

RECENT ADVANCES in COMMUNICATIONS, SIGNAL PROCESSING and COMPUTERS

**Proceedings of the 2014 International Conference on Communications,
Signal Processing and Computers (CSCP 2014)**

**Interlaken, Switzerland
February 22-24, 2014**

RECENT ADVANCES in COMMUNICATIONS, SIGNAL PROCESSING and COMPUTERS

**Proceedings of the 2014 International Conference on Communications,
Signal Processing and Computers (CSCP 2014)**

**Interlaken, Switzerland
February 22-24, 2014**

Copyright © 2014, by the editors

All the copyright of the present book belongs to the editors. All rights reserved. No part of this publication may be reproduced, stored in a retrieval system, or transmitted in any form or by any means, electronic, mechanical, photocopying, recording, or otherwise, without the prior written permission of the editors.

All papers of the present volume were peer reviewed by no less than two independent reviewers. Acceptance was granted when both reviewers' recommendations were positive.

Recent Advances in Electrical Engineering Series – 30

ISSN: 1790-5117

ISBN: 978-1-61804-215-6

RECENT ADVANCES in COMMUNICATIONS, SIGNAL PROCESSING and COMPUTERS

**Proceedings of the 2014 International Conference on Communications,
Signal Processing and Computers (CSCP 2014)**

**Interlaken, Switzerland
February 22-24, 2014**

Organizing Committee

General Chairs (EDITORS)

- Professor Kleanthis Psarris
The City University of New York,
USA
- Professor Ryszard S. Choras
Institute of Telecommunications,
University of Technology & Life Sciences,
Bydgoszcz, Poland
- Professor Sandra Sendra
Instituto de Inv. para la Gestión Integrada de Zonas Costeras (IGIC)
Universidad Politécnica de Valencia
Spain

Senior Program Chair

- Professor Maurice Margenstern,
Université de Lorraine,
France

Program Chairs

- Professor Theodore B. Trafalis,
University of Oklahoma,
USA
- Professor Claudio Talarico,
Gonzaga University, Spokane,
WA, USA
- Professor Zhuo Li,
Beijing University Of Technology,
Beijing, China

Tutorials Chair

- Professor Pradip Majumdar
Department of Mechanical Engineering
Northern Illinois University
DeKalb, Illinois, USA

Special Session Chair

- Professor Shuliang Li,
The University of Westminster,
London, UK

Workshops Chair

- Professor Dimitrios A. Karras,
Sterea Hellas Institute of Technology,
Greece

Local Organizing Chair

- Professor Jan Awrejcewicz,
Technical University of Lodz,
Lodz, Poland

Publication Chair

- Professor Vincenzo Niola
Departement of Mechanical Engineering for Energetics
University of Naples "Federico II"
Naples, Italy

Steering Committee

- Professor Aida Bulucea, University of Craiova, Romania
- Professor Zoran Bojkovic, Univ. of Belgrade, Serbia
- Professor Claudio Talarico, Gonzaga University, Spokane, USA
- Professor Imre Rudas, Obuda University, Budapest, Hungary

Program Committee

Prof. Bharat Doshi, John Hopkins University, Mayrland, USA
Prof. Gang Yao, University of Illinois at Urbana - Champaign, USA
Prof. Lu Peng, Luisian State University, Baton Rouge, LA, USA
Prof. Pavel Loskot, Swansea University, UK
Prof. Abdullah Eroglu, Indiana University & Purdue University Fort Wayne (IPFW), USA
Prof. Francesco Zirilli, Sapinenza Universitat di Roma, Rome, Italy
Prof. Yoon-Ho Choi, Samsung Electronics Co. Ltd, South Korea
Prof. Winai Jaikla, KMITL University, Bangkok, Thailand
Prof. Ki Young Kim, Samsung Advanced Institute of Technology, Korea
Prof. Stamatios Kartalopoulos, The University of Oklahoma, USA
Prof. Vyacheslav Tuzlukov, Kyungpook National University, South Korea
Prof. Stevan Berber, The University of Auckland, New Zeland
Prof. Alexander Zemliak, Autonomous University of Puebla, Mexico
Prof. Zoran Bojkovic, University of Belgrade, Serbia
Prof. Etsuji Tomita, The University of Electrocommunications, Japan
Prof. Lawrence Mazlack, University of Cincinnati, USA
Prof. Dragana Krstic, University of Nis, Serbia
Prof. Natasa Zivic, University of Siegen, Siegen, Germany
Prof. Tomas Zelinka, Czech technical University in Prague, Czech Republic
Prof. Andrzej Chydzinski, Silesian University of Technology, Gliwice, Poland
Prof. Winai Jaikla, King Mongkut's Institute of Technology Ladkrabang, Thailand
Prof. Prof. Kemal Tutuncu, Selcuk University, Konya, Turkey
Prof. Zhuo Li, Beijing University Of Technology, Beijing, China
Prof. Charles Suffel, Stevens Institute of Technology, Hoboken, NJ, USA
Prof. Shuliang Li, The University of Westminster, London, UK
Prof. Kun Chang Lee, Sungkyunkwan University, Korea
Prof. Dimitri Bertsekas, IEEE Fellow, MIT, USA
Prof. Demetri Terzopoulos, IEEE Fellow, ACM Fellow, UCLA, USA
Prof. Georgios B. Giannakis, IEEE Fellow, University of Minnesota, USA
Prof. Jun Wang, Beijing Jiaotong University, P. R. China

Prof. Josip Musić, University of Split, Croatia
Prof. Gen Qi Xu, Tianjin University, Tianjin, China
Prof. Alexander Gelbukh, National Polytechnic Institute (IPN), Mexico
Prof. Charles Suffel, Stevens Institute of Technology, Hoboken, NJ, USA
Prof. Kun Chang Lee, Sungkyunkwan University, Korea
Prof. Andre A. Keller, Universite de Lille Nord de France, France
Prof. Vaclav Skala, University of West Bohemia, Czech Republic
Prof. Bimal Kumar Bose (Life Fellow IEEE), The University of Tennessee, Knoxville, USA
Prof. Wasfy B. Mikhael, IEEE Fellow, Vice President IEEE Circuits and Systems, University of Central Florida, Orlando, USA
Prof. Yuriy S. Shmaliy (IEEE Fellow), Universidad de Guanajuato, MEXICO
Prof. D. Subbaram Naidu (Fellow IEEE), Idaho State University, USA
Prof. Narsingh Deo, IEEE Fellow, ACM Fellow, AAAS Fellow, ICA Fellow Orlando, Florida, USA
Prof. Panagiotis Agathoklis, University of Victoria, British Columbia, Canada
Prof. Imre J. Rudas, Óbuda University, Budapest, Hungary
Prof. Jiri Hrebicek, Masaryk University, Brno, Czech Republic
Prof. Brett Nener, The University of Western Australia, Australia
Prof. Branimir Reljin, University of Belgrade, Serbia
Prof. Humberto Varum, University of Aveiro, Aveiro, Portugal
Prof. Ronald Tetzlaff, Technical University Dresden, Germany
Prof. Peter Szolgay, Pazmany Peter Catholic University, Hungary
Prof. Xiang Bai, Huazhong University of Science and Technology, China
Prof. Carla Pinto, Polytechnic of Porto, Porto, Portugal
Prof. Hung-Yuan Chung, National Central University, Taiwan
Prof. Sorinel Oprisan, College of Charleston, Charleston, South Carolina, USA
Prof. Brian Barsky (IEEE Fellow, University of Berkeley, USA)
Prof. Aggelos Katsaggelos (IEEE Fellow, Northwestern University, USA)
Prof. Leonid Kazovsky (Stanford University, USA)
Prof. Anastassios Venetsanopoulos (Fellow IEEE, University of Toronto, Canada)
Prof. Steven Collicott (Purdue University, West Lafayette, IN, USA)
Prof. Nikolaos G. Bourbakis (IEEE Fellow, Wright State University, USA)
Prof. Hashem Akbari (University of California, Berkeley, USA)
Prof. Lei Xu (IEEE Fellow, Chinese University of Hong Kong, Hong Kong)
Prof. Patrick Wang (MIT, USA)
Prof. Sunil Das (IEEE Fellow, University of Ottawa, Canada)
Prof. Nikolaos D. Katopodes (University of Michigan, USA)
Prof. Biswa N. Datta (IEEE Fellow, Northern Illinois University, USA)
Prof. Mihai Putinar (University of California at Santa Barbara, USA)
Prof. Wlodzislaw Duch (Nicolaus Copernicus University, Poland)
Prof. Michael N. Katehakis (Rutgers, The State University of New Jersey, USA)
Prof. Dimitri Kazakos, Dean, (Texas Southern University, USA)
Prof. Ronald Yager (Iona College, USA)
Prof. Alexey L Sadovski (IEEE Fellow, Texas A&M University, USA)
Prof. Ryszard S. Choras (University of Technology and Life Sciences Bydgoszcz, Poland)
Prof. Remi Leandre (Universite de Bourgogne, Dijon, France)
Prof. Alexander Grebennikov (Autonomous University of Puebla, Mexico)
Prof. Guennadi A. Kouzaev (Norwegian University of Science and Technology, Norway)
Prof. Weilian Su (Naval Postgraduate School, USA)

Additional Reviewers

Matthias Buyle	Artesis Hogeschool Antwerpen, Belgium
Lesley Farmer	California State University Long Beach, CA, USA
Deolinda Rasteiro	Coimbra Institute of Engineering, Portugal
Sorinel Oprisan	College of Charleston, CA, USA
Santoso Wibowo	CQ University, Australia
Yamagishi Hiromitsu	Ehime University, Japan
Kei Eguchi	Fukuoka Institute of Technology, Japan
Shinji Osada	Gifu University School of Medicine, Japan
Tetsuya Yoshida	Hokkaido University, Japan
Xiang Bai	Huazhong University of Science and Technology, China
Philippe Dondon	Institut polytechnique de Bordeaux, France
José Carlos Metrôlho	Instituto Politecnico de Castelo Branco, Portugal
João Bastos	Instituto Superior de Engenharia do Porto, Portugal
Takuya Yamano	Kanagawa University, Japan
Hessam Ghasemnejad	Kingston University London, UK
Konstantin Volkov	Kingston University London, UK
Eleazar Jimenez Serrano	Kyushu University, Japan
Jon Burley	Michigan State University, MI, USA
Manoj K. Jha	Morgan State University in Baltimore, USA
Frederic Kuznik	National Institute of Applied Sciences, Lyon, France
Stavros Ponis	National Technical University of Athens, Greece
Ole Christian Boe	Norwegian Military Academy, Norway
Imre Rudas	Obuda University, Budapest, Hungary
Masaji Tanaka	Okayama University of Science, Japan
Francesco Rotondo	Polytechnic of Bari University, Italy
George Barreto	Pontificia Universidad Javeriana, Colombia
Dmitrijs Serdjuks	Riga Technical University, Latvia
Andrey Dmitriev	Russian Academy of Sciences, Russia
Tetsuya Shimamura	Saitama University, Japan
Francesco Zirilli	Sapienza Universita di Roma, Italy
Minhui Yan	Shanghai Maritime University, China
Valeri Mladenov	Technical University of Sofia, Bulgaria
Jose Flores	The University of South Dakota, SD, USA
James Vance	The University of Virginia's College at Wise, VA, USA
Genqi Xu	Tianjin University, China
Zhong-Jie Han	Tianjin University, China
Kazuhiko Natori	Toho University, Japan
Moran Wang	Tsinghua University, China
M. Javed Khan	Tuskegee University, AL, USA
Bazil Taha Ahmed	Universidad Autonoma de Madrid, Spain
Alejandro Fuentes-Penna	Universidad Autónoma del Estado de Hidalgo, Mexico
Miguel Carriegos	Universidad de Leon, Spain
Angel F. Tenorio	Universidad Pablo de Olavide, Spain
Abelha Antonio	Universidade do Minho, Portugal

Table of Contents

Plenary Lecture 1: Discrete Lyapunov Controllers for an Actuator in Camless Engines <i>Paolo Mercorelli</i>	12
Plenary Lecture 2: EMG-Analysis for Intelligent Robotic based Rehabilitation <i>Thomas Schrader</i>	13
Plenary Lecture 3: Atmospheric Boundary Layer Effects on Aerodynamics of NREL Phase VI Windturbine in Parked Condition <i>Mohammad Moshfeghi</i>	14
Plenary Lecture 4: Laminar and Turbulent Simulations of Several TVD Schemes in Two-Dimensions <i>Edisson S. G. Maciel</i>	15
Plenary Lecture 5: The Flocking Based and GPU Accelerated Internet Traffic Classification <i>Zhiguang Xu</i>	17
Plenary Lecture 6: The State of Civil Political Culture among Youth: Goals and Results of Education <i>Irina Dolinina</i>	18
Signal Processing in Power State Variables for Sound and Electromagnetic Environment by Introducing Fuzzy Probability <i>Akira Ikuta, Hisako Orimoto</i>	19
Second Order Statistics of SC Receiver Output SIR in the Presence of α-k-μ Multipath Fading and Co-Channel Interference <i>S. Jovkovic, D. Milic, D. Djosic, S. Panic, S. Veljkovic, C. Stefanovic</i>	27
Subdivided Weight Interpolation based on Multiscale Gradients for Color Filter Array <i>Yonghoon Kim, Jechang Jeong</i>	32
Implementation of Sparse Representation Classifier (SRC) to Heartbeat Biometrics <i>W. C. Tan, D. A. Ramli</i>	36
Stochastic Modeling of Sound Environment System with Multiplicative Noise and Noise Cancellation Method <i>Hisako Orimoto, Akira Ikuta</i>	43
A Novel Symmetric Text Encryption Algorithm based on Logistic Map <i>M. A. Murillo-Escobar, F. Abundiz-Pérez, C. Cruz-Hernández, R. M. López-Gutiérrez</i>	49
Deterministic Sequences from a Fibonacci Series For PAPR Reduction in SLM-OFDM Systems <i>Saheed A. Adegbite, Scott G. McMeekin, Brian G. Stewart</i>	54

Classification of Intravascular Ultrasound Signal by Kernel Density Estimation and Bayes Theorem for Identification of Coronary Plaque Tissue	60
<i>Hiroki Tanaka, Kazuhiro Tokunaga, Eiji Uchino, Noriaki Suetake</i>	
Automated Surveys and Integrated Auto-Location by Laser Scanner and GPS	65
<i>V. Barrile, G. Bilotta</i>	
PA-SLNR Multi-User MIMO Precoding Based on GSVD	73
<i>Varun Jeoti, Elsadig Saeid</i>	
Detection of Lightning Pattern Changes Using Machine Learning Algorithms	78
<i>Aimee Booyens, Serestina Viriri</i>	
Multiple Types of Heterogeneous Spatial Data Integration Process Using Business Intelligence Approach	85
<i>M. Mustafa, A. Aliff, M. Yazid</i>	
An Approach to Enhance Security in the Access Layer of the IMS Networks	89
<i>E. Belmekki, M. Bellafkih, A. Belmekki</i>	
Quality based Speaker Verification Systems using Fuzzy Inference Fusion Scheme	96
<i>L. A. Hamid, D. A Ramli</i>	
Fault Tolerance and Load Balancing on the Example of GlassFish	104
<i>Arne Koschel, Michael Heine, Lars Knemeyer, Irina Astrova</i>	
Laser Based Tomographic System for Visualization and Characterization of Tissue Optical Phantoms	108
<i>R. Sivakumar, N. Sujatha</i>	
A Suitable Approach for Evaluating Bus Arrival Time Prediction Techniques in Egypt	113
<i>M. Tantawy, M. Zorkany</i>	
Considering Partially Developed Artifacts in Change Impact Analysis Implementation	118
<i>Nazri Kama, Sufyan Basri, Roslina Ibrahim</i>	
Modeling and Performance Analysis of PCI Express	125
<i>Miguel Angel Orozco, Mario Siller, Adán Ruiz</i>	
Monitoring Land-Cover Changes Using Satellite Imagery	131
<i>Wayne Goosen, Serestina Viriri</i>	
PSCM: Proxy Server Cache Mechanism for Video on Demand System	138
<i>Saleh Ali Alomari, Putra Sumari</i>	

Comparative Study of Different Methods for Measurement of “Smartness” of Smart Devices	145
<i>Ahmet Al Zarqa, Tarik Ozkul, A. R. Al-Ali</i>	
A High End Capacity in Digital Image Steganography: Empowering Security by Mottling through Morphing	151
<i>Sanjay Bajpai, Kanak Saxena</i>	
Sparse Feature Based Analysis of RF Signal for Coronary Plaque Tissue Classification with Reference to the Neighboring Information of the Target Tissue	157
<i>Shota Furukawa, Eiji Uchino, Tadahiro Azetsu, Noriaki Suetake</i>	
Fixed-Point Implementation of Classifier for Tropical Wood Recognition System	161
<i>Enas Dhuhri Kusuma, Rubiyah Yusof, Mohammad Fauzi Othman</i>	
A Method for Context Aware Web Service Discovery	167
<i>Vahab Ghasemi, Hasan Haghighi</i>	
Comparative Study on Different Classifiers for Frog Identification System Based on Bioacoustic Signal Analysis	172
<i>H. Jaafar, D. A Ramli, B. A. Rosdi</i>	
Early Termination of Transform Skip Mode for High Efficiency Video Coding	177
<i>Do-Kyung Lee, Miso Park, Hyung-Do Kim, Je-Chang Jeong</i>	
Pathloss Analysis at 900 MHz for Outdoor Environment	182
<i>Zia Nadir, Mohammed Bait-Suwaitam</i>	
Simulation and Analysis of a Full Duplex DWDM RoF System Using Optimized Phase Modulator and an OADM	187
<i>Joseph Zacharias, Raji K., Vijayakumar Narayanan</i>	
Fingerprint Image Encryption based on Rossler Map	193
<i>F. Abundiz-Perez, C. Cruz-Hernandez, M. A. Murillo-Escobar, R. M. Lopez-Gutierrez</i>	
Design of Compact RF Filters with Narrow Band-Pass and Wide Stop-Band by Open-Stub & T-shaped Microstrip Resonators and Defected Ground Structure (DGS)	198
<i>Shervin Amiri, Nafiseh Khajavi, Mahboubeh Khajavi</i>	
Authors Index	203

Plenary Lecture 1

Discrete Lyapunov Controllers for an Actuator in Camless Engines



Professor Paolo Mercorelli
Leuphana University of Lueneburg
Germany
E-mail: mercorelli@uni.leuphana.de

Abstract: This paper deals with a hybrid actuator composed by a piezo and a hydraulic part controlled using two cascade Lyapunov controllers for camless engine motor applications. The idea is to use the advantages of both, the high precision of the piezo and the force of the hydraulic part. In fact, piezoelectric actuators (PEAs) are commonly used for precision positionings, despite PEAs present nonlinearities, such as hysteresis, saturations, and creep. In the control problem such nonlinearities must be taken into account. In this paper the Preisach dynamic model with the above mentioned nonlinearities is considered together with cascade controllers which are Lyapunov based. The sampled control laws are derived using the well known Backward Euler method. An analysis of the Backward and Forward Euler method is also presented. In particular, the hysteresis effect is considered and a model with a switching function is used also for the controller design. Simulations with real data are shown.

Brief Biography of the Speaker: Paolo Mercorelli received the (Laurea) M.S. degree in Electronic Engineering from the University of Florence, Florence, Italy, in 1992, and the Ph.D. degree in Systems Engineering from the University of Bologna, Bologna, Italy, in 1998. In 1997, he was a Visiting Researcher for one year in the Department of Mechanical and Environmental Engineering, University of California, Santa Barbara, USA. From 1998 to 2001, he was a Postdoctoral Researcher with Asea Brown Boveri, Heidelberg, Germany. From 2002 to 2005, he was a Senior Researcher with the Institute of Automation and Informatics, Wernigerode, Germany, where he was the Leader of the Control Group. From 2005 to 2011, he was an Associate Professor of Process Informatics with Ostfalia University of Applied Sciences, Wolfsburg, Germany. In 2010 he received the call from the German University in Cairo (Egypt) for a Full Professorship (Chair) in Mechatronics which he declined. In 2011 he was a Visiting Professor at Villanova University, Philadelphia, USA. Since 2012 he has been a Full Professor (Chair) of Control and Drive Systems at the Institute of Product and Process Innovation, Leuphana University of Lueneburg, Lueneburg, Germany.

Research interests: His current research interests include mechatronics, automatic control, signal processing, wavelets; sensorless control; Kalman filter, camless control, knock control, lambda control, robotics.

The full paper of this lecture can be found on page 19 of the Proceedings of the 2014 International Conference on Circuits, Systems and Control, as well as in the CD-ROM proceedings.

Plenary Lecture 2

EMG-Analysis for Intelligent Robotic based Rehabilitation

Professor Thomas Schrader

University of Applied Sciences Brandenburg
Germany

E-mail: thomas.schrader@computer.org

Abstract: The establishment of wireless sensor network (WSN) technology in physiotherapy and rehabilitation is a clue for improvement of the therapeutic process, quality assessment and development of supporting technologies such as robotics. Especially for complex therapeutic interventions such as sensorimotor training, a continuous monitoring during the therapy as well as for all sessions would be quite useful. For the usage of robotic support in rehabilitation various input information about the status of patient and his/her activity status of various muscles have to be detected and evaluated. The critical point for robotic intervention is the response time. Under physiotherapeutic and rehabilitation conditions, the robotic device should be able to react differently and in various patterns. A complex analysis procedure of input signals such as EMG is essential to ensure an effective response of the robot. However sensor nodes in a wireless (body) area network have limited resources for calculating and storage processes. A stepwise procedure with distributed analysis tasks is proposed. Electromyogram (EMG) measurements of eight muscles were collected and evaluated in an experimental setting of a sensorimotor training using different types of balance boards. Fast and easy methods for detection of activity and rest states based on time domain analysis using low pass IIR filter und dynamic threshold adaption. These procedures can be done on the sensor nodes themselves or special calculation nodes in the network. More advanced methods in frequency domain or analysis of dynamical system behavior request much more system power in calculation as well as storage. These tasks could be done on the level of mobile devices such as mobile phones or tablet computer. A broad range of resources can be provided by cloud/internet. Such level based organization of analysis and system control can be compared with biological systems such as human nervous system.

Plenary Lecture 3

Atmospheric Boundary Layer Effects on Aerodynamics of NREL Phase VI Windturbine in Parked Condition



Professor Mohammad Moshfeghi
Sogang University, South Korea
E-mail: mmoshfeghi@sogang.ac.kr

Abstract: In a natural condition, the wind is affected by the groundcover and the type of terrains which impose vertical velocity profile to the wind. This wind profile, which is also called atmospheric boundary layer (ABL), dramatically influences the aerodynamic behaviors and loadings of horizontal axis wind turbines. However, for the sake of simplicity, many numerical simulations only deal with the uniform wind speed. To consider the effects of the ABL, numerical simulations of the two-bladed NREL Phase VI wind turbines aerodynamic at the parked condition are conducted under both uniform and ABL. The Deaves-Harris (DH) model is applied to the ABL. The wind turbine blades are kept at the six o'clock position and are considered at two different pitch angles. The aerodynamic forces and moments of the uniform the DH model are compared. The results show that the pitch angle at which the HAWT is parked plays an important role on the blade loading. Also it is observed that for the fully separated conditions, the Down-blade and the blade in the uniform wind are under approximately similar aerodynamic loadings, while the Up-blade encounters more aerodynamic loads, which is even noticeable value for this small wind turbine. This in turn means that for an appropriate and exact design, effects of ABL should be considered with more care.

Brief Biography of the Speaker: Dr. Mohammad Moshfeghi works in Multi-phenomena CFD Engineering Research Center (ERC) Sogang University, Seoul, South Korea. He is also Lecturer in Qazvin Azad University. He has a registered patent: "Split-Blade For Horizontal Axis Wind Turbines" (Inventors: Mohammad Moshfeghi, Nahmkeon Hur).

Plenary Lecture 4

Laminar and Turbulent Simulations of Several TVD Schemes in Two-Dimensions



Professor Edison S. G. Maciel

Federal University of Great Dourados, Brazil

E-mail: edisavio@edissonsavio.eng.br

Abstract: This work, first part of this study, describes five numerical tools to perform perfect gas simulations of the laminar and turbulent viscous flow in two-dimensions. The Van Leer, Harten, Frink, Parikh and Pirzadeh, Liou and Steffen Jr. and Radespiel and Kroll schemes, in their first- and second-order versions, are implemented to accomplish the numerical simulations. The Navier-Stokes equations, on a finite volume context and employing structured spatial discretization, are applied to solve the supersonic flow along a ramp in two-dimensions. Three turbulence models are applied to close the system, namely: Cebeci and Smith, Baldwin and Lomax and Spalart and Allmaras. On the one hand, the second-order version of the Van Leer, Frink, Parikh and Pirzadeh, Liou and Steffen Jr., and Radespiel and Kroll schemes is obtained from a “MUSCL” extrapolation procedure, whereas on the other hand, the second order version of the Harten scheme is obtained from the modified flux function approach. The convergence process is accelerated to the steady state condition through a spatially variable time step procedure, which has proved effective gains in terms of computational acceleration (see Maciel). The results have shown that, with the exception of the Harten scheme, all other schemes have yielded the best result in terms of the prediction of the shock angle at the ramp. Moreover, the wall pressure distribution is also better predicted by the Van Leer scheme. This work treats the laminar first- and second-order and the Cebeci and Smith second- order results obtained by the five schemes.

Brief Biography of the Speaker: Professor Edison Sávio de Góes Maciel was born in Recife, Pernambuco, Brazil in 1969, February, 25. He studied in Pernambuco until obtains his Master degree in Thermal Engineering, in 1996, August. With the desire of study aerospace and aeronautical problems using numerical methods as tools, he obtains his Doctor degree in Aeronautical Engineering, in 2002, December, in ITA and his Post-Doctor degree in Aerospace Engineering, in 2009, July, also in ITA. He is currently Professor at UFGD (Federal University of Great Dourados) – Mato Grosso do Sul – Brasil. He is author in 47 papers in international journals, 2 books, 67 papers in international conference proceedings. His research interestes includes a) Applications of the Euler equations to solve inviscid perfect gas 2D and 3D flows (Structured and unstructured discretizations) b) Applications of the Navier-Stokes equations to solve viscous perfect gas 2D and 3D flows (Structured and unstructured discretizations) c) Applications of the Euler and Navier-Stokes to solve magneto gas dynamics flows 2D and 3D; (Structured and unstructured discretizations) d) Applications of algebraic, one-equation, and two-equations turbulence models to predict turbulent effects in viscous 2D flows (Structured and unstructured discretizations), e) Study of artificial dissipation models to centered schemes

in 2D and 3D spaces (Structured and unstructures discretizations) f)Applications of the Euler and Navier-Stokes equations to solve reentry flows in the Earth atmosphere and entry flows in Mars atmosphere in 2D and 3D (Structured and unstructured discretizations).

The full paper of this lecture can be found on page 79 of the Proceedings of the 2014 International Conference on Mechanics, Fluid Mechanics, Heat and Mass Transfer, as well as in the CD-ROM proceedings.

Plenary Lecture 5

The Flocking Based and GPU Accelerated Internet Traffic Classification



Professor Zhiguang Xu
Valdosta State University
USA
E-mail: zxu@valdosta.edu

Abstract: Mainstream attentions have been brought to the issue of Internet traffic classification due to its political, economic, and legal impacts on appropriate use, pricing, and management of the Internet. Nowadays, both the research and operational communities prefer to classify network traffic through approaches that are based on the statistics of traffic flow features due to their high accuracy and improved robustness. However, these approaches are faced with two main challenges: identify key flow features that capture fundamental characteristics of different types of traffic in an unsupervised way; and complete the task of traffic classification with acceptable time and space costs. In this paper, we address these challenges using a biologically inspired computational model that imitates the flocking behavior of social animals (e.g. birds) and implement it in the form of parallel programs on the Graphics Processing Unit (GPU) based platform of CUDA from NVIDIA™. The experimental results demonstrate that our flocking model accelerated by GPU can not only effectively select and prioritize key flow features to classify both well-known and unseen network traffic into different categories, but also get the job done significantly faster than its traditional CPU-based counterparts due to the high magnitude of parallelism that it exhibits.

Brief Biography of the Speaker: Prof. Zhiguang Xu received his Ph.D. in Computer Science from University of Central Florida, FL, USA in 2001. He is currently Professor of Computer Science in the Department of Math and Computer Science at Valdosta State University, GA, USA. His research and teaching interests include Computer Networking, Artificial Intelligence, Parallel and Distributed Computing, and Computer Science Education. Professor Xu is author or co-author of more than 25 published papers in refereed journals or conference proceedings. He has been awarded many grants from both academic and industrial entities. He is actively serving as committee member, reviewer, or lecturer of many national and international conferences and organizations.

The full paper of this lecture can be found on page 88 of the Proceedings of the 2014 International Conference on Mathematical Methods, Mathematical Models and Simulation in Science and Engineering, as well as in the CD-ROM proceedings.

Plenary Lecture 6

The State of Civil Political Culture among Youth: Goals and Results of Education



Professor Irina Dolinina

Perm National Research University, Russia

E-mail: irina_edu@mail.ru

Abstract: Political culture is viewed as a phenomenon of social reality. Attitudes toward it (its meaning or significance) are historically conditioned. This research studies enduring presuppositions about (dispositions toward) society and the state, and how these are reflected in conscious stereotypes and cognitive structures among young people within the sociocultural mechanisms that form and modify the basic characteristics of political culture.

Brief Biography of the Speaker: Prof. Irina Dolinina was born in 1960, in Perm, Russia. She is Team Leader in the Research Project «Formation of the political culture of the students», and Professor of Philosophy and Law of the Faculty of Humanities, Perm National Research Technical University since 2012. She has received a lot of honors and awards (2012 - Diploma of the All-Russian Roswitha fund national education and the Education Committee of the State Duma of the Federal Assembly of the Russian Federation. 2013 - Diploma of the All-Russian Roswitha fund national education and the Education Committee of the State Duma of the Federal Assembly of the Russian Federation. Diploma-Russian contest "Best Science Book in the humanitarian sphere - 2013). Prof. Dolinina has various professional organizations and activities.

(Expert on the legislative activities of the Council of Federation of Russia. Board member of the Interregional Association "For civic education." Director of the Research Centre of the political culture).

The full paper of this lecture can be found on page 57 of the Proceedings of the 2014 International Conference on Educational Technologies and Education, as well as in the CD-ROM proceedings.

Signal Processing in Power State Variables for Sound and Electromagnetic Environment by Introducing Fuzzy Probability

Akira Ikuta, and Hisako Orimoto

Abstract— In the actual sound and electromagnetic waves, the specific signal frequently shows some very complex fluctuation forms and the observed data are inevitably contaminated by the background noise of arbitrary distribution type. In this study, static and dynamic signal processing methods for estimating a specific signal with the existence of background noise of non-Gaussian distribution forms are proposed. More specifically, by paying attention to the power state variable for a specific signal in the sound and electromagnetic environment, which exhibits complex probability distribution forms, a new type of signal processing method for noise cancellation is proposed. The proposed method positively utilizes the additive property of power state variable in the derivation process of the noise cancellation method. Furthermore, the effectiveness of the proposed theoretical method is experimentally confirmed by applying it to an estimation problem in actual sound and electromagnetic environment.

Keywords— Background noise, fuzzy probability, power state variable, sound and electromagnetic environment.

I. INTRODUCTION

THE specific signal in the actual sound and electromagnetic environment usually shows some complex fluctuation forms of non-Gaussian type owing to natural, social and human factors [1]. Furthermore, the observed data are inevitably contaminated by external noise (i.e., background noise) of arbitrary distribution type [2]. In these situations, it is often necessary to estimate several evaluation quantities such as the peak value, the amplitude probability distribution, the average crossing rate, the pulse spacing distribution, and the frequent distribution of occurrence etc. of the specific signal. In order to consider universally these evaluation quantities without losing their mutual relationships, it is indispensable to estimate the probability distribution or the original wave fluctuation form itself of the specific signal by focusing on the specific signal in time domain.

In this study, static and dynamic state estimation methods are proposed for estimating the specific signal by removing

background noise of several non-Gaussian probability distributions. More specifically, by paying attention to the specific signal in the real sound and electromagnetic environment, which exhibits complex probability distribution forms, a signal processing method is considered for estimating the probability distribution and the fluctuation wave form of the specific signal based on the observation contaminated by background noise. The proposed theory considers a power state variable satisfying an additive property between the specific signal and background noise, and introduces Gamma distribution and Laguerre polynomial suitable for the power state variable [3], which fluctuates within only the positive region.

First, a static signal processing method is considered for predicting the probability distribution of electromagnetic wave leaked from several kinds of electronic information equipment in the real working environment. More specifically, in real situation where a background noise exists, a signal processing method is derived for predicting the probability distribution of electromagnetic wave based on the measurement of sound radiated from the identical electronic information equipment. It is necessary to note that the real observed data often contain fuzziness due to confidence limitations in sensing devices, permissible errors in the experimental data, and quantizing errors in digital observations [4]. In this study, by applying the probability measure of fuzzy events [5] to a joint probability density function on sound and electromagnetic waves in an orthogonal series type expression, a method for estimating correlation information with lower and higher orders between the sound and electromagnetic waves is proposed on the basis of fuzzy observation data, under real situation in the existence of a background noise. On the basis of the estimated correlation information, the probability distribution for the electromagnetic wave based on the observed fuzzy data of the sound can be predicted.

Next, a dynamic state estimation method with the aid of digital computer is proposed for estimating only the specific signal by removing background noise based on the observation data in the sound and electromagnetic environment under the existence of background noise. Though hitherto many methodological studies have been reported on the state estimation, most of the standard estimation methods proposed previously are restricted only to Gaussian distribution of the fluctuation [6], [7]. On the other hand, there is a restriction for energy variables fluctuating only in the non-negative region

This work was supported in part by fund from the Grant-in Aid for Scientific Research No.24560529 from the Ministry of Education, Culture, Sports, Science and Technology-Japan.

A. Ikuta is with the Department of Management Information Systems, Prefectural University of Hiroshima, Hiroshima 734-8558, Japan (phone: 82-251-9763; fax: 82-251-9405; e-mail: ikuta@pu-hiroshima.ac.jp).

H. Orimoto is with the Department of Management Information Systems, Prefectural University of Hiroshima, Hiroshima 734-8558, Japan (e-mail: orimotor@pu-hiroshima.ac.jp).

(i.e., any fluctuation width around the mean value has necessarily to tend zero when the mean value tends zero), and it is obvious that the Gaussian distribution regarding the mean and variance as independent parameters is not adequate for energy variables. In this study, a new state estimation method applicable to realistic cases with fuzzy observation is proposed by introducing the Gamma distribution and the Laguerre polynomial suitable for variables with a positive fluctuation region.

The effectiveness of the theoretically proposed static and dynamic signal processing methods for removing a background noise is experimentally confirmed by applying those to real data in the sound and electromagnetic environment.

II. STATIC SIGNAL PROCESSING FOR NOISE CANCELLATION IN SOUND AND ELECTROMAGNETIC ENVIRONMENT

A. Prediction for Probability Distribution of Specific Signal from Fuzzy Fluctuation Factor

In real sound and electromagnetic environment, the measuring instruments and observed data generally involve permissible error tolerances for the reliability, and contain several uncertain factors like quantization errors in digitizing the observed data. Furthermore, the phenomena originally contain uncertainty in themselves. In this study, the observation data with some uncertainty are considered as fuzzy data.

True values of sound and electromagnetic waves leaked from the identical electronic information equipment are expressed as x and y . Furthermore, the observed fuzzy data with uncertainty are expressed as X and Y respectively. Then, there exist the mutual correlation relationships between x and y , and also between X and Y . Therefore, by finding the relationships between X and x , and also between Y and y , based on the probability measure of fuzzy events [5], it is possible to predict y from X , or x from Y . For example, for the prediction of the probability distribution $P_s(y)$ of y from X , averaging the conditional probability distribution $P(y|X)$ on the basis of the observed fuzzy data X , $P_s(y)$ can be obtained as $P_s(y) = \langle P(y|X) \rangle_X$. Considering a property on conditional probability:

$$P(y|X) = \frac{P(X,y)}{P(X)}, \quad (1)$$

the joint probability distribution $P(X,y)$ is expanded into an orthonormal polynomial series on the basis of the fundamental probability distributions $P_0(X)$ and $P_0(y)$, which can be artificially chosen as the probability functions describing approximately the dominant parts of the actual fluctuation pattern, as follows:

$$P(X,y) = P_0(X)P_0(y) \sum_{m=0}^{\infty} \sum_{n=0}^{\infty} E_{mn} \varphi_m^{(1)}(X) \varphi_n^{(2)}(y), \quad (2)$$

$$E_{mn} \equiv \langle \varphi_m^{(1)}(X) \varphi_n^{(2)}(y) \rangle. \quad (3)$$

The information on various types of linear (and) nonlinear correlations between X and y is reflected in each expansion

coefficient E_{mn} . Two functions $\varphi_m^{(1)}(X)$ and $\varphi_n^{(2)}(y)$ are orthonormal polynomials with the weighting functions $P_0(X)$ and $P_0(y)$. Form (2), the following relationship can be derived.

$$\begin{aligned} P(X) &= \int P(X,y) dy \\ &= P_0(X) \sum_{m=0}^{\infty} E_{m0} \varphi_m^{(1)}(X). \end{aligned} \quad (4)$$

By substituting (2) and (4) into (1), the predicted probability distribution $P_s(y)$ of y can be expressed in an expansion series form, as follows:

$$P_s(y) = P_0(y) \sum_{n=0}^{\infty} \left\langle \frac{\sum_{m=0}^{\infty} E_{mn} \varphi_m^{(1)}(X)}{\sum_{m=0}^{\infty} E_{m0} \varphi_m^{(1)}(X)} \right\rangle_X \varphi_n^{(2)}(y). \quad (5)$$

B. Estimation of Higher Order Correlation by Introducing Fuzzy Probability and Prediction of Probability Distribution

When X is a fuzzy number expressing an approximated value, it can be treated as a discrete variable with a certain level difference. Therefore, as the fundamental probability function $P_0(X)$, the generalized binomial distribution with a level difference interval h_X [1] can be chosen as a trial:

$$\begin{aligned} P_0(X) &= \frac{\binom{N_X - M_X}{h_X}!}{\binom{X - M_X}{h_X}! \binom{N_X - X}{h_X}!} p_X^{\frac{X - M_X}{h_X}} (1 - p_X)^{\frac{N_X - X}{h_X}}, \\ p_X &\equiv \frac{\mu_X - M_X}{N_X - M_X}, \quad \mu_X \equiv \langle X \rangle, \end{aligned} \quad (6)$$

where M_X and N_X are the minimum and maximum values of X . In the measurement of the electromagnetic and sound environment, the observation data are generally contaminated by an external noise (i.e., background noise). The power state variables satisfying the additive property of the specific signal and the background noise are considered in this study. A Gamma distribution suitable for random variables fluctuating within only a positive range is adopted as the fundamental probability distribution of the specific signal y in a power scale.

$$\begin{aligned} P_0(y) &= \frac{y^{m_y - 1} e^{-\frac{y}{s_y}}}{\Gamma(m_y) s_y^{m_y}}, \\ m_y &\equiv \frac{\mu_y^2}{\sigma_y^2}, \quad s_y \equiv \frac{\sigma_y^2}{\mu_y}, \\ \mu_y &\equiv \langle y \rangle, \quad \sigma_y^2 \equiv \langle (y - \mu_y)^2 \rangle, \end{aligned} \quad (7)$$

where $\Gamma(\bullet)$ is a Gamma function. The orthonormal polynomials $\varphi_m^{(1)}(X)$ and $\varphi_n^{(2)}(y)$ can be determined as [1], [3]

$$\varphi_m^{(1)}(X) = \left\{ \left(\frac{N_X - M_X}{h_X} \right)^m m! \right\}^{\frac{1}{2}} \left(\frac{1 - p_X}{p_X} \right)^{\frac{m}{2}} \frac{1}{h_X^m}$$

$$\sum_{j=0}^m \frac{m!}{(m-j)!j!} (-1)^{m-j} \left(\frac{p_X}{1-p_X} \right)^{m-j} (N_X - X)^{(m-j)} (X - M_X)^{(j)}, \quad (8)$$

$$(X^{(n)} \equiv X(X - h_X)(X - 2h_X) \cdots (X - (n-1)h_X), X^{(0)} \equiv 1),$$

$$\varphi_n^{(2)}(y) = \sqrt{\frac{\Gamma(m_y)n!}{\Gamma(m_y+n)}} L_n^{(m_y-1)}\left(\frac{y}{s_y}\right), \quad (9)$$

where $L_n^{(m-1)}(\bullet)$ is a Laguerre polynomial of n -th order, defined by the following equation:

$$\begin{aligned} L_n^{(m)}(y) &\equiv \frac{e^y y^{-m}}{n!} \frac{d^n}{dy^n} (e^{-y} y^{n+m}) \\ &= \sum_{r=0}^n (-1)^r \binom{n}{r} \frac{1}{n!} \frac{\Gamma(m+n)}{\Gamma(m+r)} y^r. \end{aligned} \quad (10)$$

The expansion coefficients E_{mn} in (3) have to be estimated on the basis of the fuzzy observation data, since the true value y is unknown. Furthermore, in the measurement of the sound and electromagnetic environment, the effects of background noise are inevitable. Then, based on the additive property of power state variables, the observed power variable z is expressed as

$$z = y + v, \quad (11)$$

where v is a background noise in a power scale. We assume that the statistics of background noise are known. Therefore, by paying our attention to the available observation data z , the joint probability distribution $P(X, z)$ has to be considered instead of $P(X, y)$ in (2).

$$P(X, z) = P_0(X) P_0(z) \sum_{m=0}^{\infty} \sum_{n=0}^{\infty} B_{mn} \varphi_m^{(1)}(X) \varphi_n^{(3)}(z), \quad (12)$$

$$B_{mn} \equiv \langle \varphi_m^{(1)}(X) \varphi_n^{(3)}(z) \rangle, \quad (13)$$

where $P_0(z)$ and $\varphi_n^{(3)}(z)$ are the fundamental probability distribution and the orthonormal polynomial of z , and are expressed in a Gamma distribution and a Laguerre polynomial as follows:

$$\begin{aligned} P_0(z) &= \frac{z^{m_z-1}}{\Gamma(m_z) s_z^{m_z}} e^{-\frac{z}{s_z}}, \\ m_z &\equiv \frac{\mu_z^2}{\sigma_z^2}, \quad s_z \equiv \frac{\sigma_z^2}{\mu_z}, \\ \mu_z &\equiv \langle z \rangle, \quad \sigma_z^2 \equiv \langle (z - \mu_z)^2 \rangle, \end{aligned} \quad (14)$$

$$\varphi_n^{(3)}(z) = \sqrt{\frac{\Gamma(m_z)n!}{\Gamma(m_z+n)}} L_n^{(m_z-1)}\left(\frac{z}{s_z}\right). \quad (15)$$

When fuzzy observation data corresponding to z are expressed as Z , the joint probability distribution $P(X, Z)$ of X and Z can be given by the joint probability distribution of X and z , by applying probability measure of fuzzy events [5] to $P(X, z)$, as follows:

$$P(X, Z) = \frac{1}{K} \int \mu_Z(z) P(X, z) dz, \quad (16)$$

where K is a constant satisfying the normalized condition:

$$\sum_X \sum_Z P(X, Z) = 1. \quad (17)$$

Furthermore, $\mu_Z(z)$ is the membership function of the fuzzy data Z , and the following function suitable for the Gamma distribution is newly introduced by considering the flexibility of membership function.

$$\mu_Z(z) = (Z^{-\alpha} e^{\alpha}) \exp\left\{-\frac{\alpha}{Z} z\right\}, \quad (18)$$

where $\alpha (> 0)$ is a parameter and can be determined on the basis of the prior information on the actually measured data.

Substituting (12) and (18) into (16), the following relationship is derived (cf. APPENDIX).

$$P(X, Z) = \frac{1}{K} P_0(X) \sum_{m=0}^{\infty} \sum_{n=0}^{\infty} B_{mn} a_n(Z) \varphi_m^{(1)}(X), \quad (19)$$

$$a_n(Z) = \frac{Z^{-\alpha} e^{\alpha}}{\Gamma(m_z) s_z^{m_z}} \Gamma(M) D^M \sqrt{\frac{\Gamma(m_z)n!}{\Gamma(m_z+n)}} g_{n0}, \quad (20)$$

$$M \equiv m_z + \alpha, \quad D \equiv \frac{s_z Z}{\alpha s_z + Z}. \quad (21)$$

The function g_{n0} in (20) can be expressed as follows:

$$\begin{aligned} g_{00} &= 1, \quad g_{10} = m_z - M \frac{D}{s_z} \\ g_{20} &= \frac{1}{2} (m_z + 1) m_z - (m_z + 1) M \frac{D}{s_z} + \frac{1}{2} (1 + M) M \left(\frac{D}{s_z}\right)^2 \\ g_{30} &= \frac{1}{6} (m_z + 2) (m_z + 1) m_z - \frac{1}{2} (m_z + 2) (m_z + 1) M \frac{D}{s_z} \\ &\quad + \frac{1}{2} (m_z + 2) (1 + M) M \left(\frac{D}{s_z}\right)^2 \\ &\quad - \frac{1}{6} (2 + M) (1 + M) M \left(\frac{D}{s_z}\right)^3. \end{aligned} \quad (22)$$

The conditional N th order moment of the fuzzy variable X is given from (19) as

$$\begin{aligned} \langle X^N | Z \rangle &= \sum_X X^N P(X | Z) \\ &= \sum_X X^N P(X, Z) / P(Z) \\ &= \sum_X X^N P_0(X) \sum_{m=0}^{\infty} \sum_{n=0}^{\infty} B_{mn} a_n(Z) \varphi_m^{(1)}(X) / \sum_{n=0}^{\infty} B_{0n} a_n(Z). \end{aligned} \quad (23)$$

After expanding X^N in an orthogonal series expression, by considering the orthonormal relationship of $\varphi_m^{(1)}(X)$, (23) is expressed explicitly as

$$\langle X^N | Z \rangle = \sum_{m=0}^N \sum_{n=0}^{\infty} d_m^N B_{mn} a_n(Z) / \sum_{n=0}^{\infty} B_{0n} a_n(Z), \quad (24)$$

where d_m^N is an appropriate constant satisfying the following relationship:

$$X^N \equiv \sum_{i=0}^N d_i^N \varphi_i^{(1)}(X). \quad (25)$$

The right side of (24) can be evaluated numerically from the fuzzy observation data. Accordingly, by regarding the

expansion coefficients B_{mn} as unknown parameters, a set of simultaneous equations in the same form as in (24) can be obtained by selecting a set of N and/or Z values equal to the number of unknown parameters. By solving the simultaneous equations, the expansion coefficients B_{mn} can be estimated.

In order to predict the pdf $P_s(y)$ by using (5), the expansion coefficients E_{mn} defined in (3) have to be calculated on the basis of the expansion coefficients B_{mn} estimated from (24). Substituting the definition of Laguerre polynomial and (11) into (13), the expansion coefficient B_{mn} can be expressed as

$$B_{mn} = \frac{\Gamma(m_z)n!}{\Gamma(m_z+n)} \sum_{r=0}^n (-1)^r \binom{n}{r} \frac{1}{n!} \frac{\Gamma(m_z+n)}{\Gamma(m_z+r)} \left\langle \varphi_m^{(1)}(X) \left(\frac{y+v}{s_z} \right)^r \right\rangle. \quad (26)$$

Furthermore, by expanding $(y+v)^r$ and using the dual relationship for (10):

$$z^n = \sum_{r=0}^n (-1)^r \binom{n}{r} \frac{1}{r!} \frac{\Gamma(m+n)}{\Gamma(m+r)} L_r^{(m-1)}(z), \quad (27)$$

and by introducing two arbitrary parameters m_y and s_y , the following relationship of B_{mn} can be derived.

$$B_{mn} = \Gamma(m_z)n! \sum_{r=0}^n (-1)^r \binom{n}{r} \frac{1}{n!} \frac{1}{\Gamma(m_z+r)} \frac{1}{s_z} \sum_{i=0}^r \binom{r}{i} s_y^i \sum_{j=0}^i (-1)^j \binom{i}{j} \frac{1}{j!} \frac{\Gamma(m_y+i)}{\Gamma(m_y+j)} \left\langle \varphi_m^{(1)}(X) L_j^{(m_y-1)} \left(\frac{y}{s_y} \right) \right\rangle \left\langle v^{r-i} \right\rangle. \quad (28)$$

The correlation $\left\langle \varphi_m^{(1)}(X) L_j^{(m_y-1)} \left(\frac{y}{s_y} \right) \right\rangle$ in (28) can be expressed by using the expansion coefficient E_{mj} defined by (3) as:

$$\left\langle \varphi_m^{(1)}(X) L_j^{(m_y-1)} \left(\frac{y}{s_y} \right) \right\rangle = \sqrt{\frac{\Gamma(m_y+i)}{\Gamma(m_y)j!}} E_{mj}. \quad (29)$$

Therefore, by solving (28) inversely, the expansion coefficients E_{mj} ($j = 0, 1, 2, \dots$) can be obtained recursively from B_{mj} ($j = 0, 1, 2, \dots$). Furthermore, by using the property of statistical independence between y and v , two parameters m_y and s_y in (29) can be obtained as

$$m_y \equiv \frac{\mu_y^2}{\sigma_y^2}, \quad s_y \equiv \frac{\sigma_y^2}{\mu_y}, \quad (30)$$

$$\mu_y = \mu_z - \langle v \rangle, \quad \sigma_y^2 = \sigma_z^2 - \langle (v - \langle v \rangle)^2 \rangle.$$

By using the estimated expansion coefficients E_{mn} and the parameters m_y and s_y , the probability distribution $P_s(y)$ can be predicted from (5).

III. DYNAMIC SIGNAL PROCESSING FOR SPECIFIC SIGNAL IN SOUND ENVIRONMENT

A. Formulation of Fuzzy Observation under Existence of Background Noise

A sound environmental system with power state variables exhibiting a non-Gaussian distribution is considered. Let the specific signal power at a discrete time k be x_k , and express the dynamical model for the specific signal as:

$$x_{k+1} = Fx_k + Gu_k, \quad (31)$$

where u_k denotes the random input power with known statistics, and x_k , u_k are uncorrelated each other. Furthermore, F and G are unknown system parameters and can be estimated by use of the system identification method [5] when these parameters cannot be determined on the basis of the physical mechanism of system.

The observed data in the actual sound environment often contain the fuzziness due to several causes, for example, the permissible error of the accuracy in measurements, the quantized error in the digitization of observation data, and the variety of human response to the physical stimulus. Therefore in addition to the inevitable background noise, the effects of the fuzziness contained in the observed data have to be first considered in order to derive a state estimation method for the specific signal. The observation equation can be formulated by dividing it into two types of operation from functional viewpoint:

1) The additive property of power state variable, under the existence of external noise:

$$y_k = x_k + v_k. \quad (32)$$

We assume that the statistics of the background noise power v_k are known in advance.

2) The fuzzy observation z_k obtained from y_k : The fuzziness of z_k is characterized by the membership function $\mu_{z_k}(y_k)$.

B. State Estimation Based on Fuzzy Observation

In order to derive an estimation algorithm for a specific signal power x_k , based on the successive observations of fuzzy data z_k , we focus our attention on Bayes' theorem [8]:

$$P(x_k | Z_k) = \frac{P(x_k, z_k | Z_{k-1})}{P(z_k | Z_{k-1})}, \quad (33)$$

where $Z_k (= (z_1, z_2, \dots, z_k))$ is a set of observation data up to a time k . After applying probability measure of fuzzy events [5] to the right side of (33), expanding it in a general form of the statistical orthogonal expansion series [8], the conditional probability density function $P(x_k | Z_k)$ can be expressed as:

$$P(x_k | Z_k) = \frac{\int_0^\infty \mu_{z_k}(y_k) P(x_k, y_k | Z_{k-1}) dy_k}{\int_0^\infty \mu_{z_k}(y_k) P(y_k | Z_{k-1}) dy_k}$$

$$= \frac{\sum_{m=0}^{\infty} \sum_{n=0}^{\infty} A_{mn} P_0(x_k | Z_{k-1}) \varphi_m^{(4)}(x_k) I_n(z_k)}{\sum_{n=0}^{\infty} A_{0n} I_n(z_k)} \quad (34)$$

with

$$I_n(z_k) \equiv \int_0^{\infty} \mu_{z_k}(y_k) P_0(y_k | Z_{k-1}) \varphi_n^{(5)}(y_k) dy_k, \quad (35)$$

$$A_{mn} \equiv \langle \varphi_m^{(4)}(x_k) \varphi_n^{(5)}(y_k) | Z_{k-1} \rangle, \quad (36)$$

where $\langle \cdot \rangle$ denotes the averaging operation with respect to the random variables. The functions $\varphi_m^{(4)}(x_k)$ and $\varphi_n^{(5)}(y_k)$ are the orthogonal polynomials of degrees m and n with weighting functions $P_0(x_k | Z_{k-1})$ and $P_0(y_k | Z_{k-1})$, which can be artificially chosen as the probability density functions describing the dominant parts of $P(x_k | Z_{k-1})$ and $P(y_k | Z_{k-1})$. These two functions must satisfy the following orthonormal relationships:

$$\int_0^{\infty} \varphi_m^{(4)}(x_k) \varphi_{m'}^{(4)}(x_k) P_0(x_k | Z_{k-1}) dx_k = \delta_{mm'}, \quad (37)$$

$$\int_0^{\infty} \varphi_n^{(5)}(y_k) \varphi_{n'}^{(5)}(y_k) P_0(y_k | Z_{k-1}) dy_k = \delta_{nn'}. \quad (38)$$

Based on (34), and using the orthonormal relationship of (37), the recurrence algorithm for estimating an arbitrary N th order polynomial type function $f_N(x_k)$ of the specific signal can be derived as follows:

$$\begin{aligned} \hat{f}_N(x_k) &\equiv \langle f_N(x_k) | Z_k \rangle \\ &= \frac{\sum_{m=0}^N \sum_{n=0}^{\infty} A_{mn} C_{Nm} I_n(z_k)}{\sum_{n=0}^{\infty} A_{0n} I_n(z_k)}, \end{aligned} \quad (39)$$

where C_{Nm} is the expansion coefficient determined by the equality:

$$f_N(x_k) = \sum_{m=0}^N C_{Nm} \varphi_m^{(1)}(x_k). \quad (40)$$

In order to make the general theory for estimation algorithm more concrete, the well-known Gamma distribution is adopted as $P_0(x_k | Z_{k-1})$ and $P_0(y_k | Z_{k-1})$, because this probability density function is defined within positive region and is suitable to the power state variables.

$$\begin{aligned} P_0(x_k | Z_{k-1}) &= P_{\Gamma}(x_k; m_{x_k}^*, s_{x_k}^*), \\ P_0(y_k | Z_{k-1}) &= P_{\Gamma}(y_k; m_{y_k}^*, s_{y_k}^*) \end{aligned} \quad (41)$$

with

$$\begin{aligned} P_{\Gamma}(x; m, s) &\equiv \frac{x^{m-1}}{\Gamma(m) s^m} e^{-\frac{x}{s}}, \\ m_{x_k}^* &\equiv (x_k^*)^2 / \Gamma_k, \quad s_{x_k}^* \equiv x_k^* / m_{x_k}^*, \\ x_k^* &\equiv \langle x_k | Z_{k-1} \rangle, \quad \Gamma_k \equiv \langle (x_k - x_k^*)^2 | Z_{k-1} \rangle, \\ m_{y_k}^* &\equiv (y_k^*)^2 / \Omega_k, \quad s_{y_k}^* \equiv y_k^* / m_{y_k}^*, \\ y_k^* &\equiv \langle y_k | Z_{k-1} \rangle = x_k^* + \langle v_k \rangle, \\ \Omega_k &\equiv \langle (y_k - y_k^*)^2 | Z_{k-1} \rangle \\ &= \Gamma_k + \langle (v_k - \langle v_k \rangle)^2 \rangle. \end{aligned} \quad (42)$$

Then, the orthonormal functions with two weighting probability density functions in (41) can be given in the Laguerre polynomial [3]:

$$\begin{aligned} \varphi_m^{(1)}(x_k) &= \sqrt{\frac{\Gamma(m_{x_k}^*) m!}{\Gamma(m_{x_k}^* + m)}} L_m^{(m_{x_k}^* - 1)}\left(\frac{x_k}{s_{x_k}^*}\right), \\ \varphi_n^{(2)}(y_k) &= \sqrt{\frac{\Gamma(m_{y_k}^*) n!}{\Gamma(m_{y_k}^* + n)}} L_n^{(m_{y_k}^* - 1)}\left(\frac{y_k}{s_{y_k}^*}\right). \end{aligned} \quad (43)$$

As the membership function $\mu_{z_k}(y_k)$, the following function suitable for the Gamma distribution is adopted.

$$\mu_{z_k}(y_k) = (z_k^{-\alpha} e^{\alpha}) y_k^{\alpha} \exp\left\{-\frac{\alpha}{z_k} y_k\right\}, \quad (44)$$

where $\alpha (> 0)$ is a parameter. Accordingly, (35) can be given by

$$\begin{aligned} I_n(z_k) &= \frac{z_k^{-\alpha} e^{\alpha}}{\Gamma(m_{y_k}^*) (s_{y_k}^*)^{m_{y_k}^*}} \Gamma(M_k) D_k^{M_k} \\ &\int_0^{\infty} \frac{y_k^{M_k-1}}{\Gamma(M_k) D_k^{M_k}} e^{-\frac{1}{D_k} y_k} \sqrt{\frac{\Gamma(m_{y_k}^*) n!}{\Gamma(m_{y_k}^* + n)}} \\ &\sum_{r=0}^n d_{nr} L_r^{(M_k-1)}\left(\frac{y_k}{D_k}\right) dy_k \end{aligned} \quad (45)$$

with

$$M_k \equiv m_{y_k}^* + \alpha, \quad D_k \equiv \frac{s_{y_k}^* z_k}{\alpha s_{y_k}^* + z_k}, \quad (46)$$

where the fuzzy data z_k are reflected in D_k . Furthermore, d_{nr} ($r=0, 1, 2, \dots, n$) are the expansion coefficients in the equality:

$$L_n^{(m_{y_k}^* - 1)}\left(\frac{y_k}{s_{y_k}^*}\right) = \sum_{r=0}^n d_{nr} L_r^{(M_k-1)}\left(\frac{y_k}{D_k}\right). \quad (47)$$

By considering the orthonormal condition of Laguerre polynomial [3], (45) can be expressed as follows:

$$I_n(z_k) = \frac{z_k^{-\alpha} e^{\alpha}}{\Gamma(m_{y_k}^*) (s_{y_k}^*)^{m_{y_k}^*}} \Gamma(M_k) D_k^{M_k} \sqrt{\frac{\Gamma(m_{y_k}^*) n!}{\Gamma(m_{y_k}^* + n)}} d_{n0}, \quad (48)$$

where a few concrete expressions of d_{n0} in (48) can be expressed as follows:

$$\begin{aligned} d_{00} &= 1, \quad d_{10} = m_{y_k}^* - M_k \frac{D_k}{s_{y_k}^*}, \\ d_{20} &= \frac{1}{2} (m_{y_k}^* + 1) m_{y_k}^* - (m_{y_k}^* + 1) M_k \frac{D_k}{s_{y_k}^*} \\ &\quad + \frac{1}{2} (1 + M_k) M_k \left(\frac{D_k}{s_{y_k}^*}\right)^2, \\ d_{30} &= \frac{1}{6} (m_{y_k}^* + 2) (m_{y_k}^* + 1) m_{y_k}^* \end{aligned}$$

$$\begin{aligned}
 & -\frac{1}{2}(m_{y_k}^* + 2)(m_{y_k}^* + 1)M_k \frac{D_k}{s_{y_k}^*} \\
 & + \frac{1}{2}(m_{y_k}^* + 2)(1 + M_k)M_k \left(\frac{D_k}{s_{y_k}^*}\right)^2 \\
 & - \frac{1}{6}(2 + M_k)(1 + M_k)M_k \left(\frac{D_k}{s_{y_k}^*}\right)^3. \quad (49)
 \end{aligned}$$

Especially, the estimates for mean and variance can be obtained as follows:

$$\begin{aligned}
 \hat{x}_k & \equiv \langle x_k | Z_k \rangle \\
 & = \frac{\sum_{n=0}^{\infty} \{A_{0n}C_{10} + A_{1n}C_{11}\} I_n(z_k)}{\sum_{n=0}^{\infty} A_{0n} I_n(z_k)}, \quad (50)
 \end{aligned}$$

$$\begin{aligned}
 P_k & \equiv \langle (x_k - \hat{x}_k)^2 | Z_k \rangle \\
 & = \frac{\sum_{n=0}^{\infty} \{A_{0n}C_{20} + A_{1n}C_{21} + A_{2n}C_{22}\} I_n(z_k)}{\sum_{n=0}^{\infty} A_{0n} I_n(z_k)} \quad (51)
 \end{aligned}$$

with

$$\begin{aligned}
 C_{10} & = m_{x_k}^* s_{x_k}^*, \quad C_{11} = -\sqrt{m_{x_k}^* s_{x_k}^*}, \\
 C_{20} & = \hat{x}_k^2 - 2m_{x_k}^* s_{x_k}^* \{\hat{x}_k - (m_{x_k}^* + 1)s_{x_k}^*\} \\
 & \quad - m_{x_k}^* (m_{x_k}^* + 1)s_{x_k}^{*2}, \\
 C_{21} & = 2\sqrt{m_{x_k}^* s_{x_k}^*} \{\hat{x}_k - (m_{x_k}^* + 1)s_{x_k}^*\}, \\
 C_{22} & = \sqrt{2m_{x_k}^* (m_{x_k}^* + 1)s_{x_k}^*}, \quad (52)
 \end{aligned}$$

where, by considering (32), some of the expansion coefficients defined by (36) can be expressed in a form reflecting the statistics of the external noise power, as follows:

$$A_{00} = 1, \quad A_{10} = A_{01} = A_{20} = A_{02} = A_{21} = 0,$$

$$A_{11} = \sqrt{\frac{m_{x_k}^* s_{x_k}^*}{m_{y_k}^* s_{y_k}^*}},$$

$$\begin{aligned}
 A_{12} & = \frac{s_{x_k}^*}{s_{y_k}^*} \sqrt{\frac{2m_{x_k}^*}{m_{y_k}^* (m_{y_k}^* + 1)}} \left\{ (m_{y_k}^* + 1)m_{y_k}^* - \frac{\langle v_k \rangle}{s_{y_k}^*} \right. \\
 & \quad \left. - (m_{x_k}^* + 1) \frac{s_{x_k}^*}{s_{y_k}^*} \right\},
 \end{aligned}$$

$$A_{22} = \sqrt{\frac{(m_{x_k}^* + 1)m_{x_k}^*}{(m_{y_k}^* + 1)m_{y_k}^*}} \left(\frac{s_{x_k}^*}{s_{y_k}^*}\right)^2. \quad (53)$$

Finally, by considering (31), the prediction step which is essential to perform the recurrence estimation can be given by

$$\begin{aligned}
 x_{k+1}^* & \equiv \langle x_{k+1} | Z_k \rangle = F\hat{x}_k + G \langle u_k \rangle, \\
 \Gamma_{k+1} & \equiv \langle (x_{k+1} - x_{k+1}^*)^2 | Z_k \rangle \\
 & = F^2 P_k + G^2 \langle (u_k - \langle u_k \rangle)^2 \rangle. \quad (54)
 \end{aligned}$$

By replacing k with $k + 1$, the recurrence estimation can be achieved.

IV. APPLICATION TO SOUND AND ELECTROMAGNETIC ENVIRONMENT UNDER EXISTENCE OF BACKGROUND NOISE

A. Prediction of Electric Field in Electromagnetic Environment for PC

By adopting a personal computer (PC) in the actual working environment as specific information equipment, the proposed method is applied to investigate the mutual relationship between electromagnetic wave and sound leaked from the PC under the situation of playing a computer game.

Some studies on electromagnetic energy leaked from electronic equipment in the actual working environment have become important recently because of the increased use of various information, communication systems, and automatic, labor-saving systems highly performed, digitalized and diversified, especially concerning the effects on a living body [9], [10]. In the experiment of the proposed study, after paying our attention to the PC environment with increasing number of users and long working time, the electric and magnetic fields leaked from PC in the actual parallel working environment were considered, and a fundamental experiment to evaluate quantitatively those was performed.

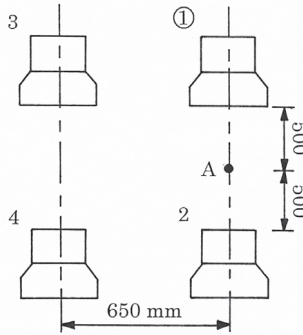


Fig. 1 a schematic drawing of the experiment

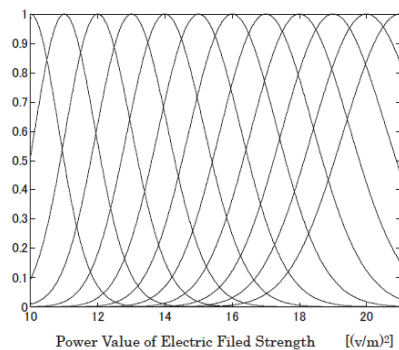


Fig. 2 membership function of electric field

Table 1 statistics of the specific signal and the background noise

Statistics of specific signal		Statistics of background noise	
Mean [v/m]	Standard Deviation [v/m]	Mean [v/m]	Standard Deviation [v/m]
2.77	0.0952	0.815	0.245

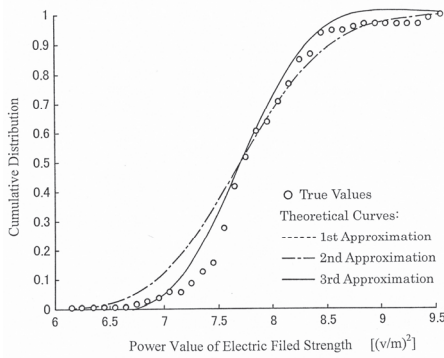


Fig. 3 prediction of the cumulative distribution for the power value of electric field strength based on the fuzzy observation of sound (in the case when $Z = 17, 22 [(v/m)^2]$ and $N = 1, 2$ in (24))

More specifically, in the actual office environment of using four computers as shown in Fig. 1, the probability distribution of the electric field strength R leaked from a specific PC denoted by circle 1 was predicted at a point A on the basis of the observation data of sound in order to evaluate the electric field strength at the position of the operator for circle 1. The electric field from other three computers was regarded as background noise n . The RMS value [v/m] of the electric field radiated from the PC and the sound intensity level [dB] emitted from a speaker of the PC were simultaneously measured with a sampling interval of 1 [s] for 600 data points. The statistics of the specific signal R and the background noise n are shown in Table 1. In order to utilize the additive property of (11), the RMS value of electric field strength R was transformed to the power variable $y (= R^2)$. Two kinds of fuzzy data with the quantized level widths of 1.0 [v/m] for the electric field strength and 5.0 [dB] for the sound intensity level were obtained. Based on the 400 data points, the expansion coefficients E_{mn} (i.e., E_{11}, E_{12}, E_{21} and E_{22}) were first estimated by use of (24), (28) and (29). Membership function of the electric field is shown in Fig. 2. The parameter α is decided so as to express the distribution of data as precisely as possible. Next, the 200 sampled data within the different time interval used for the estimation of the expansion coefficients were adopted for predicting the probability distribution of the electric field based on the sound.

One of the experimental results for the prediction in the power value y of electric field strength is shown in Fig. 3 (in the case when $Z = 17, 22 [(v/m)^2]$ and $N = 1, 2$ in (24)) in a form of cumulative distribution easier for comparisons of the prediction accuracy. In this figure, the predicted results by considering the expansion terms up to $n = 0, 1, 2$ in (5) are shown as the 1st, 2nd and 3rd approximations. From this figure, it can be found that the theoretically predicted curves show good agreements with the true values by considering the expansion coefficients with several higher orders.

B. Estimation of Specific Signal in Sound Environment

In order to examine the practical usefulness of the proposed dynamic signal processing based on the fuzzy observation, the

proposed method is applied to the actual sound environmental data. The road traffic noise is adopted as an example of a specific signal with a complex fluctuation form. Applying the proposed estimation method to actually observed data contaminated by background noise and quantized with 1 dB width, the fluctuation wave form of the specific signal is estimated. The statistics of the specific signal and the background noise used in the experiment are shown in Table 2.

Table 2 statistics of the specific signal and the background noise

Statistics of Specific Signal		Statistics of Background Noise	
Mean (watt/m ²)	Standard Deviation (watt/m ²)	Mean (watt/m ²)	Standard Deviation (watt/m ²)
2.9×10^{-5}	2.8×10^{-5}	2.9×10^{-5}	1.4×10^{-6}

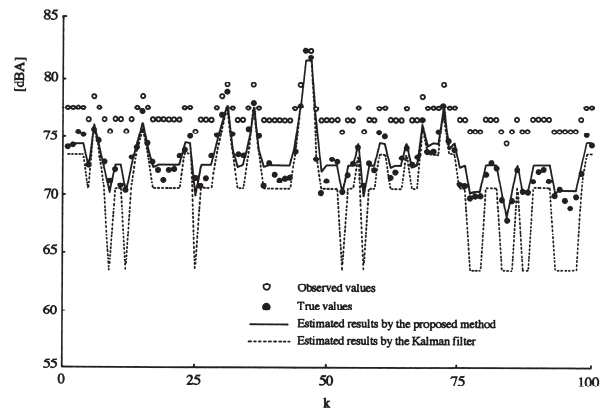


Fig. 4 state estimation results for the road traffic noise during a discrete time interval of [1, 100] sec., based on the quantized data with 1 dB width

Table 3 root-mean squared error of the estimation (in dB)

	Proposed Method	Kalman Filter
$\sqrt{\frac{1}{N} \sum_{k=1}^N (x_k - \hat{x}_k)^2}$	0.90	2.52

Figure 4 shows one of the estimation results of the fluctuation wave form of the specific signal. In this estimation, the finite number of expansion coefficients $A_{mn} (m, n \leq 2)$ is used for the simplification of the estimation algorithm. In this figure, the horizontal axis shows the discrete time k , of the estimation process, and the vertical axis expresses the sound level taking a logarithmic transformation of power-scaled variables, because the actual sound environment usually is evaluated on dB scale connected with human effects. For comparison, the estimation results calculated using the usual method without considering any membership function are also shown in this figure. Since Kalman's filtering theory is widely used in the field of stochastic system [11], [12], this method is also applied to the fuzzy observation data as a trail.

The results estimated by the proposed method considering the membership function show good agreement with the true values. On the other hand, there are great discrepancies between the estimates based on the standard type dynamical estimation method (i.e., Kalman filter) without consideration of

the membership function and the true values, particularly in the estimation of the lower level values of the fluctuation.

The squared sum of the estimation error is shown in Table 3. These results clearly show the effectiveness of the proposed method for application to the observation of fuzzy data.

V. CONCLUSION

In this study, by extending our previously reported paper in a form applicable to the actual situation in the presence of a background noise, a new method for removing background noise has been proposed from two viewpoints of static and dynamic signal processing. Power state variables have been first considered in order to utilize the additive property of the specific signal and background noise, and next by introducing a Gamma distribution and a Laguerre polynomial suitable for the power variables, a theoretical method has been derived.

More specifically, first, a Laguerre expansion series expression of the probability distribution based on the Gamma distribution has been considered, and a membership function of Gamma distribution type has been introduced in order to treat fuzzy observation data with uncertainty. By applying probability measure of fuzzy events to the probability expression, a static signal processing method has been derived for estimating correlation information between electromagnetic wave and sound based on the fuzzy observation for both variables radiated from information equipment under existence of background noise. Furthermore, a prediction method of the probability distribution of electromagnetic wave based on the observation of sound has been theoretically derived. Next, a dynamic signal processing method has been considered for estimating the fluctuation wave of the specific signal based on the fuzzy observation data under the existence of background noise.

The effectiveness of the proposed signal processing method has been confirmed experimentally by applying it to the real sound and electromagnetic data.

APPENDIX

Substituting (12) and (18) into (16), the joint probability distribution $P(X, Z)$ is expressed as (19). The function $a_n(Z)$ in (19) can be calculated as follows:

$$\begin{aligned}
 a_n(Z) &= \frac{Z^{-\alpha} e^{\alpha}}{\Gamma(m_z) s_z^{m_z}} \int_0^{\infty} z^{m_z + \alpha - 1} e^{-\left(\frac{\alpha}{Z} + \frac{1}{s_z}\right)z} \\
 &\quad \sqrt{\frac{\Gamma(m_z)n!}{\Gamma(m_z+n)}} L_n^{(m_z-1)}\left(\frac{z}{s_z}\right) dz \\
 &= \frac{Z^{-\alpha} e^{\alpha}}{\Gamma(m_z) s_z^{m_z}} \Gamma(M) D^M \int_0^{\infty} \frac{z^{M-1}}{\Gamma(M) D^M} e^{-\frac{z}{D}} \sqrt{\frac{\Gamma(m_z)n!}{\Gamma(m_z+n)}} \\
 &\quad \sum_{r=0}^n g_{nr} L_r^{(M-1)}\left(\frac{z}{D}\right) dz, \tag{A1}
 \end{aligned}$$

where two parameters M and D are defined by (21). The fuzzy data Z are reflected in D . Furthermore, g_{nr} ($r=0,1,2,\dots,n$) are the expansion coefficients in the equality:

$$L_n^{(m_z-1)}\left(\frac{z}{s_z}\right) = \sum_{r=0}^n g_{nr} L_r^{(M-1)}\left(\frac{z}{D}\right). \tag{A2}$$

By considering the orthonormal relationship of Laguerre polynomial:

$$\int_0^{\infty} \frac{z^{M-1}}{\Gamma(M) D^M} e^{-\frac{z}{D}} \sqrt{\frac{\Gamma(M)n!}{\Gamma(M+n)}} L_n^{(M-1)}\left(\frac{z}{D}\right) \sqrt{\frac{\Gamma(M)r!}{\Gamma(M+r)}} L_r^{(M-1)}\left(\frac{z}{D}\right) dz = \delta_{nr}, \tag{A3}$$

(21) can be derived.

REFERENCES

- [1] A. Ikuta, M. Ohta, and H. Ogawa, "Various Regression Characteristics with Higher Order among Light, Sound and Electromagnetic Waves Leaked from VDT--Measurement and Signal Processing in the Actual Working Environment," *J. International Measurement Confederation*, vol. 21, no.1-2, pp.25-33, 1997.
- [2] A. Ikuta, M. O. Tokhi and M. Ohta, "A Cancellation Method of Background Noise for a Sound Environment System with Unknown Structure," *IEICE Trans. Funds. of Electronics, Communications and Computer Sciences*, vol.E84-A, no.2, pp.457-466, 2001.
- [3] M. Ohta, and T. Koizumi, "General Treatment of the Response of a Non-linear Rectifying Device to a Stationary Random Input," *IEEE Trans. Information Theory*, vol.14, no.4, PP.595-598, 1968.
- [4] A. Ikuta, M. Ohta and N. Nakasako, "A State Estimation Method in Acoustic Environment Based on Fuzzy Observation Contaminated by Background Noise -Utilization of Inverse Probability and Digital Filter," *IEICE Trans. Funds. of Electronics, Communications and Computer Sciences*, vol.E80-A, no.5, pp.825-832, 1997.
- [5] L. A. Zadeh, "Probability Measures of Fuzzy Events," *J. Math. Anal. Appl.*, vol.23, pp.421-427, 1968.
- [6] P. Eykhoff, *System Identification: Parameter and State Estimation*, John Wiley & Sons, London, 1984.
- [7] P. Young, *Recursive Estimation and Time-Series Analysis*, Springer-Verlag, Berlin, 1984.
- [8] M. Ohta, and H. Yamada, "New methodological trials of dynamical state estimation for the noise and vibration environmental system---Establishment of general theory and its application to urban noise problems," *Acustica*, vol.55, no.4, pp.199-212, 1984.
- [9] Measurement Technique Research Committee on Biological Effect of High Frequency Electromagnetic Field, The Institute of Electrical Engineers of Japan (ed.), *Biological Effect of High Frequency Electromagnetic Field and Measurement*, Corona-sha, Tokyo, 1995 (in Japanese).
- [10] Y. Akao, The Institute of Electrical Engineers of Japan (ed.), *Fundamentals of Electromagnetic Environment Engineering*, The Institute of Electrical Engineers of Japan, 1991 (in Japanese).
- [11] R. E. Kalman, "A New Approach to Linear Filtering and Prediction Problems", *Trans. ASME, Series D, J. Basic Engineering*, vol.82, no.1, pp.35-45, 1960.
- [12] R. E. Kalman, and R. S. Bucy, "New Results in Linear Filtering and Prediction Theory", *Trans. ASME, Series D, J. Basic Engineering*, vol.83, no.1, pp.95-108, 1961.

Second order statistics of SC receiver output SIR in the presence of α - k - μ multipath fading and co-channel interference

S. Jovkovic, D. Milic, D. Djosic S. Panic, S. Veljkovic, C. Stefanovic

Abstract—in this paper, the wireless communication system with dual branch signal-to-interference ratio (SIR) based selection combining diversity operating over α - k - μ multipath fading channel in the presence of co-channel interference subjected to α - k - μ multipath fading is considered. The closed form expressions for probability density function, cumulative distribution function and average level crossing rate of the ratio of two α - k - μ random variables are derived and used for calculation of LCR and AFD of SC receiver output SIR. Numerical results are presented graphically to show the influence of fading parameters on LCR and AFD.

Keywords—Average fade duration, α - k - μ distribution, co-channel interference, level crossing rate.

I. INTRODUCTION

IN wireless communication system, the received signal experiences multipath fading, resulting in signal envelope variation. There are many well-known distribution which can be used to describe signal envelope variation in fading channels such as Reyleigh, Rician, Nakagami-m, Weibull, α - μ , α - k - μ distributions [7, 8]. Reyleigh distribution can be used to describe signal envelope variation in linear, non-line-of-sight fading environments. Rician model can be used in linear, line-of-sight multipath fading environments. In non-linear, non-line-of-sight fading environment signal envelope variation can be described with Weibull and α - μ distribution [11].

In this paper, the wireless communication system with dual branches, SIR based SC diversity receiver operating over α - k - μ fading environment in the presence of co-channel interference subjected also to α - k - μ multipath fading is considered. The α - k - μ distribution can be used to describe small scale signal envelope variation in non-linear and non-line-of-sight fading environment. The α - k - μ distribution has three parameters. The parameter α is related to nonlinearity of systems. The parameter k is related to the ratio of dominant components power and

scattering components power. The parameter μ is associated with the number of clusters in propagation environment. The α - k - μ distribution is general distribution. Other, well-known distributions can be obtained as special cases from α - k - μ distribution.

There are several diversity combining techniques that can be used to reduce fading effects and influence of co-channel interference on outage probability, bit error probability and system capacity. In this paper SC diversity combining techniques is used to reduce α - k - μ fading effects and co-channel interference effect on average level crossing rate and average fade duration. In interference limited environment, the SC receiver selects at outputs the branch with the highest signal-to-interference ratio. The MRC and EGC receivers provide better system performance than SC receiver but SC receiver is simpler for practical realization [4, 5, 6]. There are more works considering second order statistics in open technical literature [1, 2, 3, 13]

In this paper the probability density function, cumulative distribution function and level crossing rate of the ratio of two α - k - μ random variables are calculated. By using these results, the outage probability and average level crossing rate of dual, SIR based, SC diversity receiver in co-channel interference α - k - μ fading environment is calculated. Furthermore, average fade duration of proposed system is derived as ratio of outage probability and level crossing rate.

II. THE RATIO OF TWO α - k - μ RANDOM VARIABLES

The ratio of two α - k - μ random variables is [8]

$$z = \left(\frac{x}{y}\right)^{\frac{2}{\alpha}}$$

S. J. Author is with the College of Applied Technical Sciences, Aleksandra Medvedeva 20, 18000 Nis, Serbia (e-mail: srdjansms11@gmail.com).

D. M. Author is with Faculty of Electrical Engineering, University of Nis, Aleksandra Medvedeva 18, 18000 Nis, Serbia (e-mail: dejan.milic@elfak.ni.ac.rs).

S.P. Author is with Faculty of Natural Sciences and Mathematics, University of Pristina, Ive Lole Ribara 29, 38220 KosovskaMitrovica, Serbia (e-mail: stefanpnc@yahoo.com).

S. V. Author is with Faculty of Electrical Engineering, University of Nis, Aleksandra Medvedeva 18, 18000 Nis, Serbia. He is Ph.D student at the Department of Telecommunication (e-mail: stanislav.veljkovic@gmail.com).

C. S. Author is with Faculty of Natural Sciences and Mathematics, University of Pristina, Ive Lole Ribara 29, 38220 Kosovska Mitrovica, Serbia (phone: 00381-69-5505069; e-mail: caslav.stefanovic@gmail.com).

D. Dj. Author is with Faculty of Natural Sciences and Mathematics, University of Pristina, Ive Lole Ribara 29, 38220 Kosovska Mitrovica, Serbia (e-mail: danijeldjosic@gmail.com).

$$\frac{\alpha}{z^2} = \frac{x}{y} \quad (1)$$

where x and y are k - μ random variables. The first derivative of z is:

$$\begin{aligned} \frac{\alpha}{2} z^{\frac{\alpha}{2}-1} \dot{z} &= \frac{\dot{x}}{y} - \frac{xy}{y^2} \\ \dot{z} &= \frac{2}{\alpha z^{\frac{\alpha}{2}-1}} \left(\frac{\dot{x}}{y} - \frac{xy}{y^2} \right) \end{aligned} \quad (2)$$

The squared k - μ random variables x can be written in the form:

$$x^2 = x_1^2 + x_2^2 + \dots + x_{2\mu}^2 \quad (3)$$

Where $x_i, i = 1, 2, \dots, 2\mu$ are independent Gaussian random variables with average values of A and the variances δ_x^2 :

$$P_{x_i}(x_i) = \frac{1}{\sqrt{2\pi} \delta_x} e^{-\frac{(x_i-A)^2}{2\delta_x^2}}, i = 1, 2, \dots, 2\mu \quad (4)$$

The first derivatives of x is:

$$\dot{x} = \frac{1}{x} (x_1 \dot{x}_1 + x_2 \dot{x}_2 + \dots + x_{2\mu} \dot{x}_{2\mu}) \quad (5)$$

The squared k - μ random variables y can be written in the form:

$$y^2 = y_1^2 + y_2^2 + \dots + y_{2\mu}^2 \quad (6)$$

where $y_i, i = 1, 2, \dots, 2\mu$ are independent Gaussian random variables with average values of A and the variances δ_y^2 :

$$P_{y_j}(y_j) = \frac{1}{\sqrt{2\pi} \delta_y} e^{-\frac{(y_j-A)^2}{2\delta_y^2}}, j = 1, 2, \dots, 2\mu \quad (7)$$

The first derivatives of y is:

$$\dot{y} = \frac{1}{y} (y_1 \dot{y}_1 + y_2 \dot{y}_2 + \dots + y_{2\mu} \dot{y}_{2\mu}) \quad (8)$$

After substituting (5) and (8) in (2), the expression for the first derivative of the ratio of two random α - k - μ variable becomes:

$$\dot{z} = \frac{2}{\alpha z^{\frac{\alpha}{2}-1}} \left(\frac{1}{yx} (x_1 \dot{x}_1 + x_2 \dot{x}_2 + \dots + x_{2\mu} \dot{x}_{2\mu}) - \frac{x}{y^3} (y_1 \dot{y}_1 + y_2 \dot{y}_2 + \dots + y_{2\mu} \dot{y}_{2\mu}) \right) \quad (9)$$

The first derivative of Gaussian random variable is Gaussian random variable. The linear transformation of Gaussian random variables is Gaussian random variable. Therefore, the first

derivative of two α - k - μ random variables is conditional Gaussian distribution.

The average value of \dot{z} is:

$$\bar{\dot{z}} = \frac{2}{\alpha z^{\frac{\alpha}{2}-1}} \left(\frac{1}{yx} (x_1 \bar{\dot{x}}_1 + x_2 \bar{\dot{x}}_2 + \dots + x_{2\mu} \bar{\dot{x}}_{2\mu}) - \frac{x}{y^3} (y_1 \bar{\dot{y}}_1 + y_2 \bar{\dot{y}}_2 + \dots + y_{2\mu} \bar{\dot{y}}_{2\mu}) \right) = 0 \quad (10)$$

Since:

$$\bar{\dot{x}}_1 = \bar{\dot{x}}_2 = \dots = \bar{\dot{x}}_{2\mu} = 0$$

$$\bar{\dot{y}}_1 = \bar{\dot{y}}_2 = \dots = \bar{\dot{y}}_{2\mu} = 0 \quad (11)$$

The variance of \dot{z} can be obtained as follows:

$$\delta_{\dot{z}}^2 = \frac{4}{\alpha^2 z^{\alpha-2}} \left(\frac{1}{(yx)^2} (x_1^2 \delta_{\dot{x}_1}^2 + x_2^2 \delta_{\dot{x}_2}^2 + \dots + x_{2\mu}^2 \delta_{\dot{x}_{2\mu}}^2) + y_1^2 \delta_{\dot{y}_1}^2 + y_2^2 \delta_{\dot{y}_2}^2 + \dots + y_{2\mu}^2 \delta_{\dot{y}_{2\mu}}^2 \right) \quad (12)$$

Where:

$$\delta_{\dot{x}_1}^2 = \delta_{\dot{x}_2}^2 = \dots = \delta_{\dot{x}_{2\mu}}^2 = \pi^2 f_m^2 \delta_x^2 = f_1^2 \quad (13)$$

$$\delta_{\dot{y}_1}^2 = \delta_{\dot{y}_2}^2 = \dots = \delta_{\dot{y}_{2\mu}}^2 = \pi^2 f_m^2 \delta_y^2 = f_2^2 \quad (14)$$

After substituting, the expression for variance \dot{z} becomes:

$$\delta_{\dot{z}}^2 = \frac{4}{\alpha^2 z^{\alpha-2}} \left(\frac{1}{(yx)^2} (f_1^2 (x_1^2 + x_2^2 + \dots + x_{2\mu}^2)) + \frac{x^2}{y^6} (f_2^2 (y_1^2 + y_2^2 + \dots + y_{2\mu}^2)) \right) = \frac{4}{\alpha^2 z^{\alpha-2}} \frac{1}{y^2} (f_1^2 + f_2^2 z^\alpha) \quad (15)$$

The conditional probability density function of \dot{z} is:

$$\begin{aligned} p_{\dot{z}/zy}(\dot{z}/zy) &= \frac{1}{\sqrt{2\pi} \delta_{\dot{z}}} \cdot e^{-\frac{\dot{z}^2}{2\delta_{\dot{z}}^2}} \\ &= \frac{\alpha z^{\frac{\alpha-2}{2}} y}{2\sqrt{2\pi} \sqrt{f_1^2 + f_2^2 z^\alpha}} \cdot e^{-\frac{\dot{z}^2 \alpha^2 z^{\alpha-2} y^2}{8(f_1^2 + f_2^2 z^\alpha)}} \end{aligned} \quad (16)$$

The joint probability density function of z, \dot{z} and y is:

$$p_{z\dot{z}y}(z\dot{z}y) = p_{\dot{z}/zy}(\dot{z}/zy) \cdot p_{zy}(zy) = p_{z/zxy}(zy) p_y(y) p_{z/y}(z/y) \quad (17)$$

The conditional probability density function of z is:

$$p_z(z/y) = \left| \frac{dx}{dz} \right| p_x \left(y z^{\frac{\alpha}{2}} \right) \quad (18)$$

Where:

$$\frac{dx}{dz} = \frac{\alpha}{2} y z^{\frac{\alpha}{2}-1} \quad (19)$$

After substituting, the expression for $p_{z\dot{z}y}(z\dot{z}y)$ becomes:

$$p_{z\dot{z}y}(z\dot{z}y) = p_{z/zxy}(zy) p_y \frac{\alpha}{2} y z^{\frac{\alpha}{2}-1} \quad (20)$$

By integrating with respect to y :

$$p_{zz}(z\dot{z}) = \int_0^\infty p_z(\dot{z}/zy) p_x\left(y\frac{\alpha}{z}\right) p_y(y) y dy \quad (21)$$

The probability density functions of k - μ random variables x and y are:

$$P_x(x) = \frac{2\mu(k+1)^{\frac{\mu+1}{2}}}{k^{\frac{\mu-1}{2}} e^{\mu k \Omega_1}} \left(\frac{x}{\Omega_1}\right)^\mu e^{-\mu(1+k)\left(\frac{x}{\Omega_1}\right)^2} * I_{\mu-1}\left(2\mu\sqrt{k(1+k)}\frac{x}{\Omega_1}\right) \quad (22)$$

$$P_y(y) = \frac{2\mu(k+1)^{\frac{\mu+1}{2}}}{k^{\frac{\mu-1}{2}} e^{\mu k \Omega_2}} \left(\frac{y}{\Omega_2}\right)^\mu e^{-\mu(1+k)\left(\frac{y}{\Omega_2}\right)^2} * I_{\mu-1}\left(2\mu\sqrt{k(1+k)}\frac{y}{\Omega_2}\right) \quad (23)$$

The average level crossing rate of the ratio of two α - k - μ random variables can be calculated as average value of the first derivative of the ratio of two α - k - μ random variables:

$$N_z = \int_0^\infty d\dot{z} z p_{zz}(z\dot{z}) = \frac{1}{\sqrt{2\pi}} \frac{4\mu^2(k+1)^{\mu+1}}{k^{\mu-1} e^{2\mu k(\Omega_1\Omega_2)^{\mu+1}}} \sqrt{f_1^2 + z^\alpha f_2^2} * \sum_{i_1=0}^{\infty} \left(\frac{\mu\sqrt{k(1+k)}}{\Omega_1}\right)^{2i_1+\mu-1} \frac{1}{i_1! \Gamma(i_1 + \mu)} z^{\alpha(i_1+\mu-\frac{1}{2})} * \sum_{i_2=0}^{\infty} \left(\frac{\mu\sqrt{k(1+k)}}{\Omega_2}\right)^{2i_2+\mu-1} \frac{1}{i_2! \Gamma(i_2 + \mu)} \frac{1}{2} \left(\frac{\Omega_1^2 \Omega_2^2}{\mu(1+k)(z^\alpha \Omega_2^2 + \Omega_1^2)}\right)^{2\mu+i_1+i_2-1/2} \Gamma(2\mu + i_1 + i_2 - 1/2) \quad (24)$$

The probability density function of the ratio of two α - k - μ random variables is:

$$p_z(z) = \int_0^\infty dy P_{z/y}(z/y) P_y(y) = \frac{4\mu^2(k+1)^{\mu+1}}{k^{\mu-1} e^{2\mu k(\Omega_1\Omega_2)^{\mu+1}}} * \sum_{\lambda_1=0}^{\infty} \left(\frac{\mu\sqrt{k(1+k)}}{\Omega_1}\right)^{2\lambda_1+\mu-1} \frac{1}{\lambda_1! \Gamma(\lambda_1 + \mu)} z^{\alpha(i_1+\mu-\frac{1}{2})} * \sum_{\lambda_2=0}^{\infty} \left(\frac{\mu\sqrt{k(1+k)}}{\Omega_2}\right)^{2\lambda_2+\mu-1} \frac{1}{\lambda_2! \Gamma(\lambda_2 + \mu)} \frac{1}{2} \left(\frac{\Omega_1^2 \Omega_2^2}{\mu(1+k)(z^\alpha \Omega_2^2 + \Omega_1^2)}\right)^{2\mu+i_1+i_2} * \Gamma(2\mu + i_1 + i_2) \quad (25)$$

Cumulative distribution function of the ratio of two α - k - μ random variables can be calculated as follows [12]:

$$F_z(z) = \int_0^z dt p_z(t) = \frac{4\mu^2(k+1)^{\mu+1}}{k^{\mu-1} e^{2\mu k(\Omega_1\Omega_2)^{\mu+1}}} \sum_{\lambda_1=0}^{\infty} \left(\frac{\mu\sqrt{k(1+k)}}{\Omega_1}\right)^{2i_1+\mu-1} \frac{1}{i_1! \Gamma(i_1 + \mu)} * \sum_{\lambda_2=0}^{\infty} \left(\frac{\mu\sqrt{k(1+k)}}{\Omega_2}\right)^{2i_2+\mu-1} \frac{1}{i_2! \Gamma(i_2 + \mu)} * \frac{1}{2} \left(\frac{\Omega_1^2 \Omega_2^2}{\mu(1+k)}\right)^{2\mu+i_1+i_2} \Gamma(2\mu + \lambda_1 + \lambda_2) * \frac{1}{2} \Omega_1^{-2(2\mu+i_1+i_2)} \left(\frac{\Omega_1}{\Omega_2}\right)^{2(\mu+i_1)} B_{z_1}(\mu + i_1, \mu + i_2) \quad (26)$$

Where,

$$z_1 = \frac{\Omega_2^2 z^\alpha}{\Omega_1^2 + \Omega_2^2 z^\alpha}$$

III. SECOND ORDER PERFORMANCE OF SC DIVERSITY RECEIVER

In this section performance analysis of wireless communication system with SIR based, dual branches SC receiver operating in α - k - μ fading environment is considered. Desired signal and co-channel interference signal are presented at inputs of SC receiver. Desired signal envelopes at inputs of SC receiver are x_1 and x_2 and co-channel interference envelopes at inputs are y_1 and y_2 . The SC receiver input SIR-s are:

$$\lambda_1 = \frac{x_1}{y_1}, \lambda_2 = \frac{x_2}{y_2} \quad (27)$$

Joint probability density function of λ and its the first derivative is [10]:

$$p_{\lambda\dot{\lambda}}(\lambda\dot{\lambda}) = p_{\lambda_1\dot{\lambda}_1}(\lambda\dot{\lambda}) F_{\lambda_2}(\lambda) + p_{\lambda_2\dot{\lambda}_2}(\lambda\dot{\lambda}) F_{\lambda_1}(\lambda) = 2p_{\lambda_1\dot{\lambda}_1}(\lambda\dot{\lambda}) F_{\lambda_2}(\lambda) \quad (28)$$

The average level crossing rate of λ is:

$$N_\lambda(\lambda) = \int_0^\infty \dot{\lambda} p_{\lambda\dot{\lambda}}(\lambda\dot{\lambda}) d\dot{\lambda} = 2F_z(\lambda) N_z(\lambda) \quad (29)$$

The cumulative distribution function of dual selection diversity receiver output SIR is:

$$F_{\lambda}(\lambda) = F_{\lambda_1}(\lambda) * F_{\lambda_2}(\lambda) = (F_{\lambda_1}(\lambda))^2 = (F_z(\lambda))^2 \quad (30)$$

The average fade duration is:

$$AFD_{\lambda} = F_{\lambda}(\lambda) / N_{\lambda}(\lambda) = \frac{F_z(\lambda)^2}{2F_z(\lambda)N_z(\lambda)} = \frac{F_z(\lambda)}{2N_z(\lambda)} \quad (30)$$

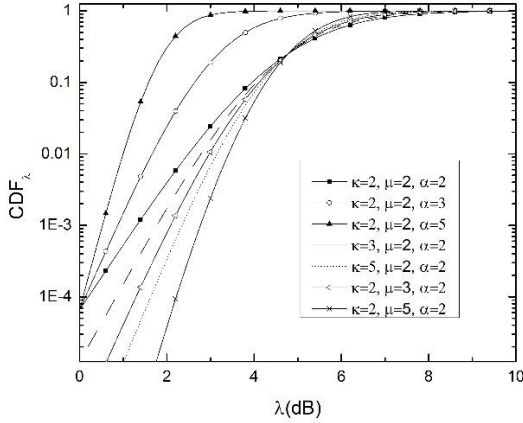


Fig.1 CDF versus SC output SIR for different parameters α, k, μ and $\Omega_1 = 3, \Omega_2 = 1$

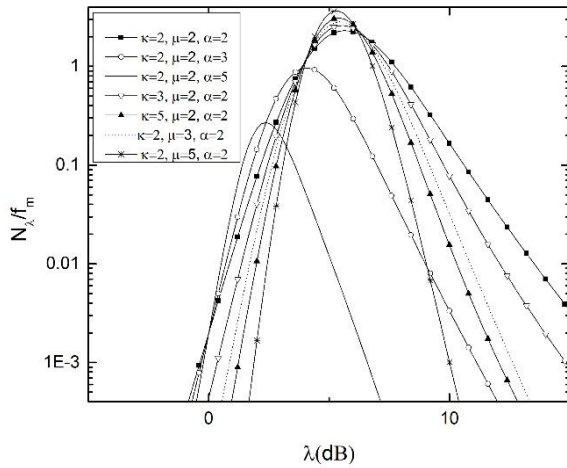


Fig.2 Normalized LCR versus SC output SIR for different parameters α, k, μ and $\Omega_1 = 3, \Omega_2 = 1$

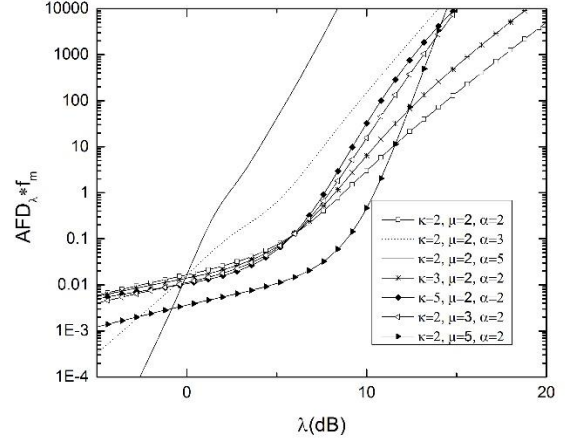


Fig.2 Normalized AFD versus SC output SIR for different parameters α, k, μ and $\Omega_1 = 3, \Omega_2 = 1$

At Figure 1, the cumulative distribution function is presented versus SC receiver output SIR for several values of fading parameters α, k and μ and constant values powers of desired signal and co-channel interference. As parameters k and μ increase the CDF decreases. The influence of parameter μ of SC output SIR for performance improvement, regarding CDF is greater. As parameter α increases, CDF increases.

At Figure 2, the LCR versus SC receiver output SIR is shown. For lower values of SC receiver output SIR, the LCR increases as SC receiver output SIR increases and for higher values of SC receiver output SIR, LCR decreases as output SIR increases. The curves for LCR have maximum, which depends on parameters α, k and μ .

In Figure 3, the average fade duration is presented in term of SC output SIR for various values of fading parameters and constant values of desired signal envelope power and co-channel interference envelope power. The influence of fading parameters on average fade duration cannot be ignored. As SC output SIR increases, the average fade duration is greater. As parameter μ increases, average fade duration decreases and improves system performances. For greater values of parameter α , the system performance degrade.

IV. CONCLUSION

In this paper, wireless communication system in the presence of multipath fading and co-channel interference is considered. Received signal experiences α - k - μ multipath fading resulting in system performance degradation. The SC diversity receiver is used to reduce effects of α - k - μ multipath fading and co-channel interference on second order performance of wireless communication system. Performance analysis is studied in interference limited fading environment. The probability density function, cumulative distribution function and average level crossing rate of the ratio of two α - k - μ random variables are calculated in closed form expressions. These expression are used for evaluation of average level crossing rate and average fade duration of SC receiver output SIR of wireless

communication system. The average level crossing rate of the ratio of two α - k - μ random variables is determined as average value of the first derivative of the ratio of two α - k - μ random variables. The average fade duration of proposed wireless system is calculated as ratio of outage probability and average level crossing rate. The α - k - μ distribution is general distribution. For different parameters α , k and μ , Rayleigh, Rician, Nakagami- m , Weibull and α - k - μ distribution can be derived from α - k - μ distribution. Numerical results obtained in this paper are represented graphically to show α - k - μ fading parameters effects on LCR and AFD of proposed wireless communication system.

REFERENCES

- [1] A. S Panajotovic, M. C Stefanovic, D. LJ Draca, N. M Sekulovic, Average Level Crossing Rate of Dual Selection Diversity in Correlated Rician Fading with Rayleigh Cochannel Interference, IEEE COMMUNICATIONS LETTERS, vol. 14, No. 7, July 2010.
- [2] Z. H Velkov, "Level Crossing Rate and Average Fade Duration of Selection Diversity With Rician-Faded Cochannel Interferers", IEEE Communications Letters, Vol. 10, No. 9, Sept. 2006.
- [3] X. Dong and N. C. Beaulieu, "Average level crossing rate and average fade duration of low-order maximal ratio diversity with unbalanced channels," IEEE Communications Letters, vol. 6, no. 4, pp. 135–137, July 2002.
- [4] N. Zlatanov, and Z. HVelkov, and G. K Karagiannidis, "Level crossing rate and average fade duration of the double Nakagami- m random process and application in MIMO keyhole fading channels. IEEE Communications Letters. IEEE COMMUNICATIONS LETTERS, vol. 12, no. 11, November 2008.
- [5] Z. H Velkov, "Level Crossing Rate and Average Fade Duration of Dual Selection Combining With Cochannel Interference and Nakagami Fading", IEEE Transactions On Wireless Communications, Vol. 6, No. 11, Nov. 2007.
- [6] Z. H Velkov, "Level crossing rate and average fade duration of EGC systems with cochannel interference in Rayleigh fading", IEEE Transactions On Communications, Vol. 55, No. 11, Nov. 2007.
- [7] M. D. Yacub "The α - μ distribution: a physical fading model for the stacy distribution" IEEE Transactions on Vehicular Technology 2007; 56.
- [8] M. K. Simon, M. S. Alouini, Digital Communication over Fading Channels, USA, New York: Wiley, 2005.
- [9] E. Mekic, N.Sekulovic, M.Bandjur, M. Stefanovic, P. Spalevic, " The distribution of ratio of random variable and product of two random variables and its application in performance analysis of multi-hop relaying communications over fading channels PRZEGLAD ELEKTROTECHNICZNY, (2012), vol. 88 br. 7A, str. 133-137.
- [10] A. Matovic, E. Mekic, N. Sekulovic, M. Stefanovic, M. Matovic and C. Stefanovic, "The distribution of the ratio of the products of two independent α - μ variates and its application in the performance analysis of relaying communication systems", MATHEMATICAL PROBLEMS IN ENGINEERING, (2013).
- [11] J. Proakis, "Digital Communications", 4thed. New York: McGraw-Hill, 2001.
- [12] I. Gradshteyn, I. Ryzhik. Tables of Integrals, Series, and products. Academic Press, New York 1994.
- [13] Panajotovic Aleksandra S , Sekulovic Nikola M , Stefanovic Mihajlo C , Draca Dragan Lj, "Average Level Crossing Rate of Dual Selection Diversity over Correlated Unbalanced Nakagami- m Fading Channels in the Presence of Cochannel Interference (Article)", IEEE COMMUNICATIONS LETTERS, (2012), vol. 16 br. 5, str. 691-693.

Subdivided Weight Interpolation based on Multiscale Gradients for Color Filter Array

Yonghoon Kim and Jechang Jeong

Abstract—Single sensor is inevitable choice for the low-cost digital camera. As a result of this limitation, only one color channel must be chosen for a pixel position, although full color image need three colors at a pixel position. There are many color filter array (CFA) pattern and bayer pattern is the most commonly used structure. To interpolate missing pixels in the CFA pattern, many interpolation filters are developed. In this paper, we proposed subdivided weight interpolation based on multiscale gradients. This algorithm uses subdivided weight for red and blue pixel interpolation and it have better CPSNR than multiscale gradients algorithm (MG) by 0.13 dB.

Keywords—Bayer pattern, color filter array interpolation, demosaicing, subdivided weight Interpolation

I. INTRODUCTION

MSOT image data uses the RGB color format, which contains red, green and blue data for each pixel. Typical digital camera employs only one charge-coupled device therefore it can capture only one color of those three channels. Using this obtained pixels, other two color channel need to be interpolated to make complete color image. This process of generating a full color image from the subset color image is called color filter array (CFA) interpolation or demosaicing.

The most common CFA pattern is Bayer pattern as shown in Fig.1. Half of the pixel of bayer pattern allocated to green channel, because it is more useful for represent detail and less suffers from aliasing. The characteristic of bayer pattern is each color pixel aligned regular distance and it helps accurate interpolation using correlation between the color channels.

The simplest method generating missing pixels is that separately fills the missing pixels of each channel using bilinear or bicubic interpolation algorithm which is spatially invariant interpolation method. These algorithms normally show good result at the homogenous region however they produce artifacts such as aliasing or blurring at the texture and edge structure.

To achieve better performance [1] and [2] use spectral correlation which can be modeled by constant color ratio model. This idea based on assumption that color ratio inside given

This research was supported by the MSIP (Ministry of Science, ICT & Future Planning), Korea, under the ITRC (Information Technology Research Center) support program supervised by the NIPA (National IT Industry Promotion Agency), (NIPA-2013-H0301-13-1011).

Y. Kim is with Hanyang University, Haengdangdong, Sungdonggu, Seoul, South Korea (e-mail: charismakyh@gmail.com).

J. Jeong is with Department of Electronics and Computer Engineering, Hanyang University, Haengdangdong, Sungdonggu, Seoul, South Korea (corresponding author, e-mail: jjeong@hanyang.ac.kr).

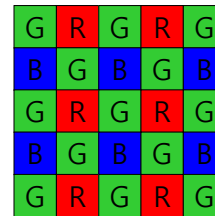


Fig. 1 Bayer color filter array

object is constant over a local area. This assumption shows good performance, therefore many other demosaicing algorithm try to adopt or adaptively utilize it. However they have too much dependency on spectral correlation, sometimes zipper artifacts are occurred when the image has many objects and the boundaries.

Based on directional interpolation algorithm with different decision rules is proposed in [3]-[6], and [7] proposed a hard direction decision using variance of color differences. Zhang *et al.* [8] proposed Linear Minimum Mean Square Error Estimation (LMMSE) which uses soft direction decision. It combines color differences along horizontal and vertical directions optimally. In [9], Paliy *et al.* suggest directional approach with scale adaptive filtering based on local polynomial approximation (LPA). Reference [10] and [11] try to making a decision criteria based on horizontal and vertical directions and especially [10] compared local homogeneity of horizontal and vertical interpolation results. In [11], to determine the direction decision author utilizes color gradients over a local window.

Recently, even though many demosaicing algorithms are proposed, they still suffer from aliasing and false coloring. The problem is point-wise edge information cannot give accurate direction. Pekkucuksen *et al.* proposed orientation-free edge strength filter (ESF) [12] and multiscale gradients based color filter array interpolation (MG) [13]. Both algorithm utilizes accumulated gradient to calculate the weight for vertical and horizontal direction and it estimate edge direction more accurately and [13] uses edge calculation more efficiently makes green channel update non-iteratively.

In this paper, we proposed improved scheme based on MG. The rest of paper is organized as follows. Proposed CFA algorithm is introduced in Section II. Experiments based on 12 Kodak images will be shown in Section III, and Section IV concludes the paper.

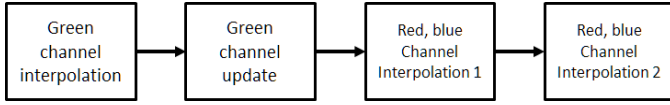


Fig. 2 Color filter array interpolation

II. PROPOSED ALGORITHM

A. Algorithm Background

Recently, most of the color filter interpolation algorithm used 4 step interpolation method in fig. 2. First and second step are for the green channel and red and blue channel interpolated at the third and fourth step. Missing green channel interpolated in the first step and interpolated green pixels are updated using neighboring correlation between green and other channel. In the third step, red channel at the blue position and blue channel at the red position is created and then rest missing channel is interpolated.

Every step uses gradient information because it can give directional information. It is very valuable for determining which pixel we use around the target pixel position. Therefore, before the initial step vertical and horizontal gradient is calculated respectively:

$$D^v(i, j) = \left| \frac{I(i+1, j) - I(i-1, j)}{2} - \frac{I(i+2, j) - I(i-2, j)}{3.5} \right. \\ \left. + \frac{I(i+3, j) - I(i-3, j)}{7} - \frac{I(i+4, j) - I(i-4, j)}{14} \right. \\ \left. + \frac{I(i+5, j) - I(i-5, j)}{28} \right| \quad (1)$$

$$D^h(i, j) = \left| \frac{I(i, j+1) - I(i, j-1)}{2} - \frac{I(i, j+2) - I(i, j-2)}{3.5} \right. \\ \left. + \frac{I(i, j+3) - I(i, j-3)}{7} - \frac{I(i, j+4) - I(i, j-4)}{14} \right. \\ \left. + \frac{I(i, j+5) - I(i, j-5)}{28} \right|, \quad (2)$$

where I is the pixel intensity in the bayer pattern image plane and (i, j) denotes pixel location. In fig.3 gradient map of each direction is created for the every pixel position.

B. Initial Green Channel Interpolation

The green channel interpolation utilizes the horizontal and vertical combination using green values calculated from each direction separately as follows:

$$G^v(i, j) = [g(i-3, j), g(i-1, j), g(i+1, j), g(i+3, j)] \cdot f_1^T \\ + [r(i-2, j), r(i, j), r(i+2, j)] \cdot f_2^T \\ G^h(i, j) = [g(i, j-3), g(i, j-1), g(i, j+1), g(i, j+3)] \cdot f_1^T \\ + [r(i, j-2), r(i, j), r(i, j+2)] \cdot f_2^T$$

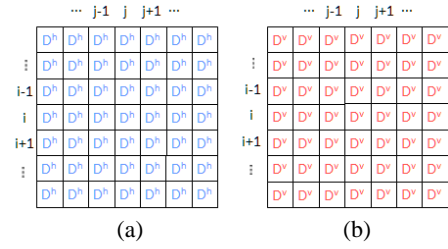


Fig. 3 Horizontal (a) and vertical (b) gradient map

$$f_1 = [1/16, 7/16, 7/16, 1/16] \quad (3) \\ f_2 = [-1/4, 1/2, -1/4],$$

Where G^v and G^h are the estimated green value of vertical and horizontal direction at the blue pixel position, and g is green pixel intensity and r is red pixel intensity. Each directional weight for the 5x5 widow is calculated as follow:

$$w_v = 1 / \left(\sum_{m=i-2}^{m=i+2} \sum_{n=j-2}^{n=j+2} D^v(m, n) \right)^3 \\ w_h = 1 / \left(\sum_{m=i-2}^{m=i+2} \sum_{n=j-2}^{n=j+2} D^h(m, n) \right)^3. \quad (4)$$

The estimated G of vertical and horizontal directions are combined using directional weight given by:

$$G^v(i, j) = \frac{G^h \cdot w_h + G^v \cdot w_v}{w_h + w_v}. \quad (5)$$

From (3) to (5) can be equally adapted to green channel interpolation at the blue pixel position.

C. Green Channel Update

To improve the interpolated green channel, it is updated using four closest neighboring pixels. In this step, four weights based on gradient information are utilized. To avoid blurring effect from the average sum, each neighboring pixel has subdivided weight unlike step 1. The four weights are calculated as follows:

$$w_u = 1 / \left(\sum_{m=i-4}^{m=i} \sum_{n=j-1}^{n=j+1} D^v(m, n) \right)^2 \\ w_d = 1 / \left(\sum_{m=i}^{m=i+3} \sum_{n=j-1}^{n=j+1} D^v(m, n) \right)^2 \\ w_l = 1 / \left(\sum_{m=i-1}^{m=i+1} \sum_{n=j-3}^{n=j} D^h(m, n) \right)^2 \\ w_r = 1 / \left(\sum_{m=i-1}^{m=i+1} \sum_{n=j}^{n=j+3} D^h(m, n) \right)^2, \quad (6)$$

where w_u , w_d , w_l and w_r represent weight of up, down, left and right respectively. To utilize the correlation between green

channel and other color channel, color difference is employed for green channel refinement and it is given as:

$$\begin{aligned} d_{g,r}(i, j) &= G(i, j) - R(i, j), \\ d_{g,b}(i, j) &= G(i, j) - B(i, j) \end{aligned} \quad (7)$$

and green channel update at the red pixel location is as follows:

$$\begin{aligned} d'_{g,r}(i, j) &= d_{g,r}(i, j) \cdot (1 - w) + \\ & (d_{g,r}(i-2, j) \cdot w_u + d_{g,r}(i+2, j) \cdot w_d \\ & + d_{g,r}(i, j-2) \cdot w_l + d_{g,r}(i, j+2) \cdot w_r) \cdot w / w_t \end{aligned} \quad (8)$$

$$w_t = w_u + w_d + w_l + w_r$$

$$G'(i, j) = R(i, j) + d'_{g,r},$$

where w is experimentally determined as 0.3 and green pixel at the blue pixel position is performed same by replacing R to B . The green channel update step refines green pixel more close to original pixel value and it help to other color channel interpolation at the next step.

D. Red and Blue Channel Interpolation

The red and blue channel interpolation consists of two steps, because available neighboring pixels are different by the position. At the third step, red pixel at blue position and blue pixel at red position is interpolated. These pixels do not have vertical and horizontal neighbors and they only have diagonal pixel can be used therefore diagonal weight is required. Instead of calculating diagonal weight using summation of gradient map, we reuse the pre-calculated weight. In fig. 4, available pixel position and proposed weight of each position is explained. Each weigh is calculated as follow:

$$\begin{aligned} w_{ul} &= w_u + w_l \\ w_{ur} &= w_u + w_r \\ w_{dl} &= w_d + w_l \\ w_{dr} &= w_d + w_r, \end{aligned} \quad (9)$$

where w_u , w_d , w_l and w_r are obtained using (6) therefore it requires 4 addition to make diagonal direction weight. We modified the 7x7 filter proposed in [10] and it is given by:

$$\begin{bmatrix} 0 & 0 & -1 & 0 & -1 & 0 & 0 \\ 0 & 0 & 0 & 0 & 0 & 0 & 0 \\ -1 & 0 & 8 & 0 & 8 & 0 & -1 \\ 0 & 0 & 0 & 0 & 0 & 0 & 0 \\ -1 & 0 & 8 & 0 & 8 & 0 & -1 \\ 0 & 0 & 0 & 0 & 0 & 0 & 0 \\ 0 & 0 & -1 & 0 & -1 & 0 & 0 \end{bmatrix} \cdot \frac{1}{24} \quad (10)$$

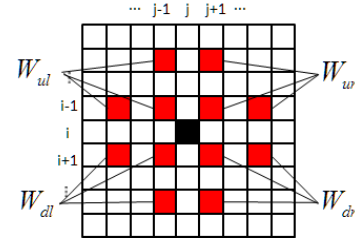


Fig. 4 available pixel position and subdivided weight in step 3

The weights calculated in (9) and matrix (10) can be combined as follow:

$$m = \begin{bmatrix} 0 & 0 & -w_{ul} & 0 & -w_{ur} & 0 & 0 \\ 0 & 0 & 0 & 0 & 0 & 0 & 0 \\ -w_{ul} & 0 & 8 \cdot w_{ul} & 0 & 8 \cdot w_{ur} & 0 & -w_{ur} \\ 0 & 0 & 0 & 0 & 0 & 0 & 0 \\ -w_{dl} & 0 & 8 \cdot w_{dl} & 0 & 8 \cdot w_{dr} & 0 & -w_{dr} \\ 0 & 0 & 0 & 0 & 0 & 0 & 0 \\ 0 & 0 & -w_{dl} & 0 & -w_{dr} & 0 & 0 \end{bmatrix} \cdot \frac{1}{24 \cdot w_t} \quad (11)$$

$$w_t = w_{ul} + w_{ur} + w_{dl} + w_{dr}.$$

This filter can be adapted red and blue position equally. The red and blue pixel reconstructed as follow:

$$\begin{aligned} R'(i, j) &= G(i, j) - d_{g,r}(i-3:j+3, j-3:j+3) \otimes m \\ B'(i, j) &= G(i, j) - d_{g,b}(i-3:j+3, j-3:j+3) \otimes m, \end{aligned} \quad (12)$$

where \otimes denotes element-wise matrix multiplication and summation of whole elements.

The rest missing red and blue pixels are located at green pixel position. These pixels have vertical and horizontal neighboring pixels therefore we can reuse w_v and w_h , which pre-calculated in step 1. The red and blue interpolation of step 4 is given by:

$$\begin{aligned} R(i, j) &= G(i, j) - \frac{w_v \cdot (d_{g,r}(i-1, j) + d_{g,r}(i+1, j))}{2 \cdot (w_v + w_h)} \\ & - \frac{w_h \cdot (d_{g,r}(i, j-1) + d_{g,r}(i, j+1))}{2 \cdot (w_v + w_h)} \\ B(i, j) &= G(i, j) - \frac{w_v \cdot (d_{g,b}(i-1, j) + d_{g,b}(i+1, j))}{2 \cdot (w_v + w_h)} \\ & - \frac{w_h \cdot (d_{g,b}(i, j-1) + d_{g,b}(i, j+1))}{2 \cdot (w_v + w_h)}. \end{aligned} \quad (13)$$

III. EXPERIMENTAL RESULT

To evaluate the performance of the proposed algorithm, we tested proposed algorithm on 12 Kodak images listed in fig. 5 and CPSNR, which is average PSNR of three color plane (red, green, blue), is used as a measurement. When we calculate the PSNR, 10 pixel distance from the border are excluded. We



Fig. 5 12 Kodak images

experimented several demosaicing algorithms: Local Polynomial Approximation (LPA) [10], Regularization Approaches to Demosaicing (RAD) [14], Edge Strength Filter based interpolation (ESF) [12], Integrated Gradients color Demosaicing (IGD) [15], and MG.

The results are summarized in Table I and The best CPSNR value of each sequence is marked with bold text. IGD and MG are the best method in terms of CSPN but the proposed algorithm gives the better CPSNR results than the other demosaicing method. It presents 0.13 dB higher CPSNR value than MG and whole sequences evenly show better performance. The weight utilized for red and blue pixel interpolation gives image quality improvement. Step 3 need slightly more operation compare with MG algorithm but proposed algorithm has simple initial green channel interpolation, therefore whole complexity almost same with MG.

IV. CONCLUSION

In this work, we present subdivided weight interpolation based on multiscale gradients to further improve the overall image quality for CFA. By interpolating red and blue channels more accurately using simply created weight, the proposed algorithm have 0.13 dB higher CPSNR than MG algorithm which gives the best performance. Our further research will be about estimated gradient accurately and applying subdivided weight to each color channel interpolation effectively.

REFERENCES

- [1] R. Kimmel, "Demosaicing: Image reconstruction from color CCD samples," *IEEE Trans. Image Process.*, vol. 8, no. 9, pp. 1221–1228, Sep. 1999.
- [2] R. Lukac and K. N. Plataniotis, "A normalized model for color-ratio based demosaicking schemes," in *Proc. Int. Conf. Image Process.*, 2004, pp. 1657–1660.
- [3] J. F. Hamilton and J. E. Adams, "Adaptive color plane interpolation in single sensor color electronic camera," U.S. Patent 5 629 734, May 1997.
- [4] C. A. Laroche and M. A. Prescott, "Apparatus and method for adaptively interpolating a full color image utilizing chrominance gradients," U.S. Patent 5 373 322, Dec. 1994.
- [5] R. H. Hibbard, "Apparatus and method for adaptively interpolating a full color image utilizing luminance gradients," U.S. Patent 5 382 976, Jan. 1995.
- [6] J. E. Adams and J. F. Hamilton, "Adaptive color plane interpolation in single color electronic camera," U.S. Patent 5 506 619, Apr. 1996.

Table I

CPSNR of 12 Kodak images by different demosaicing method

	LPA	RAD	ESF	IGD	MG	Proposed
1	43.47	42.12	42.55	43.42	43.72	43.94
2	40.86	40.69	40.45	40.68	41.54	41.67
3	37.54	38.02	37.55	38.43	39.05	39.25
4	43.02	42.44	42.15	42.70	43.51	43.68
5	37.13	36.03	37.19	37.46	37.56	37.60
6	43.49	42.40	42.96	43.56	43.78	43.88
7	43.98	43.20	43.80	44.25	44.45	44.62
8	36.97	36.12	36.11	37.33	37.97	38.23
9	40.09	39.89	39.27	39.92	40.30	40.44
10	37.42	37.51	37.72	37.75	38.24	38.28
11	38.49	38.30	38.41	38.63	39.05	39.09
12	43.89	42.36	42.45	43.33	44.02	44.03
average	40.53	39.92	40.05	40.62	41.10	41.23

- [7] K.-H. Chung and Y.-H. Chan, "Color demosaicing using variance of color differences," *IEEE Trans. Image Process.*, vol. 15, no. 10, pp.2944–2955, Oct. 2006.
- [8] L. Zhang and X. Wu, "Color demosaicking via directional linear minimum mean square-error estimation," *IEEE Trans. Image Process.*, vol. 14, no. 12, pp. 2167–2178, Dec. 2005.
- [9] D. Paliy, V. Katkovnik, R. Bilcu, S. Alenius, and K. Egiazarian, "Spatially adaptive color filter array interpolation for noiseless and noisy data," *Int. J. Imag. Syst. Technol.*, vol. 17, no. 3, pp. 105–122, 2007.
- [10] K. Hirakawa and T. W. Parks, "Adaptive homogeneity-directed demosaicing algorithm," *IEEE Trans. Image Process.*, vol. 14, no. 3, pp. 360–369, Mar. 2005.
- [11] D. Menon, S. Andriani, and G. Calvagno, "Demosaicing with directional filtering and a posteriori decision," *IEEE Trans. Image Process.*, vol. 16, no. 1, pp. 132–141, Jan. 2007.
- [12] I. Pekkucuksen and Y. Altunbasak, "Edge strength filter based color filter array interpolation," *IEEE Trans. Image Process.*, vol. 21, no. 1, pp. 393–397, Jan. 2012.
- [13] I. Pekkucuksen and Y. Altunbasak, "Multiscale Gradients-Based Color Filter Array Interpolation," *IEEE Trans. Image Process.*, vol. 22, no. 1, pp. 157–165, Jan. 2013.
- [14] D. Menon and G. Calvagno, "Regularization approaches to demosaicking," *IEEE Trans. Image Process.*, vol. 18, no. 10, pp. 2209–2220, Oct. 2009.
- [15] K. H. Chung and Y. H. Chan, "Low-complexity color demosaicing algorithm based on integrated gradients," *J. Electron. Imag.*, vol. 19, no. 2, pp. 021104-1–021104-15, Jun. 2010.

Yonghoon Kim received a B.S degree from the Department of Electronics and Computer Engineering from Hanyang University, Korea, in 2009. He is currently pursuing a Ph.D. candidate in Electronic and Computer Engineering at Hanyang University. His research interests include motion estimation, intra prediction of video compression in H.264, and Image processing include demosaicing and denoising.

Jechang Jeong received a BS degree in electronic engineering from Seoul National University, Korea, in 1980, an MS degree in electrical engineering from the Korea Advanced Institute of Science and Technology in 1982, and a PhD degree in electrical engineering from the University of Michigan, Ann Arbor, in 1990. From 1982 to 1986, he was with the Korean Broadcasting System, where he helped develop teletext systems. From 1990 to 1991, he worked as a postdoctoral research associate at the University of Michigan, Ann Arbor, where he helped to develop various signal-processing algorithms. From 1991 through 1995, he was with the Samsung Electronics Company, Korea, where he was involved in the development of HDTV, digital broadcasting receivers, and other multimedia systems. Since 1995, he has conducted research at Hanyang University, Seoul, Korea. His research interests include digital signal processing, digital communication, and image and audio compression for HDTV and multimedia applications. He has published numerous technical papers.

Implementation of Sparse Representation Classifier (SRC) to heartbeat biometrics

W. C. Tan and D. A. Ramli

Abstract— Biometrics is a new trend of human identity verification technologies nowadays to replace conventional methods such as pin number and password or token-based authentication. These biometric traits include face, iris, fingerprint, voice and etc. In this paper, heart sound is proposed and used as biometric trait for human identity authentication. The proposed heart sound biometric system consists of four main modules, which are heart sound acquisition, pre-processing, feature extraction, training and classification using classifier. A new and efficient classification technique, Kernel Sparse Representation Classifier (KSRC) based on Sparse Representation Classifier (SRC) and kernel trick is implemented in this paper. The reconstructive and discriminative nature of SRC provides a high performance of classification even with noisy data. By introducing the Kernel trick into SRC, the classification performance of the classifier is further improved by implicitly map features data into a high-dimensional kernel feature space. The results of the system prove the possibility of heart sound as a biometric trait for human authentication system. Meanwhile, KSRC shows a promising result as classifier for heart sound recognition and has outperformed the other classifiers i.e. Support Vector Machines (SVM), SRC and K-Nearest Neighbor (KNN) with 85.45% accuracy.

Keywords—biometrics, heart sound, kernel trick, sparse representation classifier.

I. INTRODUCTION

THE use of traditional authentication systems to prove legitimate user are exposed to several weaknesses such as the authenticator could be easily lost or stolen and the link between authenticator and legitimate user is weak. Thus, the use of biometric traits as a reliable authentication system to identify authentic user is becoming important to replace its traditional counterpart in order to increase the security of the authentication system. Biometric authentication system can be divided into two types which are based on physical or behavioral traits. Physical traits are characteristics which is fixed or unvarying such as face, iris, fingerprint, heart sound as well as DNA. Behavioral traits are characteristics which represented by skills or functions performed by an individual such as gait, voice and signature.

Recently research [1], [2] have been proved that heartbeat or heart sound can be used as the biometric trait for human authentication. Human heart sounds are noises generated by the beating heart and the resultant flow of blood through it. Two heart sounds are normally produced during each cardiac cycle namely S1 and S2. The first heart sound S1 is normally longer, low-pitch tone and sound like “lup” whereas the second heart sound S2 is shorter, high-pitch and sound like “dup”. These natural signals have been applied in auscultation by doctors for health monitoring and diagnosis.

Since heart sounds contain information about an individual’s physiology, it can be potentially used as a biometric traits and provide unique identity for each person. Besides, heart sounds are very difficult to counterfeit or imitate by others and therefore reduces falsification in authentication systems. In 2006, the possibility of using heart sound as biometric trait for human identification is investigated and a preliminary results indicate an identification rate of up to 96% for a database consists of 7 individuals, with heart sounds collected over a period of 2 months [2]. Their system is based on the cepstral analysis with a specified configuration called Linear Frequency Bands Cepstral (LFBC) as feature extraction method, combined with Gaussian Mixture Modeling (GMM) and Vector Quantization (VQ) as classifier.

In 2007 [1], a heart sound biometric system is proposed by the authors using a feature extraction method called chirp-Z transform (CZT) and K-Nearest Neighbor (KNN) based on Euclidean distance as the classifier. Their system achieved 0% false rejection rate (FRR) and 2.2% false acceptance rate using a database containing heart sound recorded from 20 different people. The weakness of the CZT feature extraction method is that the locations of the S1 and S2 heart sounds have to be well aligned for each sample.

In 2010 [3], three different types of features are extracted which are auto-correlation, cross-correlation and cepstrum. The classifiers applied in their system are Mean Square Error (MSE) and KNN. KNN classifier achieved 93% identification rate evaluated using a database of 400 heart sound that were recorded from 40 individuals by 10 heart sound recordings for each individuals.

In 2013 [4], a new feature set called marginal spectrum is extracted from the heart sounds and classifier VQ based on Linde-Buzo-Gray algorithm (LBG-VQ) is used for classification the heart sounds. The identification rate of their system achieved 94.40% evaluated using a database of 280 heart sounds from 40 participants.

In this paper, a heart sound authentication system based on Mel Frequency Cepstral Coefficient (MFCC) and Sparse

This work was supported by Universiti Sains Malaysia under Research University Grant 814161 and Fundamental Research Grant Scheme (FRGS) 6071266.

W. C. Tan is a PhD student at School of Electrical & Electronic Engineering, Universiti Sains Malaysia. (e-mail: zero_0317@hotmail.com).

D. A. Ramli is a senior lecturer at School of Electrical & Electronic Engineering, Universiti Sains Malaysia. (corresponding author to provide phone: +604-5996028; e-mail: dzati@eng.usm.my).

Representation Classifier (SRC) are used as feature extraction and classification method respectively. The SRC is a new and powerful classifier especially for noisy or corrupted samples data. Thus, this research aims to develop a robust and reliable heart sound authentication system which can work well with noisy heart sound sample. The proposed system consists of four main phases; data acquisition, signal pre-processing, feature extraction, and training and classification phases. The rest of this paper is organized as follows. Section II briefly states the methods and architecture of the heart sound authentication. Section III presents the classification using SRC and KSRC. The result and discussion are illustrated in section IV. Finally, section V summarizes conclusions.

II. METHODOLOGY

A. Database

An open heart sounds database HSCT-11 collected by the University of Catania Italy is applied to evaluate the performance of proposed heart sound authentication system. This database is a collection of heart sounds to be used for biometric research purpose and freely available on the internet [5]. It contains heart sounds collected from 206 people, i.e. 49 female and 157 male. Only 10 female and 5 male heart sounds are randomly selected from the database and have been used in this research. The heart sounds recordings are recorded in WAV format at a sampling frequency of 11.025 kHz, near the pulmonary valve and contains only sequences recorded in resting condition.

B. Signal Pre-processing

Although it is impossible to remove all noises from the recorded sound signal, it can be minimized to certain acceptable level. The recorded heart sound signals which are corrupted by various types of noise can reduce the accuracy of identification. Therefore, a fifth order Chebyshev type I lowpass filter with cutoff frequency at 880 Hz is applied to the signals. In this context, background noise or sound that its frequency higher than the filter cut off frequency will be eliminated. Then, the signals were normalized to absolute maximum according to the equation (1)

$$x_{norm}(k) = x(k) / \max_i(|x(i)|) \quad (1)$$

C. Segmentation

The heart produces two strong and audible sounds namely S1 and S2. These two heart sounds contain important features for human identity verification. Therefore, the heart sound segmentation is the first step of this automatic heart sound biometric system [6].

The segmentation technique that is employed in this system is based on zero-crossing rate (ZCR) and short-term amplitude (STA). First, the noise-filtered and normalized signal is blocked into frames of 5ms length with 66.7% overlapped. Next, the short-term amplitude and zero-crossing rate of each frames is calculated based on equation 2 and 3 respectively.

$$A_n = \sum_{m=n-N+1}^n [x(m)w(n-m)] \quad (2)$$

where $x(m), m = 1, \dots, N$ is the audio samples of the n^{th} frame. This simple feature can be used for detecting silent part in audio signals.

$$Z_n = \frac{1}{2} \sum_{m=0}^{N-1} |x(m) - x(m+1)| \quad (3)$$

Z_n is especially helpful for detecting speech from noisy background and for start and end point detection. Then, the upper and lower of STA and ZCR threshold is set as shown in table 1.

Table 1: Threshold value for heart sound segmentation process.

Upper Short-term amplitude threshold, $STA1$	3
Lower Short-term amplitude threshold, $STA2$	0.5
Zero-crossing rate threshold, ZCR	5

These threshold values is obtained from trial and error. After defined the threshold values, the frames of the signal is evaluated by the following rules.

Rule 1: the frame's STA is greater than $STA1$ threshold is considered as a part of heart sound and the starting point of the heart sound will be calculated.

Rule 2: the frame's with STA is greater than $STA2$ threshold or ZCR is greater than ZCR threshold is considered as possible heart sound signal and will be further evaluated next frames. If the next frame matches rule 2, the evaluation will be repeated until it matches rule 1 or rule 3. Once the next frame matches rule1, the starting point of the heart sound will be equal to the starting point of the very first frame which matches rule 2. The ending point of this heart sound is evaluated when the following frame matches rule 3. If the next frames does not matches rule 1 and directly matches rule 3, this sequence of frames will not consider as a heart sound.

Rule 3: the frame's with STA is lower than $STA2$ threshold and ZCR is lower than ZCR threshold is considered as not a heart sound.

The flow chart of the segmentation technique is shown in figure 1.

D. Feature Extraction

The extraction of the best parametric representation of acoustic signals is an important task in the design of any sound-based biometric recognition system so that a better identification performance can be produced. Mel Frequency Cepstral Coefficients (MFCC) is one of the most commonly used feature extraction method in speech recognition. MFCC takes human hearing perception sensitivity with respect to frequencies into consideration [7], [8].

After the heart sound signal is segmented, framed, and windowed, MFCC is used to extract meaningful parameter in the heart sound signal. The steps to implement MFCC in this system are as the following.

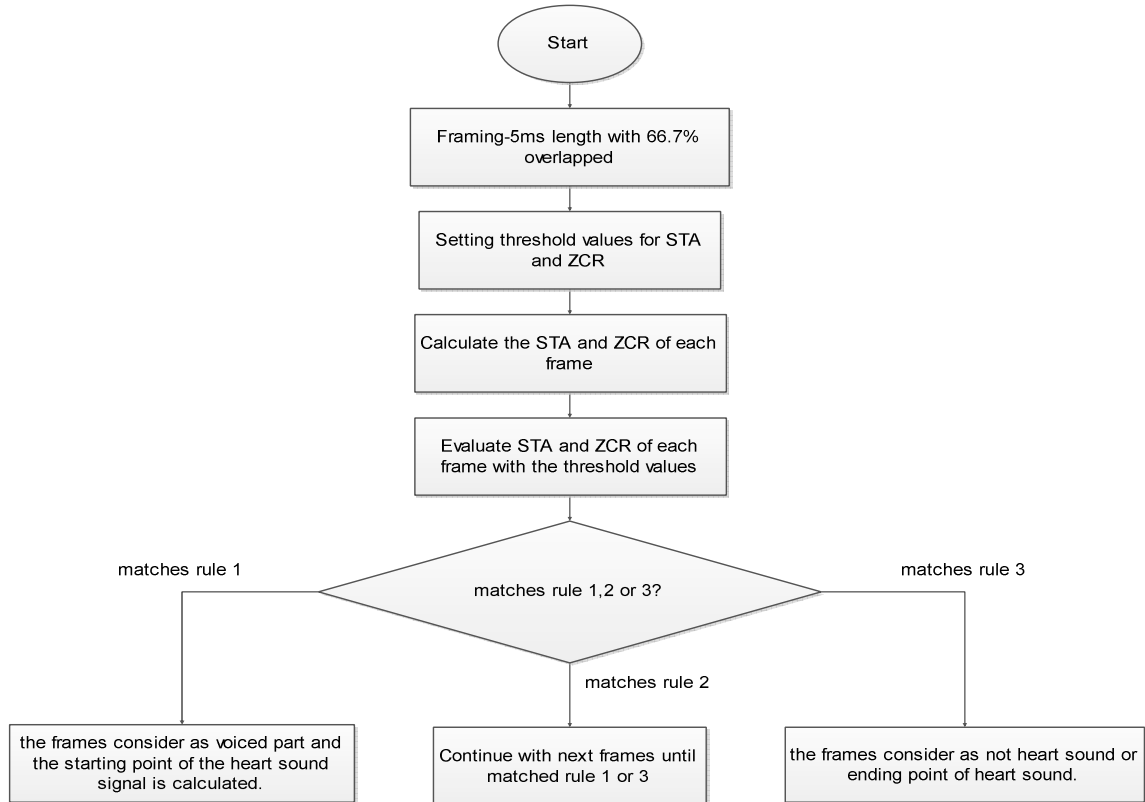


Fig. 1 Heart sound segmentation flow chart based on ZCR and STA

1. Discrete Fourier Transform (DFT) of each frame is computed. Each frame of N samples is converted from time domain into frequency domain in this step. The DFT of all frames of the pre-processed heart sound signal is

$$X_t(\omega) = \sum_{n=1}^N x'_t(n) e^{-j2\pi kn/N}, 1 \leq k \leq K \quad (4)$$

where n is the number of samples in a frame, and k is the domain index of the DFT.

2. The signal spectrum is then processed by mel filter bank processing. The magnitude of frequency is multiplied by Mel filter bank. This is to obtain the log energy of each triangular band-pass filter in the filter bank. The filter bank used in this project consists of 24 triangular band-pass filter that is emphasize on processing the spectrum which frequency is below 1 kHz.

The positions of these filters are equally spaced along the Mel frequency scale and related by following equation:

$$f_{mel} = 2595 \log_{10}(1 + f/700) \quad (5)$$

where f_{mel} is the subjective pitch in Mels corresponding to a frequency in Hz.

3. Normally, log energy is obtained by computing the logarithm of square magnitude of the coefficients $Y_t(m)$. $Y_t(m)$ is the m^{th} filter bank output. In this project, the log energy is obtained by computing logarithm of the magnitude of the coefficients. This is done in purpose of reducing the complexity of computing.
4. Inverse DFT is computed on the logarithm of the magnitude of the filter bank output as shown following:

$$y_t^{(m)}(k) = \sum_{m=1}^M \log \{|Y_t(m)|\} \cdot \cos(k(m - 0.5)\pi/m), \quad k = 0, \dots, L \quad (6)$$

where M is the number of triangular filters in the Mel filter bank, and L is the number for mel-scale cepstral coefficients. The obtained features are referred to as mel-scale cepstral coefficients, or MFCC. In this project, the value of N is 20 and L is 12. The energy within a frame is added to the 12 number of mel-scale cepstral coefficients.

5. Delta cepstrum—the first and second order time derivatives of 13 numbers of features which are the

frame energy and mel-scale cepstral coefficients is computed.

$$y_t = \{y_t^{(m)}(k), e_t, \Delta\{y_t^{(m)}(k)\}, \Delta\{e_t\}, \Delta^2\{y_t^{(m)}(k)\}, \Delta^2\{e_t\}\} \quad (7)$$

According to equation 7, the results from first and second derivatives are added as new features. Hence, a 39-dimensional MFCC features per frames is extracted from the digitized heart sound signal.

The features extracted from S2 heart sound will be appended to the features extracted from S1 sound so that features of a complete heart sound cycle is used in classification process.

III. CLASSIFICATION

A. Sparse Representation Classifier (SRC)

Sparse representation is originally applied for signal representation and reconstruction. Sparse representation of signal is an expression of the signal as a linear combination of atoms in an overcomplete dictionary in which many of the coefficients are zero. The original goal of sparse representation is to represent and compress a signal using lower sampling rates than the Shannon-Nyquist rate [9]. Thus, the performance of the compress algorithm is based on the degree of sparsity of the representation to the original signal. Among all the atoms in an over complete dictionary, the sparse representation selects the subset of the atoms which most compactly expresses the input signal and rejects all other less compact representation. Therefore, the sparsest representation of a signal is naturally discriminative and can be developed for signal classification purpose. Equation 8 shows the input signal y is linearly represented by a dictionary, D and sparse representation, x .

$$y_{m \times 1} = D_{m \times n} x_{n \times 1} \quad (8)$$

Sparse representation classifier is a nonparametric learning method which can directly predict or assign a class label to a test sample based on dictionary composed of training samples. This method is similar to Nearest Neighbor and Nearest Subspace classifier which do not have a training process in its classification process. Sparse representation for classification is first introduced in 2009 in face recognition research [10]. They experimentally proved that sparse representation classifier (SRC) has better classification performance than nearest neighbor and nearest subspace.

In sparse representation classifier, the dictionary is constructed from training samples from various classes. The j^{th} class training samples are arranged as column of a matrix D_j as shown in equation 9. The columns of dictionary are referred as atoms.

$$D_j = [d_{j,1}, \dots, d_{j,n_j}] \in R^{m \times n_j} \quad (9)$$

where $d_{j,i}$ denotes the training sample belonging to the j^{th} class, and n_j is the number of the training samples for j^{th}

class. The dictionary, D is form using all the dictionary from each class as shown in equation 10.

$$D = [D_1, D_2, \dots, D_c] \in R^{m \times n} \quad (10)$$

where $n = \sum_{j=1}^c n_j$. and c is the number of class.

Based on the equation 1, for SRC problem, the sparse representation x , is the vector of coefficients associated with the training sample in the dictionary matrix. The entries of x that corresponds to the class which the test sample y belongs to is expected to be nonzero while the entries of x that corresponding to other classes is expected to be zero.

$$x = [0, \dots, 0, x_{j,1}, \dots, x_{j,n_j}, 0, \dots, 0]^T \quad (11)$$

where $x_{j,i} \in R$ is the coefficient corresponding to the training sample $d_{j,i}$. The sparse representation based classification method looks for the sparsest representation by solving the following l_0 minimization problem.

$$\min \|x\|_0 \quad s.t. \quad y = Dx \quad (12)$$

where $\|x\|_0$ denotes the l_0 norm, which count the number of nonzero elements of sparse representation, x . Equation 12 is known as NP (nondeterministic polynomial) hard problem and difficult to approximate. The developed theory from sparse representation and compressive sensing research reveals that the sparsest solution from equation 12 can be obtained by replacing the l_0 norm with the l_1 norm given that the solution, x is sparse enough [11]–[13].

$$\min \|x\|_1 \quad s.t. \quad y = Dx \quad (13)$$

where $\|x\|_1$ denotes the l_1 norm, which sum the absolute values of all elements in the sparse representation, x . The advantage of sparse representation based classification is its ability to deal with corrupted or noisy data within the same framework. This property of sparse representation classifier provides the advantage for heart sound biometric authentication system because usually the heart sound contains noise signal. To deal with noisy data, equation 8 is modified as

$$y_{m \times 1} = D_{m \times n} x_{n \times 1} + \xi_{m \times 1} \quad (14)$$

where $\xi_{m \times 1} \in R^m$ denotes the noise vector with bounded energy $\|\xi_{m \times 1}\|_2 < \epsilon$, where $\|\cdot\|_2$ denotes the l_2 norm. While equation 13 can be modified as

$$\min \|x\|_1 \quad s.t. \quad \|y - Dx\|_2 \leq \epsilon \quad (15)$$

Equation 15 is one standard formulation for sparse reconstruction problems in compressive sensing, called the quadratically constrained l_1 minimization problem [14], [15]. Both the l_1 minimization problems are solved using spectral projected gradient method, SPGL1 toolbox in this research. The minimum of the representation error or the residual error

of class c is calculated by keeping the coefficients associated with that class and while setting the other entries to zero. This is done by introducing a characteristic function, ζ as follow.

$$r_c(y) = \|y - D\zeta_i x\|_2 \quad (16)$$

where $r_c(y)$ denotes the residual error. The vector ζ has value one at locations associated to the class i and zero for other entries. The class, d , of the test signal, y is computed as the one that produces smallest residual error.

$$d = \min_i r_i(y) \quad (17)$$

The algorithm summarizes the complete classification procedure of SRC is shown as the following.

Algorithm 1: Sparse Representation Classifier (SRC)

1. The input for SRC are a matrix of training samples form a dictionary $D = [D_1, D_2, \dots, D_c] \in R^{m \times n}$ for c classes, a test sample $y \in R^m$ and an optional error tolerance $\epsilon > 0$.
2. Normalize the atoms of D to have unit l_2 norm.
3. Solve the l_1 minimization problem in equation 13 or 15 using SPGL1 toolbox:
4. Compute the residuals $r_i(y) = \|y - D\zeta_i x\|_2$ for $i = 1, \dots, c$.
5. The class of the given test sample, y is determined by $identity(y) = \min_i r_i(y)$.

B. Kernel Sparse Representation Classifier (KSRC)

Kernel tricks is applied into a classifier to change the distribution of samples by mapping it into a high dimensional kernel feature space [16] in order to change the linear inseparable samples in the original feature space into linear separable in the high dimensional feature space. This mean a test sample can be represented as the linear combination of training samples from same class more accurately by applying kernel trick into SRC. The classification performance of SRC will be improved as the nonzero entries of sparse representation, x of the test sample are more associated with training samples from same class as itself. In this work, radial basis function (RBF) kernel is employed in KSRC as following.

$$k(x, y) = e^{-t\|x-y\|^2} \quad (18)$$

where $t < 0$ is the parameter for RBF kernels. KSRC classification method is also able to overcome the disadvantages of SRC which cannot classify samples in the same direction which belong to different classes [17].

In KSRC, kernelized dictionary and testing sample is computed by the following equation.

$$D_{kernel} = [k(d_i, d_j)]_{n \times n} \quad (19)$$

$$y_{kernel} = [k(y, d_j)]_{n \times 1} \quad (20)$$

where $i, j = 1, \dots, n$, and n is the number of training samples. The kernelized dictionary dimension of the training samples is reduced by kernel mapping if the number of atoms is smaller than feature dimension in original dictionary and vice-versa. In KSRC, the classification task is executed by replacing D and y in SRC problem with D_{kernel} and y_{kernel} . Hence, the l_1 minimization problem for KSRC is expressed as following.

$$\min \|x\|_1 \quad s.t. \quad y_{kernel} = D_{kernel}x \quad (21)$$

$$\min \|x\|_1 \quad s.t. \quad \|y_{kernel} - D_{kernel}x\|_2 \leq \epsilon \quad (22)$$

The algorithm summarizes the complete classification procedure of KSRC is shown in following.

Algorithm 2: Kernel Sparse Representation Classifier (KSRC)

1. Step 1: The input for KSRC are a matrix of training samples form a dictionary $D = [D_1, D_2, \dots, D_c] \in R^{m \times n}$ for c classes, a test sample $y \in R^m$ and an optional error tolerance $\epsilon > 0$.
2. Kernelize of D and y to yield D_{kernel} and y_{kernel}
3. Normalize the atoms of D_{kernel} and y_{kernel} to have unit l_2 norm.
4. Solve the l_1 minimization problem in equation 21 or 22 using SPGL1 toolbox:
5. Compute the residuals $r_i(y_{kernel}) = \|y_{kernel} - D_{kernel}\zeta_i x\|_2$ for $i = 1, \dots, c$.
6. The class of the given test sample, y is determined by $identity(y_{kernel}) = \min_i r_i(y_{kernel})$.

IV. RESULT AND DISCUSSION

The segmentation results of S1 and S2 heart sounds are illustrated in figure 1. According to the figure, the STA and ZCR based segmentation method is able to correctly segment out S1 and S2 heart sounds.

The heart sounds used in this paper consist of heart sounds from 15 participants which is randomly selected from HSCT11 open database. A total of 775 heart sounds samples are divided in to two groups which are training sample and testing sample. 20 samples of heart sounds from each participants have been used as training samples and the rest have been used as testing samples. Support Vector Machine (SVM) and K-Nearest Neighbor (KNN) are also implemented to provide a comparison with the SRC and KSRC method. In this work, the value of $k=3$ is used for kNN, and polynomial kernel is adopted for SVM.

The recognition methods are tested as a function of two parameters i.e., the number of training samples per participant and the feature dimension of heart sound samples. In first experiment, N numbers of training samples are randomly selected from all of the heart sound while the remaining are used for testing. The classification performance of heart sounds for various numbers of training samples using SVM, SRC, KSRC and KNN is as shown in table 2.

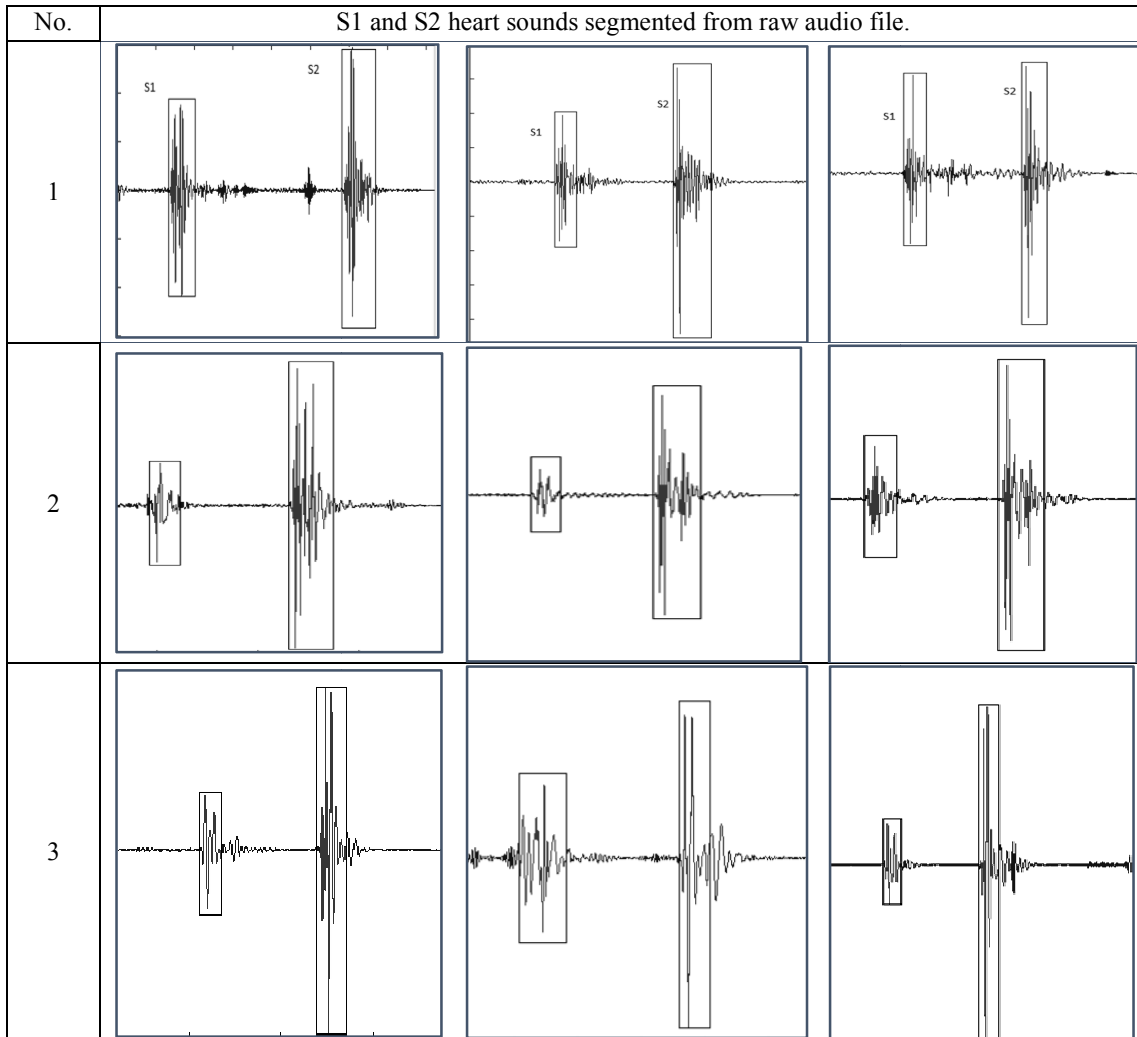


Table 1: Segmentation of S1 and S2 heart sounds from three different participants

Table 2: Classification performance based on different numbers of training samples and classifiers

Classifier	Number of Training Samples		
	10	15	20
SVM	76.96%	81.09%	84.87%
SRC	75.52%	81.18%	84.45%
KSRC	78.72%	82.00%	85.45%
KNN (K=3)	70.40%	69.82%	78.78%

Table 3: Classification performance based on different feature dimensions and classifiers

Classifier	Feature Dimension of Heart Sound Features		
	200	392	450
SVM	82.98%	84.87%	84.24%
SRC	82.14%	84.45%	84.03%
KSRC	79.41%	85.45%	82.35%
KNN (K=3)	77.31%	78.78%	75.42%

For second experiment, the effect of feature dimensions has been investigated by using three different feature lengths i.e., 200, 392 and 450. The classification performances of heart sounds for various feature dimension of heart sound using SVM, SRC, KSRC and KNN is as shown in table 3.

The results in table 2 and 3 show that KSRC achieves the highest recognition rate compared to other classifiers for 20 training samples and 392 feature dimension. KSRC shows very good results which have proved its ability in classification of heart sound (mono-dimensional) data.

V. CONCLUSION

A promising results obtained by KSRC in classifying heart's audible activity proves that its viability as classifier to be used in heart sound based biometric authentication system. The proposed segmentation method to segment out the heart sounds from recording is also crucial in order for the system to work automatically. Robust feature extraction method which is common in speech recognition i.e. MFCC shows that it is also suitable to be executed as features for heart sound. Future work will investigate the potential of applying combined-classification method to improve the result obtained.

- [17] Z. Li, Z. Wei-Da, C. Pei-Chann, L. Jing, Y. Zhe, W. Ting, *et al.*, "Kernel Sparse Representation-Based Classifier," *Signal Processing, IEEE Transactions on*, vol. 60, pp. 1684-1695, 2012.

REFERENCES

- [1] F. Beritelli and S. Serrano, "Biometric identification based on frequency analysis of cardiac sounds," *Information Forensics and Security, IEEE Transactions on*, vol. 2, pp. 596-604, 2007.
- [2] K. Phua, T. H. Dat, J. Chen, and L. Shue, "Human identification using heart sound," in *Second International Workshop on Multimodal User Authentication, Toulouse, France, 2006*.
- [3] N. El-Bendary, H. Al-Qaheri, H. M. Zawbaa, M. Hamed, A. ella Hassanien, Z. Qiangfu, *et al.*, "HSAS: Heart Sound Authentication System," in *Nature and Biologically Inspired Computing (NaBIC), 2010 Second World Congress on*, 2010, pp. 351-356.
- [4] Z. Zhao, Q. Shen, and F. Ren, "Heart Sound Biometric System Based on Marginal Spectrum Analysis," *Sensors*, vol. 13, pp. 2530-2551, 2013.
- [5] A. Spadaccini and F. Beritelli, "Performance Evaluation of Heart Sounds Biometric Systems on An Open Dataset," in *Proceedings of the 5th IAPR International Conference on Biometrics*, 2012.
- [6] Y. Xiaoling, T. Baohua, D. Jiehua, Z. Jinye, and G. Jiaoli, "Comparative Study on Voice Activity Detection Algorithm," in *Electrical and Control Engineering (ICECE), 2010 International Conference on*, 2010, pp. 599-602.
- [7] S. Kim, T. Eriksson, H.-G. Kang, and Y. Dae-Hee, "A pitch synchronous feature extraction method for speaker recognition," in *Acoustics, Speech, and Signal Processing, 2004. Proceedings. (ICASSP '04). IEEE International Conference on*, 2004, pp. 1-405-8 vol.1.
- [8] S. Memon, M. Lech, and H. Ling, "Using information theoretic vector quantization for inverted MFCC based speaker verification," in *Computer, Control and Communication, 2009. IC4 2009. 2nd International Conference on*, 2009, pp. 1-5.
- [9] E. J. Candès and M. B. Wakin, "An introduction to compressive sampling," *Signal Processing Magazine, IEEE*, vol. 25, pp. 21-30, 2008.
- [10] J. Wright, A. Y. Yang, A. Ganesh, S. S. Sastry, and M. Yi, "Robust Face Recognition via Sparse Representation," *Pattern Analysis and Machine Intelligence, IEEE Transactions on*, vol. 31, pp. 210-227, 2009.
- [11] E. J. Candès, J. K. Romberg, and T. Tao, "Stable signal recovery from incomplete and inaccurate measurements," *Communications on Pure and Applied Mathematics*, vol. 59, pp. 1207-1223, 2006.
- [12] D. L. Donoho, "For most large underdetermined systems of linear equations the minimal " *Communications on Pure and Applied Mathematics*, vol. 59, pp. 797-829, 2006.
- [13] E. J. Candès and T. Tao, "Near-Optimal Signal Recovery From Random Projections: Universal Encoding Strategies?," *Information Theory, IEEE Transactions on*, vol. 52, pp. 5406-5425, 2006.
- [14] M. A. T. Figueiredo, R. D. Nowak, and S. J. Wright, "Gradient Projection for Sparse Reconstruction: Application to Compressed Sensing and Other Inverse Problems," *Selected Topics in Signal Processing, IEEE Journal of*, vol. 1, pp. 586-597, 2007.
- [15] S. Becker, J. Bobin, and E. J. Candès, "NESTA: a fast and accurate first-order method for sparse recovery," *SIAM Journal on Imaging Sciences*, vol. 4, pp. 1-39, 2011.
- [16] K. Yu, L. Ji, and X. Zhang, "Kernel nearest-neighbor algorithm," *Neural Processing Letters*, vol. 15, pp. 147-156, 2002.

Stochastic Modeling of Sound Environment System with Multiplicative Noise and Noise Cancellation Method

Hisako Orimoto, and Akira Ikuta

Abstract— In the actual situation of sound environment systems, the observed data often contain several fluctuating noises. Therefore, it is necessary to estimate the specific signal based on the observed data by introducing some noise cancellation methods. In this study, a sound environment system considering both noises of the external noise based on the additive property of energy variable and the internal noise dependent on the specific signal expressing in a multiplicative form is first paid our attention. Next, a noise cancellation method to estimate recursively the specific signal is derived on the basis of Bayes' theorem in an expansion series form suitable to a signal processing with lower and higher order statistics for the observation data. More specifically, an expansion expression of the conditional probability distribution reflecting the information on linear and nonlinear correlation among the time series of the specific signal and observation is adopted to express the statistical relationship between the specific signal and the signal dependent noise. Finally, the validity of the proposed method is experimentally confirmed by applying it to the actual data observed in real sound environment.

Keywords— Additive External Noise, Noise Cancellation Method, Signal Dependent Noise

I. INTRODUCTION

IN the real sound environment system, the observed data contain the effects of various fluctuation factors such as noises in addition to the specific signal. Therefore, it is necessary to estimate only the specific signal based on the observation data by introducing some kinds of signal processing method [1],[2]. For example, in the evaluation of sound environment, the background noise always exists in our daily life because the background noise means every kind of noises except the specific signal sound. Therefore, in order to evaluate the sound environment, it is very important to estimate the specific signal based on the observation data contaminated by the background noise. Furthermore, the fluctuation characteristics of the specific signal and the noises show complex forms of non-Gaussian type.

This work was supported in part by fund from the Grant-in-Aid for Scientific Research No.24760322 from the Ministry of Education, Culture, Sports, Science and Technology-Japan.

H. Orimoto is with the Department of Management Information Systems, Prefectural University of Hiroshima, 734-8558 Japan (corresponding author to provide phone: +82-251-9804; e-mail: orimoto@pu-hiroshima.ac.jp).

A. Ikuta is with the Department of Management Information Systems, Prefectural University of Hiroshima, 734-8558 Japan (e-mail: ikuta@pu-hiroshima.ac.jp).

In general, the fluctuation factors can be classified into two categories of external and internal factors. The former factor can be expressed in an additive model because this factor can exist independently even when the input signal does not exist. On the other hand, the later factor can be reasonably expressed in a multiplicative model with correlation for the input signal because this factor exists in only case of existence of the input signal.

Several noise cancellation methods such as Kalman filter [3],[4], extended Kalman filter [5], unscented Kalman filter [6], and particle filter [7] have been proposed up to now. However, these studies have been focused on the suppression of additive noise, and the countermeasure methods of signal dependent noise have not been proposed.

In this study, by paying our attention to the observation mechanism in a sound environment system which is considered both of the additive external noise based on the additive property of energy variable and the internal noise dependent on the input signal expressing in a multiplicative form, a noise cancellation method applicable to cases for signal dependent noise is proposed. More specifically, an expansion expression of the conditional probability distribution reflecting the information on linear and nonlinear correlation among the time series of the specific signal and observation is adopted to express the relationship between the specific signal and the signal dependent noise. Next, based on Bayes' theorem in an expansion series form suitable to a signal processing with lower and higher order statistics for the observation data, a recursive estimation algorithm of the specific signal is derived. Finally, the validity of the proposed method is experimentally confirmed by applying it to the actual data observed in real sound environment.

II. CANCELLATION METHOD FOR ADDITIVE AND MULTIPLICATIVE NOISES

A. Modeling for Sound Environment System

As shown in Fig. 1, in sound environment system containing an internal noise w_k dependent on the input signal x_k , and an external noise v_k of non-Gaussian type with known statistics, a noise cancellation method to estimate x_k based on the recursive output observation y_k at a discrete time k is proposed.

In the case of focusing on energy variables satisfying the additive property, the output observation y_k is expressed as

$$y_k = ax_k + \varepsilon_k x_k + v_k + b, \quad (1)$$

where a and b are known parameters, and $\varepsilon_k x_k (= w_k)$ denotes generally the internal noise dependent on the input x_k . Furthermore, a time transition model:

$$x_{k+1} = Fx_k + Gu_k, \quad (2)$$

is introducing for the input x_k . Here, u_k is a random input, and two parameters F , G can be decided on the basis of the correlation information of time series of x_k .

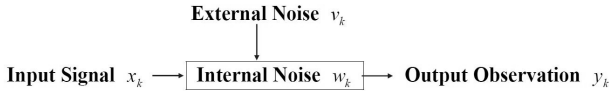


Fig. 1 sound environment system contaminated by noises

As an example of complex sound environment systems, input and output sound data measured indoors and outdoors for a house shown in Fig. 2 is considered. The sound energy variables satisfying the additive property are paid our attention. More specifically, after generating a sound inside the house, the sound energy data measured indoors and outdoors are regarded as the input signal x_k and the output observation y_k .

The scatter diagram between the input and output signals is shown in Fig. 3. It is reasonable to express the relationship between x_k and y_k as the following system model.

$$y_k = (a + \varepsilon_k)x_k + b = ax_k + \varepsilon_k x_k + b, \quad (3)$$

where two parameters a and b are regression coefficients in a linear regression model between the input x and the output y :

$$y = ax + b. \quad (4)$$

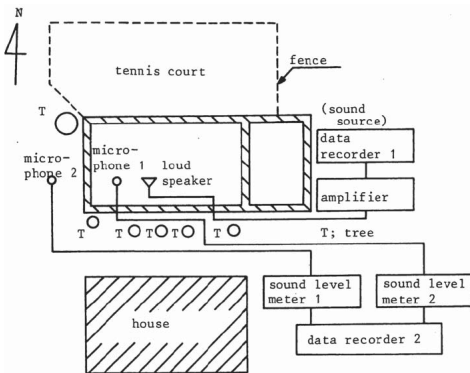


Fig. 2 a schematic drawing of the experimental set up in sound insulation system

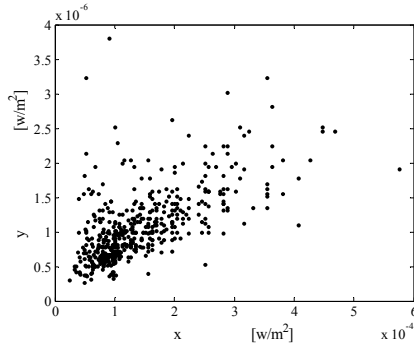


Fig. 3 scatter diagram between the input and output data for the sound environment system

Furthermore, ε_k in (3) denotes the fluctuation of the inclination a in the linear regression, and $\varepsilon_k x_k$ expresses the fluctuation around the linear regression model in (4). For random variables with the non-negative fluctuation region $[0, \infty]$ like energy, power, intensity and amplitude, the fluctuation width around the regression curve is not principally independent of the mean value (i.e., regression function). In general, the fluctuation around the mean value becomes larger (or smaller) as the mean value becomes larger (or smaller). Since the scatter diagram between the input and output data for the sound insulation system in Fig. 2 show the tendency that the fluctuation around the regression function corresponding to mean value becomes larger as the input and output data become larger as shown in Fig. 3, the system model in (3) is introduced as the input and output relationship. The term $\varepsilon_k x_k$ in (3) denotes the fluctuation around the linear regression $y_k = ax_k + b$, and the values of $\varepsilon_k x_k$ depend on the input x_k . Furthermore, since the output data are usually measured under existence of an external noise (i.e., background noise), the relationship in (1) can be derived from (3).

B. Derivation of Noise Cancellation Method

To derive an estimation algorithm for the specific signal x_k , we place our basis on the Bayes' theorem for the conditional probability distribution [1],[2].

$$P(x_k | Y_k) = \frac{P(x_k, y_k | Y_{k-1})}{P(y_k | Y_{k-1})}, \quad (5)$$

where $Y_k (= \{y_1, y_2, \dots, y_k\})$ is a set of observation data up to time k . By expanding the conditional joint probability distribution $P(x_k, y_k | Y_{k-1})$ in a statistical orthogonal expansion series [8] on the basis of the well-known standard probability distributions describing the dominant part of the actual fluctuation, the following expression is derived.

$$P(x_k | Y_k) = \frac{P_0(x_k | Y_{k-1}) \sum_{m=0}^{\infty} \sum_{n=0}^{\infty} A_{mn} \varphi_m^{(1)}(x_k) \varphi_n^{(2)}(y_k)}{\sum_{n=0}^{\infty} A_{0n} \varphi_n^{(2)}(y_k)} \quad (6)$$

with

$$A_{mn} = \langle \varphi_m^{(1)}(x_k) \varphi_n^{(2)}(y_k) | Y_{k-1} \rangle. \quad (7)$$

The above two functions $\varphi_m^{(1)}(x_k)$ and $\varphi_n^{(2)}(y_k)$ are orthonormal polynomials of degrees m and n with weighting functions $P_0(x_k | Y_{k-1})$ and $P_0(y_k | Y_{k-1})$. Based on (6), the estimate of the polynomial function $f_M(x_k)$ of x_k with M th order can be derived as follows.

$$\hat{f}_M(x_k) = \langle f_M(x_k) | Y_k \rangle = \frac{\sum_{m=0}^M \sum_{n=0}^{\infty} C_m^M A_{mn} \varphi_n^{(2)}(y_k)}{\sum_{n=0}^{\infty} A_{0n} \varphi_n^{(2)}(y_k)}, \quad (8)$$

where C_m^M is an appropriate constant satisfying the following equality:

$$f_M(x_k) = \sum_{m=0}^M C_m^M \varphi_m^{(1)}(x_k). \quad (9)$$

As examples of standard probability functions for the specific signal, the parameter and observation, Gaussian distribution is adopted:

$$\begin{aligned} P_0(x_k | Y_{k-1}) &= N(x_k; x_k^*, \Gamma_{x_k}), \\ P_0(y_k | Y_{k-1}) &= N(y_k; y_k^*, \Omega_k) \end{aligned} \quad (10)$$

with

$$\begin{aligned} N(x; \mu, \sigma^2) &= \frac{1}{\sqrt{2\pi\sigma^2}} \exp\left\{-\frac{(x-\mu)^2}{2\sigma^2}\right\}, \\ x_k^* &= \langle x_k | Y_{k-1} \rangle, \quad \Gamma_{x_k} = \langle (x_k - x_k^*)^2 | Y_{k-1} \rangle, \\ y_k^* &= \langle y_k | Y_{k-1} \rangle, \quad \Omega_k = \langle (y_k - y_k^*)^2 | Y_{k-1} \rangle. \end{aligned} \quad (11)$$

The orthonormal polynomials with two weighting probability distributions in (10) are then specified as

$$\begin{aligned} \varphi_m^{(1)}(x_k) &= \frac{1}{\sqrt{m!}} H_m\left(\frac{x_k - x_k^*}{\sqrt{\Gamma_{x_k}}}\right), \\ \varphi_n^{(2)}(y_k) &= \frac{1}{\sqrt{n!}} H_n\left(\frac{y_k - y_k^*}{\sqrt{\Omega_k}}\right), \end{aligned} \quad (12)$$

where $H_m(\bullet)$ denotes the Hermite polynomial with m th order [8]. Therefore, by selecting

$$f_1(x_k) = x_k, \quad f_2(x_k) = (x_k - \hat{x}_k)^2, \quad (13)$$

in (9), the estimates for mean and variance (i.e., conditional mean and variance) of x_k which are the first and second order statistics, can be expressed as follows:

$$\hat{x}_k = \langle x_k | Y_k \rangle = \frac{\sum_{n=0}^{\infty} \{A_{0n}C_0^1 + A_{1n}C_1^1\} \varphi_n^{(2)}(y_k)}{\sum_{n=0}^{\infty} A_{0n} \varphi_n^{(2)}(y_k)}, \quad (14)$$

$$\begin{aligned} P_{x_k} &= \langle (x_k - \hat{x}_k)^2 | Y_k \rangle \\ &= \frac{\sum_{n=0}^{\infty} \{A_{0n}C_0^2 + A_{1n}C_1^2 + A_{2n}C_2^2\} \varphi_n^{(2)}(y_k)}{\sum_{n=0}^{\infty} A_{0n} \varphi_n^{(2)}(y_k)} \end{aligned} \quad (15)$$

with

$$\begin{aligned} C_0^1 &= x_k^*, \quad C_1^1 = \sqrt{\Gamma_{x_k}}, \quad C_0^2 = \Gamma_{x_k} + (x_k^* - \hat{x}_k)^2, \\ C_1^2 &= 2\sqrt{\Gamma_{x_k}}(x_k^* - \hat{x}_k), \quad C_2^2 = \sqrt{2}\Gamma_{x_k}. \end{aligned} \quad (16)$$

Using (1), two variables y_k^* and Ω_k in (11) can be calculated as follows:

$$y_k^* = ax_k^* + \langle \varepsilon_k \rangle x_k^* + \langle v_k \rangle + b, \quad (17)$$

$$\Omega_k = (a^2 + 2a \langle \varepsilon_k \rangle + \langle \varepsilon_k^2 \rangle) \Gamma_{x_k} + \langle (v_k - \langle v_k \rangle)^2 \rangle + \langle \varepsilon_k^2 \rangle - \langle \varepsilon_k \rangle^2 x_k^{*2} \quad (18)$$

Furthermore, using (1), each expansion coefficient A_{mn} defined by (7) can be given in functional forms of x_k^* , Γ_{x_k} and statistics of v_k . Some of the expressions are shown as follows:

$$\begin{aligned} A_{00} &= 1, \quad A_{01} = A_{02} = A_{10} = A_{20} = 0, \\ A_{11} &= \sqrt{\frac{\Gamma_{x_k}}{\Omega_k}} (a + \langle \varepsilon_k \rangle), \quad A_{21} = A_{12} = 0, \\ A_{22} &= \frac{\Gamma_{x_k}}{\Omega_k} (a^2 + 2 \langle \varepsilon_k \rangle a + \langle \varepsilon_k^2 \rangle). \end{aligned} \quad (19)$$

Furthermore, from (2), the following relationships are obtained.

$$x_{k+1}^* = F\hat{x}_k + G \langle u_k \rangle, \quad (20)$$

$$\Gamma_{x_{k+1}} = F^2 P_{x_k} + G^2 \langle (u_k - \langle u_k \rangle)^2 \rangle. \quad (21)$$

By combining (14), (15) with (20), (21), the estimation of the specific signal can be performed in a recursive way.

C. Prediction of Output Probability Distribution for Sound Environment System

In the practical evaluation and regulation of the environmental noise and vibration, a (100- x) percentile level L_x ($x=5, 10, 50, 90, 95$) directly connected with a whole probability distribution is frequently used as one of noise evaluation indices. Therefore, prediction of the output response probability distribution is considered on the basis of the system model in (1).

First, in order to estimate the regression parameters a and b , by introducing the system models:

$$y_k = a_k x_k + \varepsilon_k x_k + v_k + b_k, \quad (22)$$

$$a_{k+1} = a_k, \quad b_{k+1} = b_k, \quad (23)$$

instead of (5), the following Bayes' theorem is considered.

$$P(a_k, b_k | Y_k) = \frac{P(a_k, b_k, y_k | Y_{k-1})}{P(y_k | Y_{k-1})}. \quad (24)$$

The conditional joint probability distribution $P(a_k, b_k, y_k | Y_{k-1})$ can be generally expanded in a statistical orthogonal expansion series:

$$\begin{aligned} P(a_k, b_k, y_k | Y_{k-1}) &= P_0(a_k | Y_{k-1}) P_0(b_k | Y_{k-1}) P_0(y_k | Y_{k-1}) \\ &\quad \sum_{l=0}^{\infty} \sum_{m=0}^{\infty} \sum_{n=0}^{\infty} B_{lmn} \varphi_l^{(3)}(a_k) \varphi_m^{(4)}(b_k) \varphi_n^{(2)}(y_k) \end{aligned} \quad (25)$$

with

$$B_{lmn} = \langle \varphi_l^{(3)}(a_k) \varphi_m^{(4)}(b_k) \varphi_n^{(2)}(y_k) | Y_{k-1} \rangle, \quad (26)$$

where the functions $\varphi_l^{(3)}(a_k)$ and $\varphi_m^{(4)}(b_k)$ are orthonormal polynomials of degree degrees l and m with weighting functions $P_0(a_k | Y_{k-1})$ and $P_0(b_k | Y_{k-1})$, which can be chosen as the probability functions describing the dominant parts of the actual fluctuation describing the dominant parts of the actual fluctuation or as the well-known standard probability distributions. After substituting (25) into (24), expanding an arbitrary polynomial function $f_{L,M}(a_k, b_k)$ of a_k and b_k with (L, M) th order in a series expansion form using $\{\varphi_l^{(3)}(a_k)\}$ and $\{\varphi_m^{(4)}(b_k)\}$:

$$\begin{aligned} f_{L,M}(a_k, b_k) &= \sum_{l=0}^L \sum_{m=0}^M C_{lm}^{LM} \varphi_l^{(3)}(a_k) \varphi_m^{(4)}(b_k), \\ (C_{lm}^{LM} : \text{Appropriate constants}), \end{aligned} \quad (27)$$

through the same calculation process as Section 2.2, the estimation algorithms of the function $f_{L,M}(a_k, b_k)$ can be derived as

$$\hat{f}_{L,M}(a_k, b_k) = \langle f_{L,M}(a_k, b_k) | Y_k \rangle = \frac{\sum_{l=0}^L \sum_{m=0}^M \sum_{n=0}^{\infty} C_{lm}^{LM} B_{lmn} \varphi_n^{(2)}(y_k)}{\sum_{n=0}^{\infty} A_{00n} \varphi_n^{(2)}(y_k)}. \quad (28)$$

Furthermore, by considering (23), the prediction step to perform the recurrence estimation can be given for an arbitrary function $g_{L,M}(a_k, b_k)$ with (L, M) th order, as follows:

$$g_{L,M}^*(a_{k+1}, b_{k+1}) = \langle g_{L,M}(a_{k+1}, b_{k+1}) | Y_k \rangle = \langle g_{L,M}(a_k, b_k) | Y_k \rangle. \quad (29)$$

The above equation means that the predictions of a_{k+1} and b_{k+1} at a discrete time k are given in the form of estimates for the polynomial functions of a_k and b_k . Therefore, by combining the estimation algorithm of (28) with the prediction algorithm of (29), the recurrence estimation of the parameters can be achieved.

Based on the estimated parameters \hat{a} and \hat{b} , the statistics of the output y were predicted on the basis of input x different from the data using in the estimation of the parameters, as follows:

$$\langle y^n \rangle = \sum_{i=0}^n \binom{n}{i} \langle x^i \rangle \hat{b}^{n-i} \sum_{j=0}^i \binom{i}{j} \langle \varepsilon^j \rangle \hat{a}^{i-j}, \quad (30)$$

Based on the moment statistics in (30), the probability distribution of the output in decibel scale connected with the noise evaluation index L_x ((100- x) percentile level) can be predicted in an expansion series form based on the logarithmic normal distribution [9]:

$$P(L) = \frac{K}{\sqrt{2\pi}\sigma} e^{-\frac{(\ln y_0 + KL - \mu)^2}{2\sigma^2}} \left\{ 1 + \sum_{n=1}^{\infty} D_n \psi_n(y_0 e^{KL}) \right\}, \quad (31)$$

$(K = \ln 10 / 10)$

with

$$\mu = \ln(\langle y \rangle^2 / \sqrt{\langle y^2 \rangle}), \quad \sigma^2 = \ln(\langle y^2 \rangle / \langle y \rangle^2),$$

$$D_n = \sum_{i=0}^n \xi_{ni} \langle y^i \rangle, \quad (32)$$

where, the relationship between energy variable y (i.e., sound intensity [W/m^2]) and decibel variable L (sound pressure level [dB]) is expressed as

$$L = 10 \log_{10}(y / y_0), \quad (y_0 = 10^{-12} \text{ W}/\text{m}^2). \quad (33)$$

Furthermore, $\psi_n(y) (= \sum_{i=0}^n \xi_{ni} y^i)$ is an orthonormal polynomial having the logarithmic normal distribution as the weighting function, and ξ_{ni} are coefficients determined by Schmidt's orthogonalization method.

III. APPLICATION TO ACTUAL SOUND ENVIRONMENT

A. Estimation of Input Signal for Sound Environment

The proposed method was applied to input and output sound data measured indoors and outdoors for a house shown in Fig. 2, as an example of complex sound environment systems.

After generating a music sound inside the house, the sound energy data measured indoors and outdoors are regarded as the input signal x_k and the output observation y_k . The input and output data were measured simultaneously with a sampling interval of 1 s as 500 learning data points and 200 prediction data points. Two parameters a and b in (1) were estimated from the learning data by applying the least squares method. Furthermore, by applying the proposed method to the prediction data, the fluctuation wave of x_k is estimated on the

basis of the recursive observation of y_k . Though the estimation algorithm derived in this study is expressed in an infinite expansion series, only the finite expansion series can be applied to the actual estimation problem. Since many state estimation methods like Kalman filter consider the statistics until the second order like mean and variance of external noise, the proposed method considering the statistics until the second order was also applied to the actual estimation in order to compare the proposed method with the previous methods in the same condition. More specifically, the estimation algorithms considering (14) with $n \leq 1$, and (15) with $n \leq 2$ were adopted.

For comparison, estimation results in three cases of (i) regarding $\varepsilon_k x_k$ as external additive noise w_k independent of the input signal, by introducing a system model: $y_k = ax_k + w_k + v_k + b$ instead of (1), where the statistics of w_k are obtained from the data of w_k after evaluating from $w_k = y_k - ax_k - b$ by use of the learning data, (ii) ignoring w_k by introducing a system model: $y_k = ax_k + v_k + b$ instead of (1), (iii) applying Kalman filter to the system model in (ii), (iv) applying the extended Kalman filter to the system model in (1), are shown in Figs. 4-7 as compared with the proposed method. In these figures, the estimation results in the cases of (i) and (ii) are shown as "Compared Method 1" and "Compared Method 2" respectively. The RMS errors of the estimation are shown in Table 1. The proposed method shows more accurate estimation than the results by the compared methods, and the practical usefulness of the proposed method has been confirmed.

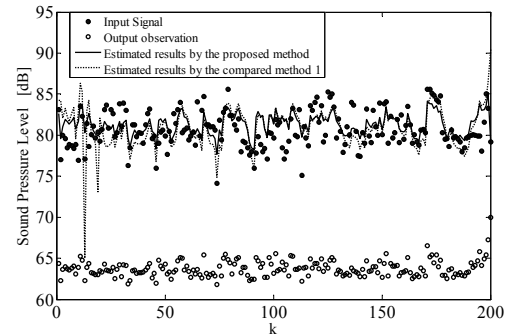


Fig. 4 comparison between two estimated results by the proposed method and the compared method 1

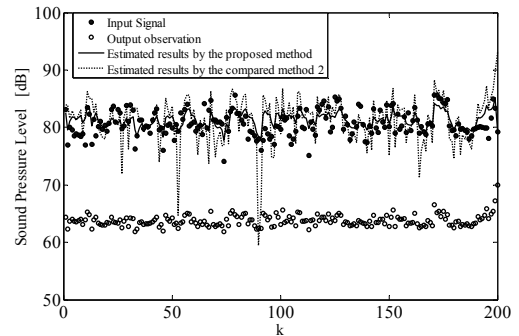


Fig. 5 comparison between two estimated results by the proposed method and the compared method

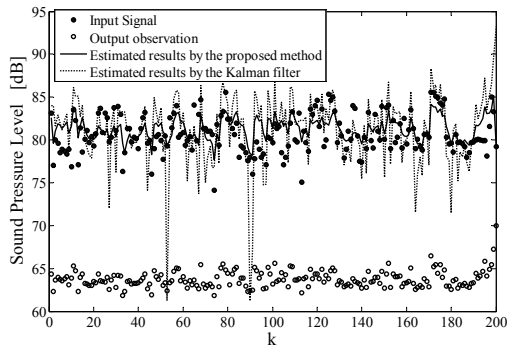


Fig. 6 comparison between two estimated results by the proposed method and the Kalman filter

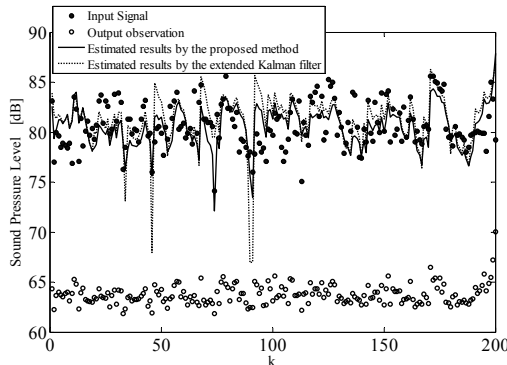


Fig. 7 comparison between two estimated results by the proposed method and the extended Kalman filter

Table 1 root mean squared error of the estimation in [dB]

Proposed Method	Compared Method 1	Compared Method 2	Kalman Filter	Extended Kalman Filter
2.09	2.58	3.67	3.72	2.60

B. Prediction of Output Probability Distribution

The prediction method of output probability distribution proposed in Section 2.3 was applied to the measured data at indoors and outdoors for a house shown in Fig. 2.

The prediction result of the output probability distribution is shown in Fig. 8 in the form of cumulative distribution connected with noise evaluation index L_x . In this figure, theoretical curves with 1st, 2nd, and 3rd approximations consider only the first term, the expansion coefficients with $n \leq 1$ and $n \leq 2$ in (27) respectively. The theoretical curve considering the higher order statistics shows a good agreement with the experimentally sampled values. For comparison, the prediction result based on the model without considering the multiplicative noise $\varepsilon_k x_k$ in (22) is shown in Fig. 9. The result based on the proposed method considering the signal dependent noise shows more accurate prediction than the result based on the model without considering the multiplicative noise, especially in the region of higher level important from the viewpoint of noise evaluation. Furthermore, after estimating the parameters in (4) based on the well-known least squared method, the predicted result of the output probability

distribution by use of (30)-(32) is shown in Fig. 10. There are large prediction errors between the theoretical curves and the experimental values as compared with Fig. 8.

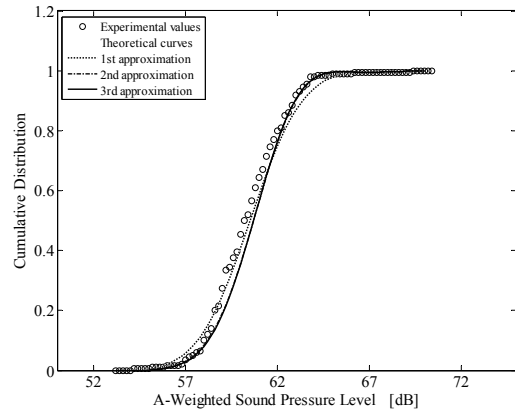


Fig. 8 comparison between experimentally sampled values and theoretically predicted curves on the output probability distribution by considering the signal dependent noise

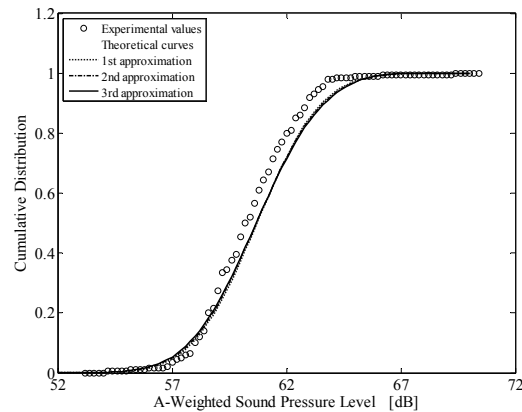


Fig. 9 comparison between experimentally sampled values and theoretically predicted curves on the output probability distribution without considering the signal dependent noise

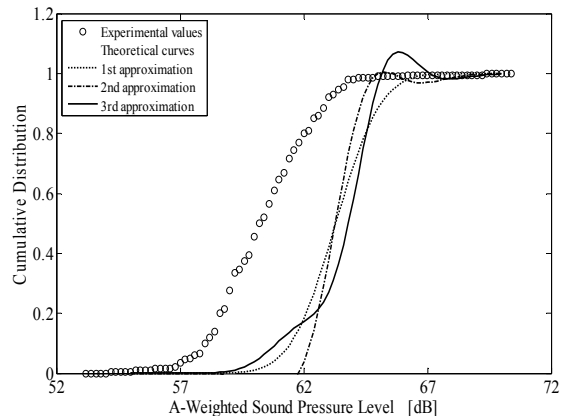


Fig. 10 comparison between experimentally sampled values and theoretically predicted curves on the output probability distribution based on the parameters estimated by the least squared method

IV. CONCLUSIONS

In this study, sound environment system involving both of external noise satisfying the additive property of energy variable and internal noise dependent on the specific signal have been considered. A noise cancellation method for sound environment system with the external and internal noises has been derived on the basis of Bayes' theorem in an expansion series form suitable to the signal processing by utilizing the higher order correlation information. More specifically, by expressing the internal fluctuation factor as multiplicative noise dependent of the input signal, and by introducing an orthogonal expansion expression of the conditional probability distribution reflecting the correlation information in the expansion coefficients, an estimation algorithm has been derived. Furthermore, by applying the proposed method to actual data in a sound environment system, the effectiveness of the theory has been confirmed experimentally.

The proposed method is quite different from the traditional standard approach. However, it is still at its early stage of study, and there are a number of practical problems to be explored in the future, starting from the result of the basic study in this paper. Some of the problems are the following.

(i) The proposed method should be applied to actual estimation and prediction problems for many other sound environment systems, and its practical usefulness should be verified in each actual situation.

(ii) By considering the higher order statistics as many as possible, the accuracy of estimation and prediction should be improved.

(iii) An optimal number of expansion terms in the proposed estimation algorithm of expansion expression type should be found.

REFERENCES

- [1] M. Ohta and H. Yamada, "New methodological trials of dynamical state estimation for the noise and vibration environmental system," *Acustica*, vol.55, no.4, pp.199-212, Jul 1984.
- [2] A. Ikuta, M. O. Tokhi and M. Ohta, "A cancellation method of background noise for a sound environment system with unknown structure," *IEICE Trans. Fundamentals*, vol.E84-A, no.2, pp.457-466, Feb 2001.
- [3] R. E. Kalman, "A new approach to linear filtering and prediction problems," *Trans. ASME, Series D, J. Basic Eng.*, vol.82, no.1, pp.35-45, 1960.
- [4] R. E. Kalman and R. S. Buch, "New results in linear filtering and prediction theory," *Trans. ASME Series D, J. Basic Eng.*, vol.83, no.1, pp.95-108, Mar 1961.
- [5] H. J. Kushner, "Approximations to optimal nonlinear filter," *IEEE Trans. on Automatic Control*, vol.12, no.5, pp.546-556, Oct 1967.
- [6] S. Julier and J. Uhlmann, "Unscented filtering and nonlinear estimation," *Proceedings of IEEE*, vol.92, no.3, pp.401-421, Mar 2004.
- [7] G. Kitagawa, "Monte carlo filter and smoother for non-Gaussian nonlinear state space model," *J. Computational and Graphical Statistics*, vol.5, no.1, pp.1-25, 1996.
- [8] M. Ohta and T. Koizumi, "General statistical treatment of response of a non-linear rectifying device to a stationary random input," *IEEE Trans. Information Theory*, vol.14, no.4, pp.595-598, Sep 1968.
- [9] M. Ohta, N. Nakasako and K. Nakamura, "A stochastic evaluation method for the arbitrary memory-type acoustic system with a non-linear observation and its application to the room acoustics," *J. Acoust. Soc. Jpn.*, vol.47, no.1, pp.13-20, 1991.

A novel symmetric text encryption algorithm based on logistic map

M. A. Murillo-Escobar, F. Abundiz-Pérez, C. Cruz-Hernández, R. M. López-Gutiérrez

Abstract—Nowadays, text encryption is recommendable when it is transmitted or stored on insecure channels as Internet. By the other hand, the chaotic systems have excellent characteristics as mixing data, ergodicity, sensitivity to initial conditions, and control parameters, etc., all them useful to design cryptographic algorithms with big size keys and an efficient permutation–diffusion process. In this work, we present a novel symmetric text cipher algorithm based on chaos; we use a 128 bit secret key, two logistic maps with optimized pseudorandom sequences, plain text characteristics, and only one permutation–diffusions round. Several security analysis are presented as secret key size, secret key sensitivity, frequency with histograms, autocorrelation analysis, information entropy analysis, differential analysis, classic attacks analysis, and encryption/decryption time. Based in numerical simulation results, the proposed encryption algorithm presents high security, an excellent encryption time, and it can resist a powerful chosen/known plain text attack; therefore, it can be implemented in real-time applications.

Keywords—chaos, logistic map, permutation–diffusion round, text encryption.

I. INTRODUCTION

In last years, people use the Internet to transmit and store data in text format. Internet is a comfortable media to transmit data but at the same time it is dangerous because the data are exposed and can be stolen by hackers to use them in an ilegal way as fraud, theft, warlike purposes, and other. Text encryption is one solution to this security problem; its objective is generate cipher text (unrecognizable text) from plain text (original text) using a symmetric algorithm (one secret key) or asymmetric algorithm (two secret keys). The telecommunications, industry, military, bank, medicine or personal data are some applications where the text encryption is needed.

Currently, 3DES (Triple Data Encryption Standard) and AES (Advanced Encryption Standard) are used as symmetric data

encryption, both are accepted as data encryption standard in EE.UU. [1]; AES has advantage as speed, low memory space, easy to implement, and it is based in permutation-diffusion architecture. The RSA (Rivest, Shamir y Adleman) algorithm is an asymmetric data cipher with security advantage but it is slow than any other symmetric cipher. Recently, the DNA (Deoxyribonucleic acid) characteristics have been proposed for text encryption where the four DNA basis are characterized by binary data, DNA complement operations are used to data encryption, and DNA sequences are used as secret key [2]-[7]. By other hand, chaos has excellent properties as mixing data, ergodicity, initial condition sensitivity, control parameters sensitivity, etc., all them are very useful to design cryptographic algorithms for text or images [8]-[14].

In this work, we present a novel symmetric text encryption algorithm based on chaos. The algorithm uses the plain text characteristics to resist a chosen/known plain text attack with just one permutation–diffusion round (change the position and the symbol value) and two logistic maps. Also, a 32 hexadecimal digits (128 bits) secret key is used. In addition, a complete security analysis is realized and we found the proposed algorithm is highly secure, practical in key handling, and it can be implemented in real-time applications. In Section 2, the encryption algorithm is presented. The analisis results are shows in Section 3. Finally, in Section 4 this work is concluded.

II. PROPOSED ALGORITHM

We assume a plain text P with length ℓ based in ASCII printable codes (lowercase letter, uppercase letter, space, numbers, and punctuation signs) characterized by 95 characters: `space!"#$%&'()*+,-./0123456789:;<=>?@ABCDEFGHIJKLMNPOQRSTUVWXYZ[\]^_`abcdefghijklmnopqrstuvwxyz{|}~` and each one has a decimal value between 32 – 126 according to ASCII table. In Fig. 1, the block diagram of the encryption scheme is shown.

The one-dimensional logistic map is described as follows

$$x_{i+1} = ax_i(1 - x_i) \quad (1)$$

where $x_i \in (0, 1)$ is the discrete state, with initial condition $x_0 \in (0, 1)$ and a is the control parameter with $a \in (3.5699, 4)$ to generate chaotic sequences.

This work was supported by the CONACYT, México under Research Grant No. 166654.

M. A. Murillo-Escobar, F. Abundiz-Pérez, and R. M. López-Gutiérrez are with the Engineering, Architecture and Design Faculty, Baja California Autonomous University (UABC), Ensenada, B.C., 22860 México (e-mail: murillo.miguel@uabc.edu.mx, abundizf@uabc.edu.mx, roslopez@uabc.edu.mx).

C. Cruz-Hernández is with the Electronics and Telecommunications Department, Scientific Research and Advanced Studies of Ensenada (CICESE), Ensenada, B.C., 22860 México (e-mail: ccruz@cicese.mx).

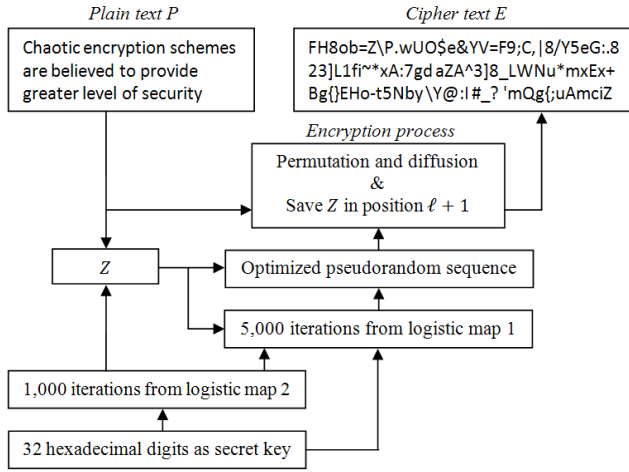


Figure 1: Block diagram of the proposed encryption scheme, where Z is the sum of all plain text characters with chaotic data from logistic map 2.

A. Secret Key Definition

In this section, the secret key is characterized and defined [15]. The initial conditions and control parameters of a chaotic system are not recommended to be used as secret key. In this work, a secret key of 32 hexadecimal digits is used (128 bits) to calculate the initial condition x_0 and the control parameter a of two logistic maps [11], [16]; with this technique the small key's size from one-dimensional maps is eliminated [17]. TABLE I shows how the initial condition and control parameter are calculated in both logistic maps. In Fig. 2, the largest Lyapunov exponent for all possible secret keys is presented; a positive Lyapunov exponent means a strong key, therefore all secret keys are considered strong.

B. Calculation of Z Value

The Z value is very important to improve the security in the proposed algorithm; in this process, all plain text symbols are summed with chaotic data from logistic map 2 to increase the security against differential attacks. First, the logistic map 2 is iterated $I = \ell + 100$ times by using a_2 and x_{2_0} from TABLE I to generate the chaotic sequence $x^{L2} = \{x_1^{L2}, x_2^{L2}, x_3^{L2}, \dots, x_I^{L2}\}$ with $x^{L2} \in (0, 1)$ and 10^{-15} decimal precision. After that, the sum of all plain text symbols is calculated as follows

$$S = S + \left[P(i) \times x_{(I+1-i)}^{L2} \right] \bmod 1, \quad (2)$$

where $i = 1, 2, 3, \dots, \ell$, P represents the plain text in decimal value, S is a variable initialized in zero, and \bmod is the module operation. Then, the Z value needs to be any proportional value between $32 - 126$; this is resolved with the following expression

$$V = \text{round}(S \times 94) + 32, \quad (3)$$

where round is the round operation. Finally, the Z value used on logistic map 1 and encryption process is

$$Z = V/127. \quad (4)$$

TABLE I. CALCULATION OF CONTROL PARAMETER a AND INITIAL CONDITION x_0 IN BOTH LOGISTIC MAPS.

Secret key:	Control parameter: a		Initial condition: x_0	
32 hexadecimal digits	$x_1, x_2, x_3, \dots, x_{32}$ where $x \in (0 - 9, A - F)$			
calculations	$A = \frac{(x_1, x_2, \dots, x_8)_{10}}{2^{32} + 1}$	$B = \frac{(x_9, x_{10}, \dots, x_{16})_{10}}{2^{32} + 1}$	$C = \frac{(x_{17}, x_{18}, \dots, x_{24})_{10}}{2^{32} + 1}$	$D = \frac{(x_{25}, x_{26}, \dots, x_{32})_{10}}{2^{32} + 1}$
logistic map 1	$a_1 = 3.999 + [((A + B + Z) \bmod 1) \cdot 0.001]$		$x_{1_0} = (C + D + Z) \bmod 1$	
logistic map 2	$a_2 = 3.999 + [((A + B) \bmod 1) \cdot 0.001]$		$x_{2_0} = (C + D) \bmod 1$	
ranges	$3.999 < a_{1,2} < 4$		$0 < x_{1,2_0} < 1$	
precision	10^{-15}		10^{-15}	
	where $(a \bmod b) = (a - b) \times (a/b)$ with $b \neq 0$			

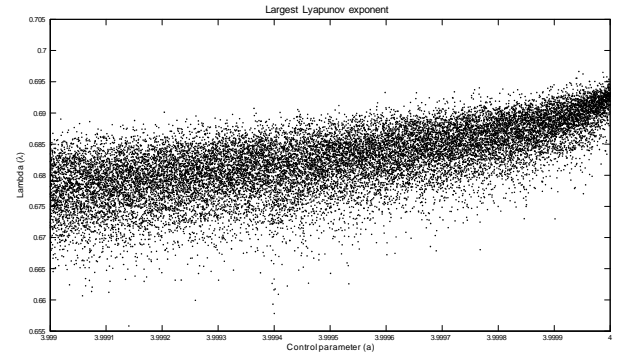


Figure 2: Maximum Lyapunov exponent graphic in $3.999 < a < 4$ range.

C. Encryption Process

The logistic map 1 is iterated $T = 5,000$ times with a_1 and x_{1_0} from TABLE I to generate other chaotic sequence $x^{L1} = \{x_1^{L1}, x_2^{L1}, x_3^{L1}, \dots, x_T^{L1}\}$ with $x^{L1} \in (0, 1)$ and 10^{-15} decimal precision. After that, a sub-sequence from x^{L1} is calculated according to ℓ plain text symbols as follows

$$PERM_i = \text{round} \left\{ \left[\left(x_{(T-\ell+i)}^{L1} \right) \cdot (\ell - 1) \right] + 1 \right\}, \quad (5)$$

where $i = 1, 2, 3, \dots, \ell$, $PERM \in [1, \ell]$ is a vector with length ℓ , round is the round operation, and \cdot represents the multiplication of each value x^{L1} per $(\ell - 1)$. In an efficient permutation process, all plain text symbols must be repositioned. In Equation (5) some values are repeated and it is important to know which ones are repeated to change them by other that are not on it; we look at the repeated values in $PERM$ as follows

$$G_h = \{k_h\}, \quad h \ll \ell \quad (6)$$

where k is the missing value from smallest to largest; the vector of missing values G is divided in two parts, after that, each missing value is replaced by each repeated value in $PERM$ directly in an alternated mode. When this process is completed, we have a pseudorandom sequence $PERM$ with all positions of plain text.

A second sub-sequence of length ℓ from x^{L1} is generated to the diffusion process. The logistic map generates many values near to 0 and 1 (Fig. 6(a)) and this would result in an inefficient diffusion process; to avoid this drawback, the logistic map sequence is modified as

$$M_i = \left\{ \left[\left(x_{(T-\ell+i)}^{L1} \right) \cdot (100) \right] + Z \right\} \bmod 1, \quad (7)$$

where $i = 1, 2, 3, \dots, \ell$, $M_i \in (0, 1)$ is a vector with length ℓ , \bmod is the module operation, and "." represents the multiplication of each value x^{L1} per 100. The Equation (7) has better distribution (Fig. 6(b)) than data directly from logistic map. Then, M_i data are transformed as follows

$$Y_i = \text{round}\{[M_i \cdot 94] + 1\}, \quad (8)$$

where $i = 1, 2, 3, \dots, \ell$, $Y_i \in [1, 95]$ is a vector with length ℓ , round is the round operation, and "." represents the multiplication of each value M_i per 94. Finally, the permutation–diffusion process and encryption are calculated as

$$E_i = \{[(P(PEM_i) - 32) + Y_i] \bmod 95\} + 32, \quad (9)$$

where $i = 1, 2, 3, \dots, \ell$, $E_i \in [32, 126]$ is the cipher text, $P \in [32, 126]$ represents the plain text in decimal value, and \bmod is the module operation.

D. Z Encryption

The Z value must be used in decryption process but it cannot be calculated from cipher text E directly, so it needs to be added in the cryptogram as follows

$$E_{\ell+1} = V, \quad (10)$$

where $V \in [32, 126]$.

E. Decryption Process

We assume that the cryptogram is not altered during its transmission. The decrypt process is invert the encrypt process (Fig. 3). First, Z is obtained from the cryptogram with

$$Z = E_{(\ell+1)}/127. \quad (11)$$

The Z value can be known by any person, but he can not decrypt correctly if it does not has the correct secret key. After that, with the 128 bits correct key and the Z value, 5,000 chaotic data are calculated in logistic map 1 to determine $PERM$, M y Y as well as in encryption process. Afterwards, the permutation–diffusion process and decryption are calculated with the next expression

$$D_i(PEM_i) = \{[(E(i) - 32) - Y_i] \bmod 95\} + 32 \quad (12)$$

where $i = 1, 2, 3, \dots, \ell$, $D_i \in [32, 126]$ is the plain text recovered, and \bmod is the module operation.

III. EXPERIMENTAL RESULT

All the analysis are implemented in a Laptop with AMD Turion 64 2.0 GHz CPU, 3.18 GB RAM, and Windows XP 32 bit

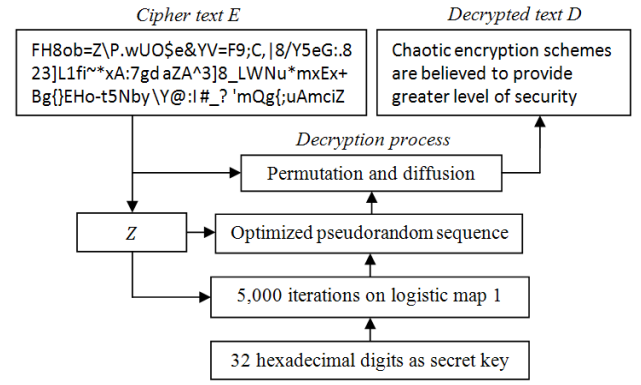


Figure 3: Block diagram of decryption process.

operative system. MatLab software is used with floating point representation type double (64 bits); therefore we use a 10^{-15} decimal precision.

A. Encryption

The proposed algorithm has the capacity to encrypt any printable characters from ASCII table with T maximum length. The first plain text P used is “*Chaotic encryption schemes are believed to provide greater level of security than conventional ciphers*” and the secret key used is “1234567890ABCDEF1234567890ABCDEF” to generate the cipher text: FH8ob=Z\P.wUO\$e&YV=F9;C,|8/Y5eG:.823]L1fi~*xA:7gdaZA^3]8_LWNU*mxEx+Bg{}EHO;t5Nby\Y@:I#_?'mQg{;uAmciZ

B. Secret Key Size Analysis

Nowadays, a cryptosystem must have more than 2^{100} possible secret key (all them strong) to be infallible versus a brute-force attack [15]. The proposed scheme uses 128 bits secret key, therefore the key size is 2^{128} all them strong based in Fig. 2. The key size can be increase to 256 bits with little modifications on the cipher algorithm.

C. Secret Key Sensitivity Analysis

A good cryptosystem must be sensitive at secret keys; this means that two cipher text generated with similar secret key should be very different. In TABLE II(a), the decrypted text is presented with correct secret key; in TABLE II(b)-(c), the decrypted text is presented with two incorrect secret keys but very similar between them. The decrypted text with incorrect key does not show any information related with plain text, therefore the proposed scheme is sensitive to secret key.

D. Frequency Analysis

The frequency analysis is based in histograms. The histogram shows how many times a symbol appears in some text; this kind of attack can give information to find the plain text, the secret key or both. If the histogram of the cipher text has all symbols in a uniform way, the algorithm could resist a frequency attack. In other side, if the histogram is not uniform, it means a weak encryption and it could be subject to a successful frequency attack in the language it was originally encrypted.

TABLE II. SECRET KEY SENSITIVITY ANALYSIS: a) DECRYPTED TEXT WITH CORRECT SECRET KEY “1234567890ABCDEF1234567890ABCDEF”, b) DECRYPTED TEXT WITH INCORRECT SECRET KEY “1234567990ABCDEF1234567890ABCDEF” AND c) DECRYPTED TEXT WITH INCORRECT SECRET KEY “1234567890ABCDEF1234567990ABCDEF”.

a) Chaotic encryption schemes are believed to provide greater level of security than conventional ciphers
b) 2 b kE".Qs'SZVh.;n.guh00TNz^&hVqSepPi8}+Ixk%L8E6#dxwJDsB/=R;*v[1pTwH,dM2f<H^=,7H!5!57A{czz.>P}kn3*2EDJ
c) p>n]X+1'd>OE1u'rTY[HI%S6)8EHh4(ABweXevK#pJh)j9s(,2M1/5=Gf;!HQ(sBJW&+'[oi[t?+)w8^u\$<Z=Q;&mNr8vLMet-'^

The plain text (abstract of this work with 1126 characters) histogram is shown in Fig. 4(a). In Fig. 4(b), the cipher text histogram is shown; it is uniform, so the proposed scheme is robust against histogram attacks and letter frequency attacks.

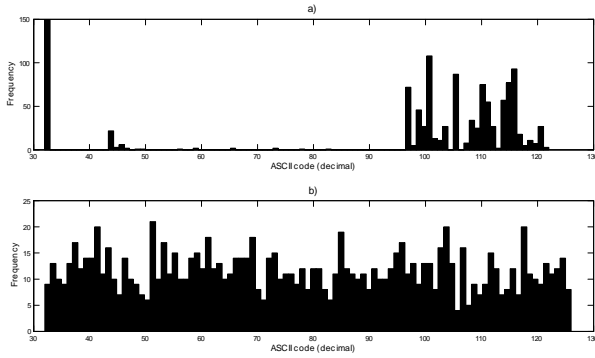


Figure 4: Histograms: a) plain text and b) cipher text.

E. Autocorrelation Analysis

The autocorrelation calculates the similitude between two sequences: the plain text and the plain text displaced t positions. The autocorrelation analysis can be used to determine the secret key length in classic cipher methods. In Fig. 5, the plain text (upper line) and cipher text (lower line) autocorrelation are showed from Fig. 4(a)-(b), respectively. The graphic shows that cipher text autocorrelation is reduced and it is uniform compared with the plain text autocorrelation. Therefore, the proposed scheme can resist an autocorrelation attack.

F. Information Entropy Analysis

When the plain text is encrypted in diffusion stage, the value of all the symbols must be modified. If this process is inefficient, the cipher text would have many identical symbols and it can be subject to an entropy attack. The entropy $H(m)$ from a message m can be calculated as follows

$$H(m) = \sum_{i=0}^{2^N-1} p(m_i) \log_2 \left(\frac{1}{p(m_i)} \right), \quad (13)$$

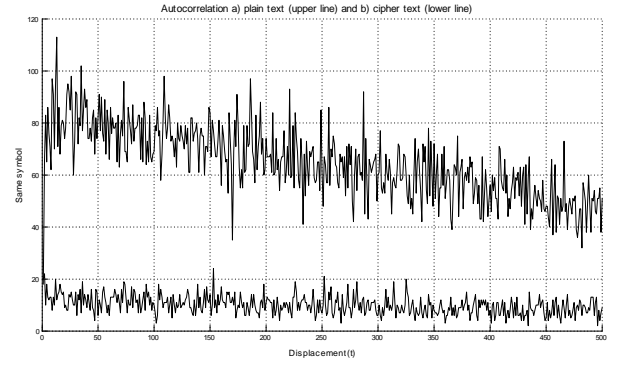


Figure 5: Autocorrelation of a) plain text and b) cipher text.

where N is the number of bits of the message m , 2^N means all possible symbols, $p(m_i)$ represents the probability of m_i , \log_2 represent the base 2 logarithm, and the entropy is expressed in bits. If a message m is encrypted with 2^N possible symbols, the entropy should be $H(m) = N$ ideally. In the proposed scheme are 95 different symbols, so the maximum entropy is $H \approx 6.56$.

The plain text entropy (from Fig. 4(a)) is $H(\text{plain text}) \approx 4.21$ and the corresponding cipher text entropy (from Fig. 4(b)) is $H(\text{cipher text}) \approx 6.48$, this means all cipher symbols appear with almost the same probability; therefore, the diffusion process is strong.

G. Differential Analysis

In this section, the plain text sensitivity is presented to determine the robustness against differential attacks. The attack is based in the encryption of two similar plain text with same secret key to determine some relation between plain text and cipher text. If a little change in plain image generates a big change in cipher text, then the differential attack results inefficient [12]. There are two metrics to determine this robustness: NPCR (Net Pixel Change Rate) and UACI (Unified Average Changing Intensity); NPCR measures the number of characters that are different between two cipher texts E_1 and E_2 from two similar plain text, the value of NPCR is represented in percentage, where 100% means both cipher texts are totally different. The NPCR is calculated with

$$NPCR = \frac{\sum_{i=1}^{\ell} W(i)}{\ell} \times 100, \quad (14)$$

where ℓ is the text length and

$$W(i) = \begin{cases} 0, & \text{if } E_1(i) = E_2(i) \\ 1, & \text{if } E_1(i) \neq E_2(i) \end{cases} \quad (15)$$

By the other hand, UACI is the intensity difference average between two cipher texts E_1 and E_2 , where 100% indicates both texts are totally different in amplitude. The UACI is calculated as follows

$$UACI = \frac{100}{\ell \times 95} \sum_{i=1}^{\ell} |E_1(i) - E_2(i)| \quad (16)$$

where ℓ is the text length, $E_1(i)$ and $E_2(i)$ are the symbol value of the cipher text E_1 and E_2 . In the scheme proposed, the NPCR and UACI are obtained with the following steps: first, the plain text from Fig. 4(a) is encrypted with one secret key to generate the cipher text E_1 ; after that, the first symbol of plain text is change from "I" to "J" and the encryption process is repeated with the same secret key to generate the cipher text E_2 . In TABLE III shows the result of NPCR and UACI. Therefore, the scheme proposed is robust against differential attacks.

TABLE III. DIFFERENTIAL ANALYSIS RESULTS OF NPCR AND UACI.

NPCR (%)	98.85
UACI (%)	33.31

H. Robustness Against Classic Attacks

The cryptanalyst knows the encryption algorithm but he does not know the secret key, this is known as Kerckhoffs principle. If a cryptanalyst has access to the encryption machinery, it can implement some differential attacks as cipher text only attack and known/chosen plain text attack [18].

In cipher text only attack, the cryptanalyst has a cipher text and he can decrypt it until find a plain text with sense, therefore is basically a brute force attack. Known/chosen plain text attack are more powerful; its objective is find the secret key to decrypt others cipher texts encrypted with the same secret key. In the proposed scheme, the permutation–diffusion process is realized in one stage; in addition, the chaotic data are calculated from both the secret key and the plain text characteristics. If the same secret key is used to encrypt many plain texts, the cipher texts will result from different chaotic data.

It is known that the logistic map generates many values close to 0 and 1 (Fig. 6(a)) and they are not appropriate to be used in diffusion process; we modified chaotic data in Equation (7) for a better pseudorandom data distribution (Fig. 6(b)) to prevent a known/chosen plain text attack.

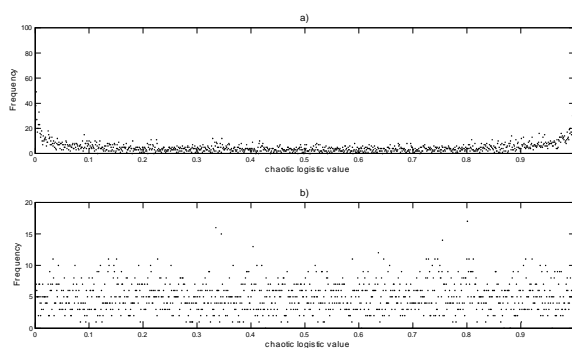


Figure 6: Distribution of 5000 chaotic logistic values with 0.001 of separation, a) data directly from logistic map and b) data used in diffusion process.

I. Encryption Time Analysis

A good encryption algorithm must be robust but it must be fast for real-time applications. The encryption time of 1126

symbols (abstract of this paper) is just 0.140 seconds; the decryption time is 0.109 seconds. Therefore, the algorithm proposed is fast to encrypt text and it can be implemented in real-time applications.

IV. CONCLUSION

A novel symmetric text encryption algorithm based in chaos was presented. A 128 bits secret key was used in a 32 digit hexadecimal format. A complete security analysis was realized over the algorithm with excellent results based in MatLab simulations: it has a big secret key size to resist a force-brute attack, all secret keys are considered strong based in Lyapunov exponent analysis, it is sensitive at secret key and plain text, it can resist an entropy attack, it generates a uniform histogram with low autocorrelation, it is robust against classic attacks, and the encryption time is fast. Therefore, the algorithm proposed can encrypt text with high performance, high security, and it can be implemented in real-time applications.

REFERENCES

- [1] Federal Information Processing Standards Publication 197, "Advanced Encryption Standard (AES)", 2001.
- [2] L. M. Adleman, "Molecular computation of solution to combinatorial problems", *Science*, Vol. 266, pp. 1021–2024, 1994.
- [3] C. Taylor, V. Risca and C. Bancroft, "Hiding messages in DNA microdots", *Nature*, Vol. 399, pp. 533–534, 1999.
- [4] X. Guozhen, L. Mingxin, Q. Lei and L. Xuejia, "New field of cryptography: DNA cryptography", *Chinese Science Bulletin*, Vol. 51 No. 12, 1413–1420, 2006.
- [5] M. Bordoia and O. Tornea, "DNA secret writing techniques", 8th International Conference on Communications (COMM), 2010.
- [6] M. R. Abbasy, A. A. Manaf and M. A. Shahidan, "Data hiding method based on DNA basic characteristics", *DEIS 2011*, CCIS 194, pp. 53–62, 2011.
- [7] L. XueJia, L. MingXin, Q. Lei, H. JunSong and F. XiWen, "Asymmetric encryption and signature method with DNA technology", *Sci China Inf Sci*, 53: 506–514, doi: 10.1007/s11432-010-0063-3, 2010.
- [8] M. Mishra and V.H. Mankar, "Message embedded cipher using 2-D chaotic map", *International Journal of Chaos, Control, Modelling and Simulation (IJCCMS) Vol.1, No.1*, 2012.
- [9] L. Hongjun, W. Xingyuan, "Color image encryption based on one-time keys and robust chaotic maps", *Computers and Mathematics with Applications* 59, 3320–3327, 2010.
- [10] Z. Peng and W. Liu, "Color image authentication based on spatiotemporal chaos and SVD", *Chaos, Solitons and Fractals* 36, 946–952, 2008.
- [11] N.K. Pareek, V. Patidar, K.K. Sud, "Image encryption using chaotic logistic map", *Image and Vision Computing* 24, 926–934, 2006.
- [12] V. Patidar, N.K. Pareek, K.K. Sud, "A new substitution–diffusion based image cipher using chaotic standard and logistic maps", *Commun Nonlinear Sci Numer Simulat* 14, 3056–3075, 2009.
- [13] D. Chen, Y. Chang, "A Novel Image encryption algorithm based on logistic maps", *Advances in Information Sciences and Service Sciences*, Vol. 3, No. 7, 2011.
- [14] X. Wang, L. Teng, X. Qin, "A novel colour image encryption algorithm based on chaos", *Signal Processing* 92, 1101–1108, 2012.
- [15] G. Alvarez and S. Li, "Some basic cryptographic requirements for chaos-based cryptosystems", *International Journal of Bifurcation and Chaos*, Vol. 16, No. 8, pp. 2129–2151, 2006.
- [16] G. Chen, Y. Mao, C.K. Chui, "A symmetric image encryption based on 3D chaotic maps", *Chaos Solitons Fractals* 21, 749–761, 2004.
- [17] H. Gao, Y. Zhang, S. Liang, D. Li, "A new chaotic algorithm for image encryption", *Chaos, Solitons and Fractals* 29, 393–399, 2006.
- [18] T-H Chen, C-S Wu, "Compression-unimpaired batch-image encryption combining vector quantization and index compression", *Information Sciences* 180, 1690–1701, 2010.

Deterministic Sequences From a Fibonacci Series For PAPR Reduction in SLM-OFDM Systems

Saheed A. Adegbite, Scott G. McMeekin and Brian G. Stewart

Abstract—Chaotic-Binary (CB) sequences have been successfully employed in selected mapping (SLM) schemes to reduce peak-to-average power ratio (PAPR) in Orthogonal Frequency Division Multiplexing (OFDM) systems. However, construction and implementation of CB sequences on a Digital Signal Processor (DSP) require a significant number of complex computations and therefore put additional constraints on limited DSP resources. This paper presents and investigates the PAPR reduction capabilities of Binary-Polynomial (BP) sequences whose coefficients are selected from numbers in a Fibonacci series. Simulations compare PAPR reduction performance and the computational complexity of the proposed sequences over CB sequences. Results show that the proposed BP sequences offer comparable PAPR reduction performance to CB sequences but have the advantage of significantly reduced computational complexity.

Keywords—Binary-Polynomial, Chaotic-Binary, Fibonacci series, OFDM, PAPR, SLM sequences.

I. INTRODUCTION

ORTHOGONAL Frequency Division Multiplexing (OFDM) has been chosen as one of the key physical layer technologies for many high speed communication systems including the 4G-Long Term Evolution (4G-LTE) system. OFDM offers immunity to multipath fading, high spectral efficiency and very high data rate transmission [1]. However, since OFDM is a multi-carrier modulation technique, it has very large peak amplitude signals which often leads to high Peak-to-Average Power Ratio (PAPR) [2], [3]. High PAPR may increase the dynamic range of OFDM signals and hence the need for higher precision Analogue-to-Digital (A/D) and Digital-to-Analogue (D/A) converters [3], [4]. Also, large PAPR values may lead to non-linear operation of Power Amplifiers (PA) which may cause non-linear distortion and hence degradation of system performance [4], [5]. Therefore, occurrence of high PAPR must be suppressed to avoid system performance degradation and to reduce design complexities associated with some aspects of an OFDM system such as PAs, A/D and D/A converters [6], [7].

Reviews of various PAPR reduction techniques have already been carried out in the literature [8]–[10]. These techniques include signal clipping [11]–[13], constellation shaping [14], partial transmit sequences (PTS) [15] and selected mapping (SLM) [16]. Of all these methods, SLM is considered as an effective PAPR reduction method because it offers more PAPR reduction performance compared to other PAPR reduction schemes [17]–[19]. Also, since high peak amplitude signals exist in OFDM at some time instant when there is coherent addition of subcarrier symbols, then since orthogonality of these subcarrier symbols is independent of

their phases, changing the phase for each subcarrier symbol can reduce the occurrence of high PAPR values [20]. This is the basic theory behind PAPR reduction in SLM.

In SLM, multiple phase sequences are used to create alternative time domain OFDM signals. One of these signals, which has the lowest PAPR value is selected and transmitted. However, one of the major disadvantages of SLM is that it requires the transmission and detection of some side information (SI). This SI represents the optimum phase sequence vector that produced the transmitted signal with the lowest PAPR [21], [22]. Several authors [23]–[25] have already developed SLM techniques which do not require transmission of SI, but these methods require complex signal processing to recover the data.

In addition, in an attempt to reduce SI, deterministic sequences have already been applied in the literature [26]–[28]. With deterministic sequences, only the u^{th} index of the optimum sequence vector is transmitted. This reduces the amount of SI transmission from at least N to just $\log_2(U)$ bits where N represents the number of subcarrier symbols in an OFDM symbol and U is the number of SLM sequence vectors.

Chaotic-Binary (CB) [26] sequences belong to a family of deterministic binary sequences. These sequences are referred to as binary sequences because their elements have values chosen from the set $\{\pm 1\}$ to produce 0 and π phase shifts. In [26], application of CB sequences in SLM schemes produce improved PAPR reduction performance [26] over Shapiro-Rudin (SR) sequences. This improved performance was later attributed to the low cross correlation value of any two alternative SLM-OFDM signals created as a result of applying CB sequences [26].

However, despite this improved PAPR reduction capability, the selection and subsequent application of CB sequences in SLM schemes may not be effective since its implementation on a Digital Signal Processor (DSP) requires significant signal processing power. Thus, the power consumption by the DSP during construction of CB sequences may be larger than the amount of power saved due to reduced PAPR.

Therefore, the focus of this paper is to develop alternative SLM sequences which have lower computational complexity and comparable PAPR reduction performance compared to CB sequences. This paper presents a new category of binary sequences derived from binary representation of a polynomial and hence referred to as Binary-Polynomial (BP) sequences. The coefficients i.e. the exponents of non-zero terms of such a polynomial are taken from the numbers in a Fibonacci

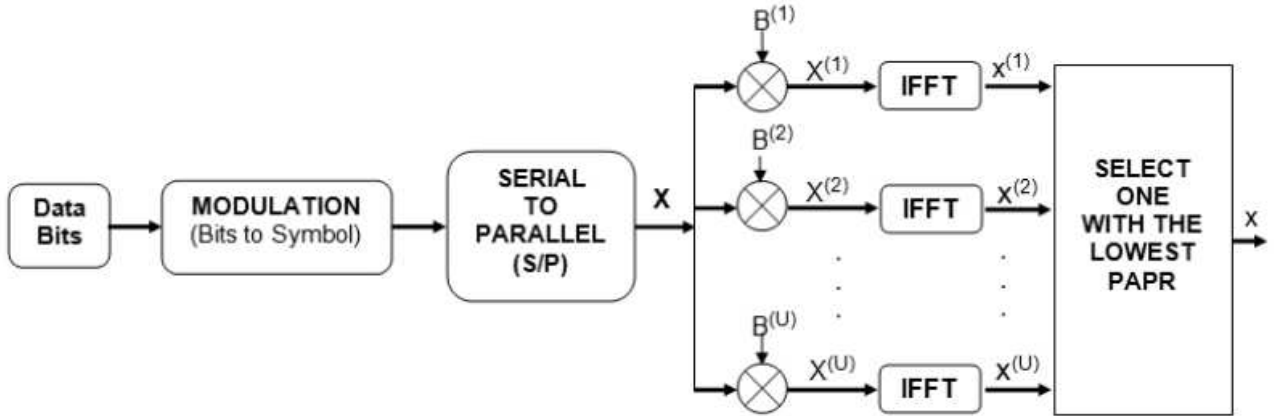


Fig. 1: Block Diagram: SLM-PAPR reduction in OFDM System

series. Simulations evaluate and compare PAPR performance and computational complexity associated with the application and construction of the CB and proposed BP sequences.

The paper is structured as follows. Section II describes a typical SLM-OFDM system model. Section III presents the method for constructing CB sequences while section IV describes the construction of the proposed BP sequences. Section V presents and discusses simulation PAPR reduction performance while section VI discusses the computational requirements of constructing CB and BP sequences. Finally, conclusions based on these results are presented in section VII.

II. SLM-OFDM SYSTEM MODEL

This section gives a brief description of an SLM-OFDM system. A block diagram of a typical SLM-OFDM system is presented in Fig. 1.

In an SLM-OFDM system, data bits are first mapped to complex data symbols according to a chosen modulation scheme such as M-ary Quadrature Amplitude Modulation (QAM). This is followed by the SLM scheme which involves the following processes:

(a) *Multiplication*: Let X_k and $B_k^{(u)}$ be the original data subcarrier symbols of an OFDM symbol and U SLM sequence vectors respectively for $k = 0, 1 \dots N - 1$ and $u = 1, 2, \dots U$ where N is the number of data subcarrier symbols. An alternative OFDM symbol $X_k^{(u)}$ is created by rotating phases of each data subcarrier symbol. This is equivalent to multiplying $B_k^{(u)}$ with X_k as expressed by

$$X_k^{(u)} = X_k \cdot B_k^{(u)} \quad (1)$$

where $X_k^{(u)}$ is the resulting frequency domain SLM-OFDM symbol.

(b) *Transformation*: After multiplication, $X_k^{(u)}$ is transformed

to a time domain signal $x_n^{(u)}$ through

$$x_n^{(u)} = IFFT\{X_k^{(u)}\} = \frac{1}{\sqrt{N}} \sum_{k=0}^{N-1} X_k^{(u)} e^{j2\pi nk} \quad (2)$$

where $IFFT$ is an inverse fast Fourier transform (IFFT) function.

(c) *PAPR Calculation*: PAPR of each alternative SLM-OFDM signal $x_n^{(u)}$ is calculated through

$$PAPR\{x_n^{(u)}\} = \frac{\max\{|x_n^{(u)}|^2\}}{E\{|x_n^{(u)}|^2\}} \quad (3)$$

where $E\{\cdot\}$ represents the expectation function which is used for evaluating the average power of a time domain signal.

(d) *Signal Selection*: The time domain signal with the lowest PAPR is selected and transmitted. First, the optimum index \bar{u} that correspond to the signal with the lowest PAPR is determined, i.e.

$$\bar{u} = \arg \min_{u=1,2, \dots U} PAPR\{x_n^{(u)}\} \quad (4)$$

where $\bar{u} \in u$. Then the signal \bar{x}_n with the lowest PAPR is selected i.e.

$$\bar{x}_n = x_n^{\bar{u}} = IFFT\{X_k \cdot B_k^{(\bar{u})}\} \quad (5)$$

where $B_k^{(\bar{u})}$ denotes the optimum SLM sequence vector. This is the SI which is normally transmitted and must be received without error for successful data recovery.

III. CONSTRUCTION OF CB SEQUENCES

This section describes the method of constructing CB sequences as outlined in [26].

TABLE I: Binary Sequence From 7 to 10 terms of a Fibonacci Series

Terms	Polynomial	Bit Format	Binary Format
$F_7(x)$	[8, 5, 3, 2, 1, 0]	100101111	-111 - 11 - 1 - 1 - 1 - 1
$F_8(x)$	[13, 8, 5, 3, 2, 1, 0]	10000100101111	-11111 - 111 - 11 - 1 - 1 - 1 - 1
$F_9(x)$	[21, 13, 8, 5, 3, 2, 1, 0]	1000000010000100101111	-11111111 - 11111 - 111 - 11 - 1 - 1 - 1 - 1 - 1
$F_{10}(x)$	[34, 21, 13, 8, 5, 3, 2, 1, 0]	10000000000001000000010000100101111	-11111111111111 - 11111111 - 11111 - 111 ... -11 - 1 - 1 - 1 - 1 - 1

TABLE II: Simulation Parameters

Parameters	Values
Number of OFDM symbol blocks, S_T	1E6
Number of data subcarriers, N	512 and 1024
Number of SLM sequence vectors, U	16
Modulation Schemes	16-QAM

CB sequences have already been applied in several applications such as compressive sensing [29] and spread spectrum multiple access schemes [30], [31]. Also, they have been applied in SLM schemes to reduce PAPR in OFDM systems [26], [32].

CB sequences are constructed using an iterative equation given by

$$c_{n+1} = 1 - 2c_n^2 \quad (6)$$

where $c_0 \in (-1, 1)$. An $N \times 1$ CB vector is first formed as follows:

- step 1: Calculate c_n for $n = 0, 1, 2, \dots, N-1$ where $c_n \in \mathbb{R}$. This step requires $2N$ real floating point multiplications and N real floating point subtractions.
- step 2: Obtain equivalent CB vector C_n from c_n using the transformation

$$C_n = \text{sgn}(c_n) \quad (7)$$

where $\text{sgn}(\cdot)$ is the signum function and $C_n \in \{\pm 1\}$.

The required U CB sequence vectors are then formed by circular shifting of C_n .

IV. PROPOSED: BINARY POLYNOMIAL

This section presents the method for generating proposed BP sequences using polynomial coefficients defined from the numbers in a Fibonacci series.

The Fibonacci series was first introduced by Leonardo Fibonacci in 1202 [33]. These series have been employed in many subject areas such as art, architectural designs, geometry and mathematics [33]. Also, they have been found to be useful in search algorithms [34] [35]. The original Fibonacci series is a sequence of integers [33] defined by $F_n = F_{n-1} + F_{n-2}$ where $F_0 = 1$ and $F_n = 0$ for $n < 0$. However, in modern representation of the series $F_0 = 0$ and $F_1 = 1$. Thus, the modern form of the series is referenced as 0, 1, 1, 2, 3, 5, 8, 13, 21, 34, 55 ...

By re-arranging the numbers in a Fibonacci series in descending order, these numbers can be used to define a polynomial since polynomials can be represented using either an integer or a bit format. An integer representation of a polynomial defines an array of the exponents of non-zero terms while in bit format, 1s and 0s are assigned to non-zero and zero polynomial terms respectively. As an example, consider a polynomial $P(x) = x^{10} + x^7 + x^1 + 1$ which can be written as [10 7 1 0] using the integer format and as 1001000011 using the bit representation format.

In SLM schemes, this bit format can be transformed to a binary sequence of 1s and -1s by replacing 0s and 1s in the bit representation with 1 and -1 respectively. Thus, binary form of $P(x)$ above becomes -111-111111-1-1. Therefore, similar to CB sequences, phase elements 1 and -1 in BP sequences will also produce 0 and π phase shifts respectively when applied in SLM.

Also, since SLM requires $N\dot{U}$ phase elements in total, then in SLM schemes, BP sequences are constructed from the cyclic shifting of this binary polynomial representation until the number of elements in BP sequences $\geq N\dot{U}$.

Table I shows resulting binary sequence derived from the integer and bit representations of 8, 13, 21 and 34-degree polynomials where the coefficients are taken from the first 7 to 10 terms of a Fibonacci series represented by the polynomial $F_7(x)$, $F_8(x)$... $F_{10}(x)$ respectively. Also, since there are two 1s at the start of a Fibonacci series, only the first one is selected when defining the polynomial for BP sequences.

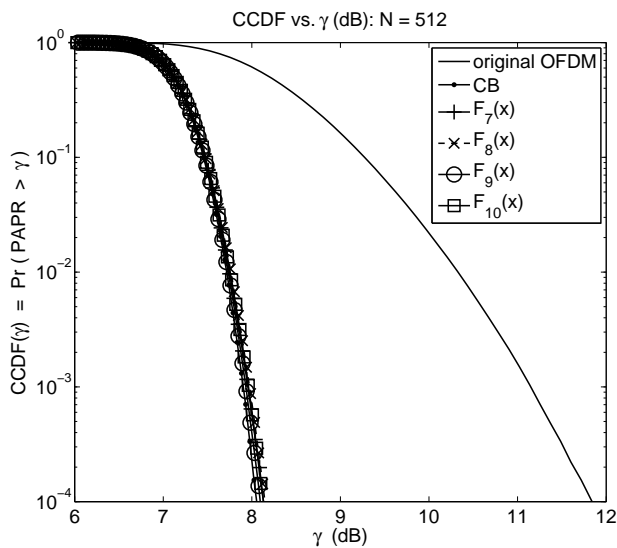
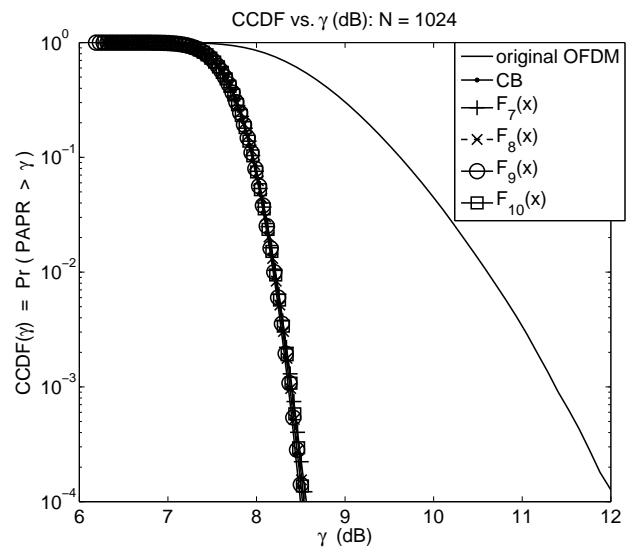
V. SIMULATION RESULTS

Matlab simulations were carried out to evaluate and compare the PAPR reduction performance of an SLM-OFDM system based on parameters presented in Table II. SLM-PAPR reduction is then performed using CB and BP sequences.

The Complementary Cumulative Distribution Function (CCDF) is chosen as a metric for evaluating the PAPR reduction performance. CCDF gives the probability of a calculated PAPR value $PAPR$ (dB) exceeding a given threshold γ dB level. CCDF is thus defined [9] as

$$CCDF\{\gamma\} = \text{Prob}(PAPR > \gamma) \quad (8)$$

Before obtaining CCDF, PAPR value of each transmitted OFDM signal block is calculated. CCDF is then evaluated for each OFDM signal blocks at various threshold PAPR level γ .


 Fig. 2: CCDF vs. γ ($N = 512$)

 Fig. 3: CCDF vs. γ ($N = 1024$)

Figs. 2 and 3 show the resulting CCDF curves as a function of γ (dB) from the application CB and 4 sets of BP sequences used in SLM schemes when N is set to 512 and 1024 respectively. Results in Figs. 2 and 3 show that BP sequences produce slightly less but comparable PAPR reduction performance to CB sequences. Also, these result show that there is very little difference in the PAPR reduction performance of each set of BP sequences.

In addition, the actual PAPR reduction gain $\Delta\gamma$ (dB) i.e. the difference between the PAPR values of original OFDM signal and SLM-OFDM signal is also evaluated for CCDF probability values of 10^{-3} and 10^{-4} to provide a simpler numerical comparison of PAPR reduction performance between CB and BP sequences. Thus, $\Delta\gamma$ (dB) may be calculated as

$$\Delta\gamma = \gamma_{OFDM} - \gamma_{SLM}^{\bar{u}} \quad (9)$$

where γ_{OFDM} and $\gamma_{SLM}^{\bar{u}}$ are the PAPR values of the original OFDM signals and SLM-OFDM signals respectively with the same CCDF probability level.

Table III shows the evaluated values of $\Delta\gamma$ (dB) at CCDF values of 10^{-4} and 10^{-3} when N is set to 512 and 1024. Data presented in this table clearly shows that both CB and BP sequences provide similar PAPR reduction gain for a CCDF probability value of 10^{-3} . However, at a lower CCDF probability value of 10^{-4} , CB sequences are likely to produce ≈ 0.1 dB more PAPR reduction compared to BP sequences.

Although, CB sequences seem to produce improved PAPR reduction performance compared to BP sequences, its implementation require a floating point DSP since it involves floating point mathematical operations. This may result in an increase in the computational complexity of constructing CB sequences compared to BP sequence implementation which

 TABLE III: Comparison of $\Delta\gamma$ (dB) at CCDF = 10^{-4} and 10^{-3}

Sequences/CCDF	$N = 512$		$N = 1024$	
	10^{-4}	10^{-3}	10^{-4}	10^{-3}
CB	3.800065	3.201392	3.599991	3.000719
$F_7(x)$	3.700011	3.200360	3.500075	2.999588
$F_8(x)$	3.700079	3.199847	3.500132	3.000136
$F_9(x)$	3.799919	3.200858	3.500156	3.000318
$F_{10}(x)$	3.700111	3.200168	3.500140	2.999811

requires reduce computational complexity. Also, BP sequences can easily be implemented on a fixed point DSP. Therefore, to provide an insight into the added value of applying BP sequences over CB sequences, the next section compares the computational requirements associated with the construction of CB and BP sequences.

VI. COMPUTATIONAL COMPLEXITY

In this section, the computational complexity involved in the construction of CB and BP sequences for SLM-PAPR reduction is discussed to further show some of the advantages of the proposed BP sequences over CB sequences, when implemented on a DSP.

As an example, consider the Texas Instruments (TI) TMS320C67x DSP [36] device. On this platform single precision (32-bit) floating point multiplication, addition and subtraction operations each take 5 clock cycles while floating point compare, fixed point unsigned integer addition and bit-wise logical operations are single cycle operations. Fig. 4 shows graphs of the estimated number of total DSP clock cycles for CB and BP sequences as a function of various numbers of subcarriers, i.e. $N = 64, 128, 256 \dots 4096$. Fig. 4 shows that BP sequences require significantly less DSP resources even for large values of N compared to CB

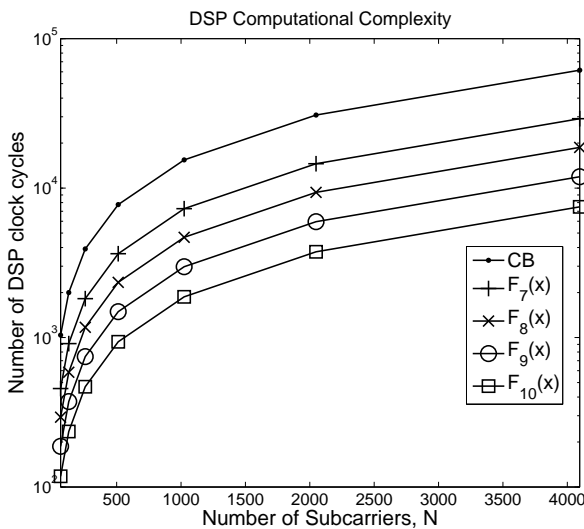


Fig. 4: DSP complexity (clock cycles) vs. N

sequences.

VII. CONCLUSIONS

Low complexity binary deterministic SLM sequences obtained from a Fibonacci series have been proposed. These sequences are referred to as BP sequences and have been shown to offer slightly less but comparable PAPR reduction performance to CB sequences. However in terms of complexity, proposed BP sequences require a much reduced number of computational resources compared to CB sequences which require significantly high computational requirements. Therefore, when reduced complexity in combination with good PAPR reduction is required, the proposed BP sequences may be a preferred choice of SLM sequences compared to CB sequences.

ACKNOWLEDGEMENTS

This work was supported by the School of Engineering and Built Environment of Glasgow Caledonian University through a University sponsored research scholarship.

REFERENCES

- [1] S. Adegbite, B. Stewart, and S. McMeekin, "Least Squares Interpolation Methods for LTE System Channel Estimation over Extended ITU Channels," *International Journal of Information and Electronics Engineering*, vol. 3, no. 4, pp. 414–418, July 2013.
- [2] A. Vallavaraj, B. Stewart, D. Harrison, and F. McIntosh, "Reduction of Peak-to-Average Power Ratio of OFDM symbols using phasing schemes combined with companding," in *GCC Conference (GCC), 2006 IEEE*, 2006, pp. 1–5.
- [3] J. Armstrong, "OFDM for Optical Communications," *Lightwave Technology, Journal of*, vol. 27, no. 3, pp. 189–204, 2009.
- [4] B. Stewart and A. Vallavaraj, "The Application of u-Law Companding to the WiMax IEEE802.16e Down-Link PUSC," in *Parallel and Distributed Systems, 2008. ICPADS '08. 14th IEEE International Conference on*, 2008, pp. 896–901.

- [5] K. Bae, C. Shin, and E. J. Powers, "Performance Analysis of OFDM Systems with Selected Mapping in the Presence of Nonlinearity," *Wireless Communications, IEEE Transactions on*, vol. 12, no. 5, pp. 2314–2322, 2013.
- [6] A. Vallavaraj, B. Stewart, D. Harrison, and F. McIntosh, "Reduction of peak to average power ratio of OFDM signals using companding," in *Communications Systems, 2004. ICCS 2004. The Ninth International Conference on*, 2004, pp. 160–164.
- [7] H.-S. Joo, S.-J. Heo, H.-B. Jeon, J.-S. No, and D.-J. Shin, "A New Blind SLM Scheme With Low Decoding Complexity for OFDM Systems," *Broadcasting, IEEE Transactions on*, vol. 58, no. 4, pp. 669–676, 2012.
- [8] S. H. Han and J. H. Lee, "An overview of peak-to-average power ratio reduction techniques for multicarrier transmission," *Wireless Communications, IEEE*, vol. 12, no. 2, pp. 56–65, April 2005.
- [9] T. Jiang and Y. Wu, "An Overview: Peak-to-Average Power Ratio Reduction Techniques for OFDM Signals," *Broadcasting, IEEE Transactions on*, vol. 54, no. 2, pp. 257–268, 2008.
- [10] D.-W. Lim, S.-J. Heo, and J.-S. No, "An overview of peak-to-average power ratio reduction schemes for OFDM signals," *Communications and Networks, Journal of*, vol. 11, no. 3, pp. 229–239, 2009.
- [11] J. Armstrong, "Peak-to-average power reduction for OFDM by repeated clipping and frequency domain filtering," *Electronics Letters*, vol. 38, no. 5, pp. 246–247, 2002.
- [12] H. Ochiai and H. Imai, "Performance analysis of deliberately clipped OFDM signals," *Communications, IEEE Transactions on*, vol. 50, no. 1, pp. 89–101, 2002.
- [13] L. Wang and C. Tellambura, "A simplified clipping and filtering technique for PAR reduction in OFDM systems," *Signal Processing Letters, IEEE*, vol. 12, no. 6, pp. 453–456, 2005.
- [14] A. Mobasher and A. Khandani, "Integer-based constellation-shaping method for PAPR reduction in OFDM systems," *Communications, IEEE Transactions on*, vol. 54, no. 1, pp. 119–127, 2006.
- [15] S. Muller and J. Huber, "OFDM with reduced peak-to-average power ratio by optimum combination of partial transmit sequences," *Electronics Letters*, vol. 33, no. 5, pp. 368–369, 1997.
- [16] R. Bauml, R. Fischer, and J. Huber, "Reducing the peak-to-average power ratio of multicarrier modulation by selected mapping," *Electronics Letters*, vol. 32, no. 22, pp. 2056–2057, Oct. 1996.
- [17] Z. Latinovic and Y. Bar-Ness, "SFBC MIMO-OFDM peak-to-average power ratio reduction by polyphase interleaving and inversion," *Communications Letters, IEEE*, vol. 10, no. 4, pp. 266–268, 2006.
- [18] E. Hassan, S. El-Khany, M. Dessouky, S. El-Dolil, and F. El-Samie, "Peak-to-average power ratio reduction in space-time block coded multi-input multi-output orthogonal frequency division multiplexing systems using a small overhead selective mapping scheme," *Communications, IET*, vol. 3, no. 10, pp. 1667–1674, 2009.
- [19] E. Hong, H. Kim, K. Yang, and D. Har, "Pilot-Aided Side Information Detection in SLM-Based OFDM Systems," *Wireless Communications, IEEE Transactions on*, vol. 12, no. 7, pp. 3140–3147, 2013.
- [20] L. Korowajczuk, *LTE, WiMAX and WLAN Network Design, Optimization and Performance Analysis*. Wiley, 2011.
- [21] A. Vallavaraj, B. Stewart, D. Harrison, and F. McIntosh, "Reducing the PAPR of OFDM Using a Simplified Scrambling SLM Technique with No Explicit Side Information," in *Parallel and Distributed Systems, 2008. ICPADS '08. 14th IEEE International Conference on*, 2008, pp. 902–907.
- [22] E. Badran and A. El-Helw, "A Novel Semi-Blind Selected Mapping Technique for PAPR Reduction in OFDM," *Signal Processing Letters, IEEE*, vol. 18, no. 9, pp. 493–496, 2011.
- [23] A. D. S. Jayalath and C. Tellambura, "SLM and PTS peak-power reduction of OFDM signals without side information," *Wireless Communications, IEEE Transactions on*, vol. 4, no. 5, pp. 2006–2013, 2005.
- [24] R. Baxley and G. Zhou, "MAP metric for blind phase sequence detection in selected mapping," *Broadcasting, IEEE Transactions on*, vol. 51, no. 4, pp. 565–570, 2005.
- [25] S. Le Goff, S. Al-Samahi, B. K. Khoo, C. Tsimenidis, and B. Sharif, "Selected mapping without side information for PAPR reduction in OFDM," *Wireless Communications, IEEE Transactions on*, vol. 8, no. 7, pp. 3320–3325, 2009.
- [26] C. Peng, X. Yue, D. Lili, and L. Shaoqian, "Optimized phase sequence set for SLM-OFDM," in *Communications, Circuits and Systems, 2007. ICCAS 2007. International Conference on*, 2007, pp. 284–287.
- [27] N. Ohkubo and T. Ohtsuki, "Design criteria for phase sequences in

- selected mapping,” in *Vehicular Technology Conference, 2003. VTC 2003-Spring. The 57th IEEE Semi-annual*, vol. 1, 2003, pp. 373–377.
- [28] D.-W. Lim, S.-J. Heo, J.-S. No, and H. Chung, “On the phase sequence set of SLM OFDM scheme for a crest factor reduction,” *Signal Processing, IEEE Transactions on*, vol. 54, no. 5, pp. 1931–1935, 2006.
- [29] L. Yu, J. P. Barbot, G. Zheng, and H. Sun, “Compressive Sensing With Chaotic Sequence,” *Signal Processing Letters, IEEE*, vol. 17, no. 8, pp. 731–734, 2010.
- [30] A. Kurian, S. Puthusserypady, and S. M. Htut, “Performance enhancement of DS/CDMA system using chaotic complex spreading sequence,” *Wireless Communications, IEEE Transactions on*, vol. 4, no. 3, pp. 984–989, 2005.
- [31] C.-C. Chen, K. Yao, K. Umeno, and E. Biglieri, “Design of spread-spectrum sequences using chaotic dynamical systems and ergodic theory,” *Circuits and Systems I: Fundamental Theory and Applications, IEEE Transactions on*, vol. 48, no. 9, pp. 1110–1114, 2001.
- [32] T. Liang-rui, L. Lin-yang, and Z. Qin, “An Improved SLM Method Based on Chaotic Phase Sequences,” in *Wireless Communications, Networking and Mobile Computing, 2009. WiCom '09. 5th International Conference on*, 2009, pp. 1–4.
- [33] S. Aghaian, M.-C. Chen, and C. L. P. Chen, “Noise reduction algorithms using Fibonacci Fourier transforms,” in *Systems, Man and Cybernetics, 2008. SMC 2008. IEEE International Conference on*, 2008, pp. 1048–1052.
- [34] S. Nishihara and H. Nishino, “Binary Search Revisited: Another Advantage of Fibonacci Search,” *Computers, IEEE Transactions on*, vol. C-36, no. 9, pp. 1132–1135, 1987.
- [35] R. Stankovic, M. Stankovic, J. Astola, and K. Egiazarian, “Fibonacci decision diagrams and spectral Fibonacci decision diagrams,” in *Multiple-Valued Logic, 2000. (ISMVL 2000) Proceedings. 30th IEEE International Symposium on*, 2000, pp. 206–211.
- [36] “Texas Instruments (TI): TMS320C67x/C67x+ DSP, CPU and Instruction Set Reference Guide,” Nov. 2006.

Classification of Intravascular Ultrasound Signal by Kernel Density Estimation and Bayes Theorem for Identification of Coronary Plaque Tissue

Hiroki Tanaka, Kazuhiro Tokunaga, Eiji Uchino, and Noriaki Suetake

Abstract—We propose a method for tissue characterization of coronary plaque using IntraVascular UltraSound (IVUS) data. In the proposed algorithm, the probability density function of each plaque is calculated by the kernel density estimation and neural gas. The probability distributions vary continuously and overlap one another in the feature space. The class labels of tissue are determined by using Bayes estimation. This algorithm enables to give more delicate information to a medical doctor, which matches with the real situation of plaque composition. In this paper, the proposed algorithm is presented brief and its effectiveness is confirmed by applying it to the real IVUS data.

Index Terms—IntraVascular UltraSound (IVUS), Tissue Characterization, Kernel Density Estimation, Neural Gas, Bayes Estimation.

I. INTRODUCTION

ACUTE Coronary Syndrome (ACS) is caused by a failure of plaque built inside the coronary arteries. ACS is a heart disease leading to death in the worst case.

A coronary plaque consists of three types of tissue. There are Fibrous, Fatty and Fibrofatty. The plaque is classified into the stable plaque or the unstable plaque depending on the structure of plaque. The stable plaque has thick fibrous tissue and small lipid core. In contrast, the unstable plaque has thin fibrous tissue and large lipid core. The tissue characterization of plaque is very important in order to prevent ACS.

The current tissue characterization uses the Radio Frequency (RF) signal measured by the IntraVascular UltraSound (IVUS) method [1]. In IVUS method, RF signals are obtained by using a catheter attached to an ultrasound probe, and then, tomograms of coronary artery (B-mode images) are made from the RF signals. A medical doctor diagnoses ACS from the B-mode images. However it is difficult even for an experienced medical doctor to diagnose ACS from B-mode image alone.

This work was supported by Grant-in-Aid for Scientific Research (B) of Japan Society for promotion of Science (JSPS) under the Contract No. 23300086.

Hiroki Tanaka is with the Graduate School of Science and Engineering, Yamaguchi University, 1677-1 Yosida, Yamaguchi 753-8512, Japan (e-mail: s015vc@yamaguchi-u.ac.jp).

Kazuhiro Tokunaga is with the Department of Ocean Mechanical Engineering, National Fisheries University, 2-7-1 Nagata-Honmachi, Shimonoseki 759-6595, Japan (phone: +81-832-86-5111; e-mail: tokunaga@fish-u.ac.jp).

Eiji Uchino is with the Graduate School of Science and Engineering, Yamaguchi University (phone: +81-83-933-5699; e-mail: uchino@yamaguchi-u.ac.jp), and also with the Fuzzy Logic Systems Institute, 680-41 Kawazu, Iizuka 820-0067, Japan.

Noriaki Suetake is with the Graduate School of Science and Engineering, Yamaguchi University (e-mail: nsuetake@yamaguchi-u.ac.jp).

Therefore, a tissue characterization system is needed to assist medical doctors.

In the previous studies, some researchers indicated that the frequency analysis is effective in the tissue characterization [2] [3] [4]. Furthermore, we have proposed the Multiple k- Nearest Neighbor (MkNN) method using the power spectra as feature vectors [5]. In those methods, each tissue is characterized as one specific tissue.

However, the actual tissues of the coronary plaque blend with each other. That is, the region characterized as one kind of tissue must include a combination of different tissues. A medical doctor diagnoses the plaque as the stable plaque or the unstable plaque based on the difference in the regions of interest. Therefore, it helps medical doctors to indicate the delicate difference in the regions.

In this paper, we propose a tissue characterization method and representation method of the tissues included in the regions of interest as continual colors.

The details are as follows; firstly, the feature vectors are extracted from RF signals by using Fast Fourier Transform (FFT) after performing some preprocessing. Then, probability density functions of each kind of tissue in the feature space are estimated by using Kernel Density Estimation (KDE) and Neural Gas (NG).

When using NG, the probabilities of tissue are calculated more efficiently in KDE. The existence probabilities of the tissues are characterized by using Bayes estimation. The color of tissue is determined on the values of probabilities. Consequently these colors represent the delicate differences of the tissues.

II. METHOD

A. IVUS Method

IntraVascular UltraSound (IVUS) method gives the tomographic images of coronary arteries. In IVUS method, a catheter with an ultrasound probe attached to its end is inserted in a blood vessel.

Figure 1 shows the catheter inserted in the blood vessel. The probe emits the Radio Frequency (RF) ultrasound signals continually, and then the probe also receives the signals reflected from the vascular wall. Depending on the kind of tissue the RF signal reflects onto, the received signal characteristics are different. The tomographic images (B-mode images) are made by transforming the amplitude values of RF signals into the luminosity values. Figure 2 shows a B-mode image.

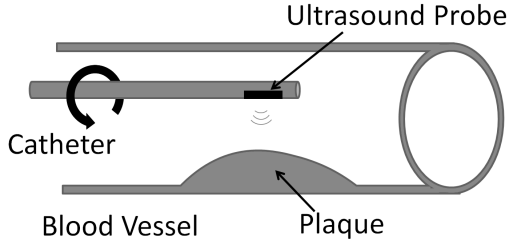


Fig. 1. A catheter with an ultrasound probe is inserted in blood vessel. The emitted ultrasound signals reflect or pass through at the vascular wall.

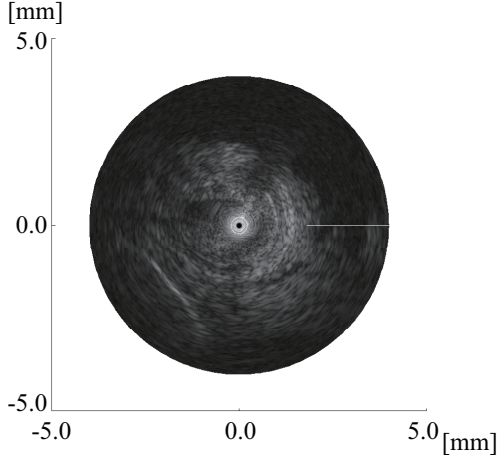


Fig. 2. B-Mode image obtained by using the IVUS method. The amplitudes of RF signal are converted to the luminosity values. A medical doctor refers to the B-mode images to diagnose ACS.

A medical doctor diagnoses ACS and decides the remedies by using a B-mode image. However, a medical doctor should be experienced as it is difficult to diagnose the ACS from the B-mode image alone.

B. Kernel Density Estimation

Kernel Density Estimation (KDE) is a basic nonparametric method for estimating the probability density function. Suppose that the D -dimensional data vectors $\mathbf{x}_i (i = 1, \dots, N)$ are given. The probability density function $p(\mathbf{x})$ which generates the data vectors \mathbf{x}_i is estimated by using the kernel functions $\phi(\mathbf{x})$ as follows:

$$p(\mathbf{x}) = \frac{1}{N} \sum_{i=1}^N \frac{1}{V} \phi\left(-\frac{\mathbf{x} - \mathbf{x}_i}{h}\right). \quad (1)$$

In (1), V is a normalization constant of each kernel function, and h is a bandwidth. The bandwidth is a smoothing parameter for the probability density function $p(\mathbf{x})$. When a small bandwidth is given, the probability density function is sensitive to noise. In contrast, when a big bandwidth is given, the probability density function becomes excessively smooth. Therefore, h is an important parameter for appropriately estimating the probability density function.

Kernel function can be any function if it satisfies the following:

$$\phi(\mathbf{u}) \geq 0, \quad (2)$$

$$\int \phi(\mathbf{u}) d\mathbf{u} = 1. \quad (3)$$

The Gaussian function is generally used as a kernel function. In this paper, we use Gaussian kernel function. The probability density function $p(\mathbf{x})$ is thus expressed as follows:

$$p(\mathbf{x}) = \frac{1}{N} \sum_{i=1}^N \frac{1}{(2\pi h^2)^{D/2}} \exp\left\{-\frac{\|\mathbf{x} - \mathbf{x}_i\|^2}{2h^2}\right\}, \quad (4)$$

where the bandwidth is a standard deviation of a Gaussian function.

In kernel density estimation, this probability density function is equivalent to the true probability density function if the sufficient number of data vectors is provided. However, the computing time is increased greatly.

C. Neural Gas

In the proposed method, Neural Gas (NG) [6] is used for calculating the probability density function of tissue efficiently. The NG is one of the vector quantization methods. It has been reported that the quantization error of NG is smaller than the other methods.

The following shows the algorithm for a batch type NG. The algorithm of the batch type NG repeats the following processes, i.e., evaluation process, competitive process, and adaptation process.

1) Initialization:

Suppose that the D -dimensional data vectors $\mathbf{x}_i (i = 1, 2, \dots, N)$ are given. Moreover, suppose that the NG is composed of the reference vectors $\mathbf{w}_k (k = 1, 2, \dots, K)$. In the first stage of learning, \mathbf{w}_k are initialized by random numbers.

2) Evaluation process:

The distances $d_{i,k}$ between all the reference vectors \mathbf{w}_k and all the data vectors \mathbf{x}_i are calculated by:

$$d_{i,k} = \|\mathbf{x}_i - \mathbf{w}_k\| \forall i, \forall k. \quad (5)$$

3) Competitive process:

The ranking of the reference vectors for each data vector \mathbf{x}_i is evaluated by the distances calculated by (5). After that, the learning rate of each reference vector is determined according its ranking. Here, the learning rate $\psi_{i,k}$ of the k -th reference vector \mathbf{w}_k for the i -th data vector \mathbf{x}_i is defined as follows:

$$\psi_{i,k} = \frac{\phi}{\sum_i \phi_{i,k}}, \quad (6)$$

$$\phi = \exp\left(-\frac{r_{i,k}}{\lambda(i)}\right), \quad (7)$$

where $r_{i,k}$ is a rank of the k -th reference vector \mathbf{w}_k for the i -th data vector \mathbf{x}_i . In addition, $\lambda(t)$ is a monotonically decreasing function for the learning step t . In this work, $\lambda(t)$ is defined as follows:

$$\lambda(t) = (\lambda_{max} - \lambda_{min}) \exp\left(-\frac{t}{\tau}\right) + \lambda_{min}, \quad (8)$$

where τ is a time constant.

4) Adaptation process:

The update rule of all the reference vectors \mathbf{w}_k is defined as follows:

$$\mathbf{w}_k = \sum_{i=1}^N \psi_{i,k} \mathbf{x}_i. \quad (9)$$

In this paper, the semi-batch type NG is employed to provide the consistent results and to process much data.

III. TISSUE CHARACTERIZATION BY IVUS DATA USING KERNEL DENSITY ESTIMATION

The proposed method is divided into the following 3 steps, i.e., feature vector extraction, estimating probability density functions, and characterization.

A. Feature Vector Extraction by Using Fast Fourier Transform

It is reported that the frequency analysis is valid for tissue characterization [2]. In the present method, the power spectra of RF signals are used as feature vectors. Specifically, the RF signals before and after the points of interest are processed by a Fast Fourier Transform (FFT) with a hamming window. As a preprocessing, removing of bias on the RF signal and Time-Gain Compensation (TGC) [7] are performed. TGC is generally done for compensating the attenuation of the ultrasound signal in IVUS method.

B. Estimating Probability Density Function

In the present method, the probability density functions of each tissue are estimated by the using Kernel Density Estimation (KDE) [8]. However, KDE takes much time to calculate the probability density function $p(\mathbf{x})$ if there are a lot of data vectors. The reference vectors $\boldsymbol{\mu}_j (j = 1, \dots, M)$ are thus used as the data vectors $\mathbf{x}_i (i = 1, \dots, N)$ in KDE ($N > M$).

In order to estimate the probability density function with high accuracy and the small number of data vectors, Neural Gas (NG) is used for quantization. It is reported that there are less quantization errors of NG than the other methods. NG is applied to the feature vectors of each tissue. A conditional probability density function $p(\mathbf{x}|\omega)$ is calculated by using (4) and reference vectors $\boldsymbol{\mu}_j$. ω is a class label of tissue.

C. Characterization by Using Bayes Estimation

The proposed method characterizes and represents the delicate and sophisticated differences of the tissue for better helping a medical doctor for diagnosis of ACS. In characterizing, the class label ω of a tissue is determined by:

$$\omega = \arg \max_{\omega_i} p(\omega_i|\mathbf{x}), \quad (10)$$

$$p(\omega_i|\mathbf{x}) = \frac{p(\mathbf{x}|\omega_i)p(\omega_i)}{\sum_{i=1}^I p(\mathbf{x}|\omega_i)p(\omega_i)}, \quad (11)$$

$$p(\mathbf{x}, \omega_i) = p(\mathbf{x}|\omega_i)p(\omega_i), \quad (12)$$

where $p(\omega)$ is a-priori probability. The conditional probability is calculated by (4). Equations (10) and (11) are the maximum a-posteriori probability estimation.

Equation (12) is a joint probability density function. This joint probability density function expresses a probability of characterizing a tissue in the point of interest as each class ω_i : We call this joint probability density existing probability. In this paper, each value of $p(\mathbf{x}, \omega_i)$ is allocated to the luminosity value for representing the delicate and sophisticated differences of tissue. The values of joint probability density functions $p(\mathbf{x}, \omega_1)$, $p(\mathbf{x}, \omega_2)$ and $p(\mathbf{x}, \omega_3)$ are allocated to R, G, and B values, respectively.

IV. EXPERIMENTS

In the experiments, the proposed method is compared with the Multiple k -Nearest Neighbor (MkNN) method proposed by the authors in the past [5]. Firstly, the results of the proposed method and MkNN are compared qualitatively. And then, the accuracy of tissue characterization is numerically evaluated in order to confirm the validity of the proposed method.

A. Experimental Settings

In the experiments, three different sections of the blood vessel were used. The findings in the sections are obtained by a medical doctor. There are three types of tissue, Fibrous, Fatty and Faibrofatty.

The present method is compared with Multiple k -Nearest Neighbor (MkNN) method [5]. MkNN is a method proposed by the authors for tissue characterization [5].

In MkNN method, the class label is determined by considering not only a feature space but also an observation space, under the presumption that adjacent feature vectors in the observation space should be in the same class.

In order to quantitatively evaluate the performance of tissue characterization, each method was compared by using True Positive Rate (TPR) and True Negative Rate (TNR). Leave-one-out cross-validation was also used. TPR and TNR is calculated by the following:

$$TPR = \frac{\text{the number of } TP}{\text{the number of } TP + \text{the number of } FN}, \quad (13)$$

$$TNR = \frac{\text{the number of } TN}{\text{the number of } TN + \text{the number of } FP}, \quad (14)$$

where TP (True Positive) means correct identification, FN (False Negative) means incorrect rejection, TN (True Negative) means correct rejection, and FP (False Positive) means incorrect identification. For using leave-one-out cross-validation, the data are classified into two groups. One is the test data and the other is the training data. Every possible combination of the data is evaluated.

The width of the hamming window for FFT was 64 points. In both the proposed method and the MkNN method, 40 reference vectors were calculated for each tissue by NG. In MkNN method, the number of browsed teaching vectors in the feature space is 9. The bandwidth of the kernel function is 1.7. The experiments were tried 20 times.

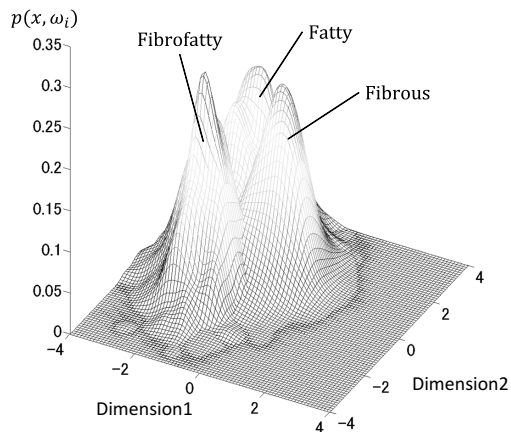


Fig. 3. Probability density function of each tissue. The probability densities are estimated by the kernel density estimation. The characteristic feature space is calculated by the multiple discriminant analysis. In this feature space, the probability densities of each tissue overlap one another.

B. Experimental Results

Fig.3 shows the joint probability density function of each tissue in the two dimensional subspace. The subspace is calculated as to separate most clearly each joint probability density function using the multiple discriminant analysis. It is seen that the probability density functions overlap one another.

Fig.4 (a) shows the tissue composition given by a medical doctor by examining the dyed tissue using a microscope. Fig.4 (b) and (c) are the results by MkNN and by the proposed method. The results of both methods show similar image to the ideal image.

Fig.5 shows the existence probabilities of each tissue. Fig.5 (a), (b), and (c) show the existence probabilities of Fibrous, Fatty, and Fibrofatty. Higher probability is represented by brighter colors. In Fig.5 (d), the values of probabilities of (a), (b), and (c) are allocated to R, G, and B values, respectively. Fig.5 (d) shows the difference in the same section of Fig.4 (c). It also shows the gradual and continuous changes of tissue, which matches with the real situation of plaque composition.

Table I shows the tissue characterization accuracy of the proposed method and MkNN. Proposed method is as accurate as MkNN in classification of Fibrous and Fibrofatty.

As for TNR of Fatty, the accuracy of the proposed method is lower than MkNN. However, the results of both methods designate well the position of the Fibrous tissue in the ideal image of Fig.4 (a). The standard deviations of the proposed method are smaller than MkNN. This means that the present method is more stable than MkNN.

V. CONCLUSIONS

In this paper, we have proposed a tissue characterization method by using a kernel density estimation and a Bayes estimation for IVUS data.

In the present method, the power spectra of RF signals are employed as feature vectors. The probability density functions of each tissue are estimated by using a kernel density estimation based on the quantized feature vectors.

The existence probabilities of unknown input vectors are estimated by using Bayes estimation. The class labels are determined based on the existence probabilities. Furthermore, allocating the existence probabilities to R, G, and B values, the delicate and sophisticated information in the tissue characterization could be visually expressed.

In the experiments, the proposed method was compared with MkNN. The proposed method is more stable than MkNN and it enables to give more delicate information to a medical doctor for a diagnosis.

VI. ACKNOWLEDGEMENTS

Many thanks are due to Prof. Takafumi Hiro of Nihon University, School of Medicine, for providing the IVUS data and for his helpful discussions.

REFERENCES

- [1] J. B. Hodgson, S. P. Graham, A. D. Savakus, S. G. Dame, D. N. Stephens, P. S. Dhillon, H. S. D. Brands, and M. J. Eberle, "Clinical percutaneous imaging of coronary anatomy using an over-the-wire ultrasound catheter system," *The International Journal of Cardiovascular Imaging*, vol. 4, pp. 178–193, 1989.
- [2] M. P. Moore, T. Spencer, D. Salter, P. Kearney, T. Shaw, I. Starkey, P. Fitzgerald, R. Erbel, A. Lange, N. McDicken, G. Sutherland, and K. Fox, "Characterisation of coronary atherosclerotic morphology by spectral analysis of radiofrequency signal: in vitro intravascular ultrasound study with histological and radiological validation," *Heart*, vol. 79, no. 5, pp. 459–467, 1998.
- [3] A. Nair, B. D. Kuban, E. M. Tuzcu, P. Achenbach, S. E. Nissen, and D. G. Vince, "Coronary plaque classification with intravascular ultrasound radiofrequency data analysis," *Clinical Investigation*, vol. 106, no. 17, pp. 2200–2206, 2002.
- [4] E.-S. Shin, H. M. Garcia-Garcia, J. M. R. Ligthart, K. Witberg, C. Schultz, A. F. W. van der Steen, and P. W. Serruys, "In vivo findings of tissue characteristics using imaptm ivus and virtual histologytm ivus," *Eurointervention*, vol. 6, no. 8, pp. 1017–1019, 2011.
- [5] E. Uchino, N. Suetake, R. Kubota, T. Koga, G. Hashimoto, T. Hiro, and M. Matuzaki, "An ROC performance validation of hierarchical k-nearest neighbor classifier applied to tissue characterization using IVUS-RF signal," *Proceedings of the 2009 RISP International Workshop on Nonlinear Circuits and Signal Processing*, pp. 333–336, 2009.
- [6] T. Martinez and K. Schulten, "A "neural gas" network learns topologies," *Artificial Neural Networks*, vol. 1, pp. 397–402, 1991.
- [7] F. Ciompi, C. Gatta, O. Pujol, O. Rodriguez-Leor, J. M. Ferré, and P. Radeva, "Reconstruction and analysis of intravascular ultrasound sequences," *New Advances in Biomedical Signal Processing*, pp. 231–250, 2011.
- [8] E. Parzen, "On estimation of a probability density function and mode," *The Annals of Mathematical Statistics*, vol. 33, no. 3, pp. 1065–1076, 1962.

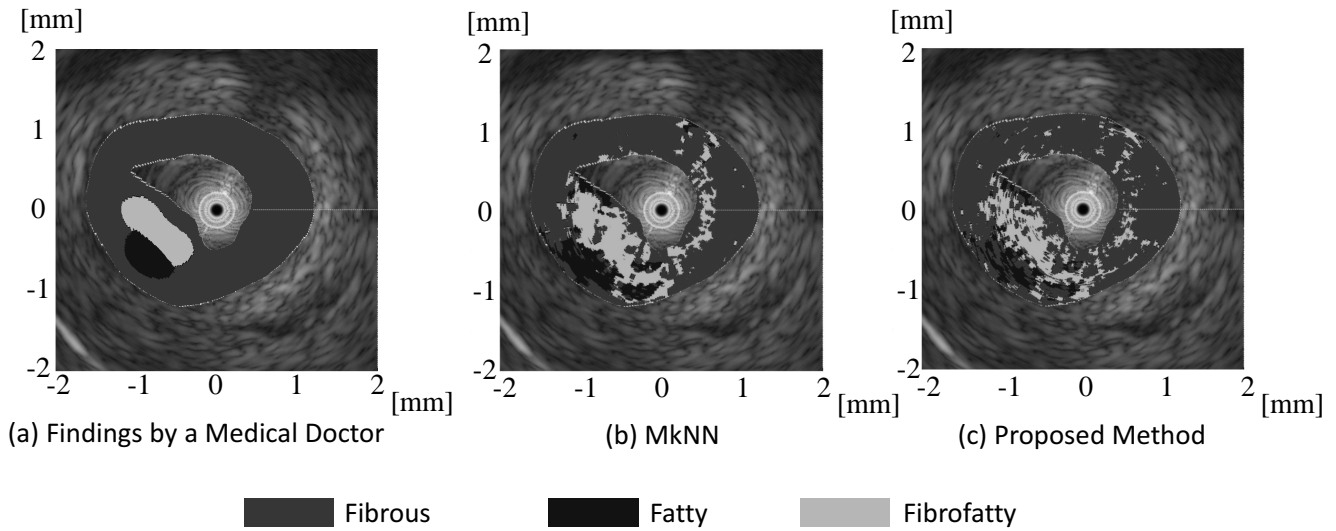


Fig. 4. The tissue characterization results by the conventional method (MkNN) and the proposed method. (a) The tissue composition given by a medical doctor by examining the dyed tissue using microscope. (b) The tissue characterization results by the MkNN. (c) The tissue characterization results by the proposed method. (b) and (c) give almost the same results.

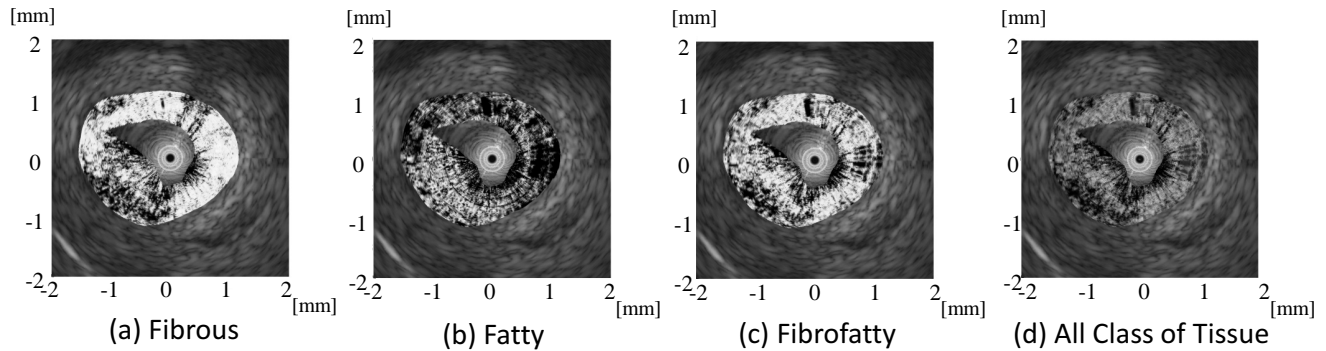


Fig. 5. The probability of each class of tissue. (a), (b), and (c) show the probabilities of each class; Fibrous, Fatty and Fibrofatty. Brighter points have higher probabilities. In (d), the probability values of each tissue, i.e., the probabilities of (a) Fibrous, (b) Fatty, and (c) Fibrofatty, are allocated to R, G, and B values, respectively. The general and continuous changes of tissue can be seen.

TABLE I
QUANTITATIVE EVALUATION OF THE PROPOSED METHOD.

Method	Fibrous		Fatty		Fibrofatty	
	TPR	TNR	TPR	TNR	TPR	TNR
Proposed Method	77.8 ± 0.8	72.4 ± 2.3	54.6 ± 4.7	94.2 ± 0.3	67.8 ± 2.4	83.6 ± 0.8
Conventional Method (MkNN)	74.6 ± 1.4	80.7 ± 2.8	72.5 ± 3.2	92.2 ± 0.4	74.2 ± 3.1	82.8 ± 1.3

Automated surveys and integrated auto-location by Laser Scanner and GPS

V. Barrile and G. Bilotta

Abstract— The present contribution is mainly based on studies, research and applications aimed to a “quick” resolution of an integrated problem oriented towards the self-localization and perimetrization through mobile devices. The methodology adopted is applied on a real case study (outdoors) by using the following surveying tools: a kinematic Global Positioning System (GPS) and a Laser Scanner supporting a “mobile platform” (deployed on a mobile platform). A “GS14” GPS receiver provided by Leica Geosystem and a two-dimensional Laser Scanner provided by the Automation and Control Laboratory of the University “Mediterranea” of Reggio Calabria were positioned on an experimental mobile system specifically designed to simulate the behaviour of a future and fully automated platform. The study focuses on the experimental development of a “quick” methodology to use in order to conduct the traditional land surveying through a Laser Scanner alongside with GPS receivers in a three dimensional centimetric resolution within one single system of reference made up of individual scans operated by a “Stop-and-Go “ device.

Keywords— Auto-location, GPS, Laser scanner 3D, Survey.

I. INTRODUCTION - THE EXPERIMENTAL CAMPAIGN

AS part of a collaboration between the Geomatics Lab and the Automation and Controls Laboratory of the Mediterranean University of Reggio Calabria, aimed to the possible development and implementation of an algorithm based on the use of a laser-scanner sensor for applications mobile robotics, we carried out a first experiment in the yard behind the university (Fig. 1). This experiment was aimed to an automated kinematic perimetrization of the area under investigation with simultaneous auto-location detection sensor through the integration of laser scanner and GPS measurements.

In particular we used a rudimentary "moving platform" (trolley mobile), equipped with a laser-scanner (which currently allows to perform scans only within the planimetric) mounted on a trolley with wheels (Fig. 2); on the same carriage, above the laser sensor, was placed the GPS receiver (Fig. 3).

V. Barrile is with the DICEAM Department, Faculty of Engineering Mediterranean University of Reggio Calabria, Reggio Calabria 89100 IT (phone: +39-0965-875-301; e-mail: vincenzo.barrile@unirc.it).

G. Bilotta was with the Department of Planning, IUAV University of Venice, Venice 30135 IT. She now collaborates with the DICEAM Department, Faculty of Engineering Mediterranean University of Reggio Calabria, Reggio Calabria 89100 IT (e-mail: giuliana.bilotta@gmail.com).



Fig. 1 survey area behind the university building



Fig. 2 mobile platform



Fig. 3 survey operations

The sensor is connected to the USB port of a laptop that sends to the LRF instructions to be executed through the use of

the programming language Matlab (programming language used for all the algorithms implemented for the management and implementation of the system).

It should be noted preliminarily that the automation of the procedure is not yet currently available and that today the operations are carried out manually.

In particular there has been a 360 ° rotation of the basket by making the acquisitions at regular intervals of time trying to ensure the continuity of motion, simulating a behavior as much as possible regular.

Prior to the integration operations between the different survey methods, was independently carried out a perimeter of the study area through GPS survey in classic mode rtk; processing of the acquired data performed with the commercial program of the Leica LGO allowed to obtain the coordinates of the points shown in the diagram of Figure 4 representing the perimeter of the study area.

ID	X (m)	Y (m)	Z (m)
1011	558340.830	4219463.856	71.060
1010	558351.745	4219464.071	70.979
1009	558353.802	4219462.929	71.011
1008	558353.486	4219460.726	71.041
1007	558348.486	4219448.349	71.161
1006	558357.896	4219447.128	71.199
1005	558362.532	4219455.262	71.131
1004	558364.995	4219463.866	71.055
1003	558360.563	4219463.981	71.065
1002	558362.141	4219464.797	71.061
1001	558361.499	4219467.919	71.014

Fig. 4 GPS data



Fig. 5 GPS data in map

The same data were subsequently reported on georeferenced map; these data, connected each other, allowed therefore to delimit the perimeter of interest (Figure 5). These data are considered as data "reliable" to be used for comparison with the survey methods later proposed. In particular, it has been positioned in this regard (integrated laser scanner - GPS - mobile cart) on the platform above the laser scanner sensor, a GPS antenna (Fig. 6) in such a way to obtain simultaneous measurements.

II. MEASUREMENT BY LASER SCANNER



Fig. 6 simultaneous positioning Laser Scanner and GPS on "mobile equipped trolley"

Therefore were made seven scans with the "equipped mobile trolley" doing as said, manually moving it (360°), with a view to its future and complete automation.

For each scan was carried out at the same position detected by GPS measurements useful for linking the different scans through the measurement of external targets.

Scans are shown below (Fig. 7).

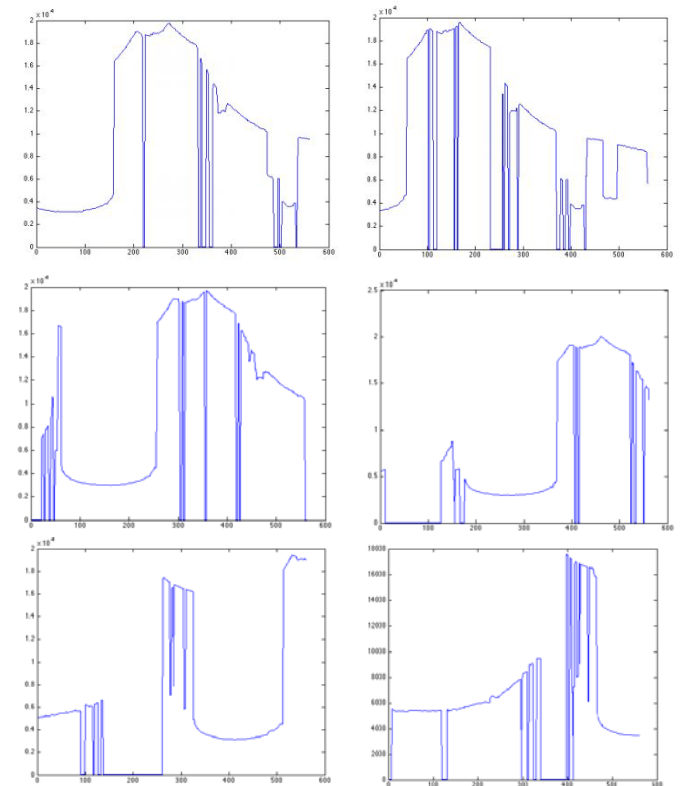


Fig. 7 Laser Scanner scans nn. 1 - 6

Single scans were processed and linked together by means of an algorithm implemented in Matlab (lab AeC), in the testing phase and the subsequent development by deriving a series of segments that describe, with little margin for error,

the geometry of the square (Fig. 8).

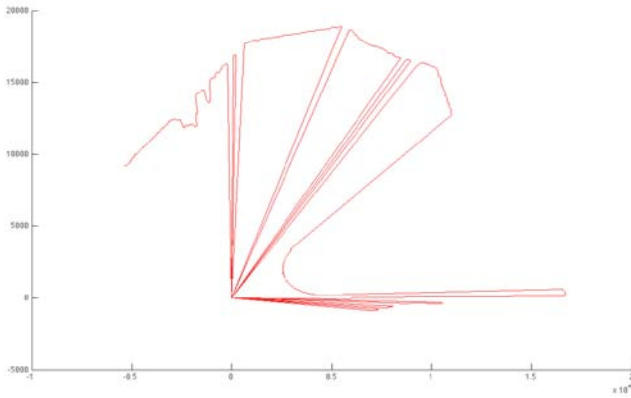


Fig. 8 result of localization algorithm

III. THE ALGORITHM

The algorithm implemented in Matlab and used in this experiment does not use the common return target detected externally but makes a connection of several scans through statistical autocorrelation methods by using the distinctive features that the robot (mobile equipped trolley) is able to perceive the environment through the use of the laser scanner sensor. These characteristics may be the geometric shapes, such as edges, circles or rectangles, or additional data such as barcodes. The features must have a precise and fixed position within the environment and should be easily detectable by the sensor. The methodology used can be divided into two phases: extraction of features from the measurements made by the sensors; coupling between features belonging to different measures so as to determine the deviation between the two measures in terms of a shift (D_x , D_y) and a rotation $D\alpha$. We thus introduced an algorithm of “SLAM” based exclusively on information from a laser scanner. This algorithm introduces a new model for the prediction of the future state (described in Fig. 9).

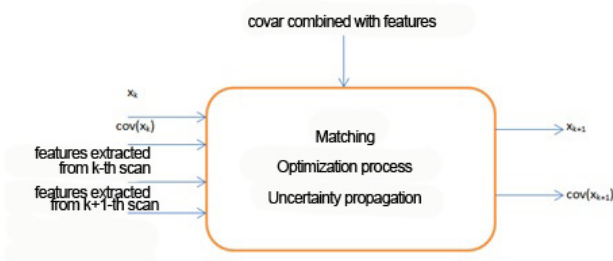


Fig. 9 prediction model of future state

The methods of location-based laser odometry differs depending on what data are used to search the correspondence between scans. The algorithm that will be described below is based on matching through the use of features and is shown schematically in Figure 10:

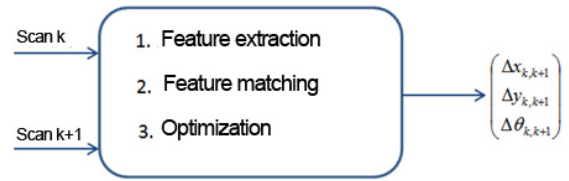


Fig. 10 diagram of localization algorithm based on use of features

From the knowledge of the current pose of the robot, x_k , its covariance, $cov(x_k)$, the extracted features to scan the k -th and $k+1$ -th scan and the covariance associated with the features you want to calculate the pose of the robot to the next step, x_{k+1} , and its covariance, $cov(x_{k+1})$. To do this you must perform three steps:

- A) Features extraction;
- B) Matching between features;
- C) Optimization process.

A. Features extraction

The matching techniques through the use of features presuppose a preliminary phase concerning the extraction of features from the scan. The features are divided into two types: “jump-edges” and “corners”.

To detect the features jump-edges, a scan is divided into groups (called “clusters”) of consecutive scan points. In this way, each cluster consists of a starting point, p_i , and an end point, p_j , and the k -th cluster is defined in the following way:

$$c_k = \{p_m \mid p_m \in S, i \leq m \leq j\} \quad (1)$$

The start and end points of each cluster are candidates to become features jump-edges as long as these points are invariant with respect to the movement of the robot.

To extract the features “corners” within a scan is instead necessary to extract lines from each cluster using an algorithm such as “split-and-merge”. Each line extracted is characterized by the following parameters: $l_q = [\alpha_q, n_q, len_q]$, where α_q is the angle between the line and the x -axis; n_q is the number of points that constitute the line and len_q is the length of l_q .

If the intersection of two successive lines is such that $|\alpha_{q+1} - \alpha_q| > \Delta\alpha_{th}$ and that, for both for l_q that l_{q+1} , or $len > len_{th}$ or $n_q > n_{th}$ (where len_{th} is the minimum length and n_{th} is the minimum number of points of the lines that make up the corner) then p_{cc} , which is the end point of l_q , is a candidate to become a feature corner.

B. Matching between features

Once extracted, by two successive scans, the features that represent the same physical point of the environment, is necessary to couple. To do so we use a matching algorithm which is based on a function of dissimilarity, d . We define this function for two points p_i and p_j , belonging to two successive scans:

$$d(p_i, p_j) = \left\| p_i - p_j \right\|_2 + B \quad (2)$$

If $|\alpha_{\text{next}} - \alpha'_{\text{next}}|$ or $|\alpha_{\text{pre},i} - \alpha'_{\text{pre},j}|$ exceeds a certain threshold, p_i and p_j are not coupled and B becomes equal to infinity, otherwise B is equal to zero. Once constructed the matrix containing all the functions of dissimilarity (called dissimilarity matrix), the smallest value of this matrix is eliminated and the corresponding features are coupled. This is done at each step, until all the elements of the matrix are eliminated or until the remaining elements have a value above a certain threshold.

C. Optimization process

To calculate the new installation of the robot in an optimal way is necessary to establish a model of uncertainty for the features extracted, i.e. a model which takes account of errors (such as the noise of the measurement process, e_{ob} , and the quantized nature of the angles of the rays, e_q); it could cause that the actual position of the feature differs from that calculated. The position of the k -th feature must therefore be written as:

$$f_k = p_i + e_{ob_i} + e_{q_i} \quad (3)$$

And the expected value of the position of features, f_k , is given by:

$$\hat{f}_k = E(f_k) = p_i + E(e_{ob_i}) + E(e_{q_i}) \quad (4)$$

where $E(\cdot)$ is the expected value operator.

At this point it is necessary to calculate the covariance of f_k :

$$\text{Cov}(\hat{f}_k) = E\left(\left(f_k - \hat{f}_k\right)^T \cdot \left(f_k - \hat{f}_k\right)\right) = \text{Cov}(e_{ob_i}) + \text{Cov}(e_{q_i}) \quad (5)$$

Using the measurement of the features and their corresponding covariance, the algorithm calculates the displacement (defined in terms of translation, T , and rotation, R) effected by the robot between the two scans. To find the optimal values of T and R the following error function must be minimized:

$$E = \sum_{j=1}^m \left(\hat{f}_{j,\text{pre}} - (R\hat{f}_{j,\text{new}} + T) \right)' C_j^{-1} \left(\hat{f}_{j,\text{pre}} - (R\hat{f}_{j,\text{new}} + T) \right) \quad (6)$$

Where m is the number of features coupled, $f_{j,\text{pre}}$ and $f_{j,\text{new}}$ are two new features coupled refer respectively to the previous scan and the current one; $v_j = (\hat{f}_{j,\text{pre}} - (R\hat{f}_{j,\text{new}} + T))$ is the j -th vector innovation and C_j is its covariance.

Assuming that the errors in the scans are independent, we can write:

$$C_j = \text{cov}(e_{ob}^{\text{pre}} + e_q^{\text{pre}}) + R \text{cov}(e_{ob}^{\text{new}} + e_q^{\text{new}}) R^T \quad (7)$$

There is the possibility of writing the variables in vector form. In such form, the displacement of the robot can be indicated in the following way:

$$X = (q_1 \quad q_2 \quad t_1 \quad t_2)^T \quad (8)$$

Where t_1 and t_2 are respectively the translations along the x direction and the y direction. The rotation R and translation T matrices become defined as follows:

$$R = \begin{pmatrix} q_1^2 - q_2^2 & -2q_1q_2 \\ 2q_1q_2 & q_1^2 - q_2^2 \end{pmatrix} \quad T = \begin{pmatrix} t_1 \\ t_2 \end{pmatrix} \quad (9)$$

The optimization problem is solved using the SQP method, "Sequential Quadratic Programming".

Assuming that X^* is the deviation between the two scans that minimizes the function E described above, for calculating the covariance of X^* should exist Jacobian, J , projecting the uncertainty of the features in the uncertainty of X^* . If there is an explicit function, g , which relates X^* to F , which is the vector of all the features coupled, we have $X^* = g(F)$. The Taylor series expansion of g in the neighborhood of $E(F)$ will be:

$$X^* = g(\hat{F}) + (F - \hat{F}) \frac{\partial X^*}{\partial F} + O(F - \hat{F})^2 \quad (10)$$

The last summand represents the higher order terms.

The Jacobian between X^* and F projects the uncertainty of X^* in F , namely:

$$\text{cov}(X^*) = J \text{cov}(F) J^T \quad (11)$$

However, there is an explicit relationship between F and X^* , then they are related by an implicit function, $I(X^*, F) = 0$, which is derived from $\partial E / \partial X = 0$. You can obtain this Jacobian using the equation:

$$J = -\left(\frac{\partial \gamma}{\partial X^*} \right)^{-1} \left(\frac{\partial \gamma}{\partial F} \right) \Rightarrow J = -\left(\frac{\partial^2 E}{\partial X^2} \right)^{-1} \left(\frac{\partial^2 E}{\partial F \partial X} \right) \quad (12)$$

with $X = X^*$.

Conducting additional steps and substitutions you can get the desired Jacobian matrix. The independence of the features of a scan brings to obtain a total diagonal covariance matrix.

Furthermore, assuming that the features extracted by two successive scans are independent, the covariance of each pair will be:

$$\text{cov}(F) = \begin{bmatrix} \text{cov}(F_1) & & 0 \\ & \ddots & \\ 0 & & \text{cov}(F_m) \end{bmatrix}, \text{cov}(F_j) = \begin{bmatrix} \text{cov}(f_{j,\text{new}}) & 0 \\ 0 & \text{cov}(f_{j,\text{pre}}) \end{bmatrix} \quad (13)$$

Substituting the expressions of J and $\text{cov}(F)$ we get $\text{cov}(X^*)$,

i.e. the uncertainty of the deviation.

The pose of the robot at the generic instant k can be defined as:

$$x_{r,k} = [x_{r1,k}, x_{r2,k}, x_{r3,k}] \quad (14)$$

where $x_{r1,k}$ e $x_{r2,k}$ represent the translations along the x and y axes, while $x_{r3,k}$ is the orientation. The new robot pose is then determined by the equation:

$$\hat{x}_{r,k+1} = \hat{x}_{r,k} + \begin{pmatrix} \cos \hat{\theta}_k & -\sin \hat{\theta}_k & 0 \\ \sin \hat{\theta}_k & \cos \hat{\theta}_k & 0 \\ 0 & 0 & 1 \end{pmatrix} \begin{pmatrix} t_1 \\ t_2 \\ \Delta\theta \end{pmatrix}, \hat{\theta}_k = \hat{x}_{r3,k} \quad (15)$$

where t_1 and t_2 are the translations along the x and y between the instants k and $k+1$ while $\Delta\theta$ is the rotation in the same time interval.

The calculation of the covariance of $X_{r,k+1}$ requires its differentiation with respect to the random parameters of the right side of the equation just written:

$$J_p = \frac{\partial x_{r,k+1}}{\partial (x_{r,k}, q_1, q_2, t_1, t_2)} \quad (16)$$

Given the independence between $x_{r,k}$ and X , the covariance of the parameters of the right side of the equation $x_{r,k+1}$ will be:

$$P^* = \begin{pmatrix} \text{cov}(P_k) & 0_{3 \times 4} \\ 0_{4 \times 3} & \text{cov}(X^*) \end{pmatrix} \quad (17)$$

The covariance of $x_{r,k+1}$ can be calculated in the following way:

$$\text{cov}(x_{r,k+1}) = J_p P^* J_p^T \quad (18)$$

The state vector x_k of the system is composed of the state of the robot, $x_{r,k}$, and the state of all the features, $x_{f,k}$. The state vector and its covariance before the prediction will be:

$$\hat{x}_k = \begin{pmatrix} \hat{x}_{r,k} \\ \hat{x}_{f,k} \end{pmatrix}, \text{cov}(x_k) = \begin{pmatrix} \text{cov}(x_{r,k}) & \text{cov}(x_{r,k}, x_{f,k}) \\ \text{cov}(x_{f,k}, x_{r,k}) & \text{cov}(x_{f,k}) \end{pmatrix} \quad (19)$$

The movement of the robot does not affect the status of the features, so we have:

$$\hat{x}_{k+1} = \begin{pmatrix} \hat{x}_{r,k+1} \\ \hat{x}_{f,k} \end{pmatrix}, \text{cov}(x_{k+1}) = \begin{pmatrix} \text{cov}(x_{r,k+1}) & \text{cov}(x_{r,k+1}, x_{f,k}) J_p^T \\ J_p \text{cov}(x_{f,k}, x_{r,k}) & \text{cov}(x_{f,k}) \end{pmatrix} \quad (20)$$

J_p is the truncated form of J_p and includes only the differentiation of $x_{r,k+1}$ with respect to $x_{r,k}$.

The next step is the association of the data and update the

map. For data binding, the positions of features belonging to the map must be predicted relative to the robot. This is done by a model of the observation that, for the i -th feature, is:

$$f_i^r = h_i(x_r, f_i^{map}) \quad (21)$$

The superscript r and map refer respectively to the coordinates of the robot and global ones.

In the present case, the model h_i is:

$$\begin{pmatrix} f_{i1}^r \\ f_{i2}^r \end{pmatrix} = \begin{pmatrix} \sqrt{(f_{i1}^{map} - x_{r1})^2 + (f_{i2}^{map} - x_{r2})^2} \\ a \tan\left(\frac{f_{i2}^{map}}{f_{i1}^{map}}\right) - \theta_r \end{pmatrix} \quad (22)$$

The total observation model, h , is obtained considering all the features in a single vector. The features that are not coupled with any feature in the map are added to the latter through data binding. The features which would be coupled with map features create new relationships between persistent objects in the map. In this case the state vector of the system and the covariance matrix do not increase in size, but are updated.

The obtaining of information from sensors in the current scan is described by a function of measurement:

$$\begin{aligned} \hat{F}^r &= h(\hat{x}_r, \hat{F}^{map}) = h(\hat{x}) \\ \text{cov}(F^r) &= H_x \text{cov}(x) H_x^T \end{aligned} \quad (23)$$

where:

$$H_x = \frac{\partial h(x)}{\partial x} \Big|_{x=\hat{x}_{k+1}^{(-)}}$$

The models of the process and observation are not linear, so the noise variables are assumed to be taken from normal distributions, and for the filtering step is chosen the iterated extended Kalman filter (IEKF), ie:

$$\begin{aligned} \hat{x}_{k+1,i+1}^{(+)} &= \hat{x}_{k+1,i}^{(-)} + K_{k+1,i} [F^{k+1} - (h(\hat{x}_{k+1,i}^{(-)}) + H_x (\hat{x}_{k+1,i}^{(-)} - \hat{x}_{k+1,i}^{(+)}))] \\ \text{cov}(\hat{x}_{k+1,i+1}^{(+)}) &= \text{cov}(x_{k+1,i}^{(-)}) - K_{k+1,i} H_x \text{cov}(x_{k+1,i}^{(-)}) \\ K_{k+1,i} &= \text{cov}(x_{k+1,i}^{(-)}) H_x^T [H_x \text{cov}(x_{k+1,i}^{(-)}) H_x^T + \text{cov}(F^{k+1})]^{-1} \end{aligned} \quad (24)$$

where:

$$H_x = \frac{\partial h(x)}{\partial x} \Big|_{\hat{x}_{k+1,0}^{(-)}, \hat{x}_{k+1,0}^{(+)} = \hat{x}_{k+1}^{(-)}}$$

D. Checks and comparison

The algorithm has allowed us to analyze the first four scans, while the last three we had difficulties due to external phenomena of noise that prevented proper data collection.

In any case, after a “cleaning” of the data from any nuisance parameters (GPS and laser scanner), overlaying the drawing of the survey to cartography is obtained as shown in Fig 11.



Fig. 11 overlaying result of algorithm on mapping

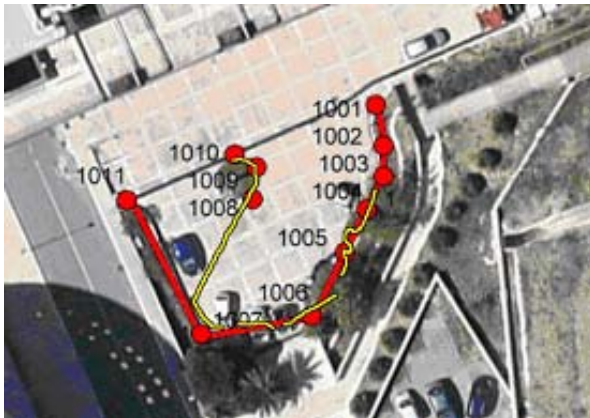


Fig. 12 comparison between the two methods

To check the validity of these results, we do a comparison between the results Laser Scanner and those GPS (red line on maps considered as “certain”), preferring the graphic display able to better show the differences between the two methods (Fig. 12) rather than the creation of complex tables and graphs summarizing and/or various statistical parameters on the accuracy of the processing, because the aim of “expeditious” of this proposal.

Although there is the same precision of the GPS data in terms of return, however, is highlighted as the algorithm proposed for the processing of the given laser scanner is able to provide by itself discrete results, as evidenced by the partial planimetric correspondence of the two tracks GPS and Laser Scanner shown in figure 12.

This is a good omen for the continuation of the trial.

IV. INTEGRATION OF GPS AND LASER SCANNER FOR CONNECTING SUBSEQUENT SCANS

As known, the main problem for laser scanner data is the assembly of the scans in order to determine a unique reference

system in which “immerse” the obtained model. The acquisition of the scans results in an immediate point cloud ordered in the plane, whose coordinates are known with respect to the center of “taking”. The scan is then locally

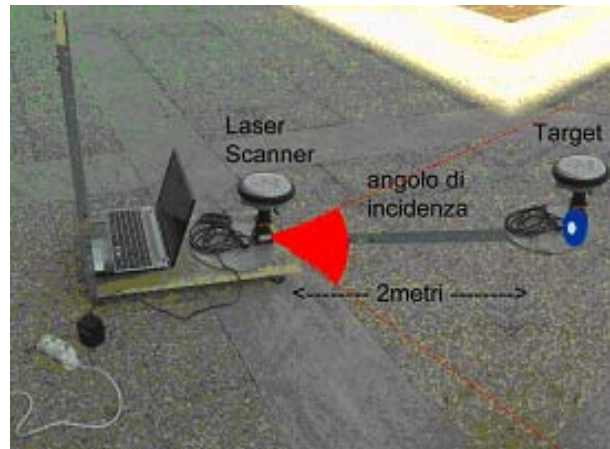


Fig. 13 system with target and dual GPS

oriented with respect to a reference system that derives from the arbitrary choice of the pickup point, which will be taken as the origin of the reference system of the scan. The assembly of multiple scans thus requires the knowledge of the parameters of rototranslation: these parameters can be calculated if the position of the origin of the reference system of each scan with respect to a single system is known through the measurement of the external “target”. Such a problem for geo - topographic applications is solved by having remarkable points (targets), of which the coordinates are known, in all the scans: in this way each scan can be oriented independently of the other. Their georeferencing can be done by using the techniques of GPS tracking.

Arm (distance between the coaxial position of the laser scanner and that of the target) of:	Deviations "average" positioning expressed in percentage
3 meters	11%
2 meters	19%
1.5 meters	37%
1 meters	Determinabile only occasionally with higher % than 65%
0.5 meters	Location not determined

Fig. 14 variation of the percentage error compared to GPS method (in the test simulated) by varying the arm in question.

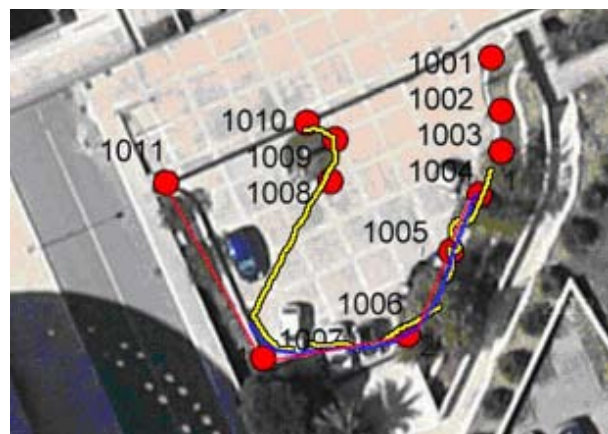


Fig. 15 integration of the two different methodological approaches

From the above considerations, the idea of experimenting with a rudimentary expeditious survey able to repeat what has already been experienced with the vehicle fully equipped (equipment includes two GPS, a laser scanner and a target all mounted on a vehicle in motion) that, by combining the two receivers GPS with the sensor laser scanner and a target audience, can overcome the issues raised; the whole mounted on a moving body that allows easy movement between the measurement sessions.

By performing measurements laser scanner and GPS simultaneously with stationary body is thus ensured a high quality of fit and positioning into a single reference system.

The system is to mount on movable equipped trolley (rigidly and coaxially) the laser scanner surmounted by a GPS and connect the trolley through a rigid arm (adjustable in length) to a "target" coaxially surmounted by other GPS reference (which will serve as the orientation of the scan), left free to rotate anyway so as to guide the laser target to the sensor. In this way, the problem of defining the coordinates of the acquisition point (Laser Scanner) and target orientation is overcome by fitting precisely coaxially two GPS receivers, respectively, the Laser Scanner and the target .

The receivers, while the laser sensor scans, acquire measurements from GNSS satellite constellations providing coordinates, both geographic both local coordinates of the laser sensor and the target orientation into a single reference system.

Once we have defined the ideal location for the first scan, we must place and stop the mobile equipped trolley at the point defined by performing both those measures GPS and Laser Scanner with the characteristics of density required by the survey. After a few minutes we must close the measures and shall move the trolley equipped cabinet in the next position chosen for the second major station, operating as before and repeating the process until completion of the survey. The processing of GPS data will allow to obtain homogeneous coordinates for all points of outlet (station laser scanner) and for all orientation target with sub-centimeter accuracy. These coordinates are assigned to stations and targets thereby allowing the software used for the management of the scans to unite and georeference all the scans made even in the absence of homologous points or targets positioned on the ground.

In this way, in addition to speed up and facilitate the steps of the survey in the field by eliminating the need of affixed targets and the necessity of their internal visibility between a measurement session and the other, will be easier georeferencing also individual scans with no points in common, decreasing processing time of "point clouds" resulting from the scans.

Taking into account what was said above, namely we have tried to make an initial experimentation in order to achieve "coarse" and "expeditious" what has already been experimented on equipped machine (cf. Leica experiment reported in bibliography).

Specifically, it was built by placing a measuring system on the mobile trolley equipped (rigidly and coaxially) the laser scanner superimposed by a GPS and connecting the trolley through a rigid arm (simulating the modulation length through the ability to extend and contract) to a "target" coaxially superimposed by other GPS reference.

In particular, measures have been simulated with arms of 3 meters, 2 meters, 1.50 meters, 1 meter, 0.5 meters (Fig. 13)

The overall reconstruction of the data, although simulated, is very interesting in particular for the test carried out with the arms of 3 meters and 2 meters (note in this regard the result of the perimeter displayed in color and overlaid on the map as reported in Fig. 15). Instead, less accurate appear the results obtained with simulated arm of 1.5 meters, while it was not possible to make reliable reconstructions with simulated arm of 1 meter or less. (Fig. 14).

V. CONCLUSIONS

Of course, although we must emphasize that the results obtained from the integration are to now only been achieved in a "simulated" way and the automation of the procedure is still under study and implementation (having now moved to the cart only by hand), yet the results seem encouraging in view of the realization of a "expeditious" process for the auto positioning and perimentering by using mobile and automated tools. The results certainly push to further study both in terms of actual full realization of the experiment, both in terms of optimization of the algorithms used for the compensation of the integrated data.

REFERENCES

- [1] G. Weiß, C. Wetzler, and E. von Puttkamer, "Keeping track of position and orientation of moving indoor systems by correlation of range-finder scans", in *Proceedings of the International Conference on Intelligent Robots and Systems 1994*, pp. 595–601.
- [2] F. Lu, E. Milios, "Robot Pose Estimation in Unknown Environments by Matching 2D Range Scans", *Journal of Intelligent and Robotic Systems*, 1997, vol. 18, no. 3, pp. 249-275.
- [3] S. Thrun, "Robotic Mapping: A Survey" in *Exploring artificial intelligence in the new millennium*. Pittsburgh: Morgan Kaufmann, 2002.
- [4] J. S. Liu, R. Chen, T. Logvinenko, "A theoretical framework for sequential importance sampling and resampling", in A. Doucet, N. de Freitas, N.J. Gordon, editors, *Sequential Monte Carlo in Practice*. New York: Springer-Verlag, January 2001.
- [5] P. Pirhjanian, N. Karlsson, L. Goncalves, E. Di Bernardo, "Low-cost visual localization and mapping for consumer robotics", in *Industrial Robot: An International Journal*, 2003, vol. 30 no. 2, pp. 139 – 144.
- [6] I. M. Rekleitis, "A particle filter tutorial for mobile robot localization", Technical Report TR-CIM-04-02, February 2004.
- [7] G. Bekey, *Autonomous Robots: From Biological Inspiration to Implementation and Control*. The MIT Press, Cambridge, MA, 2005.
- [8] K. Lingemann, A. Nüchter, J. Hertzberg and H. Surmann, "High-Speed Laser Localization for Mobile Robots", *Journal Robotics and Autonomous Systems (JRAS)*, Elsevier Science, vol. 51 no. 4, pp. 275-296, 2005.
- [9] A. Garulli, A. Giannitrapani, A. Rossi, A. Vicino, "Simultaneous localization and map building using linear features", in *Proceedings of the 2nd European Conference on Mobile Robots*, Ancona (Italy), September 7-10, 2005.
- [10] A. Garulli, A. Giannitrapani, A. Rossi, A. Vicino, "Mobile robot SLAM for line-based environment representation, Decision and Control, 2005

- and 2005 European Control Conference. CDC-ECC '05. *44th IEEE Conference on, 2005*, pp. 2041 – 2046.
- [11] A. A. Aghamohammadi, H. D. Taghirad, A. H. Tamjidi, and E. Mihankhah, “Feature-Based Laser Scan Matching For Accurate and High Speed Mobile Robot Localization” in *European Conference on Mobile Robots (ECMR'07)*, 2007.
- [12] A. A. Aghamohammadi, A. H. Tamjidi, H. D. Taghirad, “SLAM Using Single Laser Range Finder”, *Proceedings of the 17th World Congress, The International Federation of Automatic Control*, Seoul, Korea, July 6-11, 2008.
- [13] M. Secchia, F. Uccelli, *Laser Scanner e GPS -Stop&Go FIG Working Week 2012. Knowing to manage the territory, protect the environment, evaluate the cultural heritage*, Rome, Italy, 6-10 May 2012.
- [14] M. Wahde, *Introduction to autonomous robots*. Department of Applied Mechanics, Chalmers University of Technology, Goteborg, Sweden 2012.
- [15] V. Barrile, G. M. Meduri, G. Bilotta, “Laser scanner surveying techniques aiming to the study and the spreading of recent architectural structures”, in *Recent advances in signals and systems, Proceedings of the 9th WSEAS International Conference on Signal, speech and image processing 2009*, pp. 92-95. Available: <http://www.wseas.us/e-library/conferences/2009/budapest/MIV-SSIP/MIV-SSIP15.pdf>
- [16] V. Barrile, G. M. Meduri, G. Bilotta, “Laser scanner technology for complex surveying structures”, *WSEAS transactions on signal processing*, vol. 7 no. 3, July 2011, pp. 65-74. Available: <http://www.wseas.us/e-library/transactions/signal/2011/53-180.pdf>
- [17] V. Barrile, G. Bilotta, G. M. Meduri, “Least Squares 3D Algorithm for the Study of Deformations with Terrestrial Laser Scanner”, in *Recent Advances in Electronics, Signal Processing and Communication Systems, Proceedings EUROPEMENT 2013 International Conference on Electronics, Signal Processing and Communication Systems*, ESPCO 2013, Venice, Italy, September 28-30, pp. 162-165. Available: <http://www.europement.org/library/2013/venice/bypaper/ESPCO/ESPCO-24.pdf>
- [18] T. Bailey, E. Nebot, “Localisation in large-scale environments”, *Robotics and Autonomous Systems*, vol 37, no. 4, December 2001, pp. 261–281.
- [19] R. Siegwart, I. R. Nourbakhsh. *Introduction to Autonomous Mobile Robots*. A Bradford Book, The MIT Press, Cambridge, MA, London, England, 2004.
- [20] J. Borenstein, H.R. Everett, L. Feng, D. Wehe, “Mobile Robot Positioning - Sensors and Techniques”, *Journal of Robotic Systems, Mobile Robots*. vol. 14, no. 4, 1997, pp. 231-249.
- [21] V. Barrile, M. Cacciola, F. Cotroneo, F. C. Morabito, M. Versaci, “TEC Measurements through GPS and Artificial Intelligence”, *Journal of electromagnetic waves and applications*, no. 20, 2006, pp. 1211-1220.
- [22] M. N. Postorino, V. Barrile, “An integrated GPS-GIS surface movement ground control system”, *Management of Information Systems*, WIT Press (GBR), 2004, pp. 3-12.

PA-SLNR Multi-user MIMO Precoding Based on GSVD

Varun Jeoti¹, Elsadig Saeid
 Electrical and Electronic Engineering Department
 Universiti Teknologi PETRONAS
 31750, Tronoh, Perak, Malaysia
¹varun_jeoti@petronas.com.my

Abstract- In this work, a linear precoding scheme for Multi-user Multiple Input Multiple Outputs (MU-MIMO) system is introduced. The proposed method optimizes Per-Antenna Signal to Leakage plus Noise Ratio (PA-SLNR) performance criteria, and makes use of the Generalized Singular Value Decomposition (GSVD) computation to develop a simple precoding algorithm. However, the linear technique available in the literature so far uses Per-User Signal to Leakage plus Noise Ratio (PU-SLNR) performance criteria and develop a closed form precoding matrix solutions based on Generalized Eigenvalue Decomposition (GEVD) and simple algorithm based on GSVD. The PU-SLNR objective function neglects to take the intra-user antennas interference cancellation into account. In this work, a new cost function based on PA-SLNR is defined, GSVD based solution is explained and simple algorithm is developed to compute the precoding matrices for multiple users with multiple antennas. Simulation results show that the proposed precoding method has a better BER and output SINR outage performance than the conventional methods.

Index Terms— Generalized Singular Value Decomposition (GSVD), Generalized Eigenvalue Decomposition (GEVD), Multi-user Multiple Input Multiple outputs (MU-MIMO), Precoding, Per-Antenna Signal to leakage Plus Noise Ratio (PA-SLNR).

I. INTRODUCTION

Multi-user multiple input multiple output broadcast channel (MU-MIMO-BC) precoding design has received significant attention in the last decade [1-3]. This high thoughtfulness is due to the high predictable performance/capacity gain of both MIMO and the multi-user spatial dimensions. In the literature, due to the complexity of nonlinear precoding methods [4-7], several linear precoding techniques were proposed. In these methods both joint and independent optimization techniques were used to mitigate the multiuser interference (MUI) [8-12]. Given that the channel state information is available at the transmitter and receiver, various conditions and objectives were used to study this problem. In [8, 9, 13-15] various closed form solutions based on minimum mean square error (MMSE) were proposed. The methods in [8, 15] impose dimensionality restrictions that the number of base station antennas should be greater than or equal to the total numbers of receive antennas for all users. Conversely, the methods in [9, 14] relax the dimensionality constraint but with some performance loss at high SNR values when the total number of receive antennas at all users exceeds the number of base station antennas. In [10] an iterative sum mean square error (SMSE) method also called joint transceiver design was developed to compute both the precoding and decoding matrices. In spite of its high performance, computational complexity and restrictions on the number of antennas are the main demerits of this method. The work by [11] propose a beam-forming precoding design utilizing Per-User Signal to Leakage and Noise Ratio (PU-SLNR) cost function. In this method the precoding vectors for all users are obtained by solving a series of optimization

problems using generalized eigenvalue decomposition (GEVD). In [12] PU-SLNR precoding matrix design based on GEVD for MU-MIMO spatial Multiplexing is proposed. This work shows that the precoding matrix computation using GEVD is simple but it's sensitive to the singularity in the leakage plus noise power matrix, thus there is some performance loss at high SNR values. To solve the singularity problem in matrix computation, Fukunaga-Koontz transforms (FKT) and GSVD based computation were independently utilized in [16] and [17] respectively. The precoding design based on PU-SLNR cost function introduced in [12, 16, 17] were totally neglects to take into account the interference between streams multiplexed to one user (intra-user antenna interference).

In this paper, an objective function based on the PA-SLNR criteria is defined to account for the intra user antennas interference cancelation. Moreover, GSVD is utilized to develop a new precoding algorithm. Using both bit error rate (BER) and the received out SINR outage as performance metrics, simulation result shows that the combination of the proposed PA-SLNR optimization method and the GSVD computation algorithm generate numerically better results than the conventional PU-SLNR optimization with GSVD computation. The rest of this work is organized as follows: section II describes the system model and the precoding problem description is stated in section III. Section IV describes the algorithm development and the simulation results are given in section V. Section VI concludes the paper.

The superscripts $\mathbf{Q}^T, \mathbf{Q}^H$ denote the transpose and conjugate transpose of matrix \mathbf{Q} respectively. $tr(\mathbf{Q})$ and $\|\mathbf{Q}\|_F^2$ are denoting the trace and the Frobenious norm respectively. \mathbf{I}_{N_T} is an $N_T \times N_T$ identity matrix. $\mathbf{D} = diag\{\lambda_1 \lambda_2 \dots \lambda_r\}$ Denotes the diagonal matrix with diagonal elements $\{\lambda_1 \lambda_2 \dots \lambda_r\}$.

II. MU-MIMO BROADCASTING SYSTEM MODEL

We consider a downlink MU-MIMO-BC channel with a central node Base station/ Access point communicating with B number of users simultaneously at the same time and frequency. The base station is equipped with N_T transmit antennas and each individual user k is equipped with M_k receive antennas, $k = 1, \dots, B$ as depicted in figure 1. The central node spatially multiplexes and sends B data vectors to the B number of users simultaneously. We assume perfect channel state information (CSI) is available at both the transmitter and receivers.

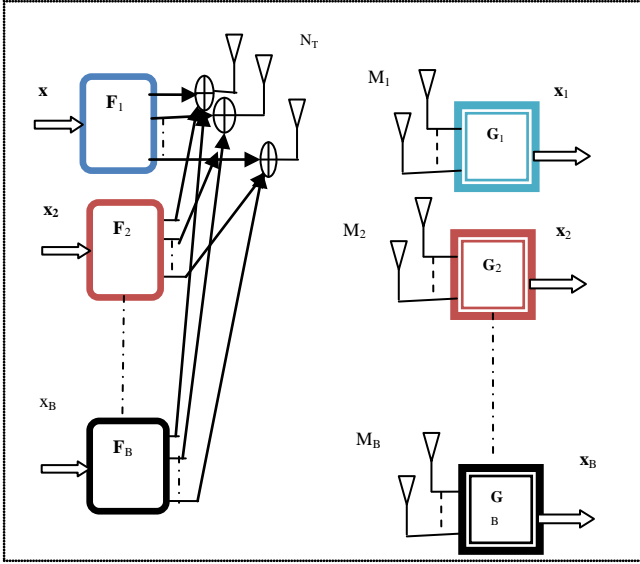


FIG. 1: MU-MIMO BROADCAST SYSTEM BLOCK DIAGRAM.

The channel from the central node to each user is assumed to be frequency flat fading and constant over all transmission block duration. The element of any user channel $\mathbf{H}_k \in \mathbf{C}^{M_k \times N_T}$ is assumed to be complex Gaussian variables with zero mean and unit-variance. The combined channel matrix for all the B users in the system is given by:

$$\mathbf{H}_{\text{com}} = [\mathbf{H}_1^T \mathbf{H}_2^T \dots \mathbf{H}_B^T]^T \quad (1)$$

and the received signal at the k^{th} user is given by:

$$\mathbf{y}_k = \mathbf{H}_k \mathbf{F}_k \mathbf{x}_k + \mathbf{H}_k \sum_{i=1, i \neq k}^B \mathbf{F}_i \mathbf{x}_i + \mathbf{n}_k \quad (2)$$

Where $\mathbf{F}_k \in \mathbf{C}^{N_T \times M_k}$ is the k^{th} user precoding matrix, while $\mathbf{x}_k \in \mathbf{C}^{M_k \times 1}$ is the k^{th} user data vector. The entries of receiving noise vector \mathbf{n}_k are assumed to be independent complex Gaussian variables with zero-mean and variance equal to σ_k^2 . Also we assume that the noise variances at all antenna elements as well as the noise at the all users are equal such that: $\sigma_1^2 = \sigma_2^2 = \dots = \sigma_{M_k}^2$. The entries of the $M_k \times N_T$ channel H_K are denoted by:

$$\mathbf{H}_k = \begin{bmatrix} h_k^{(1,1)} & \dots & h_k^{(1,N_T)} \\ \vdots & \ddots & \vdots \\ h_k^{(M_k,1)} & \dots & h_k^{(M_k,N_T)} \end{bmatrix} \in \mathbf{C}^{(M_k \times N_T)} \quad (3)$$

Also we consider that for any k^{th} user, the data vector \mathbf{x}_k and the precoding matrix \mathbf{F}_k are normalized such as that:

$$E \|\mathbf{x}_k\|_f^2 = \mathbf{I}_{M_k} ; \text{tr}(\mathbf{F}_k \mathbf{F}_k^H) = 1 \quad (4)$$

for $k = 1, \dots, B$

And for each k^{th} individual user, the decoding matrix \mathbf{G}_k will be constructed at the k^{th} user terminal to decode the received signal.

III. PA-SLNR MAXIMIZATION PRECODING

The objective function originally proposed in [11] maximizes the PU-SLNR of each user. Thus, the precoder designed cancels only the inter-user interference. This work, however, consider a new cost function that maximizes the SLNR for each individual receive antenna (PA-SLNR). This cost function would help to minimize the intra-user antennas interference and leads to a better precoder that maximizes the overall SLNR per user more efficiently. This is justified because PA-SLNR as explained in fig 2, takes into account the intra-antenna interference mitigation.

For each j^{th} receive antenna of the k^{th} user, The $PA-SLNR$, γ_k^j , is defined as ratio between the individual j^{th} received antenna desired signal power to the interference introduced by the j^{th} receiving antenna to all other antennas plus the noise power at the j^{th} receive antenna front end. So for the j^{th} receive antenna of the k^{th} user, the signal to leakage plus noise ratio γ_k^j is given by:

$$\gamma_k^j = \frac{\|\mathbf{h}_k^j \mathbf{f}_k^j\|_F^2}{\sum_{i=1, i \neq k}^B \|\mathbf{H}_i \mathbf{f}_i^j\|_F^2 + \sum_{i=1, i \neq j}^{M_k} \|\mathbf{h}_k^i \mathbf{f}_k^j\|_F^2 + \sigma_k^2} \quad (5)$$

Where $\mathbf{h}_k^j \in \mathbf{C}^{1 \times N_T}$ is the j^{th} receive antenna of the k^{th} user, received row vector. If we define an auxiliary matrix \mathbf{H}_k^j as the matrix contains all the k^{th} user receive antennas row vectors except the j^{th} antenna row vector as follows:

$$\mathbf{H}_k^j = \begin{bmatrix} h_k^{(1,1)} & h_k^{(1,2)} & \dots & h_k^{(1,N_T)} \\ \vdots & \vdots & \vdots & \vdots \\ h_k^{(j-1,1)} & h_k^{(j-1,2)} & \dots & h_k^{(j-1,N_T)} \\ h_k^{(j+1,1)} & h_k^{(j+1,2)} & \dots & h_k^{(j+1,N_T)} \\ \vdots & \vdots & \vdots & \vdots \\ h_k^{(M_k,1)} & h_k^{(M_k,2)} & \dots & h_k^{(M_k,N_T)} \end{bmatrix} \in \mathbf{C}^{((M_k-1) \times N_T)} \quad (6)$$

And the combined channel matrix for all the system received antennas except the j^{th} receive antenna of the k^{th} user desired receive antenna row as:

$$\tilde{\mathbf{H}}_k^j = [\mathbf{H}_k^j \mathbf{H}_1^T \dots \mathbf{H}_{k-1}^T \mathbf{H}_{k+1}^T \dots \mathbf{H}_B^T]^T \quad (7)$$

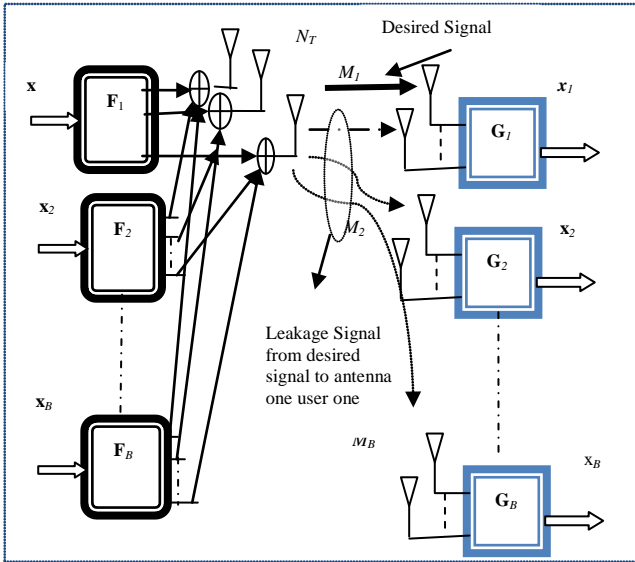


FIG.2: SYSTEM MODEL DEPICTING ALL VARIABLES.

From equation (6) and (7), the expression in (5) can be reduced to:

$$\gamma_k^j = \frac{\|\mathbf{h}_k^j \mathbf{f}_k^j\|_F^2}{\|\tilde{\mathbf{H}}_k^j \mathbf{f}_k^j\|_F^2 + \sigma_k^{2j}} \quad (8)$$

Problem statement: For any j^{th} receive antenna, at the k^{th} user, select the precoding vector \mathbf{f}_k^j , where $k = \{1, \dots, B\}$, $j = \{1, \dots, M_k\}$ such that the per-antenna signal to leakage plus noise ratio γ_k^j is maximized:

$$\mathbf{f}_k^j = \arg \max_{\mathbf{f}_k^j \in \mathbf{C}^{N_T \times 1}} \frac{\mathbf{f}_k^{jH} (\mathbf{h}_k^j \mathbf{h}_k^j) \mathbf{f}_k^j}{\mathbf{f}_k^{jH} (\tilde{\mathbf{H}}_k^j \tilde{\mathbf{H}}_k^j + \sigma_k^{2j} \mathbf{I}_{N_T}) \mathbf{f}_k^j}$$

subject to

$$\text{tr}(\mathbf{F}_k \mathbf{F}_k^H) = 1$$

$$\mathbf{F}_k = [\mathbf{f}_k^1, \dots, \mathbf{f}_k^{M_k}] \quad (9)$$

The optimization problem in the equation (9) deals with the j^{th} antenna desired signal in the numerator and a combination of total leaked power from the j^{th} antenna of the k^{th} user to all other antennas plus noise power at the j^{th} antenna front end in the denominator. To calculate the precoding matrix for each user we need to calculate the precoding vector for each receive antenna in the system independently. This requires solving the linear fractional optimization problem in the equation (9) $M_k \times B$ times using GEVD[11]. In this work, we develop a GSVD based algorithm to solve the PA-SLNR objective function of equation 9 for multiple users with multiple antennas.

IV. GSVD BASED PRECODING ALGORITHM

First formulation and generalization of singular value decomposition was introduced by Charles F. and Van Loan in [18]. There initial formulation was restricted to the dimension of the matrix pairs. More general and less restrictive version of GSVD is developed by Paige and Saunders in [19] which can be summarized as follows:

For any two matrices have the same numbers of columns i.e.

$\Psi_A \in \mathbf{C}^{P \times L}$ and $\Psi_B \in \mathbf{C}^{Z \times L}$ then for: $\Psi = \begin{pmatrix} \Psi_A \\ \Psi_B \end{pmatrix}$ and $\text{rank}(\Psi) = t$ there exists an orthogonal matrices such as $\mathbf{U} \in \mathbf{C}^{P \times P}$, $\mathbf{V} \in \mathbf{C}^{Z \times Z}$, $\mathbf{W} \in \mathbf{C}^{t \times t}$ and $\mathbf{Q} \in \mathbf{C}^{L \times L}$ such that :

$$\mathbf{U}^H \Psi_A \mathbf{Q} = \Sigma_A (\mathbf{W}^H \mathbf{R}, \mathbf{0}) \quad (10)$$

$$\mathbf{V}^H \Psi_B \mathbf{Q} = \Sigma_B (\mathbf{W}^H \mathbf{R}, \mathbf{0}) \quad (11)$$

where:

$$\Sigma_A = \begin{pmatrix} \mathbf{I}_A & & \\ & \mathbf{D}_A & \\ & & \mathbf{0}_A \end{pmatrix}, \quad \Sigma_B = \begin{pmatrix} \mathbf{0}_B & & \\ & \mathbf{D}_B & \\ & & \mathbf{I}_A \end{pmatrix}$$

$\mathbf{R} \in \mathbf{C}^{t \times t}$ is nonsingular matrix with its singular valves equal to the nonzero singular value of Ψ . The matrices $\mathbf{I}_A^{r \times r}$ and $\mathbf{I}_B^{(t-r-s) \times (t-r-s)}$ are identity matrices with value of r and s depend on the matrices Ψ_A and Ψ_B . The matrix $\mathbf{D}_A = \text{diag}(\alpha_{r+1}, \dots, \alpha_{r+s})$ and $\mathbf{D}_B = \text{diag}(\beta_{r+1}, \dots, \beta_{r+s})$ are diagonal matrices with the diagonal elements satisfies the following:

$$1 \geq \alpha_{r+1} \geq \dots \geq \alpha_{r+s} \geq 0 \quad (12)$$

$$0 \leq \beta_{r+1} \leq \dots \leq \beta_{r+s} \leq 1 \quad (13)$$

and

$$\alpha_i^2 + \beta_i^2 = 1 \quad \text{for } i = r+1, \dots, r+s \quad (14)$$

This analysis reveals that the computation of the GSVD starts with the complete orthogonal decomposition of the matrix Ψ followed by simple SVD of the orthogonal sub-matrices. Mapping the optimization problem in the equation (9) to the Paige and Saunders GSVD formulation, we can observe that for any j^{th} receive antenna of the k^{th} user, the PA-SLNR γ_k^j is a qualified GSVD problem and the eigenvector corresponding to the $(r+1)$ singular value will be the best vector in the direction of the j^{th} receive antenna of the k^{th} user (equation 14). Another notable observation is that the matrix the overall interference domain is constant for all users and receive antenna. These facts will allow the designer to reduce the computational load by making use of the matrix permutation principle. Algorithm 1, summarize

the complete steps to calculate the precoding matrices for multiple users in MU-MIMO-BC.

Algorithm 1: PA-SLNR MU-MIMO precoding based on GSVD Computation for multiple independent MU-MIMO users.

Input: all the users combined channel matrix and the received noise variance.

$$\mathbf{H}_{\text{com}} = [\mathbf{H}_1^T \mathbf{H}_2^T \cdots \mathbf{H}_B^T]^T, \sigma_k^{2j}.$$

Output: multiple users precoding matrices \mathbf{F}_k such that,

$k = 1, \dots, B$

1. Let $\boldsymbol{\psi}_k^j = [\mathbf{h}_k; [\tilde{\mathbf{H}}_k^j; \sigma_{N_T}^j]]$
2. Compute the QRD of the matrix $\boldsymbol{\psi}_k^j$ such that

$$\mathbf{Q}\boldsymbol{\psi}_k^j = \mathbf{R}$$

3. For $k = 1$ to B

4. For $j = 1$ to M_k

 Compute the vector \mathbf{v}_k^j from the

 SVD of $\mathbf{Q}((k-1)M_k + j : (k-1)M_k + j, 1 : N_T)$

 Solve for $\mathbf{R}\mathbf{f}_k^j = \mathbf{v}_k^j$

5. End

 The k^{th} user precoding matrix is

$$\mathbf{F}_k = [\mathbf{f}_k^1 \cdots \mathbf{f}_k^{M_k}]$$

6. End

V. SIMULATION AND RESULTS

The performance of the MU-MIMO system is measured in terms of the received BER and received output SINR outage. We evaluate the performance of the proposed PA-SLNR MU-MIMO precoding scheme based on the GSVD algorithm through Monte-Carlo simulation for different MU-MIMO broadcast system configurations. In each simulation setup, the entry of each k^{th} user MIMO channel \mathbf{H}_k is generated as complex white Gaussian entries with zero mean and unit variance. Furthermore, in all simulations experiments, user data symbols vector is 4-QAM modulated and spatially multiplexed at the base station. At the receivers, matched filter is used for the decoding

Figure 3, compares the received BER performance of the proposed PA-SLNR precoding which denoted in the figure By PA-SLNR-GSVD and the literature reference results of PU-SLNR-GSVD [17, 20] precoding schemes for the MU-MIMO-BC system configurations of $N_T = 12$ $B = 3$ $M_k = 3$.

In this MU-MIMO configuration, the base station modulates, spatially multiplexes and precodes a vector of length 3 symbols to each user. The BER is calculated over 5000 MU-MIMO channel realization for each algorithm. The proposed method outperforms PU-SLNR-GSVD. At BER equal to 10^{-4} there is approximately 2dB performance gain between PA-SLNR-GSVD and PU-SLNR-GSVD.

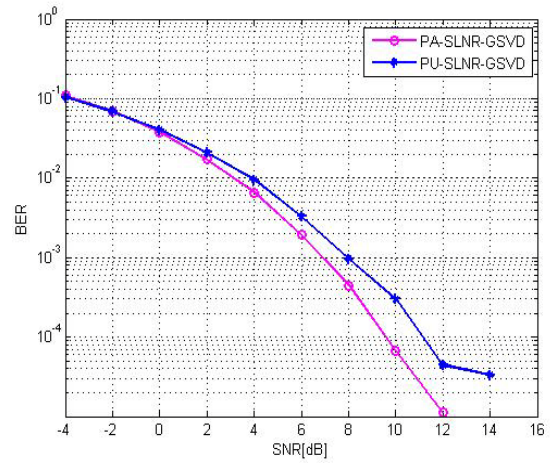


Fig 3: Shows the compression of the un-coded BER performance for PA-SLNR-GSVD, PU-SLNR-GSVD[17] precoding methods under system configuration of $B = 3$ $M_k = 3$ $N_T = 12$, 4-QAM modulated signal.

Figure 4, compares the received BER performance of the proposed PA-SLNR precoding which denoted in figure By PA-SLNR-GSVD and the literature reference results of PU-SLNR-GSVD precoding schemes for the MU-MIMO broadcast system configurations of $N_T = 10$ $B = 3$ $M_k = 3$. In this MU-MIMO configuration, the base station modulates, spatially multiplexes and precodes a vector of length 3 symbols to each user. The BER is calculated over 5000 MU-MIMO channel realization for each algorithm. The proposed method outperforms PU-SLNR-GSVD. At BER equal to 10^{-3} there is approximately 2 dB performance gain between PA-SLNR-GSVD and PU-SLNR-GSVD.

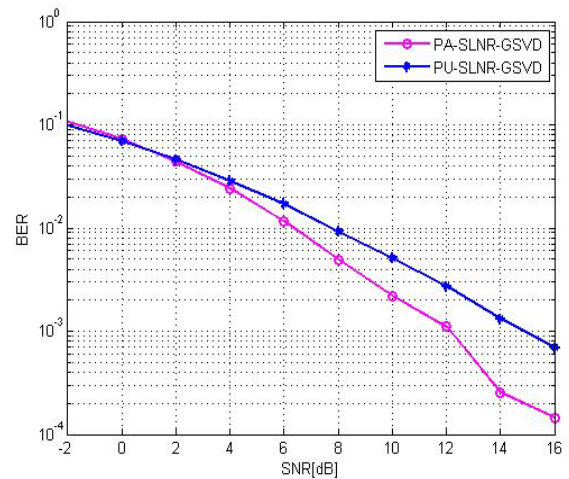


Fig 4: Shows the compression of the un-coded BER performance for PA-SLNR-GSVD, PU-SLNR-GSVD precoding methods under system configuration of $B = 3$ $M_k = 3$ $N_T = 10$, 4-QAM modulated signal.

Figure 5, compares the received output SINR outage performance of the proposed PA-SLNR-GSVD precoding and the reference PU-SLNR-GSVD. MU-MIMO system configuration of $B = 3$ $M_k = 4$ $N_T = 12$ and 4dB input SNR is considered in the simulation. The proposed method outperforms the PU-SLNR-GSVD method by 1 dB gain at 10% received output SINR outage.

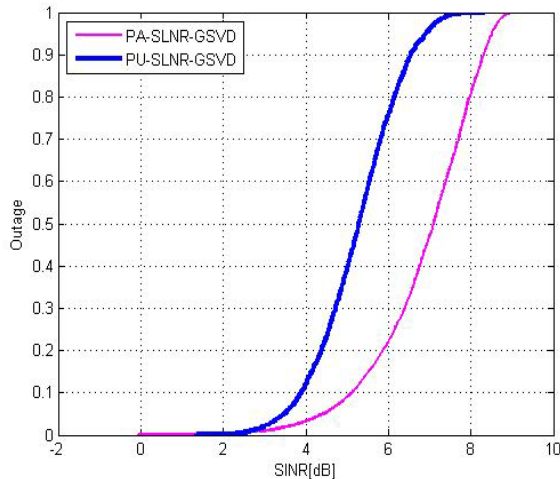


Fig 5: Shows the comparison of the un-coded output SINR outage performance PA-SLNR-GSVD and PU-SLNR-GSVD precoding methods under system configuration of $B = 3, M_k = 4, N_T = 12$, 4-QAM modulated signal at 4 dB SNR.

Figure 6, compares the received output SINR outage performance of the proposed PA-SLNR-GSVD precoding and the reference PU-SLNR-GSVD. MU-MIMO system configuration of $B = 3, M_k = 4, N_T = 12$ and 12dB input SNR is considered in the simulation. The proposed method outperforms the PU-SLNR-GSVD method by 2.5 dB gain at 10% received output SINR outage.

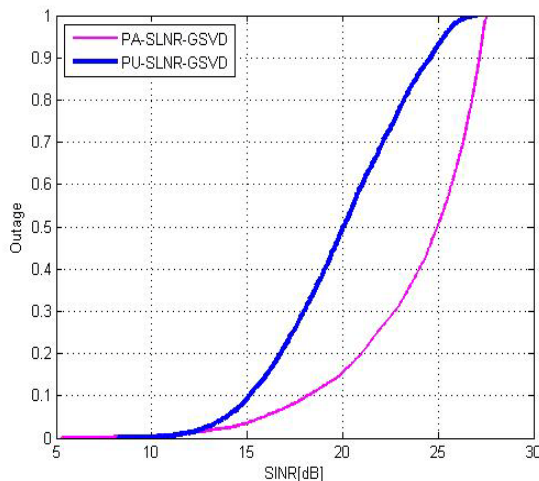


Fig 6: Shows the comparison of the un-coded output SINR outage performance PA-SLNR-GSVD and PU-SLNR-GSVD precoding methods under system configuration of $B = 3, M_k = 4, N_T = 12$, 4-QAM modulated signal at 12dB SNR.

VI. CONCLUSIONS

In this paper, a new MU-MIMO precoding method based on the combination of the PA-SLNR optimization criteria and GSVD computation algorithm is developed. Unlike the conventional method in literature which does not take into account the individual user intra-antenna interference cancellation, the proposed method transforms the MU-MIMO channel into a set of parallel single antenna channels

to effectively cancel intra-antenna interference and multiplex multiple data stream to each user. Simulation results show that the proposed method outperforms the conventional method.

References

- [1] F. Khalid and J. Speidel, "Advances in MIMO techniques for mobile communications- Asurvey," *Int'l J. of Communications, Network and System Sciences*, vol. 3, pp. 213-252, March 2010.
- [2] W. K.H., *et al.*, "Comparison of user selection methods for multiuser MIMO-OFDM downlink with limited feedback," *Inform. Technol. J.*, vol. 9, pp. 720-729, 2010.
- [3] V. Sharma and S. Lambotharan, "Multiuser Downlink MIMO Beamforming using an Iterative Optimization Approach," presented at the Vehicular Technology Conference Montreal, Que., 2006.
- [4] C. Y., *et al.*, "A leakage-based nonlinear precoder for the multi-user multi-stream MIMO broadcast channel.," *Inform. Technol. J.*, vol. 10, pp. 789-797, 2011.
- [5] S. Hyungjoon, *et al.*, "A Vector Perturbation Technique Based on Eigenvalue Normalization for Multi-User MIMO Downlink," in *Vehicular Technology Conference, 2009. VTC Spring 2009. IEEE 69th*, 2009, pp. 1-5.
- [6] N. Jindal, *et al.*, "Sum power iterative water-filling for multi-antenna Gaussian broadcast channels," *Information Theory, IEEE Transactions on*, vol. 51, pp. 1570-1580, 2005.
- [7] M. K. Karakayali, *et al.*, "On the Maximum Common Rate Achievable in a Coordinated Network," in *Communications, 2006. ICC '06. IEEE International Conference on*, 2006, pp. 4333-4338.
- [8] Q. H. Spencer, *et al.*, "Zero-Forcing Methods for Downlink Spatial Multiplexing in Multiuser MIMO Channels," *IEEE TRANSACTIONS ON SIGNAL PROCESSING*, vol. 52, pp. 461-471, Feb 2004.
- [9] V. Stankovic and M. Haardt, "Generalized design of Multi-user MIMO precoding matrices," *IEEE Trans. On wireless Comm.*, vol. 7, pp. 953-961, March 2008.
- [10] A. J. Tenenbaum and R. S. Adve, "Linear Processing and sum throughput in the Multiuser MIMO downlink," *IEEE TRANS. On wireless Comm.*, vol. 8, pp. 2652-2660, May 2009.
- [11] M. Sadek, *et al.*, "Active antenna selection in multiuser MIMO communications," *IEEE TRANS ON SIGNAL PROCESSING*, vol. 44, pp. 1498-1510, April 2007.
- [12] M. Sadek, *et al.*, "A Leakage-Based Precoding Scheme for Downlink Multi-User MIMO Channels," *IEEE TRANSACTION On Communications*, vol. 6, pp. 1711-1721, May 2007.
- [13] S. L. and Z. Z. Zhang, "Base station coordinated multi-user detection in multi-cell MIMO cellular systems," *Inform. Technol. J.*, vol. 10, pp. 134-139, 2011.
- [14] L. Min and O. Seong Keun, "A Per-User Successive MMSE Precoding Technique in Multiuser MIMO Systems," in *Vehicular Technology Conference, 2007. VTC2007-Spring. IEEE 65th*, 2007, pp. 2374-2378.
- [15] S. Shuying, *et al.*, "Physical layer multicasting with linear MIMO transceivers," in *Information Sciences and Systems, 2008. CISS 2008. 42nd Annual Conference on*, 2008, pp. 884-889.
- [16] E. Saeid, *et al.*, "FKT based linear Precoding for Multiuser multiple input multiple output," in *ICCBN-2011*, 2011.
- [17] P. Jaehyun, *et al.*, "Efficient GSVD Based Multi-User MIMO Linear Precoding and Antenna Selection Scheme," in *Communications, 2009. ICC '09. IEEE International Conference on*, 2009, pp. 1-6.
- [18] C. F. and V. Loan, "generalized singular value decomposition," *SIAM Journal on Numerical Analysis* vol. 13, March 1976.
- [19] C. Paige and M. A. Saunders, "Towards a Generalized Singular Value Decomposition," *SIAM Journal on Numerical Analysis*, vol. 18, pp. 398-405, 1981.
- [20] J. Park, *et al.*, "Generalised singular value decomposition-based algorithm for multi-user multiple-input multiple-output linear precoding and antenna selection," *IET Communication*, vol. 4, pp. 1899-1907 5 November 2010.

Detection of Lightning Pattern Changes Using Machine Learning Algorithms

Aimée Booyens
 School of Mathematics, Statistics
 and Computer Science
 University of KwaZulu-Natal
 Durban, South Africa
 210501411@stu.ukzn.ac.za

Serestina Viriri
 School of Mathematics, Statistics
 and Computer Science
 University of KwaZulu-Natal
 Durban, South Africa
 viriris@ukzn.ac.za

Abstract—The distribution of lightning across the Earth’s surface varies both with location and time. Seasonal changes in lightning activity recorded in Low Earth Orbit (LEO) satellite data have been studied by various authors, who used classical time series analysis techniques. This paper presents an alternative analysis based on automated pattern recognition, which identifies the changing state of lightning distributions using computer vision techniques. Due to the large quantity of data available, machine learning algorithms were used to predict the different lightning distribution patterns. The machine learning algorithm used to predict the seasonal patterns was K-Means which achieve a 64% global pattern detection rate. The Decision Tree machine learning algorithm was used to predict the spatial patterns this achieved 97% global pattern detection rate. The machine learning algorithm used to predict the time patterns were Naïve Bayes which achieved 31% global pattern detection rate. This system achieved a 63% global pattern detection rate for the larger dataset and for small dataset it achieved a 73% global pattern detection rate. This model not only has significant application in the analysis of historical lightning data but also helps in the forecasting of future lightning distributions.

I. INTRODUCTION

Lightning is an important and critical weather phenomenon to study, as it affects people and the environment directly and indirectly. Lightning can occur in many different forms - these are inter-cloud, intra-cloud, cloud-to-air and cloud-to-ground flashes [1], [2]. Inter-cloud occurs when lightning flashes between two different clouds and intra-cloud occurs when lightning flashes inside the same cloud. Cloud-to-air occurs when lightning flashes are discharged into the sky and strike nothing around it and cloud-to-ground occurs when lightning flashes are discharged and the flash hits the earth’s surface.

Quantification and mapping of lightning has become a very important area of research as it is beneficial to physicists trying to understand the phenomena of lightning. Along with meteorologists who can use lightning to understand climate change and severe weather storms. It is also of benefit to engineers and economists who use this information when planning buildings and infrastructure.

In this paper data from the Lightning Imaging Sensor (LIS) data aboard the Tropical Rainfall Measuring Mission (TRMM) [3], [4], [5], [6] is analysed with the aim of investigating global

distribution patterns of lightning for the four year period from May 2002 to December 2006.

The rest of the paper consists of *Section 2* Related Works, *Section 3* Methodology and Design, *Section 4* Results and Discussion and lastly *Section 5* will be the conclusion.

II. RELATED WORKS

There is minimal information available on these types of systems but the following papers described their approaches thoroughly:

Finke and Hauf [7] used Lightning Position and Tracking System (LPATS). LPATS system is used to detect cloud-to-ground lightning discharges, by taking features from this type of lightning to reject or accept whether the lightning occurred - this system had 70% detection efficiency but this was only small datasets.

LPATS has a built in algorithm that estimates the peak current amplitude of the return stroke from the measured signal strength and calculated location. The algorithm used to calculate the peak current amplitude is defined in equation (1):

$$f(t, \vec{r}) = \sum_i^N \int (t - t_i) \int (\vec{r} - \vec{r}_i) \quad (1)$$

where the t_i and \vec{r} denotes the time and location of the i^{th} detection. The Dirac function $\int (t - t_i)$ and $\int (\vec{r} - \vec{r}_i)$ are used in their convectional meaning. By applying these integrals they used statistical analysis to see how the lightning changed over time and area.

One type of analysis done was the number of lightning events which occurred during the time interval Δt around the central time t and inside the area ΔF around the location \vec{r} were integrated, as defined in equation (2).

$$N(t, \vec{r}, \Delta t, \Delta F) = \int f(t + \tau, \vec{r} + \vec{p}) d\vec{p} d\tau \quad (2)$$

However, the results found by this system have been an estimate due to the fact that this type of detection is dependent

on the location of the lightning to the location of the detection device.

Cannons and Kinsner [8] used an Axisymmetric Numerical Cloud Model (ANCM), this is an electrification model which represents a thundercloud in cylindrical axisymmetric form. This system uses equations to obtain temporal and spatial distributions. After calculating this, the Poisson's equation, as defined in equation (3), is used to calculate electrical capability, which is then used to model lightning discharges. A major problem is that the models created are large and complicated, and have difficulty in displaying the chaotic patterns of lightning discharges and this system had 60% detection efficiency.

$$f(x) = \frac{\lambda^x \cdot e^{-\lambda}}{x!} \quad (3)$$

Dlamini [5] uses the Lightning Imaging Sensor (LIS) aboard the Tropical Rainfall Measuring Mission (TRMM) to obtain data over the area of Swaziland. Dlamini uses ArcGIS to ascertain if there is a link between varying elevations in Swaziland to the lightning that has occurred. This was done by using the machine learning algorithm of the Nearest Neighbor which is a ratio of the observed distance to the expected distance. The results that the Nearest Neighbor produced were 75% detection efficiency but this machine learning algorithm could only be used for small datasets.

III. METHODOLOGY AND DESIGN

The data processing system reads in various file types, of hdf4 to hdf5. The data is then processed and analysed using machine learning algorithm, the resultant information enable the user to obtain a variety of graphs, data and maps, this is depicted in Figure 1.

A. Dataset

This paper uses data from the satellite-based Lightning Imaging Sensor (LIS) aboard the Tropical Rainfall Measuring Mission (TRMM). It was launched in November 1997 as a joint United States and Japanese mission aimed at understanding the global energy and water cycles by providing distributions of precipitation and the associated thermodynamics over the tropics [4], [5], [6]. The LIS TRMM measures all forms of lightning, inter-cloud, intra-cloud, cloud-to-air and cloud-to-ground flashes, with a high detection efficiency of every 90 seconds for both day and night conditions.

B. Data Manipulation

The data that was read into the system by the R Programming Language had to be manipulated as some variables such as location and time were in a different format. Which resulted in difficulty to produce any information.

The location values were separated by a comma to represent the Latitudinal and Longitudinal values. Due to this it had to

be separated into different columns using the split function in the R Programming Language.

The time values were recorded in International Atomic Time (TAI) which is a high precision atomic coordinate time standard based on the movement of the Earth's geoid. Using the time package POSIXlt that is found in R packages it was able to convert the time to its correct Coordinated Universal Time (UTC). This was done in order to extract the day, month, year, hour, minute and second that the lightning strikes occurs.

C. Pattern

Once the data was correctly separated it was then used to plot the points of Longitude and Latitude with the corresponding Radiance using the R package ggmap [9]. By plotting all the points from each year it was evident that there was no clear pattern that emerged from the data, as depicted in Figure 2.

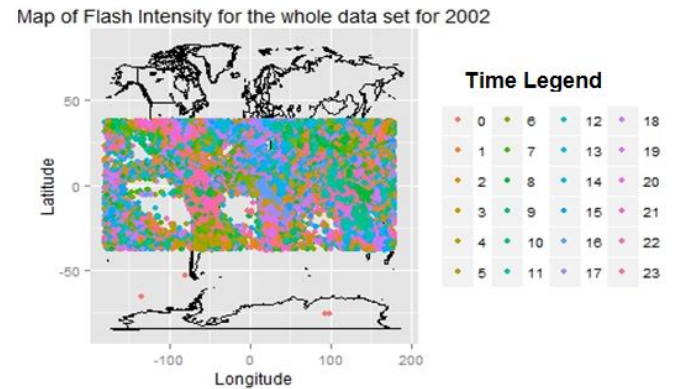


Fig. 2. The Whole Dataset

As no clear patterns were produced different maps of Radiance against variables such as the time and the month it occurred and the location were generated using the density function in ggmap. The density function uses a two-dimensional kernel density estimation with an axis-aligned bivariate normal kernel, as defined in equation (4). This equation takes a random sample of x values with a kernel (K) and a bandwidth (h) by which it tries to estimate the similarities in the x values and then links them together [9].

$$\hat{f}(x, h) = \frac{1}{nh} \sum_{i=1}^n K\left(\frac{x - X_i}{h}\right) \quad (4)$$

Once these density maps were generated, clear correlations and patterns were observed. The main patterns that emerged were seasonal, time and spatial patterns.

A seasonal pattern was observed by plotting points where the lightning occurred for each hemisphere against the month it occurred. The observation made was that every three months the Radiance values changed from extremely high values to low values [10]. This showed that seasonal change correlated with that particular hemisphere's seasons. It was evident that when the Radiance and the number of lightning flashes were high, during that hemisphere's summer season, shown in

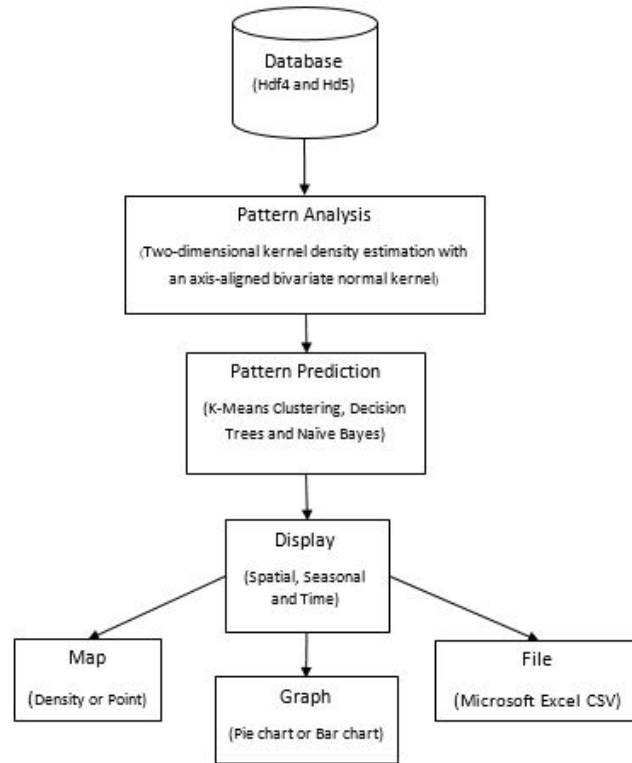


Fig. 1. The Subsystem Interaction

Figures 3 and 4. It was also evident that when the Radiance and the number of lightning flashes were low, during that hemisphere's winter season [10]. When the Radiance and the number of lightning flashes were approximately the same in both hemispheres it was either autumn or spring season. Due to this autumn and spring seasons cannot be clearly distinguished between. From these results it has been established that there is a lightning pattern that correlates to the hemisphere's summer and winter seasons.

Time patterns were observed when plotting certain time values against the Radiance experienced at the time, as depicted in Figure 5. The results showed that globally certain areas experienced the same range of intensity values for that particular time. Hence, it showed evidence that there could be a time pattern for the dataset used.

Spatial patterns were observed by plotting latitudinal values with their corresponding Radiance value. What was evident was where the Radiance value was low the corresponding latitude was close to the equator and where the Radiance value was high, the latitude was further away. Due to this change in Radiance values as latitude increased, there is evidence that there could be spatial patterns, as depicted in Figure 6

D. Prediction

A number of different supervised and unsupervised machine learning algorithms were used in order to predict seasonal,

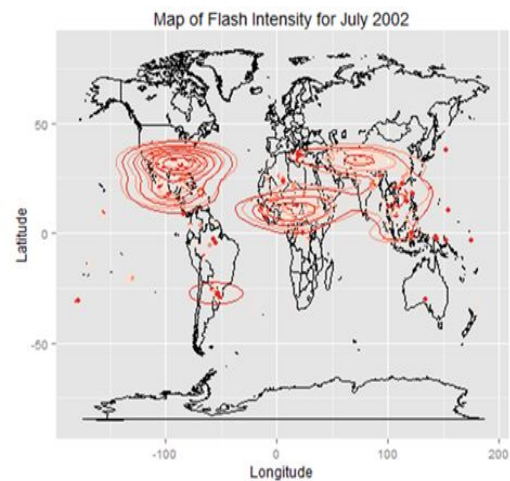


Fig. 3. Northern Hemisphere Summer Season Density Map

spatial and time patterns. The machine learning algorithms used to test supervised learning were Naïve Bayes, Support Vector Machines (SVM), Random Forest, K-Nearest Neighbor Classification, K-Means and Decision Trees. The unsupervised learning was K-Means Clustering [11].

K-Means Clustering [11], [12] is a machine learning algo-

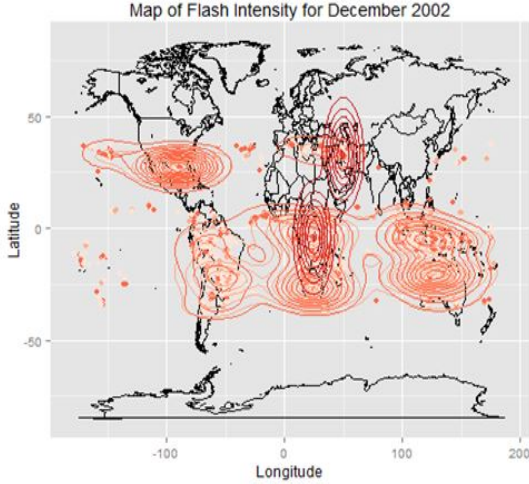


Fig. 4. Southern Hemisphere Summer Season Density Map

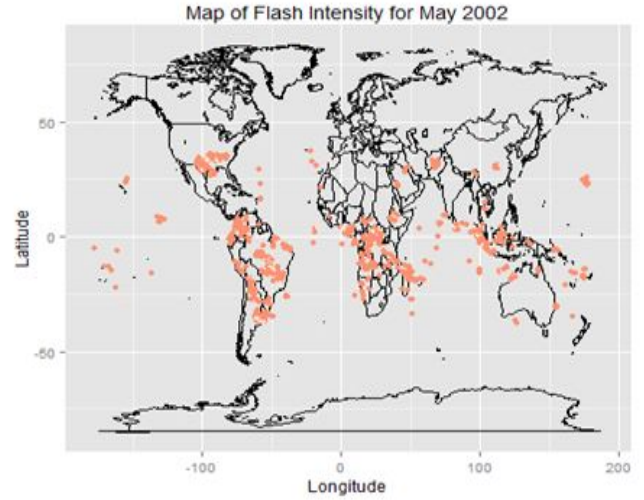


Fig. 6. Example of Spatial Pattern Density Map

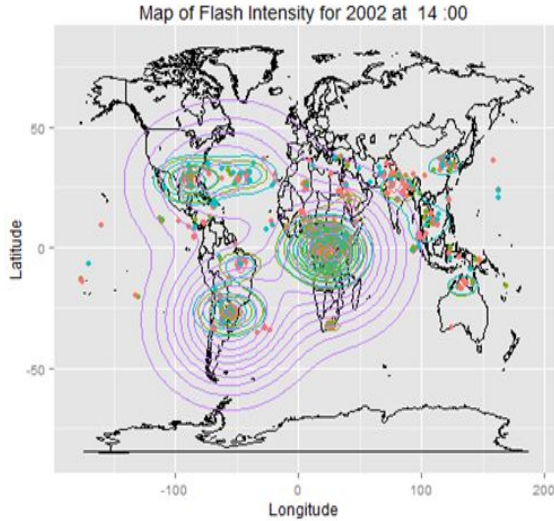


Fig. 5. Example of the Time Pattern Density Map

rithms used for seasonal pattern prediction. K-Means Clustering is calculated, by choosing a number of points c_j to be used as the initial centroid. Then subtracting all points $x_i^{(j)}$ from c_j then adding the subtracted answers together. Once the last point in the dataset has been reached and if the addition is not zero then it re-computes the centroid and restarts the calculation, as defined in the equation (5).

$$p = \sum_{j=1}^k \sum_{i=1}^n \|x_i^{(j)} - c_j\|^2 \quad (5)$$

Decision Tree[11], [13] algorithm is a suitable machine learning algorithms to use for spatial patterns. Decision Tree uses recursive partitioning to separate the dataset by finding the best variable and using the selected variable to split the data. Then using the entropy, defined in equations (6) and (7),

to calculate the difference that variable would make on the results if it is chosen. If the entropy is 0 then that variable is perfect to use, else a new variable needs to be selected.

$$H(D) = - \sum_{i=1}^k P(C_i|D) \log_k(P(C_i|D)) \quad (6)$$

$$P(C_i|D) = \frac{\text{number of correct observation for that class}}{\text{total observation for that class}} \quad (7)$$

Naïve Bayes [11], [14] is used for the prediction of the time pattern. Naïve Bayes classifies an instance by assuming the presence or absence of a particular feature and sees if it is unrelated to the presence or absence of another feature, given in the class variable. This is done by calculating the probability for which it occurred, as defined in equation (8).

$$P(x_1, \dots, x_n|y) = \frac{P(y)P(x_1, \dots, x_n)}{P(x_1, \dots, x_n)} \quad (8)$$

IV. RESULTS AND DISCUSSION

The system has been coded using the R Programming Language, the reason for this is because it has the ability to open and read hdf4 and hdf5 files by downloading an extension package. The Graphical User Interface (GUI) was also coded in R Programming Language using the packages RGtk2, gWidgetsRGtk2, cairoDevice and plotrix as R Programming Language does not have a one set GUI package as in Java [15].

The dataset utilized was for the period from May 2002 to December 2006 and was acquired from the Space Science Research Institute at the University of KwaZulu-Natal. This data consisted of information on the date, time, location, number of events, number of groups and radiance. From the

above variables this system used the time, the location and the radiance. These variables were then imported and saved as a Microsoft Excel CSV (Comma Delimited) file for spatial-temporal analysis.

The datasets used had between 900 000 - 1 050 000 lightning strikes per year. This system had a high complexity time to load data and produce the maps or graphs this could be a flaw of using R programming language. Once the dataset was loaded it was easier and quicker to work with the data.

A number of tests were done to investigate which machine learning algorithm would be suitable to determine the best results for seasonal, spatial and time patterns. The dataset sizes ranging from 0.01% to 50% of the original dataset were tested against the different machine learning algorithms. These testing datasets were filled with randomly chosen points from the original dataset.

After testing the dataset it was found that K-Means Clustering was suited for seasonal patterns, Decision Trees was suited for spatial patterns and Naïve Bayes were best suited for time patterns. The dataset sizes ranging from 0.01% to 50% of the original dataset were tested against these machine learning algorithms. These new testing datasets were filled with randomly chosen points from the original dataset.

A. Seasonal Pattern Prediction Results

Figure 7. showed the that for small amounts of data points all the machine learning algorithms have the ability to produce a result. Figure 7. also showed that the moment the dataset become too large Random Forest, Support Vector Machines and K-Nearest Neighbor could no longer produce results.

Decision Tree did produce the best results but it had high time complexity of over 3.5 minutes to compute a result for the whole dataset. Naïve Bayes produced average results but here too had a high time complexity. K-Means was found to be the best machine learning algorithm as on average had a 63% success rate for all dataset sizes. Also the time take to produce these results were less than a minute.

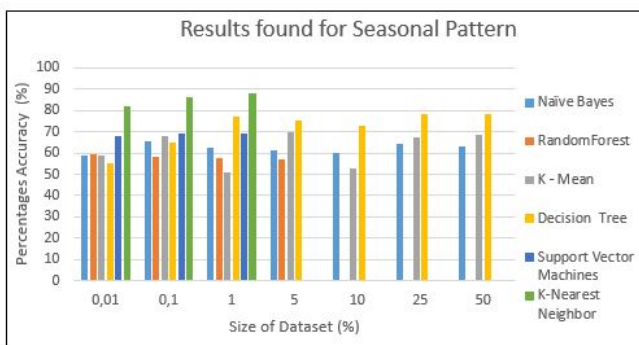


Fig. 7. Graph for percentages achieved for machine learning algorithm of the Seasonal Pattern

Hence, K-Means was used to predict the seasonal pattern for each year from 2002-2006, this produced 63%. After testing it was found that when the dataset was small it produced average

results due to the fact that the machine learning algorithm did not have enough data to produce the pattern. The large datasets yielded good results, which is needed as the size of the data is extremely large. The computational time for K-Means was short for both large and small datasets, as depicted in Figure 8.

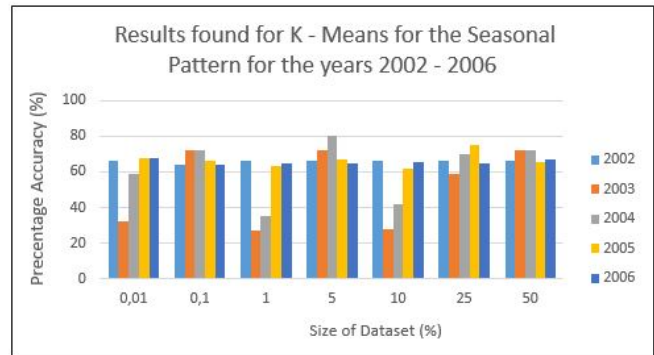


Fig. 8. Graph for percentages achieve for K-Means machine learning algorithm

B. Spatial Pattern Prediction Results

The observations made with spatial patterns and the machine learning algorithms on average produced results of about 90%. This showed that only a few points per dataset were close to the Equator and had low Radiance values hence making it easier to predict and obtain the correct results as most of the points were for the area far from the Equator and had higher Radiance. The moment the dataset became too large, once again Random Forest, Support Vector Machines and K-Nearest Neighbor could no longer produce results.

Due to the fact that the results produced were so high it was best to use the time it took to produce a result as the main factor. Naïve Bayes and K-Means both took on average 1.5 minutes for small datasets but for large datasets took 4-5 minutes to compute. Whereas with Decision Tree for both large and small datasets took about a minute to compute the result, as depicted in Figure 9.

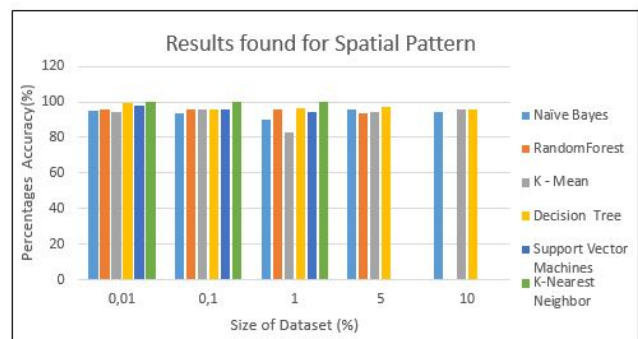


Fig. 9. Graph for percentages achieved for machine learning algorithm of the Spatial Pattern

Therefore the Decision Tree, which produced a 97% global pattern detection rate, was used to predict the Spatial Pattern for the years 2002-2006. It was found that when the size of the dataset was 0.01% for all years produced the same result of 99%. As the dataset got larger the results dropped by 1-2% but still maintained the above 90% average for all years, with some years even obtaining 100%, as shown in Figure 10 .

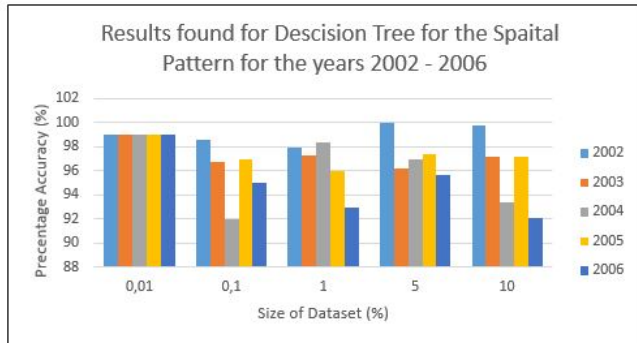


Fig. 10. Graph for percentages achieve Decision Tree machine learning algorithm

C. Time Pattern Prediction Results

Machine learning algorithms used to predict the time patterns on average produced poor results compared to the other two types of patterns as none of the percentages were above 50%. A reason that the percentage was so poor could be the fact that time patterns had 24 different categories from which it could choose from, where as seasonal and time patterns only had 2 different categories to choose from. Due to this all machine learning algorithms were finding it difficult to correctly classify the time patterns. This also showed that the time patterns were not that well defined in the dataset used. It was found that the moment the dataset became too large Random Forest, Support Vector Machines and K-Nearest Neighbor could no longer produce results, as shown in Figure 11.

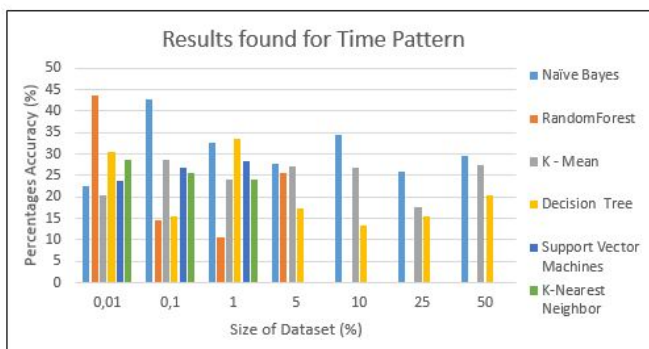


Fig. 11. Graph for percentages achieve for machine learning algorithm for the Time Pattern

The machine learning algorithm that produced better results was with Naïve Bayes with 31%. This was used to predict the

time pattern for the years 2002-2006. It was found that when the dataset was small it produced results lower than normal. The large datasets had a 2-4 % higher result, with a few datasets going above 40%. The computational time for Naïve Bayes was longer due to the fact that it had many different categories to choose from, this was found for both large and small datasets, as depicted in Figure 12.

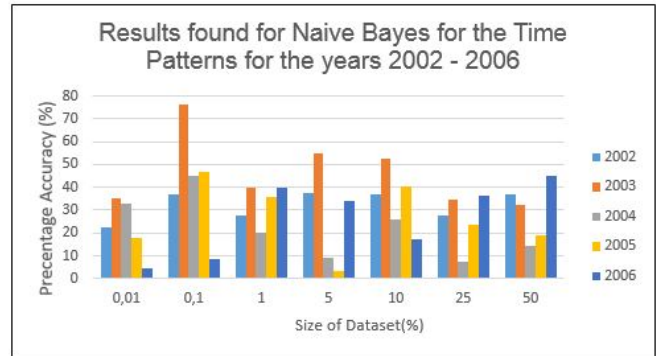


Fig. 12. Graph for percentages achieve for Naïve Bayes machine learning algorithm

V. CONCLUSION

This paper presented an alternative analysis based on automated pattern recognition, which identifies the changing state of lightning distributions using machine learning algorithm. The data file in the format hdf4 to hdf5 is processed and analysed using particular machine learning algorithm, the resultant information enable the user to obtain a variety of graphs, maps and data. The machine learning algorithm used to predict the seasonal patterns was K-Means which achieve a 64% global pattern detection rate. The Decision Tree machine learning algorithm was used to predict the spatial patterns this achieved 97% global pattern detection rate. The machine learning algorithm used to predict the time patterns were Naïve Bayes which achieved 31% global pattern detection rate. This research work achieved a 63% global pattern detection rate for the larger datasets and for small datasets it achieved a 73% global pattern detection rate. Future work for this work is to optimize the time complexity through parallel computing.

ACKNOWLEDGMENT

The authors would like to thank the National Research Foundation (NRF) and the South Africa National Space Agency (SANSA) for all forms of assistance during this research work.

REFERENCES

- [1] C. Neuwirth, W. Spitzer, and T. Prinz, "Lightning density distribution and hazard in an alpine region," *Journal of Lightning Research*, vol. 4, pp. 166 – 172, 2012.
- [2] J. W. van Wagendonk and D. R. Cayan, "Temporal and spatial distribution of lightning strikes in California in relation to large - scale weather patterns," *Fire Ecology*, vol. 4, no. 1, pp. 34 – 56, 2008.

- [3] H. R. Christian, D. Blakeslee, W. Boccippio, D. Boeck, K. Buechler, S. Driscoll, J. Goodman, W. Hall, D. Koshak, D. M. Mach, and M. Stewart, "Global frequency and distribution of lightning as observed from space by the optical transient detector," *Journal of Geophysical Research*, vol. 108, pp. 1 – 15, 2003.
- [4] A. B. Collier, S. Bremner, J. Lichtenburger, C. J. Downs, J. R. and Rodger, P. Steinbach, and G. McDowel, "Global lightning distribution and whistlers observed at dunedin, new zealand," *Annales Geophysicae*, vol. 28, pp. 499 – 513, 2010.
- [5] A. Dlamini, "Integrating satellite data and gis to map lightning distribution," *PositionIT*, vol. 12, no. 1, pp. 1 –4, 2007.
- [6] R. Marshall, U. S. Inan, T. Neubert, A. Hughes, G. Satori, J. Bórl, A. Collier, and T. H. Allinl, "Optical observation geomagnetically conjugate to sprite - producing lightning discharges," *Annales Geophysicae*, vol. 23, pp. 2231 – 2237, 2005.
- [7] U. Finke and T. Hauf, "The characteristics of lightning occurrence in southern germany," *Beitr. Phys. Atmosph.*, vol. 69, no. 3, pp. 361 – 374, 1996.
- [8] J. Cannons and W. Kinsner, *Modelling of Lightning Discharge Patterns as Observed from Space*. Manitoba: Department of Electrical & Computer Engineering Signal & Data Compression Laboratory, 2000.
- [9] H. Kahle, D. and Wickham, "ggmap: Spatial visualization with ggplot2," *The R Journal*, vol. X/Y, pp. 1 – 12, 2012.
- [10] A. Sugita and M. Matsui, "Lightning distributions in winter observed by the jldn," in *21st International Lightning Detection Conference*, Orlando, 2010.
- [11] P. Domingos, *A Few Useful Things to Know about Machine Learning*. Washington: University of Washington, 2010.
- [12] T. Kanungo, M. Mount, N. Netanyahu, C. D. Piatko, R. Silverman, and A. Y. Wu, "An efficient k - means clustering algorithm: Analysis and implementation," *Transactions on pattern analysis and machine intelligence*, vol. 24, no. 7, pp. 881 – 892, 2002.
- [13] L. Rokach and O. Maimon, *Data Mining and knowledge discovery Handbook for Beginners*. France: Tel-Aviv, 2010.
- [14] D. Lowd and P. Domingos, *Naive Bayes Models for Probability Estimation*. Washington: University of Washington, 2003.
- [15] M. F. Lawrence and J. Verzani, *Programming Graphical User Interfaces in R*. London: CRC Press Taylor and Francis Group, 2012.

Multiple Types of Heterogeneous Spatial Data Integration Process Using Business Intelligence Approach

M. Mustafa, A. Aliff and M. Yazid

Abstract-The Problem with heterogeneous sources of spatial information containing unstructured data. Here, examples of unstructured data are e-mail, maps, reports, contracts, images, movies, spreadsheets, web content and presentations are difficult to integrate and store in one database. Through a Business Intelligence Approach in the integration process, given us the best decision supporting tools for the user to make any decision related to the information that is already integrated from multiple sources and format of information in distributed locations.

Keywords-Data Integration, Spatial Information, Business Intelligence, Unstructured Data.

I. INTRODUCTION

INFORMATION integration involves a data integration process that combines data from a heterogeneous data sources in order to provide a unified view of data in a structured form [1][2]. The data integration process is done by applying a global data model and by detecting and resolving schema and data conflicts so that a homogeneous, unified view can be provided [3][4][5].

Information integration involves designing an approach that has the ability to combine data from a variety of independent data sources. Recent years, various specific aspects in information integration approaches [6][7][8] have been studied, proposed and suggested in the pursuit of achieving an ideal data integration system by the research community. The finding from reviewing some existing data integrations model showed that there was a remarkable history of previous research projects and study in the area of data integration.

Unfortunately most of these integration approaches do not abstract the users usage in marine field from heterogeneous sources of spatial data information integration through multidatabases.

Furthermore, most of organization's information nowadays was saved in unstructured contents such as e-mail, maps, reports, contracts, images, movies, spreadsheets, Web content and presentations, etc. These types of information can generate a lot more information and knowledge than some structured data in database. Most of these major unsolved problems in the information

technology (IT) industry are the difficulty to capture and store these unstructured data types in the common database storage in order to retrieve knowledge for decision.

Therefore, this paper proposes the design and develops a different spatial data integration model that based on the Business Intelligent approach. This integration model manipulates and integrates heterogeneous sources of spatial information from different databases, data format, and storages.

The proposed model will apply spatial information integration processes that also contain unstructured contents such as e-mail, maps, reports, contracts, images, movies, spreadsheets, Web content and presentations, etc., from multi-databases at different location of storage.

The rest of this paper has been structured as follows. Based on a literature review, Business Intelligence approaches were distinguished and discussed in Section II. These approaches are incorporated into a three layer BI framework that separates data, logic, and access-related BI components in Section III. The proposed spatial data integration framework is distinguished and discussed in Section IV which every component and their interactions at each layer are described. Finally, the conclusions are in Section V.

II. BUSINESS INTELLIGENT

Generally Business Intelligence provides a single view of the truth. The Business Intelligence architecture is based on the existence of a Data Warehouse on which data from all sources are integrated and from all views of information are dragged. The main objective of Business Intelligence framework is to process data from heterogeneous sources, to integrate and visualize them comprehensively. This is a user friendly that will be used as a guideline for decision making process.

As illustrated in Figure 1, multiple disparate Data sources, data integration services, data management services, reporting, analytical services, information delivery, and consumption services form the broad spectrum of the BI architecture. Heterogeneous sources of data are integrated into Data Warehouse using Extract, Transform and Load (ETL) processes that transformed all data from Data Warehouse into meaningful information.

M.Mustafa is lecturer from School of Informatics and Applied Mathematics, Universiti Malaysia Terengganu (UMT), 21030 Kuala Terengganu, Terengganu, Malaysia. (e-mail: mustafaman@umt.edu.my).

A.Aliff. is a PhD. Student from School of Informatics and Applied Mathematics, Universiti Malaysia Terengganu (UMT), 21030 Kuala Terengganu, Terengganu, Malaysia. (e-mail:taf_2nd@yahoo.co.uk).

M. Yazid is a Lecturer from Department School of Informatics and Applied Mathematics, Universiti Malaysia Terengganu (UMT), 21030 Kuala Terengganu, Terengganu, Malaysia. (e-mail: yazid@umt.edu.my)

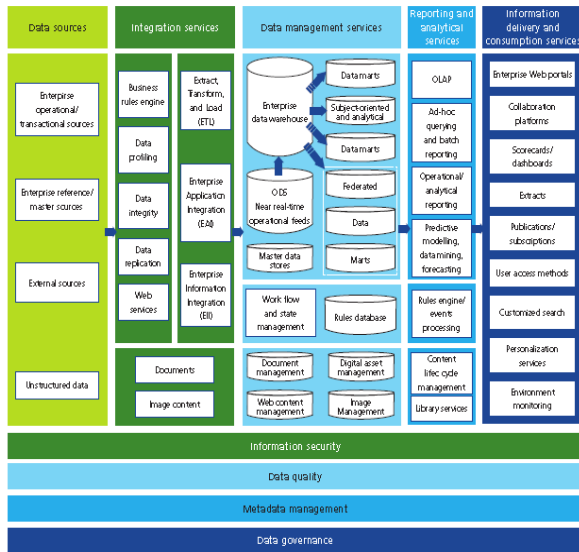


Figure 1: Typical BI Architecture

III. INTEGRATION MODEL

The Business Intelligence as an integrated model that includes two main processes as be illustrated in Figure 2.

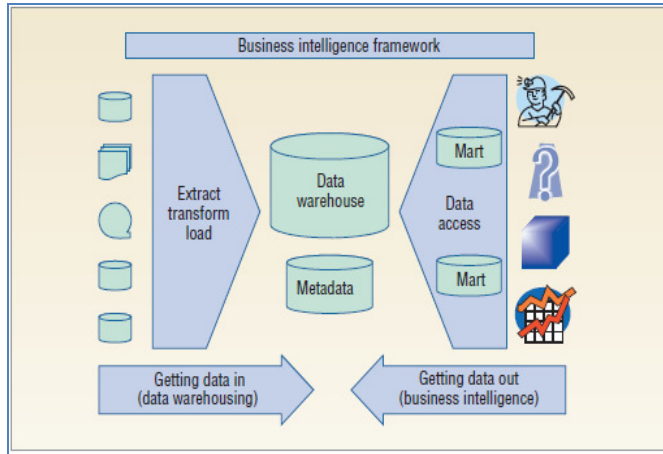


Figure 1: The BI framework includes two primary activities [9]

A. Getting Data In

This process is based on the Data Warehouse approach that involves loading the data from a set of source systems into an integrated data warehouse. The data were from heterogeneous platforms which may contain different sources, different location of databases, and different data format. These data are being to integrated and transformed for further data analysis process.

Data manipulation on this stage involves with the group of ETL processes ETP. For loading the data into the Data Warehouse, the ETL process takes place on Operational Data Store (ODS) on which data transformation is done before loading on Data Warehouse. Data Marts mostly is implemented as a data repository that served specific users (of specific department, geographic area, application). All data marts uses the same Data Warehouse in order to ensure a “single version of truth” [9].

B. Getting Data Out

This process consists of business users and applications accessing data from the data warehouse to perform enterprise reporting, OLAP, querying, and predictive analytics.

Business Intelligence framework is based on three relevant layers as illustrated in Figure 3.

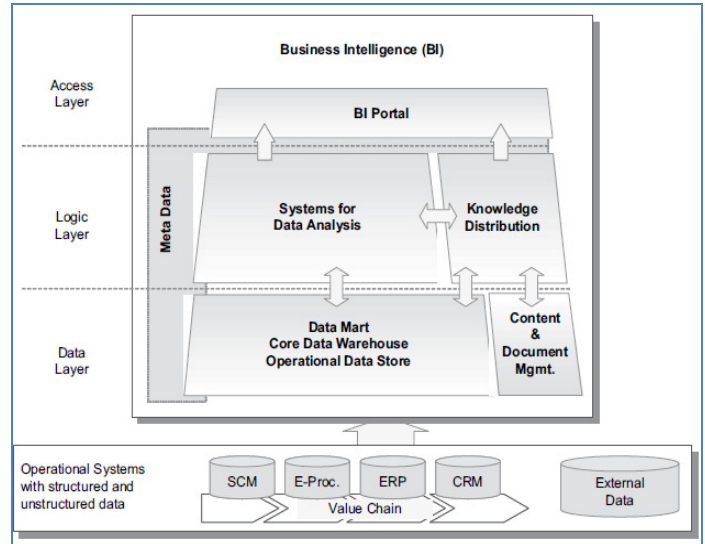


Figure 2: Business Intelligence Framework [10]

The Data Layer responsible for managing the data from heterogeneous platforms that may contained with structured and unstructured form. For structured data form, this type of data usually be loaded into data repositories such as Data Warehouses, Data Marts, and Operational Data Stores, while for unstructured data form, this type of data is loaded into Content and Document Management Systems that responsible to handle metadata content. The process of loading data from heterogeneous sources involves data extraction and transformation that included with some operational systems like ERP (Enterprise Resources Planning) systems and external data sources

The Logic Layer provides some schemas that enable the structured data or unstructured content to be analysed. Furthermore, this schema also supports the distribution of relevant knowledge.

The Access Layer provides the user with the capability to use all relevant schemas of Logic Layer in an integrated fashion. Usually at the Access Layer, all relevant schemas from the logic layer are visualised with some sort of portal software that provides a harmonized Graphical User Interface [10].

IV. PROPOSED BUSINESS INTELLIGENT APPROACH IN DATA INTEGRATION

In this section, this paper proposed spatial data integration framework which follows the three layers mentioned in Section III. As illustrated in Figure 4, the three layers of the framework will be discussed in further detail. For each layer, the components and their interactions are described. Special emphasis is given to components that handle unstructured data and to the challenges of implementing and using them.

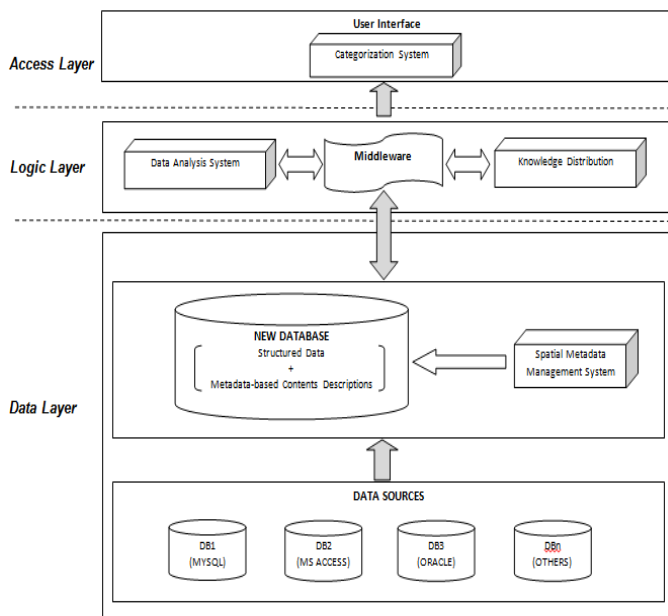


Figure 3: Business Intelligence Framework and Integration Approaches

A. Data Layer

As mentioned in Section III, the Data Layer manages data that contained with structured and unstructured form from heterogeneous data sources. Spatial information integration is managed by some applications of middleware system without requiring Mediators and Wrapper approaches. This middleware system also manages search, retrieval and management of unstructured information growth across multidatabases infrastructures. This framework also does not require data repositories such as Data Warehouses, Data Marts, and Operational Data Stores in order to retrieve information about spatial data result from multidatabase.

In order to support metadata-spatial data management, two prototype implementations are proposed. The first prototype is an existing open source modeling software called INTERLIS/UML Editor, which is extended by implementing the principles for metadata-spatial data integration [11]. The second prototype implementation explores the possibilities of creating views and functionalities of views in the relational database management system Oracle 9i.

B. Logic Layer

There are two types of systems distinguished at this layer: Data Analyze system and Knowledge Distribution System. Data Analyze System is responsible for collecting and processing data (unstructured data and metadata-based contents) from the Data Layer and transforms them into a standardize form pertinent for a visualization to the user.

The components for Knowledge Distribution System can be used to provide results and templates generated with Data Analysis Systems. In order to manage unstructured data, components for Knowledge Distribution System are needed for extracting information from integrated database. INTERLIS/UML Editor and Oracle 9i tools have been identified to help identifying, summarizing, linking, and grouping content items.

Regarding the exchange of results and templates between Analysis Systems and the knowledge distribution components, efficiency gains may be attained by the introduction of a respective middleware. The approach of this paper is based on CLARANS algorithm and Abstract Representation that will act as a hub that can communicate with several systems. Furthermore, these approaches

also include with some schemas that can converted and translated data formats. This idea shown in Figure 5. The generates reports and templates from the components in the Analysis Systems, where it is converted and transferred via the “middleware hub” to the Knowledge Distribution System. When these templates and reports need to be applied, they can be transferred back to the Analysis Systems.

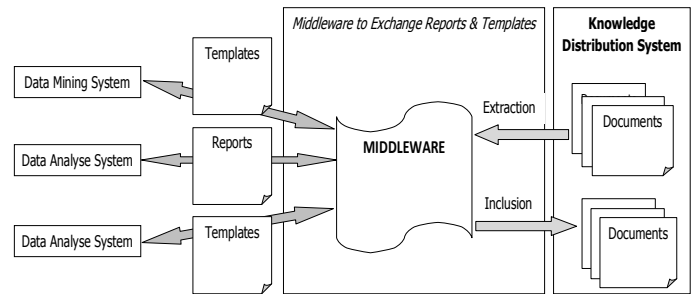


Figure 4: Middleware Hub for the Exchange of Analysis Results and Analysis Templates.

C. Access Layer

The Data Access Layer responsible for integrating all relevant components and schemas from the Logic Layer and visualizes them according to the user query. Business Intelligence usually uses “portal systems” for the implementation of this layer. Portals approach provides an integrated user interface for different content sources and application systems.

Portals and content management systems often claim to provide metadata, but they in fact rely on humans to provide any metadata beyond what they automatically capture as they store or route documents. Although this approach can work well in structured work flows, it is untenable in loosely structured knowledge work, especially as organizations focus on knowledge workers’ productivity [12]. The approach of this paper is based on a Categorization System that can generate collection catalogs or directories automatically. A Categorization System provides and maintains a hierarchical structure of categories (also called as taxonomy) and assigns documents to this category.

V. CONCLUSION

The proposed data integration system was based on Coupling Information Systems Techniques which the integration processes will be implemented by middleware software. This software has been approved to provide fast query and information retrieval process of spatial and non-spatial from heterogeneous database sources. Furthermore the data mining process from middleware software also can provide online mapping that is meaningful for the user.

REFERENCES

- [1] M. Friedman, A. Y. Levy, and T. D. Millstein, “Navigational Plans For Data Integration.” In AAAI/IAAI, 1999, pp. 67–73.
- [2] M. R. Genesereth, A. M. Keller, and O. M. Duschka, “Infomaster: An Information Integration System.” in SIGMOD Conference, 1997, pp. 539–542.
- [3] Ziegler, Patrick " User-Specific Semantic Integration of Heterogeneous Data: What Remains to be Done? " Building the Information Society 156 (2004): 3-12. Print.
- [4] M. Lenzerini, “Data Integration: A Theoretical Perspective.” in PODS, 2002, pp. 233–246.
- [5] Zachary G. Ives, Daniela Florescu, Marc Friedman, Alon Levy, and Daniel S. Weld. 1999. An adaptive query execution system for data integration. SIGMOD Rec. 28, 2 (June 1999), 299-310.,

DOI=10.1145/304181.304209,
<http://doi.acm.org/10.1145/304181.304209>

- [6] Jayaraman, Gayathri. A mediator-based data integration system for query answering using an optimized extended inverse rules algorithm. Ontario, Ottawa., 2010. Print.
- [7] K. C.-C. Chang, B. He, and Z. Zhang, "MetaQuerier over the Deep Web: Shallow Integration across Holistic Sources." in IIWeb - VLDB, 2004.
- [8] Sonia Bergamaschi, Francesco Guerra, and Maurizio Vincini. A Peer-to-Peer Information System for the Semantic Web. In Proceedings of the International Workshop on Agents and Peer-to-Peer Computing (AP2PC 2003), July 2003.
- [9] Watson, H.J.; Wixom, Barbara H., "The Current State of Business Intelligence," Computer , vol.40, no.9, pp.96,99, Sept. 2007, doi: 10.1109/MC.2007.331,
URL: <http://ieeexplore.ieee.org/stamp/stamp.jsp?tp=&arnumber=4302625&isnumber=4302594>
- [10] Henning Baars and Hans-George Kemper. 2008. Management Support with Structured and Unstructured Data-An Integrated Business Intelligence Framework. Inf. Sys. Manag. 25, 2 (March 2008), 132-148. DOI=10.1080/10580530801941058
<http://dx.doi.org/10.1080/10580530801941058>
- [11] Najar, C. (2006). A model-driven approach to management of integrated metadata-spatial data in the context of spatial data infrastructures. Zürich: Inst. für Geodäsie u. Photogrammetrie, ETH.
- [12] Rao, R., "From unstructured data to actionable intelligence," IT Professional , vol.5, no.6, pp.29,35, Nov.-Dec. 2003, doi: 10.1109/MITP.2003.1254966,
URL:<http://ieeexplore.ieee.org/stamp/stamp.jsp?tp=&arnumber=1254966&isnumber=28072>



M. Mustafa is a Lecturer at Department of Computer Science, Faculty of Science and Technology, Universiti Malaysia Terengganu (UMT). He received his Master Science in Information Technology, in 2000 from Universiti Putra Malaysia. He got his Degree and Diploma in Computer Sciences in 1998 and 1996 at the same university. He received his PHD in Spatial Databases Integration Framework at Universiti Teknologi Malaysia in 2012. His current research involved in Web Based GIS, Embedded Technology and wireless technology research. (<http://staff.umat.edu.my/~mustafaman/>).

An approach to enhance security in the access layer of the IMS networks

E.BELMEKKI , M.BELLAFKIH,A.BELMEKKI

Abstract—Migration to next generation networks (NGN) is becoming more of a necessity for operators to follow the telecommunications industry evolution. However, NGN as it is proposed by the 3GPP pose significant challenges for the deployment. Indeed IMS architecture, that includes the core NGN, includes significant gaps in terms of security of users and services. For this purpose a complete security of different interfaces is a need to solve various problems in this field. In this context we propose in this work to highlight the vulnerability of IMS access layer, with an emphasis on possible attacks, before proposing a comparative study of existing security solutions. This work will provide a meaningful improvement of existing solutions to complete the process of securing user access.

Keywords— IP Multimedia System (IMS); IPSec, HTTPDigest, TLS, S/MIME, Session Initiation Protocol (SIP).

I. INTRODUCTION

SECURITY issues in the IMS network is an important challenge as it includes a wide variety of services, protocols and components. This complexity enhances the number of vulnerabilities and risk for the IMS users and the ISP. Some of these vulnerabilities are inherent on one hand to protocols and services used and others are induced by the context of the IMS like users mobility. On the other hand, QoS is also big challenge in any IMS network as this network is designed to offer time sensitive application like video, videoconferencing and so on. The main idea in this paper is to secure IMS in the access layer [1].

In this work we will first present the IMS network architecture and we propose a state of the art of the IMS network and SIP protocol. We will summarize the most critical attacks in the C-I interface in the access network level. We will focus on the analysis of the different solution to securing the SIP protocol [2]. Second, we will analyze experimentally the vulnerability in the C-I interface the experience is limited in the procedure for registration of a customer. Third, we propose in this paper a new approach to enhancing security in the access layer in IMS networks.

E.BELMEKKI. Author is with the LR@II, Faculty des Sciences et Techniques, mohammadia, Morocco; e-mail: mbelmekki@inpt.ac.ma.

M.BELLAFKIH, Networks Laboratory, Institut nationale de Poste et Télécommunication, rabat, Morocco

A.BELMEKKI Networks Laboratory, Institut nationale de Poste et Télécommunication, rabat, Morocco

The paper is organized as following, Section 2, present architecture of the IMS network. Then, the Sections 3 present SIP protocol and his components. Section 4 and 5 describes the vulnerability and security in SIP with explications of each one, Section 6, Analysis and discussion about current security mechanism, Section 7, the security of the register method in the SIP protocol. Finally, future steps are discussed in conclusions.

II. ARCHITECTURE DE IMS

The IMS permit the convergence and the integration of data and multimedia services like voice over IP (VoIP), video, presence, instant messaging and so on. Multiple protocols are used with IMS but the main one is SIP protocol (Session Initiation Protocol). It provides method for configuring and controlling multimedia applications in IP network. The IMS architecture include four layers [3], which work together to provide reliable service.

- The access layer: The IMS user can access to IMS services through different access network like mobile network, wireless network, DSL line, enterprise network, etc. User can use basically different end IP based terminal to have access to IMS network, but can also use no IP based device.
- The transport layer: This layer offer an abstraction of different access network used which can be vendor technology dependent. It provides a unified network operation based on IP, unlike access network that can connect a no IP network users. It's responsible for assigning IP address and registration for users. The upper layers in the IMS architecture use transport layer transparently without thinking to detail behind network access.
- The control layer: It is responsible for authentication, accounting and billing, routing SIP messages to the appropriate services and forwarding traffic (mainly associated with SIP) between transport and service layers and other IMS providers. The main components in this layer are: The CSCF (Call/Session Control Function), responsible for SIP interaction Home Subscriber Service (HSS), application servers and media servers. The CSCF is itself composed by tree components, each one assume different operation: P-CSCF (Proxy CSCF), I-CSCF (Interrogation CSCF) and S-CSCF (Serving CSCF). This layer includes also HSS which content subscriber data required for handling SIP session. The other component in this

layer is PCRF (Policy Control and Charging Rules Function) responsible for charging and control [4].

- The service layer: These layers provide multimedia service over IMS network. In the 3GPP specifications, the components of this layer are referred as service platforms. The communication between SCSCF and the service layer component are based on SIP.

In the article [5] we proposed a simplified Schematic Fig 1 IMS. In this scheme we present the most vulnerable interfaces in IMS like interface C-I, S-I and C-S In this paper we propose an approach to securing the C-I interface to ensure confidentiality, the integrity and authentication. The protocols that circulated in this interface are DNS, DHCP and SIP. In the remainder of this work we concentrate in analysis of SIP protocol and we develop the different attacks related to this protocol in the context of IMS networks.

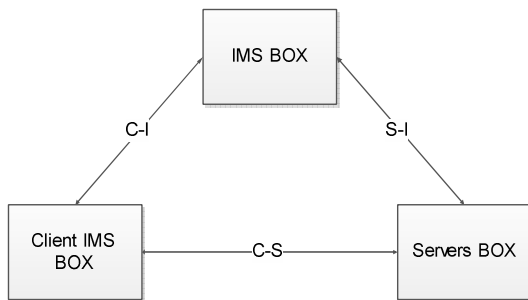


Fig. 1. Architecture of IMS simplified

III. THE PROTOCOL SIP

SIP is derived from the IETF through an RFC. It is used to initiate, modify and terminate the voice and multimedia sessions. SIP is located at the application level. To function, SIP requires additional standards and protocols. SIP is often described as a hat protocol since it is based on other protocol such as UDP [6] or TCP [7] in the transport layer. Figure 2 shows the protocol stack for SIP signaling and media.

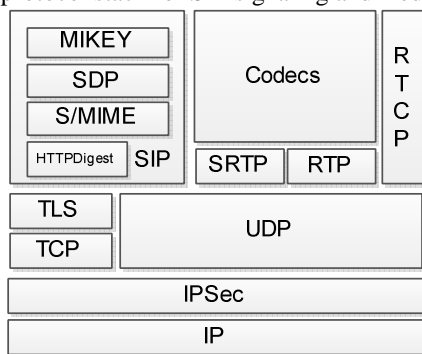


Fig. 2. Pile de SIP avec les mecanismes de securite

SIP has two categories of entities, users and servers. The user is the User Agent (UA). It transmits and receives communications. Each AU is associated with an identifier called a URI (Uniform Resource Identifier) SIP. SIP URIs is similar to e-mail addresses form, normally containing the user

name and domain membership. For servers, there are 4 types:

- Registrar Server: It focuses exclusively on the registration SIP terminals. It receives messages REGISTER. It must identify and authenticate users. It must be connected to a Proxy Server or a Redirect Server that will be in charge of the call.
- Proxy Server: It is used to relay the SIP messages. It plays the role of a server side and client side. it interprets, transforms or translate a message before transferring.
- Redirect Server: It manages call signaling as Poxy Server, but it does not relay messages. It directly redirects the UA to the required indicating the IP address and port to contact destination address.
- Location Server: it is used by the previous two types of server to obtain information on the various possible locations of a user [8].

SIP messages are divided into three parts:

- The first line.
- The header.
- The body of the message.

The first line is used to identify the type of SIP message and the recipient's address. The header contains information for routing the message as: the reference of the sender, recipient, transaction reference and session security features. Thus the header allows the establishment of a session in terms of location, naming and addressing, but it is the body of the message that describes the media stream set game session. The body of the message usually contains the elements necessary to establish the media channel. The parameter list of the message body is SDP (Session Description Protocol) format [8].

SIP was inspired by the client / server model particularly prevalent in the world of Internet. Messages are encoded using the syntax of messages HTTP/1.1 [9] and UTF-8 [10]. Exchanged messages are either requests or responses. Textual nature of trade makes it easy to interpret the messages. The association request / response transaction is called. The different possible applications in SIP messages are:

- INVITE: Request to establish a session; inviting a user (human or otherwise) to participate in a telephone or multimedia communication, the issuer of such request y indicates the types of media that is willing and able to receive, in General through an SDP session description (Session Description Protocol) [11].
- ACK Request of acquittal issued to confirm that the sending client a previous INVITE received a final response, the request may carry a session description that ends the negotiation
- BYE Request Closing a call
- CANCEL Request canceled, meaning the server to destroy the context of a call being established (this request has no effect on a call).

- **OPTIONS** this request allows a client to obtain information on the capabilities of a user, without causing the establishment of a session.
- **REGISTER** request to a SIP server and allows sending the location information (machine where the user is located).

IV. ATTACKS IN THE INTERFACE C-I

The arrival of IMS constitutes the new opportunities attacks in the world of information systems. Signaling and voice sharing the same network and the same technologies as IP data networks, IMS shares the same vulnerabilities as data networks. To this we must be added the risks specific to the signaling and voice transport. We present the different attack was associated to the signaling at the CI interfaces in the following points:

A. The attack by the BYE method

The attacker generates a BYE request and interrupts a conversation. To realize this attack, the attacker listens the traffic and takes the necessary information (such as Call-Id, the From or the To) to generate fraudulent BYE corresponding to the session which is injected into the network. The BYE is not authenticated, who receives the BYE information he executed immediately [12].

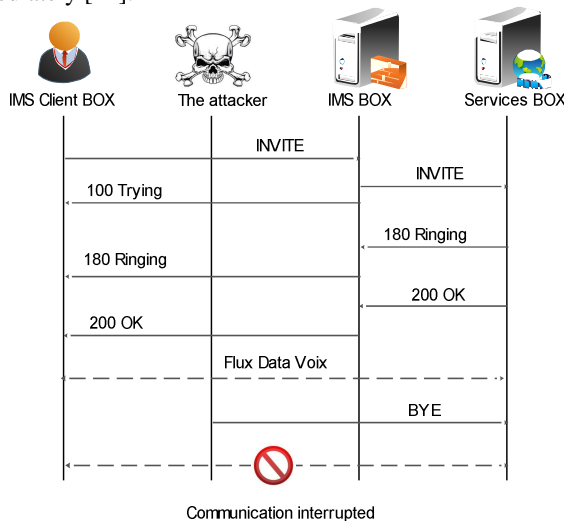


Fig. 3. The BYE attack

B. The attack by the CANCEL method

The attack by the CANCEL method is directed against a client. A third party generates a CANCEL for the establishment of a session. It operates in the same manner as for the BYE attack but this time before the establishment of the session. The server or users think that the appellant canceled. This attack is possible because the CANCEL is not authenticated [11].

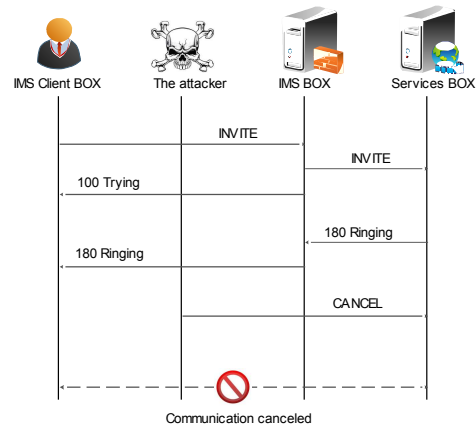


Fig. 4. The CANCEL attack

C. The attack by the REGISTER method

The attack by the REGISTER method is against the client. By listening to the network an attacker retrieves the identifier of a client. He counterfeit a REGISTER message with the "expires" zero that the REGISTRAR interrupter as deregistration. The customer is not reachable. This attack is possible if the user does not authenticate to the REGISTRAR..

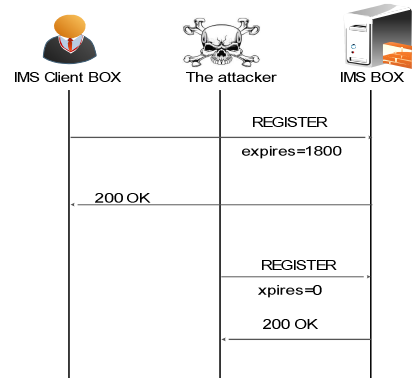


Fig. 5. The REGISTER attack

D. Identity fraud

Identity fraud may be the result of low or no authentication. Indeed a SIP proxy can provide a business service session to all requests. Fraudulent calls are attributed abusively to the SIP accounts. Identity fraud can also concern the servers by spoofing the IP address of the latter; illegitimate equipment receives all SIP traffic of the users involved. Without server authentication, the client continues to send SIP requests without knowledge that it dialogue with a pirate device. The attacker can then view the details of all calls and checking it. From that diversion of traffic, the attacker can make denial of service and have knowledge of all the traffic sent by the user. Mutual authentication is need in the context of IMS [12].

V. THE CURRENT SECURITY SOLUTION FOR SIP

RFC SIP provides a number of security mechanisms to ensure the confidentiality, integrity and authentication through signaling. We present in this section two sub section which

shows the principles of operation of the security mechanisms proposed in the SIP RFC and the security solution that proposed by the other research work.

A. Security mechanisms of RFC

The RFC of SIP protocol proposed a stack that includes all protocols that ensures the proper operating of SIP. We develop security mechanisms proposed by this stack.

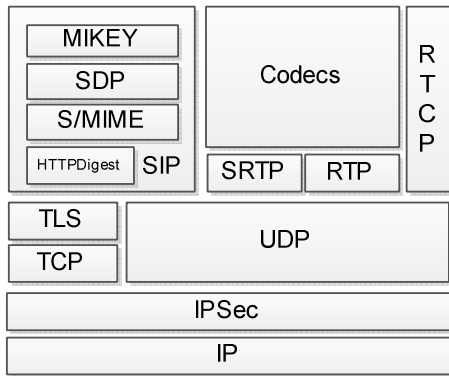


Fig. 6. the protocol stack for SIP

- 1) HTTPDigest: HTTP authentication (method "Digest" and "Basic" method) [13] is based on a challenge / response mechanism. First, it permits the SIP client to register in the REGISTRAR server and then have access to different resources when the server asks it. Authentication is usually required for an INVITE request. The server sends a challenge to the client "nonce", the client responds with a derived "response" value of the challenge and a secret it shares with the server. The server verifies that the client has the same secret by calculating the response in turn and checking the consistency of the two.
- 2) S/MIME secures a portion of SIP messages using the principle of public key encryption. It ensures the confidentiality, authentication and integrity. Certificates allow either encrypt or sign the SIP messages. Confidentiality and integrity are ensured by the use of the public key of the recipient. Authentication and integrity are assured about them using the private key of the sender. S / MIME in SIP context permits three uses, the transmission of a certificate, the signature and encryption. Encryption of all SIP messages end-to-end needs of confidentiality is not appropriate because of network intermediaries who need to see some field headers to route messages correctly: if intermediaries are excluded security associations, the messages are not routable. Security end-to-end (integrity and confidentiality) is possible for the body of SIP messages, including mutual authentication of users. The "tunnel" mode extends the security header [14].
- 3) TLS is a modular protocol which aims to secure exchanges between the client and the server independently of any type of application. TLS acts as an additional layer above of TCP. And TLS is not responsible for reliability Transport Layer or maintaining the connection. The

services offered are: authentication, integrity and confidentiality. Its native implementation in many browsers did TLS standard for securing Web applications: HTTPS corresponding to the HTTP association with TLS. Its use is mainly associated with the use of X.509 certificates for server authentication and encryption of trade (ie signaling). The initial SIP RFC describing only very briefly the SIP/TLS association [15] was published for the operation of said two protocols. TLS allows the client to authenticate the server. Using a client certificate allow mutual authentication at transport but require the server to have the certificate with the public key of all users: this would complicate significantly the system. In addition, this case is not formally described in [8]

- 4) IPSec: to protect exchanges in networks, one of the usual solution is to use IPsec (IP security) [16] protocol, the secure version of IP. As SIP provides secure exchanges at the transport layer, it envisages a network level protection with IPsec. This protocol makes it possible to authenticate the origin of IP packets, to ensure the integrity or confidentiality. IPsec therefore protects communications and signaling between two entities. Two modes: transport mode or tunnel mode. Whatever the mode, the SIP server can modify SIP headers and enable the establishment of the call. Generally, SIP clients do not implement this solution. IPsec is mainly used to protect traffic between the two areas.

B. Other research work for securing SIP

- 1) [17] proposed an authentication mechanism and integrity by adding Integrity_Auth field. The principle of this authentication is based on the pre-shared secret between the client and the supplier. As in HTTP Digest authentication, this solution uses a hash function and a secret to prove the identity of the sender. When receiving a request, the server or SIP client checks the value of Integrity_Auth calculating his own value from the SIP message, the random value and secrecy.
- 2) [18] Proposes an authentication method using both a password and certificates. The work of [SRI05] explored a solution where the customer does not trade with the SIP Proxy, Proxy for dependents to authenticate the client by exchanging with the Registrar. The servers have certificates issued by an authority.
- 3)) [19] [20] have mainly searched to strengthen the HTTP Digest authentication using a password provided by a third channel. The password for HTTP Digest challenge is provided via a mobile phone. Thus the word of OTP can use safely on a public PC without risk of identity theft.
- 4) [21] [22] have thus studied how to integrate a SSO solution in the SIP architecture. SAML (Security Assertion Markup Language) is the basis of these proposals. Based on SAML defines an XML protocol for exchanging information related to security, mainly in the SSO applications. [21] is a proposal to integrate SSO solution Liberty Alliance in a SIP environment.

Authentication is provided by centralized server applications all applications. For [22], the SSO server that centralizes applications.

VI. ANALYSIS AND DISCUSSION ABOUT CURRENT SECURITY MECHANISM

The security solutions proposed by RFCs encounter many difficulties in implementation and deployment because encryption of signaling or voice requires a mechanism to distributing secret keys or certificate management infrastructure to be used by all clients or servers. Encryption requires calculation time and increases the size of the IP packet, which is not always acceptable with a real time application such as for the transport of voice for communication. We present the limitations of each mechanism in the following table.

Table 1: The limitation of security mechanisms

Security mechanisms	Limitations
HTTPTDigest	This method allows dictionary attacks to discover passwords: it suffices to have an association nonce/responses to rebuild the calculation with the method of RFC. More password is short more attack is easy. So it is a method in which only the client authenticates the usurpation of SIP server is possible [24] This solution does not provide any confidentiality.
S/MIME	One of the major defects of this solution is the absence of infrastructure certificates. It is always possible to exchange certificates with SIP but an attacker can still intercept and modify the S / MIME message. This device also needs to associate each URI a public key that is not necessarily easy. Finally, this solution increases the size of SIP messages.
TLS	The limits described in the RFC demonstrate that it is difficult to ensure and monitor the implementation of this configuration. Moreover few clients implement SIPs and TLS [25].
IPSec	In our case, the authentication concerns the voice and signaling flows. It could be envisaged to use IPSec between the client and the server, but it must be an administrator to the configuration: in this case we prefer TLS because the user is free to insert the IMS certificate in his IMS client.

Solutions such as TLS or S/MIME allow protect themselves but require certificate management, which is not common at present in the IMS infrastructure as has already been mentioned. Thus SIP is typically deployed with HTTP Digest authentication in its simple version of a mutual authentication then is now systematic in the new architectures like 3G with AKA [26].

There are many limitations: difficulty to use certificates by absence of PKI interoperability problem, solution related to a

choice of protocol in the supports layers (transport or routing level), and difficulty to exchange symmetric keys, absence of political universal Security. This observation leads us to define the following specifications to allow a security solution for SIP signaling appears quickly: do not modify the SIP protocol does not add new fields, strengthen traditional mechanisms present.

The analysis of competing solutions shows that there are two approaches to enhance authentication in a SIP environment. The first solution is to change the syntax of messages, the second to change the architecture and nature of trade. Our logic of changing the generation of certain fields and to define a framework of interpretation can be considered as an innovative way for the security of SIP.

VII. THE SECURITY OF THE REGISTER METHOD IN SIP

In this section we prove in the first step the security problems related to the register method of the SIP protocol in the IMS context. For this we installed a test model to analyze SIP traffic in the C-I interface. This model is composed of the following elements:

- Core IMS with all entities CSCF (Proxy, interrogation and service) and the base HSS, this core is deployed by OpenCoreIMS [27].
- Two routers to transport traffic.
- the Application server
- The IMS client, we used UCTIMC client.

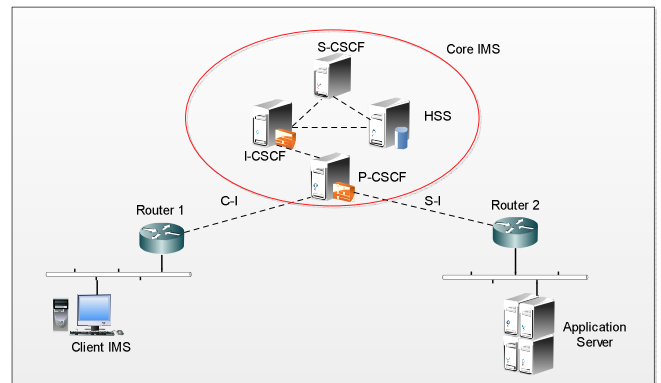


Fig. 7. the testbed

In this platform we started a test registration of client IMS in the IMS core. We capture the results shown in these figures:

```
REGISTER sip:open-ims.test SIP/2.0
Via: SIP/2.0/UDP 192.168.3.2:5060;rport;branch=z9hG4bK1469024095
From: <sip:bob@open-ims.test>;tag=1680655333
To: <sip:bob@open-ims.test>
Call-ID: 754491826
CSeq: 1 REGISTER
Contact:<sip:bob@192.168.3.2:5060;line=55001399904afab>;+sip.instance=
"<urn:uuid:9e6056da-6314-11e3-a1d3-97d88ed1e0e4>"
Authorization: Digest username="bob@open-ims.test", realm="open
ims.test", nonce=" ", uri="sip:open-ims.test", response=" "
```

```
Max-Forwards: 70
User-Agent: UCT IMS Client
Expires: 600000
Supported: path
Supported: gruu
Content-Length: 0
```

Fig. 8. the request register

```
SIP/2.0 401 Unauthorized - Challenging the UE
Via: SIP/2.0/UDP
192.168.3.2:5060;rport=5060;branch=z9hG4bK1469024095
From: <sip:bob@open-ims.test>;tag=1680655333
To: <sip:bob@open-ims.test>;tag=d7837ce6bbd631122d10546eb75bb4cf-147b
Call-ID: 754491826
CSeq: 1 REGISTER
Path: <sip:term@pcscf.open-ims.test:4060;lr>
Service-Route: <sip:orig@scscf.open-ims.test:6060;lr>
Allow: INVITE, ACK, CANCEL, OPTIONS, BYE, REFER, SUBSCRIBE, NOTIFY, PUBLISH, MESSAGE, INFO
Server: Sip EXpress router (2.1.0-dev1 OpenIMSCore (i386/linux))
Content-Length: 0
Warning: 392 127.0.0.1:6060 "Noisy feedback tells: pid=25561
req_src_ip=127.0.0.1 req_src_port=5060 in_uri=sip:scscf.open-ims.test:6060
out_uri=sip:scscf.open-ims.test:6060 via_cnt==3"
WWW-Authenticate: Digest realm="open-ims.test",
nonce="b2ea97ce7e54b65f0c2358e7191a8f55", algorithm=MD5,
qop="auth,auth-int"
```

Fig. 9. the reply with the nonce value

```
REGISTER sip:open-ims.test SIP/2.0
Via: SIP/2.0/UDP 192.168.3.2:5060;rport;branch=z9hG4bK1863722346
From: <sip:bob@open-ims.test>;tag=1680655333
To: <sip:bob@open-ims.test>
Call-ID: 754491826
CSeq: 2 REGISTER
Contact:
<sip:bob@192.168.3.2:5060;line=55001399904afab>;+sip.instance="<urn:uuid:9e6056da-6314-11e3-a1d3-97d88ed1e0e4>"
Authorization: Digest username="bob@open-ims.test", realm="open-ims.test", nonce="b2ea97ce7e54b65f0c2358e7191a8f55", uri="sip:open-ims.test", response="869392cbda09a79cbf163a684d6a7b10",
algorithm=MD5
Max-Forwards: 70
User-Agent: UCT IMS Client
Expires: 600000
Supported: path
Supported: gruu
Content-Length: 0
```

Fig. 10. the request with the response value

```
SIP/2.0 200 OK - SAR succesful and registrar saved
Via: SIP/2.0/UDP
192.168.3.2:5060;rport=5060;branch=z9hG4bK1863722346
From: <sip:bob@open-ims.test>;tag=1680655333
To: <sip:bob@open-ims.test>;tag=d7837ce6bbd631122d10546eb75bb4cf-7c5f
Call-ID: 754491826
CSeq: 2 REGISTER
P-Associated-URI: <sip:bob@open-ims.test>
Contact:
<sip:bob@192.168.3.2:5060;line=55001399904afab>;expires=600000;pub-gruu="sip:bob@open-ims.test;gr=urn:uuid:9e6056da-6314-11e3-a1d3-97d88ed1e0e4"
Path: <sip:term@pcscf.open-ims.test:4060;lr>
Service-Route: <sip:orig@scscf.open-ims.test:6060;lr>
Allow: INVITE, ACK, CANCEL, OPTIONS, BYE, REFER, SUBSCRIBE, NOTIFY, PUBLISH, MESSAGE, INFO
P-Charging-Function-Addresses: ccf=pri_ccf_address
Server: Sip EXpress router (2.1.0-dev1 OpenIMSCore (i386/linux))
```

```
Content-Length: 0
Warning: 392 127.0.0.1:6060 "Noisy feedback tells: pid=25563
req_src_ip=127.0.0.1 req_src_port=5060 in_uri=sip:scscf.open-ims.test:6060
out_uri=sip:scscf.open-ims.test:6060 via_cnt==3"
```

Fig. 11. the reply from the ims core to client

These results indicate that the procedure for registering a client passes through these steps:

- Step 1: The client sends a registration request to the proxy.
- Step 2: The proxy responds by sending a random nonce value.
- Step 3: The client sends a response derived from secret shared between the client and the proxy and the nonce value.
- Step 4: The server responds yes or no if the answer is correct.

This registration method inherits all the security problems that we develop in this section 4 article. For this we propose to strengthen the SIP register method, by changing the syntax of SIP.

The idea of our approach is to generate a significant value of nonce and not a random value.

In our approach we are looking to generate a nonce value that depends to the following value call-id, realm, URI, secret key and time. So the algorithm we want to realize in the next work is summarized in the following step:

- Step 1: the client sends a request for registration which has the following information: call-id, realm, URI and the secret crypt by the public key of proxy
- Step 2: the proxy receives the information, it begins in the first step by decrypting the secret by his privet key, in the second step the proxy generate de none by hashing the call-id, realm, URI, secret and time, then send de hashing value to the client.
- Step 3: the client receives the value of nonce; he begins by calculating the response bay hashing the nonce and the secret. The client crypt the response value by the public key of the proxy, then send the result to the proxy.
- Step 4: Proxy compares the received result with the result calculated by it even. Then send ok or reject to the client.

VIII. CONCLUSION

In this paper, in this work we present a state of art security layer access IMS networks. The work also gives a state of art on the SIP signaling protocol, with different attack related to this protocol in the context of IMS networks. the article develop the current security solutions to secure the SIP protocol, whatsoever the solutions presented in the RFC or the solution in other research work, And provides a detailed analysis about these solutions with a discussion about the limitations of these mechanisms.

We also present a new approach for securing the method registrar in the protocol SIP, because it is present point of all the attack that targets the SIP. The idea of our approach is generate a significant nonce value to ensure mutual authentication between IMS client and the IMS core.

In the future work, we want to model our approach in the modeling tool to testing the feasibility of our solution

REFERENCES

- [1] C.Chen, Y.Huang, "An efficient end-to-end security mechanism for IP multimedia subsystem" *Computer Communications* 31 (2008) 4259–4268
- [2] IMS avance : enregistrement et authentification EFORT
- [3] K Shuang, S Wang "IMS Security Analysis using Multi-attribute Model" *JOURNAL OF NETWORKS*, VOL. 6, NO. 2, FEBRUARY 2011
- [4] D Slezak E.Yvette. "Securing IP Multimedia Subsystem with the appropriate Security Gateway and IPSec Tunneling" *Security Engineering Research and Engineering*, Volume 8, N 3 Juin 2011.
- [5] E.belmekki,B.raouyne,M.bellafkih,N.bouaouda "Towards a New Approach for Securing IMS Networks" *AASRI Procedia*, Volume 4, 2013, Pages 138–146
- [6] J. Postel, « User Datagram Protocol », RFC 768, août 1980.
- [7] J. Postel, « Transmission Control Protocol STD 7 », RFC 793, septembre 1981.
- [8] J. Rosenberg, H. Schulzrinne, G. Camarillo, A. Johnston, J. Peterson, R.Sparks, M. Handley and E. Schooler, « SIP: Session Initiation Protocol », RFC 3261, juin 2002.
- [9] R. Fielding, J. Gettys, J. Mogul, H. Frystyk, L. Masinter, P. Leach, and T.Berners-Lee, « Hypertext Transfer Protocol -- HTTP/1.1 », RFC 2616, juin 1999.
- [10] F. Yergeau, « UTF-8, a transformation format of ISO 10646 », RFC 2279, janvier 1998.
- [11] M. Handley, V. Jacobson and C. Perkins, « SDP : Session Description Protocol », RFC 4566, juillet 2006.
- [12] W. Mazurczyk1, et Z. Kotulski, « New VoIP Traffic Security Scheme with Digital Watermarking », *Computer Safety, Reliability, and Security*, LCNS Volume 4166/2006, Springer Berlin / Heidelberg, 2006, pages : 170-181.
- [13] J. Franks, P. Hallam-Baker, J. Hostetler, S. Lawrence, P. Leach, A. Luotonen and L. Stewart, "HTTP Authentication: Basic and Digest Access Authentication", RFC 2617, juin 1999.
- [14] J. Peterson, « S/MIME Advanced Encryption Standard (AES) Requirement for the Session Initiation Protocol (SIP) », RFC 3853, juillet 2004.
- [15] J. Peterson, and C. Jennings, « Enhancements for Authenticated Identity Management in the Session Initiation Protocol (SIP) », RFC 4474, août 2006.
- [16] H. Krawczyk, M. Bellare, et R. Canetti , « HMAC: Keyed-Hashing for Message Authentication », RFC 2104, février 1997.
- [17] D. Geneiatakis, et C. Lambrinouidakis, « A lightweight protection mechanism against signaling attacks in a SIP-based VoIP environment», *Telecommunication System revue*, Volume 36 n° 4 décembre 2007, Springer, février 2008, pages : 153-159.
- [18] R. Srinivasan, V. Vaidehi V, K. Harish, K. Lakshmi Narasimhan, S. LokeshwerBabu, et V. Srikanth, « Authentication of Signaling in VoIP Applications », In proceedings of the Communications Asia-Pacific Conference, Perth, Australie, Octobre 2005, pages: 530-533.
- [19] S. Mizuno, K. Yama, and K. Takahashi, « Authentication Using Multiple Communication Channels », In proceedings of the 2005 Workshop on Digital Identity Management, Fairfax, USA, November 2005, pages : 54-62.
- [20] S. Hallsteinsen, I. Jøstad, and D. V. Thanh, « Using the mobile phone as a security token for unified », In proceedings of the Second International Conference on Systems and Networks Communications (ICSNC 2007), Cap Esterel, France, août 2007.
- [21] P. Nie J.-M. Tapio, S. Tarkoma, J. Heikkinen, « Flexible Single Sign-On for SIP: Bridging the Identity Chasm », In proceedings of the IEEE International Conference on Communications ICC'09, Dresde, Allemagne, juin 2009, 6 pages.
- [22] H. Tschofenig, R. Falk, Siemens, J. Peterson, J. Hodges, D. Sicker, et J. Polk, « Using SAML to Protect the Session Initiation Protocol (SIP) », *Revue IEEE Network*, septembre/octobre 2006, pages: 14-17.
- [23] L. Shan, et N. Jiang, « Research on Security Mechanisms of SIP-based VoIP System », In proceedings of the 2009 Ninth International Conference on Hybrid Intelligent Systems, Shenyang, China, August 12-August 2009, pp. 408-410.
- [24] D. Geneiatakis, G. Kambourakis, T. Dagiuklas, C. Lambrinouidakis, and S.Gritzalis, « SIP Security Mechanisms: A State-of-the-art Review », In the Proceedings of the Fifth International Network Conference (INC 2005), Samos, Grèce, juillet 2005, pages : 147-155.
- [25] A. Niemi, J. Arkko and V. Torvinen, « Hypertext Transfer Protocol (HTTP) Digest Authentication Using Authentication and Key Agreement (AKA) », RFC 3310, septembre 2002.
- [26] OpenIMScore Open source implementation of IMS Call Session Control Functions and Home Subscriber Service (HSS) <http://www.openimscore.org>

E.BELMEKKI received his MSc in Engineering, Telecommunications and Multimedia from The Faculty of Sciences, Mohammed V University Agdal, Rabat, Morocco in 2005. He is currently doing his PhD at FSTM, Mohammedia, Morocco, under the supervision of Prof. Mostafa Bellafkih. His research interests include network management, security and software Development.

M.BELLAFKIH had his PhD thesis in computer science from the University of Paris 6, France, in June 1994 and Doctorat Es Science in Computer Science (option networks) from the University of Mohammed V in Rabat, Morocco, in May 2001. His research interests include network management, knowledge management, AI, data mining and database.

A.BELMEKKI had his PhD thesis in computer science from Faculty of Science and Technology Mohammedia, Morocco in 2010 specializing in security and Network.

Quality based Speaker Verification Systems using Fuzzy Inference Fusion Scheme

L.A. Hamid and D.A Ramli

Abstract— Biometric is a science and technology of measuring and analyzing biological data i.e. physical or behavioral traits which is able to uniquely recognize a person from others. Prior studies of biometric verification systems with fusion of several biometric sources have been proved to be outstanding over single biometric system. However, fusion approach without considering the quality information of the data used will affect the system performance where in some cases the performances of the fusion system may become worse compared to the performances of either one of the single systems. In order to overcome this limitation, this study proposes a quality based fusion scheme by designing a fuzzy inference system (FIS) which is able to determine the optimum weight to combine the parameter for fusion systems in changing conditions. For this purpose, fusion systems which combine two modalities i.e. speech and lip traits are experimented. For speech signal, Mel Frequency Cepstral Coefficient (MFCC) is used as features while region of interest (ROI) of lip image is employed as lip features. Support vector machine (SVM) is then executed as classifier to the verification system. For validation, common fusion schemes i.e. minimum rule, maximum rule, simple sum rule, weighted sum rule are compared to the proposed quality based fusion scheme. From the experimental results at 35dB SNR of speech and 0.8 quality density of lip, the EER percentages for speech, lip, minimum rule, maximum rule, simple sum rule, weighted sum rule systems are observed as 5.9210%, 37.2157%, 33.2676%, 31.1364%, 4.0112% and 14.9023%, respectively compared to the performances of sugeno-type FIS and mamdani-type FIS i.e. 1.9974% and 1.9745

Keywords— Biometric, single biometric system, multibiometric system, fuzzy logic fusion scheme, sugeno-type FIS and mamdani-type FIS.

I. INTRODUCTION

PREVIOUSLY, the traditional verification uses passwords, keys or smart cards which are less secure since few problems may occur due to forgotten password, duplicated keys or stolen smart cards. Nowadays, biometric data for verification systems are commercially used in data security, internet access, ATMs, network logins, credit cards and

This work was supported by Universiti Sains Malaysia Research University Grant 81416.

L.A.Hamid is a MSc student with Intelligent Biometric Group, School of Electrical and Electronic, Universiti Sains Malaysia, Engineering Campus, 14300 Nibong Tebal, Pulau Pinang, Malaysia

D.A. Ramli is with Intelligent Biometric Group, School of Electrical and Electronic, Universiti Sains Malaysia, Engineering Campus, 14300 Nibong Tebal, Pulau Pinang, Malaysia (corresponding author to provide phone: +604-5996028; e-mail: dzati@eng.usm.my).

government records. More studies on biometric system have been done by researchers due to the increase of requirement of automatic information processing in many industrial fields [1]. Biometrics is defined as the development of statistical and mathematical methods applicable to data analysis problems in the biological sciences. Biometrics is also a technology, which uses various individual attributes of a person to verify his or her identity. Biometric characteristics can be divided into two main classes i.e. physiological and behavioral characteristics. Physiological characteristics refers to the human body such as face, fingerprints, palm print, iris, DNA, hand geometry and finger vein structure while behavioural characteristics are related to the actions of a person such as voice, keystroke dynamics, gait, typing rhythm and signature [2].

This study implements biometric system for speaker verification systems. Speaker verification system is used to verify a person's claim from the enrollment database by using speech signal as the input data.

Single biometric systems have to face few limitations such as non-universality, noisy sensor data, large intra-user variations and susceptibility to spoof attacks. For example, a single biometric system uses voice patterns to identify the individuals may fail to operate because of a noisy data signal captured by the system. Limitations faced by single biometric system can be overcome by applying the multibiometric system. Multibiometric system enhanced the matching accuracy of a biometric system in noisy condition as well as increases the population coverage with multiple traits (i.e. lip, iris, voice and face). Studies on multibiometrics are further discussed in Ben-Yacoub et al. [3] and Pan et al. [4]. Besides that, multibiometric system may continuously operate even though a certain trait is unreliable due to user manipulation, sensor or software malfunctions. However, this is only true when fusion scheme is done at the decision level where hard decision fusion for example OR operator is executed. For the score level decision fusion, the multibiometric systems are at its best performance only when all traits operate in clean condition. In noisy condition, the unreliable speech signal tends to cause the system to obtain false scores for genuine and imposter signal. This problem does not occur in clean condition since both speech and lip signal gives reliable scores for genuine and imposter signal.

This study proposes the use of quality based score fusion approach to improve the performances of multibiometric systems. The quality based fusion depends on the input current condition. This method is very useful to ensure the speaker verification system is at its best performance especially in noisy condition. The quality based fusion implements the

quality measure identification system to identify the quality of sample data. Researches on quality measure identification system have been discussed in Fierrez-Aguilar et al. [5] and Nandakumar et al. [6]. In order to take full advantage of the quality based fusion approaches, this study implements the fusion mechanism for different biometric information. For this purpose, Fuzzy Inference System is developed so as to infer the optimum weight for robust and reliable multimodal biometric based security systems. The use of fuzzy logic as the fusion scheme for quality based fusion approach improves the system performances. Similar approach has been discussed in Lau et al. [7] which generated a further improvement of 19% relative to fusion by weighted average scores.

According to Vasuhi et al. [8], the fuzzy logic decision-making is approximately the same with the human decision-making. Fuzzy design can accommodate the ambiguities of human languages and logics. It provides both an intuitive method for describing systems in human terms and automates the conversion of those system specifications into effective models. Fuzzy logic has the ability to add human-like subjective reasoning capabilities to machine intelligences as described in Prade and Dubois [9]. Fuzzification is the process where each input is assigned to a linguistic variable. Degree of membership can be obtained from the linguistic variable. The degrees of membership are combined using fuzzy rules which may be expressed in terms such as "if x is A, then y is B". The process of converting the fuzzy output based on the strength of membership is called defuzzification. Defuzzification is used in fuzzy modeling and in fuzzy logic control to convert the fuzzy outputs from the systems to crisp values [10,11].

There are two types of fuzzy inference system (FIS) i.e. mamdani and sugeno. A mamdani-type FIS has fuzzy inputs and a fuzzy output. For mamdani-type, the input is transformed into a set of linguistic variable during the fuzzification process.

The fuzzy inference system (FIS) uses the input variables and fuzzy rule to derive a set of conclusion which will be used during the defuzzification process. A crisp number is the output of the defuzzification process [12]. Mamdani-type FIS is widely accepted for capturing expert knowledge. It allows us to describe the expertise in more intuitive and human-like manner. The advantages of the mamdani-type FIS are it have widespread acceptance, intuitive and well-suited to human inputs. However, mamdani-type FIS entails a substantial burden.

In short, both mamdani-type and sugeno-type are similar in term of the fuzzification and rule evaluation process. The main different between mamdani-type and sugeno-type is the output of sugeno-type is linear or constant. Besides that, mamdani-type uses defuzzification method to extract the output while sugeno-type uses weighted average method to extract the output. Sugeno-type FIS is computationally effective and works well with optimization and adaptive techniques, which makes it is very attractive in control problems, particularly for dynamic nonlinear systems. So that it works well with linear technique and well-suited to mathematical analysis [13]. The objectives of this study are 1) to develop single and multibiometric systems based on speech and lip traits, 2) to integrate the proposed quality based fusion algorithm to the multibiometric systems and 3) to evaluate the performances of proposed fusion systems hence to compare their effectiveness with the baseline methods.

II. METHODOLOGY

Fig. 1 summarizes the data collection, feature extraction, classification, and fusion that involves in this study.

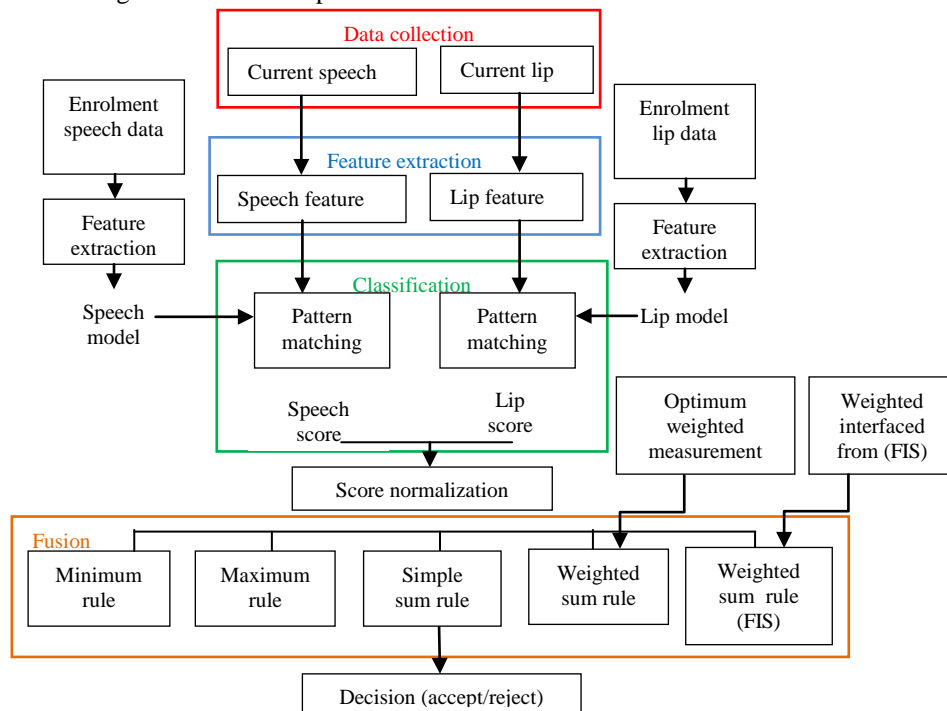


Fig. 1. Summary of the multibiometric system

A. Data Collection

In data collection, voice which is continuous electrical signal is converted to digital signal using a sampler and analog-to-digital (A/D) converter. The digitization process consists of sampling, quantization and coding. Sampling process is discussed extensively in [14]. After sampling process, the sampled signal is discrete in the time domain but still continuous in the amplitude domain. The quantization process divides the continuous amplitude range into finite subrange [15]. Finally, the coding process is done by assigning these finite values into a sequence of codes for binary number representation.

Both audio and visual data are obtained from Audio-Visual Digit Database [16]. This database contains digitized audio signals which monophonic 16 bit, 32 kHz and in WAV format corresponding to the recording voices of 37 speakers (16 female and 21 male). The recording is done in three different sessions. Each speaker performed 20 repetitions of digit zero for each session. Therefore, 60 audio data for each speaker obtained from each session. It consists of 2220 data for digit zero. The visual data of 37 speakers is stored as a sequence of JPEG images with a resolution of 512 x 384 pixels. Each speaker consists of 60 sequences of face images (20 sequences from each session) hence in total of 2220 images from entire speakers.

For the purpose of this study, the first session are used for speaker's model while data from second and third sessions are used for testing data. The clean audio data are corrupted into 40dB, 35dB, 30dB, 25dB, 20dB, 15dB, 10dB, 5dB and -5dB by using the simulated additive white Gaussian noise (AWGN) as shown in Fig. 2. The AWGN which is a white noise is commonly used to simulate background noise of the audio signal [17]. This study used salt and pepper noise method to corrupt the original image. Salt and pepper noise is an impulse noise which able to corrupt the image. Salt and pepper noise refers to single pixel noise statistics by adding white and black pixels randomly in the image matrix. For this experiment, the enrolment lip images are modified to different image qualities i.e. 0.1, 0.2, 0.3, 0.4, 0.5, 0.6, 0.7, 0.8 and 0.9 as shown in Fig. 3.

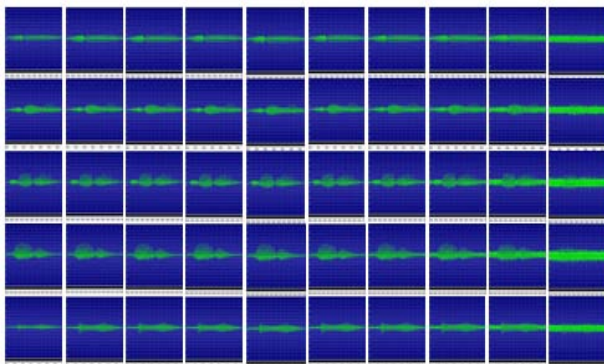


Fig. 2. Clean and noisy speech signal

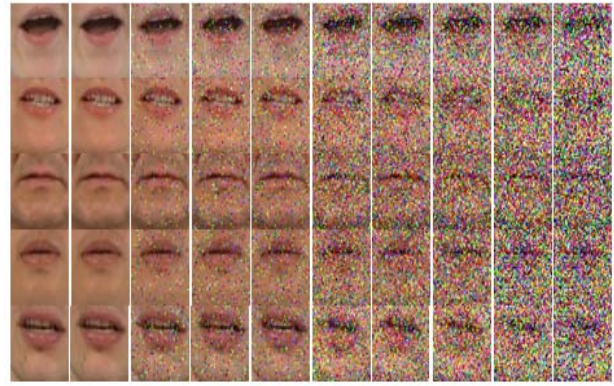


Fig. 3. Clean and noisy lip images

This study implemented Region of Interest (ROI) method to extract the lip features in this study as discussed in Iyengar et al., [18]. According to Chetty and Wagner [19,20], the lip area has been identified from the face by employing the hue/saturation colour thresholding. A binary image is then computed by setting the threshold values, $H_0 = 0.04$ and $S_0 = 0.1$ which obtained from the hue-saturation image. The lip region is identified by using the morphological image processing. Next, the 64 x 64 pixel of lip region is extracted for evaluation. The ROI database features consists of 2220 set of ROI features from 37 persons with 60 sequence per person. The ROI images of all speakers are resized to the resolution of 64 x 64 pixels in order to obtain higher accuracy for the verification process.

The database is divided to two sessions which are training and testing. During the enrolment process, 2220 audio data are developed for all 37 subjects. For training purposes, 740 data are used to train the system. Each subject is treated as the claimant and the other subjects as the imposters during the verification process. Therefore, the database has 40 testing data from the authentic speaker and 1440 from the imposter speaker. The visual data consists of 60 sequences of images (20 for training and 40 for testing) where each sequence consists of 10 images. In total, 22200 data are developed for all 37 subjects. Similar to speaker verification, each subject is treated as the claimant and the other subjects as the imposters during the verification process. Hence, the database has 400 testing data from the authentic lip image and 14400 from the imposter lip image.

This study implemented 20 training data due to results obtained from the experiments. Fig. 4 shows the performances of the MFCC-SVM systems based on 3 training data, 6 training data, 10 training data and 20 training data. The performances of the genuine acceptance rate (GAR) improve with the increment of training data. For example, at 1% false acceptance rate (FAR), the GAR performances of 3, 6, 10 and 20 training data systems are 89%, 98%, 98% and 99%, respectively. Results shown that the systems performances are at its' optimum when 20 training data are implemented.

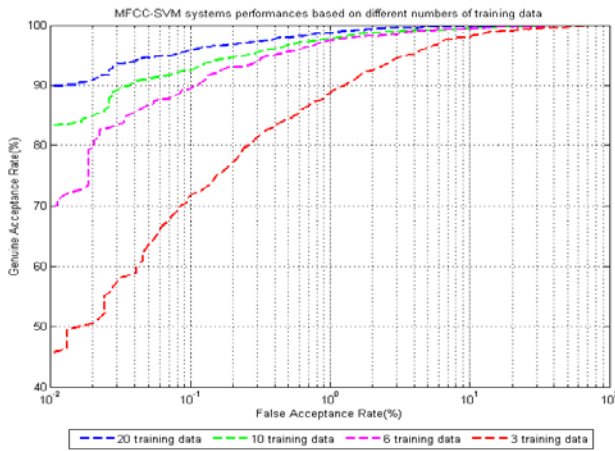


Fig. 4. ROC curves of MFCC-SVM systems performances based on different numbers of training data

B. Feature Extraction

A preemphasis of high frequencies is required to compress the signal dynamic range by flattening the spectral tilt in order to raise the SNR. The first order FIR filter is used to filtering the speech signal. The use of window function is important to minimize the signal discontinuities at the beginning and end of each frame by zeroing out the signal outside the region of interest. This study implements the Mel Frequency Cepstrum Coefficient (MFCC) processing to extract the audio features. There are few steps involved in MFCC process. First, all frames of the signal are computed using discrete fourier transform. Next, the filter bank processing formed the spectral features at defined frequency at its exit. After that, log energy computation which consists of computing the logarithm of the square magnitude of the filter bank is performed. Finally, the mel frequency cepstrum is computed [21]. This study also implements the Linear Predictive Coding (LPC) processing to extract the audio features. There are few steps involved in LPC process. First, linear predictive analysis is defined using auto-correlation method. Next, auto-correlation equation solution using auto-correlation method is executed. Finally, the LPC coefficient is computed. This study implemented ROI method for the visual features. The face detection process is firstly done before the lip localization process can be proceed. This study implemented the colour based technique and template matching for face detection process. Four steps such as development of skin colour model, skin likelihood process, skin segmentation process and determination of face region using template matching are required in this process. This study implemented Region of Interest (ROI) as the original face images in the database include the whole face images. According to Chetty and Wagner [19,20], the lip area has been identified from the face by employing the hue/saturation colour thresholding.

C. Classification

This study implements the support vector machine (SVM) as classifier. A SVM performs classification by constructing an N-dimensional hyperplane that optimally separates the data

into two categories. SVM mode is a supervised learning method that generates input-output mapping functions from a set of labeled training data. The foundation of Support Vector Machines (SVM) has been developed as discussed in [22] and becomes popular and accepted nowadays due to many attractive features and promising empirical performance. Theory regarding SVM is further explained in [23].

The SVM identifies the data points that are found to lie at the edge of an area in space which is a boundary from one class to another. The space between regions containing data points in different classes as being the margin between those classes. SVM is used to identify a hyperplane that separates the classes. The maximum margin between the different classes is found. An advantage of this method is that the modeling only deals with these support vectors, rather than the whole training dataset.

Experiments on audio systems using SVM classifiers using MFCC feature is performed in this study. In total, 13 experiments are conducted for audio systems evaluation. The first 4 experiments are implemented for audio systems evaluation with different numbers of training data (3, 6, 10 and 20 training data). The other 9 experiments are for the audio systems evaluation on different SNR levels (40dB, 35dB, 30dB, 25dB, 20dB, 15dB, 10dB, 5dB and -5dB). For visual system, 13 experiments are implemented. 4 experiments are performed in order to evaluate the systems using different numbers of training data (3, 6, 10 and 20 training data) as well as 9 experiments are conducted to evaluate the visual systems on different quality levels (0.1, 0.2, 0.3, 0.4, 0.5, 0.6, 0.7, 0.8 and 0.9).

D. Fusion scheme

The scores obtained from both single systems (speech and lip) are normalized by applying the min-max normalization technique in equation (1). The minimum and maximum scores are transformed to 0 and 1, respectively.

$$\hat{s}_i = \frac{s_i - \min_{i=1}^K s_i}{\max_{i=1}^K s_i - \min_{i=1}^K s_i} \quad (1)$$

where s_i denote the i th match score output and K is the number of the match scores available in the set [24]. Let \hat{s}_{audio} is the audio normalized score and \hat{s}_{visual} is the visual normalized score.

Minimum Rule: The normalized scores are fused using a minimum rule fusion scheme (2) which chooses the smallest score between all modalities,

$$\hat{s}_{\text{avi}} = \min(\hat{s}_{\text{audio}}; \hat{s}_{\text{visual}}) \quad (2)$$

where \hat{s}_{avi} is the score distribution and speaker's modality input data $\hat{s}_i = \hat{s}_{\text{audio}}$ and \hat{s}_{visual} . Table 3.3 shows the summary of experiments conducted during the process.

Maximum Rule: The normalized scores are fused using a maximum rule fusion scheme (3) which chooses the biggest score between all modalities,

$$\hat{s}_{avi} = \max (s_{audio}; s_{visual}) \quad (3)$$

where \hat{s}_{avi} is the score distribution and speaker's modality input data $\hat{s}_i = s_{audio}$ and s_{visual} .

Simple Sum Rule: The normalized scores are fused using a simple sum rule fusion scheme (4) where the fused score is computed by adding the scores for all modalities involved,

$$\hat{s}_{avi} = \sum_{m=1}^n X_m = s_{audio} + s_{visual} \quad (4)$$

where \hat{s}_{avi} is the score distribution and speaker's modality input data $\hat{s}_i = s_{audio}$ and s_{visual} .

Weighted Sum Rule: The normalized scores are fused using a weighted sum rule fusion scheme. The fusion scores can be obtained by using equation (5).

$$\hat{s}_{avi} = w s_{audio} + (1 - w) s_{visual} \quad (5)$$

where \hat{s}_{avi} is the score distribution and speaker's modality input data $\hat{s}_i = s_{audio}$ and s_{visual} . The overall performance is evaluated and the optimum weight, w_{opt} is defined at which the weight, $w = 0.4$ give the best system performance.

Fuzzy logic: For weighted sum rule (inferred from FIS), the weights are obtained from the Fuzzy Inference System (FIS). The weights vary depends on the input's current condition. The current audio and visual data are implemented in audio system and visual system in order to identify the weight that will be used during the fusion process. The FIS quality measure is modelled according to below steps [10,11, 25]. The fuzzy logic system procedures are proposed as below:

Step 1: Fuzzification

In this study, there are two fuzzy models for Mamdani-type and Sugeno-type, respectively. Each model has two inputs, speech and lip and one output which is weight.

Next, the inputs are identified and the degree of each input is determined according to appropriate fuzzy sets via membership function. The membership functions are Gaussian shapes because it can covers several values in one membership. The inputs are always a crisp numerical value. For input 1 (speech), the interval is varied between [0, 40] SNR and for input 2 (lip), the interval is varied between [0, 1] quality density. The output (weight) is varied between [0, 1].

Then, the speech fuzzy set is modeled for three mfs: speech (Qlow), speech (Qmed) and speech (Qhigh) and three mfs are also modelled for the lip fuzzy set: lip (Qlow), lip (Qmed) and lip (Qhigh). For the output fuzzy set, three mfs: weight (Qlow), weight (Qmed) and weight (Qhigh) are used. Output for Mamdani-type and Sugeno-type.

Step 2: Rule Evaluation

For this study, there are nine rules for the system. From the experiment, lip performs better than speech. Therefore, this study relies more on lip since uncertainty inputs condition are involved during the process. For example, when both speech (Qhigh) and lip (Qlow) are determined, the weight output is mapped to weight (Wmed). Rule editor is used to define the rules for each model. This study implemented the t-norms during the process.

1. IF speech (Qlow) AND lip (Qhigh) THEN (Wlow)
2. IF speech (Qmed) AND lip (Qhigh) THEN (Wlow)
3. IF speech (Qhigh) AND lip (Qhigh) THEN (Wmed)
4. IF speech (Qlow) AND lip (Qmed) THEN (Wlow)
5. IF speech (Qmed) AND lip (Qmed) THEN (Wlow)
6. IF speech (Qhigh) AND lip (Qmed) THEN (Whigh)
7. IF speech (Qlow) AND lip (Qlow) THEN (Wmed)
8. IF speech (Qmed) AND lip (Qlow) THEN (Wmed)
9. IF speech (Qhigh) AND lip (Qlow) THEN (Whigh)

Step 3: Aggregation

Aggregation is the process of unification of the outputs of all rules. The membership functions for all rules are scaled and combined into a single fuzzy set. The aggregation's inputs are the list of scaled membership functions and the output is one fuzzy set for each output variable. All the rules must be combined and tested in order to make a decision.

Step 4: Defuzzification

The output of aggregation will be used as input for the defuzzification process and the output is a single number (weight). For defuzzification process, the mamdani-type applied the centroid calculation method in order to obtain the centre of area under the curve while the sugeno-type used the weighted average of few data points' method. The output (w) obtained from fuzzy logic system is implemented as in equation (6) in order to calculate the fusion scores.

$$Y = w X_{speech} + (1 - w) X_{lip} \quad (6)$$

where Y is the score and w is the weight applied to speaker's modality input data which are X_{speech} and X_{lip} , respectively. Initially, the single biometric systems i.e. speech and lip single systems are evaluated separately. During the fusion process, the single biometric systems are fused using equation (2) in order to identify the overall systems performances

III. EXPERIMENTAL RESULTS

System performances for single biometric system are illustrated in Table 1 and 2, respectively. System performances for multibiometric systems executing maximum rule, simple sum rule, weighted sum rule and fuzzy logic fusion schemes are shown in Table 3, 4, 5 and 6, respectively.

Table 1 and Table 2 show the verification results in terms of equal error rate (EER) percentage for speech signal only and lip image only, respectively.

Table 1. EER percentage for speech signal

Speech	Clean	40dB	35dB	30dB	25dB	20dB	15dB	10dB	5dB	- 5dB
EER	1.1524	4.4848	4.9973	5.2862	6.3767	18.4187	25.397	33.4488	39.9381	46.8553

Table 2. EER percentage for lip image

Quality	Clean	0.1	0.2	0.3	0.4	0.5	0.6	0.7	0.8	0.9
EER	0.2684	1.0961	1.6207	3.7331	8.3399	13.719	22.2119	30.0056	37.2157	43.7125

Table 3 shows the verification results in terms of EER percentage for fusion at different combination of audio and visual conditions using maximum rule fusion scheme.

Table 3. EER percentage for different testing conditions using maximum rule fusion scheme

Visual	Audio									
	Clean	40dB	35dB	30dB	25dB	20dB	15dB	10dB	5dB	- 5dB
Clean	0.4031	0.4345	0.4699	0.4711	0.6492	3.8934	10.1001	18.2345	25.0456	35.2095
0.1	0.4201	0.4627	0.4805	0.4758	1.0087	5.3716	12.4606	21.2087	32.2748	40.2355
0.2	0.4845	0.7618	0.5537	0.9098	1.2969	5.3698	12.3098	21.1118	32.2964	21.0098
0.3	0.5212	1.1174	1.2035	1.3504	1.9206	5.3651	12.2795	20.7148	20.9206	20.9206
0.4	0.5982	1.3453	1.5010	1.9759	3.9527	2.1759	14.1159	21.1759	32.2494	21.0107
0.5	0.6014	7.4268	7.4399	7.3893	9.5420	9.5420	14.3281	24.6310	32.3142	21.6310
0.6	0.7002	16.1780	16.5478	15.7849	12.8885	15.1478	17.7768	23.5107	23.5107	23.4703
0.7	0.7501	21.5468	21.9938	20.9159	27.8895	20.3069	23.3643	27.8895	27.8565	27.7496
0.8	0.8302	30.1455	31.1364	32.6032	28.1391	28.7457	32.6032	35.5032	34.6693	32.6032
0.9	0.9867	33.9456	34.8330	34.6800	36.2378	33.2301	33.8044	36.2378	37.4114	46.2613

Table 4 shows the verification results in terms of EER percentage for fusion at different combination of audio and visual conditions using simple sum rule fusion scheme.

Table 4. EER percentage for different testing conditions using simple sum rule fusion scheme

Visual	Audio									
	Clean	40dB	35dB	30dB	25dB	20dB	15dB	10dB	5dB	- 5dB
Clean	0.0591	0.0854	0.0986	0.1998	0.3167	0.5944	4.8996	9.4555	17.3866	23.3335
0.1	0.6914	0.1548	0.1657	0.2794	0.3453	0.6554	6.0755	11.6873	18.0753	26.8928
0.2	0.1006	0.2204	0.2915	0.2965	0.5499	1.2045	7.0025	13.0623	19.9897	26.9921
0.3	0.2398	0.3963	0.2561	0.3463	1.0221	2.1896	8.6552	15.3106	22.9645	27.8065
0.4	0.3387	0.5433	0.8733	0.9552	1.4518	4.0812	10.2145	17.9542	25.1905	27.9887
0.5	0.4107	0.7723	1.0689	1.4011	3.4723	6.0998	12.4259	19.3741	27.7843	28.0000
0.6	1.0018	1.0862	2.0772	3.0261	4.2239	9.8775	15.9364	22.4521	31.0024	32.8912
0.7	2.5774	2.7450	3.8917	4.6678	8.7343	11.8872	18.8448	25.9643	33.9668	36.8666
0.8	3.5064	4.2861	4.0112	9.9972	10.7733	17.8463	23.9898	29.1601	35.2345	39.3023
0.9	7.3046	8.9912	9.2558	10.6175	15.2112	19.5111	25.8099	32.8465	39.1319	44.2990

Table 5 shows the verification results in terms of EER percentage for fusion at different combination of audio and visual conditions using weighted sum rule fusion scheme.

Table 5. EER percentage for different testing conditions using weighted sum rule fusion scheme

Visual	Audio									
	Clean	40dB	35dB	30dB	25dB	20dB	15dB	10dB	5dB	- 5dB
Clean	0.0585	0.0376	0.05311	0.2035	0.2592	0.7024	2.9301	5.3884	11.1125	17.5447
0.1	0.0299	0.1641	0.0675	0.2572	0.2871	0.8108	3.0743	7.1875	12.2466	19.4839
0.2	0.0425	0.2212	0.1625	0.2997	0.3322	1.9734	4.0005	9.0362	14.0766	20.7845
0.3	0.0528	0.3613	0.2590	0.3613	0.7835	2.2541	5.8042	10.3632	16.5664	21.7444
0.4	0.1025	0.7933	0.9614	1.0075	1.4456	4.7734	8.0074	13.7845	19.0907	23.6577
0.5	1.2423	1.8112	1.8994	2.3799	3.9274	5.6869	10.2177	15.8493	22.2410	25.1123
0.6	2.3163	3.0064	5.9274	6.0283	5.5940	11.2113	15.8776	19.8011	28.9374	29.0462
0.7	4.4412	6.8140	7.1959	8.1747	10.6284	13.6646	18.6777	22.2746	30.9056	36.0264
0.8	8.5966	10.6635	14.9023	15.8362	14.5608	21.0075	24.9173	28.5998	37.0003	40.6283
0.9	10.6519	15.5424	16.0295	17.0317	19.8746	23.1203	27.9814	35.0284	37.9795	44.3966

Table 6 and 7 show the verification results in terms of EER percentages of MFCC-ROI-SVM systems performances using mamdani-type FIS fusion scheme and sugeno-type FIS fusion scheme, respectively.

Table 6. EER percentages of MFCC-ROI-SVM system performances using mamdani-type FIS fusion scheme

Visual	Audio									
	Clean	40dB	35dB	30dB	25dB	20dB	15dB	10dB	5dB	- 5dB
Clean	0.0103	0.0122	0.0131	0.0507	0.1380	0.2562	0.2646	0.2655	0.2679	0.2683
0.1	0.0342	0.0699	0.0732	0.0882	0.1849	0.5152	0.8784	0.8971	0.9159	1.0117
0.2	0.0111	0.1053	0.1301	0.1161	0.3350	0.8230	1.1608	1.2697	1.1330	1.6002
0.3	0.0907	0.3238	0.3397	0.3491	0.8681	2.0946	3.2160	3.4328	3.5576	3.6994
0.4	0.1003	0.4133	0.5424	1.1218	1.5578	5.8117	7.2729	7.4831	7.8200	8.2377
0.5	0.5879	0.6254	0.6691	1.4011	5.9832	8.8223	9.9319	12.0796	12.3855	13.2265
0.6	0.6951	0.7189	1.4219	1.5287	6.1032	13.4035	14.5011	19.3187	20.3087	21.5643
0.7	0.8033	1.2900	1.5589	3.3483	6.2301	16.0497	22.1988	24.8179	27.0430	29.9945
0.8	1.0467	1.7502	1.9745	5.1324	6.3014	17.9221	23.3681	30.6325	34.9328	36.3332
0.9	1.1524	2.2993	4.9969	5.2800	6.3352	18.3037	29.9979	36.7324	39.6331	42.8223

Table 7. EER percentages of MFCC-ROI-SVM system performances using sugeno-type FIS fusion scheme

Visual	Audio									
	Clean	40dB	35dB	30dB	25dB	20dB	15dB	10dB	5dB	- 5dB
Clean	0.0196	0.0356	0.0528	0.0613	0.1123	0.2675	0.2679	0.2684	0.2684	0.2684
0.1	0.0304	0.0666	0.0957	0.1952	0.8530	0.6051	0.9985	1.0961	1.0961	1.0961
0.2	0.0421	0.3266	0.1342	0.1965	0.9545	1.5587	1.5878	1.6207	1.6207	1.6207
0.3	0.0909	0.5818	0.3965	0.4399	2.7768	3.9584	3.8119	3.7331	3.7331	3.7331
0.4	0.1020	0.6113	0.5599	0.5912	3.5558	8.1090	7.7664	8.5866	12.0048	8.2175
0.5	0.5923	0.8450	0.8865	1.5548	5.4002	9.0058	10.1167	13.6618	13.3855	13.6282
0.6	0.7515	1.1130	1.6006	2.7384	5.9996	13.7902	14.9134	20.4993	21.4911	22.1822
0.7	0.9961	1.1346	1.8553	4.1137	6.0058	17.1192	21.2265	26.1186	31.4956	30.0056
0.8	1.1104	1.7993	1.9971	5.2029	6.1148	17.9699	23.6049	32.4933	35.8279	37.0037
0.9	1.1393	2.3692	4.9969	5.2855	6.3700	18.4006	35.0685	37.1913	39.8754	42.1125

Fig. 5 shows the EER percentage for clean speech signal with noisy lip image while Fig. 6 illustrates the EER percentage for clean lip image with noisy speech signal.

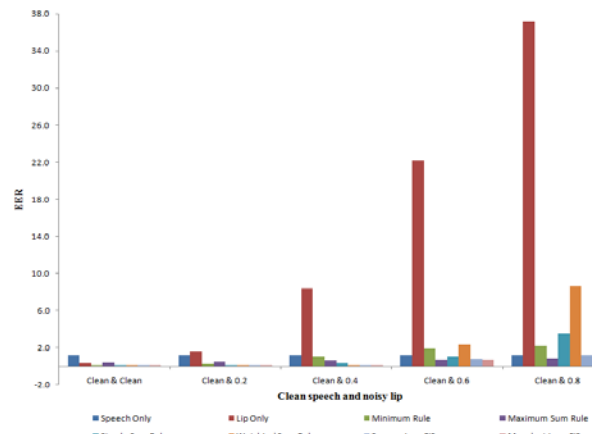


Fig. 5. EER percentage for clean speech signal with noisy lip image

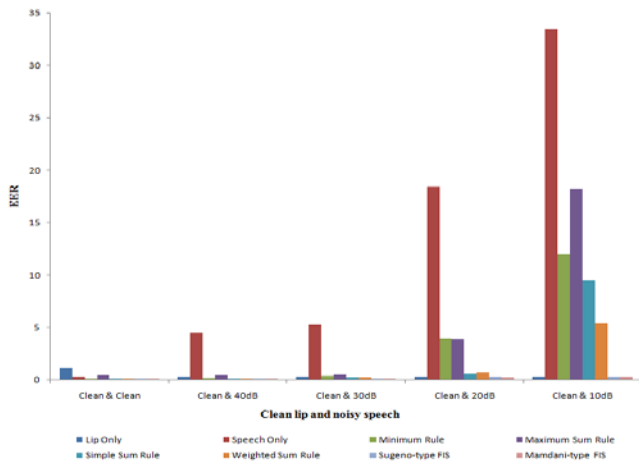


Fig. 6. EER percentage for clean lip image with noisy speech signal

IV. DISCUSSION

In this study, biometric speaker verification systems which proved to be reliable in clean and noisy condition have been successfully developed. Experimental results proved that all the objectives have been achieved.

The first objective is to develop single biometric systems based on speech and lip traits and to develop multibiometric systems based on minimum rule, maximum rule, simple sum rule and weighted sum rule fusion scheme. This objective has been accomplished by developing the feature extraction and pattern matching modules. For single biometric systems, two types of audio only biometric systems (i.e. MFCC-SVM and LPC-SVM) and one type of visual only biometric system (i.e. ROI-SVM) have been implemented successfully. For multibiometric systems, audio and visual biometric systems (i.e. MFCC-ROI-SVM and LPC-ROI-SVM) have been developed successfully. Four types of fusion schemes i.e. minimum rule, maximum rule, simple sum rule and weighted sum rule have been experimented.

The second objective for this study is to design quality based fusion algorithm using Fuzzy Inference System (FIS) for weight inference. In order to achieve this objective, experiments on two types of Fuzzy Inference System (FIS) i.e. Mamdani-type FIS and Sugeno-type FIS have been developed. The optimum fusion weights inferred from FIS are integrated to the fusion systems as a quality based multibiometric systems.

The final objective is to compare the performances of the entire single biometric systems and multibiometric systems. Performances of single biometric systems tend to drop due to degraded speech signals and lip images. Comparative study on the performances of different fusion schemes for multibiometric systems under different quality of biometric traits have been discussed in this study.

From the experimental results, in clean conditions or under minor quality degradation, it can prove that the fusion systems are able to give better performances compared to the performances of single biometric systems. Results also proved that the fusion systems based on sugeno-type FIS and mamdani-type FIS are observed as the most outstanding

systems compared to the other fusion schemes. As an example to this remark, experiment at clean speech and clean lip, the EER percentages for fusion systems based on minimum rule system, maximum rule system, simple sum rule system, weighted sum rule system, sugeno-type FIS and mamdani-type FIS fusion schemes are observed as 0.1019%, 0.4031%, 0.0591%, 0.0205%, 0.0196% and 0.0103%, respectively compared to the performances of speech and lip single systems i.e. 1.1524% and 0.2684%.

Subsequently, when one of the traits are severely corrupted by noise, the system performances of fusion systems based on minimum rule system, maximum rule system, simple sum rule system, weighted sum rule system tend to decrease. However, it can be observed that the fusion systems based on sugeno-type FIS and mamdani-type FIS are able to maintain the system performances. For example, at 35dB SNR of speech and 0.8 quality density of lip, the EER percentages for speech system, lip system, minimum rule system, maximum rule system, simple sum rule system, weighted sum rule system are observed as 5.9210%, 37.2157%, 33.2676%, 31.1364%, 4.0112% and 14.9023% respectively compared to the performances of sugeno-type FIS and mamdani-type FIS i.e. 1.9974% and 1.9745%. It can be concluded that the fusion systems based on sugeno-type FIS and mamdani-type FIS are able to overcome the problems encountered by other fusion schemes during these experiments.

Consequently, when both of the traits are severely corrupted by noise, the systems performances of fusion systems are no longer accurate. For example, experiments at 15dB SNR of speech and 0.8 quality density of lip, the EER percentages for speech system, lip system, minimum rule system, maximum rule system, simple sum rule system, weighted sum rule system, sugeno-type FIS and mamdani-type FIS fusion schemes are found as 30.7545%, 37.2157%, 33.2676%, 32.6032%, 23.9898%, 24.9173%, 23.6049% and 23.3681%, respectively. Implemented fusion systems i.e. minimum rule system, maximum rule system, simple sum rule system, weighted sum rule system as well as sugeno-type FIS and mamdani-type FIS are no longer capable to perform well due to the bad performance of both systems. Therefore, further studies on developing a system which able to filter the noise are required in order to obtain clean speech signals and lip images.

V. CONCLUSION

This paper discussed the multibiometric verification systems using fuzzy logic fusion scheme that combine two traits i.e. speech signals and lip images. The fuzzy logic fusion scheme has been proposed in order to overcome the problems faced by the unimodal systems. The unimodal systems tend to have degraded system performances due to unreliable live samples since the quality of speech signals and lip images decreased in noisy condition. The fuzzy logic fusion scheme has the ability to vary the fusion weight according to the live sample's condition which highly contributes to gain better system performances. This approach have great potential to get rid the unwanted problem such as noise in sensed live sample. Experimental

results prove that the fuzzy logic fusion method does improve the system performances.

[25] M. Hellmann, "Fuzzy logic introduction," epsilon nought radar remote sensing tutorials, 2001.

REFERENCES

- [1] C. L. Chia, and D.A. Ramli, "Comparative study on feature, score and decision level fusion scheme for robust multibiometric systems," *Frontier in Computer Education: Advances in Intelligent and Soft Computing*, vol.133, pp. 941-948, 2012.
- [2] A. K. Jain, A. Ross, and S. Prabhakar, "An introduction to biometric recognition," *IEEE Trans. On Circuits and Systems for Video Technology*, vol.14, no.1, pp. 4-20, 2004.
- [3] S. Ben-Yacoub, Y. Abdeljaoued, and E. Mayora, "Fusion of face and speech data for person identity verification," *IEEE Transactions on neural network*, vol.10, no.5, pp. 1065-1074, 1999
- [4] H. Pan, Z. P. Liang, and Z.P. Huang, "Fusing audio and visual features of speech," presented at 2000 Proceeding of IEEE International Conference on Image Processing 3, pp. 214-217.
- [5] J. Fierrez-Aguilar, Y. Chen, J. Ortega-Garcia, and A.K. Jain, "Discriminative multimodal biometric authentication based on quality measures," *Pattern Recognition*, vol.38, no.5, pp. 777-779, 2005.
- [6] K. Nandakumar, Y. Chen, S. C. Dass, and A. K. Jain, "Likelihood ratio-based biometric score fusion," *IEEE Transactions on Pattern Analysis and Machine Intelligence*, vol.30, no.2, pp. 342-347, 2008.
- [7] C. W. Lau, B. Ma, H. Meng, Y. S. Moon, and Y. Yam, Fuzzy logic decision fusion in a multimodal biometric system, presented at 2004 *Proc. ICSLP*.
- [8] S. Vasuhi, V. Vaidehi, N. T. N. Babu, and T.M. Treesa, "An efficient multi-modal biometric person authentication system using fuzzy logic," presented at 2010 Second International Conference of Advanced Computing (ICoAC), pp. 74-81.
- [9] H. Prade, D. Dubois, "What are fuzzy rules and how to use them," *Fuzzy Sets and Systems* 84, Elsevier North-holland, Inc.Amsterdam, The Netherlands, 1996.
- [10] L. A. Zadeh, "Fuzzy sets," *Information and Control*, vol. 8, pp. 338-353, 1965.
- [11] L. A. Zadeh, "Making computers think like people," *IEEE Spectrum*, vol.8, pp. 26-32, 1984.
- [12] J. Jassbi, S. H. Alavi, P. J.A. Serra, and R. A. Ribeiro, "Transformation of a mamdani FIS to first order sugeno FIS," 2007
- [13] Fuzzy Logic Toolbox, User Guide, 2010.
- [14] L. R. Rabiner, and R. W. Schafer, "Digital Signal Processing of Speech Signal," New Jersey: Prentice Hall Inc, 1978
- [15] S. Furui, "Digital speech processing, synthesis and recognition," 2nd Edn.,Dekker, New York, pp. 476, 2001.
- [16] Sanderson, and C. K. K. Paliwal, "Noise compensation in a multi-modal verification system," presented at 2001 Proceeding of International Conference on Acoustics, Speech and Signal Processing, vol.36, no.2, pp. 157-160.
- [17] T. Wark, and S. Sridharan, "Adaptive fusion and speech and lip information for robust speaker identification," *Digital Signal Processing*, vol. 11, pp. 169-186, 2001.
- [18] G. Iyengar, G. Potamianos, C. Net, T. Faruquie, and A. Verm, "Robust detection of visual ROI for automatic speech reading," presented at 2001 Proceeding Workshop on Multimedia Signal Processing, Cannes, France, pp. 79-84.
- [19] G. Chetty, and M. Wagner, "Liveness verification in audio-video authentication," presented at 2004 Int Conf on Spoken Language Processing.
- [20] G. Chetty, and M. Wagner, "Automated lip feature extraction for liveness verification in audiovideo authentication," Submitted for publication, 2004.
- [21] C. Becchetti, and L. R. Ricotti, "Speech recognition: theory and C++ implementation," 1st Edition., Wiley, England, 1999.
- [22] N. Vapnik, "The nature of Statistical Learning Theory," Berlin: Springer, 1995.
- [23] S. R. Gunn, "Support vector machines for classification and regression," Faculty of Engineering, Science and Mathematics, University of Southampton, 1998.
- [24] A. K. Jain, Nandakumar and A. Ross, "Score normalization in multimodal biometric systems," *Pattern Recognition*, vol. 38, pp. 2270-2285, 2005.

Fault tolerance and load balancing on the example of GlassFish

Arne Koschel, Michael Heine, Lars Knemeyer, and Irina Astrova

Abstract—Distributed systems are steadily gaining significance in today’s IT landscape. They are increasing in size and complexity, so is their demand on high availability. While managing distributed systems, there is a major issue to be addressed: How do we manage to keep high availability even in a case where one or more parts of the system fail? To address this issue, a distributed system should efficiently balance the load that the application has to handle and should be provided with a fault tolerance mechanism. This paper describes the principles of fault tolerance and load balancing as well as their practical implementation on the example of GlassFish.

Keywords—Apache HTTP Server, Balance, GlassFish, fault tolerance, load balancing.

I. INTRODUCTION

FAULT tolerance and load balancing are of great importance for high availability. High availability requires 24-hour per day, 7-day per week system accessibility.

A. Fault Tolerance

Generally, the term fault tolerance means that a system is able to keep operating even if some parts of the system fail. Fault tolerance is often needed when it comes to vital systems, e.g., the engines of an airliner. Although a fault tolerant system can compensate the failure of one or more parts, its performance might be compromised; e.g., an airliner would still be able to land with only one engine working, but it might not be able to take off again.

A common approach to fault tolerance is to distribute the system’s software among one or more redundant physical servers. Thus, if the primary server fails, one of the parallel running servers can take over and handle all further requests. Although a request that is processed by the primary server might get lost in the instant where the server fails, all further requests will be handled properly. In such a scenario, each redundant server would cause additional costs, but will not increase the performance of the entire system. Therefore, in practice redundant systems are often used to enhance the performance in the first place and serve as a failover only if needed.

Since it would be very inconvenient to let the user switch between the individual servers (especially for web

applications), some kind of a dispatcher so-called a *load balancer* is needed to allocate the incoming requests to the servers.

B. Load Balancing

Load balancing describes the spreading of system’s load (e.g., the incoming requests) among multiple server processes. Thereby the server processes might either be hosted on a single physical server or be distributed over multiple physical servers (one server per process). If all the processes are running on one physical server, this is called *vertical scaling*. In a case where each server process is hosted on a dedicated physical server, this is called *horizontal scaling*.

No matter which scaling is used, the motivation for load balancing is: avoiding (scalability) bottlenecks, achieving optimal resource utilization, avoiding overload, and minimizing response time [1]. Since the performance of one single server can be not good enough to handle all the incoming requests for a frequently used system (e.g., a web application), the scaling method of choice would usually be horizontal scaling. In addition, horizontal scaling enables to build an efficient and fault tolerant system. By contrast, vertical scaling relies on a single physical server and thus, it can provide no tolerance against hardware failures.

To make the distribution of the system’s software transparent to the user, the server processes are merged logically to a so-called *cluster*. This cluster is accessed through a load balancer, which appears as a single server process to the user. The load balancer itself is not part of the cluster. Rather, it runs on its own dedicated server. For the load balancer to be able to pass the incoming requests to the instances in the cluster, the IP addresses and port numbers of all server processes should be registered in the load balancer. Once an incoming request has arrived, the load balancer routes the request to a server process in the cluster. A particular server process is selected on the basis of the used load-balancing algorithm (e.g., round-robin, random, weight-based or dynamic/pending request counting).

No matter which algorithm is used, the load balancer also needs to be able to detect whether a server process is running or not. If the server process is down, the request should automatically be redirected to the next process in the cluster according to the used load-balancing algorithm.

The load balancer should also provide support for stickiness (e.g., cookie-based or URL encoding). With stickiness, the load balancer will always route all requests coming from a particular user to the same server process as the first request.

Prof. A. Koschel, Michael Heine, and Lars Knemeyer are with Faculty IV, Department of Computer Science, Hannover University of Applied Sciences and Arts, Hannover, Germany (e-mail: akoschel@acm.org).

I. Astrova is with InVision Software OÜ, Tallinn, Estonia (e-mail: irinaastrova@yahoo.com).

This enables the software hosted by the server process to keep track of the user’s actions.

II. GLASSFISH

GlassFish [2] is one of the most commonly used application servers in the field of Java applications. GlassFish uses the following terminology:

Instance: A server process that hosts the application.

Node: A physical machine hosting the GlassFish software that runs instances.

Cluster: A logical component that contains all instances on all nodes making up the cluster.

A. Fault Tolerance

GlassFish is based on a Domain Administration Architecture (DAA). This architecture enables to manage the whole cluster as if it were a single instance. The setup and configuration of the cluster with all the contained nodes and instances are done on a Domain Administration Server (DAS). The DAS is a server process. It is commonly hosted on a dedicated physical machine (see Fig. 1).

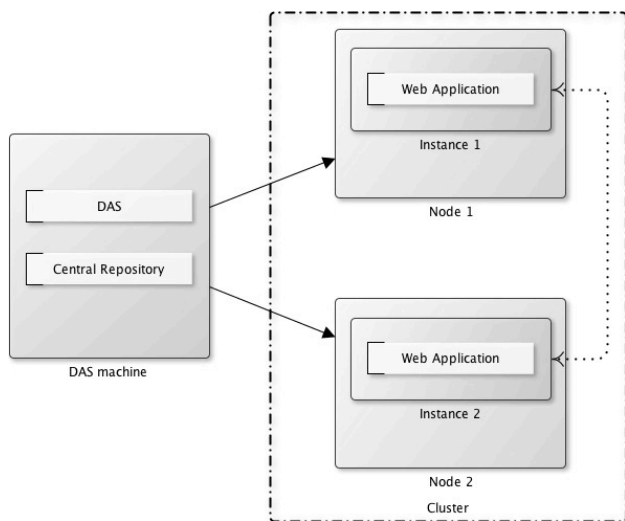


Fig. 1. GlassFish cluster

The DAS can also host web applications itself, which is usually done during the development (see Fig. 2).

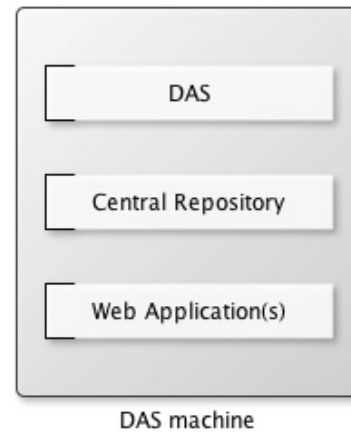


Fig. 2. Domain Administration Server (DAS)

To set up a new cluster, what is needed are a DAS (residing on its own physical machine) and one physical machine for each node in the cluster. Since the nodes should be able to run the GlassFish software, the operating system of choice for the nodes should be UNIX or Windows. For the DAS to be able to connect to the nodes, the machines should be accessible through either SSH or DCOM. Furthermore, all nodes have to be part of the same subnet as the DAS because the instances in the cluster need to communicate with one another via UDP multicasts. The setup and administration procedure can be done either from the command line interface or from the GlassFish administration console of the DAS.

At runtime, the DAS is used to manage the instances and acts as a central repository for all domain specific information (e.g. configuration information, resources and applications). If a new instance is added to the cluster, this instance will receive all necessary information from the DAS and cache it locally. Thus, once an instance has been failed, it can be reintegrated into the existing cluster without the DAS using the cached domain information.

Although a cluster can keep working properly without the DAS, it is common practice to implement a failover or at least a recovery strategy for the DAS as well. There are three basic approaches to this [3]. One is to periodically create backups of the domain data on the central repository and recreate the DAS on another GlassFish installation directory. Another approach is to periodically create backups of the whole GlassFish installation directory (including the domain root directory) and transfer it to a new host that inherits the network identity from the former host. Yet another approach is to use a hardware-based high availability solution for the DAS that automatically brings up a backup system with exactly the same configuration as the primary system where the original DAS fails.

In a cluster, fault tolerance is achieved through session replication. This means that the complete session state (including an HTTP session, EJB data and sign-on information) is replicated and stored beyond the instance that is actually handling the particular session’s requests. Before GlassFish version 3, the session state data could be saved in a

Highly Available Database (HADB). Since GlassFish version 3, this approach has been replaced by session replication. Session replication has three main advantages: (1) it is much easier to manage (since it is automatically configured by the DAS), (2) the load balancer does not need to know anything about a failover mechanism in the cluster, and (3) there is no more need for a failover of the HADB.

Session replication does not store all the session state data at one point. Rather, it distributes the replicated session information of one instance among the other instances in the cluster. A hash algorithm is used to determine which instance will store the state of a particular session. Thus in a cluster with three instances, a session S1 on an instance I1 might be replicated to an instance I2, while a session S2 from an instance I1 might be replicated to an instance I3. Fig. 3 illustrates such a scenario.

The hash algorithm can also be used to determine which instance is storing the replicated data of a particular session. This becomes important if the instance that has actually handled the session fails and the load balancer redirects the session's requests to an instance that does not have any information about the session's state. Based on Figure 3, the following scenario is possible. I1 handles S2 and replicates the session's state to I3. When I1 fails, the load balancer redirects the further requests to I2. Since I2 does not know the state of S2, it uses the hash algorithm to identify I3 as the host of the replicated session data. I2 obtains the state of S2 from I3. I3 deletes its copy of the transferred session state. I2 determines the new replication target (using the hash algorithm again) and handles the requests.

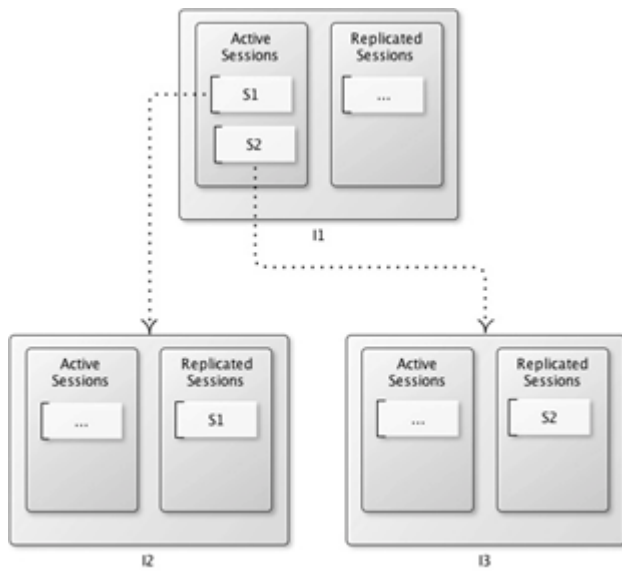


Fig. 3. Session replication

B. Load Balancing

GlassFish provides nearly all the functionality needed to set up a highly available and fault tolerant environment for web applications. The missing components are those that are not directly associated with the application server. Looking at the

logical communication flow, the missing components are, on the one hand, those that are arranged behind the application servers (e.g., a database) and, on the other hand, those that are in front of the application servers (e.g., a load balancer).

Fig. 4 illustrates a cluster that is accessed through a load balancer and has a database connected on the backend. This cluster is an abstract representation of three instances.

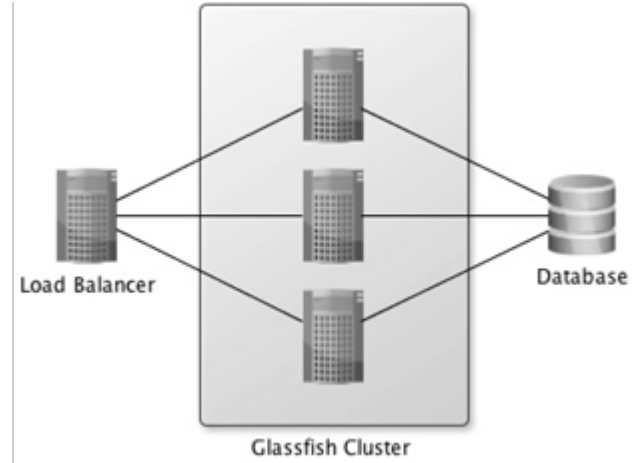


Fig. 4. GlassFish

III. EXAMPLE

To practically apply the concepts of fault tolerance and load balancing, we at first created a local cluster with two instances. By “local”, we mean that all the instances as well as the DAS were running on the same machine. Each instance had three ports: a port for HTTP connections to the server, a port for HTTPS connections to the server and an admin configuration port (which became more important later when the cluster was distributed).

After setting up the local cluster, we used Balance [4] as a load balancer to enable load balancing in the cluster. The Balance was started from the command line. The resulting setup is shown in Fig. 5.

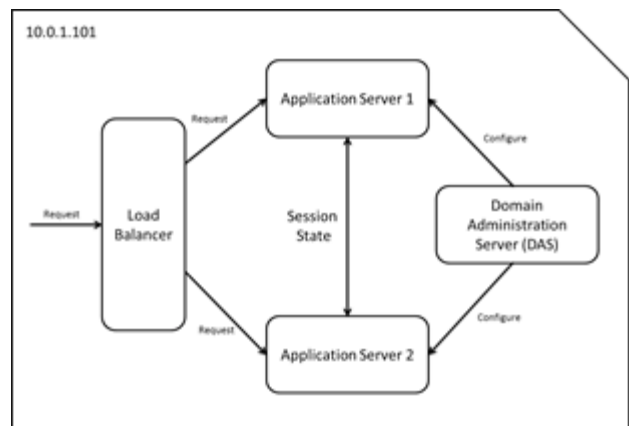


Fig. 5. Local cluster setup

We tested the local cluster by deploying a sample web

application onto the cluster and simulating different failover scenarios. The sample web application was a Java Server Faces (JSF) application. It contained three counters: one was manually stored in the HTTP session, another counter was stored inside a session scoped by JSF managed bean, and yet another counter was stored inside a session scoped by stateful session bean.

Our next step was to distribute the cluster over multiple physical nodes. The Balance and the DAS were running on one machine, whereas the other two machines hosted the two instances in the cluster (one machine per instance). The resulting setup is shown in Fig. 6. In this setup, the load balancer was connected to two servers (10.0.1.102 and 10.0.1.103); both were listening on port 8080 and hosting the sample web application.

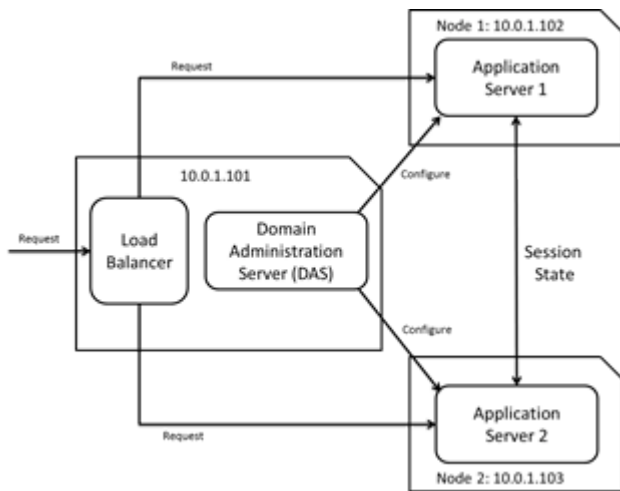


Fig. 6. Distributed cluster setup

We tested the distributed cluster against the sample web application again and particularly checked the behavior of the cluster in different failover scenarios.

To conclude the example, we critically looked at the previous setup to spot possible weaknesses of the configuration and to make suggestions for possible improvements. We identified the Balance and the DAS as single points of failure. If the Balance fails, no request will reach the instances. However, a failure of the DAS will not result in a complete failure of the cluster as the cluster can keep on running autonomously without the DAS. To solve the first problem, we suggest to have multiple Balances so that one Balance can take over if the other one fails.

IV. CONCLUSION AND FUTURE WORK

During the tests on both the local and distributed cluster, it became apparent that in some failover scenarios the Balance redirects request from a single client to different instances in the cluster. Therefore, in the future we are going to replace the Balance with the Apache HTTP Server [5]. The biggest advantage of the Apache HTTP Server is its support for stickiness.

Although the Apache HTTP Server is more sophisticated and potent than the Balance, it is more difficult to configure. To use the Apache HTTP Server as a load balancer, it should be installed with the following modules: `mod_proxy`, `mod_proxy_http`, `mod_proxy_ajp` and `mod_proxy_balancer` [6]. After the installation, the Apache HTTP Server as well as the DAS need further configuration. In the Apache HTTP Server configuration, the lines shown in Fig. 7 should be added. The placeholder `[Web-App]` stands for the name of the hosted web application, whereas the placeholders `[Instance 1]` and `[Instance 2]` represent names of the two instances that can be chosen freely. In the DAS configuration, a new property called `INSTANCE` should be added to the cluster.

```
<Proxy balancer://myCluster>
  BalancerMember
    http://10.0.1.102:[Port]
    route=[Instance 1]
  BalancerMember
    http://10.0.1.103:[Port]
    route=[Instance 2]
</Proxy>

ProxyPreserveHost On
ProxyPass                               / [Web-App]
balancer://myCluster -
/[Web-App] stickySession=JSESSIONID
<Location /balancer-manager>
  SetHandler balancer-manager
  Order Deny,Allow
  Allow from all
</Location>
```

Fig. 7. Apache HTTP Server configuration

ACKNOWLEDGMENT

We would like to thank Mats Lennart Henke from Hannover University of Applied Sciences and Arts, Hannover, Germany, for his help in preparing this paper.

REFERENCES

- [1] A. Koschel. High availability, fault tolerance, clustering concepts and sample approaches with os/hardware, corba and java ee/j2ee products. paul.inform.fh-hannover.de: /home/daten/skripte/skripte/master/qualitaet_verteilter_systeme/ss2012/Vorlesung/05_QVS_SoSe12_j2-co_lb-ft.pdf, 2012.
- [2] Oracle Corporation. Glassfish - open source application server. <http://glassfish.java.net/>
- [3] Oracle Corporation. GlassFish Server Open Source Edition High Availability Administration Guide, Release 3.1.2. Oracle Corporation, Redwood City, CA 94065.
- [4] Inlab Software GmbH. Balance. <https://www.inlab.de/balance.html>
- [5] Apache Software Foundation. The apache http server project. <http://httpd.apache.org/>
- [6] Apache Software Foundation. Apache module mod proxy balancer. http://httpd.apache.org/docs/2.2/mod/mod_proxy_balancer.html

Laser Based Tomographic System for Visualization and Characterization of Tissue Optical Phantoms

Sivakumar R, Sujatha N.

Abstract— Tomography is mathematical technique to get cross sectional details of an object from multiple trans-axial projections. A projection is a shadowgram obtained by illuminating a specimen by a penetrating radiation. In the proposed system the specimen is illuminated by using a near infrared laser and the transmitted optical radiation from the specimen are analyzed. Within the therapeutic window, from 600-1100 nm range tissues remain relatively transparent enabling us to apply tomographic principles in obtaining the cross sectional details. The developed system was tested for its imaging capabilities as well as detection of abnormalities by using tissue mimicking structures called phantoms. The prepared phantoms were scanned and the processed two dimensional tomographic images gave the outline of optical properties. Finally by using volume visualization techniques 3D visualization of the phantoms are also observed.

Keywords— shadowgram, therapeutic window, volume visualization, tissue optical phantoms, trans-axial projections.

I. INTRODUCTION

The non-invasive monitoring of physiological parameters and early diagnosis of pathological changes in tissues are of great importance for diagnosis and subsequent prevention of diseases. X-rays had been extensively used for the diagnosis of skeletal abnormalities, lesions in the chest and coronary blood vessels and breast-cancer screening. But due to its ionizing nature it cannot be used for continuous monitoring or frequent screening. On the other hand, magnetic resonance imaging, positron emission tomography, radionuclide imaging, etc. are too expensive and require contrast agents for which many people are allergic. Ultrasonography is often applied in tissue characterization and imaging, but precise localization of abnormalities in tissues at times is difficult due to similar acoustic characteristics and also the procedure requires perfect alignment of ultrasound transmitter and its receiver [1]-[3]. Therefore, optical techniques, due to their nonionizing, noninvasive and relatively inexpensive qualities,

emerge as a natural choice of an alternative diagnostic modality.

The variation in optical properties plays a major role in differentiation of tissues between the normal and abnormal states. When the light propagate through the tissue optical processes like scattering, absorption or transmission occurs based on the medium and are also strongly wavelength dependent. High energy radiations like gamma rays or X rays are not scattered to a great extent but propagates through the tissues in straight path. The radiation attenuates due to absorption which varies with tissue types. High energy photon absorption might leads to bond breaking and ionization of molecules which ultimately causes malignancy conditions in the tissues. A low energy radiation like infra red and microwave induces excitation of rotational and vibrational energy levels in the molecules leading to temperature changes only [4]. Therefore near infra red radiations has become a potential tool for diagnosis in the medical field. Near infra red spectrum occupies approximately wavelength ranging from 650-1100 nm in the electromagnetic spectrum.

The light propagation in tissues is characterized by their optical parameters viz. absorption coefficient (μ_a), scattering coefficient (μ_s), scattering anisotropy parameter (g) and refractive index (n) [5]. The reduced scattering coefficient provides a scale for isotropic scattering is given by $\mu_s = \mu_s (1-g)$ [6]. The scattering anisotropy parameter (g) can vary between -1 and +1. Zero value for g indicates isotropic scattering and $g=1$ means complete forward scattering and $g=-1$ means complete back scattering. Typical values of g in the tissue are in the range 0.7-0.95 ie. light gets forward scattered in tissues. The absorption coefficient is a measure of probability of photon being absorbed and its value in the tissue is in the order of 0.1mm^{-1} [7]. Because of variations in the refractive index in the tissues the near infra red light gets scattered and the scattering mean free path for NIR light is of the order of 10-100 microns. Absorption depends strongly on wavelength but scattering decreases very little with increasing wavelength. These parameters vary depending on the clinical conditions of the tissues [8]-[9].

Earlier applications of transillumination, technique of sample illumination by transmission of light through the sample resulted in poor-quality images due to multiple scattering of light in tissues [10]-[12]. But the availability of near infra red lasers especially within the therapeutic window region (600–1300 nm) has made significant contribution in the development of various diagnostic techniques [13]. When a

Sivakumar R is with the Department of Electronics and Communication, Government Engineering College, Idukki, Kerala, India. 685603 (phone: +91-9447454377e-mail: sivangeeci@gmail.com).

Sujatha N, is with the Department of, Applied Mechanics, IIT Madras, Madras, India 600020. (e-mail: nsujath@iitm.ac.in).

laser beam is incident on tissue surface due to mismatch in refractive index at the air–tissue interface, a part of this is backscattered, where as the remaining part is absorbed or transmitted through the tissues. Due to high scattering and low absorption, the penetration of light within the therapeutic window is more. The spatial distribution of the backscattered and transmitted components contains information on the metabolic, physiologic or possibly structural status of tissues [14], [15]. The proposed system makes use of these transmitted components to characterize the tissues as well as its visualization.

II. MATERIALS AND METHODS

A. Experimental Technique

The system proposed uses transillumination technique, the concept of imaging of biological tissues based on illuminating light on to the tissue and detecting the light coming out of the tissues. The developments in this field include development of tomographic reconstruction of head phantom system using pulsed laser [16], multilayer imaging using continuous laser [17], continuous wave laser reflectance imaging [18] etc. The schematic of the laser transillumination tomographic system used is shown in the Fig.1. The imaging system consists of the following subsystems.

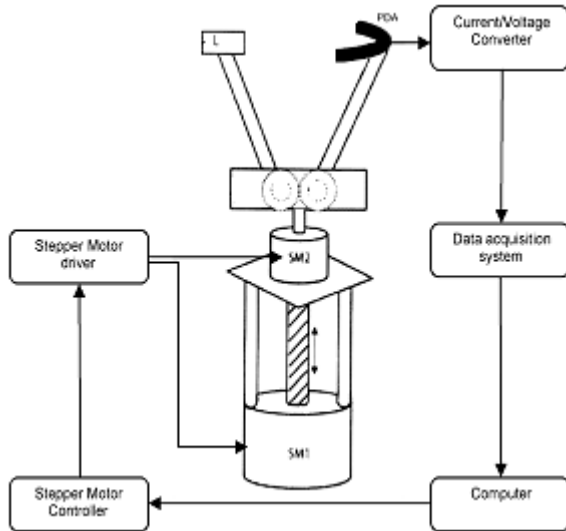


Fig.1. Schematic of laser transillumination tomography system. SM1, SM2 are stepper motors 1 and 2, L: laser source; PDA: photo diode array

1) *Mechanical System*: The mechanical system which serves the purpose of scanner helps to acquire the projections along the circumference and along the different heights of the phantom. The scanning is done by using two stepper motors. Stepper motor1 (SM1) helps in vertical scanning so that data along the various heights can be obtained and Stepper motor2 (SM2) helps in collecting data along the circumference of the phantom. A pantograph type arrangement carries laser source in one arm and an array of detectors in the other arm. The whole assembly can be moved up and down to cover the total height of the phantom by SM1.

2) *Optical System*: This system consists of laser pointer

source (690nm) of 1mw with its driver and an array of photodetectors placed on the circumference of a circle forming a fan beam configuration [19]. The photodetectors used is a silicon photodiode BPW34 having fast response, low noise and low cost with peak spectral efficiency around 900nm. The diffused components of light through the phantom, which is placed at the centre of source detector assembly, are captured by an array of 16 photodiodes which are configured in fan beam geometry.

3) *Data Acquisition System*: The phantom is placed in the centre of the source detector assembly placed in the fan beam configuration and the stepper motors are brought to the initial position. SM1(Y motor) is first activated by loading the number of slices (say 6) to be taken along the object height. SM1 makes the source detector assembly to elevate so that it comes to the base position of the phantom. SM2(X motor) is then activated by loading the number of projections (say 100) to be taken along the circumference of the phantom. For each stepping in the circumferential direction, data is collected by the data acquisition unit from the array of 16 photodiodes and is stored in the computer. When it completes one scan it records the whole data in a 16x100 matrix. When one complete scanning is over SM1 is again activated so that the whole assembly moves to the next higher position. This process continues till the scanner scans the entire phantom and the data are finally placed in a 16x100x6 matrix.

4) *Electronic System*: This includes the electronic hardware system for the data acquisition system and the designed driver electronic circuitry for motor control and optical system. Further details of the scanning system are given elsewhere [20].

B. Tomogram Visualization

The diffusely transmitted light after light tissue interaction can serve as a good measure for finding the clinical condition of the concerned tissue. By applying tomographic principles to these transmitted component cross sectional details or tomograms of the tissue can be obtained. The cross section of the object was obtained by convolution back projection algorithm [19], [21]. This was carried out in the following steps.

Step 1: Each projection $R_{\beta_i}(\gamma)$ was sampled with a sampling interval of angle α . If n denotes integer value and β_i represents angles at which projections were taken, then $R_{\beta_i}(n\alpha)$ denotes the fan beam projection. For each projection the modified projection $R'_{\beta_i}(n\alpha)$ is obtained as

$$R'_{\beta_i}(n\alpha) = R_{\beta_i}(n\alpha) D \cos n\alpha \quad (1)$$

where D is the distance of the source from origin.

$n = 0$ corresponds to the ray passing through the center of the object

Step 2: Filtered projection was obtained by convoluting each modified projection $R'_{\beta_i}(n\alpha)$ with the impulse response of a filter function $g(n\alpha)$

$$Q'_{\beta_i}(n\alpha) = R'_{\beta_i}(n\alpha) * g(n\alpha) \quad (2)$$

Step 3: Finally, the reconstructed image was obtained by

$$f(x, y) = \Delta\beta \sum_{i=1}^M \left(\frac{1}{L^2} (x, y, \beta_i) \times Q_{\beta_i}(\gamma') \right) \quad (3)$$

where

- γ' angle of the fan beam array passing through the point (x, y) and $\Delta\beta = 2\pi/M$;
- M total number of angles;
- L distance from the source S to the point (x, y)

The reconstructed images were displayed as 128×128 pixel image matrices. Further processing of image was performed by image enhancement techniques. Standard image processing techniques such as low pass filtering, median filtering, contrast stretching were done to reduce noise and to improve dynamic range of illumination.

When you submit your final version, after your paper has been accepted, prepare it in two-column format, including figures and tables.

C. Three Dimensional Reconstruction From Two-Dimensional Slices

The cross sectional details will not give a better understanding of the diagnosing problem. By applying visualization technique a better insight to the volume of the object could be obtained. Volume visualization [22] is a method of extracting meaningful information from volumetric datasets through the use of interactive graphics and imaging. It is concerned with the representation, manipulation, and rendering of volumetric datasets [23]. It involves projecting a multidimensional data into a two dimensional image plane by using an array of techniques for projecting and shading a volumetric dataset or properties. This is accomplished by series of processes like transformations, cuts, segmentation, translucency control, measurements etc. The volumetric dataset is represented as a 3D discrete regular grid of volume elements know as voxels. The numeric values associated with each voxel represents some measurable properties of the real phenomenon of object residing in the unit volume.

The scanning system scans the prepared phantom both along the circumference and also along its height. During its scanning it takes 100 projections along the circumference and each projection is registered in the array of 16 photodetectors in fan beam configuration. So after one complete scan in the circumferential direction a matrix of $16 \times 100 \times 1$ is registered in the computer. Then the stepper motor SM1 of the scanning system Fig.1. is incremented one step to take projections in the next height. Likewise the system scans the whole phantom in 6 increments and a projection matrix of size $16 \times 100 \times 6$ is obtained. This matrix is stored and processed for reconstruction by using filtered back projection technique and during this process it is resized to $128 \times 128 \times 6$ matrix. The noise removal is performed by Hamming filter. All the processes are done by using Matlab. The scalar volume data which is a collection of slices taken progressively through whole volume is further processed using image processing techniques. In the present work isosurface method of volume visualization is applied to the 3D grid containing the discrete

values of the density function which represents the optical properties of the tissue phantom. For effective visualization of the volume data, it is converted to surface form and texture map is applied to visualize the surface. The isosurface of a particular isovalue is the set of all points whose interpolated density equals that isovalue. Matlab's custom isosurface algorithm for visualization which returns a triangulated surface like marching cube algorithm is used for this purpose. When combined with isocaps this technique revealed information about interior of the isosurface. Apart from this Matlab provided several commands to control shading, lighting and camera viewpoints while rendering 3D plots and volumetric data. These controls resemble Open Graphics Library structures, style and behaviors. Appropriate Matlab functions to control the camera rotation, position, viewing direction and orientation were used for the target volume visualization to obtain better insight of the viewed surface.

D. Phantom Preparation

To evaluate the potential of developed system for imaging tissues, synthetic tissue model phantoms were prepared by using agar as a host medium, Intralipid and India ink as simulators[24]-[26]. All these constitute turbid media similar to biological tissue.

Cylindrical solid phantoms of height 6cm and diameter 4cm which matches with the dimensions of the fan beam geometry were prepared for validation. Agar powder is the host material used in tissue mimicking phantom which basically provides structural support so that solid phantom layers could be made. In order to simulate different tissue properties three phantoms Fig.2. with different concentration of absorber and scatterer are made for the testing purpose. Intralipid is used for the reason that it can simulate the scattering properties of biological tissues [24]. India ink are also used along with intralipid in different concentration which mimics the purpose of absorber in the real tissue [25].



Fig.2 Phantoms prepared: from left phantom3, phantom1 and phantom2

Agar was used in the concentrations 1:6 (6g in 100ml distilled water) in order to give more mechanical strength to the phantom sets. For these phantoms India Ink was used as absorbing medium and Intralipid simulated scattering phenomena. For phantom 1, an initial concentration of 20 μ l of India Ink was diluted to 100 ml distilled water was used as a stock solution. 1% Intralipid and 20 μ l of the stock solution diluted to 5ml are then added to the host medium. For phantom 2, 2% Intralipid and 30 μ l of the stock solution was diluted to 5ml and added to the host medium For phantom 3,

India Ink (30 μ l) was added to the host medium directly to simulate more absorption with 0.5% Intralipid. Increased absorption or scattering is an indication of malignancy in a tissue.

The mixture of agar and distilled water is heated to a temperature of about 90 degrees and is then allowed to cool for about 60 degrees [26]. When it attains this temperature intralipid and India ink of required concentration are added and is again allowed to cool till 40 degrees. During the whole process the mixture is stirred well for getting uniform concentration. Then the mixture is allowed to settle and after solidification it is taken out of the glass mould and is used for experimental purposes

III. RESULTS AND DISCUSSION

The non-invasive determination of optical parameters plays a vital role in medical diagnostic imaging. The technique presented here provides a method for studying the variations of optical parameters on tissue model phantoms using optical tomography. To analyze the variations 2D images of different layers of tissue phantoms are recorded. The obtained image is color coded which will enhance the chances of extracting information regarding abnormalities in a much simpler way. Tissue phantoms with varying concentrations of absorber and scattering medium were used for testing this tomographic method.

The phantoms with a height of 6cm are scanned using the developed system at an interval of 0.5cm. In each circumferential scanning 100 projections are made so that at the end of the whole scan a matrix of 16x100x6 is stored on the computer. This data is then used for reconstructing the tomograms and visualization of the volume. The tomograms obtained for the three phantoms are shown in Fig.3.

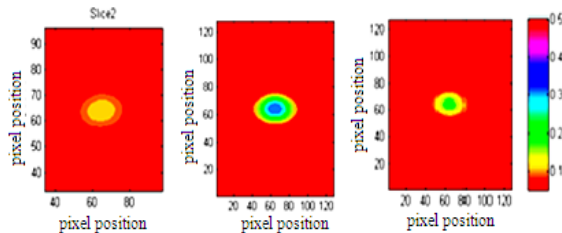


Fig.3. Tomograms obtained for three phantoms : from left phantom3, phantom1 and phantom2

The reconstructed tomogram of the phantoms shows significant differences with each other. During preparation of phantom1 the absorber and scatterer concentration included was very less and so maximum light output is obtained from that phantom. Tomograms analysis of phantom1 shows blue color in the centre followed by concentric rings of its low gradation colors. From the color bar, blue color corresponds to a maximum intensity value compared to tomograms of phantom2 and phantom3 which had green and yellow at its centre with intensity equivalent values less than that of blue. So the light output from phantom1 is maximum which means that absorption and scattering is very less when compared to other two phantoms. Phantom 1 and Phantom 2 cannot be distinguished by direct eye sight but their tomograms Fig.3.shows distinct variations because of their variations in optical properties. There is no inhomogenities included in the

phantoms and hence all the tomograms obtained for a particular phantom showed the same color map. Since variation in optical properties may be due to inhomogenities this methods finds application for distinguishing normal/abnormal tissues. Once tomograms are reconstructed an attempt to visualize the volume had been done to get a better insight to the structural variations of the phantom under consideration. For this tomograms of the six slices of the respective phantom are stacked one over the other Fig.4. Then volume rendering is done to visualize the whole volume using isosurface method of volume visualization. Fig.5 shows the reconstructed volume visualized for phantom1. Similar structures are visualized for the remaining phantoms also. The method used for volume rendering requires lot of human intervention to set the threshold values in the algorithm and hence advanced techniques could be used to enhance the visualization.

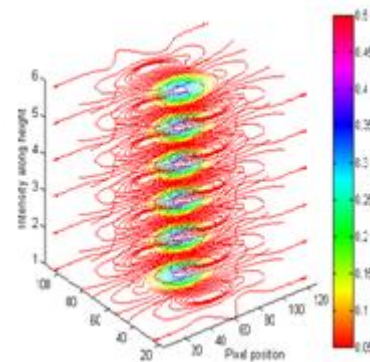


Fig.4. Placement of tomograms as a stack of six slices for Phantom1

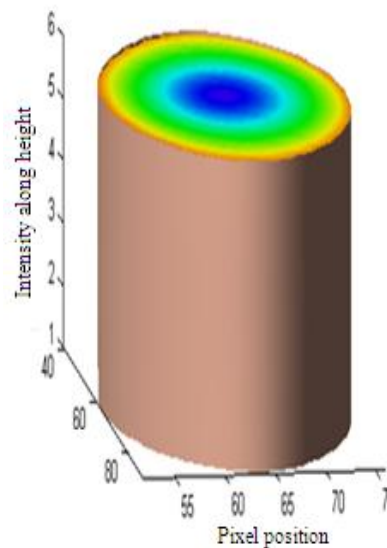


Fig.5. Volume visualized with cut away sections for Phantom1

In conclusion, a tomographic system consisting of red laser source and photodetectors has been developed. The number of detectors could be increased for better resolution and accuracy of the optical properties determination. Algorithms based on compressed sensing can be used which reduces the number of projections and thereby reduces the scanning time. Highly directional laser source with adequate

power which does not cause tissue damage can be used so that false information due to scattered output can be minimized. Advanced image processing algorithms for tomographic reconstruction and volume visualization can be implemented to provide better results. The clinical potential of this system can be further extended to real time tissue samples for further evaluation.

REFERENCES

- [1] J. D. Bronzino "The Biomedical Engineering HandBook, Second Edition." Boca Raton: CRC Press LLC, 2000
- [2] W.R.Hendee, and C. J. Morgan, W. J Med "Magnetic Resonance Imaging Part I—Physical Principles" 141(4): 491–500, October 1984
- [3] *Bushberg et al "The Essential Physics of Medical Imaging, , 2nd ed". Chapters 19, 21, 22, 24.*
- [4] J. D. Bronzino "The Biomedical Engineering HandBook, Second Edition." Boca Raton: CRC Press LLC, 2000
- [5] Renato Marchesini, A. Bertoni, S. Andreola, E. Melloni, and A. E. Sichirollo "Extinction and absorption coefficients and scattering phase functions of human tissues in vitro" *Optical Applied Optics* , Vol. 28, No. 12 ,15 June 1989
- [6] Cui, W. and Ostrander, L. E., "The relationship of surface reflectance measurements to optical properties of layered biological media" .IEEE Trans. Biomed. Eng., 1992, 39, 194–201.
- [7] John S. Maier, Scott A. Walker, Sergio Fantini, Maria Angela Franceschini, and Enrico Gratton "Correlation between blood glucose concentration and the reduced scattering coefficient of tissues in the near infrared" *Optics Letters* ,Vol. 19, No. 24 , December 15, 1994
- [8] N. Ghosh, S. K. Mohanty, S. K. Majumdar, and P. K. Gupta, "Measurement of optical transport properties of normal and malignant human breast tissue," *Appl. Opt.*, vol. 40, pp. 176–184, 2001.
- [9] *Bushberg et al "The Essential Physics of Medical Imaging, , 2nd ed". Chapters 19, 21, 22, 24.*
- [10] Nadège Roche Labarbe, Andrea Surova, Stefan A. Carp, David A. Boas, Megha Patel "Noninvasive optical measures of CBV, StO₂, CBF index, and rCMRO₂ in human premature neonates' brains" *Invest. Ophthalmol. Vis. Sci.* vol. 51 no. 52678-2685 May 2004
- [11] A. Kienle, L. Lilge, M. S. Patterson, R. Hibst, R. Steiner, and B. C. Wilson, "Spatially resolved absolute diffuse reflectance measurements for noninvasive determination of the optical scattering and absorption coefficients of biological tissue," *Appl. Opt.*, vol. 35, pp. 2304–2314, 1996.
- [12] F.Gao, P.Poulet, and Y. Yamada, "Simultaneous mapping of absorption and scattering coefficients from a three-dimensional model of time-resolved optical tomography," *Appl. Opt.*, vol. 39, pp. 5898–5910, 2000
- [13] Prah, S. A. (1998b). Some biological scatterers. Oregon Medical LaserCenter.<http://omlc.ogi.edu/classroom/ece532/class3/scatterers.html> .,Last accessed November 2009
- [14] Gopalendu Pal, S Basu, Kunal Mitra, Vo Dinh "Time resolved optical tomography using short pulse laser for tumor detection". *Applied Optics*, Vol. 45, No. 24 -August 2006
- [15] G.Jarry, J.P. Lefebvre, S. Debray and J. Perez "Laser tomography of heterogeneous scattering media using spatial and temporal resolution" *Medical and Biological Engineering and Computing* .Volume 31, Number 2, 157-164, 1993
- [16] Adam Gibson, Roza Md. Yusof, Hamid Dehghani, Jason Riley, Nick Everdell, Robin Richards, Jeremy C. Hebden, Martin Schweiger, Simon R. Arridge, and David T. Delpy "Optical tomography of a realistic neonatal head phantom" *Applied Optics* Vol. 42, No. 16 , June 2003
- [17] S. Chacko and M. Singh, "Multi-layer imaging of human organs by measurement of laser back-scattering radiation," *Med. Biol. Eng. Comput.*, vol. 37, pp. 278–284, 1999
- [18] N. S. Anand, D. Kumar, R. Srinivasan, and M. Singh, "Laser reflectance imaging of human forearms and their tissue-equivalent phantoms," *Med. Biol. Eng. Comput.*, vol. 41, pp. 28–32, 2003
- [19] Kak and Slaney, *Principles of Computerized Tomography*. Piscataway, NJ: IEEE Press, 1988.
- [20] R. Srinivasan and Megha Singh, "Multislice Tomographic Imaging and Analysis of Human Breast-Equivalent Phantoms and Biological Tissues," *IEEE Transactions on Biomedical Engineering* No 10 Volume 5, Oct. 2004
- [21] Alicia Viskoe "Computed Tomography Post acquisition Data Correction for System Alignment Errors". *IEEE Transactions on Instrumentation and Measurement*, Vol. 48, No. 5, October 1999
- [22] S. L. Wood, "Visualization and modeling of 3-D structure," *IEEE Eng. Med. Biol. Mag.*, pp. 72–79, Jan. 1992.
- [23] Kaufman, A., "Volume Visualization, IEEE Computer Society Press Tutorial", Los Alamitos, CA, 1990.
- [24] Hernández SE, Rodríguez VD, Pérez J, Martín FA, Castellano MA, Gonzalez-Mora JL. Diffuse reflectance spectroscopy characterization of hemoglobin and intralipid solutions: in vitro measurements with continuous variation of absorption and scattering. *J Biomed Opt.* 2009 May-Jun;14
- [25] Paola Di Ninni, Fabrizio Martelli, and Giovanni Zaccanti "The use of India ink in tissue-simulating phantoms" *Optics Express*, Vol. 18, Issue 26, pp. 26854-26865 (2010)
- [26] Rinaldo Cubeddu, Antonio Pifferi, Paola Taroni, Alessandro Torricelli and Gianluca Valentini "A solid tissue phantom for photon migration studies" CEQSE-CNR and Dipartimento di Fisica, Politecnico di Milano, Piazza L da Vinci 32, 20133 Milano, Italy

Sivakumar R was born in Kollam, Kerala, India, on April 29, 1977. He received the BTech degree from the Calicut University Kerala, India, in 1999 and the M.Tech. degree in Biomedical engineering from the Indian Institute of Technology, Madras, India, in 2012. His research interests include Digital image processing, Bio-optics and medical imaging.

Sujatha Narayanan received the BTech degree in Electrical Engineering from Calicut University Kerala, India, in 2000, and the Ph.D. from Nanyang Technological University, Singapore in 2005. She is currently working as Associate Professor in Biomedical Engineering division at the Indian Institute of Technology, Madras, India. Her research interests include Biomedical imaging, Bio-optics and Speckle metrology.

A Suitable Approach for Evaluating Bus Arrival Time Prediction Techniques in Egypt

M. Tantawy and M. Zorkany

Abstract—Accurate Bus arrival time prediction depending on a real-time basis has become an essential and important element in management transportation systems. This paper demonstrates the results of field tests for evaluating bus arrival time prediction in Egypt. One of the most difficult aspects of evaluating an operational field test is obtaining consumer response to products or services that are not market ready or even completely functional. Field tests were performed under real traffic situations in order to test the system in terms of prediction of bus arrival time to stations depending on two techniques consisting of Kalman filter and Neural Network. Findings from the field test at the real-world sites indicated that the system would be capable estimate the prediction time.

Keywords—Intelligent Transportation System (ITS), Neural Network, Field test, Kalman Filter.

I. INTRODUCTION

Intelligent Transport Systems (ITS) are advanced applications which aim to provide innovative services relating to different modes of transport and traffic management and enable various users to be better informed and make safer, more coordinated, and 'smarter' use of transport networks.

Improving traffic flow, reducing emissions and synchronizing traffic signals for safety and public transportation vehicle priority are just a few of the benefits of intelligent transportation systems. Intelligent traffic solutions collect information at traffic signals all around the city, correlate the real-time data and can automatically regulate traffic policies across a city.

TMUA system is designed to interconnect public transport vehicles and bus stations to “Central Room” to monitor the vehicles & traffic status. Based on the collected data and via analyzing road condition, accurate Bus arrival times will be computed via processing server at the central room and transmitted to all relevant stations. Passengers in buses will be notified of the current station and the next station using audio

This work concern is a part of research project called Transportation Management and User Awareness (TMUA) that research project is financially supported by the National Telecom Regulatory Authority (NTRA) of Egypt. Research project Team are: A. Ammar, E.M. Saad, I. Ashour, M.Tantawy, M.zorkany, M.Shiple, A.Nabil, M.Sami and A.Hamdi.

M.Tantawy is with the Network Planning Department, National Telecommunication Institute, Cairo, Egypt (e-mail: m.tantawy@nti.sci.eg.)

M.Zorkany is with the Electronic Department, National Telecommunication Institute, Cairo, Egypt; (e-mail: m.tantawy@nti.sci.eg.)

announcements. Achieving these main features will cause more improvement in public transport convenience and safety in Egypt. It will also allow “Central Rooms” to manage better their resources (mainly busses) through better route planning in relation to peak hours & congested zones.

Most Bus arrival-time predilection algorithms depend on Bus speed, traffic flow and occupancy and traffic incidents. In recent researches, other factors and parameters entered in the calculation of prediction time as daily, weekly and seasonal. For instance, daily patterns distinguish morning hours, rush hours and night traffic, while weekly patterns distinguish weekday and weekend traffic, while seasonal patterns distinguish school season and summer season.

In previous paper in the same project [1], online Bus arrival time prediction using hybrid neural network and Kalman filter techniques was proposed and tested depending on simulation data . In this paper, we re-do this implementation depending on real data of field test and propose a suitable approach for evaluating Bus arrival time predilection technique depending on a hybrid Neural Network and Kalman filter Techniques in Egypt.

This paper is organized as follows. Field Test Scenario is presented in Section 2. Testing proposed bus arrival time prediction technique is presented in Section 3. Field test results and discussions are given in Section 4 and finally conclusions are drawn in Section 5.

II. FIELD TEST SCENARIO

First, Field test scenario has been built to test TUMA integrated system and test proposed bus arrival time prediction. That scenario is carried out using different components, each aiming at a specific function. Figure 1 shows the different Field test components: Three buses and two servers (processing server & Data base server).

The available data, which was collected during more than two months for units have been installed in three Busses of the lines of NTI fleet (Our Institute) in different three routes (about 18 stations). Taking into account that these lines in different areas to cover different cases of traffic in Egypt.

In field test, five inputs are chosen to predict bus arrival time:

Day: take values from 1 (Saturday) to 7 (Friday).

Station Index Link: links index between successive stations.

Period: each day is divided into five periods.

Season: the year is divided in three categories: Ramadan, School season and Vacation season.

Route: represent route number as 1,2,3...

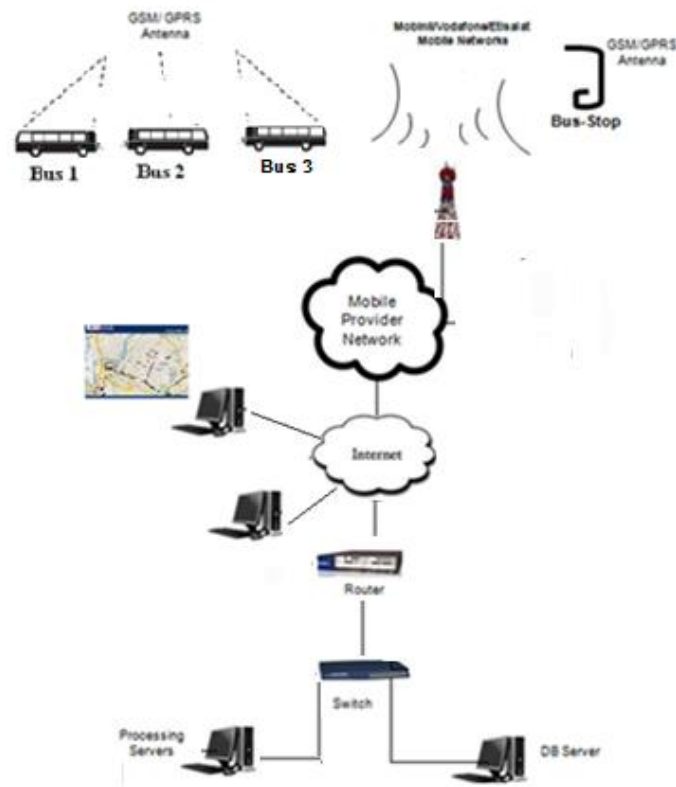


Fig. 1 Main components of Field test

III. TESTING BUS ARRIVAL TIME PREDICTION TECHNIQUE

The ability to obtain accurate predictions of bus arrival time on a real time basis is vital to both bus operations control and passenger information systems. Several studies have been devoted to this arrival time prediction problem in many countries; however, few resulted in completely satisfactory algorithms [2-9].

This paper presents an effective method that can be used to predict the expected bus arrival time at individual bus stops along a service route. This method is a hybrid scheme that combines a neural network (NN) that infers decision rules from historical data with Kalman Filter (KF) that fuses prediction calculations with current GPS measurements. The proposed algorithm relies on real-time location data and takes into account historical travel times as well as temporal and spatial variations of traffic conditions.

A. Neural Network Implementation

In previous paper in the same project [1], double hidden layer Multi Layer Perceptron (MLP) Neural Network (NN) was suggested depending on simulated data using MATLAB simulation. In this paper, re-do this implementation depending on real data of field test. And using different number of hidden

layers (single, double , three and four hidden layers) to choose the most suitable design for our application.

B. Suitable Number of Hidden Layers NN

There are really two decisions that must be made regarding the hidden layers of neural network, first, how many hidden layers to actually have in the neural network ? and how many neurons will be in each of these layers?.

Theoretically, Problem that requires fast implementation, fast learning and easy implementation single hidden layer are encountered. However, double hidden layer NN can represent functions with any kind of shape. Two hidden layers NN is also used in applications which need more accurate output and off line learning application [10,11].

Also, Deciding the number of neurons in each hidden layers is a very important to implement suitable neural network for specific application. Because using few neurons will results under- fitting problem and too large numbers of neurons will results Over-fitting problems. Also, training time can increase to the point that it is impossible to train the neural network.

The most famous rules for determining the number of neurons in the hidden layers of NN are:

- The number of hidden neurons between the size of the input layer and output layer.
- The number of hidden neurons 2/3 the size of the input layer, plus output layer.
- The number of hidden neurons less than twice the size of the input layer.

Practically, it is very difficult to determine a good network topology just from the number of inputs and outputs. It depends critically on the number of training examples and the complexity of the classification. So, for more accurate decision, the following analysis are to choose the suitable number of hidden layers neural network architecture in our project.

C. Selecting Suitable Neural Network Structure

In field test, to determine the prediction times of a moving bus to the downstream bus stations, the GPS readings of each equipped bus need to be projected onto the underlying transit network.

The proposed neural network consist of five input, and output layer. The Input Layer of the proposed neural network has 5 nodes (Day, Station Index Link, Period, Season and Route) and one output node represent bus arrival time prediction. The different neural network structures (single, double, three and four hidden layers) is studied through number of real time collected data for three different routes consisting of 18 stations (6 stations per route) during more than two months.

To select suitable number of hidden layers in neural network structure in our project, we used real data to training and simulations the different number of neural network (single, double, three and four hidden layers) to predict bus arrival

times. The MSE (Mean Square Error) and processing time were calculated for each case.

The results of MSE shown in Table 1 and Fig. 2 which indicate the MSE of single hidden layer is large (34.53), then the value decreased to 31.65 for double hidden layers and the MSE value minor decrease in case of three and four hidden layers.

The results of processing time (training time) shown in Table 2 and Fig. 3 which indicate the training time of single hidden layer is small (13 minutes), then the time increased to 16 minutes in double hidden layers and then increase in case of three and four hidden layers.

TABLE 1 : Relation between MSE and No of hidden layers

No of hidden layer	MSE (Mean Square Error)
1	34.53
2	31.65
3	31.18
4	31.43



Fig. 2 : Relation between MSE and No of hidden layers

TABLE 2 : Relation between learning processing time and No of hidden layers NN

No of hidden layer	Processing time (minute)
1	13
2	16
3	20
4	26

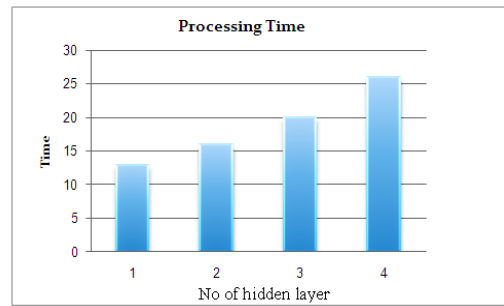


Fig. 3 : Relation between learning processing time and No of hidden layers NN

From the previous results, the double hidden layer neural network is suggested for prediction bus arrival time since MSE error of double hidden layer is better than single hidden layer and the improvement using three and four hidden layers are minor while increasing number of hidden layers increase the training processing time exponentially. Figure 4 shows the proposed neural network structure.

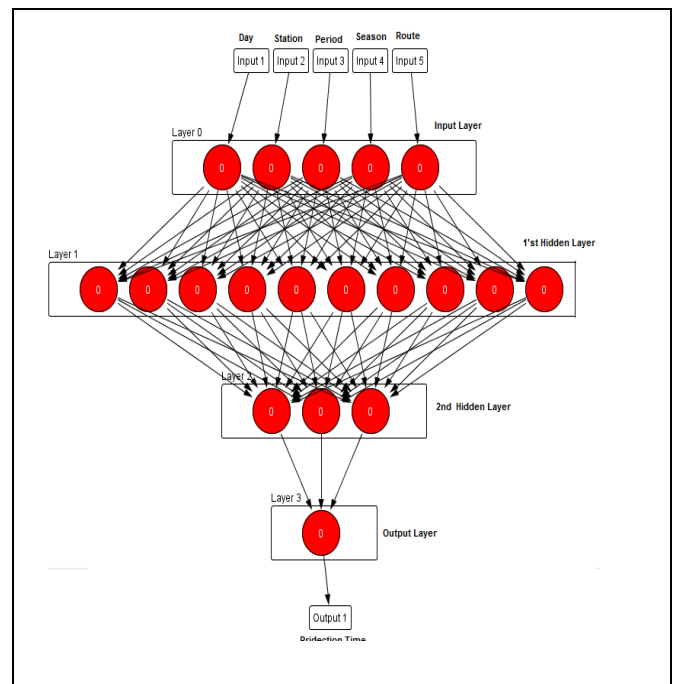


Fig. 4: The proposed neural network structure

Testing the proposed structure (double hidden layer) with single hidden layer neural network structure based on the collected real data of field test to show the quality of proposed structure in bus arrival time predictions shown in figure 5. this comparison based on Matlab simulation. The results shows advantage of double hidden layers structure in prediction.

In figure 5, the X-Axis represent *Station Index Link* in different trips and different periods in different days. and Y-Axis represent the real time (blue) and predictions times using single hidden layer (red) and double hidden layer neural network (green).

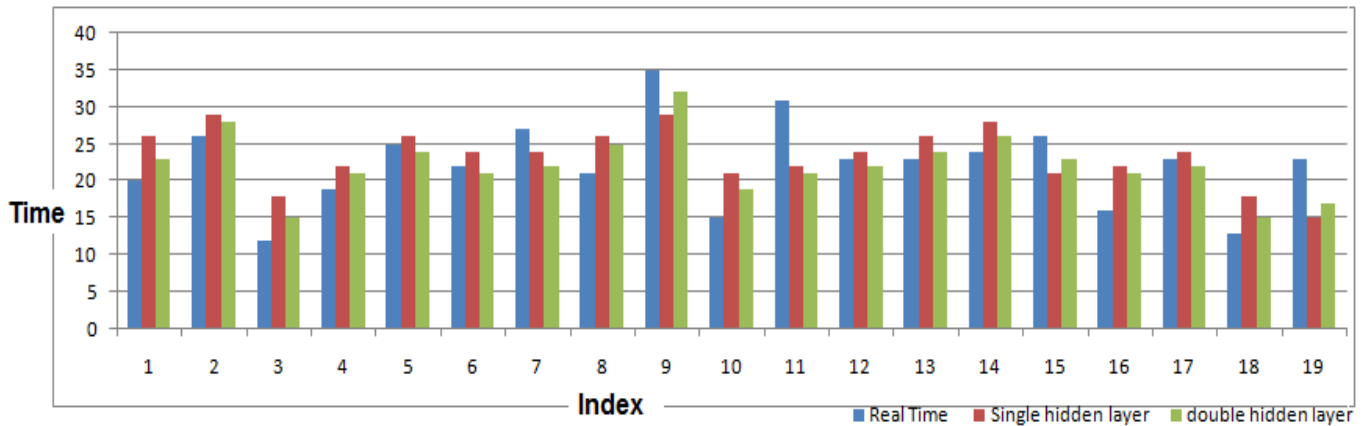


Fig. 5 : Comparison between single and double hidden layer

IV. FIELD TEST RESULTS

A. Bus Arrival Time Prediction Testing using NN:

Figure 6 shows a comparison between real arrival time and prediction time using neutral network for Kobry Al-Koba station and El-Sawah station (distance about 4 Kilometers). The RMSE (Root Mean Square Error) in this case equal 1.2 minute.

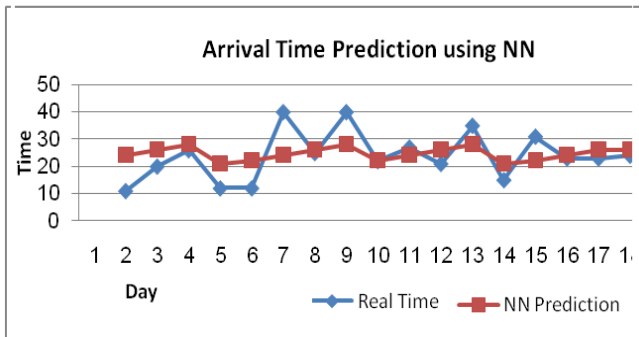


Fig. 6: Real Arrival Time and Prediction Time Using NN for Kobry Al-Koba and El-Sawah station

Figure 7 shows a comparison between real arrival time and prediction time using neutral network for NTI station to Kobry Al-Koba station (distance about 9 Kilometers).

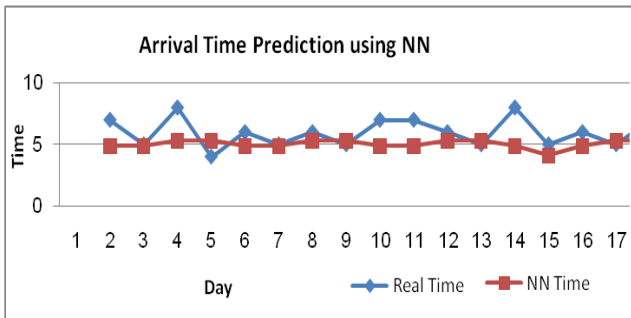


Fig. 7: Real Arrival Time and Prediction Time Using NN for NTI to Kobry Al-Koba station

B. Arrival time prediction testing using Kalman Filter

Arrival time prediction using Kalman Filter prediction algorithm is described in previous paper [1] to estimate bus arrival time. Calculations arrival time using Kalman filter in the proposed system depends on the four previous real time collected data for the same route and link. For example: figure 8 shows arrival time calculation result from NTI to Kobry Al-Koba station using Kalman Filter (distance about 9 Kilometers).

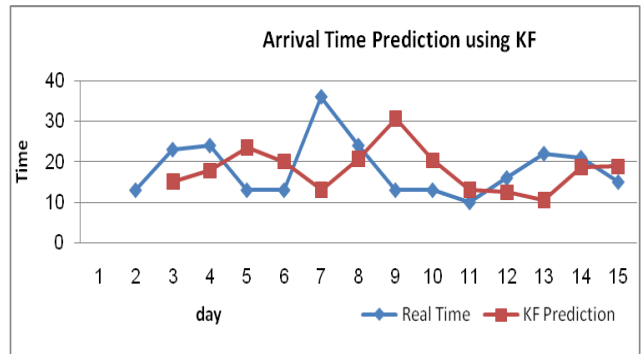


Fig. 8 Arrival Time Prediction between two stations using KF

C. Comparison Between Neural Network and Kalman Filter

The analysis of the field data has been made for 12 in-between stations distance (index). A comparison between arrival time prediction algorithms (Kalman Filter and neural network) is summarized in Table 3 and figure 9 depending on RMSE (Root Mean Square Error) value.

Table 3 and figure 9 show that, RMSE value in case of using neural network to predict bus arrival time is better than using Kalman filter in about 10 station indexes. The quality results of neural network change from 0.5 minute to 5 minutes. Kalman filter is better in only two station indexes (index number 9 and number 10). but by small value not more than 0.6 minute.

TABLE 3. Comparison Between NN and KF

Station Index	KF	NN
1	9.1	6.8
2	1.69	1.28
3	5.61	3.23
4	3.26	2.61
5	8.28	5.37
6	4.01	3.08
7	2.65	1.96
8	10.17	6.63
9	1.23	1.47
10	0.99	1.56
11	1.97	1.5
12	2.33	1.91

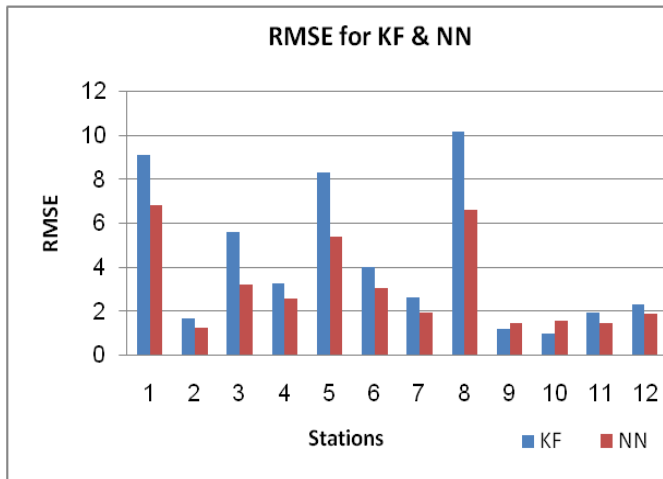


Fig. 9 : RMSE (Root Mean Square Error) for NN & KF

From the field test results using NTI fleet (low trip rate), it can be noted that calculating the arrival time using neural network algorithm gives us better results than Kalman filter algorithm in most different conditions. Nevertheless Kalman filter has show negligible improvement than neural network algorithm in two stations under test. In case of heavy daily trip rates the kalman filter algorithm shows better results.

V. CONCLUSION

In this paper, the results of field tests for Evaluating Bus Arrival Time Prediction in Egypt is proposed. Field test were performed under real traffic situations in order to test the proposed algorithms in terms of prediction of bus arrival time to stations depending on two techniques Kalman filter and Neural Network. The system was tested using NTI fleet for a field test. In the field test "at low trip rates", the arrival time calculation algorithms that were proposed in this system shows an advantage of the neutral network algorithm over kalman filter one in most cases. The kalman filter algorithm can give advantage in case of heavy daily trip rates.

ACKNOWLEDGMENT

This work concern is a part of research project called Transportation Management and User Awareness (TMUA) that research project is financially supported by the National Telecom Regulatory Authority (NTRA) of Egypt.

Research project Team are: A. Ammar, E.M. Saad, I. Ashour, M.Tantawy, M.zorkany, M.Shiple, A.Nabil, M.Sami and A.Hamdi.

REFERENCES

- [1]M. Zaki, I. Ashour, M.zorkany, B. Hesham,"Online Bus Arrival Time Prediction Using Hybrid Neural Network and Kalman filter Techniques," International Journal of Modern Engineering Research (IJMER), Vol. 3, Issue. 4, Jul - Aug. 2013 pp-2035-2041.
- [2] A. Shalaby and A. Farhan, "Bus Travel Time Prediction for Dynamic Operations Control and Passenger Information Systems", in 82nd Annual Meeting of the Transportation Research Board, National Research Council, Washington D.C., January 2003.
- [3]S.I.I. Chien, Y.Q. Ding and C.H. Wei, "Dynamic Bus Arrival Time Prediction with Artificial Neural Networks", Journal of Transportation Engineering, vol.128, no.5, pp. 429-438, 2002.
- [4]R. Jeong and L. Rilett, "The Prediction of Bus Arrival Time using AVL Data", in 83rd Annual General MeetingofTransportation Research Board, National Research Council, Washington D.C., USA, 2004.
- [5]Y. Ramakrishna, P. Ramakrishna, V. Lakshmanan and R. Sivanandan, "Bus Travel Time Prediction Using GPS Data", in Proceedings Map India, 2006,
- [6]S. Suwardo, M. Napiah, I. Kamaruddin and O. Wahyunggoro, "Bus travel time prediction in the mixed traffic by using statical neural network," in Workshop dan Simposium XII Forum Studi Transportasi antar Perguruan Tinggi (FSTP T), Universitas Kristen Petra, November 13-14, 2009.
- [7]Feng Li, Yuan Yu, HongBin Lin and WanLi Min, " Public Bus Arrival Time Prediction Based on Traffic Information Management System", IEEE International Conference on Service Operations, Logistics, and Informatics (SOLI) , Print ISBN:978-1-4577-0573-1, pp:336 - 341, 2011
- [8]R.P.S. Padmanaban1 K. Divakar1 L. Vanajakshi1 S.C. Subramanian2, "Development of a real-time bus arrival prediction system for Indian traffic conditions," Intelligent Transport Systems, IET, Vol. 4 , Issue: 3, ISSN : 1751-956X, pp: 189 - 200, 2009.
- [9] Rocco Zito, Hong-En Lin, "a review of travel-time prediction in transport and logistices," Proceedings of the Eastern Asia Society for Transportation Studies, vol. 5, 2005.
- [10] B. Karlik and A. Vehbi, "Performance analysis of various activation functions in generalized mlp architectures of neural networks," International Journal of Artificial Intelligence and Expert Systems (IJAE), vol. 1, no. 4, p. 111, 2011.
- [11] Saurabh Karsoliya," Approximating Number of Hidden layer neurons in Multiple Hidden Layer BPNN Architecture", International Journal of Engineering Trends and Technology- Volume 3, Issue6- 2012.

Considering Partially Developed Artifacts in Change Impact Analysis Implementation

Nazri Kama, Sufyan Basri, and Roslina Ibrahim

Abstract—It is important to manage the changes in the software to meet the evolving needs of the customer. Accepting too many changes causes delay in the completion and it incurs additional cost. One type of information that helps to make the decision is through change impact analysis. Current impact analysis approaches assume that all classes in the class artifact are completely developed and the class artifact is used as a source of analysis. However, these assumptions are impractical for impact analysis in the software development phase as some classes in the class artifact are still under development or partially developed that leads to inaccuracy. This paper presents a novel impact analysis approach to be used in the software development phase. The significant achievements of the approach are demonstrated through an extensive experimental validation using three case studies.

Keywords—Software development, impact analysis, traceability, static analysis.

I. INTRODUCTION

IT important to manage the changes in the software to meet the evolving needs of the customer and hence, satisfy them [1]. Accepting too many changes causes delay in the completion and it incurs additional cost. Rejecting the changes may cause dissatisfaction to the customers. Thus, it is important for the software project manager to make effective decisions when managing the changes during software development. One type of information that helps to make a decision is the prediction of the number of classes affected by the changes. This prediction can be done by performing change impact analysis [1].

Current impact analysis techniques include static analysis techniques [2]-[4] and dynamic analysis techniques [5]-[8]. These techniques are mainly developed for the software maintenance phase. The implementation of these techniques is based on the assumptions that:

- 1) All classes in the class artifacts are completely developed.
- 2) The class artifact is used as a source of analysis since it

represents the final forms of user requirements [9].

Unfortunately, these assumptions are not practical for implementing impact analysis in the software development phase since some classes in the class artifacts are still under development or partially developed [10].

The existence of partially developed classes in the class artifacts causes several problems to these static analysis and dynamic analysis techniques. The static analysis technique faces a problem related to the accuracy of program static information (i.e., class interactions) that is generated from source code through reverse engineering. The generated class interactions that involve partially developed classes may not represent the actual class interactions as some of the interactions have not been developed yet. On the other hand the dynamic analysis techniques tend to produce inaccurate method execution paths that are generated from source code through reverse engineering. This is because some method execution paths that involve partially developed classes may have not been developed yet. The inaccuracy of the generated program static information from the static analysis technique and method execution paths from the dynamic analysis technique indirectly lead to inaccuracy of impact analysis results.

We propose a new approach to perform impact analysis during software development. Our approach combines current static and dynamic analysis techniques, and supplements actual class interactions derived from source code with inferred class interactions derived from the requirements. For the static analysis technique problem, the approach develops the program static information (i.e., class interaction prediction) using a predictive technique by analysing the requirement artifacts and the design artifacts instead of reverse engineering from the source code. For the dynamic analysis technique problem, the approach introduces partially developed class analysis that is used to modify the generated method execution paths from the source code. The modification is meant to improve the accuracy of the generated method execution paths.

This paper is laid out as follows: Section 2 justifies past related works. Next, Section 3 describes the new impact analysis approach. Thereafter, Section 4 and Section 5 present evaluation strategy and results. Finally, conclusion and future work are explained Section 6 and Section 7.

II. RELATED WORK

One of the most referred definitions of impact analysis is a

The financial of this project is supported by Ministry of Higher Education Malaysia and Universiti Teknologi Malaysia under Vot No: 00K01.

N. Kama is with the Advanced Informatics School, Universiti Teknologi Malaysia, Jalan Semarak, 54100 Kuala Lumpur Malaysia (phone: 603-2180-5217; fax: 603-2180-5370; e-mail: nazrikama@ic.utm.my).

S. Basri is with the Advanced Informatics School, Universiti Teknologi Malaysia, Jalan Semarak, 54100 Kuala Lumpur Malaysia (e-mail: msufyan4@live.utm.my).

R. Ibrahim is with the Advanced Informatics School, Universiti Teknologi Malaysia, Jalan Semarak, 54100 Kuala Lumpur Malaysia (e-mail: lina@ic.utm.my).

process of identifying potential consequences of a change, or estimating what needs to be modified to accomplish a change [11]. The motivation behind the impact analysis activity is to identify software artifacts (i.e., requirement, design, class and test artifacts) that are potentially to be affected by the change. The change can be in a form of addition, removal and modification of new or existing software artifacts. With information on potentially affected software artifacts, effective planning can be made on what action will be undertaken with respect to the change.

There are two main perspectives to impact analysis which are the dependency analysis and the traceability analysis. Typically, the dependency analysis is also known as a program analysis. The program analysis focuses on identifying relationships among class artifacts or source codes by exploring the internal structure of the codes [11]. This analysis aims to determine what elements in the source codes could be potentially affected by a change. There are many types of program analysis techniques that have been introduced, such as the control dependency and the data dependency [12]. The control dependency uses a program's conditional structures for the analysis whereas the data dependency analyses the program's variable.

Comparatively to the program analysis, the traceability analysis is the analysis of relationships between software artifacts across different software phases. Since this analysis involves various software artifacts across different software phases, some researchers use this analysis to support impact analysis activity for the software development phase [13], [14]. The difference between this analysis and the program analysis is that this analysis focuses on the dependencies between software artifacts in different software phases instead of a single software artifact. There are two types of traceability analysis which are the Pre-traceability analysis and the Post-traceability analysis [15]. The pre-requirement traceability provides a mechanism to verify that all requirements have been described in a formal requirement specification document. On the other hand, the post-requirement traceability provides a mechanism to ensure all requirements in the formal requirement specification document have been implemented and how they have been implemented in the software.

Much of the work on impact analysis has been limited to source code analysis [5], [8], [11] using the dependency analysis approach. Relying on the source code analysis does not account for the overall impact to a software project [1], [16]. Software artifacts such as design and test artifacts should be kept up-to-date according to the change. This indirectly shows that these software artifacts are part of the impacted artifacts by the change. Thus, to identify thorough consequences of making a change in a software project, an effective combination between the traceability analysis and the dependency analysis is important.

III. A NEW CHANGE IMPACT ANALYSIS APPROACH

This section describes an overall structure of a new impact

analysis approach for the software development phase (will be called the Software Development Phase Change Impact Analysis (SDP-CIA)). The new approach is a direct extension of the Class Interaction Prediction with Impact Prediction Filters (CIP-IPF) technique [14]. The difference between the CIP-IPF technique [14] and this approach is the inclusion of the dynamic analysis technique in the impact analysis process implementation. In brief, there are two main stages in the approach which are:

- 1) Stage 1- Developing the program static information (i.e., class interactions prediction).
- 2) Stage 2- Performing impact analysis.

In brief, Stage 1 focuses on developing the class interactions prediction by analyzing the requirement artifacts and the design artifacts whereas Stage 2 concentrates on identifying a set of potential impacted classes using the developed class interactions prediction (Stage 1 result).

A. Stage 1: Developing Class Interactions Prediction

This approach uses a predictive technique to develop class interactions prediction model. In brief, the new predictive technique develops the class interactions prediction based on two analyses which are:

- 1) Significant object interactions analysis in the requirement artifact.
- 2) Design patterns analysis in the design artifact.

The first analysis analyses the significant object interactions in the requirement artifact to develop an initial class interactions prediction via horizontal traceability links. For the horizontal traceability links, the new predictive technique refines the selected current technique which is the Rule-based technique [17], [18].

The second analysis is the design patterns analysis. This analysis is considered as an important analysis for the new predictive technique as the current techniques [19]-[21] do not exploit the design artifacts. This analysis modifies the initial class interactions prediction produced by the first analysis according to design patterns. At this moment, this stage performs the analysis according to the Boundary-Controller-Entity (BCE) design pattern only. However, the developed steps for this analysis are flexible in that it can also be used to implement other design patterns analyses.

There are four processes in this stage which are:

- 1) Extracting software artifact elements process.
- 2) Detecting traceability link process.
- 3) Developing initial class interactions prediction process.
- 4) Modifying the initial class interactions prediction.

A brief explanation of each process is described as follows:

Extracting Software Artifact Elements Process: There are three types of software artifact involved in this process which are:

- 1) Requirement artifact.
- 2) Design artifact.
- 3) Class artifact.

However, not all elements from each software artifact are extracted. This process only extracts functional requirements and non-functional requirements from the requirement artifact, design class properties (design class name and design class attribute name) from the design artifact and actual class properties (class name and class attribute name) from the class artifact. Since, some of the elements such as design class or class are not developed yet, these elements are still extracted and they are considered as partially developed elements in the model. This process is done manually by reviewing each of the software artifacts documentation.

Detecting Traceability Links Process: There are two categories of traceability link which are:

- 1) Horizontal traceability link between requirements artifacts and design artifacts.
- 2) Vertical traceability link among requirements artifacts (or requirements interactions detection).

There are two types of links for the horizontal traceability which are from requirements in the requirement artifact to design class in the design artifact links and from design class in the design artifact to class in the class artifact links. This process only detects the horizontal traceability links from requirement to design as this process assumes that the class in the class artifact is developed according to the design class in the design artifact.

For the vertical traceability links, this process only detects the vertical traceability links among requirements in the requirement artifact (or requirement interactions) and the vertical traceability links among design classes in the design artifact (or design class interactions). This process does not specifically detect vertical traceability links among classes in the class artifact (or class interactions) as this process assumes that the design class interactions reflect the class interactions.

Developing Initial Class Interactions Prediction Process: As described earlier, this process develops initial class interactions prediction based on reflection of the significant object interactions in the requirement artifact. This process is important as this process assumes class interactions are developed based on the design class interactions, the design class interactions indirectly represent the initial class interaction prediction.

Modifying the Initial Class Interactions Prediction Process: As described earlier, this process modifies the initial class interactions prediction according to design patterns selection. However, this process only modifies the initial class interactions prediction according to the BCE design pattern.

To modify the initial class interactions prediction, there are two significant interaction rules in the BCE design pattern. The first rule is the design pattern does not allow interaction between the Boundary class and the Entity class. Any interactions between these classes are considered as invalid interactions and they need to be eliminated. The second rule is the design pattern uses the Controller class as a mediator of interactions between the Boundary class and the Entity class.

B. Stage 2: Performing Impact Analysis

This stage identifies a set of potential impacted classes using the class interactions prediction (Stage 1 result)

according to change requests. There are two main processes in this stage which are the *impact analysis process* and *filtration process*.

Impact Analysis Process: There are three steps in this process which are: Step 1: Identifying a set of impacted requirements; Step 2: Identifying a set of impacted design classes; and Step 3: Identifying an initial set of potential impacted classes. The outcome of this process is an initial set of impacted classes that will be used by the next process (the filtration process) to filter false impacted classes in the initial set of impacted classes if they exist.

Filtration Process: This process eliminates some typically false results generated by the impact analysis process. There are two filtration levels in this process which are the Class Dependency Filtration (CDF) level and the Method Dependency Filtration (MDF) level.

The CDF level implements the static analysis on the initial set of potential impacted classes produced by the impact analysis process. This implementation is important by the fact that some interaction links in the initial set of potential impacted classes have no change impact value. The interaction link that has no change impact value means that if change happens to one side of two interacting classes, the other class will not be affected. This is because the other class does not require the changed class for its implementation.

The MDF level performs another filtration on the filtered set of potential impacted classes produced by the CDF level. In brief, all method execution paths from the filtered set of potential impacted classes will be extracted and further analysed to eliminate false impacted classes. We use the backward and forward analysis technique from [5] for the elimination technique. This level can be considered as the dynamic analysis level as it uses the method execution paths to identify potential impacted classes.

Generally, most dynamic analysis techniques [6], [7], [22], [23] consist of two main steps in its implementation. These steps are extracting method execution paths from the application and analysing the generated method execution paths to identify a set of potential impacted classes (according to change request). The first step focuses on generating method execution paths from completed classes using a path generator tool. There are many existing path generator tools that can be used for the generation such as Code Surfer [24] or IBM Rational Application Developer [25]. The next step analyses the generated method execution paths to detect a set of actual impacted classes according to change requests using detection technique such as the backward or forward technique from [5], the global tracking-based algorithm and the influence graph-based algorithm from [8].

There are two main disadvantages of the current dynamic impact analysis techniques from the software development phase perspective which are:

- 1) All techniques are developed to support change impact analysis in the software maintenance phase.
- 2) All techniques do not consider or include partially developed class analysis in its implementation.

This second disadvantage occurs because of all classes in the software maintenance phase have been completely

developed or fully developed. Thus, it is not important for these techniques to have the partially developed class analysis.

From the dynamic impact analysis implementation in the software development phase, the inclusion of partially developed class analysis is an important feature. This is due to in the software development phase where situation of some classes in the class artifacts are still under construction or partially developed exist. This inclusion is required to ensure the accuracy of the extracted or generated method execution paths from class artifacts. This accuracy indirectly contributes to the accuracy of the set of potential impacted classes results.

Prior to demonstrating the importance of the inclusion of partially developed class analysis in the dynamic analysis technique, the partially developed class is defined as a class that consists of some undeveloped methods. Typically, this undeveloped method is replaced using a dummy code or a stub [26]. Fig. 1 is an example of stub.

<p>Method 1 in Class A Pseudocode: BEGIN (P1) Temperature = ThermometerRead(41) IF Temperature > 40 THEN PRINT "It's HOT!" END IF END (P1)</p>	<p>Method 2 in Class B Pseudocode: BEGIN ThermometerRead(Source insideOrOutside) // to be developed RETURN END ThermometerRead</p>
--	--

Fig. 1 Example of stub

Fig. 1 shows a Method 1 in Class A reads a temperature using a ThermometerRead function call from Method 2 in Class B. Since the Method 2 has yet to be completely developed, the ThermometerRead function is replaced using a default value (41) to represent the Method 2 functionality. In this case, the “ThermometerRead(41)” is considered as the stub. To demonstrate the importance of the inclusion of partially developed class analysis in the software development phase, the following Fig. 2 is used.

<p>M() { M1(); IF Cond1 THEN M2(); ELSE M3(); } WHILE Cond2 DO { M4(); M5(); } M6();</p>	<p>M2() { M8(); //method stub M10(); } M3() { M8();//method stub } }</p>	<p>M6() { IF Cond4 THEN M7(); ELSE M9(); } M8()*- Partially Developed { } }</p>
---	---	---

Fig. 2 Example of several methods’ algorithms

Assuming that M8 is partially developed, M2 and M3 consist of M8 stubs. This stub will not call actual M8 method (see asterisk (*) symbol represents the actual M8 implementation). Based on the path generator tool (IBM Rational Application Developer tool [25]), among the extracted method execution paths are: (1) Path 1: M, M1, M2, M10, M4, M5, M6, M7 and; (2) Path 2: M, M1, M3, M4, M5, M6, M7. However based on the actual method execution paths, the actual path (based on Path 1 and Path 2) are:
 1) Path 1: M, M1, M2, M8, M10, M4, M5, M6, M7.
 2) Path 2: M, M1, M3, M8, M4, M5, M6, M7.

The difference between the generated method execution paths using automated tool and the actual method execution paths can be seen after M2 execution. The path generator tool does not consider M8 after M2 in the generated paths as the statement to call M8 is replaced by a stub. Therefore, by looking at this example, there are two important aspects can be seen. First, the stub has caused the method execution paths generated are not reflected to the actual method execution paths. Second, the partially developed class analysis/stub analysis consideration is important to produce an accurate potential set of method execution paths.

IV. EVALUATION

This section describes the evaluation strategy that is established to measure the effectiveness of the new proposed approach (will be called the “SDP-CIA” Software Development Phase Change Impact Analysis). Basically the measurement will answer a question of “Does the SDP-CIA give better accuracy of impact analysis results than the selected current impact analysis approaches?” The selected current impact analysis approaches are:

- 1) The Class Interactions Prediction with Impact Prediction Filters (CIP-IPF) approach [27], [28].
- 2) Path Impact approach [5].

Five evaluation strategies are considered:

- 1) Subject and case study.
- 2) Evaluation metrics.
- 3) Evaluation design.
- 4) Hypothesis.
- 5) Data analysis procedure.

A. Subject and Case Study

The subjects of the experiment were three groups of final year post-graduate students of software engineering course at Advanced Informatics School, Universiti Teknologi Malaysia (UTM). During their professional attachment session in the industry, we were involved as one of the software developers in these projects. We developed some of the modules which were then used as the case study.

For the purpose of performing the impact analysis evaluation, the author issues a set of change requests to the developed modules and the impact analysis results according to the issued change requests are then identified. This experiment requires the subjects to use or implement three different impact analysis approaches which are the CIP-IPF approach [27], [28], the Path-Impact approach [5] and the SDP-CIA. The subjects were given a preliminary guideline and briefing on these techniques prior to the experiment. The guideline includes thorough technique explanations and example of its implementation.

B. Evaluation Metrics

This study employed evaluation metrics as described in [29], [30]. The reason why we choose these metrics is that these metrics have been used by several researchers [1], [5], [10] to measure the effectiveness of impact analysis prediction.

Briefly, each impacted class predictions were categorized according to four numbers:

- 1) Not Predicting and Not Changing (NP-NC): number of pairs of classes correctly predicted to not be changing
- 2) Predicting and Not Changing (P-NC): number of pairs incorrectly predicted to be changing.
- 3) Not Predicting and Changing (NP-C): number of classes incorrectly predicted to not be changing.
- 4) Predicting and Changing (P-C): number of classes correctly predicted to be changing.

These numbers are then used to calculate:

- 1) Completeness value: The ratio of the actual class interactions or impacted classes that were predicted.
- 2) Correctness value: The ratio of the predicted class interactions that were actually interacting or impacted classes that were actually impacted.
- 3) Kappa value: This value reflects the accuracy or the prediction (0 is no better than random chance, 0.4-0.6 is moderate agreement, 0.6-0.8 is substantial agreement, and 0.8-1 is almost perfect agreement [31], [32].

C. Hypothesis

A hypothesis that investigates the effectiveness of the new approach (to recap, we call it SDP-CIA) is developed. The SDP-CIA represents a combination of the static and dynamic analysis approaches whereby the selected current impact analysis approaches represent the independent technique (CIP-IPF- static analysis approach only; Path Impact- dynamic analysis approach only). If the combination is not effective, H_0 is accepted. Otherwise, H_0 is rejected. The hypothesis is:

- 1) H_0 : The SDP-CIAF does not give higher accuracy of impact analysis results than the selected current techniques results
- 2) H_a : The SDP-CIAF gives higher accuracy of impact analysis results than the selected current techniques results

D. Data Analysis

Data were collected on three cycles in the experiment. The first cycle, fifteen change requests were issued to all software projects. Each change request was analysed to identify potential impacted classes using the CIP-IPF approach and actual impacted classes. Also in the subsequent cycles for the Path Impact and SDP-CIA approaches, there were fifteen change requests issued and each change request was analysed to identify potential impacted classes and actual impacted classes.

To evaluate this hypothesis, two tables of data were created. The first table shows results between the change request id (independent data) and the pattern of prediction (combination of the Completeness and the Correctness results) produced by all approaches (dependent data). The second table shows results between the Change Request ID (independent data) and the Kappa Value (dependent data) produced by all approaches. An Independent T-Test statistical analysis technique was used to determine whether there is a statistically significant difference between the means of two unrelated

group of data (independent and dependent data) or not in both tables. The null hypothesis for the Independent T-Test was that the population means from the two independent and dependent data in each table are equal, $H_0: d1 = d2$. The alternative hypothesis for the Independent T-Test was that the population means from the two independent and dependent data in each table are not equal, $H_0: d1 \neq d2$. To do this, a significance level (alpha) that is used to either reject or accept the hypotheses is set to 0.05. To identify whether the SDP-CIA results improves the selected current impact analysis approaches (CIP-IPF approach, the Path Impact approach or not, a comparison of mean values produced by the SDP-CIA to the CIP-IPF and Path Impact approaches were then conducted.

V. EVALUATION RESULT

Table I shows impact analysis results produced by all impact analysis approaches (the CIP-IPF, the Path Impact technique and the SDP-CIA).

TABLE I.
IMPACT ANALYSIS RESULTS

CRID	CIP-IPF			Path Impact			SDP-CIA		
	Com r (%)	Cor r (%)	Kappa Value	Com r (%)	Cor r (%)	Kappa Value	Com r (%)	Cor r (%)	Kappa Value
CR1	80	100	0.785	66.7	100	0.652	86.7	100	0.876
CR2	81.3	100	0.821	78.6	100	0.789	92.9	100	0.935
CR3	76.9	100	0.768	80	92.3	0.752	100	93.8	0.944
CR4	83	94	0.795	88.7	94.1	0.85	94.4	94.4	0.903
CR5	83	91	0.767	91.7	91.7	0.852	91.7	91.7	0.852
CR6	82.4	100	0.832	76.5	92.9	0.721	94.1	94.1	0.842
CR7	81.8	90	0.734	80	94.1	0.764	95	95	0.912
CR8	80	100	0.806	78.6	100	0.787	92.9	100	0.935
CR9	75	100	0.752	87.5	100	0.884	87.5	100	0.884
CR10	76	100	0.77	88.2	100	0.892	94.1	100	0.947
CR11	85.7	100	0.863	73.7	93.3	0.695	94.7	94.7	0.908
CR12	80	100	0.773	68.8	100	0.676	87.5	100	0.884
CR13	90.9	90.9	0.83	76.5	100	0.769	94.1	100	0.947
CR14	83	100	0.843	77.8	100	0.784	94.4	100	0.95
CR15	80	92	0.749	80	100	0.804	86.7	100	0.874

To validate the hypothesis, the Independent T-Test statistical analysis is used. Two stages of analysis are created. The first stage compares Means results between the CIP-IPF approach and the SDP-CIA approach whereas the second stage compares Means results between the Path Impact technique and the SDP-CIA approach.

A. Stage 1 Analysis: The CIP-IPF Technique vs. The SDP-CIA

Table II shows the Independent T-Test results.

TABLE II.
INDEPENDENT T-TEST RESULTS BETWEEN THE CIP-IPF AND THE SDP-CIA

The Technique	Means Results
CIP-IPF Technique	0.7927
SDP-CIA	0.9060

The null hypothesis for the Independent T-Test was that the Kappa mean value from both approaches are equal, $H_0: \mu_1 = \mu_2$. The null hypothesis is accepted if the Sig. (2-tailed) value is greater than 0.05. The alternative hypothesis was used to reject the null hypothesis if the Kappa means values from both approaches are not equal, $H_0: \mu_1 \neq \mu_2$. The alternative hypothesis is accepted if the Sig. (2-tailed) value is less than 0.05.

To answer the question of “Does the SDP-CIAF give better accuracy of impact analysis results than the selected current impact analysis techniques (CIP-IPF technique)?”, the Mean results from both approaches at the Group Statistics box is reviewed. The results show the SDP-CIA value is 0.9060 and the CIP-IPF approach value is 0.7927. This shows that the SDP-CIA value is higher than the CIP-IPF approach. Thus, the values reject the null hypothesis (H_0 : The SDP-CIA does not improve on the CIP-IPF approach results) and accept the alternate hypothesis (H_a : The SDP-CIA approach gives higher accuracy of impact analysis results than the CIP-IPF approach).

B. Stage 2 Analysis: The Path Impact Technique vs. The SDP-CIAF

Table III shows the Independent T-Test results. Similarly to the Independent T-Test between the CIP-IPF approach and the SDP-CIA approach, the null hypothesis for the Independent T-Test was that the Kappa mean value from both approaches are equal, $H_0: \mu_1 = \mu_2$. The null hypothesis is accepted if the Significance (2-tailed) value is greater than 0.05. The alternative hypothesis was used to reject the null hypothesis if the Kappa means values from both approaches are not equal, $H_0: \mu_1 \neq \mu_2$. The alternative hypothesis is accepted if the Sig. (2-tailed) value or the rho value is less than 0.05. Thus, the SDP-CIA approach gives higher accuracy of impact analysis results than the selected current impact analysis approach (in particular to the Path Impact technique).

TABLE III.
INDEPENDENT T-TEST RESULTS BETWEEN THE PATH IMPACT AND THE SDP-CIA

The Technique	Means Results
Path Impact	0.7773
SDP-CIA	0.9060

To answer the question of “Does the SDP-CIA give better accuracy of impact analysis results than the selected current impact analysis techniques? (Path Impact technique)?”, the Mean values from both approaches at the Group Statistics box

is reviewed. The results show the SDP-CIA approach value is 0.9060 and the Path Impact approach value is 0.7773. This shows that the CIP-IPF approach value is higher than the Path Impact approach. Thus, the values reject the null hypothesis (H_0 : The SDP-CIA does not give higher accuracy of impact analysis results than the Path Impact approach) and accept the alternate hypothesis (H_a : The SDP-CIA approach gives higher accuracy of impact analysis results than the Path Impact approach).

VI. CONCLUSION

This paper contributes a new approach that can be used for performing impact analysis during software development through partially developed artifacts consideration in its analysis. This approach combines current static and dynamic analysis techniques, and supplements actual class interactions derived from source code with inferred class interactions derived from the requirements.

We note that the above contributions are subject to the following limitations:

- 1) This experiment measures the number of potential impacted classes according to change requests produced by the new approach compared to the selected current impact analysis approaches. The measurement does not consider performance issues such as impact calculation duration/times required to identify a set of potential impacted classes for a particular change request.
- 2) The new predictive technique includes the Boundary-Controller-Entity (BCE) design pattern only in its prediction. Extension to others design patterns in the prediction process will benefit further as most applications employ more than one design patterns.
- 3) The new approach’s implementation involves both manual and automated steps. For the automated steps, the approach uses the IBM Rational Application Developer tool [25] to support Stage 2 implementation in particular to generate method execution paths step. This combination of implementations could decrease the effectiveness of the implementation compared to a single tool that performs all steps.

As large systems are very complex, the usefulness of the new approach is only tested and applicable to a small size of software system. Large systems may involve some integrated applications of different platforms and environments.

ACKNOWLEDGMENT

The authors would like to thank the Lab of Advanced Informatics School for their offered helps, and all the members of the Lab for their useful discussions that guided us through this research. Also, to all academic staff and students of Advanced Informatics School who have been participating directly and indirectly in this study.

REFERENCES

- [1] S.A. Bohner, R. Arnold, “Software Change Impact Analysis”, Wiley-IEEE Computer Society Press

- [2] J. Hassine, J. Rilling, J. Hewitt, R. Dassouli, "Change Impact Analysis for Requirement Evolution using Use Case Maps", In Proc. of the 8th International Workshop on Principles of Software Evolution, pp. 81 - 90 http://ieeexplore.ieee.org/xpls/abs_all.jsp?arnumber=1572312
- [3] M. Shiri, J. Hassine, J. Rilling, "Feature Interaction Analysis A Maintenance Perspective", In Proc. of the 22nd IEEE/ACM International Conference on Automated Software Engineering, November 2007, 437-440
- [4] Y. Li, J. Li, Y. Yang, L. Mingshu, "Requirement-centric Traceability for Change Impact Analysis: A Case Study, In Making Globally Distributed Software Development a Success Story", 5007/2008, 100-111 http://link.springer.com/chapter/10.1007%2F978-3-540-79588-9_10
- [5] J. Law, G. Rothermal, "Whole Program Path-Based Dynamic Impact Analysis", In Proc. of the 25th International Conference on Software Engineering (ICSE 2003), May 2003, 308-318 <http://citeseerx.ist.psu.edu/viewdoc/summary?doi=10.1.1.132.5086>
- [6] T. Apiwattanapong, A. Orso, M. J. Harrold, "Efficient and Precise Dynamic Impact Analysis using Execute-after Sequences", In Proc. of the 27th Int. Conf. on Software Engineering, May 2005, 432-441 <http://dl.acm.org/citation.cfm?id=1062534>
- [7] A. Orso, T. Apiwattanapong, M. J. Harrold, "Leveraging Field Data for Impact Analysis and Regression Testing", In Proc. of the ACM SIGSOFT Symposium on Foundations of Software Engineering, September 2003, 128-137 <http://dl.acm.org/citation.cfm?id=940089>
- [8] B. Breech, M. Tegtmeier, L. Pollock, "Integrating Influence Mechanisms into Impact Analysis for Increased Precision", In Proc. of the 22nd International Conference on Software Maintenance, September 2006, 55-65 http://ieeexplore.ieee.org/xpls/abs_all.jsp?arnumber=4021320&tag=1
- [9] K. H. Bennet, V. T. Rajlich, "Software Maintenance and Evolution: A Roadmap", In Proc. of the Int. Conf. on the Future of Software Engineering, June 2000, 75-87 <http://dl.acm.org/citation.cfm?id=336534>
- [10] B. Nuseibeh, S. Esterbrook, "Requirement Engineering: A Roadmap", In Proc. of the Conference on the Future of Software Engineering (ICSE), June 2000, 35-46 <http://dl.acm.org/citation.cfm?id=336523>
- [11] R. S. Arnold, S. A. Bohner, "Impact Analysis - Towards a framework for Comparison", In Proc. of the Int. Conf. on Software Maintenance, September 1993, 292-301 http://ieeexplore.ieee.org/xpls/abs_all.jsp?arnumber=366933&tag=1
- [12] S. Horwitz, T. Reps, D. Binkley, "Interprocedural Slicing Using Dependence Graphs", ACM Transactions on Programming Languages and Systems, 12, 1, July, 1998, 26-60 <http://dl.acm.org/citation.cfm?id=53994>
- [13] J. S. O'Neil, D. L. Carver, "Analyzing the Impact of Changing Requirements", In Proc. of the IEEE International Conference on Software Maintenance, November 2001, 190-195 http://ieeexplore.ieee.org/xpls/abs_all.jsp?arnumber=972729&tag=1
- [14] N. Kama, T. French, M. Reynolds, "Impact Analysis using Class Interactions Prediction Approach", In Proc. of the 9th International Conference on New Software Methodologies, Tools and Techniques, October 2010, pp. 96-111 <http://dl.acm.org/citation.cfm?id=1860884>
- [15] O. Gotel, "Contribution Structures for Requirements Traceability", PhD. Imperial College of Science, Technology and Medicine, Department of Computing, University of London. August 1995
- [16] S. L. Pfleeger, S. A. Bohner, "A Framework for Software Maintenance Metrics", In Proc. of the Int. Conference on Software Maintenance, November 1990, 320-327 http://ieeexplore.ieee.org/xpls/abs_all.jsp?arnumber=131381
- [17] G. Spanoudakis, "Plausible and Adaptive Requirements Traceability Structures", In Proc. of the 14th International Conference on Software Engineering and Knowledge Engineering, July 2002, 135-142 <http://dl.acm.org/citation.cfm?id=568786>
- [18] G. Spanoudakis, A. Zisman, E. P. Minana, P. Krause, "Rule-based Generation of Requirements Traceability Relations", Journal of Systems and Software, 72, 2, July 2004, 105-127 <http://www.sciencedirect.com/science/article/pii/S0164121203002425>
- [19] R. C. Sharble, S. S. Cohen, "The Object-oriented Brewery: A Comparison of Two Object-oriented Development Methods", ACM Software Engineering Notes, 18, 2, April 1993, 60-73 <http://dl.acm.org/citation.cfm?id=155839>
- [20] A. Bahrami, "Object Oriented Systems Development", McGraw-Hill
- [21] Y. Liang, "From Use Cases to Classes: A Way of Building Object Model with UML", Journal of Information and Software Technology, 45, 2, February 2003, 83-93, <http://www.sciencedirect.com/science/article/pii/S0950584902001647>
- [22] L. Huang, Y. T. Seong, "Dynamic Impact Analysis using Execution Profile Tracing", In Proc. of the 4th International Conference on Software Engineering Research, Management and Applications, August 2000 237-244 http://ieeexplore.ieee.org/xpls/abs_all.jsp?arnumber=1691386
- [23] L. Huang, Y. T. Seong, "Precise Dynamic Impact Analysis with Dependency Analysis for Object-oriented Programs", In Proc. of the 5th ACIS International Conference on Software Engineering Research, Management & Applications, August 2007, 374-384 http://ieeexplore.ieee.org/xpls/abs_all.jsp?arnumber=4296961
- [24] R. C. Metzger, "Debugging by Thinking: A Multidisciplinary Approach", Elsevier Digital Press
- [25] J. Fung, C. Lau, E. Mckay, V. Birsan, C. Yu, J. Winchester, G. Mendel, G. Flood, "An Introduction to IBM Rational Application Developer: A Guided Tour (IBM Illustrated Guide Series)", Mc Press.
- [26] E. Dustin, "Effective Software Testing: 50 Specific Ways to Improve Your Testing", Addison-Wesley
- [27] N. Kama, T. French, M. Reynolds, "Considering Patterns in Class Interactions Prediction", In Advances in Software Engineering, Springer Berlin Heidelberg, 117, 11-22 http://link.springer.com/chapter/10.1007%2F978-3-642-17578-7_2
- [28] N. Kama, F. Azli, "A Change Impact Analysis for the Software Development Phase", in Proc. of the 19th Asia-Pacific Software Engineering Conference (APSEC 2012), December 2012, 583-592 http://ieeexplore.ieee.org/xpls/abs_all.jsp?arnumber=6462714
- [29] A. Finkelstein, J. Kramer, "Software Engineering: A Roadmap, in Proc of the Conference on the Future of Software Engineering", October 2000, 3-22 <http://dl.acm.org/citation.cfm?id=336519>
- [30] N. Kama, T. French, M. Reynolds, "Predicting Class Interactions from Requirement Interactions: Evaluating a New Filtration Approach", In Proc. of the IASTED International Conference on Software Engineering, February 2010, 109-116 <http://www.actapress.com/Abstract.aspx?paperId=37955>
- [31] J. Cohen, "A Coefficient of Agreement for Nominal Scales", Journal of Educational and Psychological Measurement, 20, 1, 37-46, April 1960 <http://www.garfield.library.upenn.edu/classics1986/A1986AXF2600001.pdf>
- [32] J. R. Landis, G. G. Koch, "The Measurement of Observer Agreement for Categorical Data", Journal of Biometrics, 33, 1, March 1977, 159-174 <http://www.jstor.org/stable/2529310>

Nazri Kama obtained his first degree at Universiti Teknologi Malaysia (UTM) in Management Information System in 2000, second degree in Real Time Software Engineering at the same university in 2002 and his PhD at The University of Western Australia (UWA) in Software Engineering in 2010. He has a considerable experience in a wide range on software engineering area. His major involvement is in software development.

Modeling and Performance Analysis of PCI Express

Miguel Angel Orozco, Mario Siller and Adán Ruiz

Abstract—Current computing systems require high performance networks for communication such as System-to-System, Board-to-Board or Chip-to-Chip. PCI Express is one of the most popular and successful protocols for high-performance I/O communications. This can be explained by its low power consumption, scalability in I/O signaling interconnection and bandwidth. We use teletraffic theory to address the modeling and analysis performance of PCI-E. The objective of this work is to provide an analytical framework for the design and performance evaluation of PCI-E based systems. Therefore we proposed a model based on an ergodic, non-periodic, regular and non-absorbent Markov chain. The model states represent each of the required phases when performing a write request transaction layer packet without completion. The receiver buffer is modeled using an M/M/1/B queuing system. The model takes into account network parameters such as maximum payload size, receiver buffer size, transmission capacity and bit error rate. We focus on performance metrics such as throughput and delay. The model was validated through NS3 Simulation and results of hardware tests.

Keywords— Queue systems, throughput, delay, estimation, network, Markov chain.

I. INTRODUCTION

A common problem found in current systems is the transmission capacity between end points. This occurs especially in high performance computing architectures. Therefore high performance IO technologies are required and have been a matter of research in recent years. Some of these technologies include PCI (Peripheral Component Interconnect), PCI-X, PCI Express, HyperTransport, RapidIO Parallel, Serial RapidIO, Ethernet, InfiniBand, Fibre Channel, etc. Applications of such technologies include Chip-to-Chip, Board-to-Board or System-to-System communications. PCI Express is an IO protocol, which is widely used for Board-to-Board communications, such as Ethernet cards, graphic cards, FPGAs, etc. PCI Express protocol is compatible with old PCI and PCI-X architectures. Some of the main attributes of the PCI Express protocol are bandwidth scalability (see Table 1),

and switching and bridging capacity.

PCI Express Link Width	X1	X2	X4	X8	X12	X16	X32
Aggregate Bandwidth (GBytes/seconds)	0.5	1	2	4	6	8	16

Table 1. PCI Express Bandwidth takes in consideration both directions and 8B/10B encoding.

The analysis of the protocol PCI Express can be performed in different ways. Y. Uchiyama [6] performed measurements of throughput from different memory read requests to the CPU or the memory using a test card (FPGA). The performed measurements showed a throughput capacity of 1.5Gbps. In the work [7] they used a Development Kit for PCI Express (FPGA) to analyze throughput for reading and writing requests from two different chipsets under the same conditions. They obtained faster results than theoretical results because their results were based in burst traffic.

In the works [1] and [2], they made measurements of throughput and efficiency, using a PCI Express link. They took into account the delays caused by the protocol Ack / Nak, Credit-Based Flow Control. They found that those messages affected the performance on PCI Express links. P. Böhm in [11] and [12] presented the higher order logic model and a verification methodology for PCI Express protocol transaction layer and data link layers. Their verifications focus on correctness and liveness. They verify their model using the Isabell/HOL theorem prover.

In the particular case of PCI Express[®] protocol has the problem of lack of work on performance analysis non-empirical, in other words, the performance analysis of the protocol was not carried out through a teletraffic model. Tasks for creating a model of teletraffic are identified functions, which significantly affect the performance of the protocol, the characterization for these functions and finally they are created modeling them according to teletraffic theories such as queuing theory.

A protocol teletraffic model PCI Express[®] offers researchers a way to get performance estimates such as "throughput" or latency under certain conditions, parameters and assumptions. It can be analyzed through teletraffic

This work was supported by CONACYT.

M. A. Orozco is with the Electrical Engineering and Computer Science Cinvestav Unidad Guadalajara, Zapopan, Jalisco, Mexico, Av. Del Bosque 1145, Col El Bajío (e-mail: morozco@gdl.cinvestav.mx).

M. Siller is with the Electrical Engineering and Computer Science Cinvestav Unidad Guadalajara, Zapopan, Jalisco, Mexico, Av. Del Bosque 1145, Col El Bajío (e-mail: msiller@gdl.cinvestav.mx).

A. Ruiz is with the Electrical Engineering and Computer Science Cinvestav Unidad Guadalajara, Zapopan, Jalisco, Mexico, Av. Del Bosque 1145, Col El Bajío (e-mail: aruiz@gdl.cinvestav.mx).

modeling, to have a better understanding of the protocol behavior, facilitate estimation of network performance and obtain the parameters, which can get higher performance results. That approach might facilitate the design and creation of new PCI Express[®] devices or upgrade existing devices with better performance.

This paper proposes a model based on an ergodic, non-periodic, regular and non-absorbent Markov chain for a written request transaction layer packet without completion. The receiver buffer is modeled using an M/M/1/B queuing system.

We present the mathematical framework and a brief summary of different concepts about PCI Express in section II. Then we present the modeling of PCI Express protocol and our assumptions in section III, followed by Section IV, where we present the validation of the model. We then conclude in section V.

II. MATHEMATICAL FRAMEWORK

A. Performance Metrics

The PCI Express network performance can be affected by the Credit-Based Flow Control, ACK/NAK Protocol, forwarding packets, packet size, and other mechanisms [1][2][6][7]. Some of the affected metrics include:

- Efficiency.
- Throughput.
- Delay.

Efficiency is defined as the relation between the payload and packet size as shown in (1).

$$\text{Efficiency} = \text{Payload} / (\text{Payload} + \text{Header}) \quad (1)$$

Throughput is defined as the period of time the channel is used to successfully transmit payload bits as shown in (2) as shows in the Figure 1.

$$\text{Throughput} = \text{TotalPayloadInfo} / \tau \quad (2)$$

Where:

TotalPayloadInfo = Total amount of sent payload bytes.

τ = Total time of transmissions (Packet + Ack packet + Flow Control Packet).

The total time of transmissions in this work is handled as Delay. In this model we take into account the time delays caused by packet losses due to transmission errors.as Yoo et al. [15] calculated the Delay. Also the time taken by flow control packets (FCP) and acknowledgement packets (ACK/NAK).

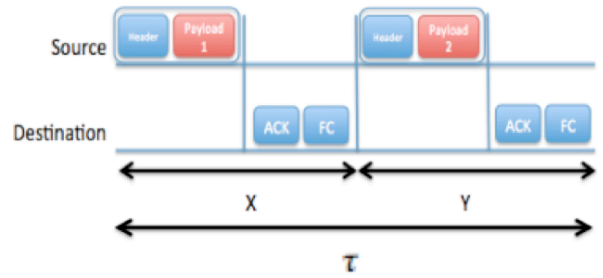


Fig. 1 This figure shows a source node sending a TLP Write Request to a Destination node and the consequent an ACK and Flow Control Packet (FCP or FC).

B. Credit-Based Flow Control.

The credit-based flow control is a technique used in Interconnection Networks Theory, which works like buffer management as described in [3][5][8] is a technique, which maintains the count of the receiver's buffer space. This prevents buffer overflow in the receiver and for that reason we avoid the packet loss.

C. Protocol ACK/NAK

The ACK / NAK protocol is a primary function within the link layer, this protocol is responsible for the verification and monitoring of TLPs packets sent from the sender to the receiver, controlling the flow of packets as shown in [3] [5] [8]. The ACK/NAK protocol is a protocol with stop and wait ARQ (Stop and Wait), assuming that PCI Express devices are set to ACK factor equal to 1.

The modeling presented in [4] on Stop and Wait ARQ protocol shows that efficiency of the protocol depends only on the size of the packet to send and the bit error rate (BER).

III. MODELING PCI EXPRESS PROTOCOL

Our model was developed using Markov chains and queuing systems. We perform an abstraction of the PCI Express protocol functions that affects performance according to [1][2][6][7], such as:

- Based Flow Control Credits.
- Protocol ACK / NAK (Acknowledgment).
- Receiver Buffer Size.
- Number of Lanes.
- Maximum Payload Size (MPS).
- Bit Error Rate (BER).

Our proposed model is based on an ergodic, no-periodic, regular and non-absorbent Markov chain. Which has several phases; each of the phases represents a system state when performing a write request TLP. Our Markov chain is the abstraction of a write request without completion. It's based on the specification [5] of PCI Express.

The Markov chain has different phases of a transmission. The probabilities to go from any state to another are discussed below.

For modeling the following assumptions were considered:

- The network is in a saturated state, in other words the device always has a packet to send
- Each TLP received, the receiver sends a Control Flow Packet and ACK / NAK Packet
- All packages DLLP (FC_Update, ACK, NAK) sent no transmission error

A. Description of the phases and probabilities

1) Idle Phase

This phase is represented by a state called “Idle” in Figure 2 and means the start of a new transmission. From this phase two possible phases may proceed. Either the “Full Phase” or the “Transmission Phase” with the probabilities “a” and “b” respectively in (3) and (4).

$$a = \frac{(1 - \rho) * \rho^B}{1 - \rho^{B+1}} * \lambda \quad (3)$$

$$b = 1 - a \quad (4)$$

Where:

$\rho = \lambda / \mu$ (Distribution Index).

λ = Arrival rate.

μ = Service rate.

B = Receiver buffer size.

2) Full Phase

This phase represents that the receiver’s buffer is completely full or the transmitter has no credits to transmit a new packet (This phase is represented by a state called “Full” in Figure 2). In order to do this we proposed a queue system M/M/1/B to represent the receiver buffer, because we consider FPGA devices provide traffic that could be modeling as Markov process as [14]. Besides the work [13] talks about PCI Express delay and they use a queue system to represent the buffer of PCI Express ports. We suppose that the traffic patterns generated by some PCI Express devices follow Poisson arrival times as them [13][14].

Equation 3 shows the probability of loss on an “M/M/1/B queuing system”, which means that the receiver does not have enough space to receive a new package and the package will be rejected by over flow. Therefore we consider this situation as a lack of credits required for packet transmission and the transmitting node must wait for them.

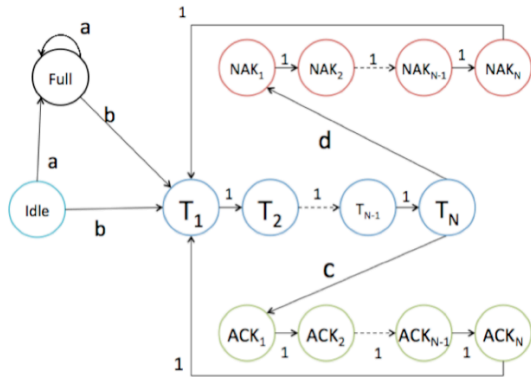


Fig. 2 State diagram by Markov chain of PCI Express.

3) Transmission Phase

This phase is represented by a set of N states called T [1], T [2], ..., T [N-1], T [N] in Figure 2. This phase corresponds to a packet transmission wing, each state corresponds to a time step required to transmit the entire package. N represents the total number of time steps required to transmit the entire package, see in (5), (Each time step is equal to 4ns). The transition probabilities between them are equal to 1. Except for the last state of this phase T[N]. Because this state can go either to “Successful Transmission Phase” with the probability of “c” or “Failed Transmission Phase” with the probability of “d” (show in (7) and (6)) according to [9].

$$N = TLPSize / Lanes \quad (5)$$

$$d = 1 - (1 - BER)^{NumBits} \quad (6)$$

$$c = 1 - d \quad (7)$$

Where:

N = Number of states of the Transmission phase.

$TLPSize$ = The number of bytes of the TLP.

$Lanes$ = Number of lanes of the device.

$NumBits$ = Number of bits of the TLP.

BER = Bit Error Rate.

4) Successful Transmission Phase

This phase represents a successful transmission of a TLP. The receiver starts to send an ACK packet. This phase is a set of M states of the Markov chain named {ACK[1],ACK[2],... ,ACK[M-1],ACK[M]} in Figure 2. Where M represents the number of time steps taken to send the ACK packet. We set M=19 according to [3]. The transition probabilities between them are equal to 1. The last state, ACK[M], has a probability transition to the “Idle Phase” equal to 1.

5) Failed Transmission Phase

This phase represents a failed transmission of a TLP. Then the receiver starts to send a NAK packet to request the re-send. This phase is a set of M states of the Markov chain named {NAK[1],NAK[2],... ,NAK[M-1],NAK[M]} in Figure 2. Where M represents the number of time steps taken to send the NAK packet. We set M=19 according to [3]. The transition probabilities between them are equal to 1. The last state, NAK[M], has a probability transition to the “Transmission Phase” equal to 1.

B. Measurements

The Steady-State Vector Distribution of our Markov chain is

$$\pi(Idle) + \pi(Full) + \sum_{n=1}^N \pi(T[n]) + \sum_{m=1}^M \pi(ACK[m]) + \sum_{m=1}^M \pi(NAK[m]) = 1 \quad (8)$$

Where:

$\pi(\mathbf{X})$ is the probability of finding our system in state “X” where X is a state of the Markov chain.

The time spent in a successful transmission (TransSuccess) will be based in (9), the time of a Failed Transmission (TransFailed) is formulated in (10), and the total time of a transmission (TransDelay) is formulated in equation 11.

$$TransSuccess = \left(\sum_{n=1}^N \pi(T[n]) + \sum_{m=1}^M \pi(ACK[m]) \right) + (N + M) \quad (9)$$

$$TransFailed = \left(\sum_{m=1}^M \pi(NAK[m]) \right) * (2N + 2M) \quad (10)$$

$$TransDelay = ((\pi(Idle) * X) + (\pi(Full) * Y) + TransSuccess + TransFailed) * Timestep \quad (11)$$

We calculate the throughput model according to (12)

$$Throughput = \frac{TotalPayloadInfo}{NumPacks * TransDelay} \quad (12)$$

Where:

TimeStep = 4ns according to [3].

X = the amount of symbols time taken to start a transmission.

Y = the amount of symbols time taken by PCI Express device to attend some TLP.

NumPacks = TotalPayloadInfo / MPS

IV. VERIFICATION OF THE MODEL AND EXPERIMENTAL RESULTS

This section shows the experiments performed in order to validate the model. These experiments consist in the comparison of the results of the proposed model against theoretical metric results obtained from a simulated scenario [10] and testing using an FPGA and chipsets [7].

The experiments were developed in the same scenario, which consists of a source node "endpoint A" and a destination node "endpoint B", connected through a PCI Express switch, as shown in Figure 3.

The following parameters were used for the development of the experiments:

- Number of lines
- Maximum Payload Size (MPS)
- Receiver Buffer Size
- Amount of information transmitted

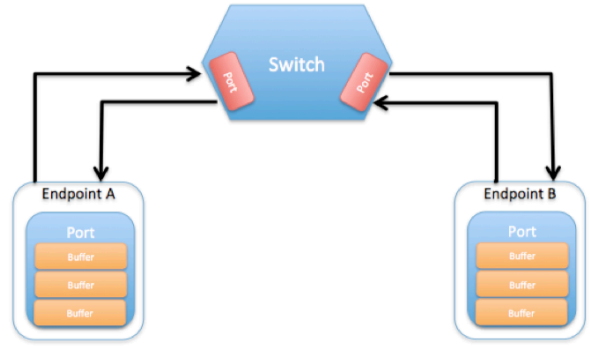


Figure 3. Shows the scenario’s topology, which we used to develop our experiments.

A. First Experiment

In our first experiment 81920 bytes were transmitted using the following parameters:

- Number of lines equal to 1 (x1).
- MPS increased from 64 bytes to 4096 bytes in increments of 128 bytes.
- BER equal to 10-12 according to [3] and [5].
- Receiver Buffer size equal to 4096 bytes.

The results obtained in this experiment are shown in Figure 4, where there are two different measures of delay. The blue line shows the delays derived from the proposed model and the green line shows the theoretical delays, which are obtained from transmission time without taking into account the delays caused by the flow control and possible errors in the transmitted TLPs [7].

Throughput measurements shown in Figure 5 were obtained from previously computed delays. The analysis of this data shows that model results are similar to theoretical results while the payload size increases. This is because when increasing the size of the payload, the number of packets required to transmit information becomes smaller and therefore the aggregate time for flow control and retransmission delays are less. Although the probability of having an error in a packet increases (according to Equation 8).

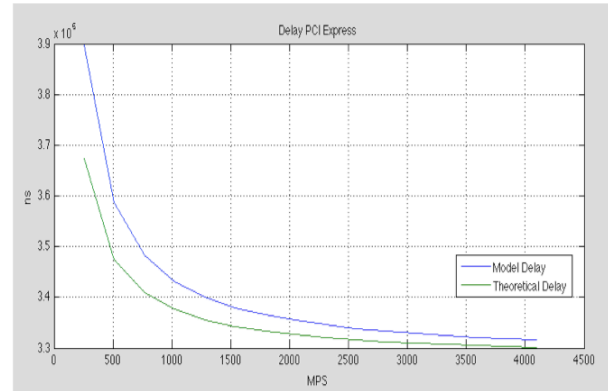


Figure 4. Shows the model’s delay and the theoretical delay in the first experiment.

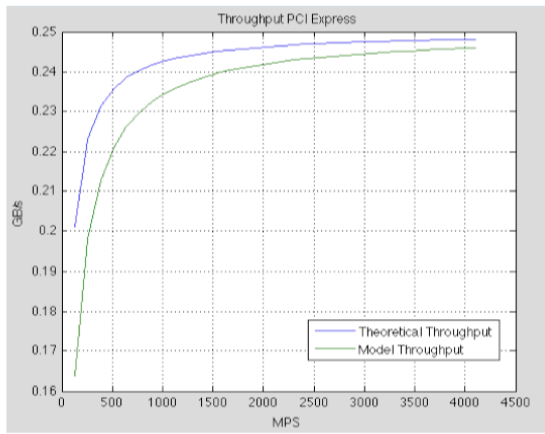


Figure 5. Shows the throughput calculated from our model and theoretically.

B. Second Experiment

In the second experiment 81920 bytes were transmitted using the following parameters:

- Number of lines x1, x2, x4, x8, x16, x32.
- MPS increased from 64 bytes to 2048 bytes in increments of 64 bytes.
- Receiver buffer size equal to 4096 bytes.
- BER equal to 10⁻¹² according to [3] and [5].

This experiment is the same as above with the difference that the execution has different runs. Each run difference is shown in the number of line, and the results obtained are shown in Figure 6. With the results obtained we can appreciate the great impact of the number of lines in the time required to transmit.

C. Third Experiment

In the third experiment a comparison of throughput measurements obtained from our model was performed against measurements from the PCI Express protocol simulator [10]. In this experiment 81920 bytes were transmitted using the following parameters:

- Number of lines equal to 1.
- Receiver buffer size equal to 1024 bytes.
- BER equal to 10⁻¹² according to [3] and [5].
- MPS increased from 64 bytes to 1024 bytes in increments of 64 bytes.

Figure 7 shows calculated results of Experiment 3, the model and simulator results were similar. These differences become negligible with increase of payload.

D. Fourth Experiment

In this fourth and last experiment the calculated results of the proposed model and the results of work [7] were compared. In work [7] the equipment used was a Virtex-5 LXT FPGA ML555 Development Kit for PCI Express as a source node and two different chipsets, the Intel 965 Chipset and the Intel E5000P Chipset as destination nodes. In this

experiment the following parameters were used:

When comparing the results obtained with the proposed model against the Intel 965 results, we obtained a good approximation of the throughput measurements as shown in Figure 8. On the other hand, the difference in the measurements obtained with Intel E5000P (see Figure 9) shows major differences using a configuration of 8 lines (x8). This is because the processor is designed for performance optimization using 8 lines and a payload size equal to 128 bytes according to [7].

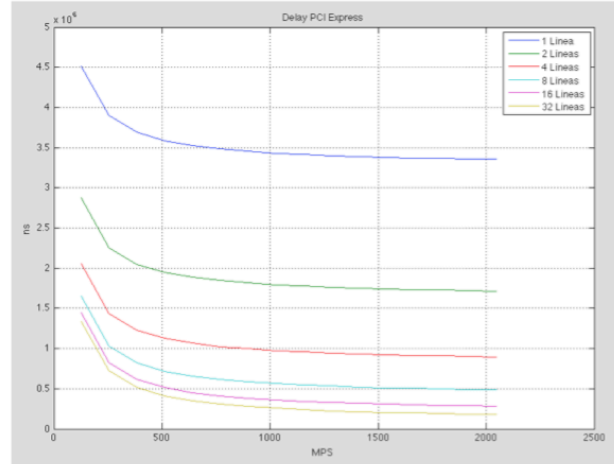


Figure 6. Shows the delays calculated in the second experiment. Using different number of lines.

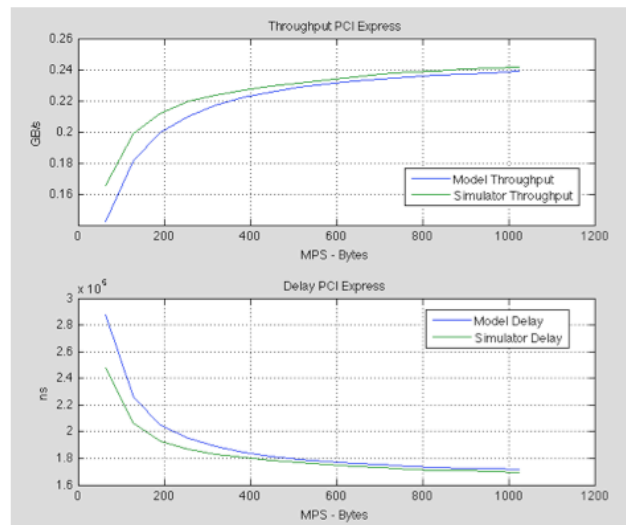


Figure 7. Shows throughput (upper side) and delay (lower side) obtained from our model and simulator.

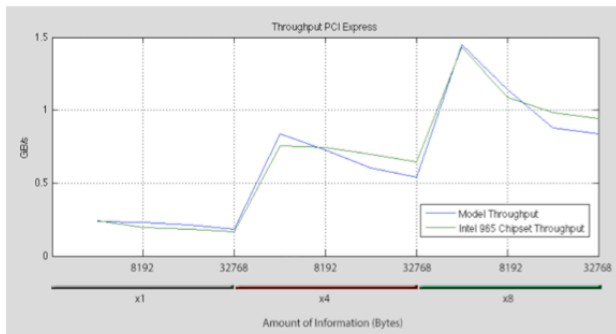


Fig. 8 Shows a comparison between throughput of our model and throughput obtained using the Intel 965 Chipset.

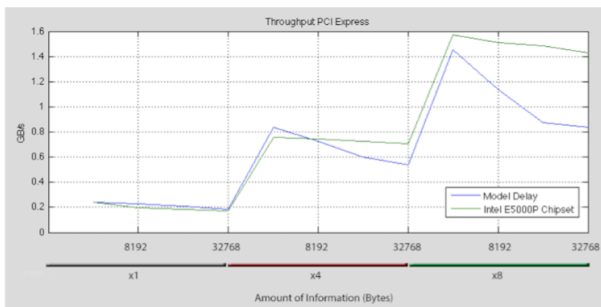


Figure 9. Shows a comparison between throughput of our model and throughput obtained using the Intel E5000P Chipset.

V. CONCLUSION

This paper provides a mathematical model based on Teletraffic Theory using Markov chains and queuing system M/M/1/B. Our mathematical model shows measurements that affect the performance of PCI Express communications such as Throughput and Delay. We noticed that the parameters of payload size, receptor’s buffer size and number of lines affect the PCI Express performance.

In the future, PCI Express switch will integrate to the model in order to represent more complex scenarios and large-scale connections, i.e. more number of interconnected nodes and information flows.

Comparing different measurements obtained from simulations and hardware tests against the model results, we can conclude that the model is a good approximation to the behavior of the protocol PCI Express.

ACKNOWLEDGMENT

We appreciate the financial support given by CONACYT.

REFERENCES

[1] R. Scherzinger, “Performance of PCI Express® devices – a case study” in PCI-SIG Developers Conf, San Jose, CA 2005.
 [2] “PCI Express Performance Measurements”, white paper, Agilent Technologies Inc, September 15, 2006.
 [3] B. Ravi, A. Don, and S. Tom, PCI Express System Architecture. Reading, MA: Mindshare Inc. and Addison Wesley, 2003, p.1049
 [4] F. Gebali, Analysis of Computer and Communication Networks, Springer, 2008, p.669

[5] PCI-SIG. PCI-Express™ base specification Rev 3.0. PCI-SIG. November, 2010
 [6] Y. Uchiyama, “Throughput Evaluation of PCIe Cores” in PCI-SIG Developers Conf, San Jose, CA 2005.
 [7] “Understanding Performance of PCI Express System”, white paper, Xilinx, September 4, 2008.
 [8] W. J. Dally and B. Towles, Principles and practices of interconnection networks, Elsevier, 2004, p.550
 [9] T. Vu and D. Reschke and W. Horn and Tu Ilmenau, “Dynamic Packet Size Mechanism (DPSM) for Multimedia in Wireless networks”, Proc. of Multimediale Informations- und Kommunikations systeme, 2002
 [10] F. Lombera, “Diseño e implementación de simulador de PCI Express”, master’s thesis, Dept. Computer Science, Cinvestav Unidad Guadalajara, 2012
 [11] Peter Böhm “Incremental and Verified Modeling of the PCI Express Protocol”, IEEE Transaction on computer aided design of integrated circuits and Systems. Vol 29 No 10, Oct 2010. pp. 1495 - 1508
 [12] Peter Böhm “Incremental modelling and verification of the PCI Express transaction layer”, Formal Methods and Models for Co-Design, 2009. MEMOCODE '09. 7th IEEE/ACM International Conference on, 13-15 July 2009, pp 36 - 45
 [13] “Overcoming Latency in PCIe Systems Using PLX”, white paper, PLX Technology, 2007
 [14] D. McConnell and P. Lysaght, “Queue Simulation Using Dynamically Reconfigurable FPGAs”, 1996
 [15] T. Yoo, R. J. Lavery, A. Goldsmith, and D. J. Goodman, "Throughput optimization using adaptive techniques." <http://wsl.stanford.edu/>, 2006.

Miguel Angel Orozco received the B.S degree in Computer Systems Engineering from Cuahtémoc University, Zapopan, Jalisco, in 2011 and the M.S degree in Computer Science from Cinvestav, Zapopan, Jalisco, in 2013. His research interests include PCI Express modeling, interconnecting communication protocols, teletraffic analysis on different communication protocols.

Monitoring Land-Cover Changes Using Satellite Imagery

Wayne Goosen
 School of Mathematics, Statistics
 and Computer Science
 University of KwaZulu-Natal
 Durban, South Africa
 209515437@stu.ukzn.ac.za

Serestina Viriri
 School of Mathematics, Statistics
 and Computer Science
 University of KwaZulu-Natal
 Durban, South Africa
 viriris@ukzn.ac.za

Abstract—Several regions around the World are currently undergoing rapid, wide-ranging changes in land cover due to human activities and natural events. These changes can have significant effect on regional and even global climate change. In this paper, focus is on urbanization in South Africa. A Post-Classification approach is employed to detect land cover changes on a specific area from a time series of satellite images. Variance in spatial resolution and radiometric resolution between images was taken into account using radiometric normalization and geometric registration. Maximum Likelihood, Neural Network, Decision tree, K-means clustering and Multi-Support Vector Machine methods were used to distinguish between the different land cover classes. All land cover class proportions are quantified in every image and this is used to monitor the change over time. For the classification using the Multi-Support Vector Machine method yielded the best classification success rate of 80.91%. The Maximum Likelihood and Neural Network methods produced 80.45% and 79.09%, respectively.

I. INTRODUCTION

There are various types of imagery produced by a number of different satellites. SPOT, QuickBird, GeoEye-1, RapidEye and Landsat are the most commonly known satellites. Each of these satellites produce imagery that contain different image resolutions and auxiliary data. These images comprise of different bands, each on a set wavelength. In the classification process, different combinations of these bands are used to detect certain types of land cover classes. These satellite imagery all have one common aspect to them, the access to this imagery is fairly difficult from the relevant organizations that run these satellites. There exist various land cover classification programs, most commonly known is ArcGis, which uses Maximum likelihood, unsupervised Clustering and Principal Components as possible classification techniques. There has not been much research into land cover classification of True Color Satellite imagery with no auxiliary data. This process involves using only three bands of the visual spectrum comprised in the image, red, green and blue components, to classify the images through various techniques and detect the corresponding change.

This paper firstly provides a summary of the back ground and related work. The Methods and Techniques are described next, covering the preprocessing, classification and change

detection methods. Finally the results are presented and discussed.

II. RELATED WORKS

There has been much research on the various change detection methods on different remotely sensed imagery. Selcuk Reis [12] Geo-referenced the images to the map of the research area, radiometric corrections were carried out by the dataset providers and the Supervised Maximum Likelihood method was used for classification. A 85.75% average classification success rate was achieved. This is higher than the result produced in this paper because of the larger testing set. The difficulties experienced stemmed from mountainous and sloping research area, noise induced by negative climate conditions and the complexity of the vegetation.

Jin Chen et al.[11] proposed a new method to improve Change Vector Analysis (CVA) in Change Detection. It attempts to determine the optimal thresholds for change detection which is the short fall of the CVA method. The process of empirically determining the threshold of change is replaced by the Double-Window Flexible Pace Search (DFPS) algorithm. The algorithm searches for the optimal threshold from training samples that leads to the maximum change detection accuracy.

Florian Sallabai [24] also utilized the Supervised Maximum Likelihood method to perform Post-Classification Change Detection and contained a number of preprocessing methods. Geometric registration was achieved by using the UTM projection. Normalization of different sun angle and solar radiance between images was achieved by calculating the Top of Atmosphere Reflectance. Spectral Radiance was used to place the images onto the same radiometric scale and cloud contaminated pixels were excluded. The results showed that the change detection suffered due to the research area being small-structured and heterogeneous.

Rupinder and Smriti Sehgal [19] compare the K-means and Back Propagation Neural Network (BPNN) methods on

a Pixel Based Classification of remotely sensed images. The two methods were performed on the same remotely sensed image. The classification success rate clearly shows the BPNN out performing the K-means producing 80.5% and 63.3%, respectively.

III. METHODOLOGY AND DESIGN

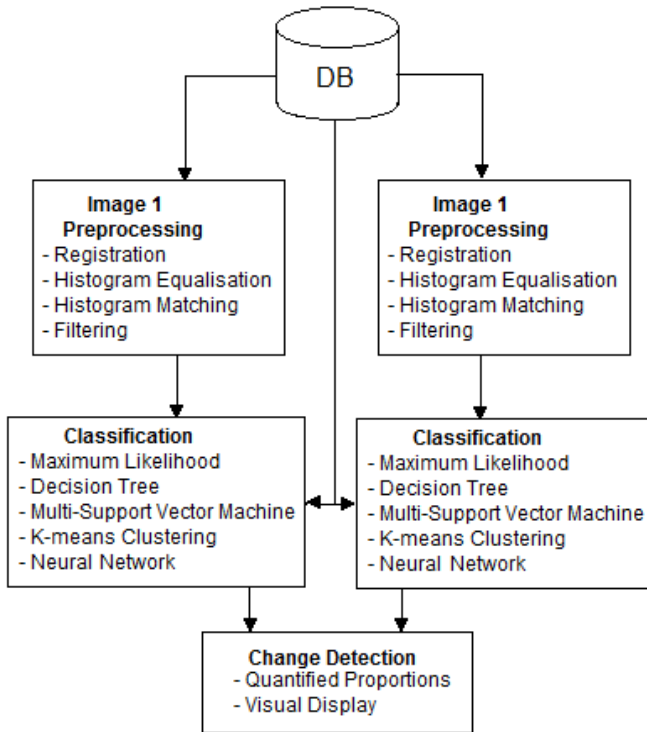


Fig. 1. Overview of the System

Figure 1 provides an overview of the system. The system is broken down into three steps, image preprocessing, classification and change detection. The image preprocessing and classification are implemented on both images. The preprocessing is divided into the following processes, Image-to-Image Registration, Histogram Equalization, Histogram Matching and Filtering. The classification consists of a number of methods, Maximum likelihood, Multi-Support Vector Machine, K-Means Clustering, Decision Tree and Neural Network methods. The change detection consists of simply quantifying the classification results.

A. Image Preprocessing

Image preprocessing consists of methods that will aid the classification process, removing any noise that will hamper the classification. Image-to-Image Registration must take place to ensure the pixels of both images correlate to one another. The three other methods are image enhancement and noise removal techniques.

1) *Image-to-Image Registration*: An Image-to-Image Registration is used whereby the one image is set as the reference image and the other input image is to be registered to the reference image. The method used to detect features was SURF (Speeded Up Robust Features) to detect scale and rotation-invariant points in both the images. The extracted feature vectors and relevant locations were stored. These extracted features were then matched between the two images. Using the locations of the feature vectors a geometric transformation matrix was produced between the matched features. This geometric transformation matrix is applied to the whole image and produces a image that is registered to the reference image.

2) *Histogram Equalization*: This method transforms the histogram of the image in an effort to enhance contrast. Once Histogram Equalization has taken place, the intensities will be better distributed on the histogram. A gray scale image G is represented by an $M \times N$ matrix of pixel intensity values. The intensity values ranging from 0 to $L-1$. Let p denote the normalized histogram of G as follows

$$P_n = \frac{\text{no. of pixels with intensity } n}{\text{total no. of pixels}} \quad n=0, \dots, L-1 \quad (1)$$

The P_n is used to create a mapping function for the pixel intensities, T ,

$$T(k) = (L-1) \left(\sum_{n=0}^K P_n \right) \quad K=0, \dots, L-1 \quad (2)$$

The intensity value K will be mapped to $T(K)$ in the outputted image. The dataset consists of images that contain three bands and thus this process will have to be performed on each band. An example can be seen in Figure 2.

3) *Histogram Matching*: This method is the process of matching a histogram to a reference histogram. Using equations (1) and (2) to produce $P1_n$ and $T1(k)$ for the original histogram, PR_n and $TR(j)$ for the reference histogram. Suppose the mapping functions for both histograms produced arbitrary values a and b , $T(k) = a$ and $TR(k1) = b$. The histogram matching utilizes a reverse mapping such that when $a=b$ (or nearest value) the value k in the original histogram is mapped to $k1$. This process will be applied to all three bands of the image.

4) *Filtering*: Filtering is a method to reduce noise in an image. It uses a 2D matrix (known as a sliding window) that scans through the image performing different mathematical calculations on this window of values and replaces the center value in the image. There are different forms of this method but they all strive to accomplish a common goal, reducing the intensity variation amongst pixels. Median filter (median of the sliding window), Mean filter (mean of sliding window) and Gaussian filter (uses a Gaussian function to set values of the sliding window and performs the sum of products) are amongst the most common filters used.

B. Classification

Classification methods can be of two types, supervised and non-supervised. With supervised classification, training

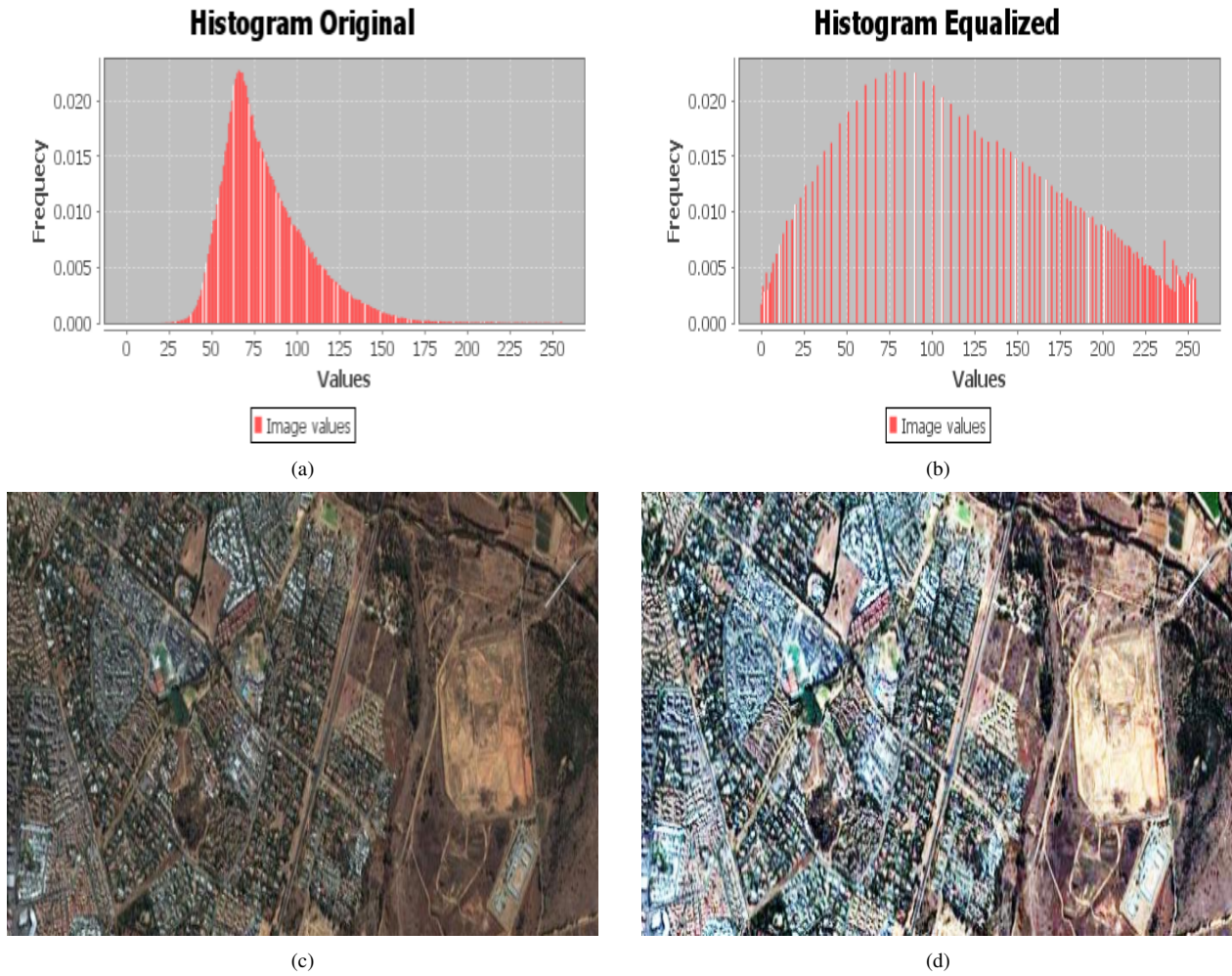


Fig. 2. (a) Histogram of Original image. (b) Transformed Histogram. (c) Original Image. (d) Resulting Image from Histogram Equalization of c.

data will have to be entered into the system to train the classifier. The number of classes and class names should be finalized before the classification process begins. The training data consists of the feature vectors of the image and the corresponding class labels. The non-supervised classifier just uses the feature vectors to classify the image into the different land cover classes. Once the pixel values are classified into the classes, a new image will be created displaying the classified pixels, each class will have a corresponding color. The images consist of a feature vector for every pixel as follows

$$F_v(i, j) = \{r, g, b\} \quad (3)$$

where i and j are co-ordinate values and r, g and b are the values from each corresponding band.

1) *Maximum Likelihood*: The Maximum Likelihood Classifier is a statistical based supervised classification method. It is derived from the Bayes Theorem and calculates a posteriori distribution known as $P(k|F_v)$. This is the probability that a pixel with feature vector F_v belongs to class k , this calculation is given by:

$$P(k|F_v) = \frac{P(F_v|k)P(k)}{P(w)} \quad (4)$$

The likelihood function is $P(F_v|k)$, $P(k)$ is the probability that the class k occurs in the data used and $P(F_v)$ is the probability that the feature vector has been observed which can be calculated using the following:

$$P(F_v) = \sum_{k=1}^L P(F_v|k)P(k) \quad (5)$$

L is the total number of classes. The whole image is traversed pixel by pixel and the pixel is assigned to class k by the following rule:

$$if P(k|F_v) > P(j|F_v) \text{ for all } j \neq k \quad (6)$$

For every pixel the probability will be calculated for each class and the one with the highest probability will be the class the pixel is assigned to.

2) *Multi-Support Vector Machines*: Support Vector machine (SVM) is a supervised learning model used in machine learning often to perform classification. The SVM classifies data into only two classes by finding the best hyperplane to separate them. An equation for a hyperplane is

$$\langle w, x \rangle + b = 0 \quad (7)$$

where $\langle w, x \rangle$ is the inner product of w and x . w is an element of R^d where d is the dimension of the input vectors. Since the data can possibly be non separable, a soft margin is employed, the hyperplane will separate a good percentage of samples but not all. The soft margin implementation utilizes slack variables s_i and a penalty parameter C as follows

$$\min_{w,b,s} (\frac{1}{2} \langle w, w \rangle + C \sum_i s_i) \quad (8)$$

Subject to

$$y_i(\langle w, x_i \rangle + b) \geq 1 - s_i \quad (9)$$

$$s_i \geq 0 \quad (10)$$

This method is used for classification when only two classes are involved, in regards to land cover classes there are usually more than two classes. To use the SVM a simple transformation from the n dimensional class space to a two dimensional class space is performed. The method consists of making a SVM for each class versus the rest of the classes (combining the rest of the classes into one class to make the class space two dimensional), to produce the Multi-Support Vector Machine. The classification process consists of the feature vector of each sample (a pixel) being inputted into each SVM and which ever SVM returns the best margin from the hyperplane, the sample is assigned to that class.

3) *Decision Tree*: A decision tree is a method that consists of various ways of splitting a dataset into segments (branches). These branches form an inverted tree, with the root located at the top. This method can be used in classification and the leaf nodes of the decision tree will represent assignment to the land cover classes. A feature vector will start at the root and pass various decisions (branches) until it reaches a leaf node and it will be classified into that land cover class. This method also requires training data to learn how to split the data. An example is shown in Figure 3, five land cover classes were used and values at the leaf nodes will be rounded off to the nearest integer (1.364 = 1, This will represent assignment to class 1).

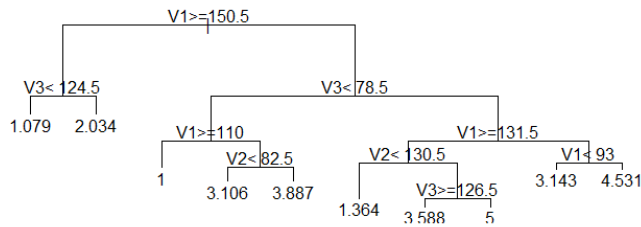


Fig. 3. Example of a Decision Tree, Input Feature Vector {V1 ,V2, V3}

4) *K-means Clustering*: This non-supervised classifier clusters the data by separating samples into K clusters to some objective function. This method requires a number of clusters to be specified which will be our land cover classes. The objective function used was a squared error function. For the

dataset X , centroid C of a cluster is calculated as follows

$$J(X, C) = \sum_{i=0}^n \min_{\mu_j \in C} (\| x_j - \mu_i \|^2) \quad (11)$$

Basic steps involved:

- 1) Initialize the centroids of all clusters.
- 2) Assign each sample to the cluster (class) that has the nearest centroid.
- 3) When all the samples have been assigned to a cluster (class), the centroids of the cluster need to be recalculated.
- 4) Repeat steps 2 and 3 until no change occurs in the centroid values. This creates clusters where by the metric to be minimized can be calculated.

5) *Neural Network*: Neural Networks are models build based on the central nervous system (typically the brain) that are capable of machine learning. These models are comprised of a large number of interconnected neurons working together to solve specific problems. In this paper the multilayer perceptron (MPL) neural network model is used. This is a supervised model which requires a desired output to learn. The MPL consists of an input layer of nodes, one or more hidden layers of nodes and output layer of nodes. The input passes through all the hidden layers to produce an output. The calculation of a two layer MPL is as follows

$$x = f(s) = BH(As + a) + b \quad (12)$$

Where x is the vector output and s the vector of inputs. A and B are the matrix of weights for the first and second layer. a and b are the bias vector for first and second layer. H is the activation function. The data flows through the hidden layers where they get summed and processed by the activation function. With each transfer to a different layer the data gets multiplied by the interconnection weights. The learning process is where by data goes through the MLP, the output gets compared to the required output, an error calculation is performed and the weights are adjusted as seen in Figure 4.

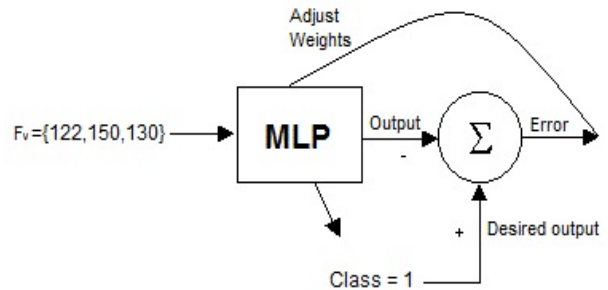


Fig. 4. Example of a MLP learning process

C. Change Detection

The Change Detection is the process of quantifying the results of the classification process. In each image the land cover proportions will be quantified, providing us with the

amount (in percentage) of each class in that image. The percentages can be compared directly or graphed to detect the change happening over time in the land cover classes. The classified images are also displayed and the change can be detected visually.

IV. RESULTS AND DISCUSSION

The change detection accuracy is directly proportional to the classification accuracy rate. Due to this, the classification results are compared and a change detection example is examined thereafter.

A. Classification Rate

The images used to test these methods are of Amanzimtoti, Durban, South Africa. These images are from Google Earth and were acquired in 2008 and 2011. A testing set and training set were abstracted from the images with the relevant land cover class labels. For this specific image, five land cover classes were selected as follows

- 1) Bare soil
- 2) Urban area
- 3) Evergreen and forests
- 4) Grass land
- 5) Roads and railways

The following confusion matrices and classification rates were produced for the Maximum Likelihood (ML), Decision Tree (DT), Multi-Support Vector Machine (MSVM) and Neural Net (NN) methods. The results in the matrices are represented in percentages.

$$ML = \begin{pmatrix} 21.36 & 2.27 & 0 & 0 & 0.45 \\ 1.8 & 13.18 & 0 & 1.36 & 1.8 \\ 0 & 0 & 23.63 & 2.27 & 1.36 \\ 0 & 2.27 & 0 & 11.81 & 2.7 \\ 0 & 3.18 & 0 & 0 & 10.45 \end{pmatrix}$$

Classification rate is: 80.45%

$$DT = \begin{pmatrix} 18.18 & 0.91 & 0 & 0 & 5 \\ 3.18 & 8.63 & 0 & 4.09 & 2.27 \\ 0 & 0 & 19.09 & 8.18 & 0 \\ 0 & 0 & 0 & 4.09 & 12.72 \\ 0.45 & 0 & 0 & 8.18 & 5 \end{pmatrix}$$

Classification rate is: 55%

$$MSVM = \begin{pmatrix} 21.82 & 0 & 0 & 0.45 & 1.8 \\ 2.7 & 8.18 & 0.91 & 0.45 & 5.91 \\ 0 & 0 & 19.09 & 3.18 & 0.45 \\ 0 & 0 & 0 & 15.45 & 1.36 \\ 0 & 0.91 & 0 & 0.91 & 11.81 \end{pmatrix}$$

Classification rate is: 80.91%

$$NN = \begin{pmatrix} 22.27 & 0 & 0 & 0.45 & 1.36 \\ 4.09 & 8.64 & 0 & 0.91 & 4.54 \\ 0 & 0 & 21.82 & 2.7 & 2.7 \\ 0 & 0 & 0 & 12.72 & 4.09 \\ 0 & 0 & 0 & 0 & 13.63 \end{pmatrix}$$

Classification rate is: 79.09%

Method	%
Maximum Likelihood	80.45
Decision Tree	55
Multi-Support Vector Machine	80.91
Neural Net	79.09

Table 1 Classification Success rate of methods.

Table 1 shows that the decision tree performs poorly and it suffers because the data can not be sequentially split up into the classes. The Maximum likelihood, Multi-Support Vector Machine and Neural Net methods perform well at an 80% average between them.

The sub images in Figure 5 show that even though the Maximum Likelihood method has given a classification rate of 80.45%, the results seem better in the Neural Net classified image which has a 79.09% rate. It is also so for the Multi-Support Vector Machine, visually the Neural Net out performs both the Maximum Likelihood and the Multi-Support Vector Machine methods. The K-means Clustering method is used to classify the same image, Figure 6 shows that the method performs poorly.



(a)



(b)

Fig. 6. (a) Original Image. (b) K-means method classified image a.

The graphical visualization of the classification in Figure 7 shows the limitations of the K-means method. The five clusters can be seen quite distinctively responding to the five classes in Figure 7 (a). They are grouped down the diagonal because of the distance measure used to create the clusters. The graph in Figure 7 (b) corresponds to the Maximum Likelihood method and the benefits are evident. In the RGB feature space the method allows classification of two classes to be parallel

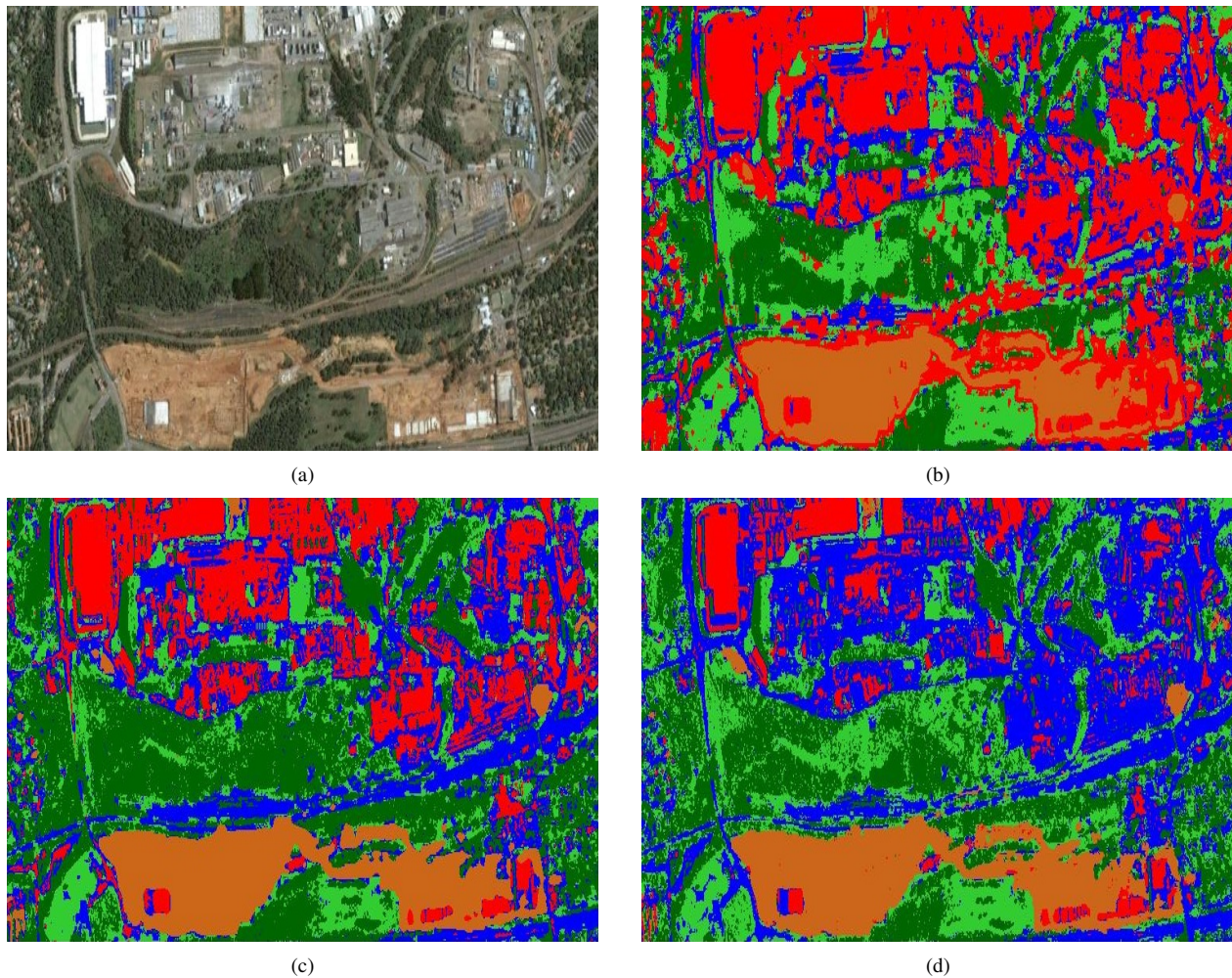


Fig. 5. (a) Original Image. (b) Maximum Likelihood method. (c) Multi-Support Vector Machine method. (d) Neural Net method.

on the diagonal. It allows a sample to be classified to a class without necessarily being in the neighborhood of the rest of the samples of that class.

B. Change Detection in Amanzimtoti

The area in Amanzimtoti was chosen because of recent developments in the small town. A golf course and surrounding areas were cleared to introduce two shopping malls and also the business park near by where development is ongoing. Evaluation of the systems potential to detect the change that is occurring in this area is performed. The resulting classification process using a Neural Network Model can be seen in Figure 8.

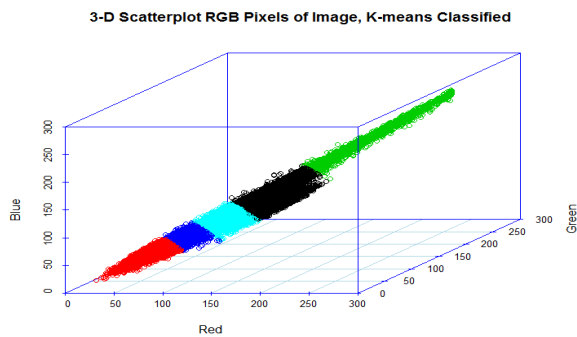
There is quite a lot of change happening and the system detects the overall change quite well as seen in Table 2. The shopping centers and adjacent roads can be seen visually occupying the bare soil over time. This is present in the system with bare soil decreasing from 10% to 1%, Urban/Residential increasing from 8% to 10% and Roads & Railways increasing from 35% to 41% in the period from 2008 to 2011.

	Year	Year
	2008	2011
Land Cover Class	%	%
Bare Soil	10	1
Urban/Residential	8	10
Evergreen/Forestry	27	14
Grass Land	18	32
Roads and Railways	35	41

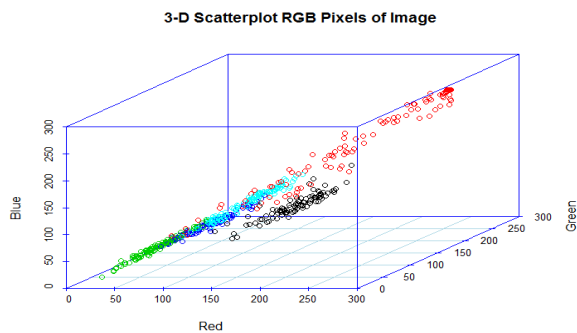
Table 2 Comparison of 2008 to 2011 Amanzimtoti Quantified Land Cover Classes.

V. CONCLUSION

This paper has compared a number of classification methods and produced competitive results compared to ones found in literature. Most notable result was a 80.91% classification success achieved by the Multi-Support Vector Machine method. The results vary compared to literature due to each change detection system using a different dataset. It can be concluded that on the dataset used, this system using a choice of preprocessing and classification methods at the users will can provide the relevant change over time from the dataset.



(a) K-means Clustering method



(b) Maximum Likelihood method

Fig. 7. 3D graph of the Classification.

Further research would be to investigate the Change Detection accuracy of these methods on images that contain more than just the three visual bands.

ACKNOWLEDGMENT

The authors would like to thank the National Research Foundation (NRF) and the South Africa National Space Agency (SANSa) for all forms of assistance during this research work.

REFERENCES

[1] H. Kopka and P. W. Daly, *A Guide to L^AT_EX*, 3rd ed. Harlow, England: Addison-Wesley, 1999.

[2] Penglin Zhang, Wenzhong Shi, Man Sing Wong and Jiangping Chen. *A Reliability-Based Multi-Algorithm Fusion Technique in Detecting Changes in Land Cover*. 2013

[3] J. F. Mas. *Monitoring Land-Cover changes: a comparison of change detection techniques*. 20 May, 1998

[4] D. Lu, E. Moran, S. Hetrick and G. Li. *Land-Use and Land-Cover Change Detection* 2010

[5] Wafa Nori, El Nour Elsiddig and Irmgard Niemeyer. *Land-Use and Land-Cover Change Detection* 2008

[6] Andrew A. Millward and Joseph M. Piwowar. *Exploring ordination a a method for normalizing disparate datasets: implications for digital change detection* 2002

[7] Limin Yang, George Xian, Jacequelin M. Klaver and Brian Deal. *Urban Land-Cover Change Detection through sub-pixel imperviousness Mapping using remotely sensed data* 2003

[8] Compton J. Tucker, John R. G. Townshend and Thomas E. Gof. *African Land-Cover Classification Using satellite Data* 25 January, 1985

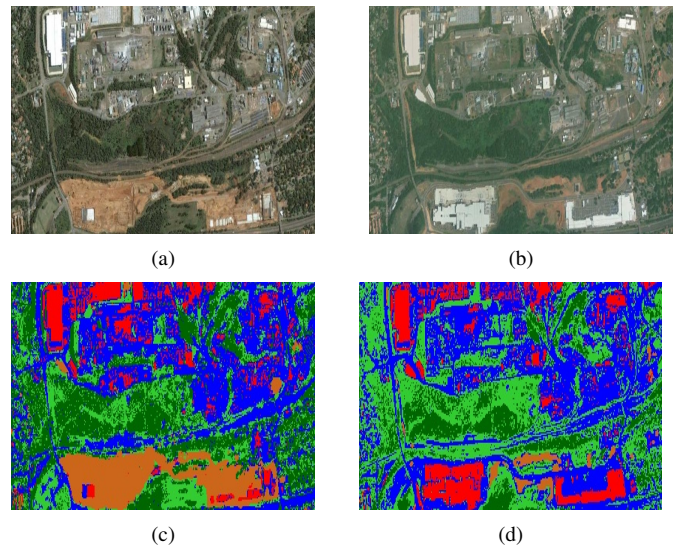


Fig. 8. (a) Amanzimtoti 2008. (b) Amanzimtoti 2011. (c) Classified image a. (d) Classified image b.

[9] Maryne Rymasheuskaaya. *Land Cover change detection in Northern Belarus* 2007

[10] I Gatsis, S. Kouskoulas, A. Vafeidis, E. Lagoudakis and K Gkoltsiou. *Monitoring and Mapping of Land cover/use changes in an agriculture and natural environment, using multitemporal satellite data and GIS(Lesvos Island, Greece*

[11] Jin Chen, Peng Gong, Chunyang He, Ruiliang Pu and Peijun Shi. *Land-Use/Land-Cover change detection using improved Change Vector Analysis* 2003

[12] Selcuk Reis. *Analyzing Land Use/Land Cover Changes using Remote Sensing and GIS in Rize, North-East Turkey* 2008.

[13] Mario Caetano. *ESA advanced training course on land remote sensing, Image Classification* 30 June, 2009.

[14] J. M. Bardsley, Marylesa Wilde, Chris Gotschalk, M. S. Lorang *MATLAB Software for Supervised Classification in Remote Sensing and Image Processing*

[15] John R. Jensen *Introductory Digital Image Processing, A Remote Sensing Perspective* Third Edition

[16] Paul M. Mather and Magaly Koch *Computer Processing of Remotely-Sensed Images, An Introduction* Fourth Edition

[17] Gang Hong, Yun Zhang *Radiometric Normalization of Ikonos image using QuickBird Image for Urban Area Change Detection*

[18] Barbara Zitova, Jan Flusser *Image Registration methods: a survey*

[19] Rupinder Kaur, Smriti Sehgal *Pixel Based Classification of Remotely Sensed Image using K-means and BPNN*

[20] Anders Karlson *Classification of high resolution satellite images* August 2003

[21] Asmala Ahmad and Shaun Quegan *Analysis of Maximum Likelihood Classification on Multi-spectral Data*

[22] T. Hastie, R. Tibshirani and J. H. Friedman *Elements of Statistical Learning* Second Edition

[23] Florian Sallabai 2009 *Potential of a Post-Classification Change Detection Analysis to Identify Land Use and Land Cover Changes*.

[24] Offer Rozenstein, and Arnon Karnieli *Comparison of Methods for Land-Use Classification incorporating Remote Sensing and GIS Input* 2011

PSCM: Proxy Server Cache Mechanism for Video on Demand System

Saleh Ali Alomari¹, Putra Sumari²

^{1,2} School of Computer Science, Universiti Sains Malaysia
Pulau Penang 11800, Malaysia

¹ Faculty of Science and Information Technology, Jadara Universeity
Irbid 21110, Jordan

omari08@jadara.edu.jo and sumari@cs.usm.my

Abstract—Video on Demand (VOD) system is being one of the emerging systems that allow the user to view a video at anytime and anywhere. One of the important elements in this system is the broadcasting technique that is used to disseminate the video to the users. In this paper, a caching scheme was proposed to reduce the service waiting time in Video on Demand (VOD) system. The proposed caching schemes called Proxy Server Cache Mechanism (PSCM) scheme to overcome the service delay. This delay is occurred when a client misses the broadcasting phase of the 1st segment from broadcasting channels. Therefore, this paper proposed a caching scheme that denote as the (PSCM) to overcome the start-up service delay. In PSCM scheme, the 1st segment of the video is stored on a stationary proxy server. The late clients can request the 1st segment directly from the proxy server rather than waiting for the next broadcast of the 1st segment. The PSCM scheme guarantees obtaining the 1st segment by the mobile clients once they arrive. This scheme presents balance technique to maintain the requests over the local proxy server in order to ensure a fair distribution of these requests. The performance of the caching scheme is evaluated by implementing the VOD system. The results show that the proposed scheme has reduced the service delay substantially compared to the best existing schemes.

Keywords—VOD, PSCM, SB, LF's, LPS, All-Cache

I. INTRODUCTION

VIDEO on Demand (VOD) system is one of the most important applications for the future internet. It became an interactive multimedia service that helps clients to playback any of the large collection of videos at anytime through public communication networks more freely after waiting for a short period of time, where they can be capable of making use of interactive services and download many videos at the same time [1]. Typically, these video files are stored in a set of central video servers, and distributed through high-speed communication networks to geographically dispersed clients. Wireless and mobile computing devices gave more flexibility and convenience to clients in order to enjoy viewing videos, and obtain flexible services from the distance video server while they are moving freely within the coverage of their wireless network. The choice of the suitable system architecture will be based on the location of the server, communication systems, available storage and other factors.

This project is part of a larger research work in the MCRG and this work was supported by Universiti RU's grant (1001 / PKOMP/ 817066) from the Universiti Sains Malaysia (USM).

The VOD system provides ubiquitous services to users (especially mobile users) in almost daily routines. For instance, VOD system allows university students to watch an educational video of their interests online anywhere and anytime. It also allows them to watch earlier recorded videos from lectures they were not able to attend. The VOD system allows people at the airport to instantly watch videos using their own PDAs while they are waiting for their flights' schedules. There are many other VOD applications, such as IPTV [2], Facebook [3], Youtub [4], Educclip [5], E-learning (digital video library) [6], On-line shopping, medical information services and etc.

The basic elements of the VOD system are servers, networks and user display equipment. The server is responsible for storing large number of videos and broadcasting them to users. Users may make requests of the videos and watch them by using users to display equipments, such as smart phone, iPad, PDA's and etc.

The characteristics of the VOD system, which include the long-lived session, high bandwidth requirements and QoS-sensitive service has made the design of the VOD system become a challenge. This is because of the nature of the video data. The video data are the real time data that has to satisfy certain QoS. Besides, the issues are how rapid a video can be watched, once requested. It is here referred to as the delay, which is the average period of time a client waits until being serviced. In other words, it determines an end-to-end time that is considered to be the difference between the times of requests for a packet travels from the source to the time of receiving at the user's destination. There are many elements influence the delay issue. The choice of the system architecture is one of the elements that influence the overall performance, especially, the location of the servers, the protocol of communication systems, and the availability of storage and other factors can contribute to the delay.

The subsequent sections are organized as follows. Section II presented the related background, while in Section III shown the cache proxy server mechanism (CPSM), the broadcasting technique for PSCM scheme presented in Section VI. In Section V described the caching mechanism of the PSCM scheme. The scenario of the playback video in the PSCM scheme for Video in Demand (VOD) system is presented in Section IV. The experimental results and discussions are

presented in Section IIV. Finally, the conclusion is presented in Section IIIV.

II. RELATED BACKGROUND

The designs of VOD systems are categorized into three main approaches; such as, Client/Server, Peer-to-Peer (P2P) and Periodic Broadcast [7], [8], [9], each of these approaches has such limitations. In the Client/Server approach [10] does not simply fit well for MANETs due to the limitation encountered in the wireless bandwidth. This limitation of wireless bandwidth creates problems when the number of request increases. In addition, the Peer-to-Peer (P2P) approach is not suggested to transmit the long video through more than one wireless hop, as this is inefficient for both; bandwidth and energy that are being used. Periodic Broadcast approaches are considered to be the better approaches in terms of bandwidth, since any number of mobile clients could be efficiently served. Particularly, the client can tune to one or more server channels and view the video. In this case, the number of the request will not effect on the server bandwidth. All broadcasting protocols, such as, [11-18], divided the video into a number of segments, then broadcasted these segments repeatedly over the number of channels.

The broadcasting method at the server is another element in contributing to the delay, as well as, the number of concurrent users of which the VOD system can support. Broadcasting is related to the scenario of handling clients who are watching different portions of the same video at any given moment. In particular, the server has to have an efficient broadcasting mechanism so that it can broadcast the video to many users as possible in a simultaneous fashion with the stringent delay requirements.

Broadcasting technique is a method of distributed video from a server to many simultaneous users. Broadcasting schemes can work with different network infrastructures [19], including cable TV, direct broadcast satellite and local area network. The idea behind the broadcasting schemes is to provide effective ways in reducing the waiting time for clients. This time refers to the interval time between requests for a video and receives the video from the beginning.

There are several researchers have been proposed to the VOD system to provide optimal services to the mobile ad hoc devices. MobiVoD [10], [20] is the latest VOD system, which provided the video services to homogeneous devices (i.e. laptop) through homogeneous network (i.e. WiFi 802.11b). MobiVoD allows the mobile clients to watch their movies at anytime and anywhere. As well as the system is composed of three main component the video server, Local forwarder (LF) and the mobile clients. The entire video files are stored on the main server. The LF's are a number of scattered stationary devices, which used as a relay for the video to the mobile clients by broadcasting video segments to its service coverage area. The server cannot transmit the video using wireless technique to wide coverage area; therefore, LF's are used to expand the transmission coverage area. Staggered Broadcast (SB) protocol has been used to broadcasting video segments repeatedly to mobile clients over number of wireless channels.

SB is considered as the best choice for broadcasting the video to the mobile devices, since the limitation of the mobile devices [10]. The main advantages of using the SB protocol in VOD system is that, at first, a zero cache space is required in the mobile client devices. In addition, the required bandwidth by the clients' device does not exceed the playback rate, while in other protocols; the bandwidth is at least twice more than the playback rate. Furthermore, the clients just need to connect one channel, while in other broadcasting techniques the client should connect to at least two channels. The disadvantage is a high service delay that is accursed when the client misses up the broadcasting of the 1st segment of the video. The client should wait for a long time until broadcasting the 1st segment again on one of the channels.

Many researchers have been proposed a caching technique to solve delay problem. In [10] proposed several types of caching, such as, All Caching, Random Caching and DSC. The author proposed PCSB1 work attempted to solve the problem of the late clients, which missed the 1st segment of the current broadcasting channel. In order to solve this problem, and make the client obtain the video segment (1st segment) without waiting for the next broadcast channel of the 1st segment, the proposed scheme helps the clients to obtain it directly from the Pool of RAM (PoR) of the existing MF, where it used a procedure to store the 1st segment of the entire videos in the PoR of the MF, when the videos are broadcasted. In other words, the PCSB scheme can minimize the delay by guaranteeing that the late client can obtain the 1st segment as soon as it arrives. The author in [21] enhanced the cache by providing the on-going video streaming in the Relay Station (RS) in order to minimize the waiting time. Proxy prefix caching for Multimedia Streams has been proposed by [22] to reduce the user perceived latency and network resource requirements in the Internet, where a proxy is used to store the initial frames of audio or video locally. Upon the request, the proxy immediately transmits the data to the client. All Cache and Random Caching schemes have been proposed [10]. In the All-Cache scheme, all the clients in the Local forwarder coverage have to save the 1st segment in the Random Caching. The random number of clients has to save the 1st segment. The late clients in both schemes can cache the missed 1st segment from their neighbor who already saves the 1st segment in their buffer. DSC scheme has been proposed [10]. In this scheme, the new client X can get the 1st segment from client Y in the same transmission area, meanwhile, Y should not forward the segment to any other clients. But if Y is not in the transmission area of X, then Y will find client Z that share the same transmission area with itself and client X, then Y will forward the 1st segment to X through Z. There are many proposed caching techniques such present in [23], [24], [25].

III. CACHE PROXY SERVER MECHANISM (CPSM)

The caching scheme proposed in this paper is called the Cache Proxy Server Mechanism (CPSM). This caching scheme minimizes the start-up delay in VOD systems. In CPSM, the 1st segments of all broadcasting movies are stored in the local Proxy Server. If a client arrives after the local forwarder broadcasts the 1st segment, the clients cannot get it, where the

client must wait till the next broadcasting channel to broadcast the 1st segment. To overcome this problem, we suggest to install stationary proxy called the Local Proxy Server to make ensure that the late mobile client can get the 1st segment as soon as arrive with less start-up delay compared to with others. In this paper, the main content of the VOD system is classified into four components, main server, local forwarders (LF), local proxy server (LPS) and number of mobile clients. The main server is a server that is used to store a lot of video files. LF is a stationary device used to replay the videos to its wireless coverage area. LPS is a stationary server used to store the 1st segment of each broadcasting video in order to reduce the delay. Clients are mobile devices which can receive and watch videos. The interconnection between the main server and LF either will be via a wired LAN or via an infrastructure-based wireless network. The devices (LF, LPS, and Clients) are equipped with a wireless network interface card (wNIC) in order to communicate with each other through IEEE 802.11b technique. The video file is divided into a number of equal-size segments. These segments are broadcast to LF's by the main sewer. The LF will disseminate the video into its coverage area by broadcasting these segments through a number of channels. Clients join one of these logical channels and view the video as shown in Figure 1, the figure shows the logical broadcasting channels of the LF, and how the clients join these channels.

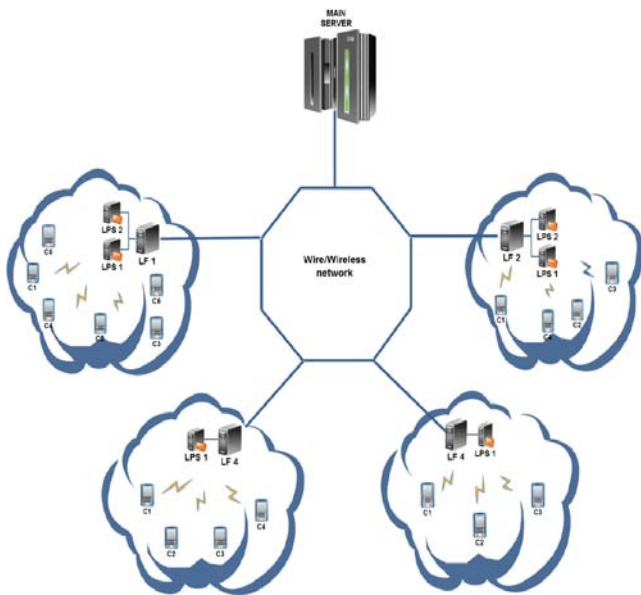


Fig.1. System Architecture of PSCM Scheme for VOD System

IV. BROADCASTING TECHNIQUE FOR PSCM SCHEME

In the main server sends the videos to the LF. The LF utilizes SB protocol as a broadcasting technique to broadcast the video to the clients where the video is classified into a number of equal-sized segments. These segments are periodically broadcasted over number of logical channels one

by one according to the scheduled time of the SB protocol. In SB protocol, the number of segments is equal to the number of logical broadcasting channels. The number of the logical broadcasting channels is determined according to the bandwidth of the transmission media. This bandwidth is logically divided into k logical broadcasting channels. Each video is broadcasted over K logical channels in order to increase the chance of the clients to get the video at the proper time.

The bandwidth required by the system is considered constant and system can meet any number of requests. This justifies the use of the broadcasting technique in the system. In the PSCM scheme, the whole video is divided into K equal size segments (Seg1, Seg2, Seg3, ..., SegK). The duration of each segment is $D_i = V/K$. The numbers of every logical broadcasting Channel i must be between ($1 \leq i \leq K$). It is decided that the provider bandwidth is $P_b * K$ for the 2nd video and so on. This bandwidth is partitioned into physical channels (Channel i) repeatedly by broadcasting the video starting from (Seg1) and until the end of the video (SegK) with a transmission rate (T_r) that is equal to the playback rate (P_b) as shown in Figure 2. The Client_x can join Channel1 and wait for the beginning of 1st segment (Seg1) to download and playback it. After that, Client_x switches to the next segment (Seg2) for playback. This process is repeated for the subsequent segments until the last segment (SegK) is downloaded from Channel1. Equation 1 and 2 follows the definition.

$$D_i = \frac{V}{K} \tag{1}$$

$$V = \sum_{i=1}^k D_i \tag{2}$$

Where, D_i is the duration of each segment, V is the length of the video and K is the number of the channels. The equation that is used to determine the number of logical channels (k) is as follows:

$$T_r \times K \times N_{vi} \leq b \quad \text{where } i = \{1, 2, \dots, n\} \tag{3}$$

Where T_r is the bandwidth transmission media, N_{vi} is the number of videos and K is the number of logical channels.

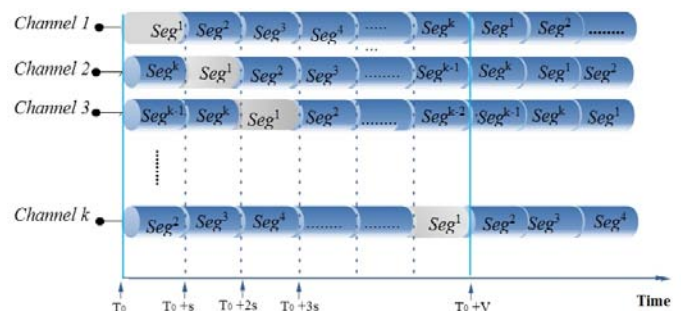


Fig. 2. Broadcasting Mechanism of PSCM scheme

Figure 2 illustrates the details of SB mechanism of broadcasting the video over the logical channels, where Channel 1 starts broadcasting the video segments sequentially. After a period of time (equals to the time of the segment), Channel 2 also starts broadcasting the segments the same way as in Channel 1. The same mechanism is achieved for the rest of channels.

In SB technique, the video can be watched directly when the client arrives at the time T_0 of the video broadcasting on LF channel where (T_0) is the time when the broadcasting of the 1st segment starts. The client has to wait for a period of time (until the next broadcasting of the 1st segment starts on another channel) if this client arrive at (T_0+s) of the 1st segment broadcasting time.

V. CACHING MECHANISM OF THE PSCM SCHEME

The caching technique proposed in this thesis aims at reducing the delay that is caused by the broadcasting technique used. The delay occurs when the client misses the broadcast of the 1st segment of the video. To view the video, the client has to wait for the next broadcasting of the 1st segment on the same or a different channel. To reduce this delay, a new caching scheme called PSCM is proposed. Figure 3 illustrates a representation of one VOD system service area. In this representation, two clients (PDA 2 and PDA5) cache the 1st segment from LPS after it is missed form LF. When these clients miss the 1st segment that is broadcasted by LF1, the clients are cached the 1st segment form the LPS1. The rest of the segments should be retrieved from the LF after tuning into one of the LF logical broadcasting channels.

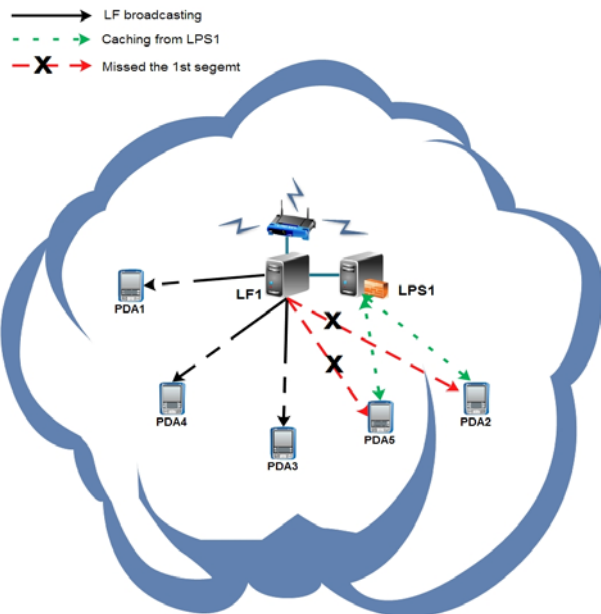


Fig. 3. A representation of one VOD System Service Area.

The PCSM scheme proposes using LPS. LPS is used for providing the 1st segment to late clients that miss broadcasting the 1st segment as soon as they arrive. The immediate provide of the 1st segment saves the clients time. This can be performed by avoiding the delay when waiting for the next broadcast of the 1st segment. In the PSCM scheme, each LF is responsible for passing a copy of the 1st segment of the videos to the neighbor LPS within its area. Figure 4 shows how the LF passes the 1st segment of the broadcasted videos to the neighboring LPS.

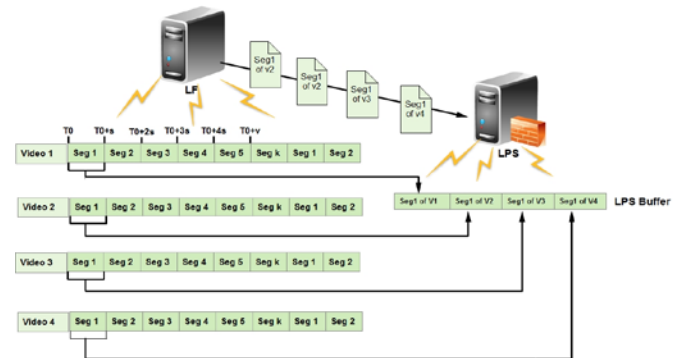


Fig. 4. The Process of Sharing the Videos 1st Segment of LF with LPS

VI. THE SCENARIOS OF PLAYBACK VIDEO IN PSCM SCHEME FOR VOD SYSTEM

In CPSM, the client can request to watch movie after one enters in the LF's areas. LF will check the arrival time of new client to know if the new client missed the 1st segment of the video or not. t_0 is the start time of the broadcasting video, so if the client arrive at time Arrival Time = ($T_0, T_0+s, T_0+2s, T_0+3s, T_0+4s$ or T_0+V), he/she can join that channel and watch the video, otherwise, if the client arrives at Arrival-Time of the broadcasting time= ($T_0+ \delta, T_0+s+\delta, T_0+2s+\delta, T_0+3s+\delta, T_0+4s+\delta$ Or $T_0+V+\delta$), where ($0<\delta<s$). This impels the client has missed the 1st segment. In this case, the LF will look up in the table to find which LPS is suitable for streaming the 1st segment of the video to the late client; then the LF sends information about the LPS. The client sends a request to the LPS and asks the 1st segment; at the same time the client joins the LF channel to get the rest of the segments. In the PSCM scheme, each LF maintains the information about the LPSs that are located in their area. Figure 5 illustrates the scenario and the LF table that are used for the load balancing of the client requests. The information in the table is used to balance the assigned requests among the LPSs in order to maintain the resources of the LPSs. Besides, by using this information in the table the CPSM can ensure a fair distribution of the requests among the LPSs, where none of the LPS has more loads than others. When late clients' request

a video, the LF check it table in order to know which LPS has less number of requests then retrieve the information about the suitable LPS and sends it to that client. The late client will cache the 1st segments from the LPS's who have less number of clients, in case that the LPSs have equal number of requests, LPS who has less ID address will handle the request of the late client. After that the LF will send the LPS which has less ID number as shown in Figure 5. The LPS will guarantee the new client to get the 1st segment as soon as he/she arrives with a less waiting time on mobile clients and with a reasonable delay.

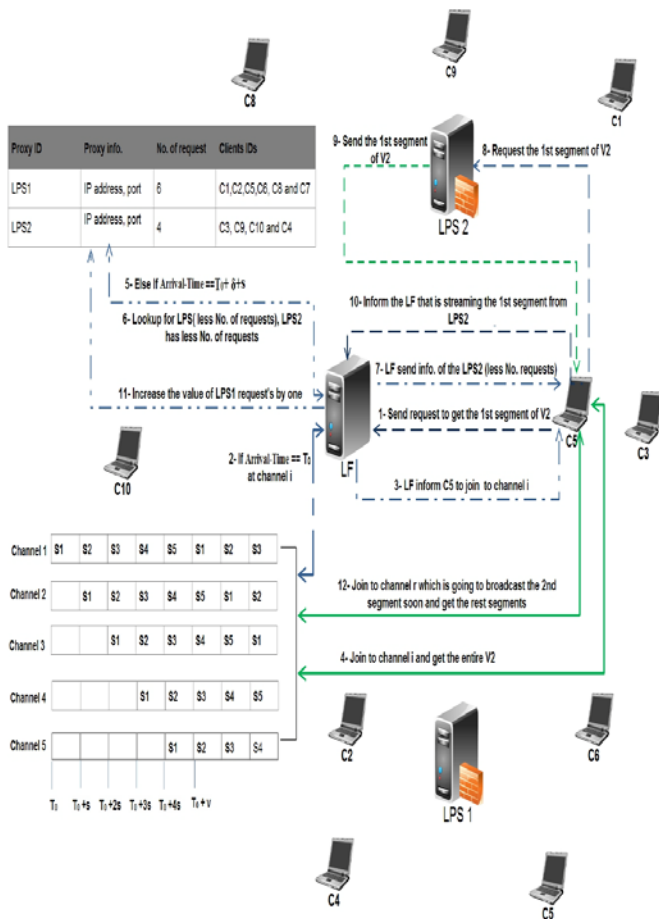


Fig.5. Shows a scenario when the late client (C5) missed the 1st segment

VII. EXPERIMENTAL RESULT AND DISCUSSION

This section represents the results that are produced by implementing the PSCM scheme for the VOD system. In addition, the following subsections discuss the service delay of requesting the video under multiple effective cases. The service delay is the time average of which a client has to spend starting from requesting the video till receiving its service. In particular, it is used to measure the way the VOD system performs as a truly on demand video service.

A. The Effects of The Number of Arrival Requests With Delay

The results of the delay effective of VOD system when it is measured depending on the number of the client's requests at a period of time as illustrated in Figure 6(a) and Figure 6(b). The results show the average delay of two caching scheme which are All-Cache and PSCM scheme. In All-Cache, needs at least one other client located in the area to cache the 1st segment and minimize the delay. In PSCM scheme, the late client cache the delay is effective even if there is one client in the area. It contributed to make the probability of the getting the video service is same for all clients. That means the client can get the 1st segment regardless if there is previous clients in the area.

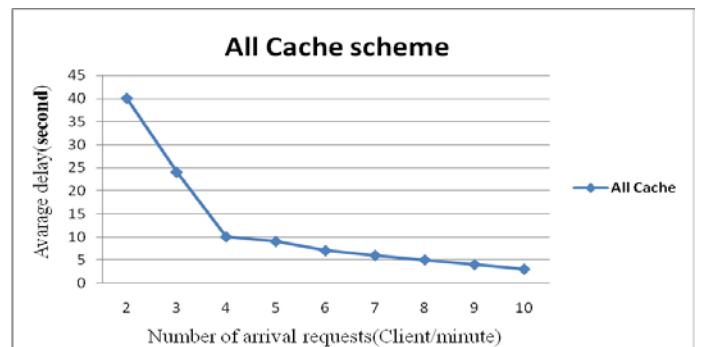


Fig.6. (a) Average service delay of All-Cache scheme depending on the number of arrival requests

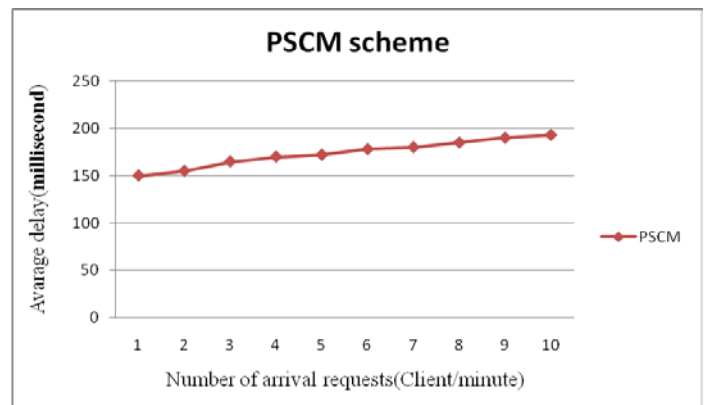


Fig.6. (b) Average service delay of PSCM Scheme depending on the number of arrival requests

B. The Effective of The Average Delay Depending n The Length Of The Video

The impact of the average delay depending on different video lengths where the VOD system is capable to handle different lengths of a video. According to Formula (2), the length of each segment can be maximized or minimized based on the total video length and the number of broadcasting

logical. Figures 7 (a) and Figures 7 (b) illustrate the effects of video length on the service delay in the All- Cache scheme and the PSCM scheme, respectively.

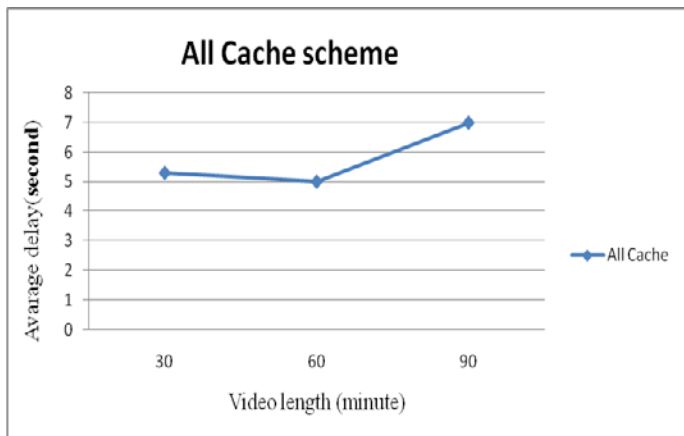


Fig.7. (a) Average delay of All-Cache scheme depending on different video lengths

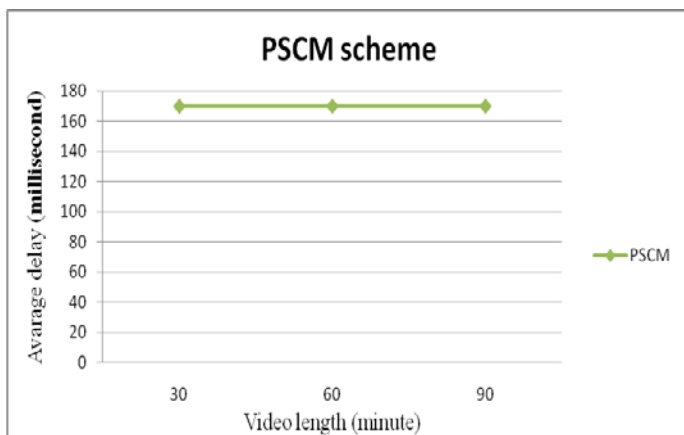


Fig. 7. (b): Average delay of the PSCM scheme depending on different video lengths

In Particular, the average of the delay is 5 seconds when the video length is 60 minutes in the All-Cache scheme, while in the PSCM scheme, the average service delay is 170 milliseconds. Besides that, the average service delay is 7 seconds when the length of the video is 90 minutes. In contrast, the average delay of the PSCM scheme maintained the same (170 milliseconds) when the length of the video is 90 minutes.

C. The Results of the Fail Probability Depending on the Number of Arrival Requests

The results of the fail probability that obtains the 1st segment video of the two caching schemes which are; the All-Cache scheme and the PSCM scheme depending on the arrival request number. As shown in Figure 8, the All-Cache scheme,

a failure is detected once the new client fails to find a free neighbor client who has already cached the 1st segment. In addition, a failure is also detected once the new clients fail to get the 1st segment video from the current cache. This failure of getting the video is due to the fact that the client who is caching the 1st segment is moved or is terminated from the system.

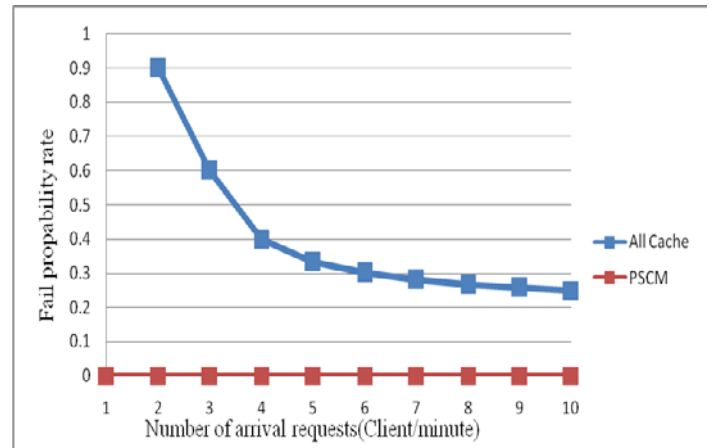


Fig.8. The results of the failure probability to get the 1st segment of the video.

VIII. CONCLUSIONS

This paper proposed a new caching scheme, which is called the Proxy Server Caching Mechanism (PSCM) for VOD system. This caching scheme proposed to solve the delay problem in mobile clients caused by using a broadcasting technique in that mobile VOD system over Ad Hoc network. In PSCM, the 1st segment of all videos is stored in a stationary server (LPS). This caching will minimize the delay by guaranteeing the late client to get the 1st segment as soon as it arrives. In order to maintain the recourses of the LPSs in the system, a load balancing method has proposed.

ACKNOWLEDGMENT

This project is part of a larger research work in the MCRG and this work was supported by Universiti RU's grant (1001 / PKOMP/ 817066) from the Universiti Sains Malaysia (USM).

REFERENCES

- [1] Saleh Ali Alomari and putra Sumari.,(2012), Effective Broadcasting and Caching Technique for Video on Demand over Wireless Mobile Network. KSII Transactions on Internet and Information Systems (TIIS), VOL. 6, NO. 3, pp. 919- 940.
- [2] Shiroom, R.G. (2007), IPTV and VoD services in the context of IMS. International Conference on IP Multimedia Subsystem Architecture and Applications, Vol. 2, No. 1, pp.1-5.
- [3] Facebook (2012). <http://www.facebook.com/> (Accessed on 2 Jan)
- [4] YouTube .(2012). http://www.youtube.com/t/press_statistics (Accessed on 2 Feb 2012).
- [5] Educlip (2012). <http://www.educclip.com/> (Accessed on 4 Nov)
- [6] Williams, B. and Camp, T. (2002). Comparison of Broadcasting Techniques for Mobile Ad Hoc Networks. In ACM Symposium on

Mobile Adhoc Networking and Computing (MOBIHOC 2002). New York, NY, USA, pp. 194 – 205.

[7] Duc AT, Thinh N.(2008). Broadcasting Techniques for Video-on-Demand in Wireless Networks. Book Chapter 1, department of Computer Science, University of Dayton, Dayton, OH 45469. Oregon State University, Corvallis, OR 97331.

[8] Gruber S, Rexford J, Basso A. (2000). Protocol considerations for a pre-caching proxy for multimedia streams, in Proc. of the 9th International WWW Conference, pp. 657-668.

[9] Park YW, Baek KH, Chung KD.(2000). Reducing network traffic using two-layered cache servers for continuous media on the internet, in Proc. Of the IEEE Int'l Conf. on Computer Software and Applications, pp. 389-394.

[10] Duc AT, Minh L, Kien AH. (2004). MobiVoD: A Video-on Demand System Design for Mobile Ad hoc Networks. Proceedings of the 2004 IEEE International Conference on MobileData Management (MDM'04). Berkeley, CA, pp. 212-223.

[11] Li-Shen J, Li-Ming T. (1998). Fast data broadcasting and receive scheme for popular video service. IEEE transactions on broadcasting, Vol. 44, No. 1, 1998.

[12] Paris JF, Carter SW, Long DDE. (1999). A hybrid broadcasting protocol for video on demand. In Proc. 1999 Multimedia Computing and Networking Conference (MMCN'99), San Jose, CA, pp 317-326.

[13] kien AH, Simon S. (1997) skyscraper broadcasting, A new broadcasting scheme for metropolitan Video on Demand systems. In Proceedings of ACM SIGCOMM 1997, Cannes, France.

[14] Hee J, Seong-min J, Sung-kwon P, Seung-hwan S, Dong-hwa Y. (2008). Interleaving harmonic staggered broadcasting scheme for video-on-demand services. Tenth IEEE International Symposium on Multimedia, 2008

[15] Kwon JB, Heom HY.(2002).Providing vcr functionality in staggered video broadcasting. IEEE Transactions on Consumer Electronics, Vol.48, No.1, pp.41-48.

[16] Gui YQ, Jung E, Choi Y, Choi HK. (2007). an efficient periodic broadcast scheme for mobile video -on demand system“ In Proc. Of international Conference on Information Technology (ITNG'07), pp. 888-889.

[17] L. Juhn and L. Tseng. Harmonic broadcasting for videoon- demand service. IEEE Transactions on Broadcasting. Vol 43, No.3, pp.268-271.

[18] Saleh Ali Alomari, Putra Sumari, Sadik Ali Taweel. (2011). An Efficient Popularity Cushion Staggered Broadcasting for Homogeneous and Heterogeneous Mobile Video-on-Demand System. International Conference on Wireless and Optical Communications (ICWOC 2011), Vol.4, pp.272-277.

[19] Liao, W. and Li, V. O. K. (1997). The split and merge protocol for interactive video on demand. IEEE Multimedia , Vol. 4, No. 4, pp.51-62.

[20] Saleh Ali Alomari, Putra Sumari. (2010). A Video on Demand System Architecture for Heterogeneous Mobile Ad Hoc Networks for Different Devices. International Conference on Computer Engineering and Technology, Vol.7, pp.700 – 707.

[21] Xie F, Hua K. (2009). A caching-based video-on-demand service in wireless relay networks. IEEE International Conference on Wireless Communications and Signal Processing, , pp. 1-5.

[22] Subhabrata S, Jennifer YR, Don T. (1999). Proxy Prefix Caching for Multimedia Streams. CMPSCI Technical Report 98-27 University of Massachusetts.

[23] Saleh Ali Alomari, Putra Sumari. (2010). A Video on Demand System Architecture for Heterogeneous Mobile Ad Hoc Networks for Different Devices. International Conference on Computer Engineering

and Technology, Vol.7, pp.700 – 707.

[24] Saleh Ali Alomari, Putra Sumari. (2010). A new Peer to Peer Caching Techniques for Transmitting the Video over Wireless Ad Hoc Network. (IJCSIS) International Journal of Computer Science and Information Security, Vol. 8, No. 3,pp. 239-245.

[25] Vaithegy D, Saleh Alomari, Putra S. (2011). Video on Demand Caching System using NIPBCS over Mobile Ad Hoc Network. JDCTA: International Journal of Digital Content Technology and its Applications, Vol.5, No.6, pp. 142 -154.

Saleh Ali K. Alomari



obtained his MSc and PhD in Computer Science from Universiti Sains Malaysia (USM), Pulau Penang, Malaysia in 2008 and 2013 respectively. He is a lecturer at the faculty of Science and Information Technology, Jadara University, Irbid , Jordan. He is Assistance Professor at Jadara University, Irbid , Jordan 2013. He is the candidate of the Multimedia Computing Research Group, School of Computer Science, USM. He is research assistant with Prof. Dr. Putra, Sumari. He is managing director of ICT Technology and Research and Development Division (R&D) in D&D Professional Consulting Company. He has published over 35 papers in international journals and refereed conferences at the same research area. He is a member and reviewer of several international journals and conferences (IEICE, ACM, KSII, JDCTA, IEEE, IACSIT, etc). His research interest are in area of multimedia networking, video communications system design, multimedia communication specifically on Video on Demand system, P2P Media Streaming, MANETs, caching techniques and for advanced mobile broadcasting networks as well.

Putra Sumari



is currently working as Assistant Professor of School of Computer Science, Universiti Sains Malaysia, Penang in 2009. Assoc. Prof Dr. Putra received his MSc and PhD in 1997 and 2000 from Liverpool University, England. Currently, he is a lecturer at the School of Computer Science, Universiti Sains Malaysia, Penang. He is the head of the Multimedia Computing Research Group, School of Computer Science, USM. He is Member of ACM and IEEE, Program Committee and reviewer of several International Conference on Information and Communication Technology (ICT), Committee of Malaysian ISO Standard Working Group on Software Engineering Practice, Chairman of Industrial Training Program School of Computer Science USM, and Advisor of Master in Multimedia Education Program, UPSI, and Perak.

Comparative Study of Different Methods for Measurement of “Smartness” of Smart Devices

Ahmet Al Zarqa, Tarik Ozkul, and A. R. Al-Ali

Abstract—“Smartness” of mobile devices is often attributed to the quality of the user interface. Quality of user interface has become a dominant factor in determining how easy to use today’s smart devices. Being intuitive, requiring fewer number of steps to achieve the goal are few of the desired characteristics expected from a well-designed user interface. Measuring the “quality of user interface” objectively has been a difficult task because of lack of appropriate yardsticks. This study tries to define “yardsticks” to measure the quality of user interface and utilizes this new tool to compare quality of several commercially available mobile phone operating systems. Study also shows several different techniques for interpreting the results generated by the tool and compares these results to opinions of real human users.

Keywords—User interface, Machine Intelligence Quotient, MIQ, User Intelligence Quotient.

I. INTRODUCTION

TODAY mobile gadgets became an important part of our lives. The intent of this study is to find an objective way of measuring quality of user interface of smart devices. As smart phones and similar swipe activated tablet devices became part of our everyday life, the issue has started to gain more and more importance. Today’s demanding customers expect their mobile devices to act as “smart” as possible when they are trying to accomplish a task with them. It is expected that modern handheld devices assist their operators to accomplish complex tasks as easily as possible. This is essentially done by the user interface and the operating system of the mobile device. There have been several studies in the literature attempting to measure user interface quality of mobile devices [1]-[4].

In this study, a new approach to measure user interface quality is suggested. The starting point of this new approach is measuring “smartness” of the user interface. Indeed what users’ desire from the mobile gadgets is “smartness”. In order to explain the process, the term “smartness” need to be defined.

A. Al-Zarqa is a graduate student in the Computer Science and Engineering Department of American University of Sharjah. PO Box 26666 Sharjah UAE. (e-mail: b00022890@aus.edu)

T. Ozkul is with the Computer Science and Engineering Department of American University of Sharjah. PO Box 26666 Sharjah UAE.(e-mail: tozkul@aus.edu, phone: +971 6 515 2455, Fax: +97165152979)

A. R. Al-Ali is with the Computer Science and Engineering Department of American University of Sharjah. PO Box 26666 Sharjah UAE. (aali@aus.edu)

Fortunately there is some ground work done by researchers in defining “intelligence” of robotic machines. The terminology is initially developed for defining intelligence of robots, but the concept of “intelligence” can be easily extended to defining “smartness” of smart devices.

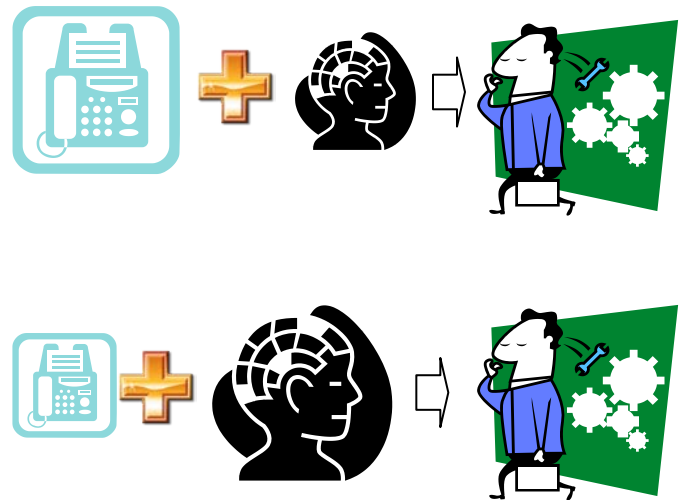


Fig. 1 Two different ways of completing a given task is shown. Top case shows an intelligent machine where operator needs to spend relatively less effort to do a task. Bottom case shows a less intelligent machine where operator needs to spend more effort to do the same task. Second machine has lower MIQ.

Machine Intelligence Quotient, or widely known as MIQ, introduces a philosophy for measuring intelligence level of machines. In this approach, “intelligence of the machine” is proportional to the level of help it provides for its master – human user- to complete his/her task. In this philosophy, tasks are for the human beings to tackle. Only human beings can initiate and finish a task. Machines can only help human beings to make their tasks easier. Intelligence level of the machines is graded according to the degree of help they provide to their human operator. Imagine two different scenarios where in the first case machine number one is very helpful in completing a task and in the second case machine number two is only marginally helpful to its human operator to complete the task. As shown in Fig. 1, machine number one is considered to have more “intelligence” than machine number two. MIQ methodology defines an elegant way of determining boundaries of what human master do, and what machine does to help. End result of this process is an

objective way of determining the amount of work done by the human master and the machine counterpart. More information about this process is available in the following references [5]-[8].

II. OVERVIEW OF TECHNIQUE USED

In this study, we have adapted MIQ philosophy to define the relationship between the human operator and the smart machine. In a typical case, human operator tries to achieve a task like finding a person's phone number from the contact number list to make a phone call or send an SMS message. Achieving this task requires human operator to go through different menu choices, make selections and then make further selections depending on the previous choices made. The human operator needs to initiate the task by tapping into appropriate buttons on the screen, and then understand the menu choices presented by the user interface on the screen to make further selections and entries. After several such iterations, user interface displays the phone number of the desired person on the screen and upon approval the call is placed. A simple task like this requires several rounds of interactions between the human operator and the mobile device. If the human operator achieves his or her purpose in the shortest possible time, with as few interactions as possible, this is attributed to the "smartness" of the mobile. If the same task is achieved with more steps and more iteration on a different mobile device, this is attributed to the smartphone being "less smart". This is in general how human operators rate the smartness level of mobile devices.

If the interaction process between the human operator and the smart phone examined carefully, the following factors appear to be effective in giving perception of "smartness" for mobile devices [9];

1. The number of steps required to achieve a given task, (e.g. How many steps required to achieve the task)
2. Ease of entering information into the smart device (e.g. Physical difficulty of swiping, entering info into device, size of buttons, sensitivity of the screen play a role in this.)
3. Ease of understandability of menu choices presented on the smart phone screen, (e.g. how cluttered the screen, how easy to decipher things on the screen, how understandable the icons are.)
4. Speed of response of the smart device. (e.g. after making an entry, how fast the device responds and displays the response screen.)

Today's discerning user is very demanding from the hardware as well as the user interface of the smart device. As far as users are concerned both hardware and software are considered contributing to the "smartness" of the smart device. Opinion polls of the users indicated that slow response rate of user interface, although it may be purely

due to hardware issues, is considered debilitating to the "smartness" of the smart device.

The developed model takes into account all the factors stated above and generates an index which is proportional to the level of help provided by the user interface to the human user for completing a task. This unit-less index is called UIQ, "User Interface Quotient". UIQ is generated in an objective manner purely by observing and timing the response of the human user. Detailed explanation of the model will be done in the next section.

A. Formal Procedure for Calculating UIQ

The basic philosophy of determining the intelligence level of a smart system is given as follows [9]. A smart system is there to help a human operator to accomplish a task. Accomplishment of the task is the sole responsibility of the human operator and machines are there to help the human operator to accomplish the task. Accomplishments of a task require effort and intelligence from the operator. This effort is called "CIQ" which stands for Complete Intelligence Quotient for accomplishing a certain task. In case of smart phones, this may be an operation of sending an SMS to a person or entering a website using the smart phone. The human operator has to spend a certain amount of effort for accomplishing this task. The amount of human effort required toward accomplishment of this task is called "HIQ" which stands for Human Intelligence Quotient. If the human operator were to complete this task on his own with a simple bare-bone phone, this would be indicated as:

$$CIQ = HIQ$$

Now, if we consider the existence of a smart phone to help the human operator, then the equation would be modified as follows:

$$CIQ = HIQ + UIQ; \text{ which can be written as:}$$

$$UIQ = CIQ - HIQ$$

In this equation, UIQ is the intelligence quotient of the smart phone helping the human operator. The smart phone helps the human operator to accomplish the task. As the smart phone is helpful in doing this, we consider that the work done the human operator becomes less (HIQ decreases and UIQ increases). When comparing the intelligence level of two different smart phones, we look into the level of help they provide to the human operator. The one that helps the human operator more in fulfilling the task at hand is considered to be the one with the higher UIQ.

In summary, the amount of total intelligence required for accomplishment of a specific task is constant. The smart phone that helps its operator to accomplish this task with the least amount of effort is considered to have UIQ (smart). The UIQ value is a relative index which indicates the level

of smartness of two or more smart phones; the higher the value, the higher the intelligence.

As in the case of sending an SMS to a person, if the task can be done easier, with less effort on a specific mobile phone, the corresponding operating system (user interface) is considered to have higher UIQ.

B. Intelligence Task Graph

Any task that needs to be tackled can be represented by a series of interactions between the human user and the smartphone. Tasks can be represented by a task graph which displays various subtasks required to complete the whole task. The state diagram, as seen in Figure 2, consists of circles that represent the task and its complexity, and arrows indicated the flow of tasks from one to another. The diagram also distinguishes and shows the tasks that are completed by the human controller and those that are completed by the intelligent machine.

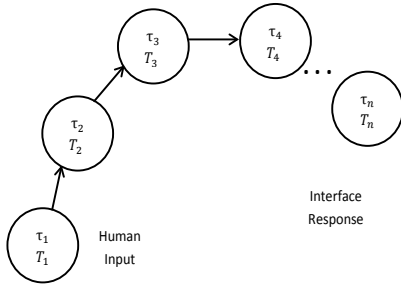


Fig. 2 Intelligence Task Graph

An intelligent task is made up of various smaller tasks, called subtasks, which are represented in a set called T:

$$T = \{T_1, T_2, T_3 \dots T_n\} \quad (1)$$

Each subtask may have a different level of complexity, represented by τ :

$$\tau = \{\tau_1, \tau_2, \tau_3 \dots \tau_n\} \quad (2)$$

Equations (1) and (2) show the set of subtasks and their complexities. As users try to tackle a subtask, there will be information transferred from user to machine or from machine to user. Data Transfer Matrix, which is designated as F, represents the amount of data transferred from one subtask to all the other subtasks during the completion of the main task. During the execution of the tasks, some tasks are handled by the smart device and some others are handled by the human operator. Task Allocation Matrix A indicates which tasks are handled by the human operator and which tasks are handled by the smart device. A and F are two matrices shown by equations (3) and (4):

$$F = \begin{bmatrix} 0 & f_{12} & f_{13} & f_{14} & \dots & f_{1j} \\ f_{21} & 0 & f_{22} & f_{23} & \dots & f_{2j} \\ f_{31} & f_{32} & 0 & f_{33} & \dots & f_{3j} \\ f_{41} & f_{42} & f_{43} & 0 & \dots & f_{4j} \\ \dots & \dots & \dots & \dots & \dots & \dots \\ f_{i1} & f_{i2} & f_{i3} & f_{i4} & \dots & 0 \end{bmatrix} \quad (3)$$

In matrix F, f_{ij} represents the amount of data being transferred from subtask T_i to T_j .

$$A = \begin{bmatrix} a_{11} & a_{12} & a_{13} \\ a_{21} & a_{22} & a_{23} \\ a_{31} & a_{32} & a_{33} \\ a_{41} & a_{42} & a_{43} \\ \dots & \dots & \dots \\ a_{n1} & a_{n2} & a_{n3} \end{bmatrix} \quad (4)$$

Matrix A has three columns. Column 1 represents tasks completed by the intelligent machine, column 2 represents tasks completed by the human operator, and column 3 represents the tasks completed by the non-intelligent machine component if there are any. Non-intelligent machine component is usually the basic electronics that take care of the phone functionalities like placing a call through GSM network.

C. Control Intelligence Quotient and Human Intelligence Quotient

Using the variables defined in the above section, the formula for “Complete Intelligence Quotient” (CIQ) and the “Human Intelligence Quotient” (HIQ) are given as follows:

$$CIQ = \sum_{i=1}^n a_{i1} \cdot \tau_i + \sum_{i=1}^n a_{i2} \cdot \tau_i$$

$$HIQ = \sum_{i=1}^n a_{i2} \cdot \tau_i + Cmh \sum_{i=1}^n \sum_{j=1}^n a_{i1} \cdot a_{j2} \cdot f_{ij} + Chm_i = 1ni = 1n a_{i2} \cdot a_{j1} \cdot f_{ij}$$

In this formula, Cmh and Chm parameters define the “interface complexity values” that describes the difficulty of transferring data from a smart device to human and from human to smart device, respectively. The values of these variables indicate the difficulty of entering or interpreting data, and typically vary from 0 to 1. In this context “0” means little or no physical difficulty entering data into the mobile device, whereas “1” means extreme difficulty in entering the data to the mobile phone. To give an example, a mobile with extremely small keypad would have higher Chm than a mobile with large keypad. For well-designed system this parameter is expected to be around 0.05.

D. User Interface Intelligence Quotient (UIQ)

UIQ user intelligence quotient is the contribution of the intelligent device towards completion of a certain task. CIQ, complete intelligence quotient, is the total effort exerted by

both human and machine together in completing the task. HIQ, human intelligence quotient, is the effort exerted by the human operator alone for completing the task. According to these definitions,

$$CIQ = UIQ + HIQ \text{ which leads to;}$$

$$UIQ = CIQ - HIQ$$

UIQ is the work done by the user interface alone toward accomplishment of the task. Task graph is color coded to distinguish human and machine tasks. Gray colored tasks in Fig. 3 are performed by the smart device.

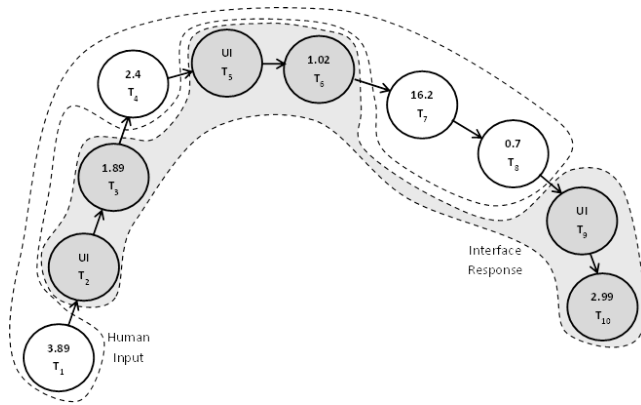


Fig. 3 Typical task graph is shown for accomplishment of a specific task. Gray colored circles indicate tasks done by the smart device.

III. PROCEDURE FOR EXPERIMENTS

The goal of the study is to find an objective procedure that generates a “smartness” score for the user interface. This score will be generated in an objective manner based on observations of the user. This score is expected to reflect the actual opinion of the user.

Experiments are conducted with 10 human operators who have similar age, education and dexterity level. Users are asked to accomplish several different tasks on a set of given smart devices.

The process is recorded so that important parameters are video recorded and parameters are extracted after the

experiment is finished. Users are asked to complete the given tasks on different smart devices and asked to rate the relative “smartness” of the devices after the completion of the experiment.

UIQ index is calculated for each one of the tasks, for each one of the user using the procedure given in the previous section.

UIQ figures are compared to the user evaluated “smartness” figures in two different ways.

1. The raw index data generated by the UIQ procedure for the task is compared to user perceptions,
2. A fuzzy logic system is developed which uses the raw data of UIQ and generates an index of “smartness” based on a fuzzy model of smartness. Later this is compared to user perceptions.

IV. FUZZY LOGIC SYSTEM

Fuzzy logic system is designed to generate a number indicating “smartness” based on raw UIQ data. The system expects the following inputs:

1. Complexity of each subtask.
2. UIQ data
3. Total number of subtasks.
4. Cmh and Chm.

The complexity of each task is evaluated by examining the time it takes to complete.

These complexities account for the human input, as for the interface input it is handled by the interface response. Each task can have a different number of subtasks with different smartphones. FIS system is used to generate one single output for a specific mobile device. Cmh and Chm values are also need to be entered into the FIS system, since they play a role in determining the smartness of the user interface.

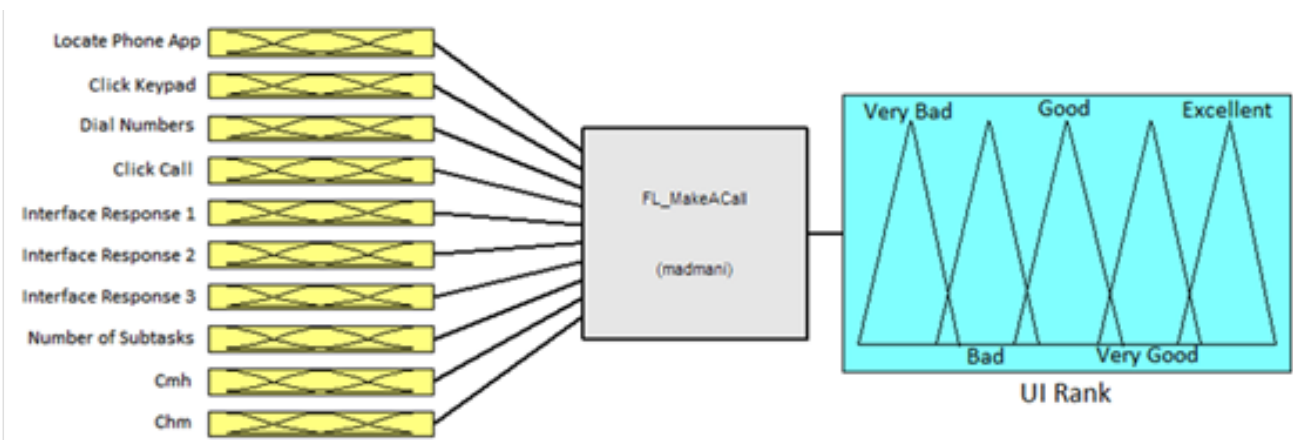


Fig. 4 FIS model for “Make a Call” Task

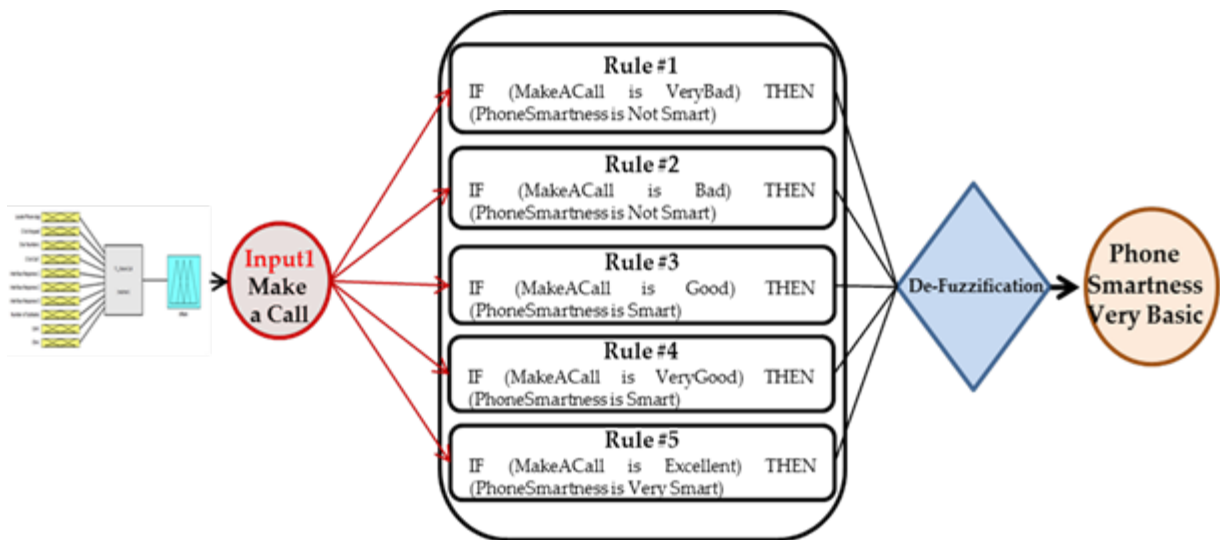


Fig. 5 FIS rules for interpreting quality of “Make a Call” Task

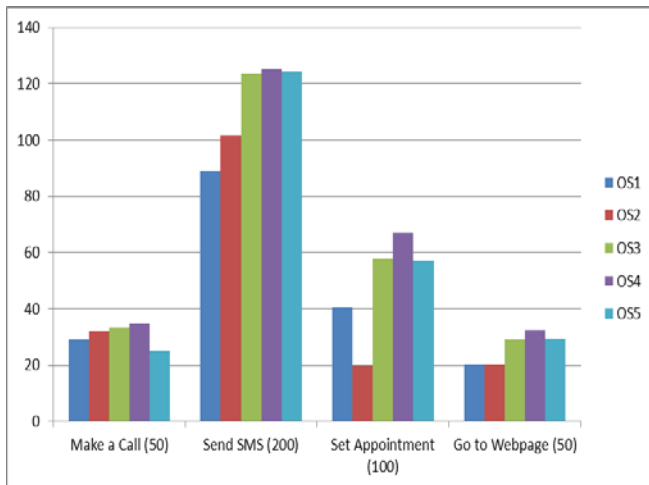


Fig. 6 UIQ results for 5 different smartphones, 4 different tasks.

Figure 4 shows the overall look of the FIS system. Figure 5 shows the some of the FIS rules. The output of the FIS indicates the “smartness rank” of the user interface.

V. RESULTS OF EXPERIMENTS

User experiments are conducted with 10 different users, with five different smart phones (each with different operating systems) for four different tasks. Altogether 200+ different experiments were conducted to get the raw data reflecting interaction between smartphones and user reactions.

Due to excessive amount of data, only refined results will be provided in this section.

All of the smartphones are selected from commercially available units at the time of study. Each smartphone is selected to be working with a different operating system. Phones are selected from the most popular units available at the time of experiment. In order to avoid any commercial

repercussions, names of smart phones and operating systems will not be revealed in the results. Since smartphones are associated with specific operating systems, only operating systems will be indicated in the results.

Figure 6 shows relative UIQ results of 5 different mobiles for 4 different tasks. The values are averaged for 10 users. The parameters were extracted from video recorded experiments while users interacted with the mobile every step of the way while performing the designated tasks. Extracted parameters were inputted to the matrix formulas and presented below.

Figure 7 shows the results of the Fuzzy logic model. The raw data gathered from the video recorded experiments were inputted into the fuzzy logic model and generated results are displayed in the figure.

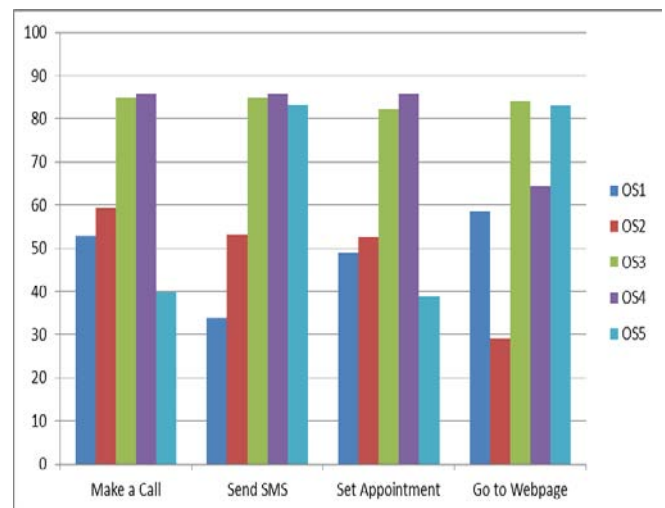


Fig 7 Results for Fuzzy Logic model

Figure 8 shows the survey results provided by the human users after conducting the experiments. The human users were asked to rank the “smartness”, in other words “ease of use” of the mobile phone for performing the designated task. Each application is ranked by the human users individually. The results were averaged for the 10 users and displayed in Figure 8. The results indicated in this figure are the actual perceptions of the users after using five different mobiles for performing the tasks.

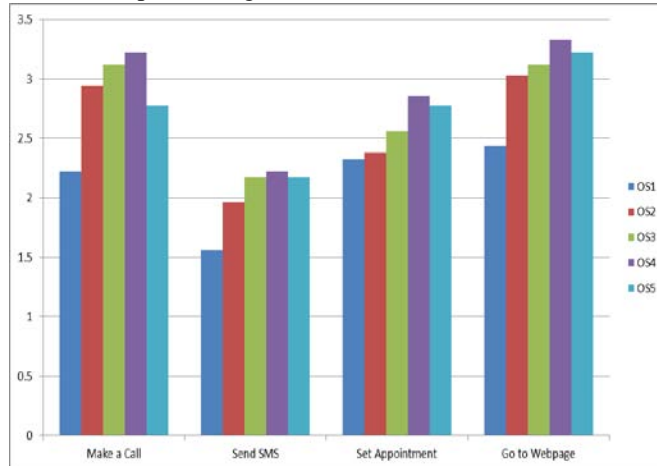


Fig. 8 Survey results reflecting opinion of the users about “smartness” of the smartphones.

VI. CONCLUSION

The results shown in Figures 6, 7 and 8 are refined results of 200+ experiments conducted with ten different users, using five different smart phones and performing four different tasks with each one of these smart phones.

Figure 8 indicates the opinion of the users regarding “smartness” of the mobiles for performing a given task. These results are found through user surveys and reflect how users feel toward the specific operating system while performing different tasks. Grading is relative and indicates that users found to perform some tasks easier in some of the smart phones. The results are averaged for all test users.

Figure 6 shows the results of UIQ methodology after extracting raw data from the experiments. The results are generated using observed and measured data from the experiments and calculated using the described UIQ process. The averaged UIQ results are found to be in parallel with the survey results shown in Figure 8.

Figure 7 shows the output of the fuzzy logic model which operates on the raw UIQ data. Rules of the fuzzy model are designed to reflect the user opinion. The results are generated by the FIS system based on data extracted through UIQ experiments.

The results indicate that there is parallelism between UIQ results and the survey results which proves validity of the approach.

REFERENCES

- [1] D. Park, J. H. Lee and S. Kim, “Investigating the affective quality of interactivity by motion feedback in mobile touchscreen user interfaces,” *International Journal of Human-Computer Studies*, vol. 69, no. 12, p. 839-853, Dec. 2011.
- [2] W. Haiyan and Y. Baozhu. “A Data-processing Mechanism for Scenario-Based Usability Testing,” *Computing, Control and Industrial Engineering (CCIE)*, vol. 1, pp. 395–398, 2011
- [3] Y. Yu and Z. Liu, “Improving the Performance and Usability for Visual Menu Interface on Mobile Computers,” in *Proc. of the International Conference on Advanced Visual Interfaces*, pp. 369-372, 2010.
- [4] H. Liang et al., “A Remote Usability Testing Platform for Mobile Phones,” *Computer Science and Automation Engineering (CSAE)*, pp. 312-316, 2011.
- [5] H. Park, B. Kim and K. Lim, “Measuring the Machine Intelligence Quotient (MIQ) of Human-Machine Cooperative Systems,” *IEEE Trans. on Systems, man and Cybernetics* 31:89-96, 2001.
- [6] H. Park, B. Kim and G. Lim, “Measuring Machine Intelligence for Human Machine Cooperative Systems using Intelligence Task Graph,” in *Proc. the International Conference on Intelligent Robots and Systems*, 1999, pp. 689-649.
- [7] A. Anthony and T. C. Jannett, “Measuring Machine Intelligence of an Agent-Based Distributed Sensor Network System,” in *Proc. International Joint Conferences on Computer, Information and Systems Sciences and Engineering*, Dec 2006.
- [8] T. Ozkul, “Determination of Machine Intelligence Quotient (MIQ) Gain of a Mechatronic System by Addition of Visual Guidance,” in *Proc. International Symposium and Mechatronics and its Applications*, Mar. 2009.
- [9] El Zarka, Ahmed, and Tarik **Ozkul**. “Assessment Metrics for Intelligence Level of Human-Computer Interface.” *Journal of Emerging Trends in Computing and Information Sciences* 4, no. 3 pp. 319-352
http://cisjournal.org/journalofcomputing/archive/vol4no3/vol4no3_1_2.pdf

A High End Capacity in Digital Image Steganography: Empowering Security by Mottling through Morphing

Sanjay Bajpai, Kanak Saxena

Abstract— One of the many techniques to provide security during data communication is digital image steganography. Embedding capacity and distortion are the two main factors that play a vital role while hiding a message in an image. A balance has to be maintained between the two so that neither does affect the other. Proposed paper discusses the techniques which comprises of two phases that leads to formulation of very secure platform with high embedding capacity. First phase mottles the arbitrary image by morphing through two parameters – text or/and image to obtain the cover image which depends upon the features of the chosen image. Second phase embeds the text message of sufficient large length incorporating multi-keys and compound operators in the algorithm to cater robust security. A bunch of images having almost the same texture are transmitted over the network to make the extraction process further complex. Our experimental results prove the horizon touching embedding capacity with extra security layer.

Keywords—Distortion, Embedding capacity, Extraction, Morphing, Mottle, Multi-keys.

I. INTRODUCTION

DATA Security is one of the most important challenges being faced by all kinds of organizations. Many companies have explored that how critical is the information to get success in their business or operations and very few have managed to adopt effective measures to make their information secure, avoiding unauthorized access, preventing intrusions, stopping secret information disclosure, etc. Data storage in digital form has out-weighed the traditional approach because of its simplicity in the operations like storing, maintaining, updating, retrieving and very easy and cheap transmission. Since vice and virtue moves together and it is not an exception. We have to compromise with privacy and security. A lot of effort has been done and is continuous to protect our valuable data and from misuse by unethical persons. Copyrights of our data can be enforced by watermarking [1] – [3]. Cryptography is another science of securing data by dismantling it using some algorithms and

encryption-keys [4], [5] but it gives a clue to the intruders that something important is hidden and it gives a thinking reason on that way. Steganography is evolving as a robust method for securing data as it does not give a clue to suspect. It is an art and science of hiding data in other innocuous medium [6] – [8].

A. Brief History and Applications

Historically, it is not new to the present era and has been in use since a long time but in other form. Plan designed by Alice and Bob [9] to escape from the prison through communication which was keenly observed by the warden Wendy. They used innocuous object to accomplish communication without giving any reason to suspect. Similarly, Greek soldiers engraved their message on the wood and pasted it with wax to hide it [10]. In 5th century BC, a slave's head was shaved to hide information and sent when his hair grew back [11] – [13]. Its application spectrum has spawned in many areas including confidential communication, secret data storage, protection of data from alteration, Medical Imaging System, biological traits, bank details, important defence information and many more [14] – [17].

B. Related Terms

It uses *cover image* which is the carrier of hidden message and should have ordinary and innocuous appearance so that it does not arouse any suspicion. *Stego image* is the cover image having the message concealed in it and used for extracting the message at the receiver end [18] – [20]. *Stego key* is a secret key that can be either single or composite, which is used to embed message in the cover image and extract message from the stego image. The key can be generated either by performing some calculations based on the texture and size of the cover image or by a pseudo random number. Basic mechanism of steganography is shown in Fig. 1. *Embedding domains* refer to the characteristics of the cover image that will be used to hide the message in it. It can use the spatial domain techniques or transform domain techniques. Former is a case when pixels of the image are modified directly for embedding and in later case images are mathematically transformed before actually embedding the message [21]. It uses the medium like

Sanjay Bajpai is with the Lakshmi Narain College of Technology, Bhopal, affiliated to Rajiv Gandhi Technical University, Bhopal (Madhya Pradesh), INDIA. M: +91 9425642238; (e-mail: sbajpai31@gmail.com).

Dr. Kanak Saxena is with Samrat Ashok Technological Institute, Vidisha (Madhya Pradesh), INDIA. (e-mail: ks.pub.2011@gmail.com)

audio, video, text file and digital images to hide information in it in such a way that it looks like natural.

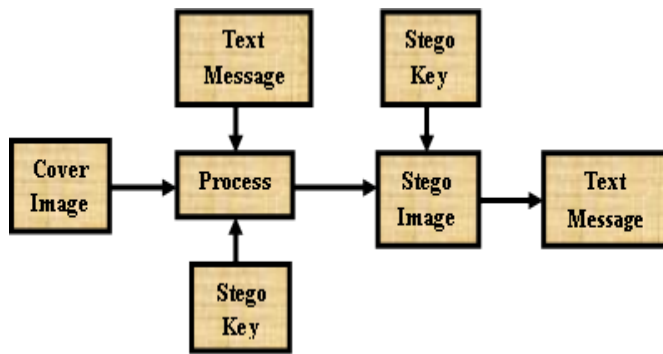


Figure 1. General Skeleton of Steganography

Remainder of the paper is organized as follows. In section 2, we shall briefly discuss about the existing methods. Section 3 describes the proposed method with analysis. Section 4 includes experimental results and comparisons with previous works. Finally, the conclusion, constraints and enhancement is presented in section 5.

II. EXISTING METHODS

Many algorithms have been developed in recent past to embed data in the cover medium. Basic principle for hiding data in the image is to replace the bits of the pixel by the bits of the text message and most common is the LSB substitution and for more detail about the LSB methods, readers are referred to [22]–[25]. LSB substitution methods works on the principle of replacing LSBs of the pixel selected either sequentially or randomly. It can be illustrated by the following relation

$$X_i * K + M_i = Y_i \quad (1)$$

where X_i is the i^{th} pixel of the cover image, K is the secret key to embed the message, M_i is the i^{th} message bit and Y_i is the i^{th} pixel of the stego image containing the message bit [26], [27]. Optimal Pixel Adjustment Procedure (OPAP) proposed by Chi-Kwon Chan [28] and et al. modifies the embedded bits to improve the visibility of the stego image. Adjustments are done on the basis of the pixel differences between the cover image and the stego image. Pixel Indicator Technique [29] is employed in the RGB images where two LSBs of one channel mark the existence of message in other two channels. Pixel Value Differencing [30] method emphasize the embedding in those areas of the image which are less susceptible to the human eyes. Since the difference between the pixels in smooth area is less than those of edge area so less distortion occurs in edge area and hence more bits can be embedded in this part. Arithmetic coding [31] can also be employed for data compression prior to embedding to increase security and embedding capacity. But it fails in case of embedding capacity as its basic principle is based on the difference between the lower bound and upper bound of each new symbol in the text message. Initially, the probability of occurrence of each

distinct symbol is calculated and its range is recorded. Upper bound and lower bound of the symbols are calculated by following formulas.

$$UB = LB + (CR \times UB \text{ of new symbol}) \quad (2)$$

$$LB = LB + (CR \times LB \text{ of new symbol}) \quad (3)$$

$$CR = UB - LB \quad (4)$$

where UB , LB and CR stands for upper bound, lower bound and current range respectively. Initially UB is set to 1 and LB is set to 0. As the length of the text message increases, both of its bounds converges to same value and hence cannot be applied. In our previous paper “submitted for publication” [32], we embedded message of very large length by compartmentalizing the pixels into its components by employing multi keys without compromising with security and distortion. Mahmud Hasan and et al. [33] devised a process which they named *block processing mechanism* and in that they divided the complete cover image into non-overlapping blocks of dimension 4×4 . They identified the Most Frequent Pixels (MFPs) and Second Most Frequent Pixels (SMFPs) of each block and deleted their occurrences. Then they encoded the secret message in these remaining pixels. We will compare their results in section 4. Sanjay Bajpai and et al. [34] incorporated Huffman coding algorithm in multi-key LSB substitution method to enhance both security and embedding capacity. Message length increased to about 1.5 times the number of pixels in the image and this number varies to both sides depending upon the domain to which this message belongs.

III. PROPOSED METHOD

A. Outlook

All the algorithms that are proposed so far like JSteg, Outguess [35], F5 [36], Singular Value Decomposition [37] which are known as transform domain techniques and spatial domain techniques which are discussed in the previous section, all focus only at point, that is, to embed the message in the image without causing any distortion. All these techniques manipulate the LSBs of the cover image. Number of LSBs generally varies from 1 to 3. Different regions of the image (smooth or edge etc.) and different pattern of pixels selected for embedding plays a vital role in stipulating the security and embedding capacity

B. Inception

Embedding capacity of stated methods vary from a few characters [31] to lakhs of characters [34]. The proposed approach is leaving this figure far behind. An arbitrary image is selected and mottled by masking all of its bits either by the bits of the text or by the bits of another image having different texture. This mottled image does not convey any specific meaning and has the look of modern art and is used as the cover image. All the bits of the cover image can be replaced by the bits of the secret message. Message length approximately

equal to three times the number of pixels in the cover image can be used for hiding. This will lead to the generation of another image having almost the same look as the cover image, a new modern art, called the stego image. Recipient is flooded with many such images in a bunch to make the process further complex. Recipient will be informed secretly later on by other means about the cover image, stego image and the keys. Both of these images will be used to extract the hidden message using the selected operation. General skeleton of the proposed process for embedding is illustrated in Fig. 2 and for extraction in Fig. 3.

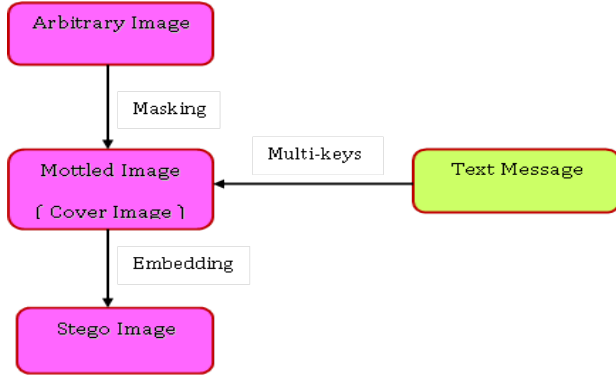


Figure 2. Embedding in the Proposed Process

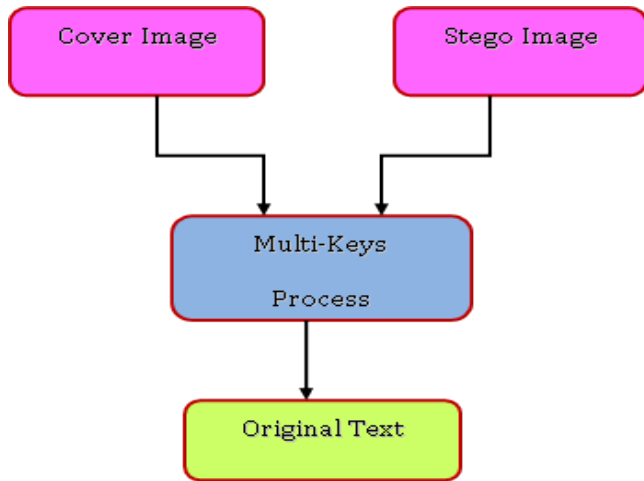


Figure 3. Extraction in the Proposed Process

C. Embedding Process

We used bitwise operators to embed data in the cover image. Bits of the pixel components are masked by the bits of the secret message using these operators. Experimental results reveal that it is impossible to extract the original message if bits are masked by either OR or AND operators. Message can be extracted if masking is done by either *Exclusive OR* (XOR) or *Exclusive NOR* (XNOR) operators. To increase the security and make the extraction process tough, we used both the (XOR and XNOR) operators for masking by varying the number of pixels.

Let N be the total number of pixels in the cover image which are equal to width × height (dimensions of the image). M slots (S) of varying capacity K are constructed to accommodate N pixels. S_i, 1 ≤ i ≤ M (M is the total number of slots) represent the ith slot of capacity K_i and K_i is the number of pixels in the slot S_i which satisfies the relation:

$$N = \sum_{i=1}^M K_i \tag{5}$$

Capacity of each slot S_i is calculated by the formula:

$$K_i = C \times K_{i-1} \tag{6}$$

where C is any constant (real number) such that 1 < C < 2. Initially K₁ is set to a value between 500 and 1000. Number of slots M depends on the constant C and

$$K_m = N - \sum_{i=1}^{M-1} K_i \tag{7}$$

We applied XOR and XNOR operators alternatively on each successive slot to mask the bits of the cover image to increase the robustness of the process. It will be almost impossible to guess that how many bits are masked by XOR operator and how many bits by XNOR since number of bits in each slot are constantly changing and governed by the constant C as shown in equation (6).

D. Algorithm-1 (Embedding)

1. Generate the mottled image from a selected image by morphing it.
2. Calculate the number of pixels, N, of the cover image by multiplying its dimensions (width×height).
3. Set the initial value for the capacity K₁ in the range (500 – 1000) and assign a value to the constant C such that 1 < C < 2 (such as 1.2, 1.45, 1.82 etc.).
4. Generate K_i = C×K_{i-1}; (i = 2 to M-1) and assign K_i pixels to slot S_i until K_i pixels are grabbed from the image and K_M = remaining pixels of the image assigned to S_M.
5. Read 3×K_i characters from the file and mask bits of these characters into the bits of the pixels of slot S_i (each pixel is fragmented into RGB components) by applying XOR and XNOR bitwise operators alternatively in the specified order.

E. Algorithm-2(Extraction)

1. Receive and decode the initial value of K, value of constant C and order of operations.
2. Decode the names of cover image and stego image.
3. Frame the slots S⁽¹⁾ and S⁽²⁾ of the cover image and stego image respectively and assign pixels to these slots by the equation (6).
4. Perform XOR and XNOR operations on the bits of the slot S⁽¹⁾ and S⁽²⁾ applying the order of operations alternatively and store the resultant bits into an temporary array T.
5. Transform the bits of array T into string to obtain the original message.

IV. EXPERIMENTAL RESULTS

Our results show that a message of very large length (3

times the number of pixels) is embedded successfully in the image. We tested our results on 20 different images and extraction is also accomplished successfully in all the cases. We achieved a high order of security by employing many parameters at the time of embedding and transmission. We constructed a set of 20 different images for transmission out of which there is only one pair of cover and stego images. To find out this pair, we have to check $^{20}C_2$ combination which itself is a big deal and after this, internal parameters play a vital role and it is almost impossible to determine which of the bits are masked by which operator. Generally, a medium size image has 4 lakh to 6 lakh pixels and each pixel is fragmented into its RGB components.

For testing purpose we reduced the size of image whose dimension varies from 160×120 pixels to 230×170 pixels. We embedded the message of length 57600 characters in one of the image whose dimension is 160×120 which is equal to $160 \times 120 \times 3$. Same pattern is adopted for images of other dimensions. Some of the images are shown for illustration which comprises of cover images, stego images and fake images. Task is to find a pair of cover and stego images to crack the code if internal parameters for embedding the messages are known. In real application, this number will be more and will increase the complexity. Images in Fig. 4 to Fig. 6 are the arbitrary selected images and images in Fig. 7 to Fig. 11 comprise the cover image, stego image and fake images.

Result Images



Figure 4. Scene-1



Figure 5. Scene-2



Figure 6. Scene-3



Figure 7. Scene-4



Figure 8. Scene-5

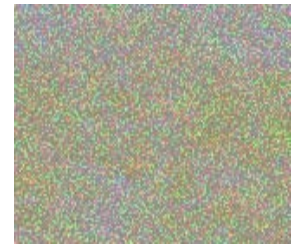


Figure 9. Scene-6

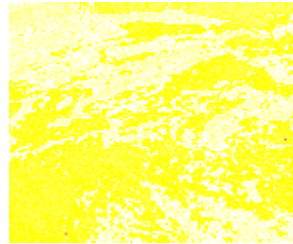


Figure 10. Scene-7

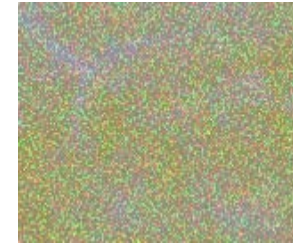


Figure 11. Scene-8

We compared the performance given by proposed algorithm with the algorithms proposed by Mahmud Hasan et al [33], our previous designed algorithms of [32] and [34] which clearly show that our results have been improved as shown in Table 1. Mahmud Hasan et al. [33] utilized only 32 bits out of 128 bits after performing calculations in their *block processing mechanism* and embedded 7 bits of a character. On an average they used 3.50 pixels per character. In [32], we fragmented the pixel into RGB components and stored one character per pixel and in [34] that is *embedding through Huffman coding*, we could store 1.5 characters per pixel. This figure fluctuates to both sides depending upon the type of message as discussed in [34]. Our proposed algorithm is able to embed 3 characters per pixel enhancing both the security and embedding capacity.

V. CONCLUSION

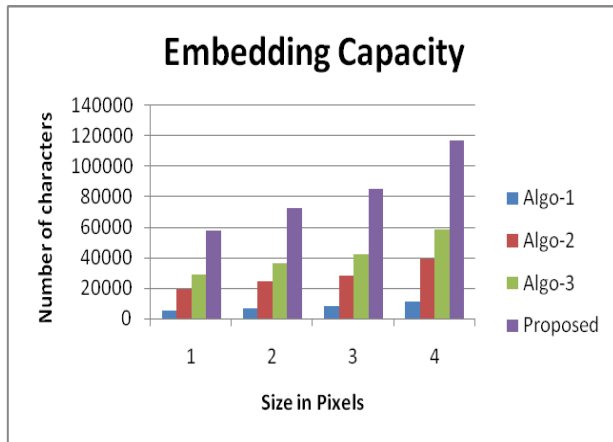
We can say with commitment that we have improved security mechanism and embedding capacity over the previous algorithms which is clearly visible in Table-1. There are other approaches also proposed by many authors but because of very low embedding capacity something around one or two bits per pixel, we have not included in the comparison process.

Here, we have to take care of that each bit (of all the pixels) of the selected image must be masked to get the cover image in mottled form. A secret message of length approximately equal to three times the number of pixels in the image can be embedded in the cover image. We observed while obtaining the stego image that there is not much difference between the cover image and stego image and both look of the same pattern. The embedding capacity can also be further enhanced by incorporating any suitable data compression technique.

Table 1
Comparative Performance Measurements

Cover Image			Number of Characters Embedded			
Size	Type	Dimension	Block Processing	Multi-key Embedding	Embedding through Huffman	Proposed

in KB		in pixels	Mechanism	Algorithm	Coding	Method
7	jpg	160×120	5485	19200	28800	57600
15	jpg	180×135	6942	24300	36450	72900
28	jpg	195×145	8078	28275	42412	84825
41	jpg	230×170	11171	39100	58650	117300



Graph – Showing the Performance Measurement

REFERENCES

[1] C. C. Chang, K. F. Hwang, M. S. Hwang, "Robust authentication scheme for protecting copyrights of images and graphics", IEE Proceedings on Vision, Image and Signal Processing 149(1) (2002), pp. 43–50.

[2] J. J. K. O' Ruanaidh, W. J. Dowling, F. M. Boland, "Watermarking digital images for copyright protection", IEE Proceedings on Vision, Image and Signal Processing 143(4) (1996), pp. 250–256.

[3] F. Y. Shih, Y.-T. Wu, "Robust watermarking and compression for medical images based on genetic algorithms", Information Sciences 175(3) (2005), pp. 200–216.

[4] H. J. Highland, "Data encryption: a non-mathematical approach", Comput. Secur. 16(1997), pp. 369–386.

[5] William Stallings, "Cryptography and Network Security: Principles and Practices." 3rd edition, 2003, pp. 259-281.

[6] D. Artz, "Digital Steganography: Hiding Data within Data", IEEE Internet Computing Magazine, Vol. 5, Issue 3, August 2002, pp. 75-80.

[7] H. Wang, S. Wang, "Cyber warfare: steganography vs. steganalysis", Commun. ACM 47(10) (2004), pp. 76–82.

[8] Alaa A. Jabbar Altaay, Shahrin bin Sahib, & Mazdak Zamani, "An Introduction to Image Steganography Techniques", 2012 International Conference on Advanced Computer Science Applications and Technologies, IEEE, 2012, pp. 122-126.

[9] Simmons G. J, "The Prisoners Problem and the Subliminal Channel", Proceedings of crypto '83, Plenum Press, 1983, pp. 51-67.

[10] Zahra Rafinezhad, Karim Faez, "Estimating PQ Algorithm Message Length Using First- and Second-order Statistics", 978-1-4673-2181-5/12/\$31.00 ©2012 IEEE, 2012, pp. 1-5.

[11] N. F. Johnson, S. Jajodia, "Exploring steganography: seeing the unseen", IEEE Computer 31(2) (1998), pp. 26–34.

[12] N. Provos, P. Honeyman, "Hide and seek: an introduction to steganography", IEEE Security and Privacy 1(3) (2003), pp. 32–44.

[13] S. Changder, N. C. Debnath, & D. Ghosh, "A Greedy Approach to Text Steganography using Properties of Sentences", Eighth International Conference on Information Technology: New Generations, IEEE, 2011, pp. 30-35.

[14] W. Bender, W. Butera, D. Gruhl, R. Hwang, F. J. Paiz, S. Pogreb, "Applications for data hiding", IBM Systems Journal 39 (3&4) (2000), pp. 547–568.

[15] S. Miaoou, C. Hsu, Y. Tsai, H. Chao, "A secure data hiding technique with heterogeneous data-combining capability for electronic patient records", in: Proceedings of the IEEE 22nd Annual EMBS International Conference, Chicago, USA, July 23–28, 2000, pp.280–283.

[16] B. Dunbar, "A detailed look at steganographic techniques and their use in an open-systems environment", Sans Info Sec Reading Room, 2002, [Online] Available: <http://www.sans.org/rr/whitepapers/cover/677.php>.

[17] Abbas Cheddad, Joan Condell, Kevin Curran, & Paul Mc Kevitt, "Digital image steganography: Survey and analysis of current methods", Signal processing 90 (2010) Elsevier, 18 August, 2009, pp. 727-752.

[18] Jamil, T., "Steganography: The art of hiding information is plain sight", IEEE Potentials, 1999.

[19] C. Munuera, "Steganography and error-correcting codes", Signal Processing Elsevier 87 (2007), pp. 1528–1533.

[20] Sanjay Bajpai, & Kanak Saxena, "Techniques of Steganography for Securing Information: A Survey", International Journal on Emerging Technologies 3(1), ISSN No. (Print): 0975-8364, 15 April, 2012, pp. 48-54.

[21] Ratankirti Roy, Suvamoy Changder, Anirban Sarkar, & Narayan C Debnath, "Evaluating Image Steganography Techniques: Future Research Challenges", 978-1-4673-2088-7/13/\$31.00 ©2013 IEEE, 2013, pp. 309-314.

[22] C. Kurak, J. McHugh, "A cautionary note on image downgrading", in: Proceedings of the IEEE 8th Annual Computer Security Applications Conference, 30 November – 4 December, 1992, pp.153–159.

[23] P. Alvarez, "Using extendeflle information (EXIF) file headers in digital evidence analysis", International Journal of Digital Evidence, Economic Crime Institute (ECI) 2(3) (2004), pp. 1–5.

[24] D. Neeta, K. Snehal, D. Jacobs, "Implementation of LSB Steganography and Its Evaluation for Various Bits", IEEE International Conference on Digital Information Management, June 2007, pp. 173-178.

[25] S. M. M. Karim, M. S. Rahman, and M.I. Hossain, "A New Approach for LSB Based Image Steganography using Secret Key", Appeared in 14th International Conference on Computer and Information Technology (ICCIT), March 2012, pp. 286-291.

[26] Bin Li, Junhui He, Jiwu Huang, & Yun Qing Shi, "A Survey on Image Steganography and Steganalysis", Journal of Information Hiding and Multimedia Signal Processing, Vol.2, Issue 2, April 2011, pp. 142-172.

[27] W. Bender, D. Gruhl, N. Morimoto, A. Lu, "Techniques for data hiding", IBM System Journal, vol. 35, no. 3, 1996, pp. 313-336.

[28] Chi-Kwong Chan, & L.M. Cheng, "Improved hiding data in images by optimal moderately significant-bit replacement", IEE Electron Lett. 37 (16), 2001, pp. 1017-1018.

[29] Adnan Gutub and et al., "Pixel indicator high capacity technique for RGB image based Steganography", WoSPA 2008 – 5th IEEE International Workshop on Signal Processing and its Applications, University of Sharjah, Sharjah, U.A.E. 18 – 20 March 2008.

[30] D. C. Wu, & W. H. Tsai, "A steganographic method for images by pixel-value differencing", Pattern Recognition Letters, vol. 24, no. 9-10, 2003, pp. 1613-1626.

[31] Paul G. Howard, & Jeffrey Scott Vitter, "Practical Implementations of Arithmetic Coding", International Conferences on Advances in Communication and Control (COMCON 3), British Columbia, Canada, 16-18 October, 1991, pp. 1-34.

[32] Sanjay Bajpai, & Kanak Saxena, "Enhancing Embedding Capacity by Compartmentalizing Pixels using LSB Techniques in Steganography", International Journal of Computers and Applications, ACTA Press, paper-id 202-3762, submitted – 03 April, 2013.

- [33] Mahmud Hasan, Kamruddin Md. Nur, & Tanzeem Bin Noor, "A Novel Compressed Domain Technique of Reversible Steganography", *International Journal of Advanced Research in Computer Science and Software Engineering* ISSN: 2277 128X, 03-March, 2012, pp. 1-6.
- [34] Sanjay Bajpai, & Kanak Saxena, "Enhancement of Security and Embedding Capacity through Huffman Coding in Steganography", *International Journal of Emerging Trends & Technology in Computer Science (IJETTCS)*, Volume 2, Issue 4, ISSN 2278-6856, July – August, 2013, pp. 73-78.
- [35] N. Provos, "Defending against statistical steganalysis", *In: Proceedings of tenth USENIX security symposium'01*, 2001, pp. 323-335.
- [36] Andreas Westfeld, "F5—A Steganographic Algorithm, High Capacity Despite Better Steganalysis", *Springer-Verlag Berlin Heidelberg*, 2001, pp. 289-302.
- [37] K S. Babu and et al., "Robust and High Capacity Image Steganography using SVD", *IET-UK International Conference on Information and Communication Technology in Electrical Sciences*, 2007, pp. 718-723.

Sparse Feature Based Analysis of RF Signal for Coronary Plaque Tissue Classification with Reference to the Neighboring Information of the Target Tissue

Shota Furukawa, Eiji Uchino, Tadahiro Azetsu, and Noriaki Suetake

Abstract—Tissue characterization of coronary plaque is important for a diagnosis of the acute coronary syndrome (ACS). In this study, we propose a method using sparse features and its neighboring information obtained by a sparse coding for the tissue characterization. In the proposed method, the radio frequency (RF) signal obtained by the intravascular ultrasound (IVUS) method is expressed by a linear combination of the basis functions extracted from learning signals by the sparse coding, and the code patterns of the expansion coefficients of the basis functions are used for the tissue characterization. The effectiveness of the proposed method has been verified by comparing the classification results of the proposed method with those of the frequency analysis applying to the data obtained from human coronary arteries.

Keywords—sparse coding, tissue characterization, coronary plaque, radio frequency signal, intravascular ultrasound

I. INTRODUCTION

THE major cause of the acute coronary syndrome (ACS) is a blood clot generated by the rupture of an unstable plaque which is abundant in lipid in a coronary artery. On the other hand, a dense fibrosis plaque tends to be stable in the coronary artery. Therefore, in the diagnosis of the ACS, it becomes very important to investigate the compositions of the plaque in order to distinguish accurately between the stable plaque and the unstable one. The intravascular ultrasound (IVUS) method is a tomographic imaging technique using an ultrasound probe mounted at the tip of a catheter. It provides a tomographic view of the coronary artery by analyzing the radio frequency (RF) signal, which is a backscattered ultrasound signal from tissues.

The IVUS method gives a real-time imaging of the section of the coronary artery. This image is called a B-mode image [1], and is often used for the diagnosis of the ACS. However, it is very difficult to perform tissue characterization of coronary plaque only by observing this B-mode image.

The integrated backscatter (IB) analysis is a typical method for the tissue characterization by using the IVUS method

[2][3]. The IB analysis employs the IB value, which is a locally averaged power of the RF signal, as a feature value for the tissue characterization. This is not always useful, because some different types of tissues have IB values similar to each other. Also the IB value is strongly affected by the measurement conditions.

The tissue characterization based on the frequency analysis of the RF signal has been proposed [4]. However, a precise tissue classification by this method is not yet achieved, because the frequency characteristics of some tissues are similar to others.

In order to realize the precise tissue classification, this paper proposes a method for the tissue characterization of coronary plaque by using the sparse coding [5]-[8], which is a feature extraction method based on the perceptual system of the mammalian visual cortex to underlying features of the observed signals. In the proposed method, the RF signal is first expanded into a series of a linear combination of the basis functions extracted by the sparse coding, and then the code patterns of the expansion coefficients are used for classification of the target tissue. Furthermore we try to adopt the neighboring information of the target tissue.

Experiments are performed to classify the tissues of the plaque into the fibrous and lipid tissues using the RF signal obtained from a human coronary arteries. The effectiveness of the proposed method has been verified by comparing the classification results by the proposed method with those by the frequency analysis.

II. CONVENTIONAL TISSUE CHARACTERIZATION METHOD

A. IVUS Method

The IVUS method is one of the medical imaging techniques. In the IVUS method, the catheter with the ultrasound probe is inserted and then rotated in the coronary artery. The ultrasound signal is transmitted from the ultrasound probe, and the RF signal reflected from the tissue is received also by its ultrasound probe. The transmitting frequency of the ultrasound is 40 MHz, and the RF signal is sampled at 400 MHz.

An IVUS B-mode image [9] is obtained by analyzing by the received RF signal. This IVUS B-mode image expresses a tomographic image of the section of the coronary artery. This image is constructed with 2,048 points in depth, and 256 lines in radial direction.

S. Furukawa, E. Uchino, and N. Suetake are with the Graduate School of Science and Engineering, Yamaguchi University, 1677-1 Yoshida, Yamaguchi 753-8512, Japan (e-mail: {t002wa, uchino, nsuetake}@yamaguchi-u.ac.jp).

E. Uchino is also with the Fuzzy Logic Systems Institute, 680-41 Kawazu, Iizuka 820-0064, Japan (e-mail: uchino@flsi.or.jp).

T. Azetsu is with the Office for Information and Technology, Yamaguchi Prefectural University, 3-2-1 Sakurabatake, Yamaguchi 753-8502, Japan (e-mail: azetsu@yamaguchi-pu.ac.jp)

Manuscript received December 15, 2013; revised January 15, 2014.

B. IB Analysis

In the IVUS-based conventional tissue characterization methods, the IB analysis is a typical method. In this analysis, the tissue is classified only by the IB value defined by [2]:

$$\text{IBS} = 20 \log \left(\frac{\frac{1}{T} \int_0^T V^2 dt}{\frac{1}{T} \int_0^T V_0^2 dt} \right), \quad (1)$$

where V is the signal voltage from a region of interest, V_0 is the smallest signal voltage that the system can detect, and T is the integration interval. In the IB analysis, the threshold of the IB value for the classification of the fibrous and lipid tissues is decided so that the learning signals are most precisely classified.

The IB analysis is simple, and is very effective in a restricted case. However, it is not always accurate to classify the tissues of the plaque, because some types of tissues have similar IB values with each other, and the strength of the IB value depends on a distance from the probe to the tissue. This is a fatal defect of the IB analysis.

C. Frequency analysis

The frequency analysis is another approach for the tissue characterization. In this method, The normalized power spectrum of the local RF signal is used as the feature vector. However, since the frequency characteristics of some tissues are similar to others, a precise tissue classification is not yet achieved.

III. TISSUE CHARACTERIZATION METHOD BY SPARSE CODING

A. Sparse Coding

The sparse coding was originally proposed to represent an image signal by using a few basis functions extracted from natural image. It is closely related to the independent component analysis (ICA)[10][11], which is well known as a statistical method to estimate underlying features of the observed signal. We try to apply the high feature extraction ability of the sparse coding to the tissue characterization using the RF signal.

1) *Representation of RF Signal:* A local RF signal \mathbf{x} in a short time interval is assumed to be represented as a linear combination of the basis functions ϕ_i as follows:

$$\mathbf{x} = \sum_{i=1}^M a_i \phi_i, \quad (2)$$

where a_i is the expansion coefficient for each basis function ϕ_i , and M is the number of the basis functions. \mathbf{x} and ϕ_i are given by:

$$\mathbf{x} = (x_1, \dots, x_L)^t, \quad (3)$$

$$\phi_i = (\phi_{i1}, \dots, \phi_{iL})^t, \quad (4)$$

where L is the dimension of \mathbf{x} sampled in the short time interval, and t is the transpose operation.

2) *Cost Function of Sparse Coding:* The basis functions ϕ_i and the coefficients a_i are statistically determined from a set of the local RF signals \mathbf{x} which are cut out randomly from the learning signals. ϕ_i and a_i are estimated only by using \mathbf{x} .

In the sparse coding, the following cost function is employed to determine ϕ_i and a_i [5][6]:

$$E = \left\langle \sum_{j=1}^L \left(x_j - \sum_{i=1}^M a_i \phi_{ij} \right)^2 + \beta \sum_{i=1}^M S \left(\frac{a_i}{\sigma} \right) \right\rangle, \quad (5)$$

where $\langle \cdot \rangle$ is the averaging operator, and β is a positive constant. σ is a scaling constant, and the standard deviation of the learning signals is used here. $S(y)$ is an arbitrary nonlinear function.

The first term of Eq. (5) indicates the signal reconstruction performance by evaluating the sum of the square error between the input signal x_j and the reconstructed signal represented by a linear combination of ϕ_i .

The second term determines the sparseness of the expansion coefficients a_i by appropriately choosing $S(y)$. $\log(1+y^2)$, $-e^{-y^2}$, and $|y|$ are given as $S(y)$. In this paper, $\log(1+y^2)$ is used as the nonlinear function $S(y)$.

3) *Learning Algorithm of Sparse Coding:* The learning algorithm of the sparse coding can be obtained by minimizing Eq. (5) with respect to a_i and ϕ_i . That is, the updating rule of a_i is given as follows [5][6]:

$$\Delta a_i = b_i - \sum_{k=1}^M R_{ik} a_k - \frac{\beta}{\sigma} S' \left(\frac{a_i}{\sigma} \right), \quad (6)$$

with

$$b_i = \sum_{j=1}^L \phi_{ij} x_j, \quad (7)$$

$$R_{ik} = \sum_{j=1}^L \phi_{ij} \phi_{kj}, \quad (8)$$

where Δa_i is an updated value of a_i and $S'(y)$ is the differential of $S(y)$.

The updating rule of ϕ_i is as follows:

$$\Delta \phi_{ij} = \eta \left\langle a_i \left(x_j - \sum_{i=1}^M a_i \phi_{ij} \right) \right\rangle, \quad (9)$$

where η is the learning rate.

a_i are updated according to Eq. (6) when each input signal is applied, and ϕ_{ij} are updated after 100 input signals are applied.

4) *Feature Extraction:* The characteristics of the basis functions obtained from the learning signals by using the sparse coding are as follows.

- 1) The frequency characteristics of the obtained basis functions and those of the learning signals are similar to each other.
- 2) The code pattern (pattern of a_i) when the learning signal is represented by the basis functions is sparse.

In this paper, we use the code pattern as the features of the RF signal for the tissue characterization.

5) *Classification*: In the proposed method, the K -Nearest Neighbor (K -NN) algorithm is used [12]. K is set to 9 in the following experiments.

The proposed method classifies the tissues by using the sparse code patterns of a_i . The basis functions for the sparse coding are first extracted from the learning signals which contain both fibrous and lipid tissues in advance. Next the local RF signals from the learning signals of the fibrous tissue are represented in the basis functions.

This obtained code patterns are used as the training samples with the class label of the fibrous tissue for the K -NN algorithm. In the same way, the training samples with the class label of the lipid tissue are obtained from the learning signals of the lipid tissue. The set \mathbf{A} of the training samples is given as follows:

$$\mathbf{A} = (\mathbf{a}_1, \dots, \mathbf{a}_N) \quad (10)$$

where N is the number of the training samples with the class label of the fibrous or lipid tissue in the set \mathbf{A} .

The target local RF signal, where its tissue is unknown, is represented in the basis functions, and then the tissue characterization is performed by applying the K -NN algorithm whose training samples are \mathbf{A} to the obtained code pattern.

IV. EXPERIMENTAL RESULTS

The proposed method is applied to the tissue characterization problem using the RF signal obtained from human coronary arteries.

In the classification, the tissues of coronary plaque are classified into the fibrous and lipid tissues. The classification performance of the proposed method by using the sparse coding is compared to that of the frequency analysis. In the proposed method and also the frequency analysis, the window size of the local RF signal is 32 points in depth and 4 lines in radial direction. Although the local RF signals are cut out from the learning signals only in the direction of depth usually, we try to expand the window size into the radial direction to take the neighboring information.

Table I shows the correct classification rates by each method. It is confirmed that the proposed method has good performance in both cases of the fibrous and lipid tissues, on the other hand, the frequency analysis gives the low correct classification rate in the case of the lipid tissue.

Figure 1 shows the classification results of the fibrous and lipid tissues by each method. The yellow and green areas correspond to the fibrous and lipid tissues, respectively.

TABLE I
CORRECT CLASSIFICATION RATES.

		Frequency analysis	Proposed method
case 1	Fibrous tissue	0.98	0.93
	Lipid tissue	0.39	0.82
case 2	Fibrous tissue	0.99	0.89
	Lipid tissue	0.49	0.88

V. CONCLUSION

This paper proposed a novel method using sparse features and its neighboring information obtained by the sparse coding for the tissue characterization. In the proposed method, the RF signal was represented by the basis functions, and the code patterns of the expansion coefficients of the basis functions were used for the tissue characterization.

The effectiveness of the proposed method was verified by comparing it with the frequency analysis. Experimental results show that the proposed method has good performance compared to the frequency analysis.

Future work is to further improve the correct classification rate by utilizing various pattern recognition methods.

REFERENCES

- [1] T. L. Szabo, *Diagnostic Ultrasound Imaging*, Elsevier Academic Press, 2004.
- [2] M. Kawasaki, H. Takatsu, T. Noda, Y. Ito, A. Kunishima, M. Arai, K. Nishigaki, G. Takemura, N. Morita, S. Minatoguchi, and H. Fujiwara, "Noninvasive quantitative tissue characterization and two-dimensional color-coded map of human atherosclerotic lesions using ultrasound integrated backscatter," *Journal of the American College of Cardiology*, Vol.38, No.2, pp. 486-492, 2001.
- [3] M. Kawasaki, H. Takatsu, T. Noda, K. Sano, Y. Ito, K. Hayakawa, K. Tsuchiya, M. Arai, K. Nishigaki, G. Takemura, S. Minatoguchi, T. Fujiwara, and H. Fujiwara, "In vivo quantitative tissue characterization of human coronary arterial plaques by use of integrated backscatter intravascular ultrasound and comparison with angioscopic findings," *Circulation*, Vol.105, pp. 2487-2492, 2002.
- [4] A. Nair, B. D. Kuban, E. M. Tuzcu, P. Schoenhagen, S. E. Nissen, and D. G. Vince, "Coronary plaque classification with intravascular ultrasound radiofrequency data analysis," *Circulation*, Vol.106, pp. 2200-2206, 2002.
- [5] B. A. Olshausen and D. J. Field, "Emergence of simple-cell receptive field properties by learning a sparse code for natural images," *Nature*, Vol.381, pp. 607-609, 1996.
- [6] B. A. Olshausen and D. J. Field, "Sparse coding with an overcomplete basis set: A strategy employed by V1?," *Vision Research*, Vol.37, pp. 3311-3325, 1997.
- [7] T. Azetsu, E. Uchino, S. Furukawa, and N. Suetake, T. Hiro, and M. Matsuzaki, "Tissue characterisation of coronary plaques using sparse feature vectors," *Electronics Letters*, Vol.46, Issue7, pp. 484-486, 2010.
- [8] M. Kotani, Y. Shirata, S. Maekawa, S. Ozawa, and K. Akazawa, "Representations of speech by sparse coding algorithm," *IEEJ Trans. on Electronics, Information and Systems*, Vol.120-C, No.12, pp. 1996-2002, 2000 (in Japanese).
- [9] B. N. Potkin, A. L. Bartorelli, J. M. Gessert, R. F. Neville, Y. Almagor, W. C. Roberts, and M. B. Leon, "Coronary artery imaging with intravascular high-frequency ultrasound," *Circulation*, Vol.81, pp. 1575-1585, 1990.
- [10] A. J. Bell and T. J. Sejnowski, "The 'independent components' of natural scenes are edge filters," *Vision Research*, Vol.37, pp. 3327-3338, 1997.
- [11] A. Hyvärinen and P. O. Hoyer, "Emergence of phase and shift invariant features by decomposition of natural images into independent feature subspaces," *Neural Computation*, Vol.12, No.7, pp. 1705-1720, 2000.
- [12] R. O. Duda, P. E. Hart, and D. G. Stork, *Pattern Classification, 2nd ed.*, Wiley-Interscience Publication, 2001.

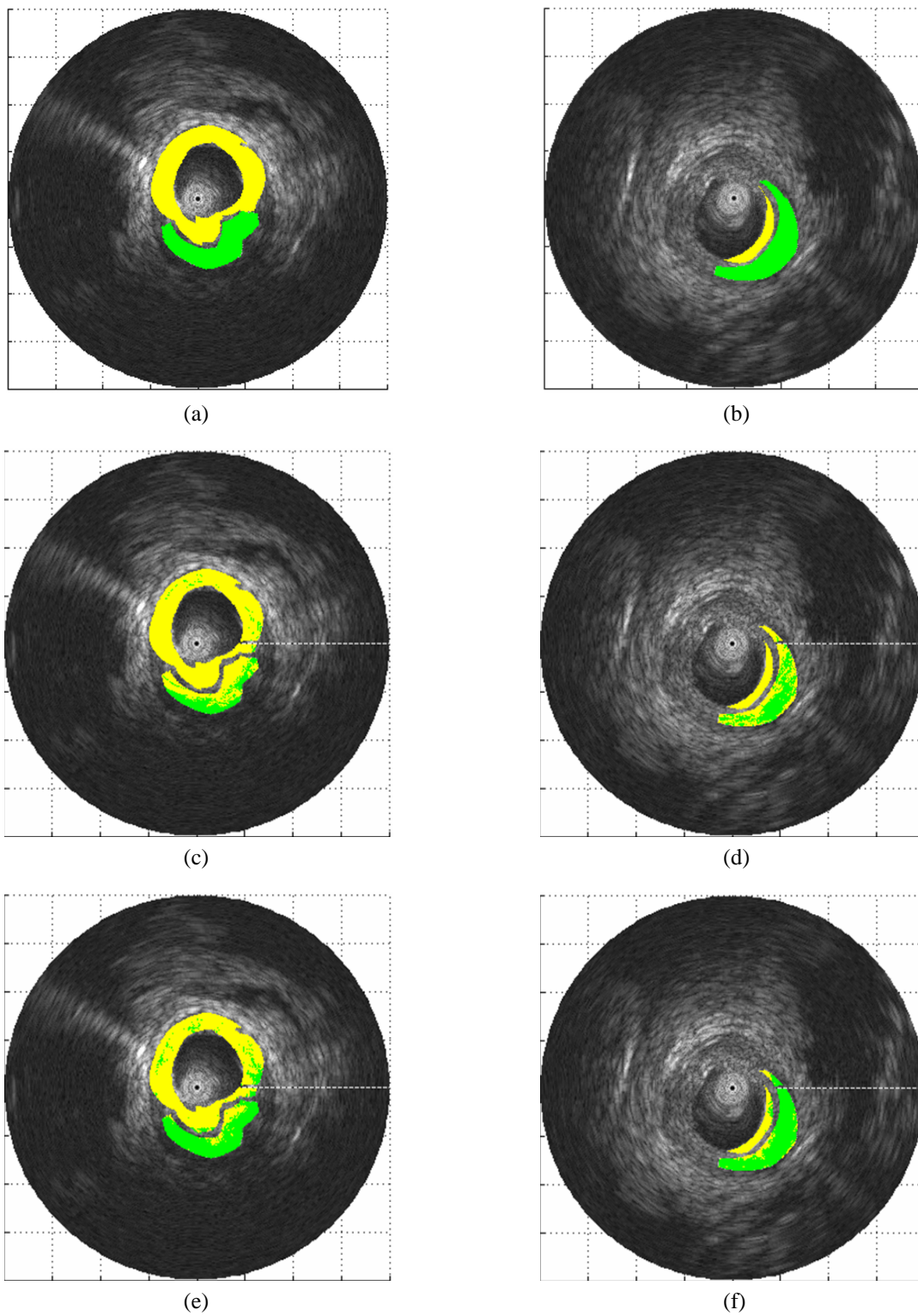


Fig. 1. Classification results. (a) Ideal result of case 1. (b) Ideal result of case 2. (c) Result of case 1 by the frequency analysis. (d) Result of case 2 by the frequency analysis. (e) Result of case 1 by the proposed method. (f) Result of case 2 by the proposed method.

Fixed-point Implementation of Classifier for Tropical Wood Recognition System

Enas Duhri Kusuma, Rubiyah Yusof, and Mohammad Fauzi Othman

Abstract—Automated wood recognition system is computationally expensive and require large data processing. The most time and resources consuming part of the system is classifier. Linear Discriminant Analysis (LDA) is used as classifier in existing wood recognition system on training stage and testing stage. Existing wood recognition system is PC based and implemented under Matlab environment. Algorithm conversion to fixed-point is required to implement system into embedded device such as FPGA. This paper will discuss fixed-point implementation of LDA, which requires QR decomposition and matrix inverse. The proposed implementation is devised to perform stable QRD and inverse algorithm for large wood recognition training data. Algorithm design, as well as word and fraction length selection for fixed-point number to get acceptable accuracy will be discussed in this paper. Finally, this paper will present fixed-point implementation result of every stage and final accuracy of fixed-point system.

Keywords– fixed-point, LDA classifier, QR decomposition, matrix inverse

I. INTRODUCTION

Automated wood recognition systems have been implemented by many researchers [1-4]. All implementations are PC based systems. Wood recognition system implemented by Khairuddin et.al[4] gets 95% accuracy for 52 species. The system consists of training and testing stage. Training stage selects most discriminative features on training data. Testing stage runs the trained system by applying input data and produce classified output data. LDA is used as classifier in both training and testing stage, which is the most time and resource consuming part. Embedded system implementation, especially in FPGA, of large matrix processing algorithm will require fixed-point arithmetic to save chip area, operation speed, and power consumption, because of complexity and hardware cost of floating point arithmetic. Fixed point number property consists of word length and fraction length. Determination of both of them is important for capitalizing fixed-point implementation. Involving large data matrices, this research will utilize fixed point toolbox from Matlab to determine the word and fraction length of fixed point number. Modification of fixed point property of the signals has been followed by performance measurement using fixed-point simulation result.

The authors would like to thank Ministry of Education Malaysia and Universiti Teknologi Malaysia for funding this research project through a research grant (04H40) titled "Dimension Reduction and Data Clustering for High Dimensional and Large Datasets".

E. D. Kusuma is with the Department of Electrical Engineering and Information Technology, Faculty of Engineering, Gadjah Mada University, Indonesia (e-mail: enas@ugm.ac.id)

R. Yusof and M.F. Othman are with Center of Artificial Intelligence and Robotics, Universiti Teknologi Malaysia (e-mail: rubiyah@ic.utm.my and fauzi@fke.utm.my respectively).

A. LDA computation

Input of feature selection unit is combination of basic gray level aura matrices (BGLAM) feature and statistical pores pattern distribution (SPPD) of preprocessed wood cross section image developed by Cordova [3] and Khairuddin et.al [4]. After pass several conditioning procedure and normalized, feature data matrix will be saved in database to be processed in classifier. In training process, training data matrix will be masked with several bit string to select which feature will be processed in the training stage. The selection is column wise, then only selected columns will be processed in stage. The final result of the computation is the selected column combination which produces highest fitness. Thus, if the number of total features is 157 and the training matrix size is $m \times n$, number of column being processed in LDA (n) will be various depends on the bit string with $n \leq 157$.

In its implementation as classifier[4,5], derived LDA computation can be shown in equation (1).

$$f_k(\mathbf{x}) = \log_2 p_k + \log_2 |R| - \frac{1}{2} [(\mathbf{x} - \boldsymbol{\mu}_k)^T (R^T R)^{-1} (\mathbf{x} - \boldsymbol{\mu}_k)] \quad (1)$$

Function $f_k(\mathbf{x})$ represents how proper sample data vector \mathbf{x} can be classified as k_{th} class member. Sample data vector \mathbf{x} will be classified as k_{th} class member if $f_k(\mathbf{x}) > f_l(\mathbf{x})$, $\forall l \neq k$. $\boldsymbol{\mu}_k$ is a vector which contains average value of training data in group k . Vector $\boldsymbol{\mu}_k$ and \mathbf{x} have the same length with number of features. $\log_2 p_k$ is base-2 logarithm of prior probability of k_{th} class. Prior probabilities for species k is equal number of species k in training database divided by number of total species in training database. R matrix is representation of normalized training data matrix, which is produced by QR decomposition of normalized training data matrix A , shown in equation (2).

$$A = QR \quad (2)$$

QR decomposition of covariance matrix is used as data reduction method in LDA based classifier. QRD can represent covariance matrix with much smaller data[6]. QRD factorizes $m \times n$ sized input matrix A with $m > n$ into $m \times n$ orthogonal Q matrix and $n \times n$ upper triangular R matrix, while Q matrix is unused.

Hence, overall computation of the classifier can be broken down to several computation modules as follows:

- 1) QRD of normalized training data from database, produce R matrix.
- 2) Inverse of R matrix.

- 3) Matrix multiplication modules to compute $(\mathbf{x} - \boldsymbol{\mu}_k)^T (R^T R)^{-1} (\mathbf{x} - \boldsymbol{\mu}_k)$
- 4) Determinant of R matrix. Because of its upper triangular characteristic, $\log_2 |R|$ is the sum of the logarithm of R's diagonal components absolute value .

QRD and Inverse will be the most resource consuming modules and have the most computation complexity among all others. Thus, this paper will emphasize more on fixed-point implementation of QRD and matrix inverse.

B. Fixed-point number

Fixed-point (FXP) numbers have finite dynamic range and quantization[7,8]. Notation (w,f, 0 unsigned/1 signed) will be used to represents the number with w is total bits and f is number of fractional bits. the integer length (IL) is the number of bits used in the integer part, and the fractional length (FL) is assigned to the fraction. Hence, total bits or total word-length (WL) of a two's complement number is $IL + FL + 1$. The IL will depends on the number's range (\mathbf{r}) and the FL will determine quantization size (Δ) of the number, which is described as $-2^{IL} \leq \mathbf{r} < 2^{IL}$ and $\Delta = 2^{-FL}$.

This work used fixed-point toolbox from Matlab to model, represent and simulate fixed-point numbers. Using fixed-point toolbox, fixed-point numbers can be modelled as *fi* structure. Important properties of *fi* object to model fixed-point number are S(sign bit), WL(word length), and FL(fraction length).

II. QR DECOMPOSITION

In the LDA computation, QRD serves as data reduction method, which R product of QRD can represent training data. Large training data matrix with $m * n$ size, $m \gg n$, will be reduced to only $n * n$. The other advantage of QRD is because R matrix is triangular, next stage process, which is matrix inverse, will be easier.

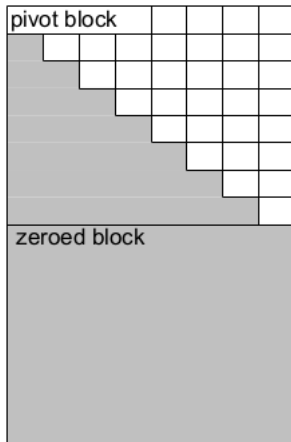


Fig. 1. Two blocks processed by individual QRD

A. Householder QRD

There are many methods of computing QRD, such as Modified Gram-Schmidt, Givens Rotation and Householder [9]. In this paper, Housholder method will be utilized. Householder method's advantage among others is the capability to simultaneously eliminate matrix elements below diagonals. Algorithm for Householder QRD is described in Algorithm 1 (HQR). Householder method processes input matrix in column wise. In every column processed, it will produce Householder vector \mathbf{v} . The vector will be multiplied to processed matrix to get all elements below diagonals zeroed. Problem will come if norm of column being processed (shown by \mathbf{d}_3 in Algorithm 1) is near zero. Thus, in pseudocode, arbitrary reflection will be performed if zero column. If algorithm get zero column, Householder vector will be replaced by identity vector, with all zero elements but first element is one.

Algorithm 1 also produces output which is used for updating rightside blocks of the processed block. Block update process is simply matrix addition and multiplication, shown in Equation 3

$$M = A + Y * W' * A; \tag{3}$$

with \mathbf{A} is matrix being updated, \mathbf{Y} and \mathbf{W} are HQR results used for update, and \mathbf{M} is updated matrix result. To apply QRD in large data size, blocked QRD algorithm will be applied since the research orientation is to implement computation in FPGA.

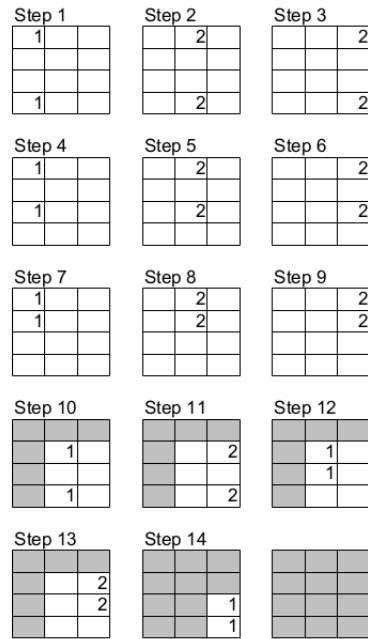


Fig. 2. Bottom-up Method of Tiled QRD

B. Blocked QRD Algorithm

In blocked algorithm, input matrix is partitioned into blocks and QRD is applied to every block with certain technique. There are several techniques in blocked QRD computation, which are tall-skinny QRD [12] and tiled QRD[10]. Tiled

QRD is preferred for implementation to resource limited device, since it works in smaller block with adjustable size. In tiled QRD, input matrix is divided into several square blocks. Individual QRD are implemented to diagonal block and all blocks below it sequentially. In one operation, individual QRD process 2 blocks, one block is diagonal block as pivot, and the other is block below diagonal.

Two blocks being processed by individual QRD is shown in Figure 1. The upper block of individual QRD is pivot block, a block which will be triangularized. Lower block is called zeroed block because all of its contents will be eliminated. Right side blocks of diagonal blocks will be modified in update processes. Tiled QRD algorithm discussed in this paper will be bottom-up variant, which is used in Fibonacci and Greedy methods [10]. In bottom-up method, shown in Figure 2, computation is done in lower blocks first while diagonal block is still used as pivot block. Shown in Figure 2, two blocks labelled 1 are blocks being processed by individual QRD and label 2 means two blocks are being updated.

Algorithm 1 : HQR

```

A = input matrix
R = output matrix, result of QRD
W and Y = output matrix, used in blocked QRD to update
the next block
1: [m, n] = size(A)
2: Y = zeros(size(A))
3: W = zeros(size(A))
4: vzero = 2-16
5: for k = 1 : n do
6:   x = A(k : m, k);
7:   d1 = x' * x;
8:   d2 = sqrt(d1);
9:   v = x;
10:  v(k) = x(k) + sign(x(k)) * d2;
11:  d3 = sqrt(v' * v);
12:  if d3 < vzero then
13:    v = zeros(size(x));
14:    v(k) = 1;
15:  else
16:    v = v/d3;
17:  end if
18:  for j = k : n do
19:    y = A(k : m, j);
20:    d4 = v' * y;
21:    y = -2 * v * d4 + y;
22:    A(k : m, j) = y;
23:  end for
24:  Y and W generation
25:  if k == 1 then
26:    Y(:, k) = v;
27:    W(:, k) = -2 * v;
28:  else
29:    z = -2 * v;
30:    for i = 1 : k - 1 do
31:      yv = Y(:, i)' * v;

```

```

32:      z = z - 2 * W(:, i) * yv;
33:    end for
34:    W(:, k) = z;
35:    Y(:, k) = v;
36:  end if
37: end for
38: R = A

```

III. TRIANGULAR MATRIX INVERSION

Triangular matrix, upper or lower, is easier and requires less number of operations. While full nxn matrix requires n^3 operations to compute its inverse, triangular system only requires $\frac{1}{2}n^2$ operations to solve [11]. The algorithm used for computing the inversion of upper triangular matrix is given in Algorithm 2. Critical point of the algorithm is division operation $X(j, j) = \frac{1}{R(j, j)}$, which will be unstable if $R(j, j)$ near zero. Thus to anticipate that, the value of $R(j, j)$ will be replaced by the smallest value in the diagonal which still greater than zero (Algorithm 2 line 7).

Algorithm 2 : InverseTriu

R = input matrix, upper triangular, result of QRD
 Ri = output matrix, inverse of R

```

1: n = size(R, 1);
2: X = zeros(n);
3: dR = |diag(R)|;
4: md = 2-4min(dR(dR > 0));
5: for j = n : -1 : 1 do
6:   if |R(j, j)| < md then
7:     R(j, j) = md;
8:   end if
9:   X(j, j) = 1/R(j, j)
10:  for k = j + 1 : n do
11:    for i = j + 1 : n do
12:      X(j, k) = X(j, k) + X(j, i)R(i, k);
13:    end for
14:  end for
15:  for k = j + 1 : n do
16:    X(j, k) = -X(j, j) * X(j, k);
17:  end for
18: end for
19: Ri = X;

```

IV. LDA FITNESS COMPUTATION

The purpose of using LDA is to compute the fitness of specific sample. Based on Equation 1, LDA computation is shown in Algorithm 3. The algorithm classified all given samples to specific class, then compared classification results to the reference. Training data fed to the algorithm depends on the masking word applied to whole training data. If classification output from algorithm was the same as the one from reference, then a counter variable was incremented, until all samples were examined. Fitness of certain training data combination was determined by the final amount of the counter.

Algorithm 3 : FitnessLDA

Training = input matrix, training data from database
fitness = scalar output, fitness of given training matrix

```

1:  $R = \text{BlockedHQR}(\text{Training});$ 
2:  $s = \text{abs}(\text{diag}(R));$ 
3:  $\log\text{DetSigma} = 2 * \text{sum}(\log_2(s));$ 
4:  $Ri = \text{InverseTriu}(R);$ 
5:  $A = \text{zeros}(\text{size}(\text{sample}));$ 
6:  $m = \text{NumberOfSamples};$ 
7: for  $k = 1 : \text{NGroups}$  do
8:   for  $i = 1 : m$  do
9:      $A(i, :) = \text{sample}(i, :) - \text{gmeans}(k, :);$ 
10:  end for
11:   $A = A * Ri;$ 
12:   $A2 = A * A;$ 
13:   $D(:, k) = \frac{1}{\text{NGroups}} - .5 * (\text{sum}(A2, 2) + \log\text{DetSigma});$ 
14: end for
15:  $n = 0;$ 
16: for  $i = 1 : m$  do
17:    $[ , \text{outclass}] = \text{max}(D(i, :));$ 
18:   if  $\text{outclass} == \text{SampleIndex}(i)$  then
19:      $\text{Counter} = \text{Counter} + 1;$ 
20:   end if
21: end for
22:  $\text{fitness} = \text{Counter} * 100/m$ 
    
```

Data obtained from database contains training data itself (**Training**), sample data for testing, which is not included in training (**sample**) and training data group average (**gmeans**). **Gmeans** was average values computed within every group in training data with **NGroups** was number of groups defined in the system, which was 52 groups. Value of classification result was in logarithmic scale to make determinant computation easier. Algorithm state $D(:, k) = \frac{1}{\text{NGroups}} - .5 * (\text{sum}(A2, 2) + \log\text{DetSigma})$; was the representation of Equation 1.

V. FIXED-POINT IMPLEMENTATION AND RESULTS

Matlab fixed-point toolbox is utilized to implement whole computation in FXP algorithm. It is decided to implement computation part-by-part, to avoid too many variables involved in a conversion process, which make conversion time longer. This paper will discuss about FXP implementation of QRD and inversion, as well as its impact to the final result. Because logarithmic part cannot directly implemented using fixed-point toolbox, it will be implemented to FXP using custom function. To compute logarithmic part, \log_2 architecture developed by Zhang, et.al [13] was used. Fixed-point design flow is shown in Figure 3. Algorithm written in Matlab is converted to FXP using fixed-point toolbox. Arithmetic operations used in the FXP algorithm such as multiplication, division, and square-root also used built-in Matlab function. The toolbox will give recommendation on FXP setting in word length (IWL and FWL). Recommended design then will be tested and compared with original (floating-point) algorithm. Fixed-point algorithm result is measured using error metric (EM) [7,8]. EM is defined

using Equation 4.

$$EM = \|e\| / \|\text{outdata}_{float}\| \quad (4)$$

With $e = \text{outdata}_{float} - \text{outdata}_{fixed}$.

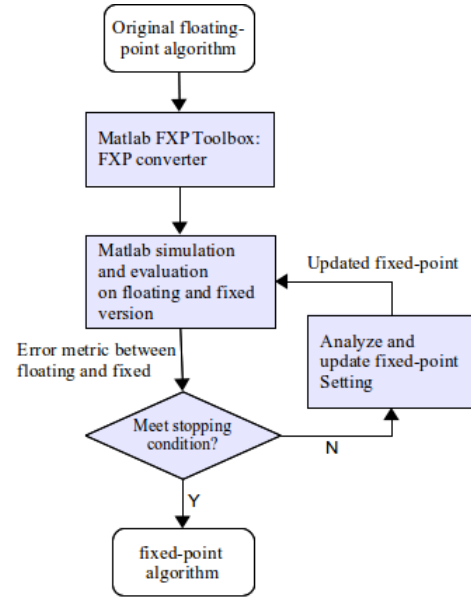


Fig. 3. Fixed-point Design Flow

In some cases, result of the toolbox sometimes is not well optimized. That is especially because of large dynamic range of variables involved in computation. Thus, to reach well optimized number, optimization algorithm proposed by Roy, et.al[7] is used. Fixed point code generation is stopped when it reaches stopping criteria. Stopping criteria is something that cannot be standardized. It depends on the objectives of the algorithms. Criteria proposed by Roy, et.al[7] and Banerjee, et.al [8] which use error metric, cannot be directly implemented to this algorithm. Therefore, the criteria will be the closest output (fitness) to the original algorithm's output. That is applied as long as FXP word length setting does not exceed word length constraint. The product or sum of FXP number also does not exceed maximum word length of product or sum. Then, there will be two possibilities of final result in generating FXP code:

- 1) FXP code reaches expected result, which is close to the original and the setting does not exceed constraint
- 2) FXP code exceeds the constraint and cannot reach expected output, which means the operation cannot be converted to FXP.

However, the second possibility sometimes only applies to a few kinds of input. When different kinds of input are applied to the FXP code, it is still able to produce expected result.

A. QRD FXP Implementation

To do FXP implementation of QRD, a defined word length was given to the toolbox. The toolbox gave result a set of inputs, outputs, and variable used in algorithm and propose the fraction lengths with given word lengths. In designing

fixed-point QRD, training data without masking (5040 x 157) were used as input to show the total dynamic range. Block size used in implementation was 32x16 and every block was processed by HQR algorithm. Overall process was arranged in tiled arrangement as shown in Figure 2. Word length (WL) of all variables were defined to 32 bits to begin the implementation. Fixed-point toolbox then gave recommended values for fraction word length. The range of variables being analyzed were also shown in the output summary. Summary of toolbox output is shown in Table I.

From Table I, it is shown that with normalized wood training data matrix as input, blocked HQR algorithm has relative static range. There is no variable in very different range compared with another variable. Therefore, it is possible to apply another WL, can be less or more than 32 bits and make comparison of error metric for every WL, which is shown in Table II. Table II also presents results from 64x32 sized block, which are not very different compared with result of 32x16. Error metric is computed using Equation 4. FW length for different WL will follow pattern from Table I. It makes sense that longer WL, and FW automatically, will produce better result. However, efficient WL which still makes good final result cannot be decided from here. Hence, it is enough to determine WL for QRD module to be 32 bits, which generally used in 32-bit system.

TABLE I
HQR SIMULATION MIN-MAX VALUE AND PROPOSED WL-FW SUMMARY

var name	sim min	sim max	S	WL	FW	FW pattern
A	-0.0685	0.0693	1	32	31	WL-1
R	-0.0685	0.0693	1	32	31	WL-1
d1	0	0.0048	0	32	32	WL
d2	0	0.0693	0	32	32	WL
d3	0	0.1382	0	32	32	WL
d4	-0.0516	0.0691	1	32	31	WL-1
x	-0.0685	0.0677	1	32	31	WL-1
y	-0.0685	0.0692	1	32	31	WL-1
v	-1	1	1	32	30	WL-2
yv	-0.5434	0.6887	1	32	31	WL-1
W	-2	2	1	32	29	WL-3
Y	-1	1	1	32	30	WL-2
z	-2	2	1	32	29	WL-3

sim min =simulation min value, sim max=simulation max value, S=0(unsigned),1(signed), WL=word length, FW=fraction word length

TABLE II
BLOCKED QR FXP ERROR METRIC (EM) FOR WL=27 TO 32 BITS

B.size	WL	27	28	29	30	31
32x16	EM(%)	14.1	6.8	3.23	3.23	1.38
64x32	EM(%)	14.1	3.71	3.13	2.66	1.54
B.size	WL	32	33	34	35	36
32x16	EM(%)	1.31	0.65	0.65	0.40	0.40
64x32	EM(%)	1.39	0.71	0.71	0.32	0.32

B.size=block size

B. FXP Triangular Matrix Inversion and Final Results

Using the same procedure and tool as QRD, triangular matrix inversion algorithm was also converted to FXP. As shown in Table III, fixed-point toolbox summarized that variables in the algorithm had very different range. Maximum values of

several variables were in the order of 10^6 and another variables were on below 0.1. That situation makes an uniform word length cannot be implemented to all variables.

TABLE III
TRIANGULAR MATRIX INVERSE SIMULATION MIN-MAX VALUE SUMMARY

var name	sim min	sim max
C	-913704.496	1049601
R	-0.0693	0.0625
X	-913704.496	1049601
d	-8626.996	1049601
x	-0.0593	0.0554
x2	-2022.728	38597.699
y	-913704.496	41733.189

To handle that situation, the FXP algorithm used variable word length. In order to get suitable word length to all variables, the fraction word length was defined (as 28 bits) and the toolbox proposed suitable word length. Complete proposed word length for all variables in the algorithm is shown in Table IV. However, input and output width are still kept at 32 bits to keep the compatibility with another stages.

TABLE IV
PROPOSED WORD LENGTH FOR TRIANGULAR MATRIX INVERSE ALGORITHM

var name	S	WL	FW	pos
R	1	32	28	in
C	1	50	28	var
X	1	50	28	var
d	1	50	28	var
x	1	32	28	var
x2	1	45	28	var
y	1	49	28	var
Ri	1	32	10	out

With specified setting, fixed-point triangular matrix inversion algorithm was applied to the previous QRD. Data input matrix to QRD algorithm was training matrix with various masks, which represent real situation of training process. From that experiment, error metrics of the inversion for different input combinations and the system's final output, the fitnesses, were obtained. The result is shown in Table V. Every combination of training data was produced by applying various mask to full column data. Masks are binary numbers with length 157 bits which are generated randomly by Matlab. In Table V, masks are generated randomly, except training data no.8, which is optimum mask.

From Table V, fixed-point algorithm for triangular inversion generates very little errors for several data combinations. After look at the matrix ranks, it is found that significant errors happened while matrix rank less than its number of columns, or it can be said as rank deficient matrix. In full rank matrix, fixed-point algorithm works well with very little errors. Rank deficiency can make a matrix close to be singular and not invertible.

Algorithm used in doing triangular matrix inversion is still classified as ordinary inverse. In order to handle rank deficient or singular matrix, a method called generalized inverse[14] should be applied. Generalized inverse (geninv) is used in floating-point version of the algorithm. The major drawback

TABLE V
ERROR METRICS OF FXP INVERSES AND FITNESS RESULTS OF FXP ALGORITHM

Train	inv EM(%)	col	rank	FXP fit	FLP fit
1	0.036	74	74	81.071	81.071
2	0.0313	86	86	84.464	84.464
3	0.0334	81	81	87.321	87.321
4	0.0356	75	75	81.964	81.964
5	0.0354	79	79	83.035	83.214
6	0.0112	78	78	88.215	88.035
7	0.0455	72	72	86.250	86.071
8	0.227	79	79	94.821	95.000

Train:training data combination number,
col:number of columns, rank: matrix rank,
FXP fit:fixed-point fitness, FLP fit:floating-point fitness,
inv EM:error metric of inverse operation

of gen_{inv} is its expensive computation. To compute gen_{inv} , one must compute 4 times matrix multiplications, 1 Cholesky decomposition, and 1 triangular inversion, which will be easy in PC level application, such as Matlab, but not in fixed-point environment. Computing many matrix calculations in FXP consecutively will increase error possibility, especially if applied to operation which requires dynamic range of data, such as inversion.

VI. CONCLUSION

This paper shows that LDA classifier for wood recognition system can be implemented in fixed-point number. LDA is implemented as combination of QR decomposition, matrix inverse, matrix multiplication, and a few scalar operations with emphasize in QRD and inverse implementation. QRD is implemented in Householder method and bottom-up tiled arrangement. With small dynamic range in its variables, QRD for wood training data can be easily implemented in fixed-point with 32-bit width. For existing wood recognition system, 32-bit fixed-point triangular matrix inversion gives satisfying result for full rank matrix. 32-bit fixed-point implementation of the classifier gives final result which is not very different compared with original algorithm for optimum input combination. Fixed-point implementation of optimum input combination can produce 94.821% accuracy, while the original produces 95%.

REFERENCES

[1] Khalid, M., Lew, Y., Yusof, R. and Nadaraj, M. Design of An Intelligent Wood Species Recognition System. IJSSST, 2008. 9.
 [2] Rosli, N. R., Khalid, M. and Yusof, R. Wood Species Recognition based on GaborFilter Image Processing Technique. Proceedings of 2008 Student Conference on Research and Development. 2008.
 [3] Cordova, F. Wood Recognition. Technical report. Centre for Artificial Intelligence and Robotics (CAIRO), Universiti Teknologi Malaysia. 2009.
 [4] Khairuddin, U., Yusof, R., Khalid, M. and Cordova, F. Optimized Feature Selection for Improved Tropical Wood Species Recognition System. ICIC Express letters, Part B: Applications, An International Journal of Research and Surveys, 2011. 2: 441446.
 [5] Bohling, G. Classical Normal-Based Discriminant Analysis. Technical report. Kansas Geological Survey. 2006
 [6] Ye, J. and Li, Q. A Two-Stage Linear Discriminant Analysis via QR-Decomposition. IEEE Transactions On Pattern Analysis And Machine Intelligence, 2005. 27: 929 942.
 [7] Roy, Sanghamitra, and Prith Banerjee. "An algorithm for converting floating-point computations to fixed-point in MATLAB based FPGA design." Proceedings of the 41st annual Design Automation Conference. ACM, 2004.

[8] Banerjee, Prithviraj, Debabrata Bagchi, Malay Haldar, Anshuman Nayak, Victor Kim, and R. Uribe. "Automatic conversion of floating point MATLAB programs into fixed point FPGA based hardware design." In Field-Programmable Custom Computing Machines, 2003. FCCM 2003. 11th Annual IEEE Symposium on, pp. 263-264. IEEE, 2003.
 [9] Trefethen, Lloyd N. "Householder triangularization of a quasimatrix." IMA journal of numerical analysis 30.4 (2010): 887-897.
 [10] Bouwmeester, Henricus, Mathias Jacquelin, Julien Langou, and Yves Robert. "Tiled QR factorization algorithms." In High Performance Computing, Networking, Storage and Analysis (SC), 2011 International Conference for, pp. 1-11. IEEE, 2011.
 [11] Burian, Adrian, Jarmo Takala, and Mikko Ylisen. "A fixed-point implementation of matrix inversion using Cholesky decomposition." Circuits and Systems, 2003 IEEE 46th Midwest Symposium on. Vol. 3. IEEE, 2003.
 [12] Rafique, Abid, Nachiket Kapre, and George A. Constantinides. "Enhancing performance of Tall-Skinny QR factorization using FPGAs." Field Programmable Logic and Applications (FPL), 2012 22nd International Conference on. IEEE, 2012.
 [13] Zhang, Ming Z., Hau T. Ngo, and Vijayan K. Asari. Design of an efficient multiplier-less architecture for multi-dimensional convolution. Advances in Computer Systems Architecture. Springer Berlin Heidelberg, 2005. 65-78
 [14] Courrieu, Pierre. Fast computation of Moore-Penrose inverse matrices. arXiv preprint arXiv:0804.4809 (2008).

A method for context aware web service discovery

Vahab Ghasemi, Hasan Haghighi

Abstract— Increasing adoption of service oriented architecture and consequent growth of web services have doubled the need for methods for web service discovery. Considering contextual information in these methods, we can recommend services that are closer to user requirements and the current context.

A lot of works have been done for service discovery some of which consider context during service discovery process, but they mainly neglect composite services. In this paper a context aware method for web service discovery will be proposed which has two main characteristics: first it considers composite services during service discovery, and second, it uses semantic approach for modeling context and describing services. Considering composite service causes decreasing of false negative in response to user's request (query); by adoption of semantic approach, we can gain benefits like inference and knowledge sharing. We will demonstrate applicability of the proposed method by applying it to a case study. Results of the case study show we can decrease false negative in service discovery by considering composite services. Also, we can set required policies for restricting user's access to available services.

Keywords—service discovery, context, composite service, ontology

I. INTRODUCTION

Service Oriented Architecture (SOA) as a way of thinking and an approach to developing enterprise applications has been considered by many experts. SOA by having properties like loose coupling and reusability can be a great help in application development [1]. In SOA, software resources are packaged and provided as services. Services are well-defined and self-contained modules which provide business functionality [2]. As stated in [3], service providers publish their services in a repository, and consumers find desired services during discovery process. Service discovery process is more successful if the proposed and found service is closer to user's requirements and constraints.

Since users are faced with lots of available services, they are interested in methods which retrieve relevant services for them. In this paper we propose a method for web service discovery which considers contextual information of user's request and contextual constraints of web service usage, in addition to requirements specified by users explicitly. Contextual constraints are defined in web service description

as enterprise policies for restricting user's access to web services. Unlike previous work for context aware service discovery, our method takes composite services into account during service discovery, which leads to reduction of false negative in service discovery.

Section II gives a review of related work. The proposed ontology for modeling contextual information is discussed in section III. Section IV demonstrates how services will be described in our approach. The proposed method and associated algorithm for indirect discovery of web services is presented in section V. Section VI shows applicability and the result of adoption of our approach using a case study. At last we conclude the paper in section VII.

II. RELATED WORKS

Context aware discovery of web services has been investigated by many researchers. In [4] an architecture for context aware discovery of web services is proposed which consider user and service contextual information during service discovery. In this architecture service discovery is performed in two steps: basic web services are selected, and then these web services are filtered with regard to current context. In [4], the contextual information used in architecture is not declared, and it is just pointed out that ontology has been used for representing contextual information. In [5] authors proposed a method for proactive context aware discovery of web services. They represented contextual information by a formal model, called HAC. As another work for context aware discovery of services, in [6] a set of search criteria is generated based on the relations among different context values. These criteria are then used for discovery of services. In [7] authors proposed a method for context aware service discovery based on rule engine. This method uses Event-Control-Action pattern; hence, after detecting context information by sensors, matching of the detected context by available patterns is checked. If the current context information matches to one of patterns in the knowledge base, corresponding actions in knowledge base will be done.

As far as we know, all methods in the related work just take atomic services into account during service discovery. In other words, they deal with service discovery problem like the information retrieval problem and neglect composite web services while service composition is a critical issue in SOA. With this drawback in mind, this paper proposes a context aware web service discovery method that regards composite services.

III. CONTEXT ONTOLOGY

In the literature term “context awareness” first appeared in [8] where the authors described context as location, identities of nearby people and objects and changes to those objects. In [9], [10] and [11] other definitions of context were presented, and different attributes of context information were enumerated. In another category of context definitions authors have tried to present a comprehensive definition instead of enumerating different context information attributes. Among these definitions, [12], [13] and [14] can be mentioned. The definition presented in [14] is one of the best definitions embraced by most of researchers in the field of context aware systems. According to [14], context is any information that can be used to characterize the situation of entities that are considered relevant to the interaction between a user and an application, including the user and the application themselves.

Therefore, we can say that contextual information includes a wide range of information which is domain specific and differ from one domain to another domain. For example, contextual information in domain of intelligent home application is different from contextual information which is used in an electronic shop. For conquering the problem of diversity of contextual information, we should limit types of contextual information which is used in our applications by appropriate modeling of context.

In [15] six different approaches for context modeling have been discussed, and ontology has been selected as the best approach for modeling context. Since we are going to use contextual information in enterprise information systems, the following ontology has been designed for representing context in our work. As seen in figure 1, the contextual information includes: requester’s related information, information related to computational entities like PCs and Networks, location of entities, temporal information and information related to requester’s activities.

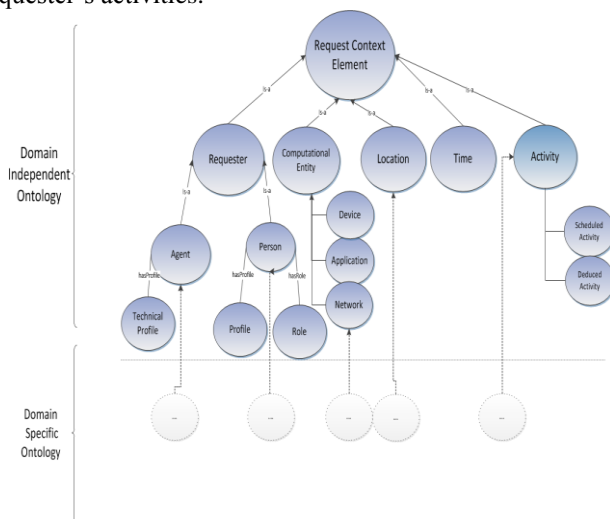


Figure 1: Context Ontology

As shown in figure 1, the designed ontology is a two-layered, hierarchal ontology. In the upper level there are domain independent concepts like computational entity, person, agent, etc. According to the domain in which this method will be applied, domain dependent concepts will

appear in the lower level ontology. In addition, the relation of these concepts with upper ones will be specified. Due to the lack of space, “is-a” relations are mostly considered in this paper, and other relations between concepts are ignored.

The two tier approach used in this paper, on the one hand, allows the use of this method in different domains and on the other hand allows reuse of existing ontologies. For example if we want to apply this method in university domain we can use ontology developed in [20] in the lower level.

IV. SERVICE DESCRIPTION

In this paper we adopt semantic approach for service description. So far, several approaches have been proposed for semantic web service description. Among them, we can mention OWL-S[16], WSMO[17] and SA-WSDL[18]. Since these approaches have a comprehensive view on the service life cycle, they have proposed a comprehensive ontology for describing all facets of web services. For example, OWL-S consists of three ontologies: service profile, service model and service grounding.

Obviously, web service description should be in accordance to our goal in this paper, i.e., proposing a context aware method for service discovery. Thus, we propose the following ontology for describing capabilities of web services. By using this ontology, we can describe atomic services in terms of their capabilities and their contextual constraints. In the following, concepts of this ontology and relations among them will be discussed.

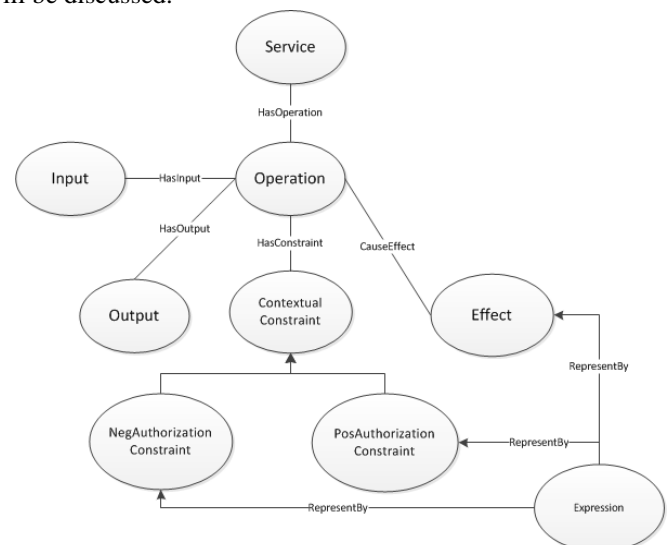


Figure 2: The Proposed Ontology For Service Description

In the proposed ontology the Service concept represents available services in the enterprise. For any instance of an available web service, there is one instance of this concept. Any instance of this concept can have one or more operation(s) which are represented by concept Operation. Each operation can have zero or more input(s) and provide one or more output(s). As shown in Figure 2, inputs and outputs are represented by Input and Output concepts, respectively.

The Effect concept in the proposed web service description

ontology is similar to Effect in OWL-S [16]. Although each web service operation can have one or more precondition, since these preconditions are checked and validated at runtime, they are not included in the service ontology. For example, a payment web service may have a precondition that checks whether the card number is valid or not. This precondition is checked at runtime after providing the card number by the user; hence, it is not necessary to consider such conditions during service discovery.

Instead of preconditions, we have contextual constraints in the service description ontology. These constraints allow us to specify policies for restricting user access to available services. Constraints are classified as PosAuthorizationConstraint and NegAuthorizationConstraint. The first one expresses situations in which a request should be able to access a web service operation. The second one, however, indicates situations in which a request of accessing a web service operation is prevented. These constraints are specified by domain engineers. For example, as a policy, we can restrict accessibility of a particular web service operation to senior managers in an enterprise.

As shown in Figure 2, contextual constraints and effects are represented by expressions. We can use SWRL for expressing expressions. Additional information about SWRL can be found in [19].

V. PROPOSED METHOD

In previous sections we discussed how services are described and context is represented. In this section we describe the proposed method for context aware discovery of web services. In the proposed method contextual information is captured on request submitting. Thus, each user request has two main parts: requirements specified by the user and contextual information related to the user request. The user specifies the goal(s) he/she wants to obtain in a request, and contextual information will be added to the request automatically. We use the proposed context ontology for attaching defined context element to user request.

Domain engineers establish relation(s) between available services and user's intended goals by means of Task concept. Using Task concept, on the one hand, we specify what tasks are fulfilled by the execution of a service operation described by service ontology, and on the other hand, we show what tasks should be performed to satisfy a specific goal defined by a domain engineer. Determining relations between goals and services, we can use a backward algorithm for constructing workflows that satisfy user goals. The proposed algorithm is shown as follows.

Algorithm 1: Service synthesizing algorithm

Service Synthesizing Algorithm

Input:User Request UR

Output: A set of candidate workflows CWFS

//This algorithm accepts user requests as input and tries to synthesize a set of workflows that can fulfill user requirements. This algorithm uses Trychain which is a recursive algorithm.

```

1. Workflow set CWFS, PWFS //
   Candidate Workflows //Set,
   Potential Workflows Set
2. For each service S in the service
   repository whose operation O
   fulfill the user goal {
3. Create a workflow W, add operation
   O of S to end of it and add W to
   CWFS
4. }
5. For each workflow W in CWFS {
6. For each operation O in W {
7. If O has unsatisfied constraint {
8. CWFS=CWFS / {W}
9. PWFS=PWFS U {W}
10.} } }
11.For each workflow W in PWFS{
12.Workflow Temp=Trychain(w,ur);
13.If Temp != Unsatisfiable // if
   there are services which can
   satisfy unresolved constraints
14.CWFS=CWFS U {temp}
15.}
16.Return CWFS

```

In algorithm 1 we have two sets of workflows: candidate workflow set (CWFS) and potential workflow set (PWFS). At the end of algorithm composite or atomic services that can fulfill user goals and their constraints are satisfiable upon contextual information of user request, are in candidate workflow set and potential workflow set consist of services that can fulfill user request but at least one of their constraints is unsatisfiable upon contextual information of user request.

In algorithm 1 we create a workflow corresponding to every service that has an operation which can satisfy user goal(s) and add the workflow to CWFS (line 1-4). Then we check for satisfaction of operation's constraints of every workflow in CWFS. If a workflow has an unsatisfied constraint we remove it from CWFS and add it to PWFS (Line 5-10). For every workflow which has unsatisfied constraint(s) in its operations we will try find services that their operations effect satisfy their constraints. This will be done using a recursive algorithm called TryChain. This algorithm tries to chain services in service repository to workflows in PWFS so that every unsatisfied constraint will be satisfied. Trychain algorithm is as follow.

Algorithm 2: Trychain Algorithm

TryChainAlgorithm

Input: a workflow W and user request ur

Output: a workflow or unresolvable value

//This recursive algorithm accepts a workflow with unsatisfied constraints and tries to chain it with available services so that all constraints are satisfied. If it cannot do that, returns unsatisfiable value.

```

1. For each operation O in W {
2. For each unsatisfied constraint C
   of O
3. {
4. If there exists service S in the
   service repository that has an
   operation Op that its effect
   satisfying C
5. Append Op to the end of W
6. Else
7. Return Unsatisfiable
8. If Op has an unsatisfied
   constraint based on ur contextual
   information
9. TryChain(W,ur)
10.Return W
11.}}
```

In TryChain algorithm we try to find services that their effects can satisfy unsatisfied constraints of an operation. This is a recursive algorithm which tries to chain services to find a composite service that all of its constraints are satisfied. If it cannot find such a composite service it return unsatisfiable.

VI. CASE STUDY

In order to demonstrate the applicability of the proposed method and the results of using it, we apply this method to the university domain. In this domain, a set of services is available which are all described by the proposed ontology for web service description. As stated before, each service may have contextual constraints. By means of these constraints, we can apply policies for restricting user’s access to available services. For example, we can make a particular operation of a web service accessible to senior managers in the university. In Table 1, a part of possible services in a university is shown.

Table 1: Part of available services in university domain

Service Name	Service Operations	Contextual Constraints
S1	-Reserve a meal -Cancel a reserved meal	NA
S2	Download paper	-Only for graduate students -Only for Internal IP
S3	Establish VPN	-Only for graduate students
S4	Search book	-Only for library members

Users in their requests for service discovery specify their intended goal(s) among available goals specified by domain engineers. After the submission of user’s requests, a set of contextual information will be added to the user request based on context ontology. For example, based on the user profile, a set of his/her personal information like age, gender and role could be added to the user request. Also, some dynamic context information will be added to the request. Among dynamic context information, we can mention devices used by the user, network which is used to send requests, and current location of the user. Now, the user request enriched by the context information can be used for context aware discovery of web services.

Suppose that user A, who is a M.S Student and is outside of the university, wants to find a suitable service for downloading papers. Based on the user request, it is obvious that service S2 can satisfy the user’s specified goal. As shown in Table 1, the ‘Download paper’ operation of this service has two constraints: first it is available only for graduate students, and second, it is available only for requests with internal IP. By considering context ontology, we can infer that M.S students are graduate students (this has been declared in the ontology using an “is-a” relation between M.S Student and Graduate Student concepts), the first constraint is satisfied. But the second one cannot be satisfied according to the user request and request context. Hence, if we only took atomic services into account, we could not find an appropriate service for the user request.

But, since in this paper we pay attention to composite services, with regard to available services and by applying algorithm 1, we can recommend an appropriate composite service to user A. since ‘Download paper’ operation of service S2 can satisfy the goal specified by user A, a workflow will be created and ‘Download paper’ operation will be appended to end of this workflow. Then by checking contextual constraints of the added operation, we can understand that ‘internal IP’ constraint cannot be satisfied. So by using Trychain which is a recursive algorithm, we try to find a chain of web services which can satisfy the unsatisfied constraint altogether.

By investigating available services, it is observable that ‘Establish VPN connection’ operation of service S3 has an effect that can satisfy ‘Internal IP’ constraint (Note that we didn’t show service effect in Table1 due to lack of space). So ‘Establish VPN connection’ operation will be appended to the end of workflow. Now in Trychain, contextual constraints of ‘Establish VPN Connection’ operation will be checked. Since this operation just has one constraint (only for graduate Students), and this constraint is satisfiable by the contextual information of the user request, the created workflow will be added to the candidate workflow set and will be recommended to the user.

VII. CONCLUSION AND FUTURE WORK

As demonstrated in the case study, with the help of the proposed method, we can use contextual information during service discovery process and suggest appropriate services to

the user. Since we consider composite services in the proposed method, it is classified as indirect services discovery approaches. Taking composite services into account causes reduction of ‘false negative’. By using the proposed approach, we also applied enterprise policies for restricting user’s access to available services.

We are going to design and implement a framework based on the proposed approach. By implementing such framework and analyzing quantitative results, we can study applicability and performance of the proposed approach more precisely. Considering non functional attributes of web services and ranking suggested web services upon these attributes could be considered as another future work.

VIII. REFERENCES

- [1] Erl, T.: Service-Oriented Architecture:Concept,Technology, and Design.Pretice Hall PTR(2005)
- [2] Srivastava, B., Koehler, J.: Web service composition-current solutions and open problems.In: ICAPS 2003 Workshop on Planning for Web Services. pp. 28–35.(2003)
- [3] Dustdar, S.,Schreiner, W., “A Survey on web service composition,”International Journal of Web and Grid Services, vol.1, pp. 1-30, (2005).
- [4] Pawar, P.,Tokmakoff, A.: Ontology-Based Context-Aware Service Discovery for Pervasive Environments. In:*Preceding of IEEE International Workshop on Services Integration in Pervasive Environments*, 2006.
- [5] Rasch, K.,Li, F., Sehic, S.,Ayani,R.,Dustdar, S.: Context-driven personalized service discovery in pervasive environments. In *World wide web*, vol. 14, no. 4, pp. 295-319, (2011)
- [6] Xiao,H.,Zou,Y.,Ng, J.,Nigul, L.: An Approach for Context-aware Service Discovery and Recommendation. In:*preceding of IEEE International Conference on Web Services*, pp. 163-170, (2010)
- [7] Patel, P.,Chaudhary,S.: Context Aware Semantic Service Discovery. In: Preceding of World Conference on Services – II, pp. 1-8, (2009).
- [8] Schilit, B.N,Theimer,M .M.: Disseminating Active Map Information to Mobile Hosts, *IEEE Network*, vol.8, no.5, 1994.
- [9] Ryan, N.,Pascoe, J,Morse, D.:Enhanced reality fieldwork: the context aware archaeological assistant.*Computer Applications and Quantitative Methods in Archaeology*, 1997.
- [10] Dey, A. K,Abowd,G. D.: Toward a better understanding of context and Context-Awareness. In:*Proceedings of the 1st international symposium on Handheld and Ubiquitous Computing*,pp. 304-307,(1999)
- [11] Dey, A. K.: Context-aware computing: The CyberDesk project. In: *Proceedings of the AAAI Spring Symposium on Intelligent Environments. Menlo Park*, 1998.
- [12] Hull, R., Neaves, P., Bedford-Roberts,J.: Towards situated computing. InProceedings of International Symposium on Wearable Computers (1997)
- [13] Peter J. Brown. The Stick-e Document: a framework for creating context-awareapplications. In Electronic Publishing, Palo Alto, 1996.
- [14] Dey, A. K.,Abowd, G.D.: Towards a better understanding of context and contextawareness. In: Proceedings of the Workshop on the What, Who, Where, When and How of Context-Awareness, affiliated with the CHI 2000 Conference on Human Factors in Computer Systems, New York, NY: ACM Press(2000)
- [15] Strang, T.,Linnhoff-Popien, C.: A context modeling survey.in*Workshop Proceedings*,(2004).
- [16] <http://www.w3.org/Submission/OWL-S/>
- [17] <http://www.w3.org/Submission/WSMO/>
- [18] <http://www.w3.org/2002/ws/sawSDL/>
- [19] <http://www.w3.org/Submission/SWRL/>
- [20] Malviya, N., Mishra,N.,Sahu,S.: Developing University Ontology using protégé OWL Tool: Process and Reasoning. In: *International Journal of Scientific & Engineering Research*, vol. 2, no. 9, p. 1, 2011.

Comparative Study on Different Classifiers for Frog Identification System Based on Bioacoustic Signal Analysis

H. Jaafar, D.A Ramli and B.A. Rosdi

Abstract—Recently, scientists have discovered that most frog species produce skin secretions of an amino acid compound called peptides that can produce several avenues of research with application for human medicine. Instead of depending on physical observation procedure to identify the particular species, this study proposes an automated frog identification system based on bioacoustic signal analysis. Experimental studies of 1260 audio data from 28 species of frogs from the Internet and Intelligent Biometric Group, Universiti Sains Malaysia, IBG, USM databases are used in this study. These audio data are then corrupted by 10dB and 5dB noise. A syllable feature extraction method i.e. Mel-Frequency Cepstrum Coefficients (MFCC) employed to extract the segmented signal. Subsequently, three classifiers i.e. Support Vector Machine (SVM), Sparse Representation Classifier (SRC) and Local Mean k-Nearest Neighbor with Fuzzy Distance Weighting (LMkNN-FDW) are developed in order to evaluate the performance of the identification system. The experimental results show that LMkNN-FDW outperforms SVM and SRC in clean SNR by 97.54% and 87.2% for the Internet and IBG, USM databases, respectively.

Keywords—Bioacoustic signal, MFCC, SVM, SRC, LMkNN-FDW.

I. INTRODUCTION

Antibiotic was discovered in the 1920s and has been used commercially in the World War II to treat a wide variety of illnesses caused by bacteria. However, for the past 20 years, numerous bacteria are able to resist against the existing drug or antibiotic. This caused a serious threat to the public health problem [1]. Hence, finding alternatives to traditional antibiotic has become an urgent need. Recently, numerous antimicrobial peptides discovered from a wide range of organisms are able to kill bacteria rapidly without being affected by resistance mechanism. Among these, an antimicrobial peptide from frogs triggers an interesting study area. This is primarily because the compounds of peptides

released from their skins depend on their habit and environment that consequently yield the structural features of effective antimicrobial peptides for medical purposes [2]. Several studies have identified the frog species based on genetic morphological characteristic [3] and molecular ecology [2]. Yet, the methods used in these studies were determined through collection of specimens and detail observation of taxonomic relationships. Such methods are often proven to be costly, time-consuming and logically difficult. Hence, bioacoustic signal is greatly needed for automatic detection and classification of frogs. Furthermore, the sound can be collected easily and continuously without interfering with the animals and disturbing their population structure [4].

In the work presented here, an automatic system for frog identification system based on their call has been developed. The system consists of three important procedures i.e. syllable segmentation, feature extraction and classification as shown in Fig. 1. 1260 audio data from 28 different species of frogs obtained from the Internet and Intelligent Biometric Group (IBG), Universiti Sains Malaysia (USM) databases are extracted with Mel Frequency Cepstrum Coefficient (MFCC) as the feature extraction. Additionally, the audio data are then corrupted and tested in clean condition, 5dB and 10dB Signal to Noise Ratio (SNR). In order to classify the frog species in the pattern matching process, various classifications have been used, including Support Vector Machine (SVM), Sparse Representation Classifier (SRC) and Local Mean k-Nearest Neighbor with Fuzzy Distance Weighting (LMkNN-FDW). The objectives of this study are twofold; (1) to test the performance of classifiers in noisy environment and (2) to compare the performance of classifiers in the frog identification system. This paper has been outlined as follows. In Section II, the methodology of this study including data acquisition, syllable segmentation, feature extraction and classification is discussed. The experimental results are presented in Section III and finally, Section IV provides the conclusion.

This work was supported in part by Universiti Sains Malaysia Short Term Grant 60311048, Research University Grant 814161 and Research University-Post Graduate Grant Scheme 8046019.

H. Jaafar, is with Intelligent Biometric Group, School of Electrical and Electronic, Universiti Sains Malaysia, Engineering Campus, 14300 Nibong Tebal, Pulau Pinang, Malaysia (e-mail: haryati_jaafar@yahoo.com).

D.A. Ramli is with Intelligent Biometric Group, School of Electrical and Electronic, Universiti Sains Malaysia, Engineering Campus, 14300 Nibong Tebal, Pulau Pinang, Malaysia (corresponding author to provide phone: +604-5996028; e-mail: dzati@eng.usm.my).

B.A. Rosdi is with the Intelligent Biometric Group, School of Electrical and Electronic, Universiti Sains Malaysia, Engineering Campus, 14300 Nibong Tebal, Pulau Pinang, Malaysia (e-mail: eebakhtiar@eng.usm.my).

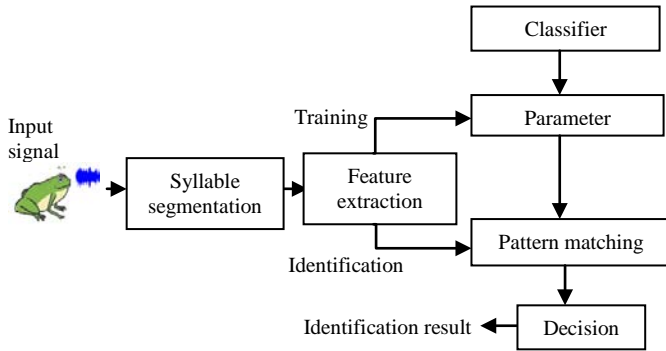


Fig. 1. Frog identification system

II. METHODOLOGY

The digital frog call samples are obtained from 2 sources i.e. the Internet and IBG, USM databases. All wave files of frog calls are recorded again at a sampling frequency of 48kHz and digitized in 32-bit and are simulated with Additive White Gaussian Noise (AGWN). 13 species are obtained from 5 families which are *Microhyla butleri* (painted chorus frog) from Microhylidae family, *Babina adenopleura* (olive frog), *Hylarana taipehensis* (Taipei brown frog), *Lithobates catesbeianus* (American bullfrog), *Rana sauteri* (Sauteri's brown frog) from Ranidae family, *Polypedates braueri* (white throated tree frog), *Kurixalus idiootocus* (surface-day tree frog) from Rhacophoridae family, *Bufo bankorensis* (Taiwan common frog) from Bufonidae family, *Litoria caerulea* (green tree frog), *Litoria splendida* (magnificent tree frog), *Litoria rothii* (roth's tree frog), *Litoria nasuta* (rocket frog) from Hylidae family and *Platyplectrum ornatus* (ornate burrowing frog) from Myobatrachidae family [12].

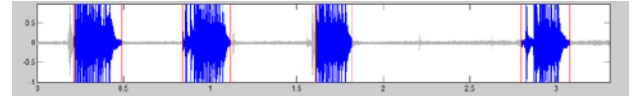
On the other hand, the frogs call provided by IBG, USM are recorded from various locations in the districts of Baling and Kulim, Kedah using Sony Stereo IC Recorder ICD-AX412F supported with Sony electret condenser microphone. These locations are selected based on the frogs' potential habitat such as near swamp areas, running streams and pond areas from 8.00 pm to 12.00pm. 12 species are obtained from the recording such as *Hylarana glandulosa* (rough sided frog), *Kaloula pulchra* (Asian painted bullfrog), *Kaloula baleata* (flower pot toad), *Microhyla heymonsi* (Taiwan rice frog), *Microhyla butleri* (painted chorus frog) from Microhylidae family, *Phrynoidis aspera* (river toad), *Duttaphrynus melanostictus* (black-spectacled toad), *Genus ansonia* (stream toad) from Bufonidae family, *Odorrana hossi* (poisonous rock frog), *Hylarana labialis* (white-lipped frog) from Ranidae family, *Polypedates leucomystax* (common tree frog), *Philautus mjobergi* (bubble-nest frog), *Philautus petersi* (kerangas bush frog), *Rhacophorus appendiculatus* (frilled tree frog) from Rhacophoridae family and *Fejervarya limnocharis* (grass frog) from Dicroglossidae family.

A. Syllables Segmentation

A syllable refers to the sound that a frog produces with a side blow of air from the lungs. Compared to human, frog syllables seem to be slightly less complex due to no-vowel-consonant and less intricate grammar [5]. Fig. 2 shows an

example of syllables waveform of *Kaloulabaleata*. Basically, the waveforms from each syllable appear to be similar. However, each syllable is different depending on how an individual frog permanently changes its calls that causes the creation of new syllables. Depending on the species, the syllables may occur in a wide range of frequencies and some are long, lasting several seconds, while others last only for a fraction of a second.

In this study, automatic syllable segmentation is employed for all frog sound signals based on Short Time Energy (STE) and short time average zero crossing rate (STAZCR). The principle of the technique is to determine the endpoint of syllable boundaries accurately where the endpoint is used to detect the syllable signal that has been segmented [6].


 Fig. 2. Example of syllables waveform of *Kaloula baleata*.

B. Feature Extraction

In this paper, MFCC is selected due to its robust features, which make it reliable to noise, hence easy to implement in an outdoor environment that contains interference of background noise for example the sound of wind, running water and other animal calls. MFCC processing consists of signal pre-emphasis, windowing, spectral analysis, filter bank processing, log energy computation and mel frequency cepstrum computation as shown in Fig. 3. 15 melcepstrum coefficients, one log energy coefficient and three delta coefficients per frame are set in the experiments [7].

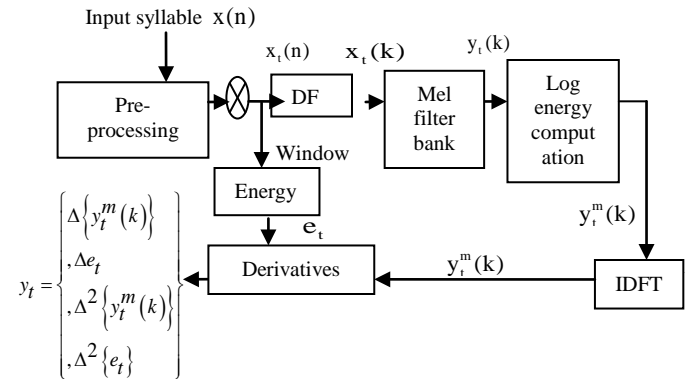


Fig. 3. MFCC process

C. Classification

SVM is a classifier based on the principle of structural risk minimization and is used for solving problems in pattern recognition. SVM is formulated in such a way that it is only capable of discriminating between two classes whereas most classification tasks typically involved more than two classes [8]. The solution of the linearly separable case is started by considering a problem of separating the set of training vectors belongs to two separate classes;

$$D = \left\{ (x^1, y^1), \dots, (x^L, y^L) \right\} \quad x \in \mathcal{R}^n \quad y \in \{-1, 1\} \quad (1)$$

with a hyperplane,

$$(w, x) + b = 0 \quad (2)$$

where w and b are the direction and position in space, respectively, and w is normal to the plane. The hyperplane that optimally separates the data which is equivalent to minimizing an upper bound on VC dimension and given as;

$$\phi(w) = \frac{1}{2} \|w\|^2 \quad (3)$$

In order to mapping the input vector x into a high dimensional feature space, the kernel function $K(x_i, x_j)$ is used and defined as;

$$K(x_i, x_j) = \phi(x_i)^T \phi(x_j) = (\gamma x_i^T x_j - r)^a \quad (4)$$

where $\gamma > 0$ and γ, r and d are kernel parameters.

On the other hand, SRC is a non-parametric learning process and this method directly assigns a class label to the test sample without the training model. Given a set of training and test sample, the basic idea of the SRC is to compute the sparse representation of the test sample on the training data. Then, the test sample is assigned to the class that minimizes the residual between itself and is reconstructed by the sparse representation that is associated to the training samples of each class. Briefly, SRC can be formulated to solve the following optimization problem [10];

$$\min \|x\|_1 \text{ subject to } \|y - Ax\|_2 \leq \varepsilon \quad (5)$$

where $\|x\|_1$ is the l_1 -norm, A and y matrix of training sample and test sample, respectively.

The test sample can be classified by minimizing the residual and yield;

$$\min r_k(y) = \|y - A\hat{\partial}_k(x)\|_2 \quad (6)$$

Where $\hat{\partial}_k$ is a characteristic function to select the coefficient of the sample belonging to class k .

The third classifier employed in this study is LMkNN-FDW [10]. Basically, LMkNN-FDW is the improvement of k-nearest neighbor (kNN) where the distance between query pattern or testing sample and local means vector is assigned using fuzzy algorithm [11]. Let $X_i = \{x_n \in R^m\}_{n=1}^N$ be a training sample where m is the number of dimensional in feature space, N is the total number of training sample and $y_n \in \{c_1, c_2, \dots, c_M\}$ denotes the class label for x_n . Then, the kNN is determined from the set X_i for each class y_n by Euclidean distance as given as;

$$d(x, x_{ij}^N) = \sqrt{(x - x_{ij}^N)^T (x - x_{ij}^N)} \quad (7)$$

The local mean vector Y_{ik} is obtained by applying k nearest neighbor of training sample such that;

$$Y_{ik} = \frac{1}{k} \sum_{j=1}^k x_{ij}^N \quad (8)$$

By applying fuzzy with distance weighting, the fuzzy membership $U_{ij}(k)$ can be computed as follows;

$$u_{ij} = \frac{\sum_{j=1}^k u_{ij} \left[\frac{1}{\|x - Y_{ik}\|^{2/(m-1)}} \right]}{\sum_{j=1}^k \left[\frac{1}{\|x - Y_{ik}\|^{2/(m-1)}} \right]} \quad (9)$$

Note the notation m denotes the fuzzy weight of the distance or fuzzy relationship. If value m increases, the neighbors are more evenly weighted. This causes the distance between training and query pattern to have less effect on each other and vice-versa.

III. EXPERIMENTAL RESULTS

The experiments are implemented using Matlab R2010 (b) and have been tested in Intel Core i5, 2.1GHz CPU, 6G RAM and Windows 7 operating system. In this experiment, the data of 45 syllables are extracted by a MFCC in which 20 syllables are used for training and 25 for testing. The value of $k=3$ is used for kNN, $\varepsilon = 0.001$ is set for the SRC and polynomial kernel is adopted for SVM. The classification accuracy (C_A) is defined as;

$$C_A = \frac{N_C}{N_T} \times 100\% \quad (10)$$

where N_C is the number of syllables which are recognized correctly and N_T is the total number of test syllables.

Table 1 lists the analytical results of the classifiers in clean, 10dB and 5dB SNR. The results show that all of the classifiers are able to identify the frog species more than 75% in all conditions. It can be seen that LMkNN-FDW always outperforms SVM and SRC and produces the best classification accuracy with more than 90%, either in clean condition or noisy environment. Moreover, two species; *Microhyla butleri* and *Litoria splendida* are able to be identified with 100% accuracy.

The classification accuracy of frog sound for every species of frogs obtained from IBG, USM is shown in Table 2. The results show that the performance accuracy for LMkNN-FDW is slightly better than SVM and SRC in clean condition with 87.2%. However, in the noisy environment, SRC shows greater performance than LMkNN-FDW with 78.93% and 74.4% in 10dB and 5dB, respectively.

Table 1. Performance results obtained from internet database

Species	SVM			SRC			LMkNN-FDW		
	Clean	10dB	5dB	Clean	10dB	5dB	Clean	10dB	5dB
<i>Babina adenopleura</i>	25	20	25	24	24	25	25	23	25
<i>Bufo bankorensis</i>	25	25	24	24	22	19	25	23	25
<i>Hylarana taipehensis</i>	23	25	24	23	22	21	21	25	24
<i>Lithobates catesbeianus</i>	25	14	25	25	14	25	25	22	25
<i>Rana sauteri</i>	25	24	20	25	8	8	25	25	17
<i>Microhyla butleri</i>	25	25	20	23	24	20	25	25	25
<i>Polypedates braueri</i>	24	24	24	24	23	21	24	25	24
<i>Kurixalus idiootocus</i>	25	25	24	25	25	23	25	25	23
<i>Litoria caerulea</i>	25	22	16	25	16	7	25	25	18
<i>Litoria splendida</i>	21	24	22	25	25	21	25	25	25
<i>Litoria rothii</i>	25	24	14	25	22	13	25	25	23
<i>Litoria nasuta</i>	25	25	24	25	22	23	25	25	24
<i>Platyplectrum ornatus</i>	25	24	25	25	18	20	25	24	25
Total	318	301	287	318	265	246	320	317	303
C_A (%)	97.85	92.62	88.31	97.85	81.54	75.69	98.46	97.54	93.23

Table 2. Performance results obtained from IBG, USM database

Species	SVM			SRC			LMkNN-FDW		
	Clean	10dB	5dB	Clean	10dB	5dB	Clean	10dB	5dB
<i>Hylarana glandulosa</i>	25	25	25	25	24	25	25	21	20
<i>Kaloula pulchra</i>	25	25	25	25	25	25	25	25	25
<i>Odorrana hossi</i>	15	13	9	13	10	10	15	11	9
<i>Polypedates leucomystax</i>	25	25	25	25	25	25	25	25	24
<i>Kaloula baleata</i>	25	25	25	25	25	25	25	25	25
<i>Philautus mjobergi</i>	25	16	13	19	17	15	24	19	15
<i>Duttaphrynus melanostictus</i>	25	25	25	25	25	25	25	25	25
<i>Phrynoidis aspera</i>	19	18	18	17	19	23	21	19	19
<i>Microhyla heymonsi</i>	12	9	7	18	14	12	13	13	10
<i>Fejervarya limnocharis</i>	22	22	20	17	20	14	21	16	20
<i>Genus ansonia</i>	21	21	12	17	15	13	24	14	18
<i>Rhacophorus appendiculatus</i>	25	25	23	25	24	22	25	18	21
<i>Hylarana labialis</i>	25	18	18	24	20	19	25	22	18
<i>Philautus petersi</i>	10	8	9	9	11	5	10	4	5
<i>Microhyla butleri</i>	22	21	20	22	22	21	24	25	24
Total	321	296	274	306	296	279	327	282	278
C_A (%)	85.60	78.93	73.07	81.6	78.93	74.4	87.2	75.2	74.13

IV. CONCLUSION

In this paper, the frog sound identification system based on bioacoustics signal has been studied and successfully implemented. The audio data are obtained from the Internet and IBG, USM databases and are segmented using STE and STAZCR. The segmented syllables are first extracted with MFCC. Subsequently, three classifiers i.e. SVM, SRC, LMkNN-FDW are used and compared in clean, 10dB and 5dB SNR. For the Internet database, the highest classification accuracies for SVM, SRC and LMkNN-FDW are obtained in clean SNR yield 97.85%, 97.85% and 98.48%, respectively. The results indicate that LMkNN-FDW provides the best classification among the four classifiers. On the other hand, for the IBG, USM dataset, it is found that LMkNN-FDW outperforms SVM and SRC in clean SNR with 87.2%

classification accuracy. However, the performance of LMkNN-FDW slightly decreased with 75.2% than SVM and SRC for 10dB with 78.93%. For 5dB SNR, it is observed that the SRC provides the best result with 74.4% better than SVM and LMkNN-FDW. Based on the results of these experiments, certain frog species are able to be easily recognized by the proposed method, whereas the characteristics of the sounds of some species, such as *Odorrana hossi* and *Philautus petersi*, clearly require further analysis.

REFERENCES

- [1] S. R. Norrby, C. E. Nord, and R. Finch, "Lack of development of new antimicrobial drugs: a potential serious threat to public health," *Lancet Infect*, vol.5, no. 2, pp.115-119, 2005.
- [2] X. Liu, R. Liu, L. Wei, H. Yang, K. Zhang, J. Liu, and R. Lai, "Two novel antimicrobial peptides from skin secretions of the frog, *Rana nigrovittata*," *Journal of Peptide Science*, vol. 17, pp. 68-73, 2010.

- [3] I. D. Gauld, M. A. O'Neill, and K.J. Gaston, "Driving Miss Daisy: the performance of an automated insect identification system," In: Austin, A. D., Dowton, M. (Eds.), *Hymenoptera: Evolution, Biodiversity and Biological Control*. CISRO, Collingwood, VIC, 2000, pp. 303–312.
- [4] M. A. Acevedo, C. J. Bravo, H. C. Bravo, L. J. V., Rivera, and T. M. Aide, "Automated classification of bird and amphibian calls using machine learning: A comparison of methods," *Ecological Information*, vol. 4, no. 4, pp. 206-214, 2009.
- [5] A. Harma, "Automatic identification of bird species based on sinusoidal modeling of syllables," presented at the 2003 5th Internat. Conf. on Acoust. Speech Signal Process, pp. 545–548.
- [6] H. Jaafar, and D. A. Ramli, "Automatic syllables segmentation for frog identification system," presented at the 2013 9th IEEE Int. Colloquium on Signal Processing and its App, 90-95.
- [7] H. Jaafar, D. A. Ramli, and S. Shahrudin, "MFCC based frog identification system in noisy environment," presented at 2013 IEEE International Conference on Signal and Image Processing Applications.
- [8] D. A. Ramli, S. A. Samad, and A. Hussain, "A multibiometric speaker authentication system with SVM audio reliability indicator," *IAENG International Journal of Computer Science (IJCS-Special Issues)*, vol. 36, no. 4, pp. 313-321, 2009.
- [9] J J. Wright, A. Y. Yang, A. Ganesh, S. S. Sastry, and Y. Ma, "Robust face recognition via sparse representation," *IEEE Trans. Pattern Analysis Machine Intelligent*, vol. 31, no. 2, pp. 210–227, 2009.
- [10] H. Jaafar, D. A. Ramli, B. A. Rosdi, and S. Shahrudin, "Frog identification system based on local means k-nearest neighbors with fuzzy distance weighting," presented at 2013 8th International Conference on Robotic, Vision, Signal Processing and Power Application.
- [11] Y. Zeng, Y., Yang, and L. Zhao, "Nonparametric classification based on local mean and class statistics," *Expert Syst. Appl*, vol. 36, pp. 8443–8448, 2009.
- [12] (Online Sources style. Available: <http://museumvictoria.com.au/bioinformatics/frog/>)

Early termination of transform skip mode for High Efficiency Video Coding

Do-Kyung Lee, Miso Park, Hyung-Do Kim and Je-Chang Jeong

Abstract—High Efficiency Video Coding (HEVC) is a recently developed video coding standard by Joint Collaborative Team on Video Coding (JCT-VC). It proves coding efficiency about half in point of bit rate reduction compared with H.264/MPEG-4 AVC. In transform process of HEVC, there is skip mode only for 4x4 transform blocks; however, for screen contents, it is helpful to extend transform block size for transform skip and has great coding performance. In this paper, we proposed early termination scheme for transform skip mode and scan order modification for computational time. The experimental results show 9% ~ 16% of saving time with small BD-PSNR loss.

Keywords—Transform skip mode, discrete cosine transform, high efficiency video coding, HEVC.

I. INTRODUCTION

WITH the popularity and the demand of high resolution video increased rapidly, new video codec technologies which has better coding efficiency than H.264/MPEG-4 AVC [1] proposed for past few years. Finally, as the successor of H.264/MPEG-4 AVC, the high efficiency video coding (HEVC) [2] was recently finalized by the Joint Collaborative Team on Video Coding (JCT-VC) consists of members in ISO/IEC MPEG and ITU-T VCEG. HEVC performs half bit-rate reduction compared to H.264/MPEG-4 AVC High Profile with the similar subjective video quality. The main difference between H.264/MPEG-4 AVC and HEVC is the basic unit of coding structure. H.264/MPEG-4 AVC utilize only 16x16 blocks which has fixed block size regardless of video characteristics. However, HEVC uses basic units with variable block size (8x8 to 64x64) which can adaptively encode the high resolution video [3]. A coding tree unit (CTU) has three coding tree blocks (CTBs) that are one luma and two chroma components and has the related syntax elements. HEVC divide CTU to coding units (CUs) employed quadtree structure, and

This research was supported by the MSIP (Ministry of Science, ICT & Future Planning), Korea, under the ITRC (Information Technology Research Center) support program supervised by the NIPA (National IT Industry Promotion Agency) (NIPA-2013-H0301-13-1011).

D. Lee is with the Department of Electronics and Computer Engineering, Hanyang University, 222, Wangsimni-ro, Seongdong-gu, Seoul, Korea (e-mail: dky1006@gmail.com).

H. Kim is with the Department of Electronics and Computer Engineering, Hanyang University, 222, Wangsimni-ro, Seongdong-gu, Seoul, Korea (e-mail: khd1207@gmail.com).

J. Jeong is with the Department of Electronics and Computer Engineering, Hanyang University, 222, Wangsimni-ro, Seongdong-gu, Seoul, Korea (corresponding author to provide phone: +82-2-2220-4369; e-mail: jjeong@hanyang.ac.kr).

CUs also can be separated into multiple prediction units (PUs) and transform units (TUs). PU is basic unit of prediction (intra-picture prediction and inter-picture prediction) and it is specified by splitting types. For each TU, integer transform based on DCT (discrete cosine transform) and quantization is applied. TU can be divided into half size of TUs followed by residual quadtree (RQT). The best sizes and modes for each CTU are determined by rate-distortion cost (RD cost), and HEVC finally can get bit-streams to binarize and entropy-code with transform coefficients.

The remainder part of this paper is organized as follows. Section II describes properties of DCT and technologies for transform skip mode (TSM). The proposed algorithm for TSM is specified in Section III. Experimental results and analysis are shown in Section IV. Finally, we conclude our proposed algorithms in Section V.

II. BACKGROUNDS

A. Properties of Discrete Cosine Transform

For signal processing and image compression, one of the most commonly used transform method is DCT. Since the cosine transform has outstanding energy compaction for highly correlated signals like images and video sequences, DCT yields great coding performance with video codec [4].

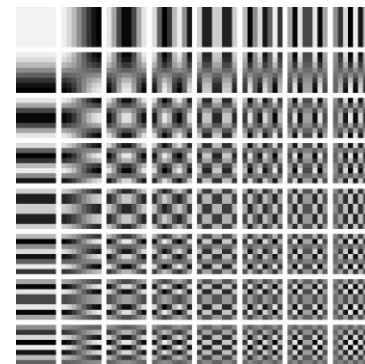


Fig. 1 Basis functions of DCT

As shown in Fig. 1, a basis function of left-upper position represents direct current (DC) component and right-bottom bases of DCT are high-frequency components in 8x8 block image. Also, first row of basis function represents vertical edges and first column shows horizontal edges. If the most of DCT coefficients congregate at nearby DC component, we can easily compress images with quantization which removes relatively

small amount of high-frequencies.

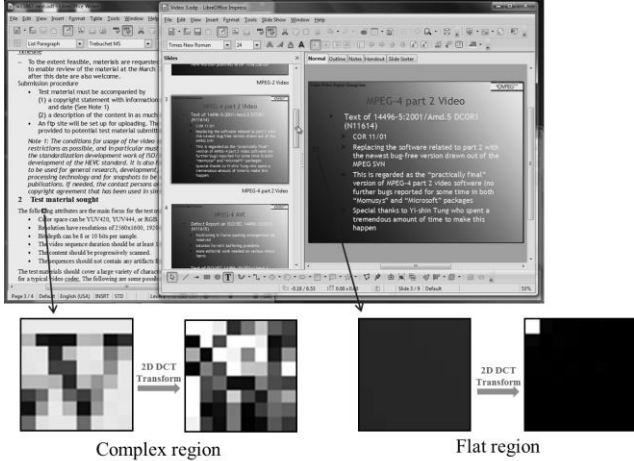


Fig. 2 Transform coefficient for complex region and flat region

For example, 8x8 DCT coefficients for screen contents are described in Fig. 2, and the test sequence is ‘SlideEditing_1280x720’ that has flat regions and also has high frequency region like text and menu icons. In complex region, coefficients spread out whole area except DC, and relatively more distributed in high frequency region than low frequency region. It is not efficient to apply DCT transform to this complex area for video codec because there is lots of important information on high frequency region. On the contrary, in flat region, whole energy of the block concentrates only DC component and we can simply disregard the rest of coefficients.

B. Transform Skip Techniques for HEVC

When the development of HEVC is in progress, a lot of experts contributed proposals about transform techniques with experimental results. Especially, proposals about transform skip method have been the focused for screen contents which is high resolution video sequences of playing computer games, editing documents and remote access. Therefore, transform skip for codec was adopted in HEVC to increase the coding efficiency for screen contents.

At 6th meeting of JCT-VC in Torino, Italy, M. Mrak with British Broadcasting Corporation (BBC) contributed proposal document was about transform skip mode [5]. It is about skipping row or column transforms or both of transforms based on RD cost, and they implemented it in HM3.2 for intra-coded blocks. They got gains of 0.2% BD-rate average for all intra coded configurations.

C. Lan of Xidian Univ. proposed transform skipping technique at 9th meeting hold in Geneva [6]. They apply transform skip method only for 4x4 intra predicted TU and, based on RD-cost, HM selects transform skip mode or 4x4 DCT. Intra transform skipping has a great coding performance for screen contents test sequences which is Class F and they have small gains for Class A, B, C, D and E.

X. Peng with Microsoft and Xidian Univ. extends intra transform skipping of C. Lan’s method to inter coded blocks [7].

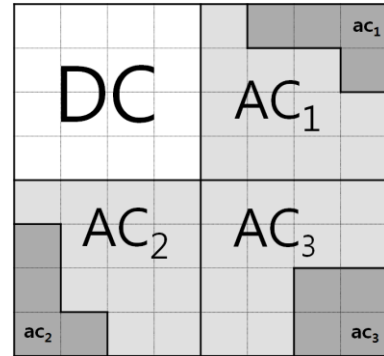
It is applied only for 4x4 TU and there are no changes in motion estimation and compensation, quantization, de-blocking filter and entropy coding. For Class F, they obtained gains about 1.8% for random access and 3.0% for low delay.

For HEVC range extension, X. Peng contributes a technique to transform skip at large size TU [8]. The author experiments transform skip for large size TU, i.e., 8x8, 16x16 and 32x32 at HM10.1_RExt3.0 anchor. For Class F and screen contents of 4-4-4 color format, the technique led to 0.9% ~ 2% BD-BR gain. Although there is coding efficiency; however, it is inevitable increasing encoding time. Since the time consumption of HM encoder and decoder has been one of the important issues of HEVC standardization, we study a novel attempt for early termination of TSM.

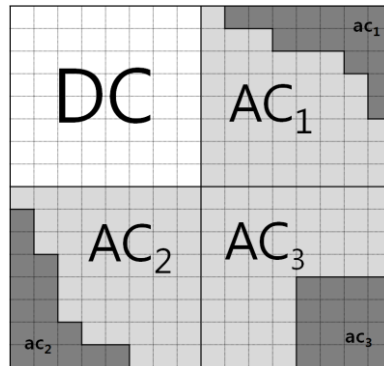
III. PROPOSED ALGORITHMS

A. Early Termination of Transform Skip Mode

The main idea is based on the assumption that if the magnitude of high frequency coefficients is larger than low frequency coefficients, the traditional transform technique for the video codec is not efficient to compress video sequences, as we mentioned in Section II-A.



(a)



(b)

Fig.3 Partition of DC and AC area for 8x8 TU (a) and 16x16 TU (b)

To calculate magnitudes of DC and AC area, we use absolute sum of each coefficients because DCT coefficients can have both of positive and negative number. First, we pre-check energy of AC area as follows:

$$sum_abs_ac = \sum_{(x,y) \in ac_1, ac_2, ac_3} |coeff(x,y)|. \quad (1)$$

$coeff(x,y)$ means DCT coefficient located (x,y) , and (x,y) is relative location of left-upper coefficient of TU. ac_1, ac_2, ac_3 have 4 coefficients respectively and located corner areas as shown in Fig. 3 (a) and (b). The reason why we firstly calculate these areas is that, in complex region, there are tendencies of DCT coefficients are gathered at each corner of ACs, as shown in Fig. 2. If sum_abs_ac equal to zero, we do not apply transform skip mode to current TU and if it is not, we calculate absolute sum of DC and AC regions by

$$sum_abs_DC = \sum_{(x,y) \in DC} |coeff(x,y)| \quad (2)$$

$$sum_abs_AC_i = \sum_{(x,y) \in AC_i} |coeff(x,y)| \quad (3)$$

for $i = 1, 2, 3$

If sum_abs_DC is larger than accumulated $sum_abs_AC_i$, TSM is not applied for current TU because energy compaction of current block is suitable for DCT. Otherwise, we add TSM as a candidate of DCT mode and determine the best mode by comparing RD-cost.

B. Scan Order Modification

For more speed enhancement, we modify scan patterns when we calculate sum of absolute values, following characteristics of coefficients.

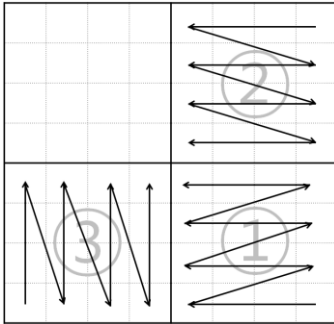


Fig. 4 Scan order for early termination

The scan order is described in Fig. 4. The order of AC part is AC_3, AC_1 and AC_2 , and it is determined experimentally. For each of AC_i , the scan order is followed by arrows; since, the ac_1, ac_2, ac_3 part have larger coefficients than others at edges and text. Finally, we compare sum_abs_DC with accumulated $sum_abs_AC_i$ as soon as the calculation of one row or column of AC_i is finished. If $sum_abs_AC_i$ is larger than sum_abs_DC , TSM is added to DCT of HEVC. The entire procedure of proposed algorithm is described in Fig. 5.

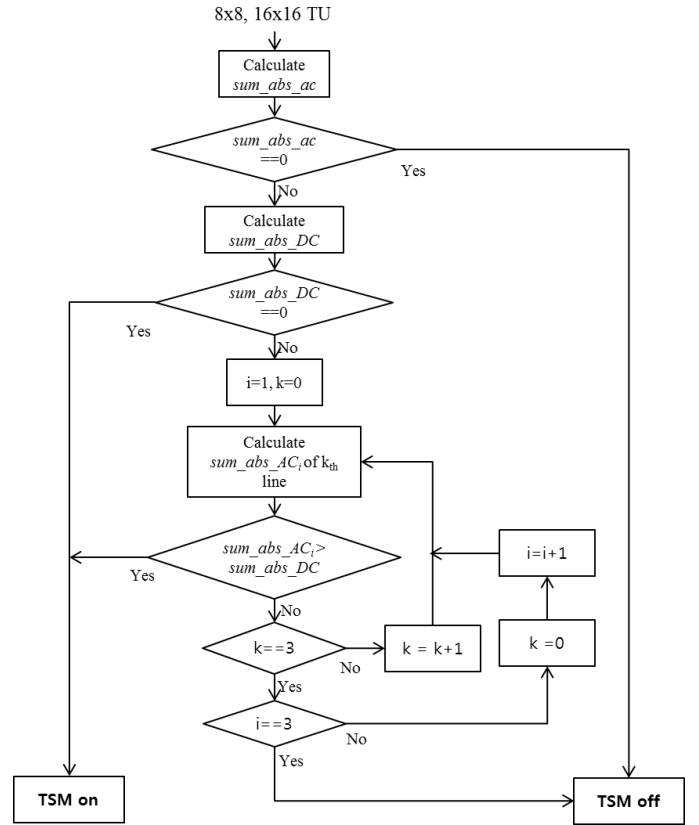


Fig. 5 Flowchart for proposed algorithms

IV. EXPERIMENTAL RESULTS

The proposed early termination method for transform skip mode is implemented in HM 12.0. We utilize the data set used for the HEVC standard development and additionally, for screen contents, we make our test sequences which are ICSP test1 and ICSP test3, as shown in Fig. 6 and Fig. 7. For experiments, all intra (AI) configuration of HEVC Main Profile is used, and largest coding unit size is 64x64 and QP = 22, 27, 32 and 37. As a measure of consuming time, $\Delta Time$ is defined as follows,

$$\Delta Time(\%) = 1 - \frac{(Time(HM12.0) - Time(proposed method))}{Time(HM12.0)}. \quad (4)$$

Table 1. Experimental results for proposed algorithms

Sequences	ET_TSM (MAX_TS=8)			ET_TSM + SOM (MAX_TS=8)		
	BD-BR	BD-PSNR	$\Delta Time$	BD-BR	BD-PSNR	$\Delta Time$
BasketballDrillText	-0.164	0.009	108%	-0.164	0.009	104%
ChinaSpeed	-0.655	0.060	109%	-0.655	0.060	106%
ICSP test1	-0.906	0.129	108%	-0.906	0.129	106%
ICSP test3	-0.934	0.128	109%	-0.934	0.128	107%
SlideEditing	-1.462	0.235	112%	-1.462	0.235	109%
SlideShow	-0.616	0.057	105%	-0.616	0.057	103%
Average	-0.790	0.103	108%	-0.790	0.103	106%

Table 2. Experimental results for proposed algorithms

Classes	Test Sequences	MAX_TS =8			MAX_TS =16			Proposed (MAX_TS =8)			Proposed (MAX_TS =16)		
		BD-rate	BD-PSNR	ΔTime	BD-rate	BD-PSNR	ΔTime	BD-rate	BD-PSNR	ΔTime	BD-rate	BD-PSNR	ΔTime
Class A 2560x1600	NebutaFestival	-0.009	0.001	117%	-0.012	0.0009	126%	-0.007	0.001	102%	-0.009	0.001	108%
	PeopleOnStreet	-0.070	0.004	118%	-0.080	0.0046	127%	-0.029	0.002	107%	-0.033	0.002	118%
	SteamLocomotiveTrain	-0.004	0.000	118%	0.001	0.0000	126%	0.004	0.000	107%	0.002	0.000	109%
	Traffic	-0.016	0.001	117%	-0.024	0.0013	125%	-0.002	0.000	107%	-0.001	0.000	95%
Class B 1920x1080	BasketballDrive	-0.046	0.001	115%	-0.064	0.0019	123%	-0.036	0.001	109%	-0.018	0.001	111%
	BQTerrace	-0.157	0.009	118%	-0.183	0.0102	125%	-0.085	0.005	109%	-0.093	0.005	109%
	Cactus	-0.102	0.004	117%	-0.109	0.0040	125%	-0.045	0.002	108%	-0.050	0.002	109%
	Kimono	-0.013	0.000	116%	-0.004	0.0002	124%	-0.004	0.000	107%	-0.004	0.000	108%
	ParkScene	-0.048	0.002	118%	-0.050	0.0023	125%	-0.014	0.001	107%	-0.014	0.001	108%
Class C WVGA	BasketballDrill	-0.246	0.012	116%	-0.253	0.0123	125%	-0.127	0.006	108%	-0.153	0.007	109%
	BQMall	-0.149	0.009	117%	-0.161	0.0096	126%	-0.083	0.005	109%	-0.083	0.005	111%
	PartyScene	-0.230	0.018	122%	-0.249	0.0192	128%	-0.155	0.012	110%	-0.155	0.012	112%
	RaceHorses	-0.122	0.008	117%	-0.119	0.0081	125%	-0.073	0.005	109%	-0.070	0.005	110%
Class D WQVGA	BasketballPass	-0.152	0.009	118%	-0.162	0.0095	125%	-0.078	0.005	108%	-0.074	0.004	110%
	BQ Square	-0.128	0.008	120%	-0.122	0.0074	129%	-0.071	0.004	109%	-0.066	0.004	110%
	BlowingBubbles	-0.283	0.025	118%	-0.289	0.0260	127%	-0.142	0.013	111%	-0.169	0.015	113%
	RaceHorses	-0.063	0.004	118%	-0.068	0.0047	127%	0.005	-0.001	109%	0.002	-0.001	109%
Class E 720p	FourPeople	-0.033	0.002	116%	-0.025	0.0015	124%	0.016	-0.001	108%	0.018	-0.001	109%
	Johnny	-0.081	0.003	113%	-0.123	0.0050	120%	-0.025	0.001	108%	-0.020	0.001	110%
	KristenAndSara	-0.073	0.004	114%	-0.095	0.0048	122%	-0.015	0.001	108%	-0.020	0.001	111%
Class F (Screen Contents)	BasketballDrillText	-0.305	0.016	117%	-0.318	0.0168	124%	-0.135	0.007	108%	-0.131	0.007	109%
	ChinaSpeed	-0.902	0.083	115%	-1.007	0.0926	122%	-0.677	0.062	109%	-0.743	0.068	111%
	ICSP test1	-1.856	0.265	115%	-2.158	0.3077	120%	-0.933	0.133	110%	-0.955	0.136	111%
	ICSP test3	-1.595	0.218	114%	-1.833	0.2494	120%	-0.906	0.124	110%	-0.968	0.132	112%
	SlideEditing	-2.193	0.352	116%	-2.537	0.4072	123%	-1.438	0.231	113%	-1.678	0.271	116%
	SlideShow	-0.806	0.075	113%	-0.875	0.0815	117%	-0.614	0.057	107%	-0.562	0.052	108%
OverallAverage		-0.297	0.033	117%	-0.334	0.0377	124%	-0.170	0.020	108%	-0.181	0.021	110%

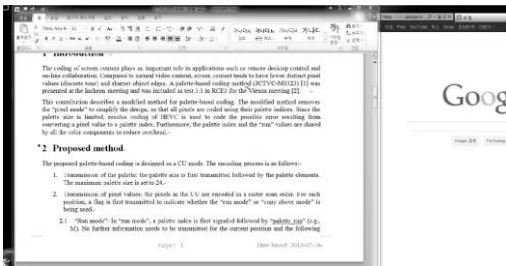


Fig. 6 Screen shot of ICSP test1



Fig. 7 Screen shot of ICSP test3

MAX_TS means maximum size of TU for transform skip, and if MAX_TS is set to 8, we allow TSM for 4x4 and 8x8 TUs. The experimental results for proposed algorithms are summarized in Table 1, and it compared with HM 12.0. Early termination for TSM (ET_TSM) has better coding efficiency in point of BD-bitrate (BD-BR) and BD-peak-to-noise-ratio (PSNR). The average Y-PSNR increased 0.103 dB and bit-rate decreased 0.790 % with increasing time consuming. However, we improve computation complexity of proposed algorithms by

the scan order modification (SOM) method. As we can be seen in Table 1, ET_TSM + SOM reduce encoding time without any loss of coding efficiency.

In Table 2, whole proposed algorithms (ET_TSM + SOM) are compared with HM12.0 (MAX_TS is set to 8 and 16). HM with extension of TSM and proposed algorithm both have good coding efficiency for Class F (screen contents). Proposed algorithm reduces computational complexity about 9% ~ 14% compared with HM with small BD-rate loss.

V. CONCLUSIONS

In this paper, we proposed algorithms for TSM of HEVC transform coding. The proposed algorithm consisted of early termination of TSM and scan order modification for speed improvement reduce computation time of HM encoder with extension of TSM. Using characteristics of DCT coefficients, we can efficiently selects whether TSM is applied for HM or not, and by changing scan order of calculating sum of absolute values, we also save computational time of transform process of HM. Therefore, our proposed algorithms are efficient for screen contents and its application.

REFERENCES

- [1] T. Wiegand, G. J. Sullivan, G. Bjontegaard, and A. Luthra, "Overview of the H.264/AVC video coding standard," IEEE Trans. Circuits Syst. Video Technol., vol. 13, no. 7, pp. 560–576, Jul. 2003.
- [2] B. Bross, W.-J. Han, G. J. Sullivan, J.-R. Ohm, and T. Wiegand, High Efficiency Video Coding (HEVC) Text Specification Draft 10, document JCTVC-L1003, ITU-T/ISO/IEC Joint Collaborative Team on Video Coding (JCT-VC), Jan. 2012.
- [3] G. J. Sullivan, J.-R. Ohm, W.-J. Han, and T. Wiegand, "Overview of the

High Efficiency Video Coding (HEVC) standard,” *IEEE Trans. Circuits Syst. Video Technol.*, vol. 22, no. 12, pp. 1648–1667, Dec. 2012.

- [4] Anil K. Jain, “Fundamentals of digital image processing,” Prentice hall, 1989, 1st ed. pp. 150-154.
- [5] M. Mrak, and A. Gabrellini, Transform skip mode, JCTVC-F077, Torino, Italy, July, 2011.
- [6] C. Lan, Intra transform skipping, JCTVC-I0408, Geneva, Switzerland, May, 2012.
- [7] X. Peng, Inter transform skipping, JCTVC-J0237, Stockholm, Sweden, July, 2012.
- [8] X. Peng, Non-RCE2: Transform skip on large TUs, JCTVC-N0288, Vienna, Austria, July, 2013.

Do-Kyung Lee received a B.S degree from the School of Electrical Engineering College of Engineering Chung-Ang University, Korea, in 2010. He is currently pursuing a Ph. D. candidate in Electronic and Computer Engineering at Hanyang University. His research interests include fast motion estimation, true motion estimation and video codec.

Miso Park received a B.S degree the Department of Electronics and Computer Engineering from Hanyang University, Korea, in 2013. She is currently pursuing a M.S in Electronic and Computer Engineering at Hanyang University. Her research interests include video processing, and high efficiency video codec.

Hyung-Do Kim received a B.S degree the Department of Electronics and Computer Engineering from Hanyang University, Korea, in 2013. He is currently pursuing a M.S in Electronic and Computer Engineering at Hanyang University. His research interests include fast motion estimation and video codec.

Je-Chang Jeong received a BS degree in electronic engineering from Seoul National University, Korea, in 1980, an MS degree in electrical engineering from the Korea Advanced Institute of Science and Technology in 1982, and a PhD degree in electrical engineering from the University of Michigan, Ann Arbor, in 1990. From 1982 to 1986, he was with the Korean Broadcasting System, where he helped develop teletext systems. From 1990 to 1991, he worked as a postdoctoral research associate at the University of Michigan, Ann Arbor, where he helped to develop various signal-processing algorithms. From 1991 through 1995, he was with the Samsung Electronics Company, Korea, where he was involved in the development of HDTV, digital broadcasting receivers, and other multimedia systems. Since 1995, he has conducted research at Hanyang University, Seoul, Korea. His research interests include digital signal processing, digital communication, and image and audio compression for HDTV and multimedia applications. He has published numerous technical papers.

Dr. Jeong received the Scientist of the Month award in 1998, from the Ministry of Science and Technology of Korea, and was the recipient of the 2007 IEEE Chester Sall Award and 2008 ETRI Journal Paper Award. He was also honored with a government commendation in 1998 from the Ministry of Information and Communication of Korea.

Pathloss Analysis at 900 MHz for Outdoor Environment

Zia Nadir, Mohammed Bait-Suwailam
ECE department, College of Engineering,
Sultan Qaboos University,
Muscat 123, Sultanate of Oman
nadir@squ.edu.om

Abstract— This paper provides an extension of pathloss analysis in Urban, Rural and Semi-Urban environments in Oman. A new software package has been developed that incorporates modified propagation models and the proposition of radio frequency (RF) network design output for proper and efficient planning to be used by RF engineers for pathloss studies. The root-mean square error (RMSE) was calculated between measured and predicted values according to the Okumura-Hata propagation model. PCHIP analysis technique has been used for the prediction of unknown data which gave good result.

Index Terms— Pathloss, Propagation models, Hata Model, Urban Area, PCHIP (Piecewise Cubic Hermite Interpolating Polynomial).

I. INTRODUCTION

In the design of any cellular mobile system, the fundamental task is to predict the coverage of the proposed system. Propagation models are useful for predicting signal attenuation or path loss which may be used as a controlling factor for system performance or coverage so as to achieve perfect reception [1]. It has been found that the mechanisms behind electromagnetic wave propagation are diverse and characterized by certain phenomena such as reflection, refraction and diffraction of waves. These phenomena induces signal scattering, fading and shadowing along the signal path and their effects can best be described (in a large scale) by the path loss exponent which defines the rate of change of attenuation that the signals suffers as it propagates from the transmitter to the receiver [2]. The wireless communication relies on the broadcast of waves in the free space. This also provides mobility for users and satisfies the demand of the customers at any location covered by the wireless network. Growth in the mobile communications field has now become slow, and has been linked to technological advancements [3-4]. The need for high quality and high capacity networks, estimating coverage accurately has become extremely important. Therefore, for more accurate design coverage of modern cellular networks, signal strength measurements must be taken into consideration in order to provide an efficient and reliable coverage area.

This article addresses the evaluations between the statistical and the experimental analysis at GSM frequency of 900 MHz using Okumara model which is most widely used [5].

The cellular concept was a major breakthrough in solving the problem of spectral bottlenecks and user's capacity. It offered high capacity with a limited spectrum allocation without any major technological change. The cellular concept is a system level idea in which a single, high power transmitter is replaced with many low power transmitters. The area serviced by a transmitter is called a cell. Each small powered transmitter, also called a base station provides coverage to only a small portion of the service area. The power loss involved in transmission mode between the base station (BTS) and the mobile station (MS) is known as the pathloss and depends particularly on the antenna height, carrier frequency, distance and environmental parameters. At higher frequencies the range for a given Pathloss is reduced, so more cells are required to cover a given area. Base stations close to one another are assigned different groups of channels. Neighboring base stations are assigned different groups of channels so that the interference between base stations or interaction between the cells is minimized. As the demand for service increases, the number of base stations may be increased, thereby providing additional capacity with no increase in radio spectrum. The key idea of modern cellular systems is that it is possible to serve the unlimited number of subscribers, distributed over an unlimited area, using only a limited number of channels, by efficient channel reuse [4].

II. THEORETICAL PROPAGATION MODELS

Propagation models are mathematical representation of results of experiments conducted on the wave propagation under different frequencies, antenna heights and locations over different periods and distances. Propagation models indicate that average received signal power decreases logarithmically with distance [6]. They are divided into two basic types; namely: Free space propagation and Plane earth propagation model.

A. Free Space Propagation Model

In free space, the wave is not reflected or absorbed. Ideal propagation implies equal radiation in all directions from the radiating source and propagation to an infinite distance with no degradation. Spreading the power over greater areas causes waves attenuation. Equation (1) illustrates how the power flux is calculated.

$$P_d = P_t / 4\pi d^2 \quad (1)$$

Where P_t is known as transmitted power (W/m^2) and P_d is the power at a distance d from antenna. If the radiating element is generating a fixed power and this power is spread over an ever-expanding sphere, the energy will be spread more thinly as the sphere expands.

B. Plane-Earth Propagation Model

The free space propagation model does not consider the effects of wave propagation over ground. When a radio wave propagates over ground, some of the power will be reflected due to the presence of ground and then received by the receiver. In order to better estimate the effect of the reflected power, the free space propagation model is modified and referred to as the 'Plane-Earth' propagation model. This model better represents the true characteristics of radio wave propagation over ground. The plane earth model computes the received signal to be the sum of a direct signal and that reflected from a flat, smooth earth. The relevant input parameters include the antenna heights, the length of the path, the operating frequency and the reflection coefficient parameter from the earth's interface. This coefficient will vary according to the terrain type (e.g. water, desert, wet ground etc). Pathloss Equation for the plane Earth Model is illustrated in equation (2)

$$L_{pe} = 40 \log_{10}(d) - 20 \log_{10}(h_1) - 20 \log_{10}(h_2) \quad (2)$$

Where d represents the path length in meters, and h_1 and h_2 are the antenna heights at the base station and the mobile, respectively. The plane earth model is not appropriate for mobile GSM systems as it does not consider the reflections from buildings, multiple propagation or diffraction effects. Furthermore, if the mobile height changes (as it will in practice), then the predicted Pathloss will also be changed.

III. EMPIRICAL PROPAGATION MODELS

Empirical propagation models will be discussed in this section; amongst them are Okumura and Hata models.

A. Cellular Propagation Models

The two basic propagation models (free space loss and plane-earth loss) would require detailed knowledge of the location, dimension and constitutive parameters of every tree, building, and terrain feature in the area to be covered. This is far too complex to be practical and would yield an unnecessary amount of detail. One appropriate way of accounting for these complex effects is via an empirical model. There are various empirical prediction models among them are, Okumura – Hata model, Cost 231 – Hata model, Cost 231 Walfisch – Ikegami model, Sakagami- Kuboi model. These models depend on location, frequency range and clutter type such as urban, sub-urban and countryside.

B. Okumura's Measurements

Okumura carried out extensive drive test measurements with range of clutter type, frequency, transmitter height, and transmitter power. It states that, the signal strength decreases at much greater rate with distance than that predicted by free space loss [5, 7-8].

C. Hata's Propagation Model

Hata model was based on Okumura's field test results and predicted various equations for Pathloss with different types of clutter. It is well suited model for the Ultra High Frequency (UHF) band [9]. The limitations on Hata Model due to range of test results from carrier frequency 150 MHz to 1500 MHz, the distance from the base station ranges from 1 Km to 20 Km, the height of base station antenna (h_b) ranges from 30 m to 200 m and the height of mobile antenna (h_m) ranges from 1 m to 10 m. It was also observed that the signal strength is a function of distance and antenna height, as we can see in this work the highest antenna has less propagation path loss and as the distance increases the path loss also increases [10]. Hata created a number of representative Pathloss mathematical models for each of the urban, suburban and open country environments, as illustrated in following equations, respectively. Okumura takes urban areas as a reference and applies correction factors as following:

$$\text{Urban areas: } L_{dB} = A + B \log_{10} R - E_{1,2,3} \quad (3)$$

$$\text{Suburban areas: } L_{dB} = A + B \log_{10} R - C \quad (4)$$

$$\text{Open areas: } L_{dB} = A + B \log_{10} R - D \quad (5)$$

Where

$$A = 69.55 + 26.16 \log_{10} f_c - 13.82 \log_{10} h_b$$

$$B = 44.9 - 6.55 \log_{10} h_b$$

$$C = 2 (\log_{10} (f_c / 28))^2 + 5.4$$

$$D = 4.78 (\log_{10} f_c)^2 + 18.33 \log_{10} f_c + 40.94$$

$$E_1 = 3.2 (\log_{10} (11.7554 h_m))^2 - 4.97$$

for large cities, $f_c \geq 300\text{MHz}$.

$$E_2 = 8.29 (\log_{10} (1.54 h_m))^2 - 1.1$$

for large cities, $f_c < 300\text{MHz}$.

$$E_3 = (1.1 \log_{10} f_c - 0.7) h_m - (1.56 \log_{10} f_c - 0.8)$$

for medium to small cities.

Definition of parameters:

h_m ; mobile station antenna height [m]

d_m ; distance between the mobile and the building [km]

h_0 ; typical height of a building above local terrain height [m]

h_b ;base station antenna height above local terrain height [m]
 r ; great circle distance between base station and mobile [m]
 $R=r \times 10^{-3}$ great circle distance between BS and mobile [km]
 $f_c=f \times 10^{-6}$ carrier frequency [MHz]
 λ ; free space wavelength [m].

The practical Pathloss can be calculated using the equation:

$$L_P \text{ (dB)} = P_t - P_r \quad (6)$$

Where P_t is the transmitted power which is equal to 47 dB and P_r is the received power

$A = 69.55 + 26.16 \log_{10} f_c - 13.82 \log_{10} h_b$, and $E_3 = (1.1 \log_{10} f_c - 0.7) h_m - (1.56 \log_{10} f_c - 0.8)$ for small and medium city [11-13]

The generation of such predictions is based on the assumption that the power of a signal decreases monotonically with the increase of the distance traveled by the signal [14]. Thus, Hata model is not suitable for micro-cell planning where antenna is below roof height and its maximum carrier frequency is 1500MHz. It is not valid for 1800 MHz and 1900 MHz systems.

IV. RESULTS AND DISCUSSIONS

Data Collection

An intensive drive test has been conducted along all pre-identified paths. GSM sample every 450 ms. This sampling rate is adequate to determine representative signal levels. The drive test process was conducted using TESt Mobile System, (TEMS) Investigation Data Collection V13.0 tool. TEMS Investigation is widely used for drive testing (Collecting handset data while moving) purpose and it supports all major technologies including GSM, Wi-MAX, UMTS and LTE. The measurement reports of radio signal strength and many other RF parameters are collected by a special purpose mobile handset connected to the PC in which the TEMS program is installed. Furthermore, the positioning information is collected via GPS antenna terminal which have direct communication with GPS satellite

Data Processing

The measured data for each path has been recorded in terms of log files. These log files have been exported to a post processing tool called ACTIX for further processing and extraction of the required data. ACTIX Analyzer is a tool used for drive test post-processing, supporting network optimization and network troubleshooting. It is capable of troubleshooting RF problems automatically for GSM, Wi-MAX, WCDMA and LTE technologies.

The data files collected from TEMS Investigation is post-processed from this tool. Also, it has been used to convert the recorded log files into graphical format for

map viewing via Google Earth program (not shown). Moreover, it has been utilized to export coverage log files into Excel worksheets format for further manipulation. After that, the required data has been manipulated as the main aim of the conversion was to obtain the path loss and the link distance. However, the road of Al Khuwair can be considered as an urban area, in which Okumura-Hata model was used. Fig. 1 below depicts the Graphical User Interface developed for this study.

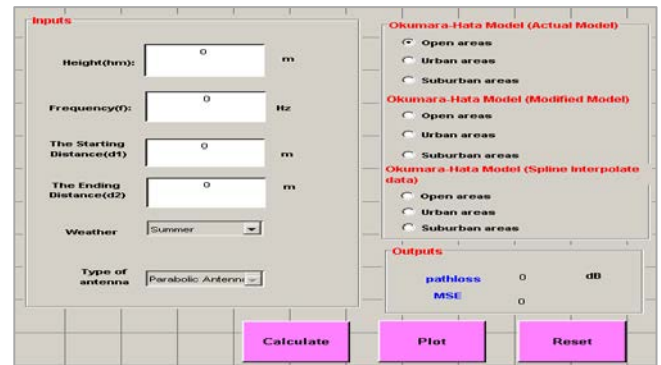


Fig. 1: GUI Development for Pathloss studies.

After determining the Pathloss of the practical measurements for each distance, the study was carried in order to make a comparison between the experimental and theoretical data and the result is as shown in Fig. 2.

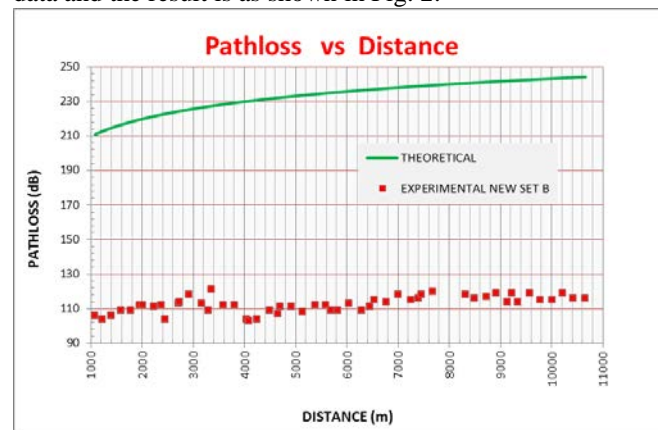


Fig. 2: Theoretical and Experimental Pathloss versus distance

From the above plot, the results clearly show that the measured Pathloss is less than the predicted Pathloss by a difference varying from 4 to 20 dB. However, there are several reasons that may have caused those significant differences. First of all, in Japan there are few areas virtually satisfying the conditions; and if any, they are narrow. Because of that reason Okumura selected the value for urban area as standard for open areas [8]. Moreover, the geographical situation of Japan is different from that in Oman due to geographical differences. As such, root mean square error (RMSE) was calculated between measured Pathloss value and those predicted by Hata model using the following equation (7) [15-16]:

$$RMSE = \sqrt{\left(\frac{\sum (P_m - P_r)^2}{(N-1)}\right)} \quad (7)$$

Where;

P_m : Measured Pathloss (dB)

P_r : Predicted Pathloss (dB)

N: Number of Measured Data Points

The RMSE was found 113.459 dB but the acceptable range is up to 6 dB. Therefore, the RMSE is adjusted with the Hata equation for urban area and the modified equation is as given below:

$$L_{pModified} (Urban) = 69.55 + 26.16 \log_{10}(f) - 13.82 \log_{10}(h_b) + (44.9 - 6.55 \log_{10}(h_b)) \log_{10}(d) \pm MSE - (1.1 \log_{10}(f) - 0.7)h_m - (1.56 \log_{10}(f) - 0.8) \quad (8)$$

The modified result of Hata equation is shown in Fig. 3 and the RMSE in this case is less than 6dB, which is acceptable.

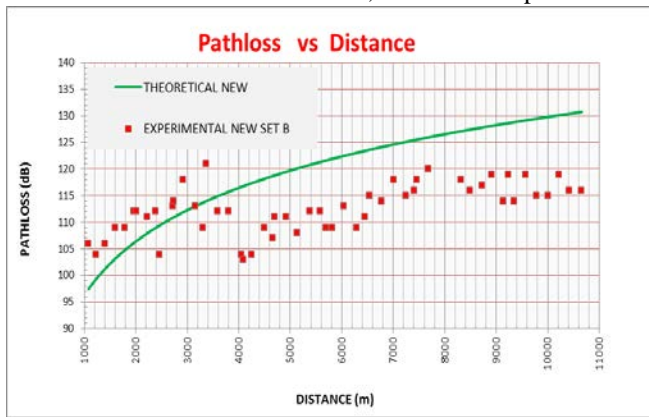


Fig. 3: Modified Hata's equation Pathloss on experimental data set B.

In order to verify that the modified Hata's equation (8) is applicable for other areas in Oman, another data generated from TEMS tool for another cell in the road of Al Khuwair has been used. Based on that practical data, the propagation Pathloss and the distance have been re-verified for another cell [11].

Theoretical simulation and the obtained experimental data are compared and analyzed further using PCHIP to interpolate on the set of the experimental data which provides quite flexibility. A PCHIP, is any Piecewise Cubic Hermite Interpolating Polynomial that interpolates the given data, and has specified derivatives at the interpolation points. Just as two points determine a linear function, two points and two given slopes determine a cubic. The data points are known as "knots". We have the y-values at the knots, so in order to get a particular PCHIP, we have to somehow specify the values of the derivative, y' , at the knots. PCHIP also provides a fairly smooth and efficient approximation without increasing the computational complexities required for higher-order polynomial approximation. A good correlation is observed for the entire range. The good agreement of the characteristics show that experimentally reproduced data is a good representation of that described by Hata propagation model.

Furthermore, the simulation and the obtained experimental data is compared and analyzed further using a cubic regression model on the set of the experimental data which gives acceptable results. After observation of experimental data, it can be predicted that the scatter plot of the experimental data on Pathloss versus distance reveals a third order polynomial trend. Therefore, the Cubic Regression Model was fitted [12-13] using method of least square error which estimates the parameters by minimizing sum of squares of the white noise. The estimated model is given as below:

$$P_m = 98.66 + (6.8e^{-3})d + (7.0e^{-7})d^2 + (4.0e^{-11})d^3 \quad (9)$$

The coefficient of determination of this regression suggested that about 90% variation in Pathloss can be explained by distance using the above equation (9). The correlation between experimental, theoretical model and fitted by cubic regression were worked out by Pearson Correlation Coefficient which shows that the Pathloss estimated by equation (9) has highly significant correlation of 0.975 with the experimental data and a correlation of 0.974 with the theoretical model. The correlation between experimental data and theoretical model was 0.948 which is also highly significant at $p < 0.01$ value

Fig.4 shows the theoretical, experimental and PCHIP plots for Hata propagation model. As can be seen, results show good agreement between various studies.

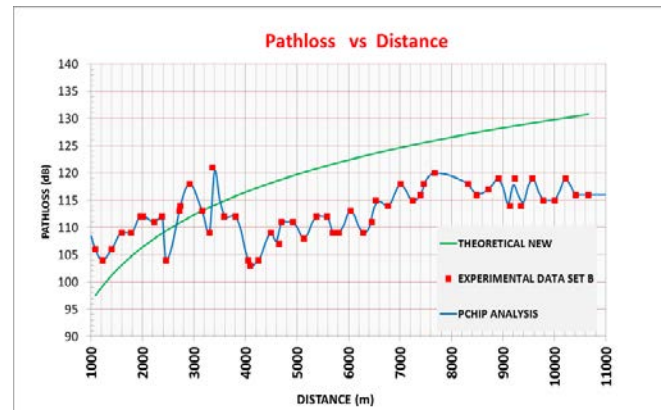


Fig. 4: Pathloss versus distance for Experimental set-B, Theoretical, and PCHIP analysis.

By calculating the RMSE for the second cell, for most of the data sets it was found to be 3.2058 dB, which is an acceptable figure. On experimental Set B, few data points were a bit far from the interpolated values which are attributed to the nature of cell B with high rise buildings. Although there are many predictions methods that are based on deterministic processes through the availability of improved databases, the Okumura-Hata model is still mostly used [17]. That is because of the ITU-R recommendation for its simplicity and its proven reliability.

V. CONCLUSION

This work focused on predicting the root mean signal strength in different areas. As most propagation models aim to predict the median Pathloss, existing prediction models differ in their applicability over different terrain and environmental conditions. The effects of terrain situation predicted at 900 MHz were analyzed. Experimental results of radio signals propagation for an urban area in Oman were compared with those predicted based on Okumura-Hata model. The contribution is the prediction by statistical techniques and verification by experimental results. If environmental information is included in the model, better prediction results might be achieved. PCHIP gave us also the missing experimental points showing a good agreement with Theoretical model.

ACKNOWLEDGMENT

The authors would like to thank SQU for the support to carry out this study and also Ms Manal Al Raisi and Ms Tabarak Al Lawati for their valuable contribution.

REFERENCES

- [1] S. Sharma and R. S Uppal, "RF coverage estimation of cellular mobile systems", *International Journal of Engineering and Technology*, Vol.3 (6), pp. 398-403, 2011-2012,
- [2] E.A. Ubom, V. E. Idigo, A.C.O. Azubogu, C.O. Ohaneme, T. L.Alumona, "Pathloss characterization of wireless propagation for South – South region of Nigeria", *International Journal of Computer Theory and Engineering*, Vol. 3, No. 3, pp. 360-364, June 2011.
- [3] D. Nobel, "The history of land to mobile radio communications", *IEEE Transactions on Vehicular Technology*, pp. 1406-1416, May 1962.
- [4] V. H. MacDonald, "The cellular concept", *The Bell Systems Technical Journal*, vol. 58, no. 1, pp. 15-43, January 1979.
- [5] A. Medeisis and A. Kajackas, "On the use of the universal Okumura-Hata propagation prediction model in rural areas", *Vehicular Technology Conference Proceedings, VTC Tokyo*, Vol.3, pp. 1815-1818, May 2000.
- [6] M. Kumari, T. Yadav, P. Yadav, "Comparative study of pathloss models in different environments", *International Journal of Engineering Science and Technology (IJEST)*, ISSN: 0975-5462 Vol. 3, No. 4, pp. 2945-2949, Apr 2011.
- [7] M. Hata, "Empirical formula for propagation loss in land mobile radio services", *IEEE Transactions on Vehicular Technology*, vol. 3 VT 29, pp. 317-326, August 1980.
- [8] R. D. Wilson and R. A. Scholtz, "Comparison of CDMA and modulation schemes for UWB radio in a multipath environment", *Proceedings of IEEE Global Telecommunications Conference*, Vol. 2, pp. 754-758, Dec 2003.
- [9] R. N., S. S. K., "A study on pathloss analysis for GSM mobile networks for urban, rural and suburban regions of Karnataka state", *International Journal of Distributed and Parallel Systems (IJDPS)* Vol.4, No.1, DOI: 10.5121/ijdps. 2013. 4105 pp.53-66 January 2013.
- [10] D. A. Shalangwa, S. K. Singh, "Measurement and modeling of pathloss for GSM900 in sub urban environment over Irregular terrain", *International Journal of Computer Science and Network Security (IJCSNS)*, Vol.10, No.8, pp. 268-274, August 2010.
- [11] Z. Nadir, N. Elfadhil, F. Touati, "Pathloss determination using Okumura-Hata model and spline interpolation for missing data for Oman" *World Congress on Engineering, IAENG-WCE-2008*, Imperial College, London, United Kingdom, 2-4 July,2008.
- [12] Z. Nadir, M. I. Ahmed, "Characterization of pathloss using Okumura-Hata model and missing data prediction for Oman", *IAENG Transactions on Engg. Tech. Vol (5): special Edition of the Int. Multiconference of Engineers and Computer Scientists 2009*. AIP conference proceeding, volume 1285, PP: 509-518; 2010.
- [13] Z. Nadir, "Empirical pathloss characterization for Oman", *IEEE Computing, Communications & Applications Conference 2012, (IEEE ComComAP 2012)*, HongKong University of Science and Technology, Hong Kong, China, 11-13 January 2012.
- [14] F. Mourad, H. Snoussi, M. Kieffer, C. Richard, "Robust bounded-error tracking in wireless sensor networks", *SYSID'12 Brussels, Belgium*, 11-13 July 2012.
- [15] D. A. Shalangwa, & G. Jerome, "Pathloss propagation model for Gombi town Adamawa State Nigeria", *International Journal of Computer Science and Network Security (IJCSNS)*, Vol.10, No.6, pp. 186-190 June 2010.
- [16] J. Wu and D. Yuan, "Propagation measurements and modeling in Jinan city", *IEEE International Symposium on Personal, Indoor and Mobile Radio Communications*, Boston, MA, USA, Vol. 3, pp. 1157-1159, 8-11 September 1998.
- [17] Y. Okumura et al., "Field strength and its variability in VHF and UHF land-mobile radio service", *Review of the Electrical Communications Laboratory*, Vol. 16, no. 9-10, September-October 1968.

Simulation and Analysis of a Full Duplex DWDM RoF System Using Optimized Phase Modulator and an OADM

Joseph Zacharias
Dept. of ECE
RIT

Kottayam joseph.zacharias@rit.ac.in

Raji K
Dept. of ECE
RIT Kottayam

rajikbhargavan@gmail.com

Vijayakumar Narayanan
Dept. of ECE
Govt. Engg College, Barton Hill
dr.nvkr@gmail.com

(WDM) networks.

Abstract- We've proposed a full duplex Dense Wavelength Division Multiplexing (DWDM) Radio over Fiber (RoF) system using an optimized phase modulator and an optical add drop multiplexer. Phase modulated carrier is suppressed using an optimized phase modulator. That is an optimized phase deviation is given to a phase modulator to suppress the central carrier of the modulated signal. An optical add drop multiplexer is used to add or drop specific channel at a particular base station. Performance of the system is analyzed. This system is compared with one which is not using an optimized phase modulator. The eye diagram and bit error rate performance of the base station and central station has been analyzed.

Keywords: Radio over Fiber (RoF), Dense Wavelength Division Multiplexing (DWDM).

I. INTRODUCTION

Optical mm wave generation through radio over fiber is an emerging technology in the area of communication. Simplification of Remote access points (RAPs) is the key advantage of this technique. It can be considered as the solution to future broad band wireless access network [1]. In Radio over Fiber (RoF) system, a microwave signal is available at the input, which is then modulated over light and transmitted over fiber towards remote radio access point (RAP). Performance of this system depends on so many factors like modulation format, transmitted power and optical fiber length and type etc. The power being transmitted after modulation can be reduced to some extent by suppressing the optical carrier. There by we can improve signal to noise ratio.

Carrier suppression through enhancing the modulation index of the phase modulator has already been proposed in [2]. i.e., tuning the modulation index will help to decrease the Bessel amplitude of the central carrier of the modulated signal. High value of the modulation index will increase the side band power, which in turn affects the performance of the system when it is used in wave length division multiplexing

In this paper, a full duplex Dense wave length division multiplexing (DWDM) RoF system, which makes use of an optimized phase modulator and an add drop multiplexer is proposed. This system makes use of an optimized phase modulator instead of Mach-Zehnder Modulator (MZM) which results in reduced power transmission of generated mm wave. The power is deducted by suppressing the central carrier of phase modulated wave. Three different Interleaver filters are used to separate first order side bands of each channel. Interleaver filter is a type of optical filter which separate incoming spectrum into two complimentary spectrums, whose separation is entirely different from the input spectrum. The principle and working of interleaver filter has already been proposed in [3], [4]. It is the best solution when Fiber brag grating (FBG) fails due to temperature variation. Optical add-drop multiplexer (OADM) is a device used in wavelength division multiplexing systems for multiplexing and routing different channels of light into or out of a construction of optical network. Two OADMs are used here to represent two base stations. The received signal shows better correlation with the input signal

In addition to this system, a single channel RoF system with and without phase modulator and interleaver filter is presented for analyzing the transmitted power and fiber range.

II. OPERATING PRINCIPLE

A phase modulated optical signal has side bands at its harmonics. The power level of each side band and central carrier is a function of modulation index. By changing the modulation index, it is possible to decrease the carrier power to some extent. Phase modulated signal can be generated by simply phase modulating the continuous wave light source. The output of the phase modulator can be expressed in terms of Bessel function [2].

$$\begin{aligned}
 E'_{out} &= E_0 e^{j\omega_0 t} e^{j\beta \cos \omega_m t} \\
 &= E_0 \sum_{n=-\infty}^{\infty} (j)^n J_n(\beta) e^{j(\omega_0 + n\omega_m)t} \\
 &\approx E_0 \{ J_0(\beta) e^{j\omega_0 t} + J_1(\beta) e^{j[(\omega_0 + \omega_m)t + \pi/2]} \\
 &\quad - J_1(\beta) e^{j[(\omega_0 - \omega_m)t - \pi/2]} \\
 &\quad - J_2(\beta) e^{j[(\omega_0 + 2\omega_m)t]} - J_2(\beta) e^{j[(\omega_0 - 2\omega_m)t]} \}
 \end{aligned}
 \tag{1}$$

Where, E_0 and ω_0 are the amplitude and frequency of carrier wave, β is the modulation index, $J_n(\beta)$ is the Bessel function of first kind order n , and ω_m is the angular frequency of driving signal.

Phase modulation index can be expressed in terms of half wave voltage [5]

$$\beta = (V_e / V_\pi) \pi / 2 \tag{2}$$

Where, V_π is the half wave voltage of phase modulator, V_e is the amplitude of electrical signal voltage.

We've the phase deviation of the phase modulator

$$\Phi = (V_e / V_\pi) \pi, \text{ in radian} \tag{3}$$

i.e., by changing the phase deviation of optical phase modulator, we can suppress the central carrier of the optical carrier. The depth of the carrier suppression depends on the modulation index value. We can achieve a carrier suppression of 41dB if a phase deviation of 276° is applied to the phase modulator. This optimized phase deviation is used in proposed DWDM system, so as to suppress the central carrier of each channel.

Here a central station with three channels and two base stations are considered to analyze the performance of optimized phase modulator in a DWDM RoF system.

III. EXPERIMENTAL SET UP

A 2.5 Gbps pseudorandom binary sequence (PBRs) signal with a word length of $2^5 - 1$ is used to modulate a transmitter at 193.1THz and is then fed into a PM driven by a 20-GHz sinusoidal wave. A phase deviation of 276° is applied to phase modulator to achieve carrier-suppressed optical up-conversion. A single channel system is shown in Fig. 1. For a DWDM system, three different channels with spacing of 100GHz are used to transmit three different data streams. Experimental set up for DWDM system is shown in Fig. 2.

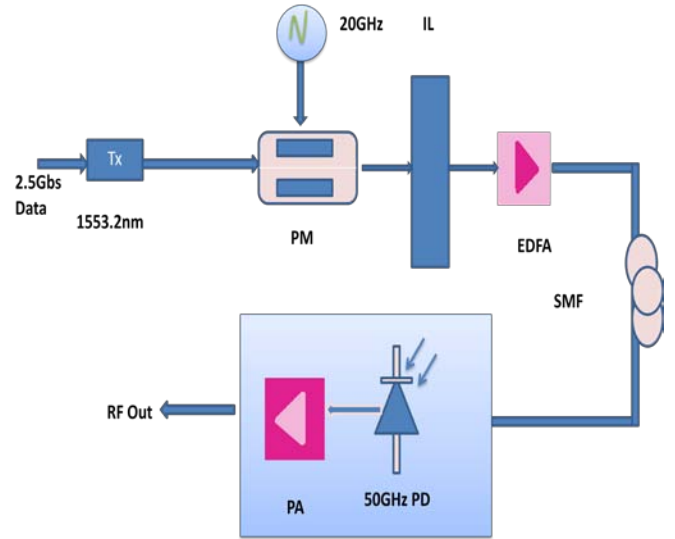


Fig. 1. Experimental model of single channel RoF system

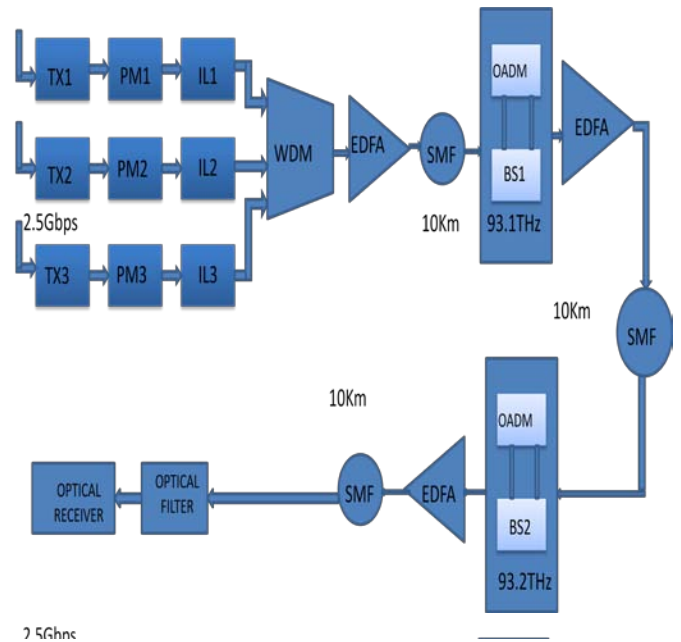


Fig. 2. Experimental model of proposed system

IV. SIMULATION AND RESULT

Simulation is done in optisystem 11 software. Optisystem is a powerful software tool for designing optical communication system. It can be used to design optical communication systems and simulate them to determine their performance by giving various component parameters.

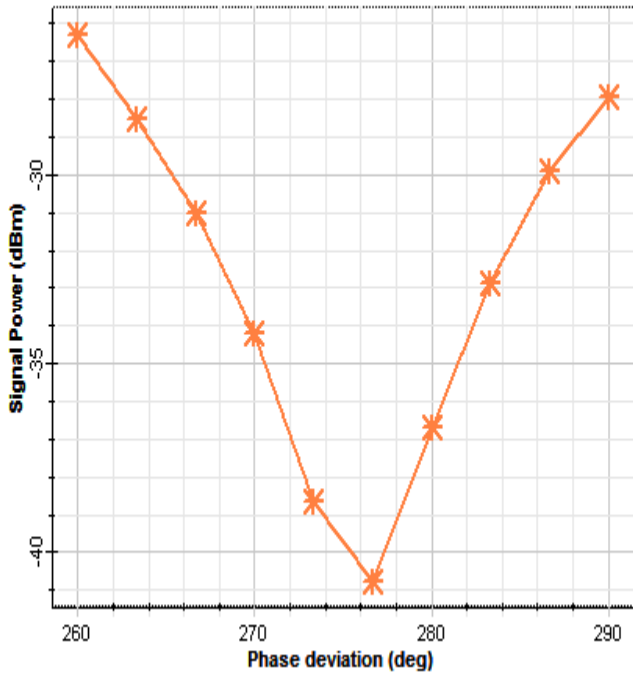


Fig. 3. Phase deviation versus carrier power

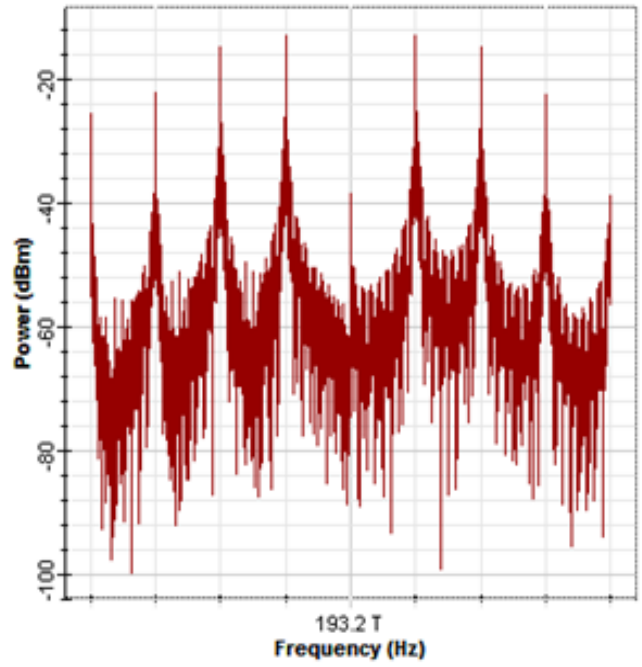


Fig. 5. Carrier suppressed spectra of channel 2

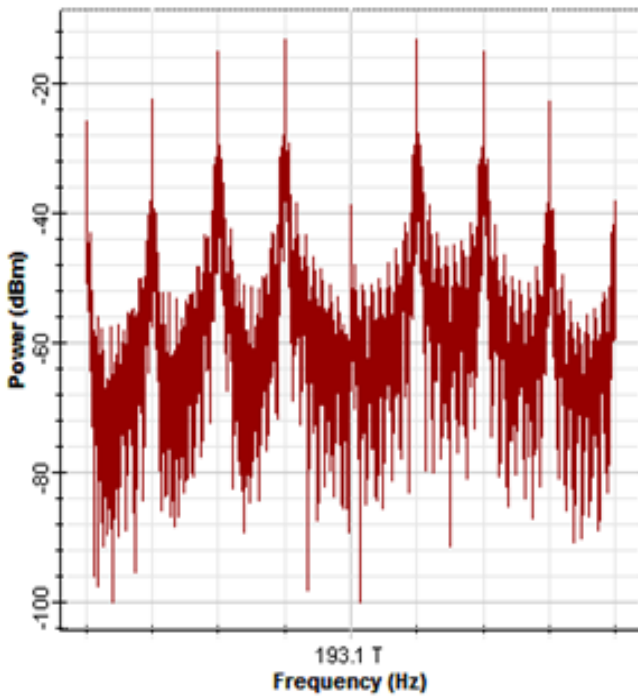


Fig. 4. Carrier suppressed spectra of channel 1

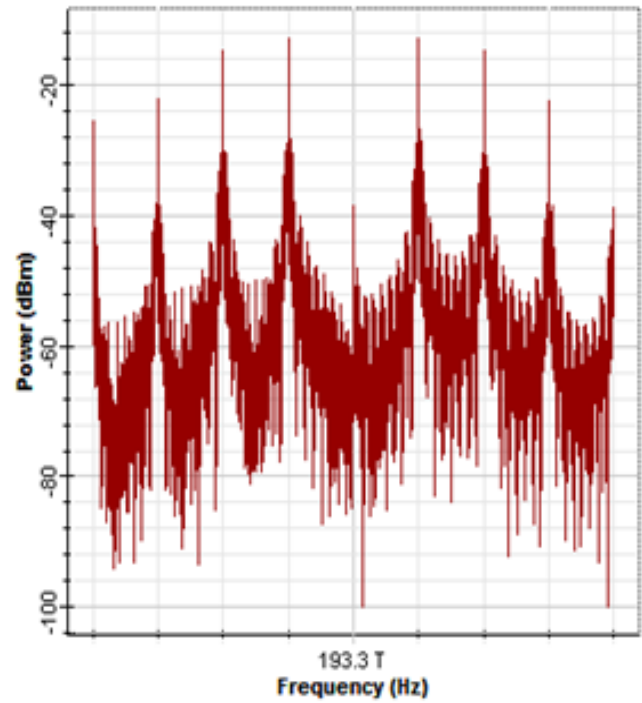


Fig. 6. Carrier suppressed spectra of channel 3

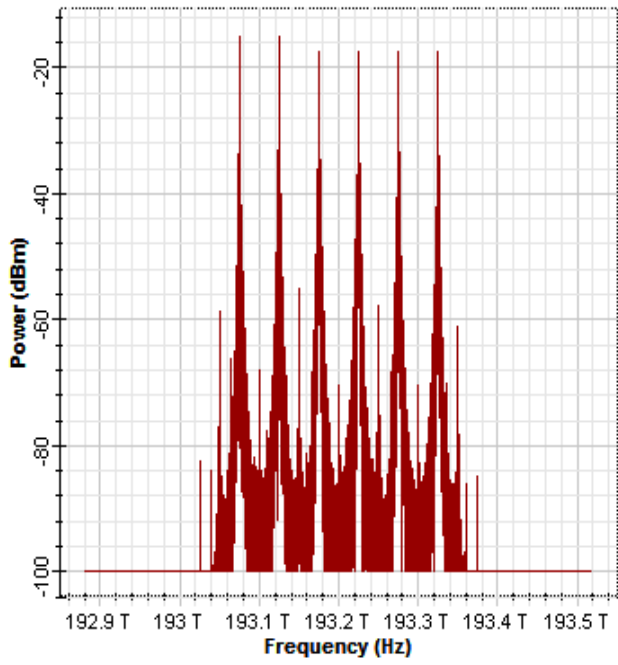


Fig. 7. Spectra of multiplexed signal

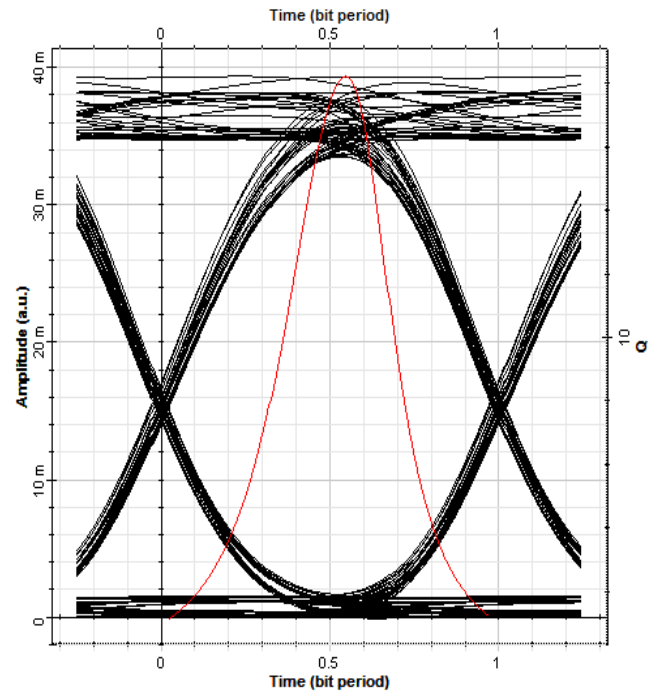


Fig. 9. Eye diagram of downlink channel of BS 2

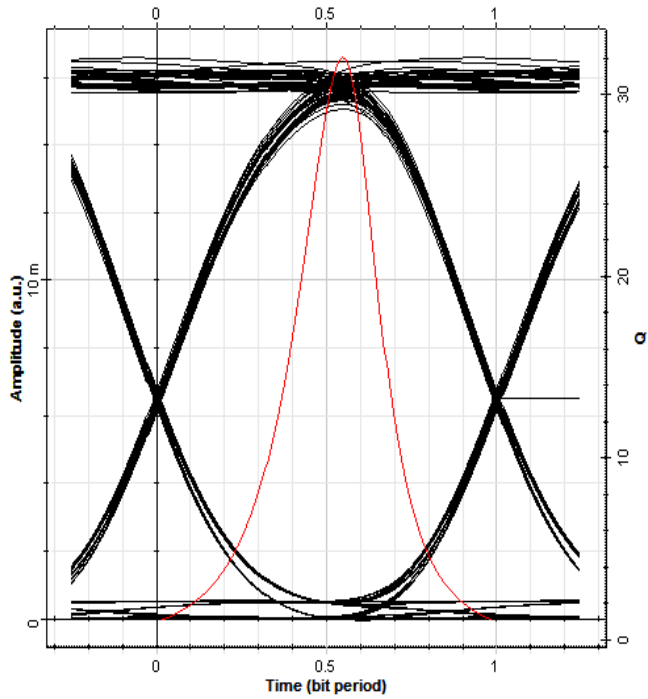


Fig. 8. Eye diagram of downlink channel of BS 1

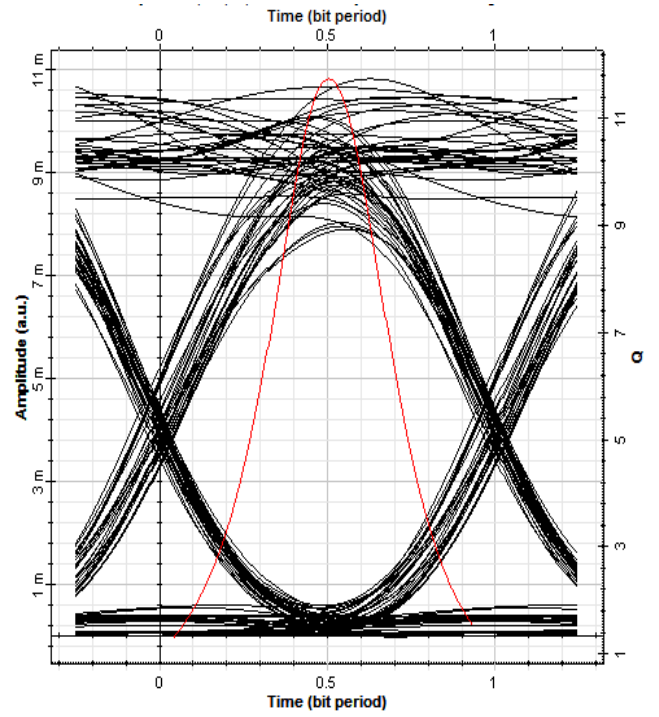


Fig. 10. Eye diagram of uplink channel of BS 1

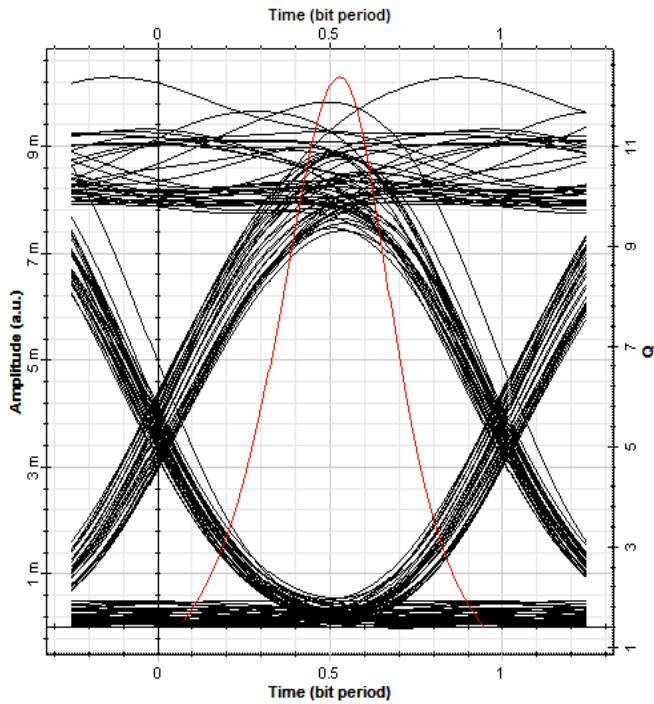


Fig. 11. Eye diagram of uplink channel of BS 2

The carrier signal power at the output of phase modulator versus phase deviation value is plotted in figure 3. It is found that a 276° the carrier is suppressed up to 41 dB. The output spectra of phase modulator of each channel are shown in figures 4, 5, and 6. It is clear from the figures that the central carrier of the modulated signal is almost fully suppressed. The multiplexed spectra of three channels are shown in figure 7. The eye diagrams of data received at base station 1 and 2 are shown in figures 8 and 9 respectively. The eye diagram of data received from the uplink channel of BS1 and BS2 at central station is shown in figures 10 and 11 respectively. The difference in the BER of two base stations is mainly due to the difference in distance travelled. Moreover each channel has different wavelengths and hence causes different dispersion as it travels through the fiber.

Table 1 shows the comparison of single channel RoF system with and without employing phase modulator and interleaver filter. It is found that, after a 30Km transmission through single mode fiber (SMF) the signal quality of the RoF system with phase modulator and interleaver filter is comparatively less than that of other methods. Even though the fiber transmission length is less, the power saved is significant in this system. The total power output at the phase modulator after suppression of the central carrier is 229µW. But in other cases it is about 484µW. i.e., half of the power is saved by employing an optimized phase modulator for modulating 2.5Gbps data.

TABLE 1
COMPARISON OF SINGLE CHANNEL ROF SYSTEM WITH AND WITHOUT PM AND IL FILTER

Fiber length (in Km)	With PM and IL			Without PM and IL		
	Max.Q Factor	Min. BER	Eye diagram	Max.Q Factor	Min. BER	Eye diagram
5	81.5867	0	Excellent	92.9538	0	Excellent
10	60.677	0	Excellent	42.2108	0	Excellent
20	23.9719	2.19659×10^{-127}	Good	23.0889	2.78003×10^{-118}	Good
30	10.3055	2.8507×10^{-25}	Good	17.5142	4.59603×10^{-69}	Good
40	5.01106	2.38576×10^{-7}	Bad	10.9394	2.85639×10^{-28}	Bad
50	2.6697	0.00396674	Bad	7.34994	7.38232×10^{-14}	Bad

V. CONCLUSIONS

A full duplex DWDM RoF system using an optimized phase modulator and optical add drop multiplexer is proposed, simulated and analyzed using optisystem 11. Good eye diagram and low BER is achieved for 5Km fiber transmission from central station. Even though OADM effectively adds/drops the desired channel to/from the DWDM feeder network, successive cascading of these interfaces in the Central Office (CO) and the remote nodes (RNs) may cause significant performance degradation and impose limitations in network dimensioning. If the multiplexing and demultiplexing functionality in the CO and the RNs can instead be combined into a single device, cost-effective architectures with reduced complexity can be realized.

REFERENCE

- [1] G. Eason, B. Noble, and I.N. Sneddon, "Radio Over Fiber Link Design for Next Generation Wireless Systems," David Wake, Anthony Nkansah, and Nathan J. Gomes, *Journal Of Lightwave Technology*, VOL. 28, NO. 16, AUGUST 15, 2010.
- [2] Yu-Ting Hsueh, Hung-Chang Chien, Arshad Chowdhury, Jianjn Yu, and Gee-Kung Chang "Performance Assessment Of Radio Linjks Using Millimeter-Wave Over Fiber Technology With Carrier Suppression Through Modulation Index Enhanced Phase Modulator," 25 *J.Opt Commun. Netw./Vol. 3, No. 3/March 2011*.
- [3] T. Chiba*, H. Arai, H. Nounen, K. Ohira, Optoelectronic System Laboratory, Hitachi Cable, Ltd., Hitaka-cho 5-1-1, Hitachi-shi, Ibaraki-ken 319-14, Japan, "Wave Guide Interleaving Filter", Active and Passive Optical Components for WDM Communications III, Achyut K. Dutta, Abdul Ahad S. Awwal, Niloy K. Dutta, Kazuo Fujiura, Proceedings of SPIE Vol. 5246 (2003) © 2003 SPIE · 0277-786X/03
- [4] Jianjun Yuju, Senior Member, IEEE, Zhensheng Jia, Lei Xu, Lin Chen, Oing Wang, and Gee-Kung Chang, Fellow, IEEE, "DWDM Optical Millimeter-Wave Generation For Raio –Over- Fiber Using an Optical Phase Modulator and an Optical Interleaver ",IEEE Photonic Technology Letters, Vol. 18, No. 13, July 1, 2006
- [5] St. Fischer ,M. Dülk, E. Gamper, W. Vogt,W. Hunziker,E. Gini, H. Melchior, A. Buxens,H. N. Poulsen,and A. T. Clausen"All-Optical Regenerative OTDM Add–DropMultiplexing at 40 Gb/s Using Monolithic InPMach–Zehnder Interferometer", *IEEE photonics technology letters*, VOL. 12, NO. 3, MARCH 2000

Fingerprint image encryption based on Rössler map

F. Abundiz-Pérez, C. Cruz-Hernández, M.A. Murillo-Escobar, and R.M. López-Gutierrez.

Abstract—Nowadays, the biometric systems based on fingerprint image like biometric's identification are the most utilized, for this reason exist several attacks to the biometric systems. One of these attacks is obtaining from the pattern or image of fingerprint in the transmitted information in the communication line, for this reason, exist several research that have realized to provide one possible solution for this problem. In this work, for provides in the security topic of the encrypted fingerprint images, is presented a method of encryption of image using the hyperchaotic Rössler map.

Index Terms—encryption, hyperchaos, fingerprint, biometric systems.

I. INTRODUCTION

SINCE centuries ago the integrity and security of the information through which to exchange information of safe form, have had a great importance, for this reason, during the history have developing several technical of encoding for information hide secure via communication line. Historically, great part of the technical of encoding was been developing for military reason, some examples are reported in [1], [2]. The used encryption information techniques that provide a communication confidential, already is not single important in question military, this is due in great part to the communication networks, that exist today, where are executed several operations, in which, is needed a confidentiality communication, examples where are applied encryption techniques are in bank operations, control access system, etc.

Nowadays is common use of systems to control the access of physical or virtual means, for example, the operative system of computer, the e-mail account, data bases, governmental buildings, cross border lines, among others. For access control, lot of this systems used magnetic card, physical key, password, biometric identifiers, etc. Today the biometric systems are one of the systems more used for access control and several of this systems encrypts the biometric identifier information for provide security, for this reason, several researcher have carried out studies for implement cryptographic algorithms in biometric systems, see, e.g. [3] and [4]. In several works of research the proposed encryption is on extracted patterns of imagen of the identifier biometric

F. Abundiz-Pérez, M.A. Murillo-Escobar and R.M. López-Gutierrez are with the Facultad of Ingeniería, Arquitectura and Diseño, Universidad Autónoma de Baja California (UABC), Km. 103, Carretera Tijuana-Ensenada, 22860 Ensenada, B.C., México. E-mail: abundizf@uabc.edu.mx, murillo.miguel@uabc.edu.mx and roslopez@uabc.edu.mx

C. Cruz-Hernández is with Departamento de Electrónica y Telecomunicaciones, Centro de Investigación Científica y de Educación Superior de Ensenada (CICESE), Carretera Ensenada-Tijuana No. 3918, Zona Playitas, 22860 Ensenada, B.C., México. E-mail: ccruz@cicese.mx

and in other works the ciphered is on imagen of the biometric identifier.

Topic related to ciphered of images, exist several works that report new alternatives of cipher, where some propose use the properties intrinsic of the ADN sequence, whereas other propose benefit of the properties pseudorandom that provide the chaotic systems, some of this research are presented in [5], [6] and [7]. In this work is presented an alternative of ciphered for fingerprint images, by using a hyperchaotic Rössler map to encrypt the image information.

The organization of this work is as follows: In Section II vulnerabilities of biometric systems are presented, Section III briefly describes hyperchaotic Rössler map used in the present work, the Section IV presents in detail the methodology used to encrypt and decrypt the image of fingerprint, In Section V are presented the results obtained from implementing the methodology developed in the present work. The conclusions are presented in Section VI.

II. VULNERABLES POINTS IN BIOMETRIC SYSTEMS

Today the biometric systems is a topic, in which, the researchers have paid very much attention due a the advantage that provide as a control systems of access safe. Nevertheless, these systems have some vulnerable points, which are shown in Figure 1. Attacks made on these points could are classified in two categories, the first classification are attacks in communication lines, in which, found the points 2, 4, 7, and 8 which are shown in Figure 1, one of attack that can be realized to these lines is break the communication so that the user will not have access, or a snooper can spy the communication line so obtain information of the biometric identifier, the which can be used after for replace a true user. The second classification are attacks to the modules, in this classification are found the points 1, 3, 5, and 6, that are illustrated in Figure 1, the attacks that will been realized in the points will have been using malicious programs (trojan horse), which, when execute emulated realize the functions of some module of the biometric system, this could will used so reason several, same examples: the trojan horse could extract the information that will prosecute in some module, which after will used in some attack to biometric system, too could be refused the user access due a the realizing bad the function of the module, etc.

Due the existence of attacks in the vulnerable points of the biometric systems shown in Figure 1, is have been implementing actions for protection the system to attacks in this vulnerable points for mitigate the danger to suffer

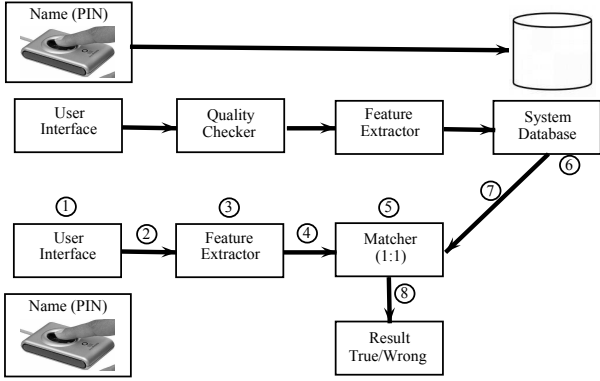


Figure 1. Vulnerable points to attacks in biometric systems.

damages to cause of them, among these actions are been used the following: random data, withhold data, on-life detection, biometric multiple, cryptography, digital signature, clean up the network and physical security. For more information look up the references [8]-[14].

III. HYPERCHAOTIC RÖSSLER MAP

Today Several digital or analogous, communication systems which, require's new model cryptographics, motivated by this fact, in recent years several researchers have reported great variety of works based on chaotic encryption, in which, exploit the pseudorandom properties of the dynamics chaotic, see e.g. [15], [16], and [17]. Some properties that benefit the chaotic encryption are:

- Easy operations can supply dynamics very complex which provide appropriate means where information can be hidden in encryption systems.
- Small variations in initial conditions from the chaotic system provide great changes in the dynamics, which benefits the number of keys that will be using in order for encryption.
- Outputs preserved the same probability distribution for any output which benefit the encryption against statistic analysis attacks.

In this work, we use the Rössler map which presents hyperchaotic dynamics [17]. That is, presents a more complex behavior than a chaotic system. one distinctive characteristic from the hyperchaotic systems is existence of more than one positive Lyapunov exponent [18], [19], and [20]. The choice of hyperchaotic map is very convenient in order to encryption purpose, due that this allows that encrypted information (fingerprint image) be more safe, due to wealth great dynamics from the Rössler map. Rössler map is described by [17]:

$$\begin{aligned}
 x_1(k+1) &= \alpha x_1(k)(1-x_1(k)) - \beta(x_3(k) + \gamma)(1-2x_2(k)), \\
 x_2(k+1) &= \delta x_2(k)(1-x_2(k)) + \varsigma x_3(k), \\
 x_3(k+1) &= \eta((x_3(k) + \gamma)(1-2x_2(k)) - 1)(1-\theta x_1(k)).
 \end{aligned}
 \tag{1}$$

Figure 2 shows the hyperchaotic dynamics of three states from the Rössler map considering the initial conditions $x(0) = (0.3, 0, 0.05)$, and parameter values $\alpha = 3.8, \beta = 0.05, \gamma = 0.35, \delta = 3.78, \varsigma = 0.2, \eta = 0.1, \theta = 1.9$, and 28000 iterations.

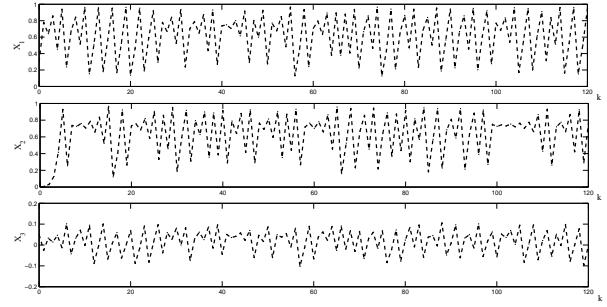


Figure 2. Hyperchaotic dynamics generated by the Rössler map.

IV. ENCRYPTION AND DECRYPTION PROCESSES

If does make a review of the safe communications literature is will find a number of methodologies to perform encryption of information, for that reason, is considered very important describe the methodology followed in the present work. The cipher process consists of two important stages, the diffusing and permutation stage, moreover, decipher process is constituted by the reverse of the above stages, that is inverse permutation and inverse diffusing stage, which are shown in Figure 3.

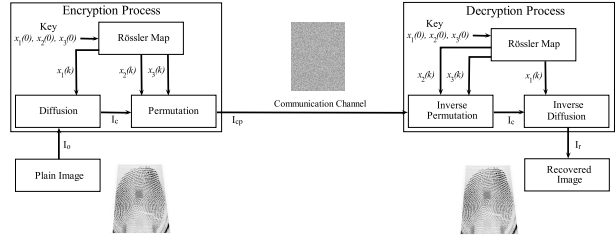


Figure 3. Block diagram of the encryption and decryption process of a fingerprint image.

A. Encryption process

To realization of encrypted stage is need, the diffusion and permutation stages, which used the same hyperchaotic Rössler map in their processes. Hyperchaotic map is used to generate a sequence of pseudorandom numbers, which are used in the stages mentioned above. To better explain what they consist each of these stages, are mentioned separately the required steps to perform the diffusion and permutation stages.

1) *Diffusion stage: Step 1:* Take a reading of the image from the fingerprint to generate a variable that the program can manipulate to perform encryption, which, in this work will be represented by the variable $I_o(i, j)$, where $i = 1, 2, \dots, n$ and $j = 1, 2, \dots, m$, therefore, it represents an array of $n \times m$, where n is the number of rows and m is the number of columns.

Step 2: Construct an array of size $n \times m$, which contains the output data from the hyperchaotic state $x_1(k)$ from the mapping Rössler see (1), where $k = 1, \dots, N$, and

$N = n \times m$, this array will be named chaotic state matrix and will be represented by the variable $M_c(i, j)$.

Step 3: Using chaotic state matrix obtained above step, will generate a new array containing only values in the set $\{a \in \mathbb{N} : 0 \leq a < 256\}$. This array is used to blur the image. To accomplish this, first is need to take into account that $M_c(i, j) \in \mathbb{R}$, as well as the value of its elements is between the range of 0 to 1 therefore has to perform a mapping of the set of real numbers (\mathbb{R}) obtained from the hyperchaotic map Rössler to a set of integers numbers (\mathbb{Z}) positive corresponding to the set $\{a \in \mathbb{N} : 0 \leq a < 256\}$, for which, the following expressions are used:

$$M_{cc} = (\{M_c(i, j) : (|M_c(i, j)| \times 100000) \in \mathbb{N}\} \bmod 256).$$

Step 4: Adding the elements of the array $M_{cc}(i, j)$ with the elements of the array image $I_o(i, j)$ by applying the modulo 256, this to ensure only the values set $\{a \in \mathbb{N} : 0 \leq a < 256\}$. With this process will get a new array that will be named dithered image matrix and will be represented by $I_c(i, j)$.

2) *Permutation stage:* **Step 1:** Read image in order to perform the process of permutation of the pixels positions. This variable is represented by $I_{in}(i, j)$, but this image is obtained in the above process, therefore, $I_{in}(i, j) = I_c(i, j)$.

Step 2: Generate a vector for the positions of the rows and a vector for the positions of the columns, which will be represented by the variables $Vren = [1 \ 2 \ 3 \ 4 \ \dots \ n]$ and $Vcol = [1 \ 2 \ 3 \ 4 \ \dots \ m]$.

Step 3: Generate two vectors that contains the data resulting from chaotic states $x_2(k)$ and $x_3(k)$ from the Rössler map (1), these shall be appointed as chaotic vector of rows and chaotic vector of columns, which will be represented by the variables $X_c(k_1) = [x_2(0) \ x_2(1) \ \dots \ x_2(N)]$ and $X_r(k_1) = [x_3(0) \ x_3(1) \ \dots \ x_3(N)]$. Where $k_1 = 1, 2, 3, \dots, N$ and $N > (21m)$.

Step 4: Generate two vectors from pseudorandom sequences from the rows and columns positions from the image. Considering that $X_r, X_c \in \mathbb{R}$, as well as that the value of its elements are smaller than the values of the elements from the vectors $Vren$ and $Vcol$, is performs a mapping of the set of real numbers (\mathbb{R}) obtained from hyperchaotic Rössler map to set of integers positive (\mathbb{Z}) corresponding to the positions of the rows and columns, for which, the following expressions are used:

$$Sren = (\{X_r : (|X_r| \times 100000) \in N\} \bmod n) + 1,$$

$$Scol = (\{X_c : (|X_c| \times 100000) \in N\} \bmod m) + 1.$$

Subsequently by using the vectors $Vren, Vcol, Sren,$ and $Scol$ are generated two vectors that containing of the pseudorandom sequence the positions from the columns and rows, for which will be used the following Algorithm 1.

Algorithm 1 Generation random sequence of positions.

Require: Order variables $N = 21m, Scao(k_1) = Sren(k_1), Vp(l) = Vren(i)$ and $N_2 = n$ for generating pseudo-random sequence from the rows positions or $Scao(k_1) = Scol(k_1), Vp(l) = Vcol(j)$ and $N_2 = m$ for generating pseudorandom sequence the columns positions.

Ensure: $Vsap$ Vector random sequence of positions.

```

1:  $p = 1; a = 1; b = N/21;$ 
2: while  $a \neq 0$  do
3:   if  $Scao(b)$  is equal to  $Vp(Scao(b))$  then
4:      $Vsap(p) = Scao(b)$ 
5:      $Vp(Scao(b)) = 0; p = p + 1$ 
6:   end if
7:    $b = b + 1$ 
8:   if sum of all elements of  $Vp$  is equal to 0 then
9:      $a = 0$ 
10:  end if
11:  if  $b$  is equal to  $N$  then
12:     $b = 1$ 
13:     $Scao = ((Scao + 1) \bmod N_2) + 1$ 
14:  end if
15: end while
16: return  $Vsap$ 

```

Step 5: Using the vectors the random sequences from the columns and rows positions, which are represented by variables $Vsap_c$ and $Vsap_r$ respectively. The pixels positions from the image will be permuted of the follows

$$I_{cp}(i, j) = I_{in}(Vsap_r(i), Vsap_c(j)).$$

B. Decryption process

To perform the decryption process is requires the inverse permutation stage and reverse diffusion stage, which use the same hyperchaotic Rössler map which was used in the encryption process with the same initial conditions. In the sequel, we describe the above stages.

1) *Inverse permutation stage:* The steps to be followed to perform the reverse permutation are similar to those made in the permutation stage, but in this time $I_{in}(i, j) = I_{cp}(i, j)$ and the main unlike of the process lies in the Step 5. To perform reverse permutation equally will be used the vectors of the pseudorandom sequences from the column ($Vsap_c$) and row ($Vsap_r$) positions, but to perform the reverse permutation will be used the following expression

$$I_c(i, j) = I_{in}(Vsap_r(i), Vsap_c(j)).$$

2) *Inverse diffusion stage:* The steps to perform the inverse diffusion process are similar to those presented in the diffusion stage, the difference lies in Step 4 of the process. To perform the reverse blurring equally will be used the matrices $M_{cc}(i, j)$ and $I_c(i, j)$, but in this time the operation performed is:

$$I_r(i, j) = (I_c(i, j) - M_{cc}(i, j)) \bmod 256,$$

also the $\bmod 256$ is to ensure that the values resulting from this operation are within the set $\{a \in \mathbb{N} : 0 \leq a < 256\}$. With

this process will be provided a new matrix which contains the retrieved data from the encrypted image previously in the encryption stage, that is, the obtained matrix corresponds to recovered image, and will denoted by the variable I_r .

V. EXPERIMENTAL RESULTS

Below is presented what has been achieved from the programs implemented in MatLab 2008a version, which, performed the procedures listed in Section IV. The results to be presented are applying the steps of encryption, decryption, permutation, diffusion, inverse permutation, and inverse diffusion.

A. Stages from the process of encryption and decryption

To better observe what performed permutation and diffusion stages, as well as the stages of their inverses, in Figure 4 are shown the results that would be obtained if input a image to these stages, this time will be entered the same image on both stages, that is, isolated stages and input the fingerprint image, this provides a idea clearer of what perform these steps.

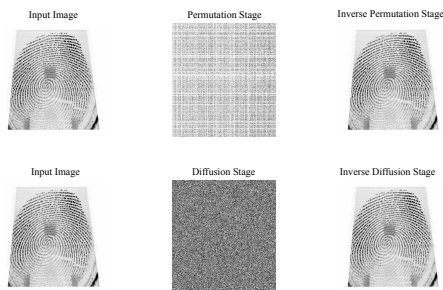


Figure 4. Results of permutation, diffusion, permutation inverse, and diffusion inverse, when an image is input to the stages and using the correct key for performing correctly the reverse processes.

In Figure 5 is shown the results of ciphered and deciphered process, without omitting any steps that are performed in each of the processes. But what would happen if will be skipped someone of the stages? if will be omitted one of the two stages that are performed in the encryption or decryption process, the imagen not will retrieve, to demonstrate this fact is presented in Figure 6 the results if omitted permutation stage or inverse permutation in the encryption or decryption depending on the case.

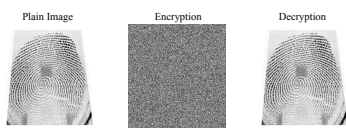


Figure 5. Results obtained if not will be omitted any stage of the cipher and decipher process.

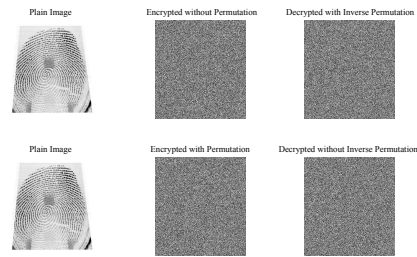


Figure 6. Results obtained if will be omitted the stage of the permutation or permutation inverse.

B. Processing time encryption/decryption

The process of encryption/decryption is performed by using MatLab 2008a version that was installed on a laptop Toshiba satellite E105-S1402, with operating system Windows Vista Home Premium SP1, Core2Duo P8400 processor speed of 2.26 Ghz, System Memory 4GB DDR2 PC6400 800 Mhz and 320 GB hard disk. The time taken by the algorithm to encrypt an image of “.bmp” format in grayscale of 355×390 with a weight of 139918 bytes is 0.2340 sec and for decryption is 0.2105 sec. For a color image of “.jpg” of size 512×512 with a weight of 69214 bytes is 2.6208 sec and for decryption is 2.6676 sec.

VI. CONCLUSIONS

Encryption performed in this study used only hyperchaotic Rössler map to perform the diffusion and permutation stages, is generated a good encryption without by using a hyperchaotic map at each stage, however if two maps are used Rössler the number of keys that can be used increase, safety by providing increased encryption.

The processing time of encryption algorithm for grayscale images is considered a good time of conversion. While the time to a color image is considered slow compared to existing algorithms today, however, this time could be reduced if it is performed in the C language, where process times can be greatly reduced.

ACKNOWLEDGMENT

This work was supported by the CONACYT, México under Research Grant No. 166654.

REFERENCES

- [1] García del Castillo Crespo Eugenio C. López Guerrero Miguel Ángel. *Introducción a la criptografía: historia y actualidad*, chapter Los primeros pasos. Cifrado por sustitución, pages 19–35. Colección Monografías, 2006.
- [2] J.C.G. Díaz. *Criptografía: Historia De La Escritura Cifrada*. sin colección. Editorial Complutense, 1995.
- [3] Daesung Moon, Yongwha Chung, Sung Bum Pan, Kiyoun Moon, and Kyo Il Chung. An efficient selective encryption of fingerprint images for embedded processors. *ETRI Journal*, 28(4):444–452, August 2006.
- [4] Juan M. Vilaridy, Cesar O. Torres, and Lorenzo Mattos. Fingerprint encryption using fractional fourier transform. *5th. European Congress on Computational Methods in Applied Sciences and Engineering (EC-COMAS 2008)*, 2008.

- [5] Hongjun Liu, Xingyuan Wang, and Abdurahman kadir kadir. Image encryption using dna complementary rule and chaotic maps. *Applied Soft Computing*, 12(5):1457–1466, 2012.
- [6] Guodong Ye. Image scrambling encryption algorithm of pixel bit based on chaos map. *Pattern Recognition Letters*, 31(5):347–354, 2010.
- [7] Qiang Zhang, Ling Guo, and Xiaopeng Wei. Image encryption using dna addition combining with chaotic maps. *Mathematical and Computer Modelling*, 52(11-12):202–2035, 2010.
- [8] Parvathi Ambalakat. Security of biometric authentication systems, 2005.
- [9] Maltoni Dario Maio Anil K. Jain Salil Prabhakar Davide. *Handbook of Fingerprint Recognition*. springer, 2003.
- [10] Anil K. Jain, Karthik Nandakumar, and Abhishek Nagar. Biometric template security. In *EURASIP Journal on Advances in Signal Processing*, 2008.
- [11] Muhammad Khurram Khan, Ling Xie, and Jiashu Zhang. Chaos and ndft-based spread spectrum concealing of fingerprint-biometric data into audio signals. *Digital Signal Processing*, 20(1):179–190, 2010.
- [12] C. Militello, V. Conti, S. Vitabile, and F. Sorbello. Embedded access points for trusted data and resources access in hpc systems. *The Journal of Supercomputing*, 55:4–27, 2011.
- [13] Alicia Hortensia Beisner Muñoz. Ataques tipo side-channel a sistemas biométricos de reconocimiento de huella dactilar. Technical report, Universidad Autónoma de Madrid, Abril 2010.
- [14] Umut Uludag and Anil K. Jain. Attacks on biometric systems: A case study in fingerprints. *Proc. SPIE-El 2004, Security, Seganography and Watermarking of Multimedia Contents VI*, pages 622–633, 2004.
- [15] A. Y. Aguilar-Bustos, C. Cruz-Hernández, R. M. López-Gutiérrez, E. Tlelo-Cuautle, and C. Posadas-Castillo. Hyperchaotic encryption for secure e-mail communication. In Richard Chbeir, Youakim Badr, Ajith Abraham, and Aboul-Ella Hassaniien, editors, *Emergent Web Intelligence: Advanced Information Retrieval*, Advanced Information and Knowledge Processing, pages 471–486. Springer London, 2010. 10.1007/978-1-84996-074-8_18.
- [16] Cruz-Hernández C., López-Gutiérrez R.M., Aguilar-Bustos A.Y., and Posadas-Castillo C. Communicating encrypted information based on synchronized hyperchaotic maps. *International Journal of Nonlinear Sciences and Numerical Simulation*, 11:337–350, March 2011.
- [17] López Gutiérrez R. M. y Posadas Castillo C. Aguilar Bustos A. Y. Cruz Hernández C. Synchronization of different hyperchaotic maps for encryption. *Nonlinear Dynamics and Systems Theory*, 8(3):221–236, july 2008.
- [18] A.Y. Aguilar-Bustos and C. Cruz-Hernández. Synchronization of discrete-time hyperchaotic systems: An application in communications. *Chaos, Solitons & Fractals*, 41(3):1301–1310, 2009.
- [19] E. J. Ngamga, A. Buscarino, M. Frasca, G. Sciuto, J. Kurths, and L. Fortuna. Recurrence-based detection of the hyperchaos-chaos transition in an electronic circuit. *Chaos*, 20(4):1089–7682, 2010.
- [20] R. Vicente, J. Dauden, P. Colet, and R. Toral. Analysis and characterization of the hyperchaos generated by a semiconductor laser subject to a delayed feedback loop. *Quantum Electronics, IEEE Journal of*, 41(4):541–548, 2005.

Design of Compact RF Filters with Narrow Band-Pass and Wide Stop-Band by Open-Stub & T-shaped Microstrip Resonators and Defected Ground Structure (DGS)

Shervin Amiri ¹, Nafiseh Khajavi ², Mahboubeh Khajavi ³

¹Scientific Member of E.E Department of IROST, Tehran, Iran, amiri@irost.ir

^{2,3}Faculty of E.E Department of Dezful Branch of Islamic Azad University, Dezful, Iran, N_khajavi89@yahoo.com , Zefins2011@yahoo.com

Abstract- This paper presents the design of a narrow band-pass filter with wide stopband for WLAN and WiMAX applications. First, open-stub and T-shaped resonators were used to design a filter (F1) with the center frequency of 2.4 GHz. In order to verify the architectures of the proposed resonators, their frequency responses were compared to the response of an LC model. Next, DGS was utilized to achieve a wide stopband within the frequency response of F1. The design of other narrow-band filters (F2 and F3) with their center frequencies of 3.7 GHz and 5.1 GHz respectively is derived only by modifying the dimensions of the resonators in the structure of F1. Advantages of these filters include simplicity, architectural symmetry, tuning for applications at other frequencies and proper bandwidth. These filters have optimal return loss and insertion loss.

Keywords- Compact microstrip filters, Narrow Band-pass, Wide Stop Band, Defected Ground Structure (DGS)

I. INTRODUCTION

High-quality compact bandpass filters are among the common elements in wireless communication systems. Wide-stopband filters are used in nonlinear elements such as power amplifiers or mixers for rejecting noise or unwanted interference in the stopband. Bandpass filters with wide stopbands may be designed for different frequencies. The frequencies of 2.4 GHz and 5.1 GHz are consistent with the IEEE 802.11 standards for WLAN systems while the frequency 3.7 GHz is among the operating frequencies for WiMAX technology. There are different techniques for designing narrow-band filters with wide stopbands. For example, ring resonators have been used to eliminate the second harmonic in a bandpass filter with the center frequency 2.6 GHz. This narrow-band filter, however, does not have an acceptable insertion loss [1]. A narrow bandpass filter has been designed by eliminating the harmonic $11f_0$ using various types of quarter-wavelength SIRs[2]. The insertion loss at the center frequency of this filter (2.4 GHz) is at the non-optimal level of 2.6 dB. DGS has been used to improve the filter parameters, including its bandwidth. Dumbbell-shaped DGS (DS-DGS) was implemented at the ground structure [3]. A bandpass filter with the center frequency 2.4 GHz has been designed by coupling two open-loop DGS slot resonators with microstrip resonators [4]. DGS technique has also been implemented on bandpass filter structures to examine how this technique impacts the results [5]. A compact microstrip single-band bandpass filter with controllable bandwidth has been designed by coupling two DGS resonators. The center frequency of this filter does not match the frequency of WLAN applications. In addition, the insertion loss of this filter is above 1 dB [6]. In this paper, a single-band bandpass filter with a wide pass band was designed by cascading

a low-pass and a bandpass filter [7]. An LC model has been developed for microstrip lines [7-11].

This paper presents narrow-band bandpass filters with wide stopbands for WLAN and WiMAX applications. Open-stub and T-shaped resonators were used to design the architecture of the filters. The frequency responses of these structures were compared to the frequency response of the LC model in order to examine the architecture of the proposed resonators. For the first filter (F1) with the center frequency 2.4 GHz, DGS was applied to improve the width of the stopband. Next, it has been shown that due the simplicity and symmetry in the architecture of this filter, two other filters with the center frequencies 3.7 GHz (for F2) and 5.1 GHz (for F3) can be constructed only by modifying the dimensions of the resonators. All simulations in this paper were implemented using Momentum simulator in ADS software.

II. DESIGNING FILTER F₁

Using open-stub resonators placed in parallel to each other (the resonators are connected through a middle stub), the basic resonator architecture shown in Fig. 1(a) was obtained. As seen in the frequency response of the basic resonator (Fig. 1(b)), this architecture has a resonance frequency of 2 GHz with insertion loss of 0.22 dB and a return loss of 32.88 dB. The presence of a neutral harmonic at 5.46 GHz limits the stopband. In addition, the center frequency of this architecture does not match the WLAN frequency. The dimensions of the basic resonator are: $L1 = 5.3$ mm, $W1 = 0.1$ mm, $L2 = 6.4$ mm, $W2 = 0.1$ mm, $L3 = 20.06$ mm, $W3 = 0.1$ mm and $G1 = 4.788$ mm.

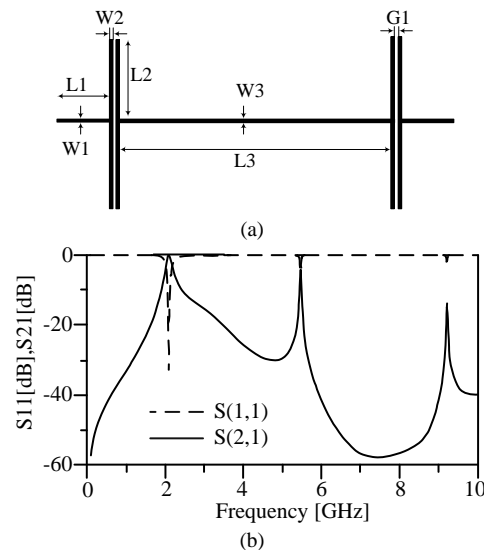


Fig.1 (a) Basic structure of the proposed resonator.(b) Frequency response of basic structure of the proposed resonator.

An LC model is presented to further examine the basic resonator. The effective dielectric constant ϵ_{re} and characteristic impedance Z_C are used to identify the characteristics of microstrip lines [12]. For substrate R04003 with the thickness $H=20\text{Mil}$ and a microstrip line with the width W (The width of microstrip lines are presented in Fig. 2), ϵ_{re} can be obtained from (1).

$$\begin{cases} \epsilon_{re\text{eff}} = \frac{\epsilon_r + 1}{2} + \left\{ \left(1 + 12 \frac{H}{W}\right)^{-0.5} + 0.04 \left(1 - \frac{W}{H}\right)^2 \right\} \frac{W}{H} \leq 1 \\ \epsilon_{re\text{eff}} = \frac{\epsilon_r + 1}{2} + \frac{\epsilon_r - 1}{2} \left(1 + 12 \frac{H}{W}\right)^{-0.5} \frac{W}{H} \leq 1 \end{cases} \quad (1)$$

Equation (2) is used to calculate C_a . ϵ_r is the permittivity of dielectric substrate. C_a is capacitance per unit length for an air substrate.

$$\begin{cases} C_a = \frac{2\pi\epsilon_0}{l_n} \frac{W}{\left(\frac{aH}{W} + \frac{W}{4H}\right)H} \leq 1 \\ C_a = \epsilon_0 \left(\frac{W}{H} + 1.393 + 0.667l_n \left(\frac{W}{H} + 1.444 \right) \right) \frac{W}{H} \leq 1 \end{cases} \quad (2)$$

L and C are derived from (3). For this purpose, one should first calculate phase velocity V_p and characteristic impedance Z_C .

$$Z_C = \frac{120\pi}{\epsilon_0 \sqrt{\epsilon_{re}}} \quad , \quad V_p = \frac{(3.0 \times 10^8) \frac{m}{s}}{\sqrt{\epsilon_{re}}}$$

$$\begin{cases} L = \frac{Z_C l}{V_p} \\ C = \frac{l}{Z_C V_p} \end{cases} \quad (3)$$

In this model, L_{t1} represents the lines which connect the ports to the basic resonator while L_{t2} shows the line which connects open-stub resonators together. The gap between the open-stub resonators is denoted by C_{g1} . The grounded capacitor C_{op} and the inductor L_{op} were used to model the open-stub resonators. The LC model is shown in Fig. 2(a). Comparison of the frequency response of the LC circuit with the simulation results indicates a proper match between the center frequencies of both frequency responses shown in Fig. 2(b). The values of inductance and capacitance for the LC model are: $L_{t1}=3\text{ nH}$, $L_{t2}=8.3\text{ nH}$, $L_{op}=0.95\text{ pF}$, $C_{op}=0.5\text{ pF}$ and $C_{g1}=0.37\text{ pF}$.

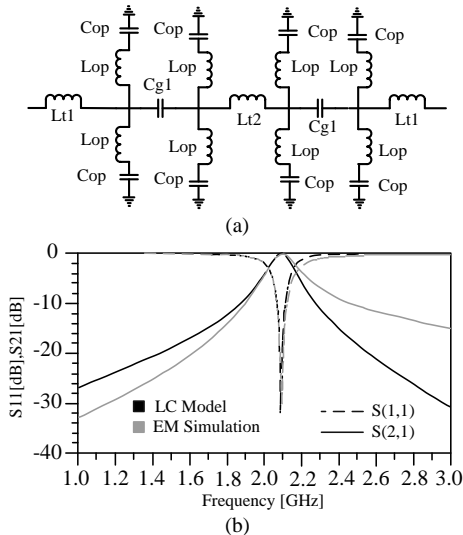


Fig.2 (a) The LC model of the basic structure, (b) Frequency response of the LC model and EM simulation of the basic structure

In the next step, T-shaped resonators were used to improve the stopband and to obtain a center frequency which is consistent with IEEE 802.11a (Fig. 3(a)). The arrangement of the T-shaped resonators has created a deep zero at 5.4 GHz. The dimensions of the T-shaped resonators are: $W_4=0.247$

mm, $L_4=10.266\text{ mm}$, $W_5=1.08\text{ mm}$, $L_5=5.74\text{ mm}$, $W_6=0.70\text{ mm}$, $L_6=1.98\text{ mm}$ and $G_1=0.24\text{ mm}$.

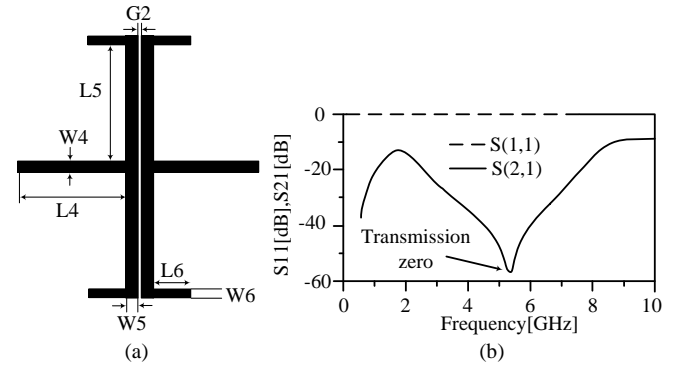


Fig.3 (a) T-shape structure resonators, (b) Frequency response of T-shape structure resonators.

Again, an LC model was used to examine these T-shaped resonators. In this model, the microstrip lines are modeled based on their corresponding indices using inductors and capacitors. C_{g2} represents the gap between the T-shaped resonators. The open-ended sections are grounded through a capacitor and the transmission lines are modeled by inductors. The model is shown in Fig. 4(a). The values of the capacitance and inductance are: $L_4=0.85\text{ nH}$, $L_5=1.45\text{ nH}$, $L_6=0.5\text{ nH}$, $C_6=0.5\text{ pF}$ and $C_{g2}=0.1\text{ pF}$.

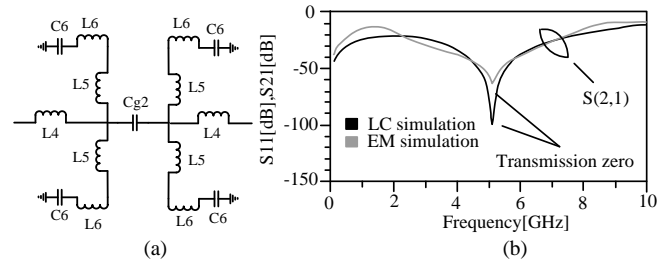


Fig.4 (a) The LC model of the T-shape structure resonators, (b) Frequency response of the LC model and EM simulation of the T-shape structure resonators

A comparison of the frequency response of the LC model for the T-shaped resonators and the associated EM simulation indicates a good match between the two simulations as seen in Fig. 4(b). The presence of a deep zero at 5.4 GHz along with a frequency response with a pole at the same frequency cancels the effect of the zero and the pole at this frequency, thereby widening the stopband. This can be seen in Fig. 5. These results in center frequency of 2.69 GHz are insertion loss of 4.36 dB, and return loss of 2.5 dB, which show a considerable drop in losses compared to the frequency response obtained for open-stub resonators.

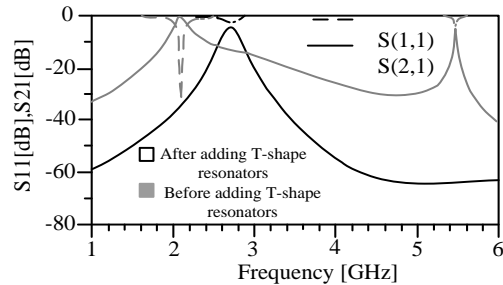


Fig.5 Comparison the frequency response of basic structure before and after adding the T-shaped resonators

In fact, the final architecture of filter F1 was obtained by putting together the open-stub resonators and the T-shaped resonators. The architecture is shown in Fig. 6(a). Desirable center frequency, insertion loss, return loss, and

bandwidth were achieved by optimizing the dimensions of different parts of the open-stub and T-shaped resonators. The dimensions of the filter structure F_1 are:

$W1=0.1\text{mm}$, $L1=3.06\text{mm}$, $W2=0.34\text{mm}$, $L2=6.50\text{mm}$, $W3=0.1\text{mm}$, $L3=1.35\text{mm}$, $W4=0.24\text{mm}$, $L4=10.26\text{mm}$, $W5=1.08\text{mm}$, $L5=5.74\text{mm}$, $W6=0.70\text{mm}$, $L6=1.98\text{mm}$, $G2=0.24\text{mm}$ and $G1=0.18\text{mm}$.

As seen in the frequency response of F_1 (Fig. 6(b)), return loss and insertion loss for this filter are 32.8 dB and 0.5 dB, respectively. The bandwidth of F_1 is 112 MHz.

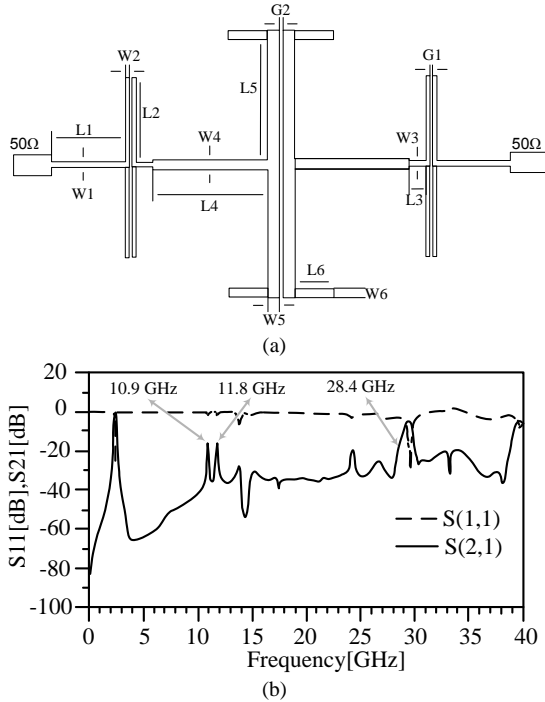


Fig.6 (a) Structure of the filter F_1 (b) Frequency response of filter F_1

Fig. 7 shows a schematic of constructed filter and a comparison of its measured frequency response to that of the simulation model. As seen in Fig. 7, the two responses are in close agreement.

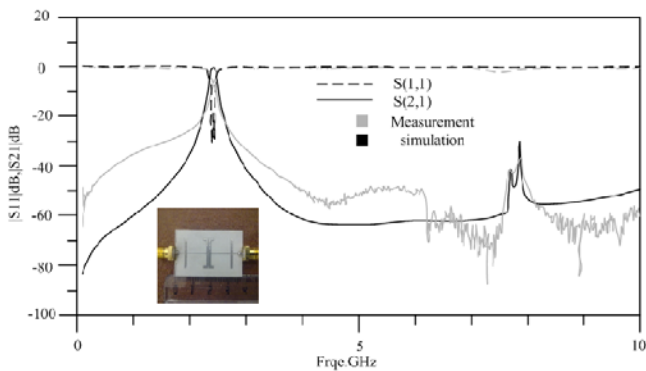


Fig.7 Comparison of the results EM-simulation and measurement for filter F_1

III. ADDING DGS TO STRUCTURE OF THE FILTER F_1

The presence of some harmonics at 10.9 GHz, 11.8 GHz, and 28.4 GHz in the frequency response of F_1 (Fig. 6(b)) has limited the stop-band of the filter. DGS was used to eliminate the neutral harmonics in the stopband and to widen this band. DGS technique was employed to create the dumbbell-shaped structure shown in Figure 8.

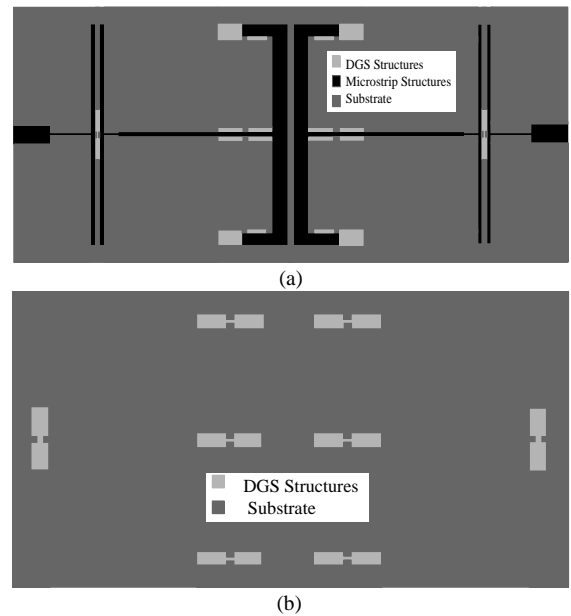


Fig.8 (a) The architecture seen from above (b) The substrate and dumbbell-shaped DGS structure seen from below

Fig. 9 compares the frequency responses of filter F_1 before and after applying DGS. Applying DGS shifts all the neutral harmonics in the stopband, up to the frequency 39 GHz, into the levels below -20 dB, thereby widening the stopband by 16.25 F_0 .

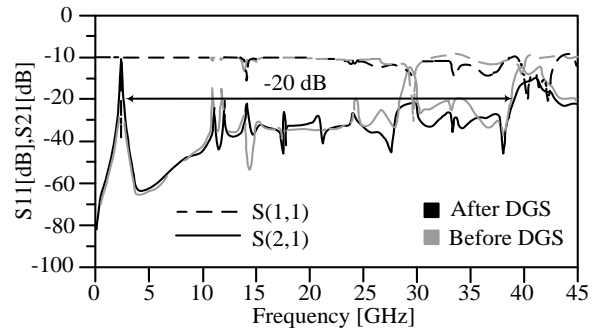


Fig. 9 compares the frequency responses of filter F_1 before and after applying DGS

According to the comparison presented in Table I, DGS improves not only the stopband, but also return loss and insertion loss.

Table.1 Comparison of the results for filter F_1 before and after applying DGS

Filter F_1	Center frequency	Limit of the stop band	Band width	Return loss	Insertion loss
Before DGS	2.42GHz	$12f_0$	0.121GHz	33.35dB	0.521 dB
After DGS	2.42GHz	$16.25F_0$	0.121GHz	38.3 dB	0.426 dB

IV. DESIGNING FILTERS WITH CENTER FREQUENCY OF 3.7GHz AND 5.1GHz

One objective in designing microstrip filters is to design small size architectures with high capabilities which are regarded as advantages of this type of architecture. These small and highly capable architectures can be designed by combining open-stub resonators with T-shaped resonators. Therefore, F_2 with the center frequency 3.7 GHz and F_3 with the center frequency 5.1 GHz were obtained simply by changing the dimensions of filter

F1. Filters F1 and F3 can be used in WLAN applications while filter F2 is suitable for WiMAX systems.

V. DESIGNING FILTER F₂

The architecture of this filter is the same as the architecture of filter F1 and the optimized dimensions are: W1=0.1 mm, L1=5.3 mm, W2=0.16 mm, L2=6.4 mm, W3=0.1 mm, L3=0.5 mm, W4=0.8 mm, L4=8.88 mm, W5=0.8 mm, L5=5.4 mm, W6=0.4 mm, L6=1.6 mm, G1=0.2 mm and G2=0.15 mm. The frequency response of this filter is shown in Fig. 10. As seen in this figure, filter F2 has its center frequency at 3.7 GHz, a bandwidth of 214 MHz, an insertion loss of 0.42 dB, and a return loss of 41.578 dB. Since magnitude of S21 is below -20 dB, for frequencies up to 11.79 GHz, the first, second, and third harmonics are eliminated in filter F2.

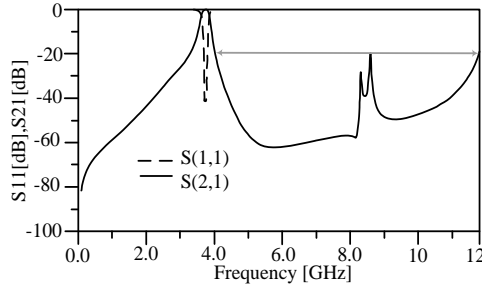


Fig.10 frequency response of the filter F₂

VI. DESIGNING FILTER F₃

The architecture of this filter is the same as the architecture of filter F1 and the optimized dimensions are: W1=0.1 mm, L1=4.69 mm, W2=0.12 mm, L2=4.48 mm, W3=0.1 mm, L3=0.76 mm, W4=0.56 mm, L4=6.16 mm, W5=0.616 mm, L5=3.66 mm, W6=0.397 mm, L6=1.12 mm, G1=0.14 mm and G2=0.105 mm.

The frequency response of this filter is shown in Fig. 11. As seen in this figure, filter F3 has its center frequency at 5.1 GHz, a bandwidth of 423 MHz, an insertion loss of 0.318 dB, and a return loss of 53.23 dB. Since magnitude of S21 is below -20 dB, for frequencies up to 16.27 GHz, the first and second harmonics are eliminated in filter F3.

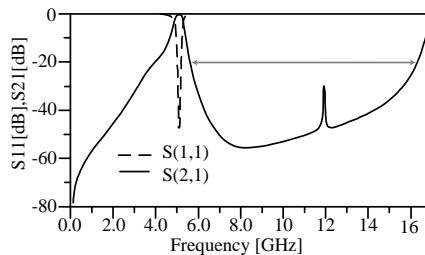


Fig.11 frequency response of the filter F₃

Comparison of the dimensions of these three filters demonstrates that for higher center frequencies, the sizes of the filter will be smaller as expected; frequency has an inverse relationship to size. Table II compares the results obtained for the filters designed in this paper. Frequency responses of the three filters are shown in Fig. 12.

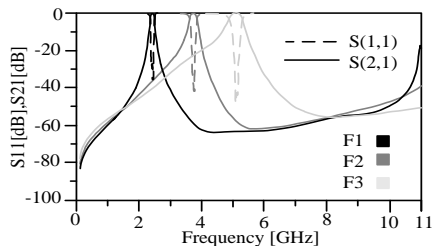


Fig.12 Frequency responses of the three proposed filters

Table.2 Final results for optimized architectures of the proposed microstrip single-band bandpass filters

Filter name	Center frequency	Insertion Loss	Return loss	Band width	Limit of the stop band	Size of the filter
F1	2.42GHz	0.521 dB	33.35 dB	0.121 GHz	12f ₀	37.182*13.45 mm ²
F2	3.7GHz	0.42 dB	41.57 dB	0.214 GHz	3f ₀	36.46*12.91 mm ²
F3	5.1GHz	0.318 dB	53.23 dB	0.423 GHz	2f ₀	29.81*9 mm ²

VII. CONCLUSION

This paper presents narrow-band bandpass filters with wide stopband for WLAN and WiMAX applications. First, using parallel open-stub resonators, the frequency response of the basic resonator was obtained with the resonance frequency 2 GHz and a pole at 5.4 GHz. T-shaped resonators were placed next to open-stub resonators, to cancel this pole, widen the stopband, and construct the final architecture for F1. The T-shaped resonators create a deep zero at the same frequency, thereby cancelling the effect of this pole. To examine the architectures of the proposed resonators, the frequency responses of these architectures were compared with the frequency responses of their corresponding LC model. Then, narrow-band filters with the center frequencies 3.7 GHz and 5.1 GHz (for F2 and F3, respectively) were obtained simply by changing the dimensions of the resonators in the basic structure of F1. Finally, DGS was utilized to achieve a wide stopband in the frequency response of F1. An advantage of these filters is having a good bandwidth. In addition, these filters have optimal return loss and insertion loss. In this paper we obtained: (a) Comparison of frequency responses before and after adding the T-shaped resonators. (b) Comparison of the results for F1 before and after applying DGS. (c) Frequency responses of the three proposed filters. (d) Final results for optimized architectures of the proposed microstrip single-band bandpass filters.

REFERENCES

- [1] J. Fraresso and C.E. Saavedra, "Narrowband bandpass filter exhibiting harmonic suppression," *Electronics letters*, Vol. 39, No. 16, 1189-1190, 2003.
- [2] S-C. Lin, P-H. Deng, Y-S Lin, C-H. Wang, and C. H. Chen, "Wide-Stop band Microstrip Bandpass Filters Using Dissimilar Quarter-Wavelength Stepped-Impedance Resonators," *IEEE transactions on microwave theory and techniques*, Vol. 54, No. 3, 1011-1018, 2006.
- [3] A. Kumar, M.V. Kartikeyan, "A design of microstrip bandpass filter with narrow bandwidth using DGS/DMS for WLAN," *Communications (NCC), 2013 National Conference on*, New Delhi, India, 1-4, 2013.
- [4] P. Vagner, M. Kasal, "A Novel Bandpass Filter Using a Combination of Open-Loop Defected Ground Structure and Half-Wavelength Microstrip Resonators," *Radioengineering*, Vol. 19, No. 3, 392-396, 2010.
- [5] M. Kufa, Z. Raida, "Comparison of Planar Fractal Filters on Defected Ground Substrate," *Radioengineering*, Vol. 21, No. 4, 1019-1024, 2012.
- [6] S. U. Rehman, A. F. A. Sheta, and M. A. S. Alkanhal, "Compact Bandpass Filters with Bandwidth Control using Defected Ground Structure (DGS)," *ACES Journal*, Vol. 26, No. 7, 624-630, 2011.
- [7] M. Shobeyri and M. H. Vadjed Samiei, "Compact ultra-wideband Bandpass Filter With Defected Ground Structure," *Progress In Electromagnetics Research Letters*, Vol. 4, 25-31, 2008.
- [8] T. Yang, M. Tamura, and T. Itoh, "Compact Hybrid Resonator With Series and Shunt Resonances Used in Miniaturized Filters and Balun Filters," *IEEE Transactions on microwave theory and techniques*, Vol. 58, No. 2, 390-402, 2010.
- [9] Z.-C. Hao, and J.-S. Hong, "UWB Bandpass Filter Using Cascaded Miniature High-Pass and Low-Pass Filters With Multilayer Liquid Crystal Polymer Technology," *IEEE Transactions on microwave theory and techniques*, Vol. 58, No. 4, 941- 948, 2010.
- [10] F. Wei, C.-J. Gao, B. Liu, H.-W. Zhang and X.-W. Shi, "UWB bandpass filter with two notch-bands based on SCRLH resonator," *Electronics letters*, Vol. 46 No. 16, 2010.

- [11] F. Wei, Q. Y. Wu, X. W. Shi, and L. Chen, "Compact UWB Bandpass Filter With Dual Notched Bands Based on SCRLH Resonator," IEEE microwave and wireless components letters, Vol. 21, No. 1, 28-30, 2011.
- [12] J. S. Hong, and M. J. Lancaster, "Microstrip Filters for RF/ Microwave Applications," Book (Hong, et al., 2001), A Wiley-Interscience Publication, John Wiley & Sons, Inc, 2001.

1) **Shervin Amiri** is Scientific Member of Electrical Engineering Department of Iranian Research Organization for Science and Technology (IROST) in Tehran, I.R.Iran. He received to associate professor degree at 2013. His research interest fields are Antenna and RF subsystems in microwave and millimeter wave bands. He is supervisor of many MSc and PhD students in these fields.

2) **Nafiseh Khajavi** received the B.Sc. degree in Medical Engineering from Islamic Azad University Dezful branch, Iran, 2007, and the M.Sc. degree in Electrical Engineering from Kermanshah Science and Research Branch Islamic Azad University, Kermanshah, Iran, 2012. She has been with the Department of Engineering Islamic Azad University Dezfull branch. Her research interests include microstrip filter, the analysis and design of high-frequency electronics and microwave passive circuits.

Authors Index

Abundiz-Pérez, F.	49, 193	Ibrahim, R.	118	Panic, S.	27
Adegbite, S. A.	54	Ikuta, A.	19, 43	Park, M.	177
Al Zarqa, A.	145	Jaafar, H.	172	Raji, K.	187
Al-Ali, A. R.	145	Jeong, J.-C.	32, 177	Ramli, D. A.	36, 96, 172
Aliff, A.	85	Jeoti, V.	73	Rosdi, B. A.	172
Alomari, S. A.	138	Jovkovic, S.	27	Ruiz, A.	125
Amiri, S.	198	Kama, N.	118	Saeid, E.	73
Astrova, I.	104	Khajavi, M.	198	Saxena, K.	151
Azetsu, T.	157	Khajavi, N.	198	Siller, M.	125
Bait-Suwailam, M.	182	Kim, H.-D.	177	Sivakumar, R.	108
Bajpai, S.	151	Kim, Y.	32	Stefanovic, C.	27
Barrile, V.	65	Knemeyer, L.	104	Stewart, B. G.	54
Basri, S.	118	Koschel, A.	104	Suetake, N.	60, 157
Bellafkih, M.	89	Kusuma, E. D.	161	Sujatha, N.	108
Belmekki, A.	89	Lee, D.-K.	177	Sumari, P.	138
Belmekki, E.	89	López-Gutiérrez, R. M.	49, 193	Tan, W. C.	36
Bilotta, G.	65	McMeekin, S. G.	54	Tanaka, H.	60
Booyens, A.	78	Milic, D.	27	Tantawy, M.	113
Cruz-Hernández, C.	49, 193	Murillo-Escobar, M. A.	49, 193	Tokunaga, K.	60
Djosic, D.	27	Mustafa, M.	85	Uchino, E.	60, 157
Furukawa, S.	157	Nadir, Z.	182	Veljkovic, S.	27
Ghasemi, V.	167	Narayanan, V.	187	Viriri, S.	78, 131
Goosen, W.	131	Orimoto, H.	19, 43	Yazid, M.	85
Haghighi, H.	167	Orozco, M. A.	125	Yusof, R.	161
Hamid, L. A.	96	Othman, M. F.	161	Zacharias, J.	187
Heine, M.	104	Ozkul, T.	145	Zorkany, M.	113